

NON-BF SLAG-BASED GREEN CEMENTITIOUS MATERIALS

EDITED BY: Lijie Guo, Tingting Zhang, Xiaolu Guo and Weina Meng
PUBLISHED IN: *Frontiers in Materials*



frontiers

Frontiers eBook Copyright Statement

The copyright in the text of individual articles in this eBook is the property of their respective authors or their respective institutions or funders. The copyright in graphics and images within each article may be subject to copyright of other parties. In both cases this is subject to a license granted to Frontiers.

The compilation of articles constituting this eBook is the property of Frontiers.

Each article within this eBook, and the eBook itself, are published under the most recent version of the Creative Commons CC-BY licence.

The version current at the date of publication of this eBook is CC-BY 4.0. If the CC-BY licence is updated, the licence granted by Frontiers is automatically updated to the new version.

When exercising any right under the CC-BY licence, Frontiers must be attributed as the original publisher of the article or eBook, as applicable.

Authors have the responsibility of ensuring that any graphics or other materials which are the property of others may be included in the CC-BY licence, but this should be checked before relying on the CC-BY licence to reproduce those materials. Any copyright notices relating to those materials must be complied with.

Copyright and source acknowledgement notices may not be removed and must be displayed in any copy, derivative work or partial copy which includes the elements in question.

All copyright, and all rights therein, are protected by national and international copyright laws. The above represents a summary only. For further information please read Frontiers' Conditions for Website Use and Copyright Statement, and the applicable CC-BY licence.

ISSN 1664-8714

ISBN 978-2-88976-774-8

DOI 10.3389/978-2-88976-774-8

About Frontiers

Frontiers is more than just an open-access publisher of scholarly articles: it is a pioneering approach to the world of academia, radically improving the way scholarly research is managed. The grand vision of Frontiers is a world where all people have an equal opportunity to seek, share and generate knowledge. Frontiers provides immediate and permanent online open access to all its publications, but this alone is not enough to realize our grand goals.

Frontiers Journal Series

The Frontiers Journal Series is a multi-tier and interdisciplinary set of open-access, online journals, promising a paradigm shift from the current review, selection and dissemination processes in academic publishing. All Frontiers journals are driven by researchers for researchers; therefore, they constitute a service to the scholarly community. At the same time, the Frontiers Journal Series operates on a revolutionary invention, the tiered publishing system, initially addressing specific communities of scholars, and gradually climbing up to broader public understanding, thus serving the interests of the lay society, too.

Dedication to Quality

Each Frontiers article is a landmark of the highest quality, thanks to genuinely collaborative interactions between authors and review editors, who include some of the world's best academicians. Research must be certified by peers before entering a stream of knowledge that may eventually reach the public - and shape society; therefore, Frontiers only applies the most rigorous and unbiased reviews.

Frontiers revolutionizes research publishing by freely delivering the most outstanding research, evaluated with no bias from both the academic and social point of view. By applying the most advanced information technologies, Frontiers is catapulting scholarly publishing into a new generation.

What are Frontiers Research Topics?

Frontiers Research Topics are very popular trademarks of the Frontiers Journals Series: they are collections of at least ten articles, all centered on a particular subject. With their unique mix of varied contributions from Original Research to Review Articles, Frontiers Research Topics unify the most influential researchers, the latest key findings and historical advances in a hot research area! Find out more on how to host your own Frontiers Research Topic or contribute to one as an author by contacting the Frontiers Editorial Office: frontiersin.org/about/contact

NON-BF SLAG-BASED GREEN CEMENTITIOUS MATERIALS

Topic Editors:

Lijie Guo, Beijing General Research Institute of Mining and Metallurgy, China

Tingting Zhang, Dalian University of Technology, China

Xiaolu Guo, Tongji University, China

Weina Meng, Stevens Institute of Technology, United States

Citation: Guo, L., Zhang, T., Guo, X., Meng, W., eds. (2022). Non-BF Slag-based Green Cementitious Materials. Lausanne: Frontiers Media SA.
doi: 10.3389/978-2-88976-774-8

Table of Contents

05	<i>Editorial: Non-BF slag-based green cementitious materials</i> Lijie Guo, Tingting Zhang, Xiaolu Guo and Weina Meng
07	<i>Experimental Study on the Compaction and Deformation of Filling Gangue by Reducing Waste Gangue for Filling Mining</i> Yue Dong, Xinguo Zhang, Jia Lin, Jinhai Zhao and Zixuan Meng
21	<i>Mechanical Modification of Nanomaterials on Fully Saturated Concrete in Groundwater Reservoir Under Long-Term Water Immersion</i> XianJie Hao, Yingnan Wei, Zeyu Chen, Honglan Zhang, Yifan Niu, Kai Chen and Ruilai Huang
37	<i>Pore Structure Characteristics and Its Effect on Mechanical Performance of Cemented Paste Backfill</i> Chao Huan, Chao Zhu, Lang Liu, Mei Wang, Yujiao Zhao, Bo Zhang and Xiaoyan Zhang
47	<i>Effect of Iron Tailings and Slag Powders on Workability and Mechanical Properties of Concrete</i> Wu Ruidong, Shen Yu, Liu Juanhong, Cheng Linian, Zhang Guangtian and Zhang Yueyue
56	<i>An Experimental Study on Strength Characteristics and Hydration Mechanism of Cemented Ultra-Fine Tailings Backfill</i> Gan Deqing, Li Hongbao, Chen Chao, Lu Hongjian and Zhang Youzhi
69	<i>Occurrence State of Carbon and Electrolyte in Anode Carbon Residue From Electrolytic Aluminum</i> Song Mao and Qin Zhang
83	<i>Effects of the Silicate Modulus of Water Glass on the Hydration and Mechanical Properties of Alkali-Activated Blast Furnace Ferronickel Slag</i> Kuisheng Liu, Zhenguo Liu and Jianwei Sun
92	<i>Effect of the Alkalized Rice Straw Content on Strength Properties and Microstructure of Cemented Tailings Backfill</i> Shi Wang, Xuepeng Song, Meiliang Wei, Wu Liu, Xiaojun Wang, Yuxian Ke and Tiejun Tao
105	<i>Effect of Cr^{6+} on the Properties of Alkali-Activated Slag Cement</i> Fu Bo and Cheng Zhenyun
113	<i>Filling Treatment of Surface Subsidence Resulted From Underground Mining in a High-Altitude Mine</i> Daiqiang Deng, Guodong Cao and Yihua Liang
126	<i>Strength Prediction of Coal-Based Solid Waste Filler Based on BP Neural Network</i> Feisheng Feng, Lirong Li, Jiqiang Zhang, Zhen Yang and Xiaolou Chi
135	<i>Experimental Investigation on Strength and Failure Characteristics of Cemented Paste Backfill</i> Zhihong Zhang and Jiacheng Li
143	<i>Basic Properties of fly Ash/Slag -Concrete Slurry Waste Geopolymer Activated by Sodium Carbonate and Different Silicon Sources</i> Yingli Gao, Kairui Duan, Shuncheng Xiang and Wei Zeng

- 156 Synergistic Excitation Mechanism of $\text{CaO-SiO}_2\text{-Al}_2\text{O}_3\text{-SO}_3$ Quaternary Active Cementitious System**
Fusheng Niu, Yukun An, Jinxia Zhang, Wen Chen and Shengtao He
- 164 Synergetic–Complementary Use of Industrial Solid Wastes to Prepare High-Performance Rapid Repair Mortar**
Jingwei Li, Dong Xu, Xujiang Wang, Kun Wang and Wenlong Wang
- 174 Improvement of Calcium Aluminate Cement Containing Blast Furnace Slag at 50°C and 315°C**
Wu Zhiqiang, Liu Hengjie, Qu Xiong, Wu Guangai, Xing Xuesong, Cheng Xiaowei and Ni Xiucheng
- 181 Mechanical Characteristics and Stress Evolution of Cemented Paste Backfill: Effect of Curing Time, Solid Content, and Binder Content**
Chen Hou, Liujun Yang, Lei Li and Baoxu Yan
- 191 Effect of Aluminum Incorporation on the Reaction Process and Reaction Products of Hydrated Magnesium Silicate**
Yuan Jia, Yuxin Zou, Xinmei Zou, Yaoting Jiang, Fangyuan Li, Wangkun Ma, Hongli Yan and Rui Hua
- 198 Durability of Concrete With Coal Gasification Slag and Coal Gangue Powder**
Xiaoliang Zhu, Zhaocheng Guo, Wen Yang and Wenjing Song



OPEN ACCESS

EDITED AND REVIEWED BY

John L. Provis,
The University of Sheffield,
United Kingdom

*CORRESPONDENCE

Lijie Guo,
guolijie@bgrimm.com

SPECIALTY SECTION

This article was submitted to Structural Materials, a section of the journal Frontiers in Materials

RECEIVED 25 June 2022

ACCEPTED 30 June 2022

PUBLISHED 18 July 2022

CITATION

Guo L, Zhang T, Guo X and Meng W (2022), Editorial: Non-BF slag-based green cementitious materials. *Front. Mater.* 9:978032. doi: 10.3389/fmats.2022.978032

COPYRIGHT

© 2022 Guo, Zhang, Guo and Meng. This is an open-access article distributed under the terms of the [Creative Commons Attribution License \(CC BY\)](https://creativecommons.org/licenses/by/4.0/). The use, distribution or reproduction in other forums is permitted, provided the original author(s) and the copyright owner(s) are credited and that the original publication in this journal is cited, in accordance with accepted academic practice. No use, distribution or reproduction is permitted which does not comply with these terms.

Editorial: Non-BF slag-based green cementitious materials

Lijie Guo^{1*}, Tingting Zhang², Xiaolu Guo³ and Weina Meng⁴

¹Beijing General Research Institute of Mining and Metallurgy, Beijing, China, ²School of Civil Engineering, Dalian University of Technology, Dalian, China, ³School of Materials Science and Engineering, Tongji University, Shanghai, China, ⁴Department of Civil, Environmental and Ocean Engineering, Stevens Institute of Technology, Hoboken, NJ, United States

KEYWORDS

slag, cementitious materials, hydration, mechanical properties, minefill

Editorial on the Research Topic

Non-BF slag-based green cementitious materials

This special issue draws attention to “Non-BF slag Based Green Cementitious Materials”, focusing on the research progress and achievements of non-BF slag-based green cementitious materials. Metallurgical slag is a kind of by-product of the metal smelting process. For many years, a huge amount of slag was deposited in waste dumps or stockpiles due to the increasing scale of metal production, which causes a series of social, environmental, and economic problems. The sustainable utilisation of waste slag has become one of the major challenges in the field of civil and environmental engineering. The use of slag in cement production as an alternative cementitious material to form new green construction materials is a critical aspect to consume this huge amount of metallurgical solid waste. So far, blast-furnace slag (BF slag) has already been widely used in cement production, however, a large amount of non-BF slag (ferrous and non-ferrous) materials are still under-utilised. At present, a lot of research has been carried out to investigate the use of non-BF slags in cement production. However, only a few examples of industrial applications have been reported. Various Research Topics are available to address this issue related to the role of non-BF slag-based green cementitious materials, including: hydration and microstructure formation of green cementitious materials; assessment of mechanical properties of green cementitious materials; methods to improve the activity of non-BF slag based green cementitious materials; results from laboratory experiments and/or large-scale projects; short and long-term performance of novel cementitious materials; case studies of green cementitious materials for mine filling.

In the present issue of Frontiers in Materials, a total of 29 manuscripts were received and 19 of them were accepted. The editors would thank all the experts and scholars for submitting excellent papers to this special issue, and the reviewers for providing many constructive comments for the special issue.

The first paper by [Dong et al.](#) provides a case study of green cementitious materials for mine filling, they studied the application of using mixed gangue composed of equal-quality washed gangue and crushed gangue is proposed as a raw material for solid filling,

and experimental work was carried out to compare and analyze the compression characteristics of solid filling. The findings show the degree of relative compaction of mixed gangue is 1.226, which is significantly lower than that of washed gangue, which is 1.33. The deformation modulus of mixed gangue is 23–135 MPa, which is better than that of washed gangue (26–100 MPa), indicating that the compressive resistance of mixed gangue is significantly improved. And the case study in the Tangkou mine also suggests that mixed gangue greatly promotes the consumption of wasted gangue and can effectively control the surface deformation. In the paper by [Deng et al.](#) the case study was done for the filling treatment of surface subsidence resulting from underground mining in a high-altitude mine.

For the use of green cementitious materials in mine filling, [Huan et al.](#) studied the pore structure characteristics and their effect on the mechanical performance of cemented paste backfill in his paper, [Wang et al.](#) studied the effect of the alkalized rice straw content on strength properties and microstructure of cemented tailings backfill. Gan et al. did a study on the mechanical properties and hydration mechanism of tailings backfill made by green cementitious materials. The paper by [Hou et al.](#) illustrates the mechanical characteristics and stress evolution of cemented paste backfill. An experimental investigation on the strength and failure characteristics of cemented paste backfill was done by [Zhang and Li](#). [Zhu et al.](#) studied the durability of concrete with coal gasification slag and coal gangue powder. [Feng et al.](#) predicted the strength of coal-based solid waste filler based on the BP neural network. In the paper done by [Hao et al.](#) mechanical modification of nanomaterials on fully saturated concrete in groundwater reservoir under long-term water immersion was studied. Basic properties of fly ash/slag-concrete slurry waste geopolymer activated by sodium carbonate and different silicon sources was also done by [Cao et al.](#)

In the paper by [Wu et al.](#), the effect of iron tailings and slag powders on the workability and mechanical properties of concrete were studied. It demonstrates that the proper addition of iron tailing powder is beneficial to the working performance of concrete and can effectively reduce the time-loss of concrete fluidity. When the content of iron tailings powder in the composite admixture is 50%, the 1080d long age strength of C30 and C50 concrete can reach 50.3 and 80.7 MPa. Based on the 28d compressive strength, the relative strength-age prediction model of iron tailings powder concrete was established. The calculation and experimental results show that the model can accurately predict the compressive strength of micro-powder concrete of iron tailings at long age, and the error rate is less than 1%. The results lay a theoretical foundation for the utilization of iron tailings in concrete.

In the paper by [Liu et al.](#), the effects of the silicate modulus of water glass on the hydration and mechanical properties of alkali-activated blast furnace ferronickel slag were studied. In the paper by [Niu et al.](#), the synergistic excitation mechanism of $\text{CaO-SiO}_2\text{-Al}_2\text{O}_3\text{-SO}_3$

SO_3 quaternary active cementitious system $\text{CaO-SiO}_2\text{-Al}_2\text{O}_3\text{-SO}_3$ was provided. [Wu et al.](#) also presented the improvement of calcium aluminate cement containing blast furnace slag at 50 and 315°C. In the paper by [Fu and Cheng](#), the effect of Cr^{6+} on the properties of alkali-activated slag cement, the effect of aluminum incorporation on the reaction process, and reaction products of hydrated magnesium silicate was done by [Jia et al.](#) The occurrence state of carbon and electrolyte in anode carbon residue from electrolytic aluminum was studied in the paper by [Mao and Zhang](#).

In the paper by [Li et al.](#), they explored an innovative approach for rapid repair mortar preparation using solid waste-based calcium sulfoaluminate cement. The test results showed that the 2-h compressive and flexural strength and 1-day bonding strength of the prepared rapid repair mortar were 32.5, 9.2, and 2.01 MPa, respectively, indicating the excellent early-age mechanical performance of the high-performance rapid repair mortar. In addition, the 28-days compressive and flexural strengths of the rapid repair mortar reached 71.8 and 17.7 MPa. And a life cycle assessment and economic analysis indicated that this approach achieved environmental-friendly utilization of industrial solid wastes and cost-effective and energy-saving natures.

Overall, we hope the contribution of this collection builds up the understanding and interest of all researchers and practitioners who are focused on the recent developments and advancements in studying green cementitious materials based on solid wastes. It is hoped that the results of this issue can provide a reference for future research on non-BF slag-based green cementitious materials, and contribute to promoting the development of green cementitious materials.

Author contributions

All authors listed have made a substantial, direct, and intellectual contribution to the work and approved it for publication

Conflict of interest

The authors declare that the research was conducted in the absence of any commercial or financial relationships that could be construed as a potential conflict of interest.

Publisher's note

All claims expressed in this article are solely those of the authors and do not necessarily represent those of their affiliated organizations, or those of the publisher, the editors and the reviewers. Any product that may be evaluated in this article, or claim that may be made by its manufacturer, is not guaranteed or endorsed by the publisher.



Experimental Study on the Compaction and Deformation of Filling Gangue by Reducing Waste Gangue for Filling Mining

Yue Dong¹, Xinguo Zhang^{2,3*}, Jia Lin⁴, Jinhai Zhao^{2,3} and Zixuan Meng²

¹College of Geodesy and Geomatics, Shandong University of Science and Technology, Qingdao, China, ²College of Energy and Mining Engineering, Shandong University of Science and Technology, Qingdao, China, ³State Key Laboratory of Mining Disaster Prevention and Control, Co-founded by Shandong Province and the Ministry of Science and Technology, Shandong University of Science and Technology, Qingdao, China, ⁴School of Civil, Mining and Environmental Engineering, University of Wollongong, Wollongong, NSW, Australia

OPEN ACCESS

Edited by:

Lijie Guo,
Beijing General Research Institute of
Mining and Metallurgy, China

Reviewed by:

Yanli Huang,
China University of Mining and
Technology, China
Shuai Cao,
University of Science and Technology
Beijing, China

*Correspondence:

Xinguo Zhang
zhangxg1229@163.com

Specialty section:

This article was submitted to
Structural Materials,
a section of the journal
Frontiers in Materials

Received: 25 April 2021

Accepted: 10 June 2021

Published: 05 July 2021

Citation:

Dong Y, Zhang X, Lin J, Zhao J and
Meng Z (2021) Experimental Study on
the Compaction and Deformation of
Filling Gangue by Reducing Waste
Gangue for Filling Mining.
Front. Mater. 8:700118.
doi: 10.3389/fmats.2021.700118

The coal mining technology of fully mechanized solid filling is an efficient and green mining method that integrates “sediment reduction” and “emission reduction.” However, the discharge of wasted gangue and surface subsidence are controlled by the amount of wasted gangue used in filling mining and the compaction rate of gangue filled into a goaf, respectively. To increase the consumption of wasted gangue and reduce surface subsidence, mixed gangue composed of equal-quality washed gangue and crushed gangue is proposed as a raw material for solid filling on the basis of gradation theory. Next, a screening experiment was performed to analyze the grain gradation of different specimens, and a compression experiment was executed to compare and analyze the compression characteristics. The results show that the nonuniformity coefficient of mixed gangue is 55.2 and the curvature coefficient is 1.53, which significantly improve the grain gradation of washed gangue. The degree of relative compaction of mixed gangue is 1.226, which is significantly lower than that of washed gangue, which is 1.33. The deformation modulus of mixed gangue is 23–135 MPa, which is better than that of washed gangue (26–100 MPa), indicating that the compressive resistance of mixed gangue is significantly improved. The case study of the Tangkou mine suggests that mixed gangue greatly promotes the consumption of wasted gangue and can effectively control the surface deformation.

Keywords: solid filling mining, grain gradation, compression characteristic, deformation modulus, surface deformation, equivalent mining height

HIGHLIGHT:

- Mixed waste gangue is used as a filling material for solid backfilling mining.
- The gradation combination of filling gangue was significantly improved.
- More wasted gangue was consumed, and the compressive strength of the filling body was enhanced.
- The compression of the filling body was reduced, and the surface settlement was controlled.

INTRODUCTION

Filling mining is a type of ecological protection mining technology that has been developed in recent years. The usage of this technology can process coal gangue and fly ash, two solid forms of waste from coal mines, and solid waste around cities while replacing coal resources under buildings (structures) such as villages, railways (roads) and overlying aquifers, and on floor pressurized water (referred to as “three under one on”). This is a type of scientific coal mining technology that is in line with the ecological mine development model of “lucid waters and lush mountains are invaluable assets,” advocated by President Xi Jinping, with great promotion and application prospects (Hu and Guo, 2018; Qian et al., 2018; Wang et al., 2018; Dong et al., 2019; Ma et al., 2019; Wang et al., 2020a; Dong et al., 2020; Liu et al., 2020; Ju et al., 2021). To date, three kinds of filling mining technology approaches have been developed in China: solid filling technology (Miao et al., 2010), paste filling technology (Zhou et al., 2010; Sun et al., 2018; Wu et al., 2020a), and high-water filling technology (Feng et al., 2010; Chang et al., 2018). Solid filling technology mainly includes fully mechanized solid filling technology, dumping gangue and filling technology, pneumatic filling technology, and the technology of coal gangue separation in underground coal flow and gangue powder pumping on-site. Due to the relatively mature filling system and equipment (the gangue feeding system, the storage system, and four-column and six-column filling support with a tamping mechanism) and the mining–filling process (single and double interlaced, and coal mining tamping), fully mechanized solid filling technology has become the main development direction of filling mining technology (Hu, 2012; Zhang et al., 2020; Zhang et al., 2019a; Guo et al., 2019). In the implementation of fully mechanized solid filling technology, the control effect of overlying strata and surface subsidence is determined by the final compaction rate of gangue in a goaf, which is equivalent to that of mining in thin coal seams. Therefore, relevant scholars have proposed the concept of “equivalent mining thickness” for surface subsidence control of fully mechanized solid filling technology (Zhang et al., 2011; Huang et al., 2012; Guo et al., 2014; Meng et al., 2020a). In summary, the study of how to reduce the final compaction ratio of gangue filled into goafs has become the key to popularizing applications and effectively predicting the control effect of surface subsidence.

At present, various scholars have performed preliminary experimental studies on compaction and deformation of gangue. Zhang Jixiong conducted compaction deformation tests on loose gangue and obtained the relationship among deformation, hulk coefficient, and compactness of the filling body and strain, as well as the characteristics related to the compaction time in the process of compaction (Miao and Zhang, 2007; Zhang, 2008). Through gangue compaction tests, Ma et al. (2003) summarized the trends of the change in the axial strain, transverse strain, Poisson’s ratio, and elastic modulus of loose gangue in the process of compaction, and analyzed the deformation mechanism of gangue during this process. Xu et al. (2011) adopted an MTS815.02 electrohydraulic servo rock mechanics test system and a self-designed compaction device

to analyze the deformation characteristics of gangue–fly ash as a filling material in the compaction process. Hu Bingnan et al. adopted a large container, large particle size, and large load and simulated coal mass to perform 23 simulated gangue compression experiments, obtained the rule that the compression ratio is proportional to the particle size and inversely proportional to the lateral pressure, and analyzed the relationship among the compression ratio, lateral pressure and coal mass strength, particle size, and gangue gradation (Hu and Guo, 2009). Several scholars have studied the compaction characteristics of gangue with different gradations. Zhang Jinhong et al. conducted compression tests on gangue with seven groups of gradation schemes, showing that the content of gangue was maintained with a particle size range of 40–70 mm, and an increased content of gangue with a small particle size can minimize the compression amount of gangue filling materials (Zhang et al., 2012). As the main source of gangue in most domestic coal mines is washed gangue (maximum particle size ≤ 50 mm), while driving gangue (maximum particle size ≥ 100 mm) accounts for less gangue, the general treatment method of coal mines is to raise the driving gangue with the raw coal sulfur flow to the surface coal washery and then dispose it off separately (Li and Guo, 2018). The Zhuanlongwan coal mine was taken as an example, where the volume of gangue produced in 2019 was 2.266 million tons, of which the gangue produced by the coal washery accounted for 90% and the gangue produced by driving accounted for 10%. Driving gangue is usually not treated underground but mixed into raw coal sulfur and raised to the surface coal washery. The particle size of the washed gangue processed by the coal washery is basically the same, and the particle size is large. As the pores between the particles cannot be filled completely by the small particles, the bearing effect is limited to a certain extent (Meng et al., 2020b).

Therefore, in order to compare and analyze the grain gradation and compression characteristics of different gangue fillings, this study carried out screening experiment and compression experiment body based on the continuous gradation theory. The grain gradation curve shows that mixed gangue composed of washed gangue, and crushed gangue with equal quality has a certain gap with the theoretical optimal grain gradation, but considering the convenience of on-site construction, mixed gangue with equal quality is the optimal filling material. Simultaneously, the compression test indicates that the compressive properties of gangue with equal mixing mass are significantly increased. Adoption of mixed gangue with equal quality as filling material can effectively reduce the “equivalent mining height,” decrease the surface discharge of gangue, and provide theoretical and reference significance to improve the on-site filling rate of gangue materials.

THEORY OF THE CONTINUOUS GRADATION OF A PARTICLE DISTRIBUTION

The gradation of solid particles refers to a continuous gradation that is made up of solid particles with various particle sizes. This

represents the quantity of the particle size in the bulk materials composed of different granularities, which is usually expressed as a percentage of the total amount (Fang et al., 2019). The cumulative curve of the particle size distribution obtained from the results of the particle size distribution can clearly reveal the thickness of solid materials, and the uniformity and continuity of the particle size distribution, thus allowing the quality of the material gradation to be determined (Chen et al., 2016; Wang et al., 2020b). The material uniformity or gradation can be analyzed based on the slope of the cumulative curve of the particle diameter. A steeper curve indicates that the sizes of the particles are almost the same, the particles are more uniform, and the gradation is poor, whereas a flat curve indicates that the size of particles is very different, the particles are uneven, and the grading is good (Cai et al., 2020; Wang et al., 2020c; Yao et al., 2020). According to the cumulative curve of the particle size, two quantitative indexes of the particle size distribution, C_u (nonuniformity coefficient) and C_c (curvature coefficient), can be determined as follows (Li et al., 2014):

$$C_u = \frac{d_{60}}{d_{10}}, \quad (1)$$

$$C_c = \frac{d_{30}^2}{d_{60} \times d_{10}}. \quad (2)$$

In the equation, d_{60} , d_{30} , and d_{10} are equivalent to the particle size corresponding to the cumulative weight percentage of the material that is less than a particle size of 60, 30, and 10%, respectively, known as the limited particle size, the median particle size, and the effective particle size.

For a solid material, the following relationship is observed: $d_{60} > d_{30} > d_{10}$. The nonuniformity coefficient C_u reflects the distribution of different fractions, that is, the size or the degree of uniformity of granularity. Generally, the larger C_u is, the larger the distribution range of granularity, the more uneven the particles, and the better the gradation (Yang et al., 2019). The curvature coefficient C_c describes the overall shape of the cumulative curve distribution and reflects the distribution of the fraction contents between the constrained particle size d_{60} and effective particle size d_{10} . In engineering practice, materials with $C_u < 5$ are generally regarded as homogeneous materials with poor gradation, and those with $C_u > 10$ exhibit good gradation. Generally, for materials with continuous gradation, a satisfactory result can be achieved by using a single index C_u . At this point, it is difficult to effectively judge the gradation of materials using only a single index C_u . It is more reasonable to judge the gradation of solid materials by using the curvature coefficient C_c as the second index together with C_u (Zhu et al., 2015; Zhu et al., 2018).

For rockfills with a high volume of rock, the specification (DL/T, 2007; DL/T, 2011) only requires that the particle content less than 5 mm shall not exceed 30%, and the fine particle content (less than 0.075 mm) shall not exceed 5%, without clear requirements on the overall composition of gradation; there is also no gradation requirement for transition material and cushion material. For gradation evaluation, currently, only gradation indicators exist, which apply to the largest diameter within

60 mm gradation index of coarse-grained soil; that is, when the nonuniformity coefficient C_u is less than 5, the gradation is poor; if it is greater than 5, it is good. However, if C_u is too large, it may lack intermediate particle size and belongs to discontinuous gradation. When the specified curvature coefficient C_c is increased between 1 and 3, the gradation is good (GB/T, 2007). If not, the soil is determined to be poorly graded. Obviously, for soil samples with the same C_u , if C_c is too large or too small, it indicates that there is a lack of intermediate fraction in the soil, the chain filling effect of pores between each fraction decreases, and the gradation worsens (Zhu et al., 2017). The particle size of washed gangue and crushed gangue in coal mines is similar to that of gravel soil, so the evaluation standard of gravel soil is adopted as that of a reasonable gradation of fully mechanized solid filling gangue in this study. Currently, the most commonly used continuous gradation theory is the theory of the maximum density curve. The maximum density curve is an ideal curve based on experiments. It is assumed that the density of loose particles is the highest when particles are composed according to the maximum density curve (Chu et al., 2020; Zuo et al., 2015). The calculation method of continuous gradation was proposed by the American scholar, Fuller, in the early 20th century on the basis of the theory of maximum density, which demonstrated that when the gradation curve was a parabola, as given by eq. 3, the loose deposit could reach the maximum density state (FULLER and THOMPSON, 1907).

$$P_d = \left(\frac{d}{D} \right)^{0.5}. \quad (3)$$

In the equation for P_d , d is the pore diameter passing through the sieve and D is the maximum particle size.

Fuller's curve became the theoretical basis for the composition forms of various gradation curves, such as the n-method improved by Talbol. Talbol demonstrated that Fuller's equation was an ideal gradation curve; in reality, there was a certain range of fluctuation required to achieve the maximum density, so Fuller's equation was modified into the following expression:

$$P_d = \left(\frac{d}{D} \right)^n. \quad (4)$$

When $n = 0.3-0.7$, there is good compactness; when $n = 0.5$, the maximum density curve is a parabola (Huang et al., 2019a; Wu et al., 2020b).

TESTS ON GANGUE SCREENING

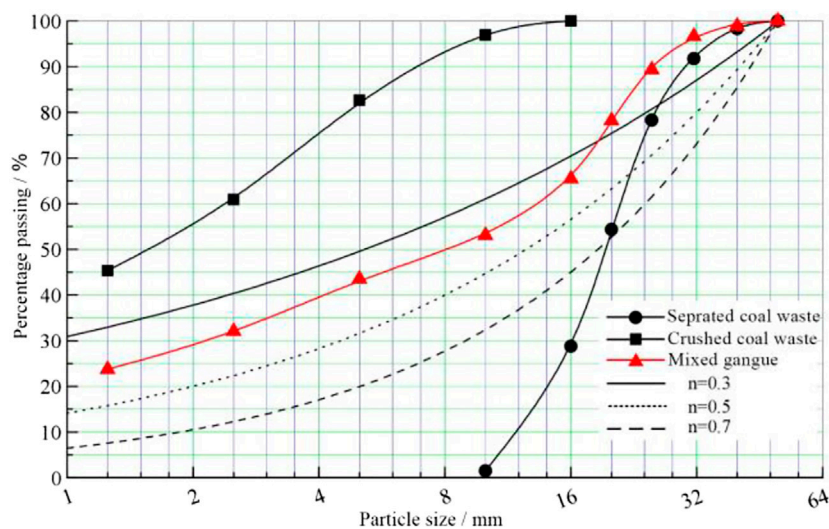
The main source of filling gangue was washed gangue ($d_{\max} \leq 50$ mm), which was used to fill gangue directly, and crushed gangue ($d_{\max} \leq 16$ mm) was used as auxiliary filling gangue. The experimental materials are sampled on site, washed gangue is directly obtained by the coal washery, the maximum diameter of washed gangue is 50 mm, and crushed gangue whose maximum diameter is less than 16 mm is obtained after the secondary

TABLE 1 | Gradation parameters of washed gangue.

Sieve pore diameter size (mm)	Residential mass (g)	Percent passing (%)	Graded retained percentage (%)	Cumulative retained percentage (%)
50	0	100.00	0.00	0.00
40	620	99.30	0.70	0.70
31.5	5,600	92.94	6.35	7.06
25	10,420	81.12	11.82	18.88
20	23,620	54.32	26.80	45.68
16	25,640	25.22	29.09	74.78
10	20,900	1.51	23.71	98.49
The bottom of the screen	1,330	0.00	1.51	100.00

TABLE 2 | Gradation parameters of crushed gangue.

Sieve pore diameter size (mm)	Residential mass (g)	Percent passing (%)	Graded retained percentage (%)	Cumulative retained percentage (%)
16	0	100.00	0.00	0.00
10	625	98.71	1.29	1.29
5	7,410	84.67	15.33	16.63
2.5	11,380	76.45	23.55	40.18
1.25	6,995	85.53	14.47	54.64
The bottom of the screen	21,915	54.65	45.35	100

**FIGURE 1** | Fuller curve and grading curve of the gangue specimen.

crushing of washed gangue. The gradation parameters of washed gangue and crushed gangue were obtained by using a new standard stone screen, as shown in **Table 1** and **Table 2**, respectively.

In light of Talbol's method related to n , n is taken as 0.3, 0.5, and 0.7; the maximum particle size is 50 mm; and the corresponding continuous gradation curve diagram and screening gradation curve diagram are drawn in semilogarithmic coordinates, as shown in **Figure 1**. In the semilogarithmic curve diagram, the abscissa is expressed as the logarithm of the particle

size ($\log_2 d_i$), and the ordinate is expressed as the cumulative pass rate, p_i (%).

According to **Tables 1** and **2**, p_{10} of washed gangue is only 1.51%, and the gradation curve of crushed gangue is above the continuous curve; that is, its fine content is far higher than that of the continuous gradation, and p_{10} is as high as 98.71%. Therefore, crushed gangue of equivalent mass can be mixed into washed gangue to compensate for the serious gradation defect of p_{10} . Simultaneously, the content of coarse material larger than 28 mm for washed gangue is adjusted indirectly under the condition that

TABLE 3 | Gradation parameters for mixed-filling gangue.

Sieve pore diameter size (mm)	Percent passing (%)	Graded retained percentage (%)	Cumulative retained percentage (%)
50	100.00	0.00	0.00
40	99.66	0.34	0.34
31.5	96.99	3.03	3.37
25	90.99	5.64	9.01
20	78.21	12.78	21.79
16	64.33	13.88	35.66
10	52.34	11.99	47.65
5	43.60	8.74	56.39
2.5	31.28	12.32	68.71
1.25	23.71	7.57	78.28
The bottom of the screen	0	23.72	100.00

TABLE 4 | Variabe index of gangue gradation.

	Washed gangue	Crushed gangue	Mixed-filling gangue
d_{60}	21.1	2.52	13.8
d_{30}	16.7	1	2.3
d_{10}	12.1	0.25	0.25
C_u	1.74	10.08	55.2
C_c	1.09	1.59	1.53

the whole quality of loose gangue is not changed. **Table 3** gives the gradation parameter table of filling gangue after equal-quality mixing, and its gradation curve is plotted in **Figure 1**. In the gradation curve of mixed gangue, the particle curve of $P_d \leq 20$ mm is between the curve of $n = 0.3$ and $n = 0.5$, and only the particle content of $P_d \geq 20$ mm is more than that of the continuous gradation curve, indicating that the gradation combination of mixed gangue is significantly better than that of washed gangue and crushed gangue.

The gradation of washed gangue, crushed gangue, and mixed gangue was evaluated by using the evaluation standard for a solid particle gradation. According to the data in **Figure 1** and **Tables 1–3** obtained by interpolation, the nonuniformity coefficient of washed gangue is 1.74, the curvature coefficient is 1.09, the nonuniformity coefficient of crushed gangue is 10.08, the curvature coefficient is 1.59, the nonuniformity coefficient of mixed gangue is 55.2, and the curvature coefficient is 1.53, as shown in **Table 4**. Obviously, the nonuniformity coefficient of washed gangue is small, and it is a poorly graded solid. The nonuniformity coefficients of gangue after crushing and in mixed gangue are large, but the nonuniformity coefficient of gangue after mixing is an excellent graded solid with the largest nonuniformity coefficient.

Because of the complexity of underground work, filling material processing, and the necessity of filling cost control, it is not possible to implement underground large-scale gradation restructuring to obtain a better filling effect. Thus, this study proposes a way to adjust the gradation of gangue filling bodies by mixing equal qualities of washed gangue and crushed waste.

**FIGURE 2** | WAW-600B electronic universal testing machine.

TESTS ON THE COMPACTNESS OF GANGUE

Experimental Equipment and Scheme

As shown in **Figure 2**, a WAW-600B microcomputer was used as the compacting and loading equipment to control the electrohydraulic servo universal testing machine. Hydraulic power servo control technology, electrohydraulic servo control technology, computer data acquisition and processing, high-precision material testing equipment with closed-loop control, and automatic detection utilized in this testing equipment can realize the closed-loop control of constant-rate loading, constant-rate deformation, constant-rate displacement, and constant-rate strain to verify the performance of materials (Li et al., 2019).

As the physical drawing of the design shows in **Figure 3**, all the instruments are made of 45# steel with a yield strength of no less than 355 MPa. The filling gangue apparatus is designed as a steel cylinder with an inner diameter of 125 mm, wall thickness of 10 mm, outer diameter of 145 mm, and height of 300 mm. The experimental charging height is 250 mm, the charging volume is $3.06 \times 10^{-3} \text{ m}^3$, and the weight is approximately 4.3 kg. The auxiliary force



FIGURE 3 | Compaction apparatus.

transmission instrument is a steel cylinder with a diameter of 100 mm, height of 150 mm, and weight of approximately 9.3 kg.

The compaction experiment of filling coal gangue was performed with the above experimental device, according to the method of compaction testing of solid backfilling materials (Nb/T, 2014). In light of the conditions of the apparatuses and equipment, the maximum permissible particle size of the gangue sample was 25 mm, and the sample was prepared by a similar method of gradation. Before the experiment, the mass of each fraction of particle size was measured on the basis of the experimental design scheme and then evenly mixed and loaded into the compacted steel cylinder. The steel cylinder was used to impose the load on the gangue specimen, and experimental data such as the load and compression displacement of gangue were recorded during the loading process. The laboratory gradation tables for washed gangue and gangue with the continuous gradation of Taltol's *n*-method (*n* is 0.3, 0.5, and 0.7) are shown in **Tables 5** and **6**, respectively, and the laboratory gradation tables of mixed gangue are shown in **Tables 7** and **8**, respectively.

To reduce the friction between gangue and the steel cylinder wall during the process of compression, a layer of grease was smeared on the inner wall of the steel cylinder before each test, and then the screened gangue was uniformly mixed and filled according to the corresponding gradation table. The charge of each test was controlled at 4,300 g, the initial filling height h_0 was measured, and the initial bulk density γ_0 was calculated. Force control was adopted in the compaction experiment, the maximum axial compressive stress was set at 185 kN, the loading speed was 1 kN/s, and the preloading speed was 1 mm/min. After loading, the load was automatically unloaded. After the end of the experiment, the height h_1 of the compacted specimen was measured, and the final compacted bulk density γ_1 was calculated.

Analysis of Compactness

Relationship Between the Compactness and Bulk Density of Gangue

The results of the final compression test on gangue specimens are shown in **Figure 4**.

TABLE 5 | Laboratory gradation table of washed gangue.

Particle size/mm	<5	5–10	10–16	16–20	20–25
Graded retained percentage (%)	1.51	52.8	38.33	6.66	0.7

The experimental data were sorted, and the initial bulk density and compacted bulk density of gangue specimens in each group were obtained, as shown in **Table 9**. According to changes in the bulk density of coal gangue specimens, it is evident that the initial bulk density of washed gangue is the smallest, close to 14 kN/m³, indicating that the initial bulk volume of washed gangue is the largest and the intergranular void of gangue is the largest. In Taltol's *n*-method, when *n* = 0.7, the bulk density of gangue reaches a maximum of 15.78 kN/m³; that is, the volume of the gangue filling body is the smallest and the intergranular void of gangue is small, and the initial bulk density of mixed gangue is close to the bulk density of the gradation group when *n* = 0.3. In the final compaction volume of the sample, when *n* = 0.5, the compaction density is the largest, and the relative compaction is also the largest in the continuous gradation. The compaction volume changes greatly, and the filling effect is poor. The compacted bulk density is basically 19.5 kN/m³, and the relative compaction is the smallest, that is, its volume compression is the smallest. The compaction effect of gangue is greatly improved after mixing.

Stress–Strain Curve

To further understand the stress–strain properties of coal gangue, the numerical analysis software Origin is used to express the curve in the form of a mathematical model, as shown in **Figures 5–9**.

Next, the fitting equation of the stress–strain is established, and the fitting degree of the curve is analyzed. According to the observed curve, **Eq. 5** is used to fit the stress–strain relationship. The stress–strain relationship of gangue specimens with different particle sizes is shown in **Table 10**.

$$\varepsilon \times 100 = a - b \ln(s + c). \quad (5)$$

In the above equation, *a*, *b* and *c* are constants.

Table 10 shows that the form of this function can effectively express the stress–strain relationship of gangue, and the correlation coefficient (*R*-squared) is very close to 1, indicating that the data have a high correlation degree and a small degree of dispersion, and the fitting result is reliable. To compare and analyze the compression performance of gangue at all levels of the above gradation groups under different axial compact loads, fitting equation curves of gangue at all levels are drawn, as shown in **Figure 10**. To analyze and compare the compression performance of the gangue filling body under the conditions of all levels, the curve of the stress–strain relationship of the gangue filling body is used to obtain the stress under different axial compressive stresses, as shown in **Table 11**.

When the axial compressive stress reaches 25 MPa (the mining depth is 1,000 m), the strain is regarded as the maximum compression strain. Before the compressive stress reaches 2 MPa, the deformation rate of compression is

TABLE 6 | Laboratory gradation table of continuous graded filling gangue.

Particle size/mm	<1.25	1.25–2.5	2.5–5	5–10	10–16	16–20	20–25
Continuous gradation, $n = 0.3$	40.71	9.41	11.58	14.26	11.5	6.06	6.48
Graded retained percentage (%)							
Continuous gradation, $n = 0.5$	22.36	9.26	13.1	18.52	16.75	9.45	10.56
Graded retained percentage (%)							
Continuous gradation, $n = 0.7$	12.28	7.67	12.46	20.24	20.51	12.38	14.46
Graded retained percentage (%)							

TABLE 7 | Mixed gangue gradation table.

Particle size/mm	<1.25	1.25–2.5	2.5–5	5–10	10–16	16–20	20–25	25–31.5	31.5–40	40–50
Graded retained percentage (%)	23.72	7.57	12.32	8.74	11.99	13.88	12.78	5.64	3.03	0.34

TABLE 8 | Laboratory gradation table of mixed-filling gangue.

Particle size/mm	<1.25	1.25–2.5	2.5–5	5–10	10–16	16–20	20–25
Graded retained percentage (%)	31.28	12.32	8.74	25.87	18.05	3.4	0.34

**FIGURE 4 |** Compaction effect of the specimen.**TABLE 9 |** Variation table of the bulk density.

Specimen group		Initial bulk density (kN/m ³)	Compacted bulk density (kN/m ³)	Degree of relative compactness
Washed gangue		14.32	19.07	1.33
Taitol's n-method	$n = 0.3$	15.60	19.51	1.25
	$n = 0.5$	15.64	19.79	1.27
	$n = 0.7$	15.78	19.56	1.24
Mixed gangue		15.50	19.46	1.226

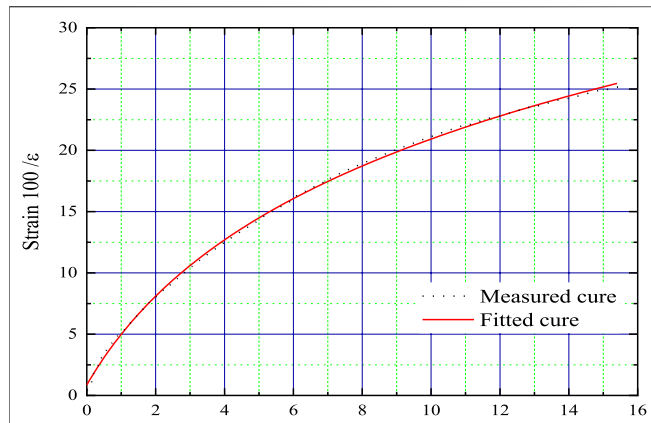


FIGURE 5 | Measured and fitted stress-strain curves (washed gangue).

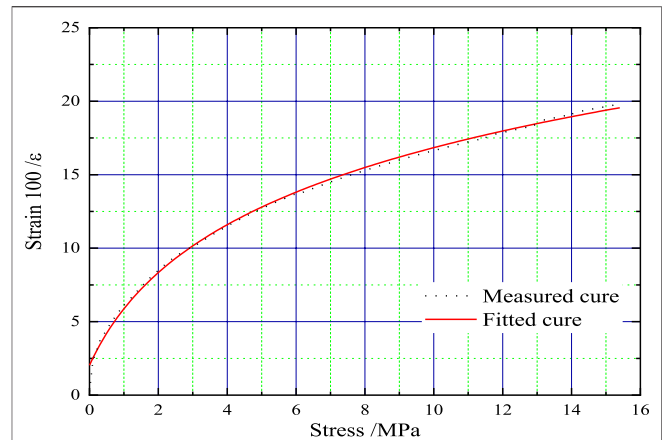


FIGURE 8 | Measured and fitted stress-strain curves ($n = 0.7$).

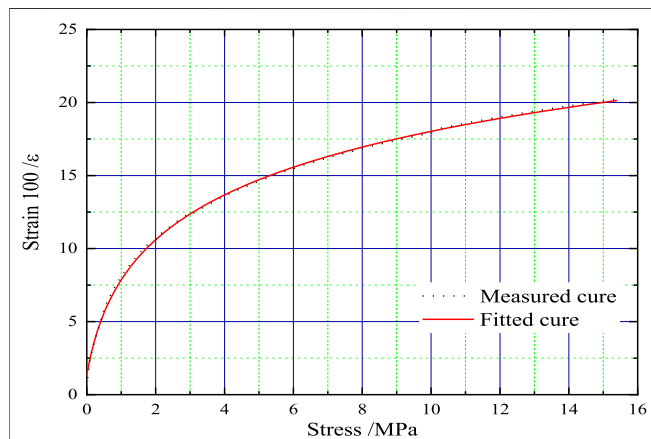


FIGURE 6 | Measured and fitted stress-strain curves ($n = 0.3$).

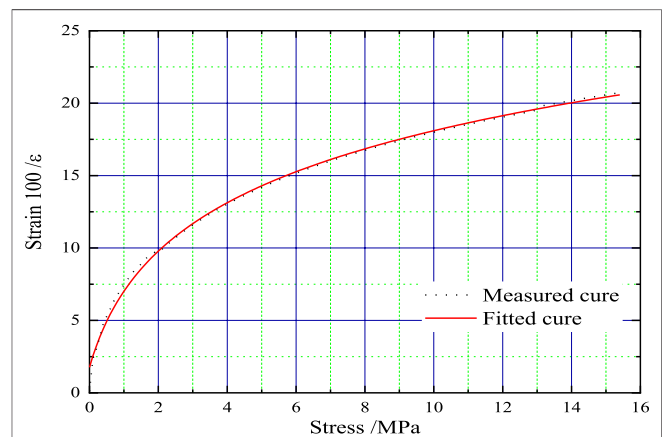


FIGURE 9 | Measured and fitted stress-strain curves (mixed-filling gangue).

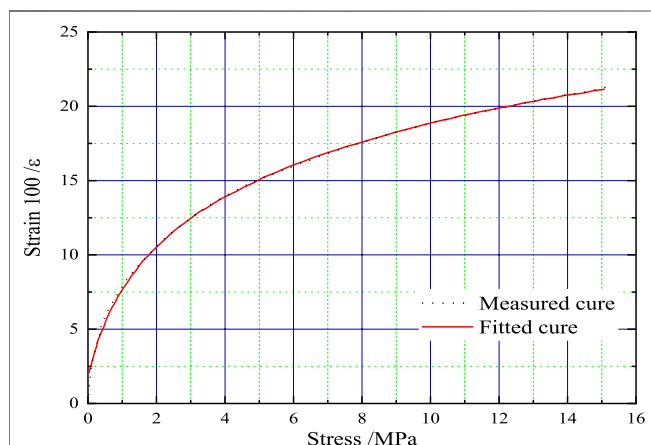


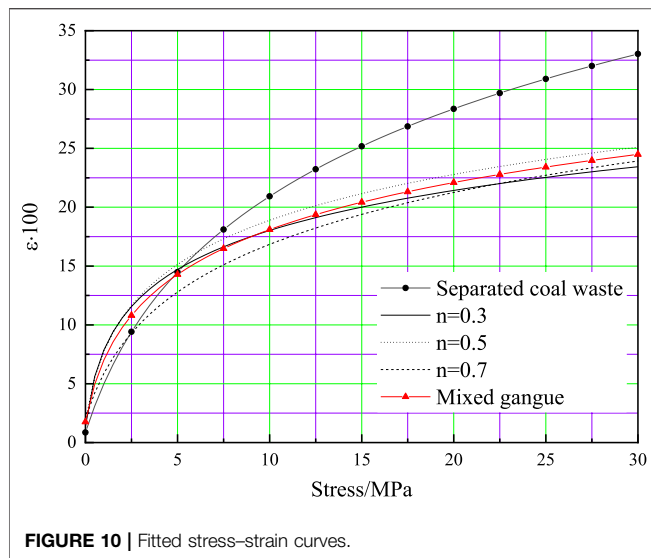
FIGURE 7 | Measured and fitted stress-strain curves ($n = 0.5$).

TABLE 10 | Stress-strain curve table.

Specimen group	Fitting equation	R ²
Washed gangue	$\varepsilon \cdot 100 = -11.367 + 12.739 \ln(\sigma + 2.61)$	0.99958
Taitol's n-method		
$n = 0.3$	$\varepsilon \cdot 100 = 6.221 + 5.044 \ln(\sigma + 0.383)$	0.99914
$n = 0.5$	$\varepsilon \cdot 100 = 5.068 + 5.858 \ln(\sigma + 0.580)$	0.99957
$n = 0.7$	$\varepsilon \cdot 100 = -0.127 + 6.982 \ln(\sigma + 1.362)$	0.99888
Mixed gangue	$\varepsilon \cdot 100 = 3.690 + 6.072 \ln(\sigma + 0.728)$	0.99916

relatively fast. At this point, the maximum amount of compression of gangue at all levels reaches 26, 47, 44, 37, and 42%. Compared with washed gangue, the final compression

deformation of gangue in the continuous gradation groups decreases by 22.15–27.08%, and the compression amount of mixed gangue decreases by 24.25%. Thus, it is evident that the initial compaction ratio and the final compaction ratio are improved to a great extent, and the initial compression rate and the final compaction rate of mixed gangue are also effectively controlled under the condition of continuous gradation. When the axial compressive stress reaches 12.5 MPa (the mining depth is 500 m), the strain is regarded as the maximum compression strain. Before the compressive stress



reaches 2 MPa, the compression of gangue at all levels reaches the maximum compression sets of 35, 55, 53, 46, and 51%. At this point, the maximum amount of compression of gangue at all levels reaches 26, 47, 44, 37, and 42%; namely, with the decrease in mining depth, the initial compaction rate of washed gangue decreases, while the initial compaction rate of mixed gangue and the initial compaction rate of gangue in the continuous gradation group are improved. Compared with washed gangue, the final compression deformation of gangue in the continuous gradation group is reduced by 13.32–21.51%, and the compression amount of mixed gangue is reduced by 16.60%. After gradation optimization, the compression performance of gangue filling material is significantly improved. Mixed gangue is not the optimal gradation group, but it can prevent large-scale screening and restructuring of particle groups to optimize the gradation of gangue. Compared with washed gangue, mixed gangue still has great advantages in controlling the movement and deformation of overlying strata.

Deformation Modulus of Gangue

According to the data acquisition results from the experimental machine and the calculation method of the deformation modulus of the loose material, the E - σ curve of the graded specimens in the process of compaction was calculated and drawn by the numerical calculation analysis software Origin, as shown in **Figure 11**.

According to the E - σ curve, when the axial stress reaches 2 MPa in the lateral constrained compression experiment, the deformation modulus E of coal gangue exhibits a basic linear relationship with the axial compressive stress σ . To describe the relationship between the two, the compressive stress of 2 MPa is regarded as the initial compaction stress. Before the compressive strength reaches 2 MPa, the deformation modulus increases exponentially, and the growth rate of the deformation modulus decreases gradually. After that, the deformation modulus increases linearly, and the anti-compression properties increase gently. Linear fitting was adopted for the data after 2 MPa to obtain the fitting equation of E - σ for the gangue sample group, as shown in **Table 12**.

In light of the fitting equation, the deformation modulus E increases with increasing compressive stress σ , and the variation range of E is 21–140 MPa in the compressive stress range of 2–30 MPa. The correlation coefficient (R -squared) of the fitting equation is very close to 1, which indicates that the data correlation is high, the degree of dispersion is not large, and the fitting result is reliable.

CASE

Most of the ground surface within the 930 mining area of the Tangkou Coal Mine is made up of buildings (structures) of Li temple and Fengtai village. There are Phoenix palace ruins (the third batch of key cultural relic protection units in Shandong Province) and six seven-story residential buildings in the village, as shown in **Figure 12**. Mining will have an impact on surface buildings (structures). To ensure the normal life of villagers, control surface deformation, and reduce the impact of surface buildings (structures), solid filling mining technology is adopted.

The mining area is approximately 0.3–0.9 km long from north to south and 1.0–1.3 km wide from east to west. The mining area is approximately 0.85 km². The basic reserves of the mining area are 3.602 million tons, and the recoverable reserves are 2.881 million tons. The western area of the mining area is adjacent to the 130 mining area. Four working faces such as 1,301, 1,302, 1,304, and 1,305 were stopped in the 130 mining area, and water was accumulated in the low-lying areas of the 130 goaf. The seep area is far away from the mining area, which has no impact on the production of the mining area. In the north, the mining area is adjacent to the protective coal pillar of the industrial square and is 1700 m away from the northern

TABLE 11 | Stress-strain table.

σ /MPa, ε -100, specimen group	Washed gangue	Taitol's n-method			Mixed gangue
		$n = 0.3$	$n = 0.5$	$n = 0.7$	
2	8.10	10.60	10.62	8.34	9.78
7.5	18.11	16.64	17.31	15.11	16.49
12.5	23.22	19.11	20.13	18.23	19.37
17.5	26.87	20.77	22.03	20.38	21.32
25	30.90	22.53	24.06	22.72	23.41

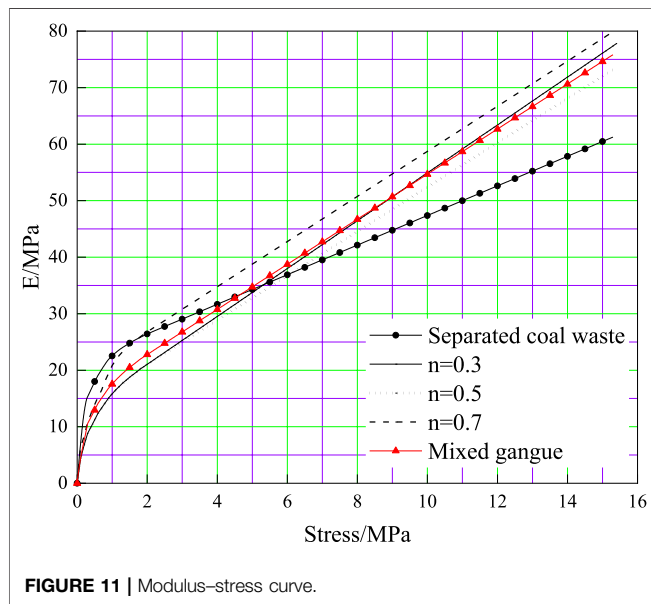


FIGURE 11 | Modulus–stress curve.

TABLE 12 | Modulus–stress curve table.

Specimen group	Fitting equation	R ²
Washed gangue	$E = 21.173 + 2.619\sigma$	0.99675
Taitol's n-method	$n = 0.3$ $E = 12.574 + 4.235\sigma$	0.99809
	$n = 0.5$ $E = 13.165 + 3.923\sigma$	0.99782
	$n = 0.7$ $E = 18.808 + 3.992\sigma$	0.99685
Mixed gangue	$E = 14.787 + 3.989\sigma$	0.99764

430 mining area. There are unmined coal areas in the east and south, as shown in Figure 13.

The main mining area is the third upper coal seam, located in the middle of the Shanxi unit, with a full thickness of 2.63–5.11 m.

Most of the coal seams in the mining area have a large angle of inclination, generally 7–16°, and the coal seam depth is 1,082–1,222 m.

The filling mining scheme for gangue of the 9,302 working face was optimized, and the gradation of the filling material was improved. After washed gangue and crushed gangue were mixed with equal quality, filling and mining were performed. In actual production, washed gangue is first broken by a crusher and then obtained after scavenging and screening by a screener; crushed gangue is obtained from washed gangue after secondary breakage by a crusher again.

After improving the filling scheme, the solid filling effect of the 9,302 working face is shown in Figures 14, 15. The practical application proves once again that the amount of waste gangue filled in a unit working face is greatly improved by using mixed gangue, the porosity of the filling body is reduced, and the filling ratio of the filling body is improved. According to engineering experience, with the increase in the filling ratio and the roof-contacted filling rate, the mining process can not only consume more wasted gangue but also better control the ground settlement of the mining area.

DISCUSSION

The stress–strain curves of gangue with different particle gradations all show nonlinear characteristics. The compression modulus increases as the compressive stress increases. With the continuation of the compression process, the rate of change in the compression modulus decreases and tends to stabilize (Zhang et al., 2019b). In the compression test, the specimen contains a large number of pores formed by internal particles. In the initial stage of the compression experiment, as the compressive stress increases, the restraining force of the specimen increases, and the stress concentration between the inner edges of the particles becomes more obvious. When the compressive stress increases to



FIGURE 12 | Distribution of surface buildings.

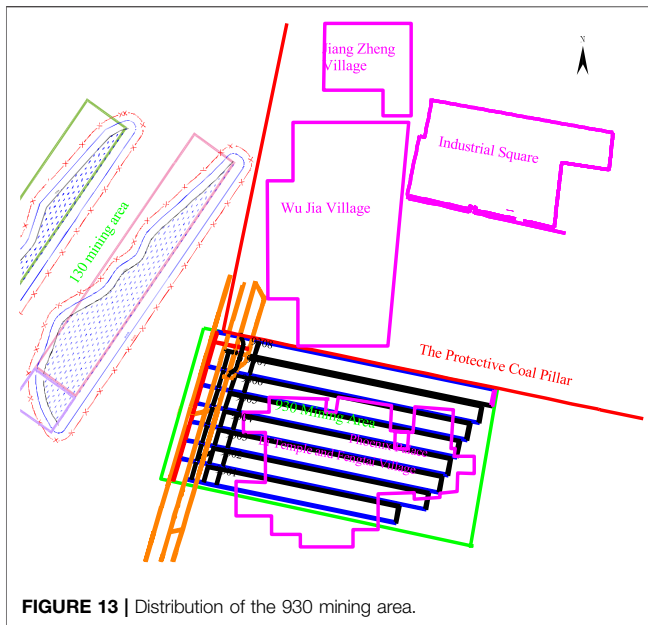


FIGURE 13 | Distribution of the 930 mining area.

a certain extent, the large particles in the specimen are crushed, and the internal pores are gradually filled (Meng et al., 2019). It is generally believed that the particle diameter and bulk density after compaction tend to be the same after extreme stress compression in tests with different particle sizes (Huang et al., 2019b).

In the compression experiment, the compressed amount of washed gangue is the largest, that of mixed gangue is greatly reduced compared with that of washed gangue, and that of continuous graded gangue is the smallest. The reason is that the more prominent the edge of large particles is, the more prone it is to stress concentration, which leads to the fragmentation of large particles (Ali et al., 2018; Li et al., 2020a). In the washed gangue specimen, large particles are dominant, and small particles cannot completely fill the pores between the large particles, resulting in an obvious stress concentration between

the large particles and maximum compression (Zhang et al., 2012). In the specimen of continuously graded gangue, the small particles basically filled the pores between the large particles and weakened the stress concentration between the large particles, and the specimen compression was the smallest. The particle gradation of mixed gangue is slightly worse than that of continuous graded gangue and is much better than that of washed gangue. The optimization degree of the internal structure of the specimen is also somewhat lower than that of continuous graded gangue and much higher than that of washed gangue, so the specimen compression is in the same way: the compression of washed gangue is the largest, that of continuous graded gangue is the smallest, and that of mixed gangue is slightly less than that of continuous graded gangue (Zhang et al., 2018).

Solid filling technology is an economical and effective surface subsidence control technology to solve the problem of “three under” coal holding down. The probability integral model of “equivalent mining height theory” can be used to calculate the surface subsidence of solid filling mining (Li et al., 2020b). The determination of “equivalent mining height” is mainly affected by three aspects: the subsidence of the immediate roof of the working face after mining and before gangue filling, the filling rate of the filling body in the filling process, and the compression of the filling body after filling (Wang et al., 2019).

In solid filling mining, on the premise of ensuring the roof-contacted filling rate, the surface subsidence is mainly affected by the filling rate of the filling body and the compression of the filling body under the compressive stress of the overlying rock after filling (Li et al., 2020c). The optimization of the particle size gradation of the filling body can greatly improve the filling rate of the filling body and enhance the compressive strength of the filling body to reduce its amount of compression. Using gangue with optimized particle size gradation for filling can further curtail the “equivalent mining height” to achieve better control of surface deformation and settlement. The filling body of mixed gangue with equal mass proposed in this study has good grain



FIGURE 14 | Transportation of filling gangue.



FIGURE 15 | Working face of filling gangue.

gradation, a high roof bonding rate, and a small compaction rate, which can effectively reduce the “equivalent mining height” and better reduce the surface deformation. In practical application, filling body of mixed gangue with equal quality has simple flow and convenient construction, which has played a guiding role in the promotion and use of gangue filling mining.

CONCLUSION

Through the screening experiment of gangue filling materials, the gradation characteristics of washed gangue are optimized to obtain gradation groups of gangue conforming to engineering applications. Laboratory specimens of washed gangue, continuous gradation gangue, and mixed gangue were prepared by a similar gradation method; their compression performance was measured; and the following conclusions were drawn:

- 1) The screening experiment shows that compared with the ideal gradation, the content of large particle size of washed gangue is too much and the content of small particle size is too little, while the small particle size of crushed gangue is dominant, but the large particle size content is too little. Combined with the continuous gradation curve and the gradation of crushed gangue, it is concluded that the gradation defects of filling gangue can be promoted by mixing two types of gangue with equal quality.
- 2) The list bulk density of gangue varies in the range of 14–20 kN/m³, and the degrees of relative compaction of washed gangue, continuous graded gangue, and mixed gangue are 1.33, 1.24–1.27, and 1.226, respectively. The degree of relative compaction of the gangue filling body decreases significantly after optimizing gangue gradation.
- 3) The stress–strain curve of gangue is nonlinear and can be described by a three-factor logarithmic function model. With the change in stress, the final compression rate of continuously

graded gangue is 70–80% and that of mixed gangue is 75–85%. After optimizing gangue gradation, the compression of the gangue filling body is significantly reduced.

- 4) According to the experimental results, when the compressive stress reaches 2 MPa, the constitutive model of the filling body is expressed by a nonlinear elastic model, and the relationship between the deformation modulus and compressive stress is described by linear fitting. With the change in compressive stress, the deformation modulus of washed gangue is 26–100 MPa, the final deformation modulus of continuous graded gangue is 21–140 MPa, and the deformation modulus of mixed gangue is 23–135 MPa. The anti-compression properties of the gangue filling body are significantly improved after optimizing the gradation of gangue.
- 5) The filling body of mixed gangue composed of washed gangue and crushed gangue with equal quality significantly improves its compressive strength and reduces its compression amount. Although it is not the optimal grain gradation, it is considered that mixed gangue is the optimal gangue filling material considering the convenience of on-site construction.

DATA AVAILABILITY STATEMENT

The original contributions presented in the study are included in the article/Supplementary Material; further inquiries can be directed to the corresponding author.

AUTHOR CONTRIBUTIONS

YD, ZM, and XZ contributed to conception and design of the study. YD and XZ organized the database. JL, JZ and ZM performed the statistical analysis. YD and XZ wrote the first draft of the manuscript. YD, JL, JZ and ZM wrote sections of the manuscript. All authors contributed to manuscript revision, read, and approved the submitted version.

FUNDING

Funding was provided by the National Key R and D Program of China (2018YFC0604705); SDUST Research Fund (grant no. 2018TDJH102); the National Natural Science Foundation of China (grant nos. 51574159, 51974172, 51974173, and 51804179); and the

SDUST Research Fund, China Postdoctoral Science Foundation (2015 M572067 and 2016T90662), the Shandong Province Natural Science Foundation Project (ZR2017 MEE055 and 2018GSF116002), and the National Experimental Teaching Demonstration Center of Mining Engineering (Shandong University of Science and Technology) Opening Fund (KYSF20180209).

REFERENCES

- Ali, S., Kamran, E., and Bibhu, M. (2018). Degradation of a Discrete Infilled Joint Shear Strength Subjected to Repeated Blast-Induced Vibrations[J]. *Int. J. Mining Sci. Technology* 28 (4), 561–571.
- Cai, Z., Zhang, D., Shi, L., Zhong, C., Biao, C., Suyang, S., et al. (2020). Compaction and Breakage Characteristics of Crushed Stone Used as the Backfill Material of Urban Pavement Subsidence. *Adv. Civil Eng.* 2020, 1–8. doi:10.1155/2020/8889199
- Chang, Q., Tang, W., Xu, Y., and Zhou, H. (2018). Research on the Width of Filling Body in Gob-Side Entry Retaining with High-Water Materials. *Int. J. Mining Sci. Technology* 28 (3), 519–524. doi:10.1016/j.ijmst.2017.12.016
- Chen, C., Liu, X., Luo, Z., and Ning, Z. (2016). Study of Strength and Deformation Characteristic of Unbound Granular Material with Different Grain Composition[J]. *J. Eng. Geology*. 24 (6), 1191–1198. doi:10.13544/j.cnki.jeg.2016.06.019 (in chinese).
- Chu, F., Zhu, J., Weng, H., and Ye, Y. (2020). Experimental Study on Maximum Dry Density of Scaled Coarse-Grained Soil[J]. *Rock Soil Mech.* 41 (5), 1599–1604. doi:10.16285/j.rsm.2019.0780 (in chinese).
- DL/T (5016—2011) Resign Specification for concrete Face Rockfill Dams[S]. (in chinese)
- DL/T (5395—2007) Resign Specification for Rolled Earth-Rock Fill Dams[S].2007. (in chinese)
- Dong, L., Deng, S., and Wang, F. (2020). Some Developments and New Insights for Environmental Sustainability and Disaster Control of Tailings Dam[J]. *J. Clean. Prod.* 269, 122270. doi:10.1016/j.jclepro.2020.122270
- Dong, L., Tong, X., Li, X., Zhou, J., Wang, S., and Liu, B. (2019). Some Developments and New Insights of Environmental Problems and Deep Mining Strategy for Cleaner Production in Mines. *J. Clean. Prod.* 210, 1562–1578. doi:10.1016/j.jclepro.2018.10.291
- Fang, M., Park, D., Singuranayo, J. L., Chen, H., and Li, Y. (2019). Aggregate Gradation Theory, Design and its Impact on Asphalt Pavement Performance: a Review. *Int. J. Pavement Eng.* 20 (12), 1408–1424. doi:10.1080/10298436.2018.1430365
- Feng, G., Sun, C., Wang, C., and Zhou, Z. (2010). Research on Goaf Filling Methods with Super High-Water Material[J]. *J. China Coal Soc.* 35 (12), 1963–1968. doi:10.1016/S1876-3804(11)60004-9 (in chinese).
- Fuller, W. B., and Thompson, S. E. (1907). The Laws of Proportioning Concrete[J]. *Trans. Am. Soc. Civil Eng.* 33, 222–298.
- Gb/T 5014—2007 Standard for Engineering Classification of Soil[S]. (in chinese)
- Guo, G.-l., Zhu, X.-j., Zha, J.-f., and Wang, Q. (2014). Subsidence Prediction Method Based on Equivalent Mining Height Theory for Solid Backfilling Mining. *Trans. Nonferrous Met. Soc. China* 24 (10), 3302–3308. doi:10.1016/S1003-6326(14)63470-1
- Guo, G., Li, H., and Zha, J. (2019). An Approach to Protect Cultivated Land from Subsidence and Mitigate Contamination from Colliery Gangue Heaps. *Process Saf. Environ. Prot.* 124 (PartB), 336–344. doi:10.1016/j.psep.2019.03.004
- Hu, B. Backfill Mining Technology and Development Tendency in China Coal Mine[J]. *Coal Sci. Technology*, 2012,40(11):1-5+18. doi:10.13199/j.cst.2012.11.7.hubn.006 (in chinese)
- Hu, B., and Guo, A. (2009). Testing Study on Coal Waste Back Filling Material Compression Simulation. *J. China Coal Soc.* 34 (8), 1076–1080. doi:10.1360/972009-754 (in chinese).
- Hu, B., and Guo, W. (2018). Mining Subsidence AREA Status, Synthe-Ses Governance Model and Governance Recommendation [J]. *Coal Mining Technology* 23 (2), 1–4. doi:10.13532/j.cnki.cn11-3677/td.2018.02.001 (in chinese).
- Huang, X., Zhang, X., Li, Z., Chen, Y., Hu, Y., and Liu, P. (2019a). Study on Grain Composition of Manufactured Sand on Basis of Fuller and Tabor Theory[J]. *Concrete* 354 (4), 97–101. doi:10.3969/j.issn.1002-3550.2019.04.022 (in chinese).
- Huang, Y., Li, J., Ma, D., Gao, H., Guo, Y., and Ouyang, S. (2019b). Triaxial Compression Behaviour of Gangue Solid Wastes under Effects of Particle Size and Confining Pressure. *Sci. Total Environ.* 693, 133607. doi:10.1016/j.scitotenv.2019.133607
- Huang, Y., Zhang, J., Zhang, Q., Nie, S., and An, B. (2012). Strata Movement Control Due to Bulk Factor of Backfilling Body in Fully Mechanized Backfilling Mining Face[J]. *J. Mining Saf. Eng.* 29 (02), 162–167. doi:10.3969/j.issn.1673-3363.2012.02.003 (in chinese).
- Ju, Y., Nie, X., Zhu, Y., and Xie, H. (2021). *In Situ* fluidized Mining and Conversion Solution to Alleviate Geological Damage and Greenhouse Gas Emissions Due to Coal Exploitation: A Numerical Analysis and Evaluation. *Energy Sci Eng* 9 (1), 40–57. doi:10.1002/ese3.812
- Li, B., Yan, H., Zhang, J., and Zhou, N. (2020). Compaction Property Prediction of Mixed Gangue Backfill Materials Using Hybrid Intelligence Models: A New Approach[J]. *Construction Building Mater.* 247, 118633. doi:10.1016/j.conbuildmat.2020.118633
- Li, B., Zhou, N., Qi, W., Li, A., Cui, Z., and Trung, N. (2020). Surface Subsidence Control during Deep Backfill Coal Mining: A Case Study[J]. *Adv. Civil Eng.* 2020, 1–12. doi:10.1155/2020/6876453
- Li, G., Liu, Y., Yin, Z., Dano, C., and Hicher, P. (2014). Grading Effect on Critical State Behavior of Granular Materials[J]. *Chin. J. Geotechnical Eng.* 03 (36), 0452–0458. doi:10.11779/CJGE201403007 (in chinese).
- Li, H., and Guo, G. (2018). Surface Subsidence Control Mechanism and Effect Evaluation of Gangue-Backfilling Mining: A Case Study in China, *Geofluids* 2018, 1–9. doi:10.1155/2018/2785739
- Li, J., Huang, Y., Wen, Z., Yingshun, L., Shenyang, O., Huadong, G., et al. (2020). Experimental Study on Acoustic Emission of Confined Compression of Crushed Gangue under Different Loading Rates: Disposal of Gangue Solid Waste[J]. *Sustainability* 12 (9), 3911. doi:10.3390/su12093911
- Li, M., Zhang, J., Wu, Z., Liu, Y., and Li, A. (2019). An Experimental Study of the Influence of Lithology on Compaction Behaviour of Broken Waste Rock in Coal Mine Backfill R. *Soc. Open Sci.*, 6 (4), 182205. doi:10.1098/rsos.182205
- Liu, J., Li, X., and Tuan, He. (2020). Application Status and Prospect of Backfill Mining in Chinese Coal Mines [J]. *J. China Coal Soc.* 45 (1), 141–150. doi:10.13225/j.cnki.jccs.YG19.1063 (in chinese).
- Ma, D., Duan, H., Liu, J., Li, X., and Zhou, Z. (2019). The Role of Gangue on the Mitigation of Mining-Induced Hazards and Environmental Pollution: An Experimental Investigation. *Sci. Total Environ.* 664, 436–448. doi:10.1016/j.scitotenv.2019.02.059
- Ma, Z., Pu, H., and Zhang, F. (2003). Study on Compacting Characteristics of Coal Gangue[J]. *Ground Press. Strata Control.* 20 (1), 95–96. (in chinese).
- Meng, Li., Li, A., Zhang, J., Huang, Y., and Li, J. (2020). Effects of Particle Sizes on Compressive Deformation and Particle Breakage of Gangue Used for Coal Mine Goaf Backfill[J]. *Powder Technology* 360, 493–502. doi:10.1016/j.powtec.2019.10.075
- Meng, Li., Zhang, J., Li, A., and Zhou, N. (2020). Reutilisation of Coal Gangue and Fly Ash as Underground Backfill Materials for Surface Subsidence Control[J]. *J. Clean. Prod.* 254, 120113. doi:10.1016/j.jclepro.2020.120113
- Meng, Li., Zhang, J., Wu, Z., and Sun, K. (2019). Calculation and Monitoring Analysis of Stress Distribution in a Coal Mine Gob Filled with Waste Rock Backfill Materials[J]. *Arabian J. Geosciences* 12 (14), 1–11. doi:10.1007/s12517-019-4584-9
- Miao, X., and Zhang, J. (2007). Analysis of Strata Behavior in the Process of Coal Mining by Gangue Backfilling[J]. *J. Mining Saf. Eng.* (04), 379–382. doi:10.3969/j.issn.1673-3363.2007.04.001 (in chinese).

- Miao, X., Zhang, J., and Guo, G. (2010). Study on Waste-Filling Method and Technology in Fully-Mechanized Coal Mining[J]. *J. China Coal Soc.* 35 (01), 1–6. doi:10.1016/S1876-3804(11)60004-9 (in chinese).
- Nb/T 5101—2014, Method of Compaction Testing of Solid Backfilling Materials [S]. (in chinese)
- Qian, M., Xu, J., and Wang, J. (2018). Further on the Sustain-Able Mining of Coal[J]. *J. China Coal Soc.* 43 (1), 1–13. doi:10.13225/j.cnki.jccs.2017.4400 (in chinese).
- Sun, Q., Zhang, J., and Zhou, N. (2018). Study and Discussion of Short- Strip Coal Pillar Recovery with Cemented Paste Backfill. *Int. J. Rock Mech. Mining Sci.* 104, 147–155. doi:10.1016/j.ijrmm.2018.01.031
- Wang, C., Lu, Y., Li, Y., Zhang, B., and Liang, Y. (2019). Deformation Process and Prediction of Filling Gangue: A Case Study in China[J]. *Geomechanics Eng.* 18 (4), 417–426. doi:10.12989/gae.2019.18.4.417
- Wang, J., Xie, H., Liu, J., Wu, L., Ren, S., Jiang, P., et al. (2018). Coal Development and Utilization Theory and Technical System of Near Zero Ecological Environment Impact[J]. *J. China Coal Soc.* 43 (5), 1198–1209. doi:10.13225/j.cnki.jccs.2018.0518 (in chinese).
- Wang, K., Yang, P., Yu, G., Yang, C., and Zhu, L. (2020). 3D Numerical Modelling of Tailings Dam Breach Run Out Flow over Complex Terrain: A Multidisciplinary Procedure. *Water* 12 (9), 2538. doi:10.3390/w12092538
- Wang, Q., Zhao, Y., Tseng, M., and Lim, M. (2020). Performance Analysis and Reuse of Construction and Demolition Waste Stone Using Fractal and Gradation Theory[J]. *J. Clean. Prod.* 271, 122208. doi:10.1016/j.jclepro.2020.122208
- Wang, Y., Yin, D., Chen, S., Zhang, L., Liu, D., Sun, Y., et al. (2020). Experimental Study on Properties of Rock-Cemented Coal Gangue-Fly Ash Backfill Bimaterials with Different Coal Gangue Particle Sizes[J]. *Adv. Civil Eng.* 2020, 1–12. doi:10.1155/2020/8820330
- Wu, J., Jing, H., Yin, Q., Yu, L., Meng, B., and Li, S. (2020). Strength and Ultrasonic Properties of Cemented Waste Rock Backfill Considering Confining Pressure, Dosage and Particle Size Effects[J]. *Construction Building Mater.* 242, 118132. doi:10.1016/j.conbuildmat.2020.118132
- Wu, J., Jing, H., Yin, Q., Meng, B., and Han, G. (2020). Strength Prediction Model Considering Material, Ultrasonic and Stress of Cemented Waste Rock Backfill for Recycling Gangue[J]. *J. Clean. Prod.* 276, 123189. doi:10.1016/j.jclepro.2020.123189
- Xu, J., Zhang, J., and Huang, Y. (2011). Experimental Research on the Compress Deformation Characteristic of Waste-Flyash and its Application in Backfilling Fully Mechanized Coal Mining Technology[J]. *J. Mining Saf. Eng.* 28 (1), 158–162. doi:10.3969/j.issn.1673-3363.2011.01.030 (in chinese).
- Yang, Y., Zhao, J., Wang, L., and Liu, X. (2019). Influence of Gradation Characteristics on Filling Standard of Sand Gravel Material for Dam Construction[J]. *J. Hydraulic Eng.* 11 (50), 1374–1383. doi:10.13243/j.cnki.slxb.20190547 (in chinese).
- Yao, Z., Fang, Y., Kong, W., Huang, X., and Wang, X. (2020). Experimental Study on Dynamic Mechanical Properties of Coal Gangue Concrete. *Adv. Mater. Sci. Eng.* 2020, 1–16. doi:10.1155/2020/8874191
- Zhang, J., Tu, S., Cao, Y., Tan, Y., Xin, H., and Pang, J. (2020). Research Progress of Technologies for Intelligent Separation and In-Situ Backfill in Deep Coal Mines in China[J]. *J. Mining Saf. Eng.* 37 (1), 1–10+22. doi:10.13545/j.cnki.jmse.2020.01.001 (in chinese).
- Zhang, J., Yu, Z., and Su, Y. (2012). Experimental Research on Compression Deformation of Coal Gangue Filling Materials[J]. *Mining Res. Development* 23 (4), 129–131. doi:10.13827/j.cnki.kyyk.2012.03.018 (in chinese).
- Zhang, J., Zhang, Q., Ju, F., Zhou, N., Meng, Li., and Zhang, W. (2019). Practice and Technique of green Mining with Integration of Mining, Dressing, Backfilling and X in Coal Resources[J]. *J. China Coal Soc.* 44 (01), 64–73. doi:10.13225/j.cnki.jccs.2018.5045 (in chinese).
- Zhang, J. (2008). *Study on Movement Control and Application of Direct Filling Fully Mechanized Coal Mining Strata with Gangue*[D]. Xu Zhou: China University of Mining and Technology. (in chinese).
- Zhang, J., Zhang, Q., Huang, Y., Liu, J., Zhou, N., and Zan, D. (2011). Strata Movement Controlling Effect of Waste and Fly Ash Backfillings in Fully Mechanized Coal Mining with Backfilling Face. *Mining Sci. Technology (China)* 21 (5), 721–726. doi:10.1016/j.mstc.2011.03.003
- Zhang, P., Zhang, Y., Zhao, T., Tan, Y., and Yu, F. (2019). Experimental Research on Deformation Characteristics of Waste-Rock Material in Underground Backfill Mining[J]. *Minerals* 9 (2). doi:10.3390/min9020102
- Zhang, Yu., Zhou, W., Li, M., Chen, Z., et al. (2018). Experimental Study on Compression Deformation and Permeability Characteristics of Grading Broken Gangue under Stress. [J]. *Processes*. 6 (12). doi:10.3390/pr6120257
- Zhou, H., Zheng, L., and Liang, Li. (2010). Strip Mining Technology with Paste Backfilling[J]. *Coal Sci. Technology* 38 (02), 10–14. doi:10.13199/j.cst.2010.02.15.liuk.009 (in chinese).
- Zhu, J., Guo, W., Wang, Y., and Wen, Y. (2015). Equation for Soil Gradation Curve and its Applicability[J]. *Chin. J. Geotechnical Eng.* 37 (10), 1931–1936. doi:10.11779/CJGE201510023 (in chinese).
- Zhu, S., Deng, S., Ning, Z., and Wang, J. (2017). Gradation Design Method for Rockfill Materials Based on Fractal Theory[J]. *Chin. J. Geotechnical Eng.* 39 (6), 1151–1155. doi:10.11779/CJGE201706023
- Zhu, S., Ning, Z., Zhong, C., Chu, J., and Gao, Z. (2018). Study on Particle Crush and Deformation Characteristics Considering Rockfill Gradation Effect[J]. *J. Hydraulic Eng.* 07 (49), 0849–0857. doi:10.13243/j.cnki.slxb.20180086 (in chinese).
- Zuo, Y., Zhang, W., and Pan, J. (2015). Effects of Gradation Scale Method on Maximum Dry Density of Coarse-Grained Soil[J]. *Rock Soil Mech.* 36 (S1), 417–422. doi:10.16285/j.rsm.2015.S1.073 (in chinese).

Conflict of Interest: The authors declare that the research was conducted in the absence of any commercial or financial relationships that could be construed as a potential conflict of interest.

Copyright © 2021 Dong, Zhang, Lin, Zhao and Meng. This is an open-access article distributed under the terms of the Creative Commons Attribution License (CC BY). The use, distribution or reproduction in other forums is permitted, provided the original author(s) and the copyright owner(s) are credited and that the original publication in this journal is cited, in accordance with accepted academic practice. No use, distribution or reproduction is permitted which does not comply with these terms.



Mechanical Modification of Nanomaterials on Fully Saturated Concrete in Groundwater Reservoir Under Long-Term Water Immersion

XianJie Hao^{1,2,3*}, Yingnan Wei⁴, Zeyu Chen³, Honglan Zhang³, Yifan Niu³, Kai Chen³ and Ruilai Huang³

¹Beijing Key Laboratory for Precise Mining of Intergrown Energy and Resources, China University of Mining and Technology (Beijing), Beijing, China, ²State Key laboratory of Coal Resources and Safe Mining, China University of Mining and Technology (Beijing), Beijing, China, ³School of Energy and Mining Engineering, China University of Mining and Technology (Beijing), Beijing, China, ⁴Zhengzhou Coal Mining Machinery (Group) Co., Ltd, Zhengzhou, China

OPEN ACCESS

Edited by:

Lijie Guo,
Beijing General Research Institute of
Mining and Metallurgy, China

Reviewed by:

Erol Yilmaz,
Recep Tayyip Erdoğan University,
Turkey
Shiqi Dong,
University of California, Los Angeles,
United States

*Correspondence:

XianJie Hao
haoxianjie@cumtb.edu.cn

Specialty section:

This article was submitted to
Structural Materials,
a section of the journal
Frontiers in Materials

Received: 29 April 2021

Accepted: 22 June 2021

Published: 15 July 2021

Citation:

Hao X, Wei Y, Chen Z, Zhang H, Niu Y,
Chen K and Huang R (2021)
Mechanical Modification of
Nanomaterials on Fully Saturated
Concrete in Groundwater Reservoir
Under Long-Term Water Immersion.
Front. Mater. 8:702308.
doi: 10.3389/fmats.2021.702308

With the increasing number of hydraulic structures in service, many scholars have investigated the performance of saturated concrete, however, there are few studies on the influences of different contents and types of nanomaterials on the performance of fully saturated concrete. In this paper, a series of experiments on concrete with different contents of nano SiO₂, nano Al₂O₃ and nano TiO₂ are performed, such as electron mirror scanning, uniaxial compression, acoustic emission, etc., and the microstructure, mechanical properties of samples are compared and analyzed. The results show that: 1) By the addition of various kinds of nanomaterials to saturated concrete, the microstructure of saturated concrete is significantly improved, and the compactness and integrity of the slurry are improved 2) The mechanical properties of saturated concrete are significantly improved by the addition of 3 wt% nanomaterials. And the compressive strength of the saturated concrete sample containing 3 wt% nano-Al₂O₃ is the largest and the deformation modulus of the saturated concrete sample containing 6 wt% nano-Al₂O₃ is the largest. 3) Compared with dry concrete, when the concrete is saturated, the modifying effect of nanomaterials on the mechanical properties of concrete is weakened. The results of this study have important guiding significance for the study of the nano-modification and the safe operation of hydraulic structures.

Keywords: saturated concrete, nanomaterials, microstructure, mechanical properties, modification

INTRODUCTION

Concrete is widely used in various construction projects because of its low cost and abundance of constituent materials (Zuo et al., 2018; Lu et al., 2019). It is most commonly used in building structures, therefore, the safety of concrete structures is very important. The mechanical properties of concrete are the foundation for ensuring the safety and stability of concrete structures.

Due to the presence of many pores and other defects in concrete, it is easily damaged: to improve the mechanical properties of concrete materials, admixtures are often used (Cao et al., 2020; Cao et al., 2021). Nanomaterials have a small particle size and high (and stable) specific surface energy. Therefore, nanomaterials are often used as admixtures to improve the mechanical properties of concrete. Much work so far has focused on nano-SiO₂, nano-Al₂O₃ and nano-TiO₂ due to their

dominate advantages in compressive strength, microstructure and price. Said et al. (Said et al., 2012) observed the significant improvement in concrete incorporating nano-silica in terms of reactivity, strength development, refinement of pore structure, and densification of the interfacial transition zone. Jalal et al. (Jalal et al., 2015) indicated the mechanical and transport properties improved in concrete containing nanomaterials especially when using a blend of silica nanoparticles and silica fume. Zhou et al. (Zhou et al., 2019) studied the hydration of Portland cement blended with 5% of nano-alumina, and identified a chemical effect of nano-alumina alongside the well-known filler effect, which is related to its solubility in pore fluids. Shaikh et al. (Shaikh et al., 2017) studied the effect of mixing methods of nano-silica on properties of recycled aggregate concrete. Du et al. (Du et al., 2015) investigated the influence of nano-silica on the mechanical and transport properties of lightweight concrete. Liu et al. (Liu et al., 2018) concluded that the effects of nano-SiO₂ on promoting the hydration, refining the pore structure, narrowing the width of microcrack, and thus reducing the permeability of cement paste become much clearer as the W/C ratio decreases. Yang et al. (Yang et al., 2019) indicated that nano-Al₂O₃ can be used for improving the chloride binding capacity of cement. Li et al. (Li et al., 2006a) showed that the addition of nano-Al₂O₃ to concrete increases the compactness of the interfacial transition zone, decreases the porosity of the cement, and increases the elastic modulus and compressive strength of the concrete. Deng et al. (Deng, 2012) demonstrated that nano-TiO₂, as a partial substitute for cement, can improve the compressive performance of concrete to some extent. Zhang et al. (Zhang et al., 2015) showed that nano-TiO₂ increases the compressive strength of cement mortar through its acceleration of cement hydration and the pore-refining effect. Hong et al. (Hong et al., 2020) proved that nano-clay could promote the hydration process of cement grouting material, and thus it weakens the chloride ion erosion due to the porosity reduction effect. It can be seen from the literature that nanomaterials can not only fill the pores in concrete, but also participate in and promote the hydration reaction of concrete materials. Adding nanomaterials to the concrete can improve the microstructure of the concrete and can increase its compressive strength and elastic modulus.

Some concrete structures must survive in water for a long time (e.g., dams and artificial dams in groundwater reservoirs). The mechanical properties of the concrete will be affected by water. Due to the surrounding water pressure and initial defects such as internal pores and cracks, the internal pores and cracks of concrete structures are filled with water, saturating the concrete. Many scholars have studied the differences in mechanical performance between saturated and dry concrete. Research shows that the strength of saturated concrete is lower than that of dry concrete, while the static and dynamic modulus is higher (Rossi et al., 1992; Ross et al., 1996; Yaman et al., 2002a; Yaman et al., 2002b; Wang and Li, 2007). Zheng et al. (Zheng and Li, 2010) proposed a method of predicting the elastic modulus of dry and saturated concrete based on the micromechanics of composite materials. Jin et al. (Jin et al., 2012) studied the effect of pore-water on the mechanical properties of saturated

concrete and established relationships between the water content and the elastic parameters of saturated concrete. Kaji et al. (Kaji and Fujiyama, 2014) found that the compressive strength of saturated concrete increases with the strain rate. Wang et al. (Wang et al., 2016) investigated the effect of saturation on the behavior of concrete under biaxial compression: the results indicated that the static compressive strength of saturated concrete is lower than that of dry concrete, but the dynamic strength of saturated concrete is higher than that of dry concrete. Siddiqui et al. (Siddiqui et al., 2016) developed an approximate analytical model for the axial strain and internal water pressure development in a saturated concrete cylinder. Bian et al. (Bian et al., 2017) proposed a coupled elastoplastic damage model to describe the mechanical behavior of saturated and dry concrete over a wide range of confining pressures. It can be seen from the published literature that the mechanical properties of concrete are significantly affected by saturation. The static strength of saturated concrete is reduced compared with dry concrete, but the dynamic strength and modulus are increased compared with dry concrete.

Due to the low static strength of saturated concrete, it is unsatisfactory in some engineering applications. For example, artificial dams of groundwater reservoir will always be subject to seepage in service, and the artificial dam often requires rebuilding.

The mechanical properties of saturated concrete may be improved by addition of nanomaterials. Adding nanomaterials may be a better measure for saturated concrete. Although many scholars have done a lot of research on saturated concrete, especially the difference between saturated concrete and dry concrete, few have studied the modifying effect of nanomaterials on saturated concrete, especially the difference in the effect of different nanomaterials. With the increasing number of construction projects in water, to ensure the safety stability and service life of these hydraulic structures, it is becoming more important to study the modifying effect of nanomaterials on the mechanical properties of saturated concrete.

The research object of this paper is fully saturated concrete, the purpose is to study the influence of different types and contents of nanomaterials on the mechanical properties of saturated concrete, and to compare the modifying effects of different types and contents of nanomaterials in this paper. A series of experiments on saturated concrete specimens with different types and contents of nanomaterials are conducted. In *Sample Preparation*, three nanomaterials (nano-SiO₂, nano-Al₂O₃, and nano-TiO₂) are selected as admixtures to prepare different types of nano-saturated concrete samples. In *Composition and Microstructure*, the composition and microstructure of the nano-saturated concrete samples are tested by XRF and SEM. In *Results and Analysis*, wave velocity tests and uniaxial compression tests are performed on saturated concrete samples, and the test results presented therein. In *Discussion*, the mechanical parameters such as strength, modulus of different nano-saturated concrete samples are compared. In *Conclusion*, the saturated concrete containing nanomaterials is compared with dry concrete containing the same nanomaterials (data sourced from the literature), and the different modifying

TABLE 1 | Chemical composition of Portland cement (PO42.5).

Chemical composition	CaO	SiO ₂	Al ₂ O ₃	TiO ₂	MgO	SO ₃	K ₂ O
Content (%)	59.72	21.15	5.93	0.51	2.31	2.23	0.53

TABLE 2 | Concrete mixes.

Type	Cement/g	River sand/g	Stones/g	Water/g	Water-reducing agent/g	Nano-SiO ₂ /g	Nano-Al ₂ O ₃ /g	Nano-TiO ₂ /g
Ordinary concrete	1,200	2,400	2,400	720	3			
3 wt% Nano-SiO ₂ sample	1,164	2,400	2,400	720	3	36		
6 wt% Nano-SiO ₂ sample	1,128	2,400	2,400	720	3	72		
3 wt% Nano-Al ₂ O ₃ sample	1,164	2,400	2,400	720	3		36	
6 wt% Nano-Al ₂ O ₃ sample	1,128	2,400	2,400	720	3		72	
3 wt% Nano-TiO ₂ sample	1,164	2,400	2,400	720	3			36
6 wt% Nano-TiO ₂ sample	1,128	2,400	2,400	720	3			72

**FIGURE 1** | Sample preparation process.

effects of nanomaterials on the mechanical properties of saturated concrete and dry concrete are analyzed. The results of this study have important guiding significance for the study of the nano-modification of saturated concrete mechanical properties and the safe operation of construction engineering work in water.

SAMPLE PREPARATION

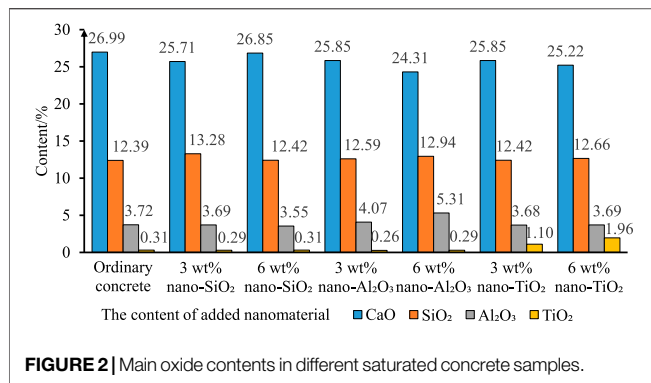
Materials

The materials used in this study included cement, river sand, stones, nano-SiO₂, nano-Al₂O₃, nano-TiO₂, and a water-reducing agent. Portland cement (PO42.5) was used in this experiment, and it was the main cementitious material used for making concrete materials, and its chemical composition

table is shown in **Table 1**. The river sand was taken from the river channels around the city, with yellow color and low mud content. The particle size of the stone was between 5 and 10 mm, with cyan color, high calcium content, and good workability. The particle size of the three nanomaterials is all 30 nm. The purity of the three nanomaterials was 99%. The water-reducing agent uses polycarboxylic acid high-performance water-reducing agent, which can improve the fluidity and strength of concrete.

Mixing Method

Two types of samples were prepared: ordinary saturated concrete samples without nanomaterials for reference and comparison. In subsequent research, this type of sample was called an ordinary saturated concrete sample, the other was the nano-saturated concrete samples, which were used to study the modifying



effects of different types and contents of nanomaterials on the mechanical properties and microstructure of saturated concrete. The ordinary saturated concrete samples were mixes of cement, river sand, and stones in the ratio of 1: 2: 2, with a water-cement ratio of 0.6 and a water-reducing agent content of 0.2% of the cement mass, made without addition of nanomaterials. For nano-saturated concrete materials, two control parameters for the content and type of nanomaterials were designed. The contents of nanomaterials included 3 wt% and 6 wt%. The added nanomaterials replaced the corresponding quantity of cement. There were three types of nanomaterials used here: nano-SiO₂, nano-Al₂O₃, and nano-TiO₂. Through the changes of these two control parameters, there were six different types of nano-saturated concrete samples. In summary, a total of seven types of concrete were prepared in the present research (four samples of each type, and a total of 28 samples were prepared). The mass ratio of raw materials of each type of concrete samples is summarized in **Table 2**.

For nano-concrete materials, a series of steps were needed to prevent the agglomeration of the added nanomaterials. Firstly, nanomaterials of the required quality were put into water and dispersed using an ultrasonic cleaning machine for 15 min to ensure their even dispersal in the water. Then, the cement, stones, and river sand of the quality described in **Table 2** were put into a bucket and mixed for 1 min. Finally, the dispersed liquid with its nanomaterials was poured into the bucket and stirred using a mixer for 10 min. The mixed slurry was poured into a mold, and

after waiting for 24 h the mold was removed, as shown in **Figure 1**. The standard cylindrical samples of $\Phi 50 \times 100$ mm were drilled from the condensed paste after demolding. A total of 28 samples were then drilled: to ensure that the concrete samples reached a state of fully saturation, after drilling they were soaked in sodium hydroxide solution with a pH of 8 for water saturation treatment. After 12 days, the samples were removed for subsequent testing. In this paper, the water retention process of concrete lasts for 12 days, so it is considered that the concrete samples have reached a fully saturated state.

Experimental Equipment

X-Ray Fluorescence (XRF)

The debris produced during sample processing was ground into 200-mesh powder using an agate mortar. Then, the element and oxide content were tested by X-ray fluorescence spectrometer (Arl Perform'X).

Scanning Electron Microscopy

The debris produced during sample processing was made into a sample of 1 cm² cross-sectional area. To observe the microstructure and pore state of different types of saturated concrete samples, the Quanta 200 F field emission environment scanning electron microscope produced by FEI was used.

Uniaxial Compression Testing

The uniaxial compression testing of saturated concrete samples was performed using an RTR-1000 triaxial rock mechanics test system (GCTS Co., United States).

COMPOSITION AND MICROSTRUCTURE

X-Ray Fluorescence (XRF)

The XRF results show that: the amount of CaO in concrete is the highest, indicating that it is the main oxide present in such concrete samples. Therefore, the CaO content and the content of various kinds of nanomaterials (SiO₂, Al₂O₃, and TiO₂) in various types of concrete samples are plotted to compare the oxide content in different saturated concrete samples (**Figure 2**).

It can be seen from **Figure 2** that the amount of CaO in each sample is around 26%, and there is no obvious difference between

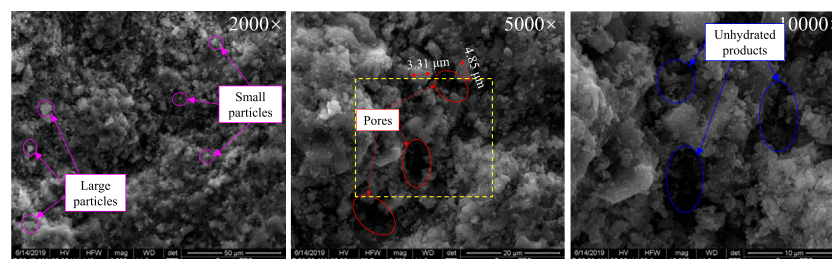


FIGURE 3 | SEM results: ordinary saturated concrete samples.

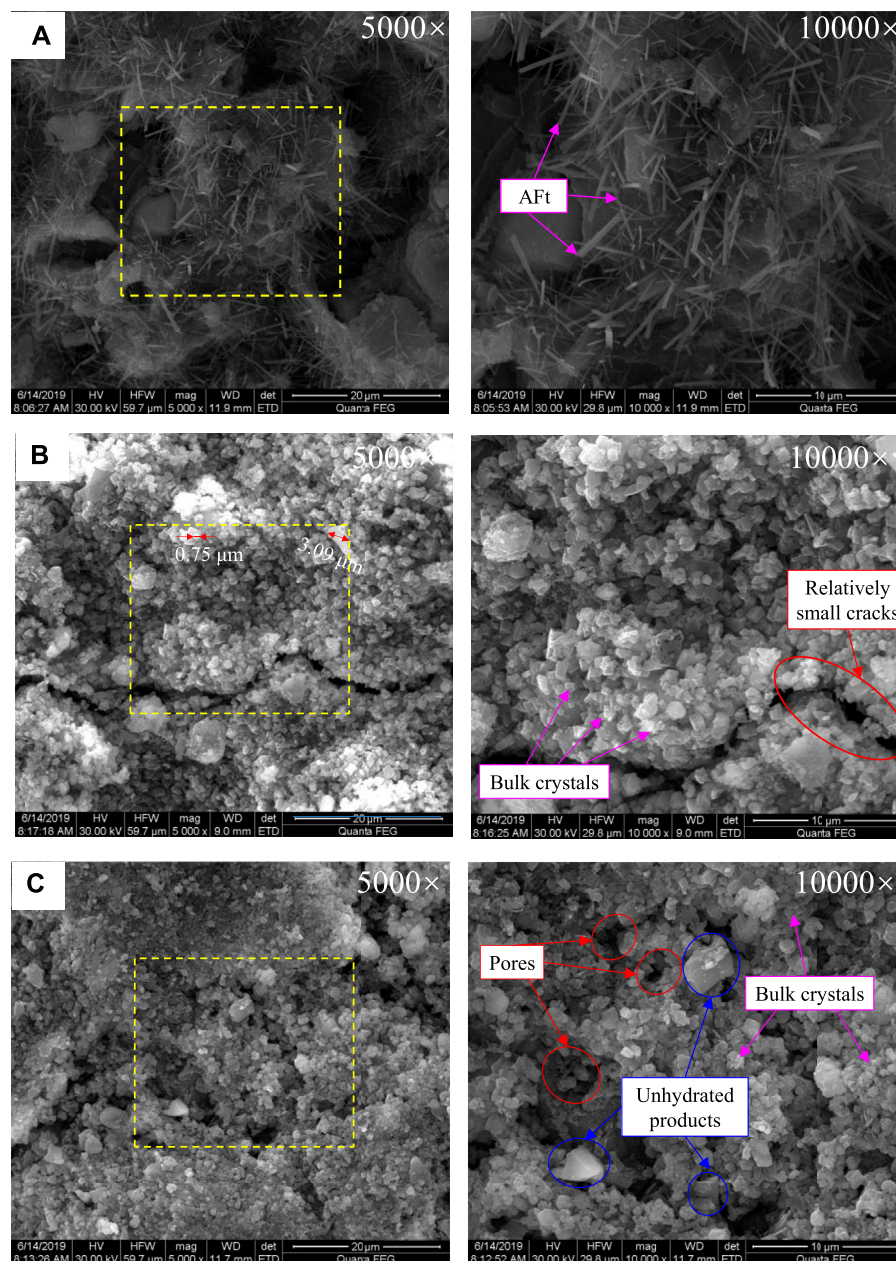


FIGURE 4 | SEM results: saturated concrete containing nanomaterials, **(A)** sample containing nano-SiO₂; **(B)** sample containing nano-Al₂O₃; **(C)** sample containing nano-TiO₂.

them. As one of the main components of concrete materials, SiO₂ accounts for a relatively large proportion of the concrete. Due to the amount of added nano-SiO₂ being relatively small, for samples containing nano-SiO₂, the content of SiO₂ shows no significant change compared with other samples; however, the Al₂O₃ and TiO₂ contents of samples containing nano-Al₂O₃ or nano-TiO₂ increase significantly. The average content of Al₂O₃ in the samples without nano-Al₂O₃ is 3.67%. The average content of Al₂O₃ in the samples mixed with 3 wt% nano-Al₂O₃ is 3.67%. The average content of Al₂O₃ in the samples mixed with 6 wt%

nano-Al₂O₃ is 4.07%. The average content of TiO₂ in the samples without nano-TiO₂ is 0.29%. The average content of TiO₂ in the samples mixed with 3 wt% nano-TiO₂ is 1.1%. These results indicate that the nanomaterial has been successfully mixed with concrete through the mixing method outlined in *Mixing Method*.

Scanning Electron Microscopy

The SEM scanning results of ordinary saturated concrete samples are shown in **Figure 3**: particulate hydration products in ordinary

TABLE 3 | Wave velocities.

	Number	Length (mm)	Time (μ s)	Wave velocity (m/s)	Standard deviation
Ordinary saturated concrete samples	C-1	105.24	37.6	2,798.94	71.03
	C-2	99.94	38	2,630	
	C-3	100.64	38.4	2,620.83	
	C-4	100.53	37.6	2,673.67	
The saturated concrete samples containing 3 wt% nano-SiO ₂	S-1	99.47	38.4	2,590.36	17.96
	S-2	100.31	38.4	2,612.24	
	S-3	100.11	38.4	2,607.03	
	S-4	100.33	38	2,640.26	
The saturated concrete samples containing 6 wt% nano-SiO ₂	S-5	99.42	38.8	2,562.37	21.71
	S-6	100.04	38.8	2,578.35	
	S-7	99.93	39.2	2,549.23	
	S-8	99.76	39.6	2,519.19	
The saturated concrete samples containing 3 wt% nano-Al ₂ O ₃	A-1	100.4	37.6	2,670.21	13.03
	A-2	100.42	37.6	2,670.74	
	A-3	100.37	37.2	2,698.11	
The saturated concrete samples containing 6 wt% nano-Al ₂ O ₃	A-5	100.17	37.1	2,700	77.13
	A-6	100.54	40.1	2,507.23	
	A-7	100.79	37.6	2,680.59	
	A-8	100.68	38.9	2,588.17	
The saturated concrete samples containing 3 wt% nano-TiO ₂	T-1	100.17	37.6	2,664.10	13.81
	T-2	100.13	37.6	2,663.03	
	T-3	99.76	37.2	2,681.72	
	T-4	100.31	37.2	2,696.51	
The saturated concrete samples containing 6 wt% nano-TiO ₂	T-5	100.84	37.4	2,696.26	19.60
	T-6	100.91	38	2,655.53	
	T-7	100.45	38	2,643.42	
	T-8	100.65	37.8	2,662.70	

saturated concrete samples vary in size and there are many micro-pores therein. There is also a significant amount of loose un-hydrated products seen in the pores and the pores are areas of accumulation of Ca(OH)₂ generated during hydration of the cement. All these combine to make the pores become areas of weakness in saturated concrete.

The microstructure of the three types of saturated concrete samples containing different nanomaterials differs: as shown in **Figure 4A**, many acicular crystals are randomly distributed within samples containing nano-SiO₂, which fill the pores and increase the compactness of the material. In the sample containing nano-Al₂O₃, as shown in **Figure 4B**, the internal hydration products are bulk crystalline in form. The internal hydration products are closely connected with the un-hydrated products, and the large cracks in the concrete are filled with these crystals before becoming relatively small cracks. The hydration product of the sample containing nano-TiO₂ (**Figure 4C**) is like that of the sample containing nano-Al₂O₃, and they are both bulk crystals, but the internal structure of the sample containing nano-TiO₂ is looser than the sample containing nano-Al₂O₃. There are still large pores inside the sample containing nano-TiO₂ and the degree of hydration is lower than that of the sample containing nano-Al₂O₃, and some un-hydrated products remain within.

In summary, compared with the saturated samples without nanomaterials, nanomaterials can improve the microstructure of saturated concrete materials. For the saturated sample containing nanomaterials, on the one hand, the internal

hydration product particles have a smaller diameter and the internal structure is more uniform and compact: such as for ordinary saturated concrete, the internal particle diameter is mostly between 3 and 5 μ m, and for saturated concrete containing with nanomaterials, although there are a few crystals with a particle diameter of 3 μ m, the internal crystal diameter is mostly around 1 μ m; on the other hand, the internal pores are much fewer in number, and the pores are filled with hydration products. This is because nanomaterials exhibit high pozzolanic activity that can promote the hydration reaction of cement, and the secondary hydration reaction with Ca(OH)₂ can produce more C-S-H gel. The secondary hydration products are filled in the pores; this can increase the content of C-S-H gel in the weak area of the interface and improve the compactness of the slurry and reform the microstructure. Among all saturated concrete samples, the saturated concrete samples containing nano-Al₂O₃ show the best microstructure in that the internal structure is more uniform and compact, and its integrity is optimal.

RESULTS AND ANALYSIS

Wave Velocity Test

Before the saturated concrete samples were subjected to uniaxial compression, the different types of saturated concrete samples were numbered. The ordinary saturated concrete samples were labeled C (a total of four samples). The saturated concrete

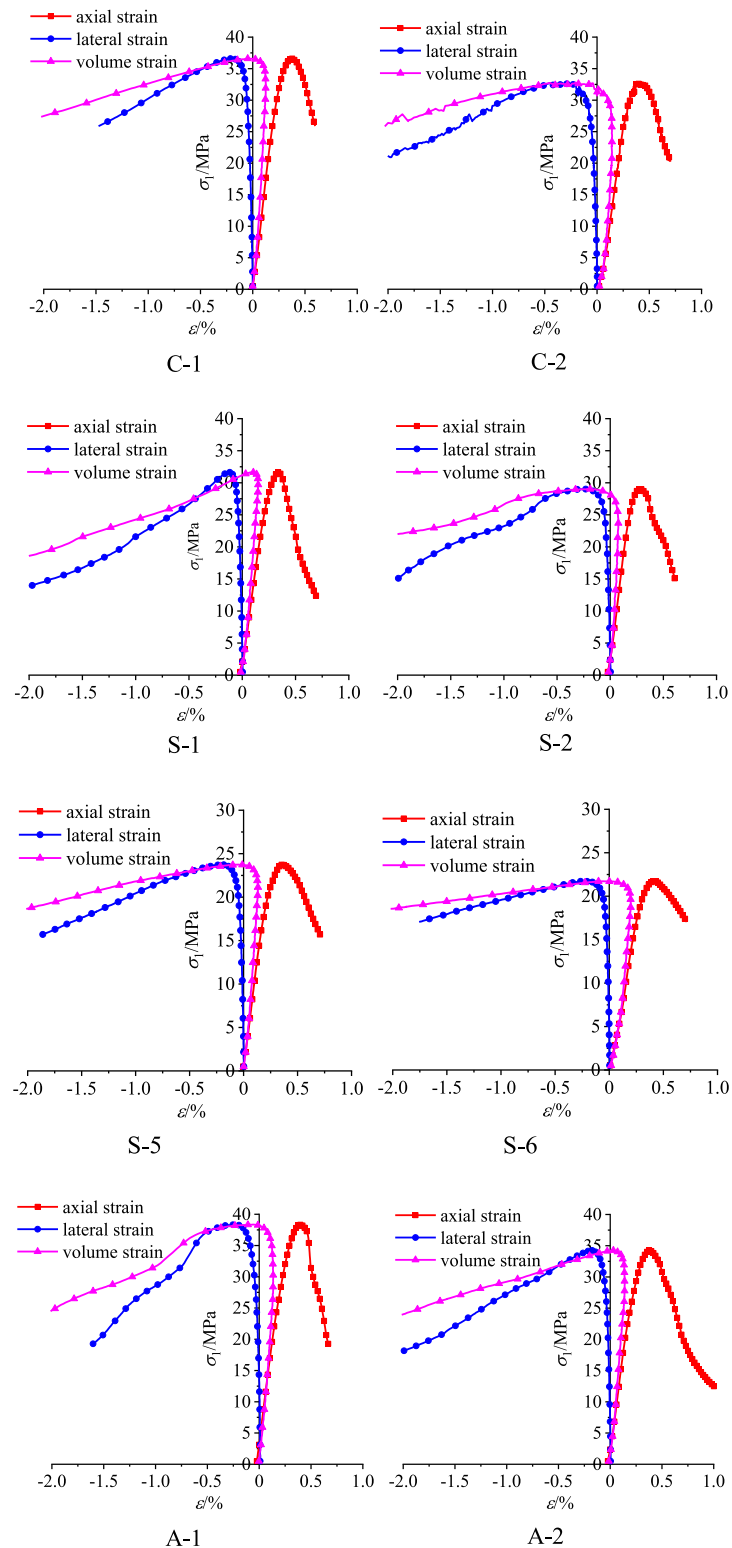


FIGURE 5 | Stress-strain curves of the samples.

samples containing nano-SiO₂ were labeled S (a total of eight samples). The saturated concrete samples containing nano-Al₂O₃ were labeled A (a total of eight samples). The saturated concrete

samples containing nano-TiO₂ were labeled T (a total of eight samples). The wave velocity of each sample was tested with a multi-frequency acoustic wave measurement system. The

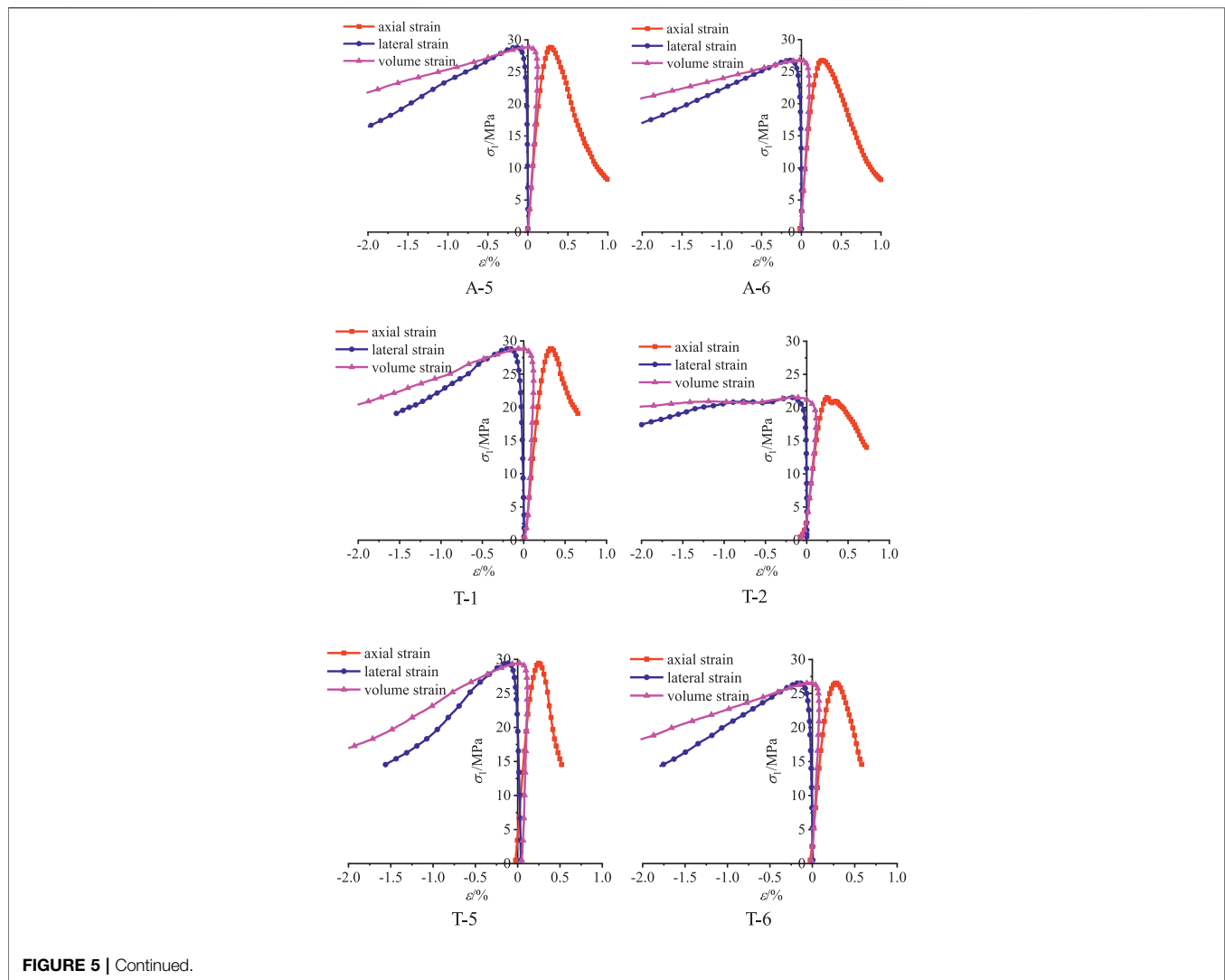


FIGURE 5 | Continued.

numbers of each sample and the results of the wave velocities are shown in Table 3.

Experimental Results: Uniaxial Compression

The axial, lateral, and volumetric stress-strain curves of the samples are shown in Figure 5. Through uniaxial compression experiments, the compressive strength of each sample can be obtained. The elastic modulus, deformation modulus, and Poisson's ratio of these samples can be calculated according to the stress-strain curves.

The damage strength is the starting point for unstable crack growth. The damage strength indicates that many cracks are interconnected. It is well known that crack propagation often leads to the failure of concrete (Hao et al., 2016; Gong et al., 2019; Pan et al., 2019; Hao et al., 2020). Therefore, it is necessary to study the damage strength of concrete. The most commonly used method to determine the damage strength is the crack volume strain calculation method (Martin and Chandler, 1994; Cai et al.,

2004). In the present work, the damage strength of the saturated concrete samples is determined according to the crack volume strain calculation method (Eq. 1):

$$\varepsilon_v = \varepsilon_1 + 2\varepsilon_3 \quad (1)$$

where: ε_1 is the axial strain of the saturated concrete sample, ε_2 is the circumferential strain, and ε_v is the volumetric strain.

Sample S-1 is taken as an example to illustrate the characteristics of the stress-strain curve and the method of determination of the damage strength of saturated concrete. The axial stress-strain curve and volumetric strain curve of sample S-1 under uniaxial compression are shown in Figure 6. It can be seen that the axial stress-strain curve and volumetric strain curve of saturated concrete are divided into five stages: crack closure (Stage I), elastic behavior (Stage II), stable crack growth (Stage III), unstable crack growth (Stage IV), and failure (Stage V). In Stage I, the crack volumetric strain is positive, and the slope of the curve is positive, which indicates the initial cracks, pores, etc. inside the sample are closed under axial stress, resulting in reduction in the volume of the crack and the sample.

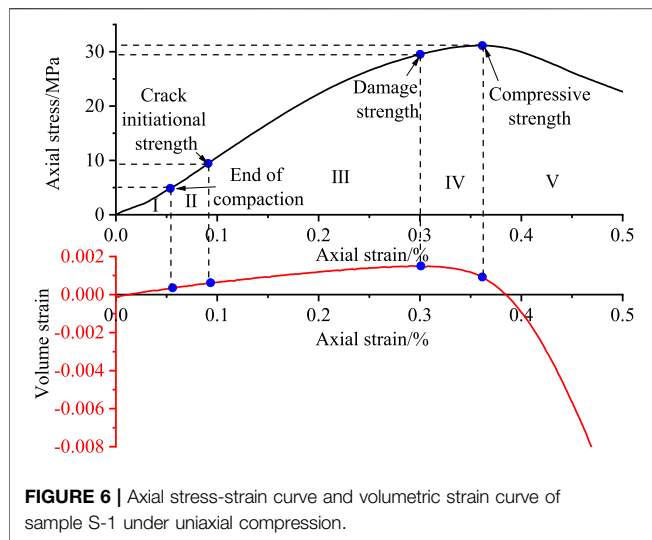


FIGURE 6 | Axial stress-strain curve and volumetric strain curve of sample S-1 under uniaxial compression.

In the elastic stage (Stage II), the axial stress-strain curve is quasi-linear, and the slope of the curve remains practically unchanged. At this stage, the volume strain of the sample is mainly elastic volume strain, there is almost no crack initiation inside the sample, and the crack volume strain has no obvious change. During stable crack growth (Stage III), the slope of the stress-strain curve begins to decrease. At this stage, cracks begin to occur inside the sample and begin to gradually expand; because the volumetric strain increases upon crack opening, the slope of the volume strain curve in this stage gradually decreases, that is, the rate of change of sample volume decreases. During unstable crack growth (Stage IV), the stress-strain graph becomes non-linear and a peak appears therein. The slope of the stress-strain curve decreases with increasing load, and the rate of change of strain also increases. Many cracks penetrate through the sample, and the volume of the sample begins to increase. Due thereto, the slope of the volumetric strain curve becomes negative. After the stress reaches its peak value, the sample begins to fail (Stage V): the sample volume increases rapidly, and the volumetric strain continuously decreases. Therefore, the demarcation point between the elastic stage and the stable crack growth stage, that is, the stress value corresponding to the inflection point of the crack volume strain slope from positive to negative is the crack initiation strength of the S-1. the demarcation point between the stable crack growth and the unstable crack growth stage, that is, the stress value corresponding to the inflection point of the volume strain slope from positive to negative is the damage strength of S-1, and the damage strength of sample S1 can be determined to be 29.653 MPa.

Using the same method, the damage strength of all samples can be determined. The compressive strength, damage strength, elastic modulus, deformation modulus, and Poisson's ratio of each sample are listed in **Table 4**.

Analysis

According to the measured compressive strength and wave velocity of ordinary saturated concrete samples, the

compressive strength of ordinary saturated concrete samples corresponding to arbitrary wave speeds can be calculated by **Eq. 2**. Comparing the compressive strength of the nano-saturated concrete sample with the compressive strength at the same wave velocity of the ordinary saturated concrete sample, the effect of nanomaterial addition on the compressive strength of saturated concrete can be obtained. The effect of nanomaterials on the deformation modulus, elastic modulus, and damage strength can also be compared by the aforementioned methods, so will not be repeated later.

$$\sigma_n = \sigma_{min} + \frac{\sigma_{max} - \sigma_{min}}{v_{max} - v_{min}} \times v_n \quad (2)$$

where: v_n is the wave velocity. σ_n is the compressive strength at the corresponding wave velocity; σ_{min} and σ_{max} are the minimum and maximum compressive strength of ordinary saturated concrete samples, respectively; v_{min} and v_{max} are the minimum and maximum wave velocity of ordinary saturated concrete samples, respectively.

Compressive Strength

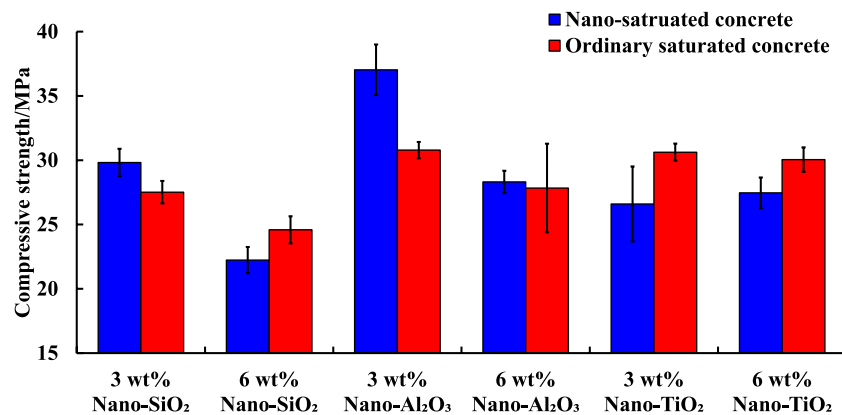
The compressive strength of various types of saturated concrete samples is shown in **Figure 7**. It can be seen that the compressive strength of saturated concrete is affected by the addition of nanomaterials, and the modifying effects of different contents and types of nanomaterials on the compressive strength of concrete also vary.

For the saturated concrete samples containing nano-SiO₂, the compressive strength of saturated concrete samples containing 3 wt% nano-SiO₂ is significantly increased compared with that of ordinary saturated concrete samples, with an average increase of 8.56%; however, when the added amount of nano-SiO₂ is increased to 6 wt%, the compressive strength of nano-saturated concrete sample is decreased relative to that of ordinary saturated concrete samples, indicating that the content of 6 wt% nano-SiO₂ has exceeded its optimum level. The above results indicate that the compressive strength of saturated concrete samples does not always increase with the increase of the nano-SiO₂ content. When the content of nano-SiO₂ exceeds a certain value, the addition of nanomaterials not only fails to increase the strength of saturated concrete but decreases it.

For the saturated concrete samples containing nano-Al₂O₃, the compressive strength of saturated concrete samples containing 3 wt% nano-Al₂O₃ is also increased compared with ordinary saturated concrete samples, with an average increase of 20.27%. The modifying effect is better than that in samples containing the same amount of nano-SiO₂. The compressive strength of the samples containing 6 wt% nano-Al₂O₃ shows two different outcomes compared with that of ordinary saturated concrete samples: some are greater than that of ordinary saturated concrete samples, such as A-6 and A-8, with an average increase of 14.69%. The increase is lower than that found with 3 wt% nano-Al₂O₃ while the strength of the remaining samples (A-5 and A-7) is lower than that of ordinary saturated concrete samples, with an average decrease of 9.19%,

TABLE 4 | Experimental results: uniaxial compression.

	Number	Compressive strength/MPa	Damage strength/MPa	Elastic modulus/GPa	Deformation modulus/GPa
Ordinary saturated concrete samples	C-1	36.59	32.27	14.26	9.51
	C-2	32.80	26.81	12.24	8.44
	C-3	27.92	22.34	10.79	6.46
	C-4	35.52	30.87	14.06	9.50
	Mean value	33.21	28.07	12.84	8.48
Standard value		3.35	3.87	1.42	1.24
The saturated concrete samples containing 3 wt% nano-SiO ₂	S-1	31.64	29.65	12.49	8.67
	S-2	29.03	23.20	14.14	9.55
	S-3	29.04	19.12	7.80	6.80
	S-4	29.58	21.30	10.22	7.64
	Mean value	29.82	23.32	11.16	8.17
Standard value		1.07	3.93	2.39	1.04
The saturated concrete samples containing 6 wt% nano-SiO ₂	S-5	23.74	19.12	10.21	6.35
	S-6	21.72	19.12	8.23	5.35
	S-7	20.98	19.84	9.42	6.02
	S-8	22.49	18.69	9.40	6.09
	Mean value	22.23	19.19	9.32	5.95
Standard value		1.02	0.41	0.71	0.37
The saturated concrete samples containing 3 wt% nano-Al ₂ O ₃	A-1	38.36	29.72	12.69	9.22
	A-2	34.25	29.49	13.18	8.46
	A-3	38.49	32.43	11.66	8.63
	Mean value	37.03	30.54	12.51	8.77
	Standard value	1.97	1.33	0.64	0.33
The saturated concrete samples containing 6 wt% nano-Al ₂ O ₃	A-5	28.87	25.28	15.44	10.03
	A-6	26.81	22.59	15.14	9.31
	A-7	28.68	23.97	15.45	9.64
	A-8	28.87	25.09	14.49	8.21
	Mean value	28.31	24.23	15.13	9.30
Standard value		0.87	1.07	0.39	0.68
The saturated concrete samples containing 3 wt% nano-TiO ₂	T-1	28.87	23.70	13.80	8.69
	T-2	21.61	17.89	10.65	6.51
	T-3	27.41	22.13	11.81	7.81
	T-4	28.48	23.07	12.84	7.83
	Mean value	26.60	21.70	12.28	7.71
Standard value		2.93	2.27	1.17	0.78
The saturated concrete samples containing 6 wt% nano-TiO ₂	T-5	29.46	25.92	15.85	10.52
	T-6	26.58	22.72	13.92	8.40
	T-7	27.30	24.91	15.59	10.08
	T-8	26.50	23.95	13.91	8.78
	Mean value	27.46	24.37	14.82	9.45
Standard value		1.19	1.18	0.91	0.88

**FIGURE 7 |** Compressive strength of various types of saturated concrete samples.

indicating that the content of nano- Al_2O_3 has exceeded its optimum content at 6 wt%.

The results of the saturated concrete samples containing nano- TiO_2 are different from the results of nano- SiO_2 and nano- Al_2O_3 . As can be seen from **Figure 7**, the compressive strength of samples containing 3 wt% nano- TiO_2 and 6 wt% nano- TiO_2 is both decreased relative to that of ordinary saturated concrete samples. The reason may be that the nano- TiO_2 has exceeded its optimal content at 3 wt%, which leads to the decrease in compressive strength of saturated concrete samples.

In summary, the compressive strength of saturated concrete can be increased by the addition of nanomaterials, but the compressive strength does not always increase with the increased dosage of nanomaterials. When the amount of added nanomaterial exceeds a certain value, the compressive strength of saturated concrete materials is decreased instead. The optimal content of different types of nanomaterials in concrete samples is also different: when the content of nanomaterials is 3 wt%, the modifying effect of nano- Al_2O_3 on the compressive strength of saturated concrete is the best, followed by that of nano- SiO_2 , whereas with nano- TiO_2 the compressive strength is decreased. At a nanomaterial content of 6 wt%, all nanomaterials have exceeded their optimum content.

In addition, for saturated concrete samples containing nano- SiO_2 and nano- Al_2O_3 , the modifying effect on the compressive strength when the content of nanomaterials is 3 wt% is better than that at 6 wt%, however, the modifying effect of nano- Al_2O_3 on the compressive strength of saturated concrete is better than that of nano- SiO_2 , which is consistent with the modifying effect of nanomaterials on the microstructure seen under the SEM.

Deformation Modulus

The deformation modulus of various types of saturated concrete samples is shown in **Figure 8**: the deformation modulus of saturated concrete samples containing nanomaterials is generally larger than that of ordinary saturated concrete, but the modifying effect of different nanomaterials is different.

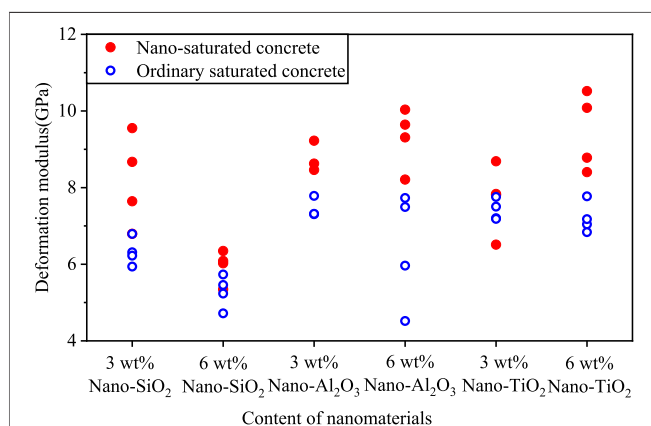


FIGURE 8 | Comparison of deformation modulus of various types of samples.

For saturated concrete samples containing nano- SiO_2 , the deformation modulus of saturated concrete samples containing 3 wt% nano- SiO_2 is increased compared with ordinary saturated concrete samples, with an average increase of 29.77%. The deformation modulus of saturated concrete samples containing 6 wt% nano- SiO_2 is also increased compared with ordinary saturated concrete samples, with an average increase of 13.39%. This shows that the modifying effect on the deformation modulus of saturated concrete when the content of nano- SiO_2 is 3 wt% is better than that at 6 wt%.

For saturated concrete samples containing nano- Al_2O_3 , the deformation modulus of saturated concrete samples containing 3 wt% nano- Al_2O_3 is increased compared with that of ordinary saturated concrete samples, with an average increase of 17.57%. The deformation modulus of saturated concrete samples containing 6 wt% nano- Al_2O_3 is also increased compared with that of ordinary saturated concrete samples, with an average increase of 50.56%. This shows that the modifying effect on the deformation modulus of saturated concrete when the nano- Al_2O_3 content is 6 wt% is better than that at 3 wt%.

For the saturated concrete samples containing nano- TiO_2 , the deformation modulus of saturated concrete samples containing 3 wt% nano- TiO_2 is increased compared with that of ordinary saturated concrete samples, with an average increase of 4.08%. The deformation modulus of saturated concrete samples containing 6 wt% nano- TiO_2 is also increased compared with that of ordinary saturated concrete samples, with an average increase of 31.11%. This shows that the modifying effect on the deformation modulus of saturated concrete when the nano- TiO_2 content is 6 wt% is better than that at 3 wt%.

These results can be explained by the fact that the addition of nanomaterials to the saturated concrete material can increase the deformation modulus, that is, the stiffness of the saturated concrete is increased. The optimal amount of different nanomaterials in saturated concrete also varies: the modifying effect of 3 wt% nano- SiO_2 on the deformation modulus of saturated concrete is better than that at 6 wt% nano- SiO_2 . For nano- Al_2O_3 and nano- TiO_2 , the modifying effect of 6 wt% nanomaterials on the deformation modulus of saturated concrete is better than that at 3 wt%. Among all the samples tested here, the modifying effect of 6 wt% nano- Al_2O_3 on the deformation modulus of saturated concrete is the best.

It can also be seen from the figure that, although the deformation modulus of most saturated concrete samples containing nanomaterials is greater than that of ordinary saturated concrete samples, there are a few exceptions: for example, the deformation modulus of S-6 and T-2 is lower than that of ordinary saturated concrete samples. The results in **Discussion section** show that the compressive strength of these two samples is also far lower than that of ordinary saturated concrete.

Elastic Modulus

The elastic modulus of various types of saturated concrete is shown in **Figure 9**. The comparison of elastic modulus between the nano-saturated concrete and ordinary saturated concrete is similar to that undertaken for deformation modulus (except for

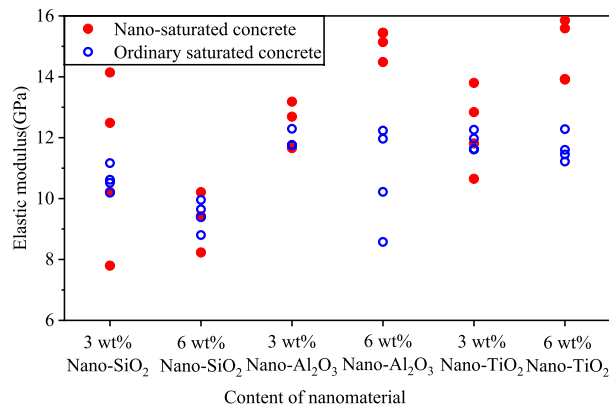


FIGURE 9 | Comparison of elastic modulus of various types of samples.

those samples containing 6 wt% nano-SiO₂, with little significant difference from that of ordinary saturated concrete).

Damage Strength

The damage strength of various types of saturated concrete is shown in Figure 10: for the saturated concrete sample containing nano-SiO₂, when the content of nano-SiO₂ is 3 wt% (S-1, S-2, S-3, and S-4), the damage strength of S-1 and S-2 is larger than that of ordinary saturated concrete, the damage strength of S-3 and S-4 is less than that of ordinary saturated concrete, but the average damage strength of nano-saturated concrete is larger than that of ordinary saturated concrete. When the content of nano-SiO₂ is 6 wt% (S-5, S-6, S-7, and S-8), the damage strength of S-7 and S-8 is larger than that of ordinary saturated concrete samples, the damage strength of S-6 is less than that of ordinary saturated concrete samples, and the damage strength of S-5 is similar to that of ordinary saturated concrete samples.

For the saturated concrete sample containing nano-Al₂O₃, when the nano-Al₂O₃ content is 3 wt% (A-1, A-2, and A-3), the

damage strength of nano-saturated concrete samples is larger than that of ordinary saturated concrete samples, and the modifying effect of 3 wt% nano-Al₂O₃ on the damage strength of saturated concrete is significantly better than that of the relative content of nano-SiO₂. When the nano-Al₂O₃ content is 6 wt% (A-5, A-6, A-7, and A-8), the damage strength of some samples (A-6 and A-8) is larger than that of ordinary saturated concrete samples, and the damage strength of other samples (A-5 and A-7) is less than that of ordinary saturated concrete samples.

For the saturated concrete sample containing nano-TiO₂, except for T-7, the damage strength of ordinary saturated concrete samples is larger than that of nano-saturated concrete samples.

In summary, for saturated concrete samples containing nano-SiO₂ and those saturated concrete samples containing nano-Al₂O₃, the damage strength of the saturated concrete is increased by the addition of nanomaterials when the content thereof is 3 wt%, and the modifying effect of 3 wt% nano-Al₂O₃ on the damage strength of saturated concrete is significantly

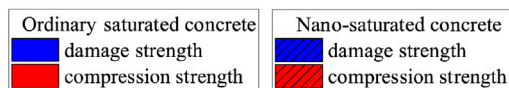
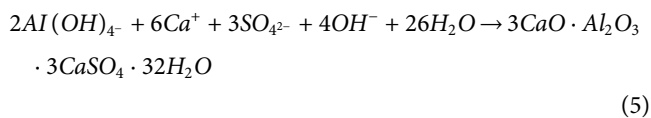
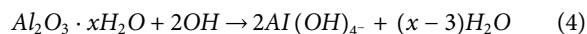
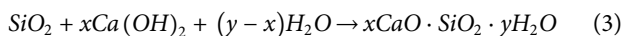


FIGURE 10 | Comparison of damage strength of various types of saturated concrete samples.

better than that of same relative amount of nano-SiO₂. When the content of nanomaterials is 6 wt%, the addition thereof has a little effect on the damage strength. For the saturated concrete sample containing nano-TiO₂, when the content of nano-TiO₂ is 3 wt%, the content may have exceeded its optimal level in saturated concrete, therefore, the addition of nano-TiO₂ reduces the damage strength of saturated concrete.

Through the above analysis, it can be seen that adding nanomaterials to saturated concrete can optimize its microstructure and improve its strength, modulus and other mechanical properties. The main reasons are the following two aspects: on the one hand, nanomaterials have a small particle size and can fill the internal pores of concrete. On the other hand, nanomaterials have higher specific surface energy, which can promote and participate in the hydration reaction of cement, reacting off excess Ca(OH)₂ (harmful to mechanical properties), and generate more C-S-H gels and other materials, which can improve mechanical properties, as shown in Eqs. 3, 4, 5.



It can also be seen from the formula that both nano SiO₂ and nano Al₂O₃ can participate in the hydration reaction of cement, while nano TiO₂ only can promote the hydration reaction of cement, which leads to the poor mechanical properties of saturated concrete samples containing nano TiO₂ compared with the other two nanomaterials. And the nano-SiO₂ and nano-Al₂O₃ participate in the cement hydration reaction to produce different products, resulting in different microstructures of the two samples. The difference in the microstructure also determines the difference in mechanical properties.

DISCUSSION

The compressive strength of concrete is affected by the amount of nanomaterial added to the concrete, and the extent of this influence may be affected by the properties of the concrete. The saturation of the concrete may also be one of the influencing factors, however, no research has been done on the different effects of nanomaterial contents on the compressive strength of saturated concrete and dry concrete (Rossi et al., 1992; Ross et al., 1996; Yaman et al., 2002a; Yaman et al., 2002b; Wang and Li, 2007; Zheng and Li, 2010; Jin et al., 2012).

To compare the different effects of nanomaterial contents on the compressive strength of saturated concrete and dry concrete, the compressive strength of saturated concrete (in this paper) and dry concrete (Li et al., 2006b; Zhang and Li, 2006; Nazari and Riahi, 2011; Said et al., 2012; Mohseni et al., 2015; Rong et al., 2015; Su et al., 2017; Niewiadomski et al.,

2018; Ren et al., 2018; Du, 2019) when the nanomaterial content was 3 wt% and the nanomaterial content exceeded 3 wt% was analyzed.

The changes in compressive strength of nano-saturated concrete and nano-dry concrete compared to ordinary concrete are shown in **Figure 11** (at a nanomaterial content of 3 wt%). For the concrete samples containing nano-SiO₂ and nano-Al₂O₃, when the nanomaterial content is 3 wt%, although the increase in compressive strength of nano-saturated concrete and nano-dry concrete compared to ordinary concrete is different, the compressive strength of nano-saturated concrete and nano-dry concrete is increased compared to that of ordinary concrete.

For concrete sample containing nano-TiO₂, when the nano-TiO₂ content is 3 wt%, the compressive strength of nano-saturated concrete is lower than that of ordinary concrete, but the compressive strength of nano-dry concrete varies compared to ordinary concrete; the compressive strength of most nano-dry concrete samples is higher than that of ordinary concrete. It is reported elsewhere (Siddiqui et al., 2016) that the compressive strength of nano-dry concrete containing 3 wt% nano-TiO₂ is lower than that of ordinary concrete, but the reduction is smaller than that for nano-saturated concrete. This suggests that, when the content of nano-TiO₂ is 3 wt%, the increase in compressive strength of saturated concrete compared to ordinary concrete is lower than that for dry concrete.

The increase in compressive strength of nano-concrete containing more than 3 wt% nanomaterials compared to nano-concrete containing 3 wt% nanomaterials is shown in **Figure 12**: for saturated concrete samples containing nano-SiO₂, when the nano-SiO₂ content exceeds 3 wt%, the compressive strength of the nano-saturated concrete sample decreases compared to that at 3 wt%. For dry concrete samples containing nano-SiO₂, when the nano-SiO₂ content exceeds 3 wt%, the compressive strength of a few samples increases compared to that when the nano-SiO₂ content is 3 wt%, and the compressive strength of most samples decreases, but the decrease in the dry concrete is less than that in the saturated concrete.

For concrete samples containing nano-Al₂O₃, when the nano-Al₂O₃ content exceeds 3 wt%, the compressive strength of each concrete sample decreases compared to that at 3 wt%, but the decrease in the saturated concrete is greatest.

For concrete samples containing nano-TiO₂, when the nano-TiO₂ content exceeds 3 wt%, the compressive strength of the nano-saturated concrete samples increases compared with that at 3 wt%. The compressive strength of most nano-dry concrete samples decreases compared with that at 3 wt%.

These results suggest that the compressive strength of both saturated concrete and dry concrete does not always increase with increasing nanomaterial content. When the content of nanomaterials exceeds its optimal level, the increase in compressive strength of the concrete is reduced: for saturated concrete samples containing more than 3 wt% nano-SiO₂ and saturated concrete samples containing more than 3 wt% nano-Al₂O₃, the compressive strength decreases more compared to nano-concrete samples containing 3 wt% nanomaterials for dry concrete samples. This shows that, when the nano-concrete is

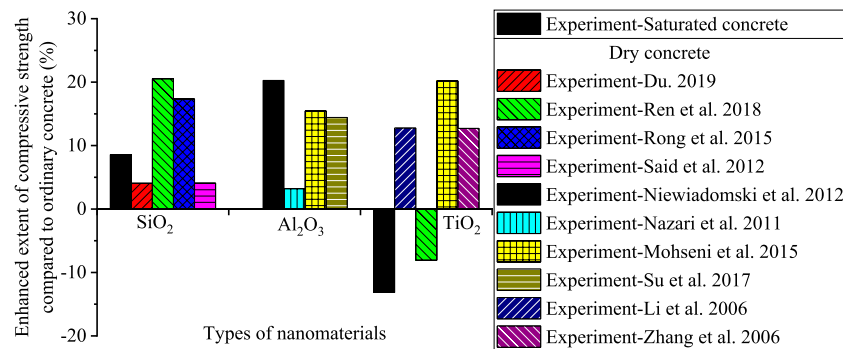


FIGURE 11 | The change in compressive strength of nano-concrete (at a nanomaterial content of 3 wt%) compared to ordinary concrete.

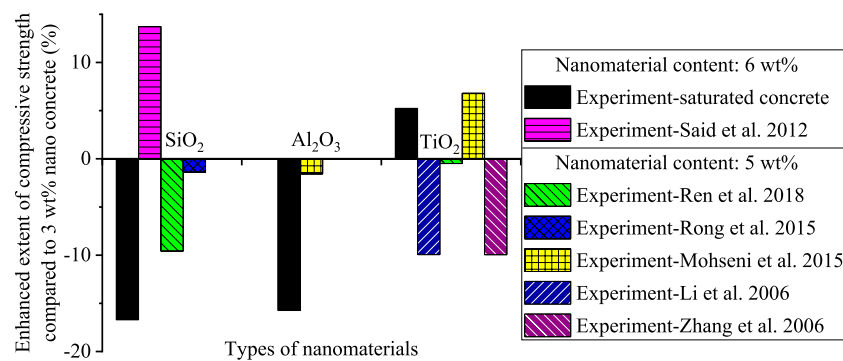


FIGURE 12 | The increase in compressive strength of nano-concrete containing more than 3 wt% nanomaterials compared to nano-concrete containing 3 wt% nanomaterials.

saturated, the modifying effect of nanomaterials on the mechanical properties of concrete is diminished.

CONCLUSION

The mechanical properties of saturated concrete are of importance when ensuring the long-term safe and stable operation of hydraulic structures. In this research, scanning electron microscopy, wave velocity, and uniaxial compression were conducted to assess the influence of different nanomaterials added in different amounts on saturated concrete. The conclusions are as follows:

- By the addition of various kinds of nanomaterials to saturated concrete, the microstructure of saturated concrete can be significantly improved, the internal particles are refined, the porosity is reduced, and the compactness and integrity of the slurry are improved. For three different types of nano-saturated concrete samples, the microstructure of samples containing nano-Al₂O₃ is more uniform and compact, and its integrity is optimal.
- Compared with ordinary saturated concrete, the mechanical properties of saturated concrete such as strength,

deformation modulus, and elastic modulus are significantly improved by the addition of 3 wt% nanomaterials; however, the mechanical properties of saturated concrete do not always increase with the increase of the nanomaterial content. When the nanomaterial content is 6 wt%, the compressive strength of the three types of nano-saturated concrete sample decreases compared with that of ordinary saturated concrete samples. Among all saturated concrete samples tested here, the compressive strength of the saturated concrete sample containing 3 wt% nano-Al₂O₃ is the largest, the deformation modulus of the saturated concrete sample containing 6 wt% nano-Al₂O₃ is the largest.

- For concrete samples containing 3 wt% nano-SiO₂ and those containing 3 wt% nano-Al₂O₃, the compressive strength of nano-dry concrete sample and nano-saturated concrete sample is larger than that of the ordinary concrete sample, and the increase in compressive strength is similar, but when the nano-SiO₂ and nano-Al₂O₃ contents are 6 wt %, the increase in compressive strength compared to ordinary concrete is decreased, and the weakening effect on the compressive strength of saturated concrete is more obvious. For the sample containing 3 wt% nano-TiO₂, the compressive strength of most of the nano-dry concrete

samples is increased compared with that of ordinary concrete but the compressive strength of the nano-saturated concrete sample is decreased compared with that of ordinary concrete. Compared with dry concrete, when the concrete is saturated, the modifying effect of nanomaterials on the mechanical properties of concrete is diminished.

The artificial dam body of coal mine underground reservoir is complicated in force. In addition to compressive stress, it will also be affected by static forces such as tensile stress and shear stress, as well as dynamic forces such as mining and earthquakes. The mechanical behavior of nanomodified concrete under different stress states will be studied later.

DATA AVAILABILITY STATEMENT

The raw data supporting the conclusion of this article will be made available by the authors, without undue reservation.

REFERENCES

- Bian, H., Jia, Y., Pontiroli, C., and Shao, J.-F. (2017). Numerical Modeling of the Elastoplastic Damage Behavior of Dry and Saturated concrete Targets Subjected to Rigid Projectile Penetration. *Int. J. Numer. Anal. Methods Geomech.* 42 (10), 312–338. doi:10.1002/nag.2744
- Cai, M., Kaiser, P. K., Tasaka, Y., Maejima, T., Morioka, H., and Minami, M. (2004). Generalized Crack Initiation and Crack Damage Stress Thresholds of Brittle Rock Masses Near Underground Excavations. *Int. J. Rock Mech. Mining Sci.* 41 (5), 833–847. doi:10.1016/j.ijrmms.2004.02.001
- Cao, S., Xue, G., Yilmaz, E., Yin, Z., and Yang, F. (2021). Utilizing concrete Pillars as an Environmental Mining Practice in Underground Mines. *J. Clean. Prod.* 278, 123433. doi:10.1016/j.jclepro.2020.123433
- Cao, S., Zheng, D., Yilmaz, E., Yin, Z., Xue, G., and Yang, F. (2020). Strength Development and Microstructure Characteristics of Artificial concrete Pillar Considering Fiber Type and Content Effects. *Construction Building Mater.* 256, 119408. doi:10.1016/j.conbuildmat.2020.119408
- Deng, Z. Y. (2012). Mechanical Properties Research on Concrete Block Doped Nano-TiO₂ under the Conditions of Common Conservation. *Appl. Mech. Mater.* 238, 9–12. doi:10.4028/www.scientific.net/AMM.238.9
- Du, H., Du, S., and Liu, X. (2015). Effect of Nano-Silica on the Mechanical and Transport Properties of Lightweight concrete. *Construction Building Mater.* 82, 114–122. doi:10.1016/j.conbuildmat.2015.02.026
- Du, H. (2019). Properties of Ultra-lightweight Cement Composites with Nano-Silica. *Construction Building Mater.* 199, 696–704. doi:10.1016/j.conbuildmat.2018.11.225
- Gong, F., Yan, J., Luo, S., and Li, X. (2019). Investigation on the Linear Energy Storage and Dissipation Laws of Rock Materials under Uniaxial Compression. *Rock Mech. Rock Eng.* 52, 4237–4255. doi:10.1007/s00603-019-01842-4
- Hao, X.-J., Feng, X.-T., Yang, C.-X., Jiang, Q., and Li, S.-J. (2016). Analysis of EDZ Development of Columnar Jointed Rock Mass in the Baihetan Diversion Tunnel. *Rock Mech. Rock Eng.* 49, 1289–1312. doi:10.1007/s00603-015-0829-4
- Hao, X., Du, W., Zhao, Y., Sun, Z., Zhang, Q., Wang, S., et al. (2020). Dynamic Tensile Behaviour and Crack Propagation of Coal under Coupled Static-Dynamic Loading. *Int. J. Mining Sci. Tech.* 30 (5), 659–668. doi:10.1016/j.ijmst.2020.06.007
- Hong, Z.-j., Zuo, J.-p., Zhang, Z.-s., Liu, C., Liu, L., and Liu, H.-y. (2020). Effects of Nano-clay on the Mechanical and Microstructural Properties of Cement-Based Grouting Material in Sodium Chloride Solution. *Construction Building Mater.* 245, 118420. doi:10.1016/j.conbuildmat.2020.118420
- Jalal, M., Pouladkhan, A., Harandi, O. F., and Jafari, D. (2015). Comparative Study on Effects of Class F Fly Ash, Nano Silica and Silica Fume on Properties of High Performance Self Compacting concrete. *Construction Building Mater.* 94, 90–104. doi:10.1016/j.conbuildmat.2015.07.001
- Jin, L., Du, X., and Ma, G. (2012). Macroscopic Effective Moduli and Tensile Strength of Saturated concrete. *Cement Concrete Res.* 42 (12), 1590–1600. doi:10.1016/j.cemconres.2012.09.012
- Kaji, T., and Fujiyama, C. (2014). Mechanical Properties of Saturated concrete Depending on the Strain Rate. *Proced. Eng.* 95, 442–453. doi:10.1016/j.proeng.2014.12.204
- Li, H., Zhang, M.-h., and Ou, J.-p. (2006a). Abrasion Resistance of concrete Containing Nano-Particles for Pavement. *Wear* 260 (11–12), 1262–1266. doi:10.1016/j.wear.2005.08.006
- Li, Z., Wang, H., He, S., Lu, Y., and Wang, M. (2006b). Investigations on the Preparation and Mechanical Properties of the Nano-Alumina Reinforced Cement Composite. *Mater. Lett.* 60, 356–359. doi:10.1016/j.matlet.2005.08.061
- Liu, R., Xiao, H., Li, H., Sun, L., Pi, Z., Waqar, G. Q., et al. (2018). Effects of Nano-SiO₂ on the Permeability-Related Properties of Cement-Based Composites with Different Water/cement Ratios. *J. Mater. Sci.* 53 (7), 4974–4986. doi:10.1007/s10853-017-1906-8
- Lu, W., Wang, Q., Jiang, B., Xu, S., Liu, B., Zhang, P., et al. (2019). Comparative Study on Bearing Mechanism and Design Parameters of Confined concrete Arch Joints in Deep Soft Rock Roadway. *Int. J. Coal Sci. Technol.* 6, 493–504. doi:10.1007/s40789-019-00272-5
- Martin, C. D., and Chandler, N. A. (1994). The progressive fracture of Lac du Bonnet granite. *Int. J. Rock Mech. Mining Sci. Geomechanics Abstr.* 31 (6), 643–659. doi:10.1016/0148-9062(94)90005-1
- Mohseni, E., Miyandehi, B. M., Yang, J., and Yazdi, M. A. (2015). Single and Combined Effects of Nano-SiO₂, Nano-Al₂O₃ and Nano-TiO₂ on the Mechanical, Rheological and Durability Properties of Self-Compacting Mortar Containing Fly Ash. *Construction Building Mater.* 84, 331–340. doi:10.1016/j.conbuildmat.2015.03.006
- Nazari, A., and Riahi, S. (2011). Effects of Al₂O₃ Nanoparticles on Properties of Self Compacting concrete with Ground Granulated Blast Furnace Slag (GGBFS) as Binder. *Sci. China Technol. Sci.* 54, 2327–2338. doi:10.1007/s11431-011-4440-y
- Niewiadomski, P., Hoła, J., and Ćwirzeń, A. (2018). Study on Properties of Self-Compacting concrete Modified with Nanoparticles. *Arch. Civil Mech. Eng.* 18 (3), 877–886. doi:10.1016/j.acme.2018.01.006
- Pan, W., Wang, X., Liu, Q., Yuan, Y., and Zuo, B. (2019). Non-parallel Double-Crack Propagation in Rock-like Materials under Uniaxial Compression. *Int. J. Coal Sci. Technol.* 6, 372–387. doi:10.1007/s40789-019-0255-4
- Ren, J., Lai, Y., and Gao, J. (2018). Exploring the Influence of SiO₂ and TiO₂ Nanoparticles on the Mechanical Properties of concrete. *Construction Building Mater.* 175, 277–285. doi:10.1016/j.conbuildmat.2018.04.181

AUTHOR CONTRIBUTIONS

XH designed the experiment and samples; YW and ZC prepared samples; YW, ZC, and HZ performed the experiments under the supervision of XH; XH, YW and YN analyzed the data; and XH, YW and ZC write the paper. All authors read and approved the final manuscript.

FUNDING

This article is supported by the National Natural Science Foundation of China (51804309), Yue Qi Young Scholar Project (2019QN02) and Distinguished Scholar Project (2017JCB02) from China University of Mining and Technology (Beijing), Joint Fund of State Key Laboratory of Coal Resources and Safe Mining- and Beijing Outstanding Young Scientist Program (Grant No SKLCSRSM20LH01 and BJWZYJH01201911413037), National Natural Science Foundation of China (51861145403, 51874312, U1910206).

- Rong, Z., Sun, W., Xiao, H., and Jiang, G. (2015). Effects of Nano-SiO₂ Particles on the Mechanical and Microstructural Properties of Ultra-high Performance Cementitious Composites. *Cement and Concrete Composites*. 56, 25–31. doi:10.1016/j.cemconcomp.2014.11.001
- Ross, C. A., Jerome, D. M., and Joseph, W. T. (1996). Moisture and Strain Rate Effects on Concrete Strength. *ACI Mater. J.* 93 (3), 293–300. doi:10.14359/9814
- Rossi, P., van Mier, J. G. M., Boulay, C., and Le Maou, F. (1992). The Dynamic Behaviour of concrete: Influence of Free Water. *Mater. Structures*. 25, 509–514. doi:10.1007/BF02472446
- Said, A. M., Zeidan, M. S., Bassuoni, M. T., and Tian, Y. (2012). Properties of concrete Incorporating Nano-Silica. *Construction Building Mater.* 36, 838–844. doi:10.1016/j.conbuildmat.2012.06.044
- Shaikh, F., Chavda, V., Minhaj, N., and Arel, H. S. (2017). Effect of Mixing Methods of Nano Silica on Properties of Recycled Aggregate concrete. *Struct. Concrete*. 19 (6), 387–399. doi:10.1002/suco.201700091
- Siddiqui, M. S., Grasley, Z., and Fowler, D. W. (2016). Internal Water Pressure Development in Saturated concrete cylinder Subjected to Coefficient of thermal Expansion Tests: Poroelastic Model. *Construction Building Mater.* 112, 996–1004. doi:10.1016/j.conbuildmat.2016.02.081
- Su, Y., Wu, C., Li, J., Li, Z.-X., and Li, W. (2017). Development of Novel Ultra-high Performance concrete: From Material to Structure. *Construction Building Mater.* 135, 517–528. doi:10.1016/j.conbuildmat.2016.12.175
- Wang, H., and Li, Q. (2007). Prediction of Elastic Modulus and Poisson's Ratio for Unsaturated concrete. *Int. J. Sol. Structures*. 44 (5), 1370–1379. doi:10.1016/j.ijsolstr.2006.06.028
- Wang, H., Wang, L., Song, Y., and Wang, J. (2016). Influence of Free Water on Dynamic Behavior of Dam concrete under Biaxial Compression. *Construction Building Mater.* 112, 222–231. doi:10.1016/j.conbuildmat.2016.02.090
- Yaman, I. O., Aktan, H. M., and Hearn, N. (2002a). Active and Non-active Porosity in concrete Part II: Evaluation of Existing Models. *Mat. Struct.* 35 (2), 110–116. doi:10.1007/BF02482110
- Yaman, I. O., Hearn, N., and Aktan, H. M. (2002b). Active and Non-active Porosity in concrete Part I: Experimental Evidence. *Mat. Struct.* 35 (2), 102–109. doi:10.1007/BF02482109
- Yang, Z., Gao, Y., Mu, S., Chang, H., Sun, W., and Jiang, J. (2019). Improving the Chloride Binding Capacity of Cement Paste by Adding Nano-Al₂O₃. *Construction Building Mater.* 195, 415–422. doi:10.1016/j.conbuildmat.2018.11.012
- Zhang, M.-h., and Li, H. (2006). The Resistance to Chloride Penetration of concrete Containing Nano-Particles for Pavement. *Proc. Spie-int. Soc. Opt. Eng.* 6175, 1–8. doi:10.1117/12.660882
- Zhang, R., Cheng, X., Hou, P., and Ye, Z. (2015). Influences of Nano-TiO₂ on the Properties of Cement-Based Materials: Hydration and Drying Shrinkage. *Construction Building Mater.* 81, 35–41. doi:10.1016/j.conbuildmat.2015.02.003
- Zheng, D., and Li, X. X. (2010). Prediction of Saturate Concrete Elastic Modulus by Considering Pores and Microcracks. *Amr.* 168–170, 594–598. doi:10.4028/www.scientific.net/AMR.168-170.594
- Zhou, J., Zheng, K., Liu, Z., and He, F. (2019). Chemical Effect of Nano-Alumina on Early-Age Hydration of Portland Cement. *Cement Concrete Res.* 116, 159–167. doi:10.1016/j.cemconres.2018.11.007
- Zuo, J.-p., Hong, Z.-j., Xiong, Z.-q., Wang, C., and Song, H.-q. (2018). Influence of Different W/C on the Performances and Hydration Progress of Dual Liquid High Water Backfilling Material. *Construction Building Mater.* 190, 910–917. doi:10.1016/j.conbuildmat.2018.09.146

Conflict of Interest: YW was employed by Zhengzhou Coal Mining Machinery (Group) Co., Ltd.

The remaining authors declare that the research was conducted in the absence of any commercial or financial relationships that could be construed as a potential conflict of interest.

Copyright © 2021 Hao, Wei, Chen, Zhang, Niu, Chen and Huang. This is an open-access article distributed under the terms of the Creative Commons Attribution License (CC BY). The use, distribution or reproduction in other forums is permitted, provided the original author(s) and the copyright owner(s) are credited and that the original publication in this journal is cited, in accordance with accepted academic practice. No use, distribution or reproduction is permitted which does not comply with these terms.



Pore Structure Characteristics and Its Effect on Mechanical Performance of Cemented Paste Backfill

Chao Huan^{1,2}, Chao Zhu^{1,2*}, Lang Liu^{1,2}, Mei Wang^{1,2}, Yujiao Zhao^{1,2}, Bo Zhang^{1,2} and Xiaoyan Zhang^{1,2}

¹Energy School, Xi'an University of Science and Technology, Xi'an, China, ²Key Laboratory of Western Mines and Hazards Prevention, Ministry of Education of China, Xi'an, China

OPEN ACCESS

Edited by:

Tingting Zhang,
Dalian University of Technology, China

Reviewed by:

Erol Yilmaz,
Recep Tayyip Erdoğan University,
Turkey
Shuai Cao,
University of Science and Technology
Beijing, China
Xin Chen,
Central South University, China

*Correspondence:

Chao Zhu
zcxx521@126.com

Specialty section:

This article was submitted to
Structural Materials,
a section of the journal
Frontiers in Materials

Received: 27 April 2021

Accepted: 09 June 2021

Published: 19 July 2021

Citation:

Huan C, Zhu C, Liu L, Wang M, Zhao Y,
Zhang B and Zhang X (2021) Pore
Structure Characteristics and Its Effect
on Mechanical Performance of
Cemented Paste Backfill.
Front. Mater. 8:700917.
doi: 10.3389/fmats.2021.700917

The development of cemented paste backfilling (CPB) technology has made an important contribution to the mining economy. As a kind of porous material, the pore structure characteristic of cemented paste backfill (CPB) is strongly correlated to its mechanical properties. In this study, CPB specimens were prepared with tailings/cement ratios (T/C ratio) of 4, 6, 10 and curing durations of 3, 7, 14, and 28 days, respectively. Pore structures characteristics of CPB specimens were investigated using nuclear magnetic resonance (NMR) and scanning electronic microscopy (SEM). The uniaxial compressive strength (UCS) was adopted to illustrate the mechanical property of CPB specimens. The coupling effects of T/C ratio and curing time on the pore characteristics of CPB as well as the effect of pore size on the UCS were analyzed. The results indicated that: 1) the microstructural integrity of CPB was highly related to the development status of the pore structure, which can be represented by micro-parameters like porosity, average pore area, etc. 2) a similar normal distribution curve was observed from the four kinds of pore structure in CPB. As the curing time increased, the peak of the pore size curve shifted left, and the peak value decreased, which means that the pore size in CPB decreased and became much concentrated; 3) the extension of the most probable pore size led to the cross-connection of pores and resulted in the fracture of CPB, which was shown as a crack on the main section.

Keywords: cemented paste backfill, pore structure characteristics, mechanical properties, integrity, damage process

INTRODUCTION

The cemented paste backfill (CPB) technology has been widely used in recent years due to technical, economical, and environmental benefits (Yilmaz et al., 2011a; Lu et al., 2018; Qi et al., 2018a; Liu et al., 2020). In the deep mining, CPB could control the ground pressure to protect mine workers from roof subsidence. Diverting tailing into underground stopes could reduce surface tailing disposal and environmental hazards as well as cut the costs of tailings management (Hu et al., 2004; Yilmaz et al., 2011b; Qi et al., 2018b; Qi et al., 2018c; Cao et al., 2019). Generally, CPB is a kind of three-phase cementitious composite material, that includes solid particles (tailings, cement, etc.), water and pores, produced with three ingredients, i.e., tailings, cement, and mixing water (Benzazaoua et al., 2002; Yilmaz et al., 2010; Li et al., 2016). During the consolidation process of CPB, large numbers of

pores with different size would form around the hydration products, which has an important influence on the mechanical properties (Huang et al., 2021) and flow characteristics (Jiang et al., 2020) of CPB.

At present, scanning electron microscope (SEM) and nuclear magnetic resonance (NMR) are widely used in microstructure analysis of various materials. Due to its good results, high efficiency, and low consumption. SEM has been successfully applied to study the microstructure of concrete, rock, and soil. Complex micro-pore structure characteristics of backfill can be observed through SEM (Xu et al., 2015; Li et al., 2016; Liu et al., 2021). Meanwhile, SEM images can be used to analyze the pore structure, hydration process and hydration products of cementing backfill (Cihangir et al., 2012; Wu et al., 2015; Chen et al., 2017; Koohestani and Belem, 2017; Liu et al., 2017; Chen et al., 2018; Zhou et al., 2014). In order to obtain the quantitative description of SEM images, Liu et al. (2011) developed Particles (Pores) and Cracks Analysis System (PCAS) software, in which the image recognition technology was employed to conduct quantitative analysis on soil microstructure. However, SEM can only analyze the local microstructure of the filling body due to the restriction of the sampling area. NMR technology can make up for the inadequacy of SEM in overall pore structure analysis and has been widely adopted in rock micro-pore structure investigation because of its advantages of no destruction and rapid detection. For example, based on NMR technology, Zhou et al. (2012) and Wang et al. (2017) studied the pore characteristics of rocks and the pore structure of cement asphalt mortar, respectively; Ji et al. (2017) examined the fractal features of pore structure in fresh cement slurry.

On the other hand, many efforts have been made to investigate the pore structure of backfill to get better unconfined compressive strength (UCS), recently. Xing et al. studied the effect of fineness of tailings on the pore structure of cementing backfill (Li et al., 2016). Liu et al. studied the effect of cement particle shapes on the capillary structure of hardened cement slurry through numerical simulations (Liu C et al., 2018). Ma et al. analysed the effects of adding superabsorbent polymer (SAP) on the performance of cement-based material and its pore structure (Ma et al., 2017). Those studies are valuable in engineering from the perspective of understanding the effects of material granularity and additives on pore structure. However, there still exists three problems that need to be further explored with respect to the microstructure of CPB: 1) how to determine the relationship between the microstructure and mechanical properties quantitatively; 2) the coupling effects of tailings cement ratio (T/C ratio) and curing time on the development process of pore structure; and 3) the relationship between the failure mechanism and the pore structure in CPB.

The objective of this paper was to assess the coupling effect of tailings cement ratio and curing time on microstructural parameters (such as average pore area, T_2 spectrum area etc.) and UCS of CPB specimens, which were prepared with different tailings cement ratios. Therefore, a series of tests including SEM test, NMR test, and UCS test have been performed, then the relationship between the pore structure parameters of CPB and the UCS was investigated. Finally, the effects of different pore sizes on the failure process in CPB was discussed. The results of

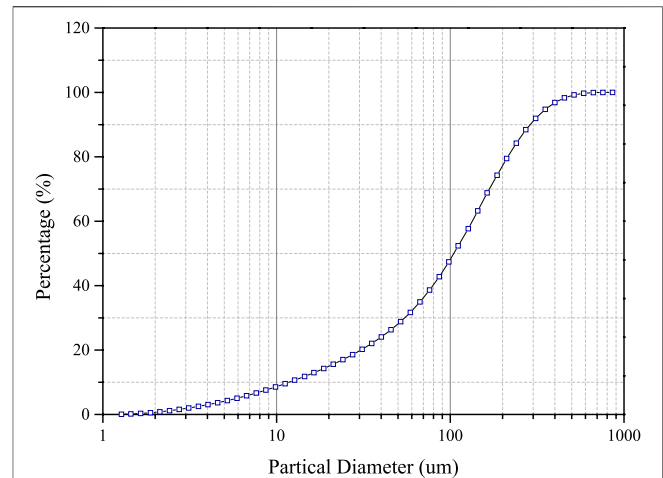


FIGURE 1 | The particle size distribution of tailings.

this study could provide a reference for the pore characteristics investigation of CPB and accelerate the application of CPB in the future.

MATERIALS AND METHODOLOGY

Materials Used

The tailings utilized in this study were obtained from Xianglushan tungstic mine, located in Jiangxi Province of China. The particle size distribution (PSD) of tailings is shown in **Figure 1**, and the related physical characteristics of tailings are summarized in **Table 1**. **Figure 1** indicates that the d_{10} , d_{50} , d_{60} were 11.8, 105, and 134.1 μm , respectively, while the non-uniformity coefficient (d_{60}/d_{10}) was 11.36. The main chemical compositions of tailings are presented in **Table 2**. The binder used was P.O 32.5 Portland cement based on China's Common Portland Cement Standard (No. GB175-2007), and its main chemical compositions are summarized in **Table 3**. The water used for CPB preparation was tap water (Liu L et al., 2018).

Preparation of CPB Specimens

Because the solid concentration of 72 wt% can ensure the liquidity requirement during CPB transportation, three kinds of CPB specimens with the solid concentration of 72 wt%, and T/C ratios of 4, 6, and 10 were prepared, respectively, (Koohestani and Belem, 2017; Qi et al., 2018a). The mine tailings, cement, and tap water were mixed with a mortar mixer. The CPB slurry was stirred evenly in cylindrical bottom-drained column moulds ($\varnothing 50 \text{ mm} \times 100 \text{ mm}$). After a rest period, CPB specimens were placed into a curing box at a temperature of $20 \pm 1^\circ\text{C}$ and a relative humidity of $95 \pm 1\%$ (Yin et al., 2018). Then the specimens, cured for 3, 7, 14, and 28 days, were evaluated by SEM test, NMR test, and UCS test, respectively. In this paper, all experiments were performed at room temperature in accordance with the related test manuals and literatures, specific methods are described as follows.

TABLE 1 | Physical characteristics of tailings.

Material	Specific gravity	Loose bulk density (t/m ³)	Compacted density (t/m ³)	Porosity (%)	Natural repose angle (°)	Specific surface area (m ² /g)
Tailings	2.992	1.392	1.955	34.659	42.997	0.631

TABLE 2 | Chemical composition of tailings used (units of wt%).

TFe	SiO ₂	Al ₂ O ₃	MgO	CaO	S	WO ₃	Other
9.450	48.220	5.010	2.960	12.680	2.750	0.055	18.875

TABLE 3 | Chemical composition of Portland cement used (units of wt%).

CaO	SiO ₂	Al ₂ O ₃	Fe ₂ O ₃	MgO	SO ₂	Na ₂ O	Other
63.66	21.26	4.50	2.80	1.66	2.58	0.18	3.36

Experimental Implementation

NMR Test

The MacroMR12-150I test system (Suzhou Niumag Analytical Instrument) was performed for NMR test, as shown in **Figure 2**. The prepared CPB specimens were covered with a layer of Polytetrafluoroethylene (PTFE) to avoid moisture loss before the NMR test. The NMR tests involve two sequential steps, i.e., excitation status and reception status. Excitation status is used to excite the signals of CPB specimens, while reception status is to convert analog signals to digital signals. According to the operational procedures, each CPB specimen (ϕ 50 mm \times 100 mm) was tested three times, the specific test method can be found in a previous study (Liu C et al., 2018). Finally the distributions of pores size in CPB could be examined through the T_2 spectra analysis.

UCS Test

After the NMR test, CPB specimens were covered with a layer of Polytetrafluoroethylene (PTFE) again and sent to the UCS laboratory immediately. The UCS measurements were performed on CPB specimens (50 mm \times 100 mm) using an electrohydraulic servo universal testing machine (MTS C43.504, MTS Systems Corporation, United States) to

investigate the relationship between the UCS and pore size in CPB specimens. The UCS tests were conducted with a constant displacement-speed of 1 mm/min. For each experimental scenario, three identical specimens were tested and their average UCS values were recorded for further analysis.

SEM Test

After the aforementioned UCS test, the samples of SEM test were obtained from the central part of each CPB specimen. The specimens were coated with a layer of metal conductive film in a vacuum coating machine, and then were scanned with a JSM-6460LV scanning electron microscope produced by Nippon Electronics Company (JEOL). To avoid the human error, we conducted three times on each specimen. After that, the SEM images were quantitatively analyzed using the software of Particles (Pores) and Cracks Analysis System (PCAS) to evaluate the micro-parameters such as apparent porosity ratio, average pore area etc. For the former, it is a ratio of the pore area to the total specimen area in SEM test. And it is a two-dimensional parameter, which could indirectly indicate the pore variation trend in CPB (Koohestani and Belem, 2017). For the latter, it is a parameter which depends on the average pore length and average pore width. It could indicate the average size of pores and reflect the pore size variation in CPB specimens (Koohestani and Belem, 2017).

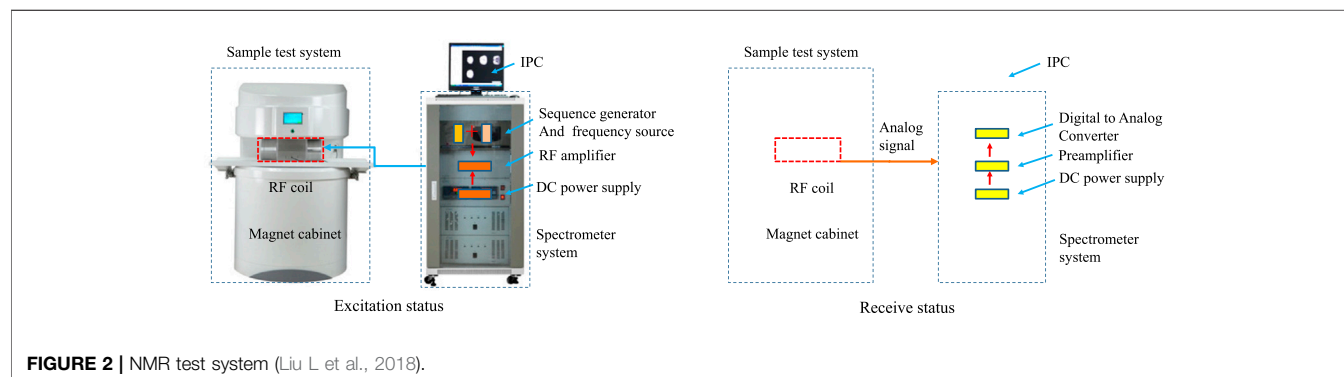
RESULTS AND DISCUSSION

Pore Characteristic Parameter Analysis

SEM Analysis

(1) Qualitative Analysis on CPB Specimens

The variation tendency of the pore structure in CPB during its curing period can be observed directly by SEM image, as shown in **Figure 3**. At the same curing time, the pore structure in CPB gradually became worse with the increased tailing/cement ratio



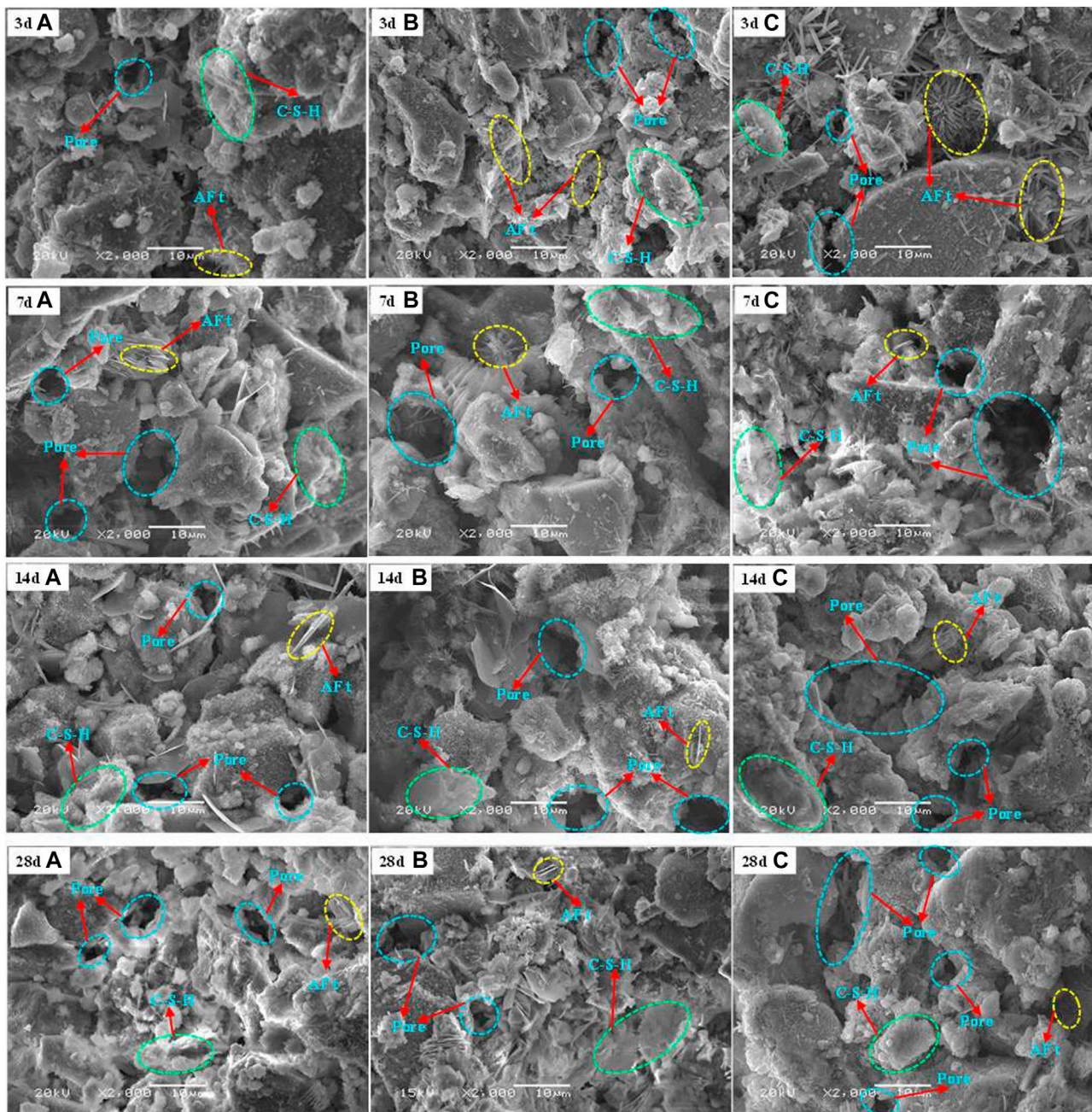


FIGURE 3 | CPB microstructures obtained by SEM test.

(T/C ratio), due to more and more generated pores (especially macro-pores) and ettringite (AFt). Because hydration productions at an early curing time (such as 3 days) were less and could not fully fill the pore structure (Chen et al., 2021). Therefore, we can clearly see that there were a large amount of needle-like ettringites and pores with different sizes. When the curing period was 14 days, on the one hand, more and more C-S-H and needle-like ettringites were produced by cement hydration. On the other hand, macro-pores were unceasingly filled by those

stuffs and subsequently became the pores with smaller size. Therefore, internal microstructure integrity of CPB specimens gradually became higher than before.

However, the hydration process in CPB specimens gradually slows down as curing time increased. such as with a curing time of 28 days. In this case, the larger pore cannot be further filled by hydration productions, therefore the change of pore structure in CPB gradually became stabilized, finally formed the unique pore characteristics of CPB. Under this circumstance, the coupling

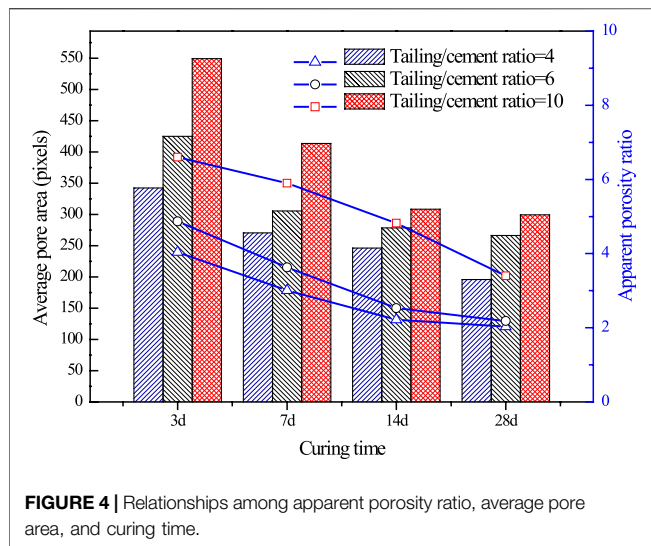


FIGURE 4 | Relationships among apparent porosity ratio, average pore area, and curing time.

effect of curing time and T/C ratio seems to be negligible. Meanwhile, it manifested that the UCS decreased with the increase of T/C ratio due to less hydration products.

(2) Quantitative Analysis on CPB Specimens

Figure 4 shows the relationships among apparent porosity ratio and average pore area of CPB and curing time. As shown in **Figure 4**, as curing time increased, the apparent porosity ratio of CPB with T/C ratios of 4, 6 and 10, decreased from 4.04 (3 days) to 2.03 (28 days), from 4.87 (3 days) to 2.18 (28 days), from 6.6 (3 days) to 3.4 (28 days), respectively. The micro-structural integrity in CPB approximately increased by 51.86%, due to the pore structure in CPB improved by curing time, although the initial T/C ratio is different. Meanwhile, the average pore area had a nearly inverse proportional relation to the curing time. As curing time increased, the average pore area decreased from 342.26 (3 days), 424.79 (3 days), and 549.33 (3 days) to 195.63 (28 days), 266.12 (28 days), and 299.38 (28 days), respectively. The micro-structural integrity in CPB increased by about 41.43%.

The results indicated that the apparent porosity ratio is highly correlated with the average pore area, both of them could illustrate the development of pore structure characteristics in CPB.

NMR Analysis

Due to the defects of SEM sampling, in this section we used T_2 spectrum area, porosity (NMR) as parameters to quantitatively investigate the pore structure characteristics in CPB. Generally, the NMR relaxation time and T_2 spectrum area were proportional to the liquid content of the rock (Zhang and Xiao., 2006). To be specific, a shorter relaxation time (T_2) indicates a smaller pore size. Thus the area of zone enclosed by the T_2 spectrum amplitude and x-axis indicates the porosity (NMR) of CPB. Furthermore, the pore size distribution in CPB could be obtained by the conversion of T_2 spectrum distribution as well.

Table 4 shows the results of T_2 spectrum of CPB. If the T/C ratio was set to be a certain value (4, 6, and 10), as the curing time increased, the spectrum area decreased. The same goes for the porosity (NMR). To be specific, the porosity (NMR) of CPB with T/C ratios of 4, 6, and 10 decreased from 11.75 (3 days), 18.65 (3 days), and 12.94 (3 days) to 2.45 (28 days), 3.57 (28 days), and 4.46 (28 days), respectively. The micro-structural integrity in CPB approximately increased by 80.86%. There seems to be a negative correlation between the integrity in CPB and the parameters, such as T_2 spectrum area, and porosity (NMR). It is also negatively correlated with UCS. Although the integrity values obtained by different analysis methods were obviously different, both SEM and NMR analyses demonstrated that the internal pore structure of CPB became much better as the curing time increased.

Pore Size Analysis

Classification of Pore Size

As aforementioned, pore structure characteristics in CPB have a close relationship with the hydration process. However, the pore structure in CPB would become stabilized to form its own unique pore characteristics as the curing period increased. The reason is that the cement hydration process gradually slows down, and even stops. Therefore, in this section, the pore size in CPB was

TABLE 4 | The NMR spectrum area.

T/C ratio	Curing time (day)	T ₂ spectrum analysis		UCS (MPa)
		T ₂ spectrum area (S)	Porosity (%)	
4	3	102,372.65	11.751	0.268
	7	44,682.32	4.49	0.87
	14	42,900.26	4.36	1.02
	28	19,637.08	2.45	1.05
6	3	114,460.20	18.65	0.23
	7	106,505.88	11.88	0.42
	14	82,891.91	7.48	0.56
	28	29,718.70	3.57	0.60
10	3	143,714.52	12.94	0.15
	7	130,927.66	12.28	0.28
	14	115,912.40	11.33	0.33
	28	38,249.38	4.46	0.41

TABLE 5 | Pores size partition in CPB (Yang et al., 2010).

Name	Gel pores	Transition pores	Capillary pores	Macro-pores
Pores size	<10 nm	10–100 nm	100–1,000 nm	>1,000 nm

divided into four types according to the related literature (Yang et al., 2010), including gel pores (pore size <10 nm), transition pores (pore size = 10–100 nm), capillary pores (pore size = 100–1,000 nm), and macro-pores (pore size > 1,000 nm), as shown in Table 5.

Pores Size Characteristics Analysis

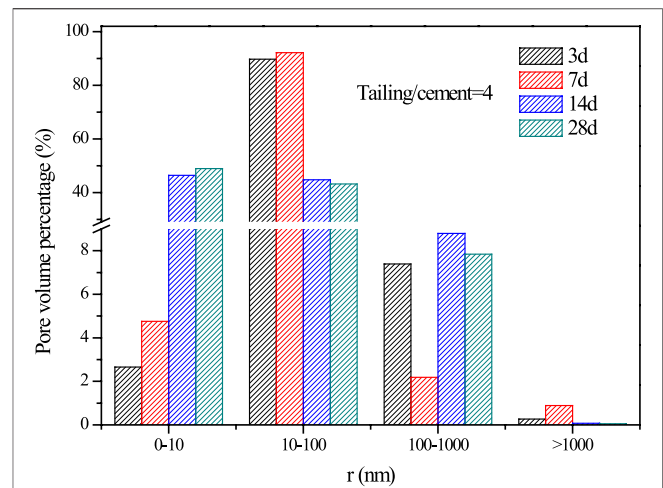
(1) Effect of Curing Time on Pore Size

In this section, CPB specimens with a T/C ratio of 4 were taken as an example to study the effect of curing time on the development of pore size in CPB. Figure 5 shows the proportion of different pore sizes in CPB during the curing period. As shown in Figure 5, as the curing time increased, the gel pore (<10 nm) increased, while the transition pores (10–100 nm) decreased. To be specific, the volume percentage of gel pores gradually increased from 2.65% (3 days) and 4.75% (7 days) to 46.37% (14 days) and 48.96% (28 days), while the transition pores decreased from 89.73% (3 days) and 92.16% (7 days) to 44.75% (14 days) and 43.14% (28 days), respectively. It is interesting that these two kinds of pores seem to maintain a dynamic balance. However, the volume percentage of capillary pores (100–1,000 nm) keeps a stable level (about 9.46%) while the macro-pores are negligible (about 0.05%) during the whole curing period. This means that the hydration products continuously increase with the curing time, but it just has a significant influence on the pore size of 10–100 nm. The effect of the hydration products has little impact on the pore sizes above 1,000 nm, which have a good agreement with the results of SEM analysis.

As shown in Figure 5, when the curing time is 3 days, the percentage of different pores in CPB exhibits a similar normal distribution. To be more specific, the peak of the curve is the most probable pore size (10–100 nm), namely the pore size with the largest proportion in CPB, the pore size between 0 and 10 nm and that between 100 and 1,000 nm located on the two sides of the peak, respectively. As the curing time increased, these four kinds of pore sizes in CPB keep the similar normal distribution, the pore sizes below 10 nm and above 100 nm distributed at the two sides all the time, while the pore size within 10–100 nm always occupies the peak of the curve. As the curing time increased, the peak shifted left due to the pore size in CPB decreased, meanwhile the peak reduced because the percentage of different pores distributed more concentrated. Generally, the dominant pore size has an important influence on material characteristics (Yaohua et al., 2018), therefore the effect of the dominant pore size on the mechanical property of CPB will be discussed in *The Effect of Pore Size on Failure Process of CPB*.

(2) Effect of T/C Ratio on Pore Size

Figure 6A shows the NMR T_2 spectrum of CPB specimens with different T/C ratios, the corresponding pore volume percentage

**FIGURE 5 |** The percentage distribution of pores with different size in CPB.

in CPB is shown in Figure 6B, in which there were two distinct peaks on T_2 spectrum when the curing time is 3 days or 7 days. Generally, the area of the first peak was about 76.105–99.701% of the total area of T_2 spectrum, while the second peak was about 0.299–23.340% of the total area. However, we found a third peak and a fourth peak when the curing periods were 14 and 28 days, respectively. The third peak or the fourth peak areas are very small, accounted for only 0.1% of the total area. This means that local pore size in CPB increased unexpectedly due to the coupling influence of C/T ratio and curing time.

Figure 6B shows that when the curing time was 3 days, the volume percentage of pores between 10 and 100 nm decreased continuously with the increase of T/C ratio, while the pore size between 100 and 1,000 nm increased. The macro-pores (pore size >1,000 nm) were very few, but it exhibited an uptrend. When the curing time increase to 7, 14 or 28 days, the volume percentages of pore size between 10–100 nm and 100–1,000 nm increased continuously with the increased T/C ratio, while pore size (< 10 nm) decreased gradually. This means that with the increase of T/C ratio, the cement content in CPB descended. As a result, the hydration products were too few to fully fill the pores with large size, which is in good agreement with the aforementioned analysis.

The Effect of Pore Size on Failure Process of CPB

In this section, CPB with a curing time of 28 days and a T/C ratio of 4 was taken as an example to evaluate the effect of pore size on the failure process of CPB. Meanwhile, because of the development characteristic of pore structure in CPB, the most probable pore size was used to study the effect of pore size on the failure process of CPB.

Figure 7 shows the failure mode of CPB after UCS test. As shown in Figure 7, the failure mechanism of CPB was mainly shear failure due to the main fracture through the shear slip

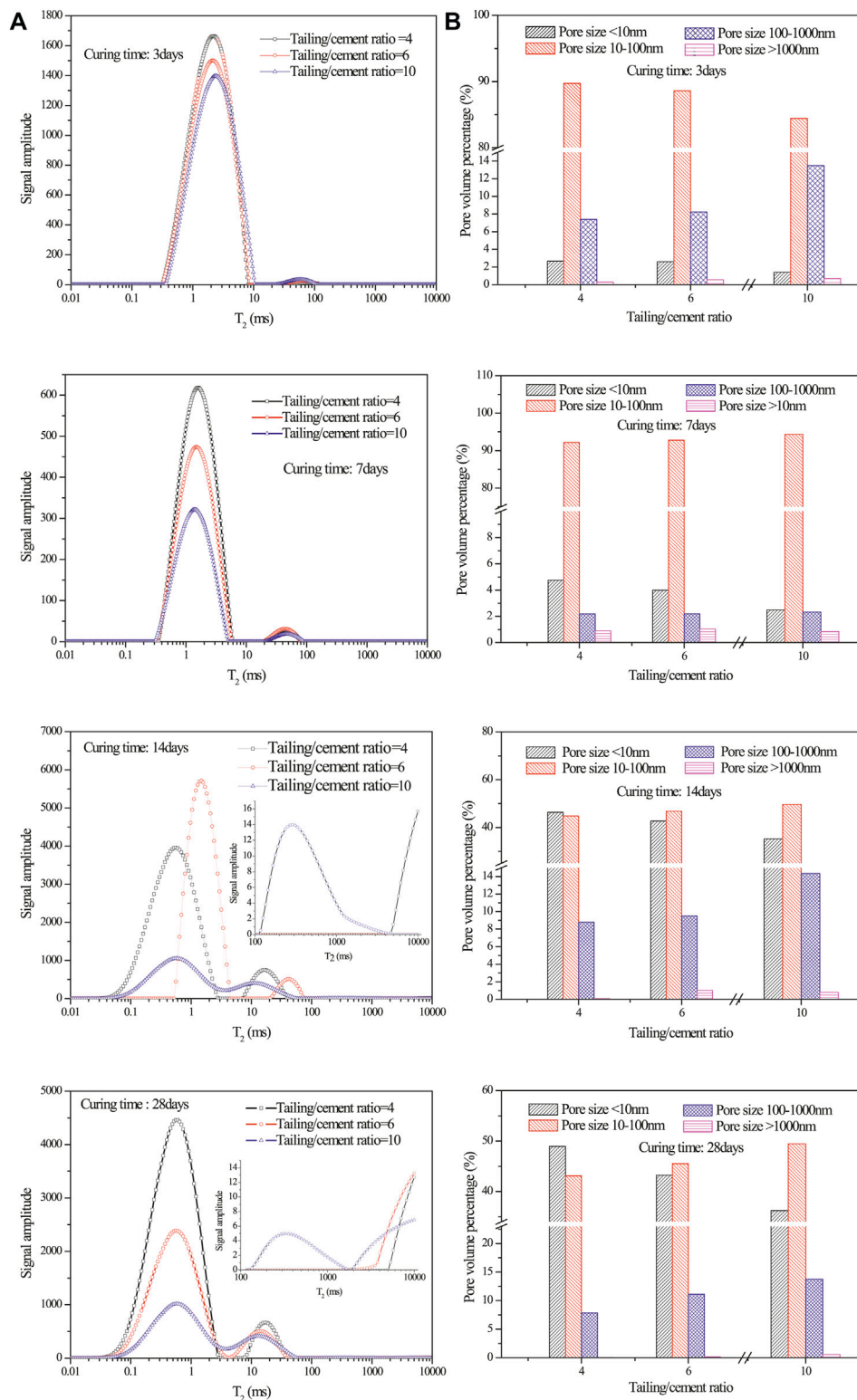


FIGURE 6 | The pore size distribution of CPB specimens at different curing time; **(A)** NMR T_2 spectrum of CPB specimens; **(B)** Pore volume percentage in CPB.

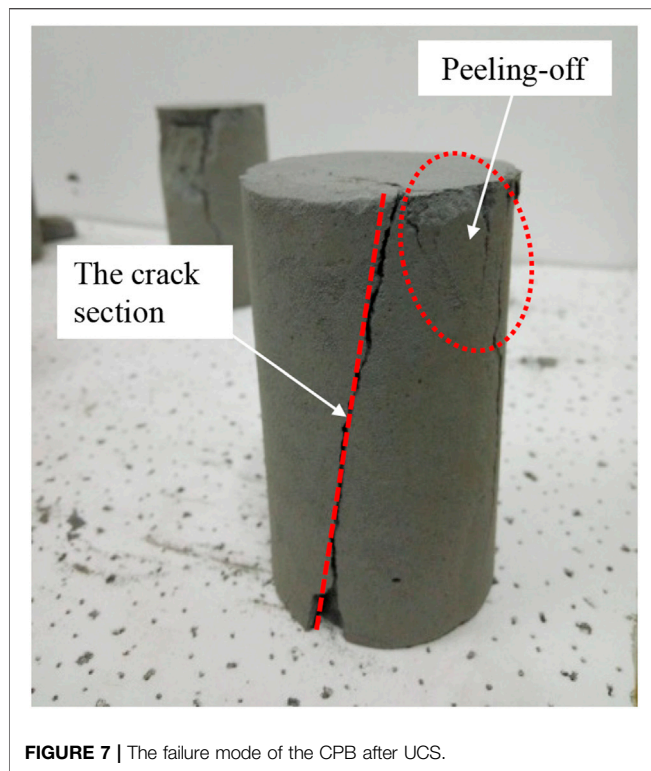


FIGURE 7 | The failure mode of the CPB after UCS.

surface. According to the mesomechanics theories and related literatures (Luo et al., 2000; Gregerová and Všianský, 2009), the failure essence of CPB is the results of micro-damage as well as the accumulation and development of micro-fracture. Generally, during the UCS test, pores with pore size within 10–100 nm (as the most probable pore size) were compacted to be micro-crack due to the gradual increase of the load. Then, the micro-fracture will not disappear but extend to form the main cracks together with the nearby micro-crack, when the higher load further added, finally resulted in the main failure surface throughout CPB. As for macro-pores, which accounted for only 0.05% of the total pores, just led to the partial peeling-off of CPB rather than the generation of the main crack section, as shown in **Figure 7**. Therefore, it is significantly important to make an investigation and control on the most probable pores size (the dominant pore sizes) for predicting the failure mechanism of CPB.

CONCLUSION

In this study, the development process of the pore structure in cemented paste backfill was systematically investigated using NMR test and SEM test. The coupling effect of curing time and T/C ratio on the pore size and failure mechanism of CPB was presented. The following conclusions could be drawn from the current study.

- a. Pore structure in CPB could be represented by the average pore area, apparent porosity ratio, porosity (NMR), and T2 spectrum area, which are negatively correlated with UCS.
- b. As the curing time increased, the amount of pores below 10 nm descended, while those between 10 and 100 nm increased. During the initial development stage of CPB pores (3 days or 7 days), almost 90% of the total pores were transition pores (10–100 nm). In the second development stage of CPB pores (14 days or 28 days), the dominant contents were gel pores (<10 nm) and transition pores (10–100 nm), occupying up to about 40% of the total pores, respectively.
- c. A similar normal distribution was observed from the volume percentages of the four kinds of pore structure in CPB. As the curing time increased, the peak of pore size distribution curve shifted left, and the peak value decreased, which means that the pore size in CPB decreased and was distributed to be highly concentrated.
- d. Pores larger than 1,000 nm have little effect on uniaxial compressive strength. The failure mode of CPB was mainly shear, which was significantly affected by pores between 10 and 100 nm. To be more specific, the extension of the most probable pore size led to the cross-connection of pores and resulted in the main failure surface in CPB.
- e. Research and control of the most probable pore size is of great significance in predicting the macro-crack generation in CPB during the UCS test. Three-dimensional testing methods (like CT) in the future studies should be adopted to rebuild the complete pore structure in CPB, as well as to monitor the pore extension process in real time during the UCS test, which can significantly accelerate the application of CPB in the future.

DATA AVAILABILITY STATEMENT

The original contributions presented in the study are included in the article/supplementary material, further inquiries can be directed to the corresponding author.

AUTHOR CONTRIBUTIONS

LL contributed to the conception of the study; CZ performed the experiment; CH, MW contributed significantly to analysis and manuscript preparation; YZ, XZ performed the data analyses and wrote the manuscript; BZ helped perform the analysis with constructive discussions. All authors agree to be accountable for the content of the work.

FUNDING

This research was supported by the National Natural Science Foundation of China (No. 52004207, 51504182, 51674188, 51404191, 51405381), the Natural Science Basic Research Plan of Shaanxi Province of China (No. 2015JQ5187), the Scientific Research Program funded by the Shaanxi Provincial Education Department (No. 15JK1466), the Project funded by China Postdoctoral Science Foundation (No. 2015M582685), and Outstanding Youth Science Fund of Xi'an University of

Science and Technology (No. 2018YQ2-01). This research was also supported by the National Research Council of Science and Technology (NST) grant by the Korea government (MSIP) (No. CRC-16- 38502-KICT).

REFERENCES

- Benzaazoua, M., Belem, T., and Bussière, B. (2002). Chemical Factors that Influence the Performance of Mine Sulphidic Paste Backfill. *Cement Concrete Res.* 32, 1133–1144. doi:10.1016/s0008-8846(02)00752-4
- Cao, S., Yilmaz, E., Song, W., and Xue, G. (2019). Assessment of Acoustic Emission and Triaxial Mechanical Properties of Rock-Cemented Tailings Matrix Composites. *Adv. Mater. Sci. Eng.* 2019, 1–12. doi:10.1155/2019/6742392
- Chen, Q.-s., Zhang, Q.-l., Fourie, A., Chen, X., and Qi, C.-c. (2017). Experimental Investigation on the Strength Characteristics of Cement Paste Backfill in a Similar Stope Model and its Mechanism. *Construction Building Mater.* 154, 34–43. doi:10.1016/j.conbuildmat.2017.07.142
- Chen, Q., Zhang, Q., Qi, C., Fourie, A., and Xiao, C. (2018). Recycling Phosphogypsum and Construction Demolition Waste for Cemented Paste Backfill and its Environmental Impact. *J. Clean. Prod.* 186, 418–429. doi:10.1016/j.jclepro.2018.03.131
- Chen, S., Wu, A., Wang, Y., and Wang, W. (2021). Coupled Effects of Curing Stress and Curing Temperature on Mechanical and Physical Properties of Cemented Paste Backfill. *Construction Building Mater.* 273, 121746. doi:10.1016/j.conbuildmat.2020.121746
- Cihangir, F., Ercikdi, B., Kesimal, A., Turan, A., and Deveci, H. (2012). Utilisation of Alkali-Activated Blast Furnace Slag in Paste Backfill of High-Sulphide Mill Tailings: Effect of Binder Type and Dosage. *Minerals Eng.* 30, 33–43. doi:10.1016/j.mineng.2012.01.009
- Gregorová, M., and Všianský, D. (2009). Identification of concrete Deteriorating Minerals by Polarizing and Scanning Electron Microscopy. *Mater. Characterization* 60 (7), 680–685. doi:10.1016/j.matchar.2009.01.018
- Hu, R. L., Yue, Z. Q., Wang, L. C., and Wang, S. J. (2004). Review on Current Status and Challenging Issues of Land Subsidence in China. *Eng. Geology*. 76 (1–2), 65–77. doi:10.1016/j.enggeo.2004.06.006
- Huang, Z., Yilmaz, E., and Cao, S. (2021). Analysis of Strength and Microstructural Characteristics of Mine Backfills Containing Fly Ash and Desulfurized Gypsum. *Minerals* 11 (4), 409. doi:10.3390/min11040409
- Ji, Y., Sun, Z., Jiang, X., Liu, Y., Shui, L., and Chen, C. (2017). Fractal Characterization on Pore Structure and Analysis of Fluidity and Bleeding of Fresh Cement Paste Based on ¹H Low-Field NMR. *Construction Building Mater.* 140, 445–453. doi:10.1016/j.conbuildmat.2017.02.151
- Jiang, H., Fall, M., Yilmaz, E., Li, Y., and Yang, L. (2020). Effect of mineral Admixtures on Flow Properties of Fresh Cemented Paste Backfill: Assessment of Time Dependency and Thixotropy. *Powder Tech.* 372, 258–266. doi:10.1016/j.powtec.2020.06.009
- Koohestani, B., and Belem, A. K. (2017). *Influence of Polymer Powder on Properties of Cemented Paste Backfill*. Amsterdam, Netherlands: International Journal of Mineral Processing.
- Liu, L., Xin, J., Huan, C., Zhao, Y. J., Fan, X., Guo, L. J., et al. (2021). Effect of Curing Time on the Mesoscopic Parameters of Cemented Paste Backfill Simulated Using the Particle Flow Code Technique. *Int. J. Minerals* 28, 590–602. doi:10.1007/s12613-020-2007-2
- Li, X., Wang, B., You, J., Yang, H., Hou, Y., Xie, L., et al. (2016). Study on Mechanical Properties and Microstructure of the Cemented Tailings Backfill. *China Mining Mag.* 25 (6), 169–172. (In Chinese). doi:10.3969/j.issn.1004-4051.2016.06.038
- Liu, C., Liu, G., Liu, Z., Yang, L., Zhang, M., and Zhang, Y. (2018). Numerical Simulation of the Effect of Cement Particle Shapes on Capillary Pore Structures in Hardened Cement Pastes. *Construction Building Mater.* 173, 615–628. doi:10.1016/j.conbuildmat.2018.04.039
- Liu, C., Shi, B., Zhou, J., and Tang, C. (2011). Quantification and Characterization of Microporosity by Image Processing, Geometric Measurement and Statistical Methods: Application on SEM Images of clay Materials. *Appl. Clay Sci.* 54 (1), 97–106. doi:10.1016/j.clay.2011.07.022
- Liu, L., Fang, Z., Qi, C., Zhang, B., Guo, L., and Song, K.-I. (2018). Experimental Investigation on the Relationship between Pore Characteristics and Unconfined Compressive Strength of Cemented Paste Backfill. *Construction Building Mater.* 179 (aug.10), 254–264. doi:10.1016/j.conbuildmat.2018.05.224
- Liu, L., Zhou, P., Feng, Y., Zhang, B., and Song, K.-i. (2020). Quantitative Investigation on Micro-parameters of Cemented Paste Backfill and its Sensitivity Analysis. *J. Cent. South. Univ.* 27 (001), 267–276. doi:10.1007/s11771-020-4294-1
- Liu, Q., Liu, D., Tian, Y., and Liu, X. (2017). Numerical Simulation of Stress-Strain Behaviour of Cemented Paste Backfill in Triaxial Compression. *Eng. Geology*. 231, 165–175. doi:10.1016/j.enggeo.2017.10.021
- Lu, H., Qi, C., Chen, Q., Gan, D., Xue, Z., and Hu, Y. (2018). A New Procedure for Recycling Waste Tailings as Cemented Paste Backfill to Underground Stopes and Open Pits. *J. Clean. Prod.* 188 (JUL.1), 601–612. doi:10.1016/j.jclepro.2018.04.041
- Luo, X., Sun, W., and Chan, S. Y. N. (2000). Effect of Heating and Cooling Regimes on Residual Strength and Microstructure of normal Strength and High-Performance concrete. *Cement Concrete Res.* 30, 379–383. doi:10.1016/s0008-8846(99)00264-1
- Ma, X., Liu, J., Wu, Z., and Shi, C. (2017). Effects of SAP on the Properties and Pore Structure of High Performance Cement-Based Materials. *Construction Building Mater.* 131, 476–484. doi:10.1016/j.conbuildmat.2016.11.090
- Qi, C., Fourie, A., Du, X., and Tang, X. (2018b). Prediction of Open Stope Hangingwall Stability Using Random Forests. *Nat. Hazards* 92 (2), 1179–1197. doi:10.1007/s11069-018-3246-7
- Qi, C., Chen, Q., Fourie, A., Zhao, J., and Zhang, Q. (2018c). Pressure Drop in Pipe Flow of Cemented Paste Backfill: Experimental and Modeling Study. *Powder Tech.* 333, 9–18. doi:10.1016/j.powtec.2018.03.070
- Qi, C., Fourie, A., and Chen, Q. (2018a). Neural Network and Particle Swarm Optimization for Predicting the Unconfined Compressive Strength of Cemented Paste Backfill. *Construction Building Mater.* 159, 473–478. doi:10.1016/j.conbuildmat.2017.11.006
- Wang, Y., Yuan, Q., Deng, D., Ye, T., and Fang, L. (2017). Measuring the Pore Structure of Cement Asphalt Mortar by Nuclear Magnetic Resonance. *Construction Building Mater.* 137, 450–458. doi:10.1016/j.conbuildmat.2017.01.109
- Wu, A., Wang, Y., Wang, H., Yin, S., and Miao, X. (2015). Coupled Effects of Cement Type and Water Quality on the Properties of Cemented Paste Backfill. *Int. J. Mineral Process.* 143, 65–71. doi:10.1016/j.minpro.2015.09.004
- Xu, W., Pan, W., and Ding, M. (2015). Experiment on Evolution of Microstructures and Long-Term Strength Model of Cemented Backfill Mass. *J. Cent. South Univ.* 46, 2333–2341. (In Chinese). doi:10.11817/j.issn.1672-7207.2015.06.046
- Yang, Y. H., Yue, L. I., and Xiu-Li, D. U. (2010). Study on Early Autogenous Shrinkage and Microcosmic Pore Distribution of Self-Compacting Concrete. *J. Building Mater.*
- Yaohua, G., Hongyan, D., Puyang, Z., and Lei, Z. (2018). Pore Structure Characteristics of SAP concrete Based on Mercury Intrusion Test. *J. Building Mater.* 21 (1), 138–142. (In Chinese). doi:10.3969/j.issn.1007-9629.2018.01.022
- Yilmaz, E., Belem, T., Benzaazoua, M., and Bussière, B. (2010). Assessment of the Modified CUAPS Apparatus to Estimate *In Situ* Properties of Cemented Paste Backfill. *Geotechnical Test. J.* 33 (5), 102689. doi:10.1520/gtj102689

ACKNOWLEDGMENTS

We would like to express our gratitude to Huaifu Qiu and Dongzhuang Hou for their assistance.

- Yilmaz, E., Belem, T., Benzaazoua, M., Kesimal, A., Ercikdi, B., and Cihangir, F. (2011b). Use of High-Density Paste Backfill for Safe Disposal of Copper_zinc Mine Tailings. *Mineral. Resour. Manage.* 27 (3), 81–94.
- Yilmaz, E., Belem, T., Bussière, B., and Benzaazoua, M. (2011a). Relationships between Microstructural Properties and Compressive Strength of Consolidated and Unconsolidated Cemented Paste Backfills. *Cement and Concrete Composites* 33 (6), 702–715. doi:10.1016/j.cemconcomp.2011.03.013
- Yin, S., Shao, Y., Wu, A., Wang, Y., and Chen, X. (2018). Expansion and Strength Properties of Cemented Backfill Using Sulphidic Mill Tailings. *Construction Building Mater.* 165, 138–148. doi:10.1016/j.conbuildmat.2018.01.005
- Zhang, Y. Z., and Xiao, L. Z. (2006). *Experimental Study of the NMR Characteristics in Rock under Uniaxial Load*. Beijing, China: Nuclear Electronics & Detection Technology. (In Chinese) doi:10.1109/icct.2006.341981
- Zhou, J., Deng, Y., Cao, Y., and Yan, J. (2014). Experimental Study of Microstructure of Hangzhou Saturated Soft Soil during Consolidation Process. *J. Cent. South Univ.* 45 (6), 1998–2005. (In Chinese).
- Zhou, K. P., Li, J. L., Xu, Y. J., and Zhang, Y. M. (2012). Measurement of Rock Pore Structure Based on NMR Technology. *Zhongnan Daxue Xuebao (Ziran Kexue Ban)/Journal Cent. South Univ. (Science Technology)* 43 (12), 4796–4800. (In Chinese).

Conflict of Interest: The authors declare that the research was conducted in the absence of any commercial or financial relationships that could be construed as a potential conflict of interest.

Copyright © 2021 Huan, Zhu, Liu, Wang, Zhao, Zhang and Zhang. This is an open-access article distributed under the terms of the Creative Commons Attribution License (CC BY). The use, distribution or reproduction in other forums is permitted, provided the original author(s) and the copyright owner(s) are credited and that the original publication in this journal is cited, in accordance with accepted academic practice. No use, distribution or reproduction is permitted which does not comply with these terms.



Effect of Iron Tailings and Slag Powders on Workability and Mechanical Properties of Concrete

Wu Ruidong^{1,2}, Shen Yu³, Liu Juanhong^{1,2*}, Cheng Linian^{1,2}, Zhang Guangtian⁴ and Zhang Yueyue^{1,2}

¹School of Civil and Resource Engineering, University of Science and Technology Beijing, Beijing, China, ²Beijing Key Laboratory of Urban Underground Space Engineering, University of Science and Technology Beijing, Beijing, China, ³CCCC-SHEC Third Highway Engineering Co., Ltd., Xi'an, China, ⁴Hebei Academy of Building Research, Shijiazhuang, China

OPEN ACCESS

Edited by:

Lijie Guo,
Beijing General Research Institute of
Mining and Metallurgy, China

Reviewed by:

Erol Yilmaz,
Recep Tayyip Erdoğan University,
Turkey
Jiaqi Li,
University of California, Berkeley,
United States

*Correspondence:

Liu Juanhong
liujuanhong66@126.com

Specialty section:

This article was submitted to
Structural Materials,
a section of the journal
Frontiers in Materials

Received: 10 June 2021

Accepted: 24 June 2021

Published: 26 July 2021

Citation:

Ruidong W, Yu S, Juanhong L,
Linian C, Guangtian Z and Yueyue Z
(2021) Effect of Iron Tailings and Slag
Powders on Workability and
Mechanical Properties of Concrete.
Front. Mater. 8:723119.
doi: 10.3389/fmats.2021.723119

Tailings are one of the largest solid wastes in stock at present. In order to improve the comprehensive utilization rate of tailings, especially to solve the problems of fine-grained tailings treatment, the concrete composite admixture was prepared by using iron tailings powder and slag powder. In order to study the influence of iron tailings powder on the workability and long-term mechanical properties of concrete, C30 and C50 concrete with different iron tailings powder dosages were prepared, and the slump, expansion, flexural strength, splitting tensile strength, and compressive strength of concrete at different ages were tested. The results showed that the proper addition of iron tailing powder is beneficial to the working performance of concrete and can effectively reduce the time-loss of concrete fluidity. When the content of iron tailings powder in the composite admixture is 50%, the 1080d long age strength of C30 and C50 concrete can reach 50.3 and 80.7 MPa. Based on the 28d compressive strength, the relative strength-age prediction model of iron tailings powder concrete was established. The calculation and experimental results show that the model can accurately predict the compressive strength of micro-powder concrete of iron tailings at long age, and the error rate is less than 1%. The results lay a theoretical foundation for the utilization of iron tailings in concrete.

Keywords: iron tailings powder, slag, mechanical properties, workability, prediction model

INTRODUCTION

With the continuous development of mineral resources, a large number of tailings have been formed after mineral dressing, and tailings is one of the most abundant solid wastes. The accumulation of tailings in tailings ponds not only pollutes groundwater and the surrounding environment but also threatens the safety of surrounding people and buildings (Pedro et al., 2019; Liu et al., 2020). Limited by science and technology, the overall utilization rate of tailings is not high at present; nearly 78% of the tailings are piled on the surface, resulting in a considerable waste of resources. The main use of tailings is to prepare filling materials and building materials, especially coarse-grained iron tailings can be used as an aggregate to prepare filling materials and concrete, iron tailings can be used as a kind of machine-made aggregate, and the performance of filling materials and concrete is good (Lv et al., 2019; Qi and Fourie, 2019; Protasio et al., 2020; Karthikeyan et al., 2021; Leong, 2021). Some tailings are used to prepare the concrete of mine pillars; the concrete has good mechanical properties by means of fiber reinforcement (Cao et al., 2020; Cao et al., 2021a; Cao et al., 2021b). However, with the continuous development of mineral processing technology, tailings become finer and finer, and

the fine-grained tailings below 75 μm can reach more than 80% (Wu et al., 2020). Fine-grade tailings will lead to the increase of cementitious substances in filling materials and cannot be used as a concrete fine aggregate, which greatly increases the difficulty of tailings utilization. The fine-grained tailings need to be classified, and a large number of fine-grained tailings cannot be used, which results in a considerable waste of resources, reduces the overall utilization rate of tailings, and increases the treatment cost. To solve the problem of fine tailings treatment is the bottleneck to improve the comprehensive utilization rate of tailings.

On the other hand, a huge amount of concrete is consumed in infrastructure construction. The production and preparation of concrete lead to the shortage of many resources, especially high-quality mineral admixtures. Mineral admixtures are essential raw materials for the modern green high-performance concrete. Under the background of low carbon and environmental protection, more and more admixtures will replace cement in concrete, which will help reduce carbon emissions and form an environment-friendly cementitious material system (Miller, 2018; Li et al., 2020a; Li et al., 2020b; Habert et al., 2020). In some areas, there is a scarcity of high-quality mineral admixtures, such as fly ash and slag powder (Granulated blast furnace slag, S95 and S105). Therefore, it is imperative to make a rational and efficient use of all kinds of resources, especially waste resources. In order to supplement the shortage of traditional admixture resources such as fly ash and slag and to make a wider use of industrial solid waste, reuse of iron tailings powder as a mineral admixture of concrete should be considered. The content of fine powder below 75 μm in iron tailings is increasing. Because the iron tailings powder is mainly composed of SiO_2 , Al_2O_3 , and other chemical components, it can be used as a kind of concrete admixture. At present, the research of iron tailings powder as a mineral admixture in concrete is mainly focused on the influence of iron tailings powder on the strength of concrete, as well as the activation and hydration of iron tailings powder. Research shows that when iron tailings powder is mixed with slag powder, concrete has relatively good mechanical properties (Wu and Liu, 2018; Han et al., 2019), and its hydration rate is very slow, which can effectively reduce the hydration heat of cement concrete (Han et al., 2017). It is found that the fineness of iron tailings powder has an important impact on the performance of concrete. Some scholars believe that iron tailings powder can promote the performance of concrete

through effective activation and further grinding (Hou et al., 2019; Liu et al., 2019; Yang and Mao, 2020). Through the study on the influence of iron tailings powder as a concrete admixture on mechanical properties and microstructure, iron tailings powder can be completely used as a mineral admixture to prepare concrete materials (Song and Liu, 2017; Song et al., 2019; Wu et al., 2019; Song and Chen, 2020).

However, as an inactive mineral admixture of concrete, iron tailings powder needs to be mixed with highly active slag powder to become a compound admixture. The influence law of iron tailings powder and slag powder on concrete strength, especially the development law of long age strength, is urgently needed to be explored. In this article, different proportions of iron tailings powder and slag powder composite admixtures are designed to prepare two common grades of concrete, C30 and C50. The compressive strength, flexural strength, and splitting tensile strength of concrete are tested, and the long-term strength prediction model is established and verified. This study can fill the research blank of iron tailings powder concrete long-term mechanical properties, which provides a theoretical basis for the application of fine-grained tailings.

RAW MATERIALS AND MIX PROPORTION

Raw Materials

Iron tailings powder comes from Fujian, China. Iron tailings are collected from mines and become iron tailings powder after drying, dehydration, and grinding. Its specific performance indexes are shown in **Table 1**.

The main chemical composition of iron tailings powder is silica, which comprises metal elements such as iron, copper, and zinc, and the main chemical composition is shown in **Table 2**. Iron tailings are a kind of mineral rich in silica, so it can be used as a mineral admixture of concrete.

Figure 1 is the X-ray diffraction pattern of iron tailings powder, which is mainly composed of quartz, SiO_2 , and a small amount of calcite, mica, and other minerals.

In order to eliminate the influence of other mineral admixtures in cement, the standard cement produced by the China Building Materials Institute, namely, pure Portland cement P.I 42.5, is selected for the test, and its basic performance indexes are shown in **Table 3**.

TABLE 1 | Technical indexes of iron tailings powder and slag powder.

	Density/g·cm ⁻³	45 μm sieve residue/%	Water requirement ratio/%	Specific surface area/m ² ·kg ⁻¹
Iron tailings	2.82	6.45	90	450
Slag	2.80	6.20	96.2	485

TABLE 2 | Main chemical components of iron tailings powder (%).

Chemical composition	SiO_2	CaO	Fe_2O_3	Al_2O_3	MgO	CuO	ZnO
Mass fraction	67.59	4.02	10.88	4.57	1.18	0.23	0.11

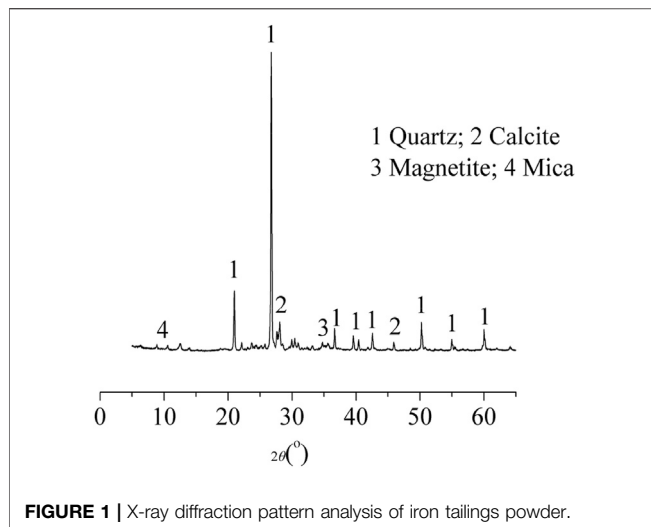


FIGURE 1 | X-ray diffraction pattern analysis of iron tailings powder.

Water quenched slag powder is an important mineral admixture for concrete. S95 slag powder produced by a factory in Hebei Province is adopted in the test. The basic performance indexes are shown in **Table 1**.

The coarse aggregate and fine aggregate used are in line with the national standard. In coarse aggregate, the particle size of large stone is 10–20 mm and that of small stone is 5–10 mm. The mass ratio of large stone and small stone is 8:2. The fine aggregate used in the test belongs to the medium sand of II area. It meets the grade I aggregate requirements of JG/T568-2019 “High performance concrete aggregate”. See **Table 4** for specific indicators.

Ordinary tap water is used to meet the requirements of mixing water. Polycarboxylate superplasticizer is used as a superplasticizer, and the solid content is about 20%.

Mix Proportion

This article designs C30 and C50, two kinds of commonly used concrete. Due to environmental protection, concrete cementitious materials introduce solid waste, so the cement

content should not be high. A low cement system is used in this experiment, and cement only accounts for 30 and 40% of the whole cementitious material system, respectively. After the preliminary test, the iron tailings powder belongs to an inactive admixture, so the water-binder is lower than that of concrete with common mineral admixtures. The water-binder ratio of C30 concrete is 0.40 and that of C50 concrete is 0.29. The composite admixture of iron tailings powder and slag powder is adopted, and the proportion of iron tailings powder in the composite admixture is 0, 30, 50, 70, and 100%, respectively. The influence of different proportion of iron tailings powder on the mechanical properties of concrete is studied. With the increase of iron tailings powder content, the water-binder ratio of concrete decreases to ensure that the strength can meet the requirements. Specific coordination is shown in **Table 5**.

In order to verify the relationship model between phase compressive strength and age of iron tailings micro-powder concrete, the verification group of concrete was prepared. The content of reference cement in C30 and C50 concrete accounted for 40 and 50% of the total cementing material, respectively, and the mixing ratio was shown in **Table 6**.

RESULTS AND DISCUSSION

Influence of Iron Tailings Powder on Concrete Performance

C30 and C50 concrete with different iron tailings powder contents were prepared according to the mix ratio, and the slump and dilatancy of each group of concrete at the time of discharge and 1 h after discharge were tested, respectively. The specific data are shown in **Table 7**.

The slump and expansion of C30 and C50 concrete mixed with iron tailings powder are greater than that of concrete mixed with slag powder alone. With the increase of iron tailings powder content, the slump and expansion of concrete first increase and then decrease. When iron tailings powder accounts for 70% of mineral admixtures (iron tailings powder and slag powder), the slump and expansion of concrete are the largest, with C30

TABLE 3 | Property indexes of reference cement.

Compressive strength/MPa		Flexural strength/MPa		Setting time/min		Specific surface area/m ² ·kg ⁻¹	Fineness/mm	Water requirement of normal consistency/%	Stability
3d	28d	3d	28d	Initial	Final				
28.3	53.2	5.5	10.3	155	215	347	0.5	27.2	Qualified

TABLE 4 | Technical indexes of coarse and aggregate.

	Fineness modulus	Apparent density/kg·m ⁻³	Bulk density/kg·m ⁻³	Porosity/%	Mud content/%	Crushing index/%	Needle and flake content/%
Coarse	-	2,743	1,569	42.8	1.0	5.2	5.5
Fine	2.7	2,595	1,534	39.0	1.6	-	-

TABLE 5 | Mix proportion of iron tailings powder concrete ($\text{kg}\cdot\text{m}^{-3}$).

		Cement	Iron tailings powder	Slag powder	Sand	Stone	Water	W/B	PC
C30	A0	113	0	264	840	1,018	151	0.40	3.4
	A30	113	79	185	840	1,018	147	0.39	3.4
	A50	113	132	132	840	1,018	143	0.38	3.4
	A70	113	185	79	840	1,018	140	0.37	3.4
	A100	113	264	0	840	1,018	136	0.36	3.4
C50	B0	191	0	287	725	1,071	139	0.29	6.7
	B30	191	86	201	725	1,071	134	0.28	6.7
	B50	191	144	144	725	1,071	129	0.27	6.7
	B70	191	201	86	725	1,071	124	0.26	6.7
	B100	191	287	0	725	1,071	119	0.25	6.7

W/B: Water–binder ratio, mass ratio of water to cementitious material.

TABLE 6 | Mix proportion of verification concrete ($\text{kg}\cdot\text{m}^{-3}$).

		Cement	Iron tailings powder	Slag powder	Sand	Stone	Water	W/B	PC
C30	E0	151	0	226	840	1,018	151	0.40	3.4
	E30	151	68	158	840	1,018	147	0.39	3.4
	E50	151	113	113	840	1,018	143	0.38	3.4
	E70	151	158	68	840	1,018	140	0.37	3.4
	E100	151	226	0	840	1,018	136	0.36	3.4
C50	F0	239	0	239	725	1,071	139	0.29	6.7
	F30	239	72	167	725	1,071	134	0.28	6.7
	F50	239	120	120	725	1,071	129	0.27	6.7
	F70	239	167	72	725	1,071	124	0.26	6.7
	F100	239	239	0	725	1,071	119	0.25	6.7

W/B: Water–binder ratio, mass ratio of water to cementitious material.

TABLE 7 | Slump and dispersion of concrete (mm).

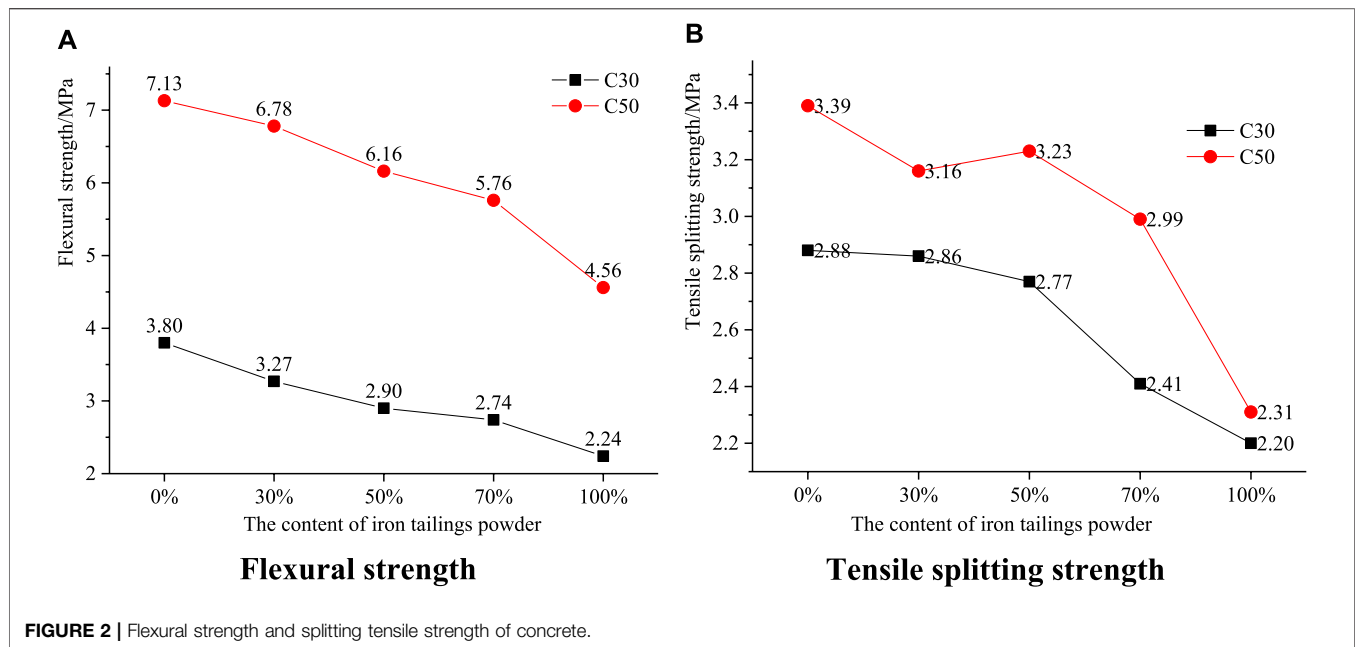
Group	Slump		Dispersion		Group	Slump		Dispersion	
	Initial	After 1 h	Initial	After 1 h		Initial	After 1 h	Initial	After 1 h
A0	215	155	450	300	B0	200	160	445	375
A30	220	170	500	390	B30	210	170	525	405
A50	230	180	515	420	B50	225	185	550	440
A70	230	190	525	450	B70	230	200	550	470
A100	225	170	510	410	B100	215	180	510	435

concrete reaching 230 and 525 mm, and C50 concrete reaching 230 and 550 mm.

The slump and expansion of C30 and C50 concrete decreased in different degrees after 1 h out of the mixer. The slump and expansion of C50 concrete are higher than that of C30 concrete after 1 h. This is due to the low water–binder ratio and high viscosity of C50 concrete. With the passage of time, the concrete has a good water retention performance, while the water–binder ratio of C30 concrete is larger, and there is more free water in the concrete. The concrete will lose water with time, and even the phenomenon of mortar bone separation appears. Therefore, the working performance of C30 concrete is not as good as that of C50 concrete after 1 h. The slump loss rate and expansion loss

rate of concrete with slag powder are the largest, and the loss rate of C30 concrete can reach 27.9 and 20.0%, respectively. The addition of iron tailing powder can effectively reduce the loss rate of slump and expansion of concrete after 1 h. When iron tailing powder accounts for 70% of mineral admixtures, the loss rate of slump and expansion is the lowest. Taking C30 as an example, it is 17.4 and 13.0%, respectively, which is 10.5 and 7.0% lower than that of concrete with slag powder alone.

In conclusion, the appropriate addition of iron tailings powder can effectively improve the particle size distribution of cement slag powder cementitious material system and make the particle distribution more uniform, thus increasing the workability of concrete. At the same time, it reduces the time loss of concrete



slump and expansion, has good working performance, and ensures the smooth pumping and construction of concrete.

Flexural Strength and Splitting Tensile Strength of Concrete

The flexural strength and splitting tensile strength of concrete after standard curing for 28d were respectively tested, and the results are shown in **Figure 2**.

The results show that the flexural strength and splitting tensile strength of concrete decrease with the increase of iron tailings powder content. The flexural strength and splitting tensile strength of A0 and B0 concrete with slag powder are the largest, which are 3.80, 7.13, 2.88, and 3.39 MPa, respectively. The A100 and B100 concrete with iron tailings powder is not suitable for single mixing. The bending strength and splitting tensile strength of A100 and B100 concrete with iron tailings powder is low, which is only 58–76% of that of concrete with single slag powder. When the ratio of iron tailings powder and slag powder is not more than 5:5, the flexural strength and splitting tensile strength of concrete are similar to those of concrete with slag powder alone. For example, when the proportion of iron tailings powder in a mineral admixture is 30%, the splitting tensile strength of C30 and C50 concrete is only 0.69 and 6.7% lower than that of concrete with single slag powder. In low-strength concrete (C30), the effect of iron tailings powder on flexural strength is greater, and the splitting tensile strength is less. In high-strength concrete (C50), the adverse effect of iron tailings powder on flexural strength is less than that of low-strength concrete, and the adverse effect on splitting tensile strength is greater than that of low-strength concrete. On the whole, the effect of iron tailings powder on the flexural strength of concrete is much greater than that on the tensile strength of concrete.

Long-Term Compressive Strength Law of Concrete

In order to explore the influence law of iron tailings powder on the long-term compressive strength of concrete, the 3, 7, 28, 90, 180, 270, 360, 540, 720, and 1080d compressive strength of C30 and C50 concrete were tested, respectively. The development law of concrete strength with age is shown in **Table 8**.

The results show that the strength of C30 and C50 concrete decreases with the increase of the iron tailings powder content. Iron tailings powder is a kind of non-active admixture, a very small amount of which can participate in the hydration reaction and produce less hydration products. Slag powder is a kind of mineral admixture with higher activity, which has a faster hydration reaction and can produce more hydration products, so it has higher strength. When the ratio of iron tailings powder to mineral admixtures (slag powder and iron tailings powder) is less than 50%, the compressive strength of concrete with different ages has little difference from that with single slag powder. The maximum reduction of compressive strength of C30 and C50 concrete at 28d was only 2.0 and 10.2% compared with that of the concrete with slag powder. When the proportion of iron tailings powder in a mineral admixture is more than 50%, the compressive strength of concrete at different ages decreases greatly compared with concrete mixed with slag powder alone. The maximum reduction ranges of 28d compressive strength are 19.4 and 33.8% compared with that of slag powder concrete. The content of iron tailing powder in concrete should not exceed 50% of the whole mineral admixture.

The influence of iron tailings powder on the strength of high-strength concrete (C50) is greater than that of low-strength concrete (C30). The reason is that high-strength concrete needs more cementitious materials, and the water–binder ratio is also relatively low. Although the addition of non-active

TABLE 8 | Compressive strength of iron tailings powder concrete (MPa).

Group	Iron tailing powder content/%	3d	7d	28d	90d	180d	360d	540d	720d	1080d
A0	0	14.4	28.7	35.5	45.5	46.3	47.2	48.1	50.5	52.1
A30	30	11.3	26.8	36.3	43.8	45.1	47.8	48.6	49.2	50.5
A50	50	9.6	23.9	34.8	42.9	43.6	44.1	45.5	48.1	50.3
A70	70	6.9	19.1	32.9	34.2	34.7	38.6	40.2	42.1	43.5
A100	100	4.2	17.4	28.6	30.4	31	35.5	35.9	36.4	37.3
B0	0	24.9	50.2	71.4	75.1	78.3	85.6	88.2	90.5	91.1
B30	30	22.1	48.7	64.4	77.0	79.3	82.5	83.4	85.6	88.2
B50	50	19.8	44.9	64.1	71.5	72.2	78.4	79.1	79.9	80.7
B70	70	15.7	34.5	53.8	58.4	60.6	62.8	66.6	67	67.5
B100	100	8.1	29.9	47.3	50.2	53.3	53.8	53.5	55.2	56.1

The content of iron tailing powder is the mass percentage of iron tailing powder in mineral admixture.

TABLE 9 | Relative compressive strength of iron tailing powder concrete.

Group	Iron tailing powder content/%	3d	7d	28d	90d	180d	360d	540d	720d	1080d
A0	0	0.41	0.81	1.00	1.28	1.30	1.33	1.35	1.42	1.47
A30	30	0.31	0.74	1.00	1.21	1.24	1.32	1.34	1.36	1.39
A50	50	0.28	0.69	1.00	1.23	1.25	1.27	1.31	1.38	1.45
A70	70	0.21	0.58	1.00	1.04	1.05	1.17	1.22	1.28	1.32
A100	100	0.15	0.61	1.00	1.06	1.08	1.24	1.26	1.27	1.30
B0	0	0.35	0.70	1.00	1.05	1.10	1.20	1.24	1.27	1.28
B30	30	0.34	0.76	1.00	1.20	1.23	1.28	1.30	1.33	1.37
B50	50	0.31	0.70	1.00	1.12	1.13	1.22	1.23	1.25	1.26
B70	70	0.29	0.64	1.00	1.09	1.13	1.17	1.24	1.25	1.25
B100	100	0.17	0.63	1.00	1.06	1.13	1.14	1.13	1.17	1.19

The content of iron tailing powder is the mass percentage of iron tailing powder in mineral admixture.

admixtures can change the particle size distribution of cementitious materials to a certain extent, and the microaggregate effect can improve the performance of concrete, its effect is not as good as the hydration reaction of active admixtures. Therefore, the adverse effect of iron tailings powder on the strength of low-strength concrete is small, and the adverse effect of iron tailings powder on the strength of high-strength concrete is obvious. Therefore, in the design mix proportion of high-strength concrete, the amount of iron tailings powder should be reduced appropriately under the low clinker system. For example, when the proportion of iron tailings powder to a mineral admixture is 30%, the compressive strength of group B30 concrete is equivalent to that of group B0 concrete, even if at some age exceeds the strength of group B0. At the same time, the compressive strength of concrete can not only be based on the 28d compressive strength as the standard system in the case of introducing the non-active admixture iron tailings powder. The curing age should be extended so that the non-active admixture can give full play to its effect. For example, when the age reaches 90 days, the strength of concrete with iron tailings powder accounting for less than 50% of the mineral admixture is very close to that of concrete with slag powder alone; it is more

suitable to evaluate the mechanical properties of concrete with inactive admixtures by the strength of longer age.

Relative Compressive Strength and the Age Prediction Model

The 28d strength of concrete in each group was taken as the reference value 1, and the strength of other ages was divided by the 28d compressive strength to calculate the relative compressive strength of concrete at different ages, as shown in **Table 9**.

The addition of iron tailings powder is not conducive to the early strength of concrete, but the appropriate addition of iron tailings powder (30%) is conducive to the growth of long-term strength of concrete. From the point of view of long age, after 360 days, the strength development law of concrete with appropriate amount of iron tailings powder is similar to that of concrete with slag powder only. Taking 1080d strength as an example, the compressive strength of A50 group increased by 45% compared with 28d compressive strength.

In order to study the relationship between compressive strength and age, the development model of compressive strength and age was established, which can provide

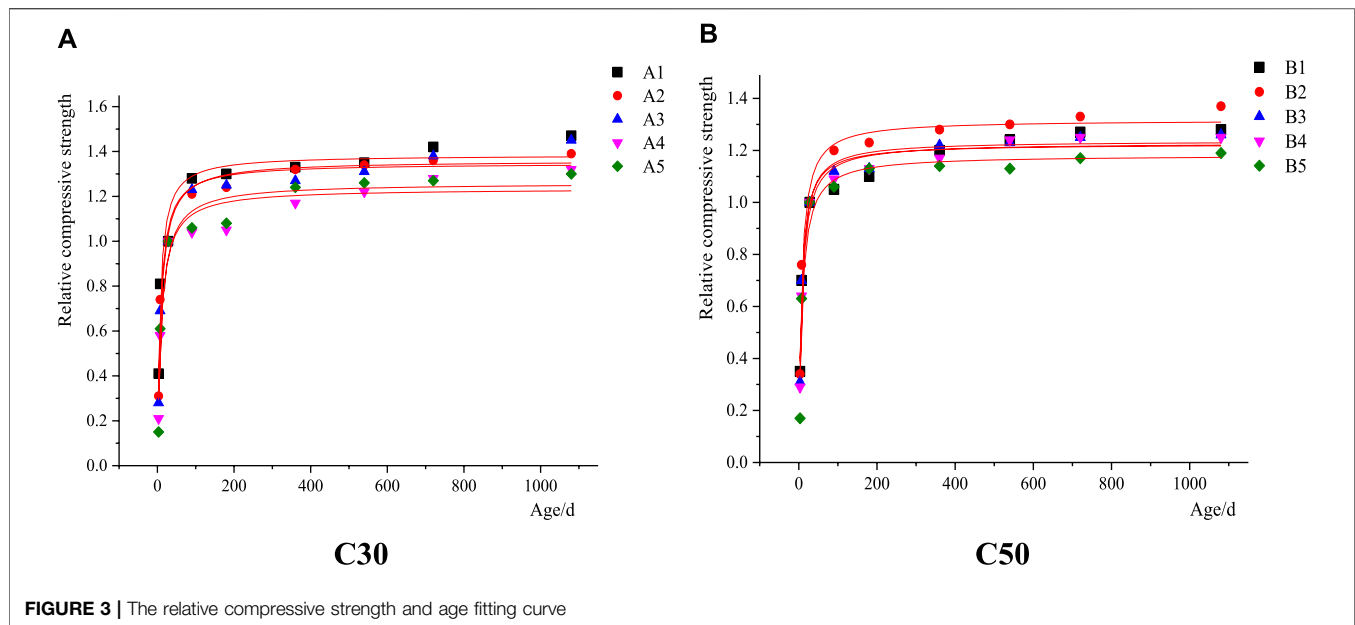


FIGURE 3 | The relative compressive strength and age fitting curve

TABLE 10 | Relative compressive strength and age fitting parameters.

Group	Content of iron tailings powder/%	A	B	C	Correlation coefficient R^2
A0	0	1.26	5.54	0.911	0.948
A30	30	1.19	6.37	0.879	0.969
A50	50	1.22	7.42	0.898	0.964
A70	70	0.878	6.22	0.711	0.934
A100	100	0.729	5.28	0.579	0.937
B0	0	1.11	5.33	0.906	0.950
B30	30	1.15	5.51	0.871	0.967
B50	50	1.02	5.10	0.826	0.973
B70	70	0.932	5.21	0.758	0.977
B100	100	1.01	6.30	0.852	0.945

The content of iron tailing powder is the mass percentage of iron tailing powder in mineral admixtures, and the coefficients retain three significant figures.

theoretical basis for the prediction of long-term compressive strength of iron tailings powder concrete. By using the software to fit the curve of compressive strength and age of C30 and C50 concrete with different iron tailings powder contents, it is found that the regularity of single compressive strength and age is not strong, but the better regularity is found by using the relative compressive strength and age fitting of each age to 28d strength. The fitting curve is shown in Figure 3.

In order to more accurately determine the relationship between reaction intensity and age, three parameter equation is chosen as the fitting formula, and the fitting reliability is high. The formula is as follows:

$$f_t = A \ln \left(1 + \frac{1}{B + Ct} \right)$$

In the formula, the fitting parameters of different concrete groups are shown in Table 10.

TABLE 11 | Model calculation value and the real value of concrete compressive strength (MPa).

Group		28d	90d	180d	360d	540d	720d	1080d
E0	Real	45.3	56.7	59.2	60.1	61.0	61.8	62.5
	Calculated	-	58.3	60.4	61.5	61.9	62.1	62.3
E30	Real	43.3	53.6	56.5	57.3	58.2	58.5	58.7
	Calculated	-	53.9	56.2	57.4	57.8	58.0	58.2
E50	Real	40.9	49.8	53.5	54.3	54.8	55.1	55.5
	Calculated	-	50.6	53.0	54.2	54.7	54.9	55.1
E70	Real	36.0	41.6	42.9	43.5	43.8	44.0	44.4
	Calculated	-	40.2	42.2	43.3	43.7	43.9	44.1
E100	Real	30.5	34.2	36.9	37.5	37.8	38.2	38.2
	Calculated	-	34.6	36.4	37.4	37.7	37.9	38.0
F0	Real	65.4	79.5	87.1	88.4	89.6	91.1	91.5
	Calculated	-	74.8	77.4	78.7	79.2	79.4	79.7
F30	Real	69.7	83.1	88.5	90.1	90.5	90.8	91.3
	Calculated	-	85.5	88.6	90.3	90.9	91.2	91.4
F50	Real	63.4	73.2	75.5	76.7	77.5	78.1	78.5
	Calculated	-	72.8	75.4	76.8	77.3	77.6	77.8
F70	Real	58.3	65.8	67.8	69.4	70.3	70.8	71.5
	Calculated	-	66.1	68.8	70.2	70.7	70.9	71.2
F100	Real	52.4	56.8	58.9	60.1	60.8	61.1	61.3
	Calculated	-	57.1	59.5	60.8	61.2	61.4	61.7

It can be seen from Table 10 that the range of parameters A, B, and C in the model of relative compressive strength and age relationship of iron tailings powder concrete is relatively concentrated, and the fitting correlation coefficient is also very high, all above 0.930, with a strong correlation, indicating that the model selection is more appropriate. Parameter A is related to the content of iron tailings powder. Parameter A increases with the increase of iron tailings powder contents. The A value of C30 concrete is between 0.7 and 1.3. The A value of group A5 with iron tailings powder is smaller and the dispersion is larger than that of the other four groups. The A value of C50 concrete is

TABLE 12 | Error rate of model calculation value and experiment measured value (%).

Group	Content of iron tailings powder/%	90d	180d	360d	540d	720d	1080d
E0	0	2.82	2.03	2.33	1.48	0.49	0.32
E30	30	0.56	0.53	0.17	0.69	0.85	0.85
E50	50	1.61	0.93	0.18	0.18	0.36	0.72
E70	70	3.37	1.63	0.46	0.23	0.23	0.68
E100	100	1.17	1.36	0.27	0.26	0.79	0.52
F0	0	5.91	11.1	10.9	11.6	12.8	12.9
F30	30	2.89	0.11	0.22	0.44	0.44	0.11
F50	50	0.55	0.13	0.13	0.26	0.64	0.89
F70	70	0.46	1.47	1.15	0.57	0.14	0.42
F100	100	0.53	1.02	1.16	0.66	0.49	0.65

relatively concentrated, ranging from 0.9 to 1.2. It shows that the influence factor (parameter a) of non-active admixtures on the strength of iron tailings under the condition of low water–binder ratio is much smaller than that under the condition of high water binder ratio. The range of B value and C value in the model is relatively concentrated, except for the points with large individual dispersion, B value ranges from 5.10 to 6.30, and C value ranges from 0.711 to 0.911.

To verify the correctness of the prediction model, 30% of the original C30 concrete cement is increased to 40%, the original C50 concrete 40% cement content is increased to 50%, and the concrete is prepared according to the mix proportion shown in **Table 9**. Based on the measured value of 28d compressive strength, the compressive strength of different age is calculated according to the model, and compared with the measured value of the same age. The results are shown in **Table 11**.

In order to intuitively show the reliability of the relative compressive strength and age prediction model, based on the experiment data of each age, the difference between the calculated value of the model and the real value is divided by the real value, and the error rate of strength predicted model is calculated, as shown in **Table 12**.

It can be seen from the above table that the prediction error of the relative compressive strength and age prediction model for E0 and F0 groups with single slag powder is relatively large, which indicates that the prediction effect of the concrete without iron tailings powder is general. However, the model has a good prediction effect on the strength of concrete mixed with iron tailings, and the prediction error of different proportion of iron tailings is relatively small. When the age is over 90 days, the error between the predicted value and the measured value is very small, and the error rate is basically within 1%. It shows that the model can effectively predict the long-term service strength of concrete based on the 28 days compressive strength, and the model has a

good prediction effect on the long-term service performance of concrete.

This study has found out the influence of iron tailings powder and slag powder on the workability and long-term mechanical properties of concrete. The appropriate proportion of tailings powder and slag powder can increase the workability of concrete and contribute to the long-term strength. In the future research, we should pay attention to the long-term hydration mechanism of iron tailings powder and explore the hydration process of composite admixtures.

CONCLUSION

- 1) Appropriate addition of iron tailings powder is beneficial to the working performance of concrete and can effectively reduce the time loss of concrete fluidity.
- 2) When the content of iron tailings powder in the compound admixture is 50% or less, the mechanical properties of concrete are equivalent to that of the single slag powder concrete. The long-term strength of 1080d in C30 and C50 concrete can reach 50.3 and 80.7 MPa.
- 3) Based on the 28d compressive strength, the relative strength and age prediction model of iron tailings powder concrete is established. The calculation and experimental results show that the model can accurately predict the long-term compressive strength, and the error rate is less than 1%.

DATA AVAILABILITY STATEMENT

The raw data supporting the conclusions of this article will be made available by the authors, without undue reservation.

AUTHOR CONTRIBUTIONS

LJ and WR conceived and designed the experiments; WR, CL, ZG, and ZY performed the experiments; SY contributed materials; WR and LJ wrote the article. All authors read and approved the manuscript.

FUNDING

This research was financially supported by the National Natural Science Foundation of China (No. 51834001) and Fundamental Research Funds for the Central Universities (FRF-BD-20-01B).

REFERENCES

Cao, S., Xue, G., Yilmaz, E., Yin, Z., and Yang, F. (2021b). Utilizing concrete Pillars as an Environmental Mining Practice in Underground Mines. *J. Clean. Prod.* 278, 123433. doi:10.1016/j.jclepro.2020.123433

Cao, S., Yilmaz, E., Yin, Z., Xue, G., Song, W., and Sun, L. (2021a). CT Scanning of Internal Crack Mechanism and Strength Behavior of Cement-Fiber-Tailings Matrix Composites. *Cement and Concrete Composites* 116, 103865. doi:10.1016/j.cemconcomp.2020.103865

Cao, S., Zheng, D., Yilmaz, E., Yin, Z., Xue, G., and Yang, F. (2020). Strength Development and Microstructure Characteristics of Artificial concrete Pillar

- Considering Fiber Type and Content Effects. *Construction Building Mater.* 256, 119408. doi:10.1016/j.conbuildmat.2020.119408
- Habert, G., Miller, S. A., John, V. M., Provis, J. L., Favier, A., Horvath, A., et al. (2020). Environmental Impacts and Decarbonization Strategies in the Cement and concrete Industries. *Nat. Rev. Earth Environ.* 1 (11), 559–573. doi:10.1038/s43017-020-0093-3
- Han, F., Li, L., Song, S., and Liu, J. (2017). Early-age Hydration Characteristics of Composite Binder Containing Iron Tailing Powder. *Powder Techn.* 315, 322–331. doi:10.1016/j.powtec.2017.04.022
- Han, F., Song, S., Liu, J., and Huang, S. (2019). Properties of Steam-Cured Precast concrete Containing Iron Tailing Powder. *Powder Techn.* 345, 292–299. doi:10.1016/j.powtec.2019.01.007
- Hou, Y. F., Liu, J. T., Zhao, S. R., and Peng, X. D. (2019). Effect Mechanism of Iron Tailing Powder on Cement Mortar Properties. *Journal Basic Sci. Eng.* 27 (05), 1149–1157. doi:10.16058/j.issn.1005-0930.2019.05.018
- Karthikeyan, B., Kathyayini, R., Aravindh Kumar, V., Uthra, V., and Senthil Kumaran, S. (2021). Effect of Dumped Iron Ore Tailing Waste as fine Aggregate with Steel and basalt Fibre in Improving the Performance of concrete. *Mater. Today Proc.* 2021, 2021 March. doi:10.1016/j.matpr.2021.01.906
- Leong, Y.-K. (2021). Controlling the Rheology of Iron Ore Slurries and Tailings with Surface Chemistry for Enhanced Beneficiation Performance and Output, Reduced Pumping Cost and Safer Tailings Storage in Dam. *Minerals Eng.* 166, 106874. doi:10.1016/j.mineng.2021.106874
- Li, J., Zhang, W., Li, C., and Monteiro, P. J. M. (2020a). Eco-friendly Mortar with High-Volume Diatomite and Fly Ash: Performance and Life-Cycle Assessment with Regional Variability. *J. Clean. Prod.* 261, 121224. doi:10.1016/j.jclepro.2020.121224
- Li, J., Zhang, W., Xu, K., and Monteiro, P. J. M. (2020b). Fibrillar Calcium Silicate Hydrate Seeds from Hydrated Tricalcium Silicate Lower Cement Demand. *Cement Concrete Res.* 137, 106195. doi:10.1016/j.cemconres.2020.106195
- Liu, W. B., Yao, H. Y., Wang, J. F., Chen, C. M., and Liu, Y. T. (2020). Current Situation of Comprehensive Utilization of Iron Tailings. *Mater. Rep.* 34 (Z1), 268–270.
- Liu, Y. X., Li, X. G., Zhang, C. M., and Lv, B. N. (2019). Properties of Iron Tailing Sand Cement Based Grouting Material. *J. Building Mater.* 22 (04), 538–544. doi:10.3969/j.issn.1007-9629.2019.04.006
- Lv, X., Shen, W., Wang, L., Dong, Y., Zhang, J., and Xie, Z. (2019). A Comparative Study on the Practical Utilization of Iron Tailings as a Complete Replacement of normal Aggregates in Dam concrete with Different Gradation. *J. Clean. Prod.* 211 (Nov), 704–715. doi:10.1016/j.jclepro.2018.11.107
- Miller, S. A. (2018). Supplementary Cementitious Materials to Mitigate Greenhouse Gas Emissions from concrete: Can There Be Too Much of a Good Thing?. *J. Clean. Prod.* 178, 587–598. doi:10.1016/j.jclepro.2018.01.008
- Pedro, D. D., Castro, G. B., Lima, M. M. F., and Lima, R. M. F. (2019). Characterisation and Magnetic Concentration of an Iron Ore Tailings. *J. Mater. Res. Techn.* 8 (1), 1052–1059. doi:10.1016/j.jmrt.2018.07.015
- Protasio, F. N. M., Avillez, R. R., Letichevsky, S., and Silva, F. A. (2020). The Use of Iron Ore Tailings Obtained from the Germano Dam in the Production of a Sustainable concrete. *J. Clean. Prod.* 278, 123929. doi:10.1016/j.jclepro.2020.123929
- Qi, C., and Fourie, A. (2019). Cemented Paste Backfill for mineral Tailings Management: Review and Future Perspectives. *Minerals Eng.* 144, 106025. doi:10.1016/j.mineng.2019.106025
- Song, S. M., and Chen, H. Y. (2020). Influence of Iron Tailings Powder on Performance of Low Clinker Cementitious Material concrete. *Bull. Chin. Ceram. Soc.* 39 (08), 2557–2566. doi:10.16552/j.cnki.issn1001-1625.2020.08.026
- Song, S. M., and Liu, X. D. (2017). Influence of Iron Ore Tailings Powder on the Performance of High Fluidity concrete. *Concrete* 11, 77–80. doi:10.3969/j.issn.1002-3550.2017.11.018
- Song, S. M., Zhang, L. Y., and Li, Z. Y. (2019). Effect of Iron Tailings Micropowder on Late-Property of Cement concrete. *Concrete* 01, 128–131+145. doi:10.3969/j.issn.1002-3550.2019.01.031
- Wu, R. D., Zhang, G. T., and Wang, K. (2019). Study on Strength and Chloride Diffusion Coefficient of Iron Tailings Powder concrete. *Construction Techn.* 48 (03), 25–27+54. doi:10.7672/sjgs2019030025
- Wu, R., and Liu, J. (2018). Experimental Study on the concrete with Compound Admixture of Iron Tailings and Slag Powder under Low Cement Clinker System. *Adv. Mater. Sci. Eng.* 2018, 1–7. 2018. doi:10.1155/2018/9816923
- Wu, R., Liu, J., Zhang, G., Zhang, Y., and An, S. (2020). Research on Carbonation Characteristics and Frost Resistance of Iron Tailings Powder concrete under Low-Cement Clinker System. *Adv. Mater. Sci. Eng.* 2020, 1–11. doi:10.1155/2020/9192757
- Yang, Y. C., and Mao, Y. G. (2020). Influence of Iron Tailing Powder of Different Fineness on Properties of Cement-Based Material. *J. Xi'an Univ. Architecture Techn.* 52 (02), 241–247. doi:10.15986/j.1006-7930.2020.02.013

Conflict of Interest: SY was employed by CCCC-SHEC Third Highway Engineering Co., Ltd.

The remaining authors declare that the research was conducted in the absence of any commercial or financial relationships that could be construed as a potential conflict of interest.

Publisher's Note: All claims expressed in this article are solely those of the authors and do not necessarily represent those of their affiliated organizations, or those of the publisher, the editors and the reviewers. Any product that may be evaluated in this article, or claim that may be made by its manufacturer, is not guaranteed or endorsed by the publisher.

Copyright © 2021 Ruidong, Yu, Juanhong, Linian, Guangtian and Yueyue. This is an open-access article distributed under the terms of the Creative Commons Attribution License (CC BY). The use, distribution or reproduction in other forums is permitted, provided the original author(s) and the copyright owner(s) are credited and that the original publication in this journal is cited, in accordance with accepted academic practice. No use, distribution or reproduction is permitted which does not comply with these terms.



An Experimental Study on Strength Characteristics and Hydration Mechanism of Cemented Ultra-Fine Tailings Backfill

Gan Deqing, Li Hongbao, Chen Chao*, Lu Hongjian and Zhang Youzhi

College of Mining Engineering, North China University of Science and Technology, Tangshan, China

OPEN ACCESS

Edited by:

Lijie Guo,

Beijing General Research Institute of
Mining and Metallurgy, China

Reviewed by:

Chen Qiusong,

Central South University, China

Jiaqi Li,

University of California, Berkeley,
United States

*Correspondence:

Chen Chao

13931501518@163.com

Specialty section:

This article was submitted to
Structural Materials,
a section of the journal
Frontiers in Materials

Received: 11 June 2021

Accepted: 05 July 2021

Published: 06 August 2021

Citation:

Deqing G, Hongbao L, Chao C,
Hongjian L and Youzhi Z (2021) An
Experimental Study on Strength
Characteristics and Hydration
Mechanism of Cemented Ultra-Fine
Tailings Backfill.
Front. Mater. 8:723878.
doi: 10.3389/fmats.2021.723878

In order to study the strength characteristics and hydration mechanism of the cemented ultra-fine tailings backfill (CUTB), the uniaxial compressive strength (UCS) tests of CUTB and cemented classified tailings backfill (CCTB) with cement-tailing ratio (C/T ratio) of 1:4 and 1:6 and curing ages of 3, 7, 14 and 28 days were carried out. The hydration products and morphology of the cemented paste backfill (CPB) were analyzed by X-ray diffraction (XRD) and scanning electron microscope (SEM). The results show that the UCS of the CUTB is significant compared to the CCTB under the same conditions; the greater the C/T ratio and curing age, the greater the UCS difference value. The UCS growth curve of the CUTB is approximately S-shaped, and there is a relationship between the UCS and curing age. The ultra-fine tailings particles in the CUTB have potential activity; in the alkaline environment-generated cement hydration, active SiO_2 and Al_2O_3 particles undergo secondary hydration reaction, resulting in no or very little $\text{Ca}(\text{OH})_2$ crystals generated in the CUTB, and the hydration products and morphology are also different.

Keywords: cemented ultra-fine tailings backfill, uniaxial compressive strength, regression equation, hydration mechanism, secondary hydration reaction

INTRODUCTION

The ultra-fine particles of mineral monomer exist in iron ore; therefore, iron ore must be ground to ultra-fine size to separate minerals and gangue (Deng et al., 2017a). The tailings particles discharged after mineral processing of the concentration plant are extremely fine, classified as ultra-fine tailings (UT). The tailings are usually discharged into the tailing pond or transported to the backfill plant to be used as cemented aggregates (Wang et al., 2014).

Generally speaking, the uniaxial compressive strength (UCS) of cemented paste backfill (CPB) is mainly determined by the cement-tailing ratio (C/T ratio), mass concentration, and curing age. Taking the underground mining environment into consideration, the UCS is affected by many factors such as temperature and mixing water (Benzaazoua et al., 2004; Fall et al., 2010; Yilmaz et al., 2012; Ercikdi et al., 2013; Jiang et al., 2019). The classified tailings have gotten promising results in CPB for several years, making the technological process more perfect. In recent years, the study is aimed at studying specific mines, focusing on the proportioning scheme optimization under the premise of satisfying UCS, ore recovery rate and settlement, and the rheological characteristics and transport characteristics of the filling slurry (Wang et al., 2009; Liu et al., 2019). The design optimization of mine filling process parameters and reasonable adjustment of the proportioning scheme in CPB can reduce the amount of cementing materials and improve the utilization of tailing

(Lu et al., 2018). In addition, some experts measured and analyzed the stress state and pore water pressure of underground CPB, indicating that filling and settlement time schedules have a significant impact on the pore water pressure of the cemented backfill, which in turn affects the quality of CPB (Doherty et al., 2015). The constitutive model and percolation model of CPB contributing to the efficient use of tailings are also studied (Helinski et al., 2007). Some of the industrial waste byproducts, including fly ash, slag, water granulated slag, and limestone powder, have been applied as potential active materials to CPB to reduce cement consumption and reduce filling costs (Ouellet et al., 2007; Wang et al., 2009; Cihangir et al., 2012; Yin et al., 2012; Zheng et al., 2016; Deng et al., 2017b). Many studies have shown that the choice of cement type also affects the UCS of CPB (Ercikdi et al., 2009; Xue et al., 2018).

The traditional research of CPB is based on the theory of building materials; the aggregates are not allowed to contain a large amount of ultra-fine particles. With the extensive application of classified tailings, a series of problems have arisen: low utilization of tailing, polluted underground environment, long cycle of filling mining, and high filling costs. Therefore, many studies have been carried out to analyze the fineness of tailings on the quality of CPB (Kesimal et al., 2003; Fall et al., 2005; Fall et al., 2008; Yilmaz et al., 2014; Ke et al., 2015; Ke et al., 2016). In recent years, with the increase of UT output, there are some signs of progress in relevant research. Kawatra has analyzed the mineral composition and particles morphology of UT in several regions (Kawatra, 2017). Wang et al. have investigated and analyzed the current status of UT, also discussed the key technical problems of slow settlement rate and the low water recovery rate in the recycling of UT, and proposed a solution (Wang et al., 2014). The theoretical and applied research on UT is currently concentrated on the rheological characteristics and conveying characteristics of slurry. Many experimental studies have been carried out on the influencing factors, parameter optimization, and transportation performance optimization (Yang et al., 2017; Zhou et al., 2017a; Zhou et al., 2017b; Deng et al., 2018a; Deng et al., 2018b). There is less literature on the UCS of cement ultra-fine tailings backfill (CUTB). Qiu et al. have researched the effect of C/T ratio, mass concentration, and curing age on the UCS of CUTB. The results show that UT has certain activity and the curing age is the most important factor affecting UCS, followed by the C/T ratio and mass concentration (Qiu et al., 2017). Niroshan et al. have designed a uniaxial compressive strength test with different cementitious materials and contents and found that CUTB of slag + cement had a higher early strength. Compared with CPB, CUTB of slag and cement had a higher stiffness, summing up the prediction model of UCS (Nircoshan et al., 2017). Based on the UCS test and the physicochemical properties of UT, Xu et al. have discussed the diagenesis mechanism of CUTB (Xu et al., 2013).

Most of the current research involved the application and optimization material of UT and the cemented backfill to UT; however, few studies discussed the strength characteristics and the hydration reaction mechanism of CUTB. Because the particles sizes of most UT are smaller than those of cement particles, the strength formation mechanism and hydration

reaction of CUTB are different from CCTB, which is essentially different. Therefore, it is very important to research the strength characteristics and hydration reaction mechanism of CUTB. In this article, the ultra-fine tailings and classified tailings of iron were used as experimented materials. Based on the analysis of the basic physical and chemical properties, the strength experiment of different schemes of CPB was designed, the strength variation law of CUTB analyzed, and a prediction model based on the strength value of tailings gradation characteristics and curing age constructed. X-ray diffraction (XRD) and scanning electron microscope (SEM) were used to compare and analyze the hydration products of different CPB, research the hydration reaction mechanism of CUTB, and discuss the strength formation mechanism of CUTB.

MATERIALS AND METHODS

Test Material

Tailings

The test materials are the ultra-fine tailings and the classified tailings in an iron ore mine in northern North China. The composition of the tailings is shown in **Figure 1** and **Table 1**. The size of the median grain of the ultra-fine tailings is 14.97 μm , and the restricted rain size is 20.7 μm , and it is classified into UT according to the Design Reference Materials for Tailing Facilities. The median grain size of the classified tailings is 190.78 μm , and the restricted grain size is 269.5 μm . The coefficients of uniformity for the two types of tailings are 5.88 and 5.12, respectively. The coefficients of curvature for the two types of tailings are 1.1 and 0.86, respectively (Xu et al., 2013). The two types of tailings belong to the better gradation tailings.

Figure 2 shows that the ultra-fine tailings are mainly composed of cohesive particles and powder particles, containing a small number of sand particles, and the shape of the particles is mostly irregular (Wolff et al., 2011). The surface of the particles is smooth with large surface energy. There is an agglomeration phenomenon found in the ultra-fine tailings (Wolff et al., 2011). The classified tailings are composed of sand particles. The surface of the particles is relatively rough, mostly the crystal grain boundary surface and a small amount of staggered fracture surface. A small number of cohesive particles and powder particles attach to the surface of sand particles.

Figure 3 shows the XRD spectrum results. The tailings contain a large amount of SiO_2 (Wolff et al., 2011), which belongs to high silicon tailings, and contain MgO , CaO , Al_2O_3 , and total Fe. **Figure 3** also shows that the intensity of the diffraction peak of the classified tailings is greater than that of the ultra-fine tailings; especially, the main diffraction peak of SiO_2 is significant. The intensity of the main diffraction of SiO_2 in the classified tailings is about 15,000, while the main diffraction peak intensity of SiO_2 in the ultra-fine tailings is less than 9,000. It can be seen that the ultra-fine tailings particles have a low degree of crystallization, and the amorphous particles have high surface energy, high content, and large specific surface area, so the activity of the ultra-fine is relatively higher than that of the classified tailings.

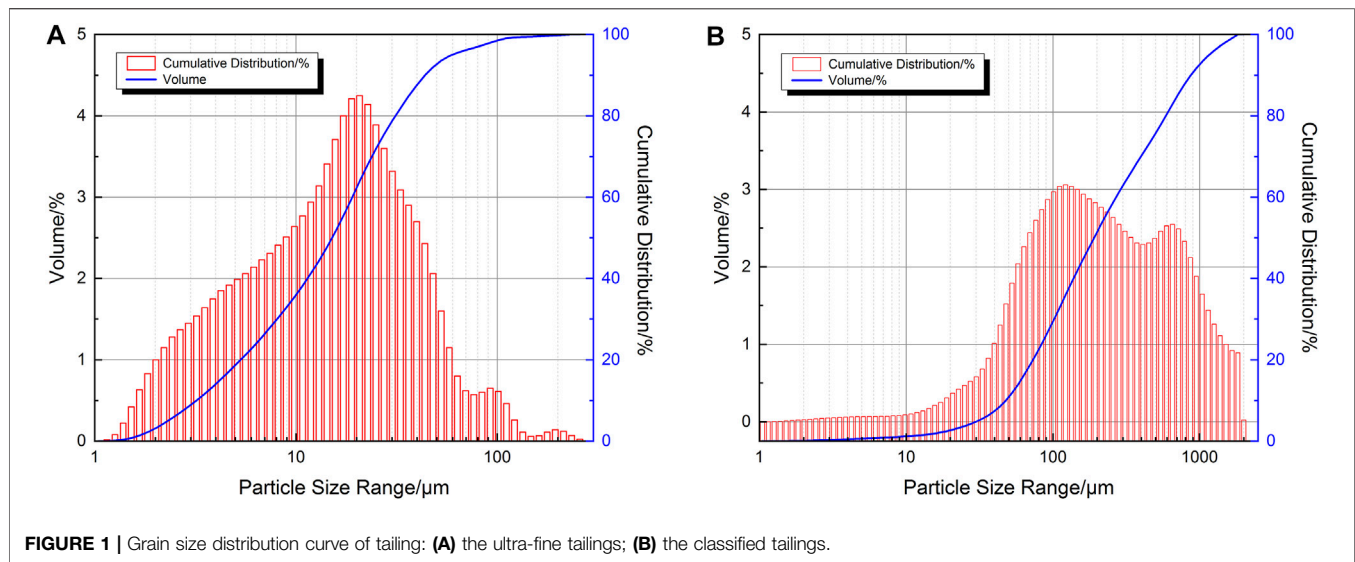


FIGURE 1 | Grain size distribution curve of tailing: **(A)** the ultra-fine tailings; **(B)** the classified tailings.

TABLE 1 | Physical and chemical characterization of the tailings and binder.

Characteristics		The ultra-fine tailings	The classified tailings	Binder
Chemical composition	SiO ₂	67.58%	74.24%	20.8%
	MgO	5.60%	3.34%	3.23%
	CaO	4.04%	2.96%	56.2%
	Al ₂ O ₃	7.30%	7.65%	10.0%
	Fe ₂ O ₃	—	—	4.4%
	SO ₃	—	—	2.49%
	Total Fe	6.00%	4.29%	—
	Total	90.52%	92.48%	97.12
	Alkalinity coefficient	0.13	0.08	—
	Quality coefficient	0.25	0.19	—
	Activity coefficient	0.06	0.04	—
Physical properties	Effective grain size ($d_{10}/\mu\text{m}$)	3.52	52.62	1.55
	Median grain size ($d_{50}/\mu\text{m}$)	14.97	190.78	14.1
	Control grain size ($d_{60}/\mu\text{m}$)	20.7	269.5	17.3
	Coefficient of uniformity (Cu)	5.88	5.12	11.16
	Coefficient of curvature (Cc)	1.10	0.86	1.13

Table 1 also shows the main chemical components of tailings, the mass ratios of 90.52% (the ultra-fine tailings) and 92.48% (the classified tailings). The ultra-fine tailings have an alkalinity coefficient of 0.13, which belongs to the acidic tailings. The quality coefficient of the ultra-fine tailings is 0.25; the quality is a little poor. The activity coefficient of the ultra-fine tailings is 0.06; the ultra-fine tailings have a lower activity (Xu et al., 2013).

Binder

The cement used in the tests is the production batch of Jidong brand ordinary Portland cement (325#), which was produced in Tangshan city, Hebei Province, China.

Mixing Water

The tailings discharged from the plant contain water. In the test preparation stage, the tailings were placed into a drying box to be dried; then, they will be naturally cooled at room temperature to avoid the influence of moisture in the tailings on the test

(Benzaazoua et al., 2004). Tap water from Lunan District of Tangshan City was used as mixing water to mix binder and tailings and prepare ultra-fine tailings backfill slurry.

Uniaxial Compressive Strength Tests

Experiment Mixing Ratio

According to the research experience and application (Qiu et al., 2017), the C/T ratios were 1:4 and 1:6, and the curing age was 3, 7, 14, and 28 days. Because of the obvious difference at the same mass concentration of the ultra-fine tailings and the classified tailings, the mass concentration was determined to be 70%.

Experiment Method

According to the experiment scheme, calculate and weigh the quality of cement and tailings. Then, they will be mixed evenly and poured into the mixing vessel. After that, add water and mix for 2 min to complete the backfill slurry. The backfill slurry is injected into the standard triple test strip of 7.07 cm × 7.07 cm × 7.07 cm

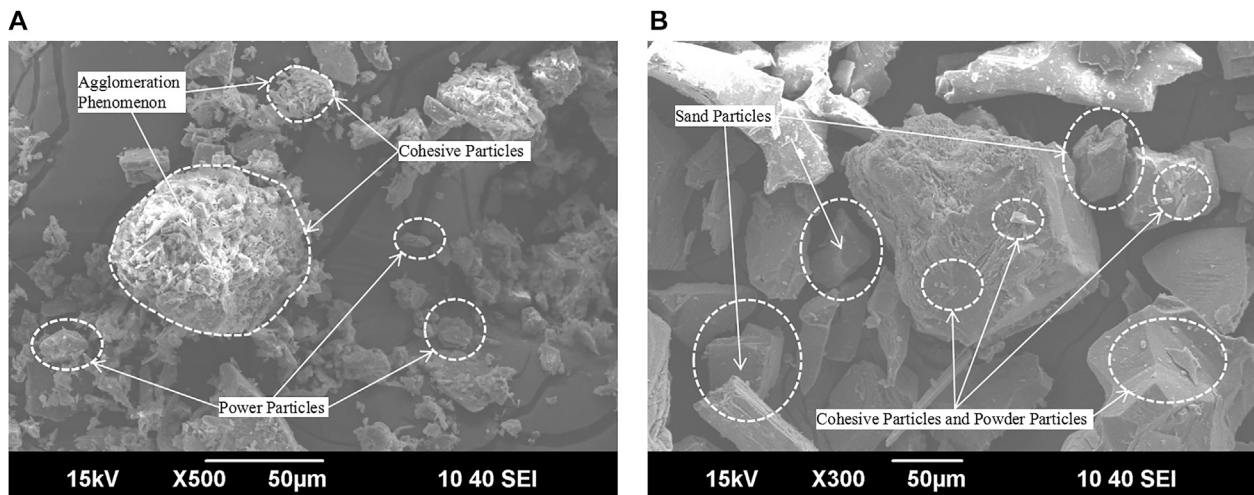


FIGURE 2 | SEM images of the tailings: **(A)** the ultra-fine tailings; **(B)** the classified tailings.

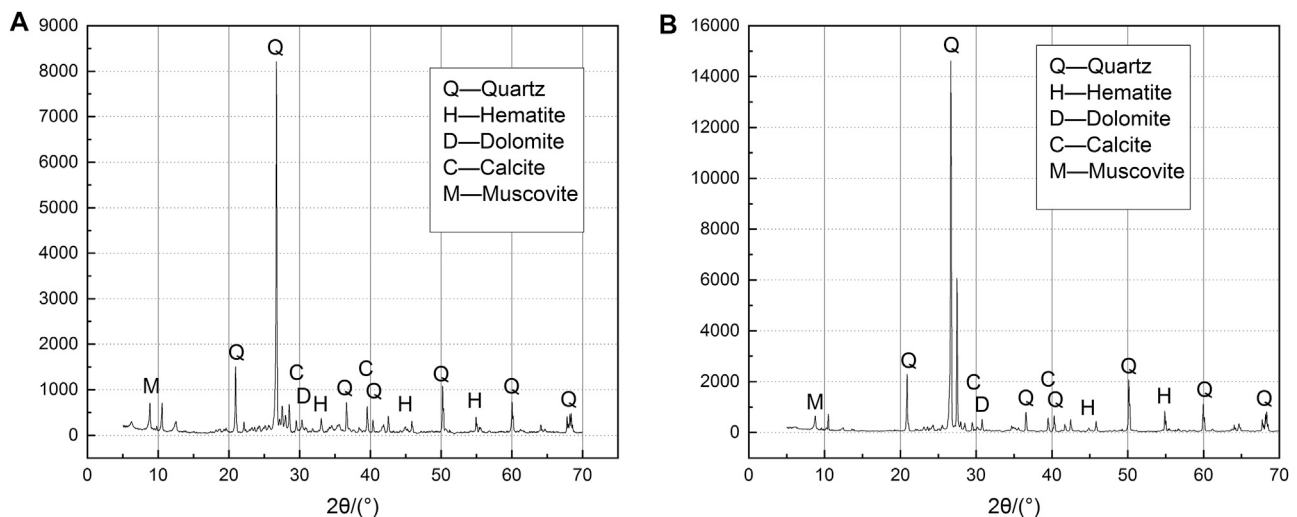


FIGURE 3 | XRD spectrum results of tailings: **(A)** the ultra-fine tailings; **(B)** the classified tailings.

(Xue et al., 2018). After being tamped and smoothed, it will be placed in the curing box for 24 h and then demolded. The CPB was numbered and labeled and then placed in the curing box for maintenance. The curing environment temperature is $20 \pm 1^\circ\text{C}$, the relative humidity is 90%, and the curing time is controlled according to the experimental scheme. The cured CPB was placed on the test platform of the uniaxial press, aligned with the axis. To determine the UCS of the backfill, each group of CPB is measured 3 times and averaged (Fall et al., 2005).

XRD and SEM

After the uniaxial compressive strength test, the internal samples of CPB were stored in a sealed bottle containing anhydrous ethanol. The purpose is to replace the moisture in the CPB sample and terminate the hydration reaction. A small amount of CPB in the

sealed bottle was taken out and naturally air-dried, then ground to about 200 mesh. The scanning angle was $5^\circ\text{--}7^\circ$ and the scanning speed was $0.02^\circ/\text{min}$ by X-ray diffractometer (Bruker D8 ADVANCE) (Fall et al., 2005). Another complete sample of CPB in the sealed bottle was taken and naturally air-dried. The microscopic morphology of the original fracture surface of CPB was taken by the scanning electron microscope (JSM-6390A), and the acceleration voltage was 15 kV (Fall et al., 2005).

RESULTS AND DISCUSSION

UCS Variation Law of CUTB

At present, domestic and foreign researchers generally believe that the higher the proportion of cement and the longer the

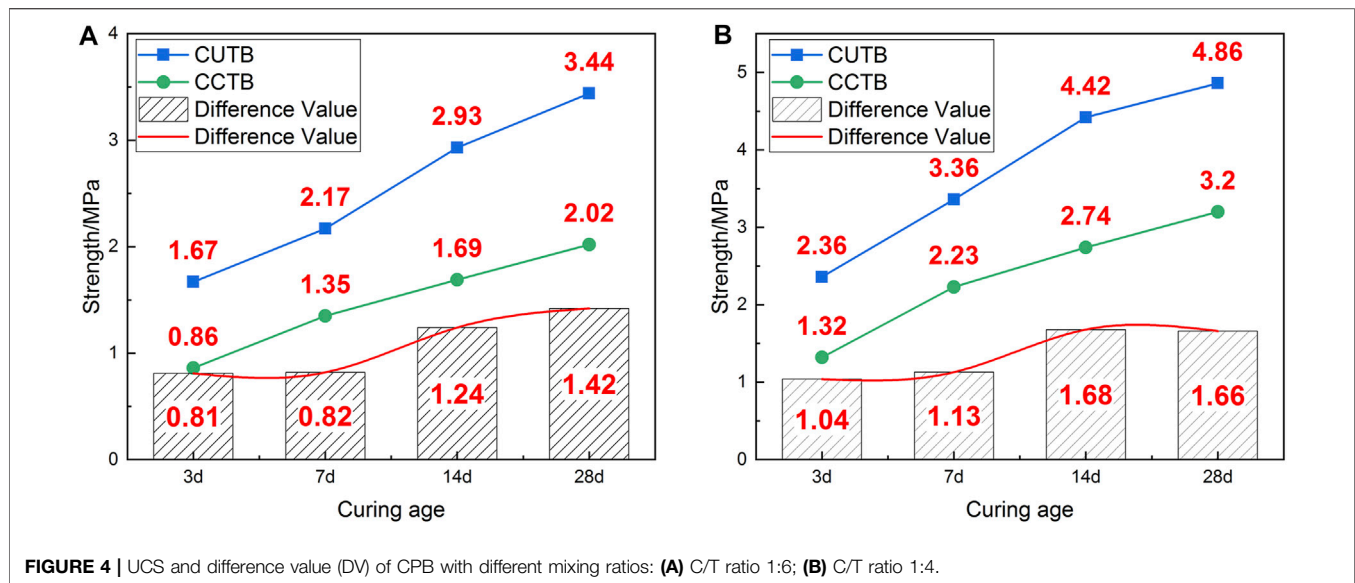


FIGURE 4 | UCS and difference value (DV) of CPB with different mixing ratios: **(A)** C/T ratio 1:6; **(B)** C/T ratio 1:4.

TABLE 2 | UCS of CPB with different mixing ratio.

Number	Mass concentration (%)	C/T ratio	Tailings	Curing age (d)	UCS/MPa
1	70	1:4	UT	3	2.36
2	70	1:4	UT	7	3.36
3	70	1:4	UT	14	4.42
4	70	1:4	UT	28	4.86
5	70	1:6	UT	3	1.67
6	70	1:6	UT	7	2.17
7	70	1:6	UT	14	2.93
8	70	1:6	UT	28	3.44
9	70	1:4	CT	3	1.32
10	70	1:4	CT	7	2.23
11	70	1:4	CT	14	2.74
12	70	1:4	CT	28	3.20
13	70	1:6	CT	3	0.86
14	70	1:6	CT	7	1.35
15	70	1:6	CT	14	1.69
16	70	1:6	CT	28	2.02

curing age, the greater the UCS of the CPB (Kesimal et al., 2003). **Figure 4** and **Table 2** show that the CUTB also follows the rule in terms of C/T ratio and curing age.

Figure 4 also shows that the UCS of the CUTB is significantly higher than the CCTB at the same conditions and the greater the C/T ratio, the greater the UCS difference value. When the C/T ratio is 1:6, the UCS differences value of CPB are 0.81 MPa (3 days), 0.82 MPa (7 days), 1.24 MPa (14 days), and 1.42 MPa (28 days), and the average value is 1.07 MPa. Moreover, when the C/T ratio is 1:4, the UCS differences value of CPB are 1.04 MPa (3 days), 1.13 MPa (7 days), 1.68 MPa (14 days), and 1.66 MPa (28 days), and the average value is 1.38 MPa. With the increase of the curing age, when the UCS difference value increases, the ultra-fine tailings are more conducive to the increase of UCS in the CUTB and increase faster than those of the CCTB. Especially during the curing age of 7–14 days, the UCS differences value

increases by 0.42 MPa (C/T ratio 1:6) and 0.55 MPa (C/T ratio 1:4), respectively, and the UCS difference value of the CUTB increases sharply, which is approximately an S-shaped curve. With the increase of the C/T ratio (cement content), the UCS difference value of the CUTB increases. When the C/T ratio is 1:6, the UCS difference value of CUTB is 1.07 MPa, and when the C/T ratio is 1:4, the UCS difference value is 1.38 MPa. It shows that the CUTB is more sensitive to the change of cement content, increasing the same quality of cement; the UCS of CUTB increases more.

Figure 5 shows that the UCS variation laws of the CUTB and the CCTB are different under the same mixing ratio. The CUTB has a relatively large early strength, which reaches 1.67 MPa at a C/T ratio of 1:6 and a curing age of 3 days. Under the same mixing ratio, the UCS of the CCTB is only 0.86 MPa. The UCS growth curve of the CUTB is approximately S-shaped, and during the curing age of 3–7 days, the UCS growth rate of the CUTB is slow,

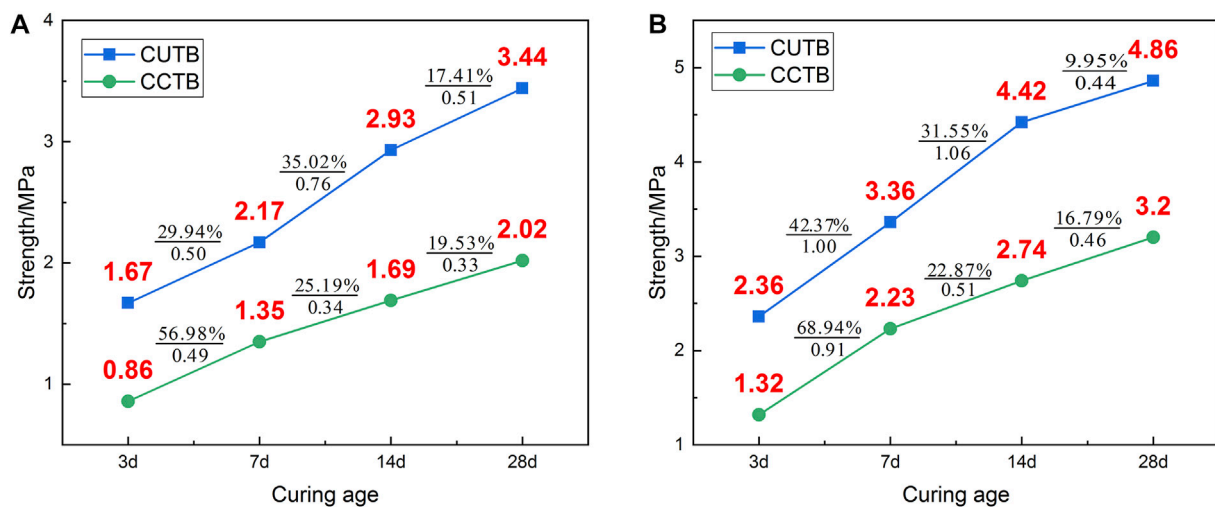


FIGURE 5 | UCS variation law of CPB with different mixing ratios: (A) C/T ratio 1:6; (B) C/T ratio 1:4.

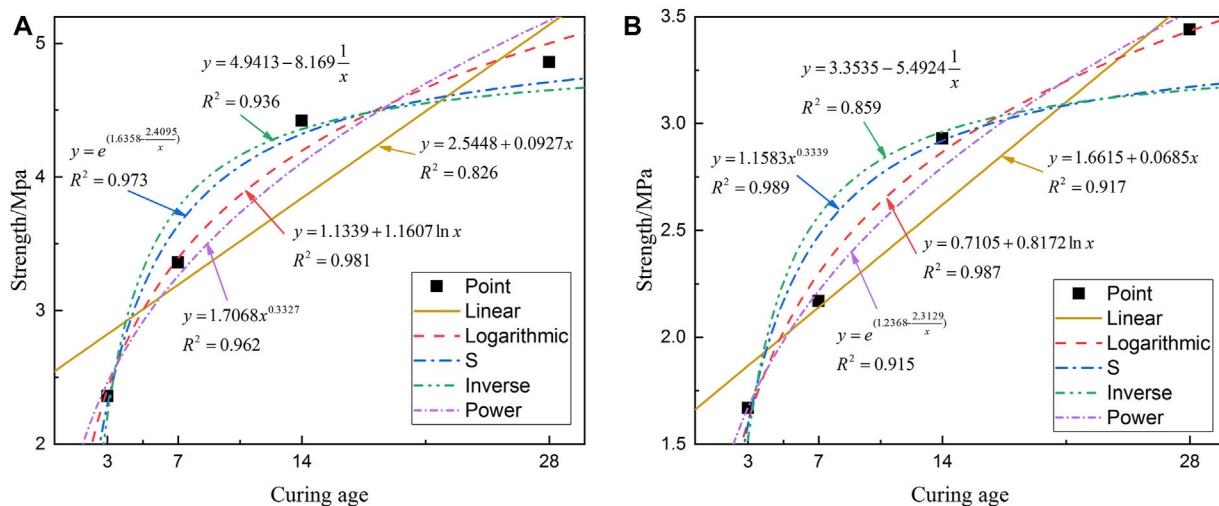


FIGURE 6 | Fitting curve and regression equation of UCS with curing age: (A) C/T ratio 1:6; (B) C/T ratio 1:4.

with an increase of 0.5 MPa (29.94%). The UCS growth rate of the CUTB is accelerated during the curing age of 7–14 days, with an increase of 0.76 MPa (35.02%). In the later period of curing age (14–28 days), the UCS growth rate of the CUTB decreases, with an increase of 0.51 MPa (17.41%). In contrast, the UCS growth curve of the CCTB is of an approximately convex shape, and the UCS growth rate decreases with curing age. When the C/T ratio is 1:6, the UCS growth rate of CCTB is 0.49 MPa (56.98%), 0.34 MPa (25.19%), and 0.33 MPa (19.53%), respectively.

UCS Regression Fitting of CUTB

Figure 6 shows that there is a nonlinear relationship between the UCS and curing age of CUTB. According to the variation law of UCS and curing age of CUTB, the least-square method is used for curve regression analysis and to obtain a significant regression

equation. The function expression of regression equation is as follows:

$$\hat{P}_k = f(T_k, b_1, b_2, \dots, b_m),$$

where \hat{P}_k is regression value of UCS, T_k is curing age, and b_1, b_2, \dots, b_m are regression parameters.

The principle of the least-square method is to minimize the sum of squares deviations between all observed values and regression values:

$$Q(b_1, b_2, \dots, b_m) = \sum_{i=1}^n \{P_k - f(T_k, b_1, b_2, \dots, b_m)\}^2,$$

where $Q(b_1, b_2, \dots, b_m)$ is the sum of squares deviations and P_k is the observation value.

TABLE 3 | Regression equation and test results.

C/T ratio	Equation type	Expression	R	R ²	ADJ R ²	F	p
1:4	Linear	$P = 2.5448 + 0.0927T$	0.909	0.826	0.739	9.5153	0.091
	Logarithmic	$P = 1.1339 + 1.1607 \ln T$	0.99	0.981	0.971	100.8506	0.0098
	S	$P = e^{(1.6358 - \frac{2.4955}{T})}$	0.986	0.973	0.960	72.1308	0.0136
	Inverse	$P = 4.9413 - 8.169\frac{1}{T}$	0.968	0.936	0.904	29.3922	0.0324
	Power	$P = 1.7068T^{0.3327}$	0.981	0.962	0.943	51.0318	0.019
1:6	Linear	$P = 1.6615 + 0.0685T$	0.957	0.917	0.874	21.9546	0.0427
	Logarithmic	$P = 0.7105 + 0.8172 \ln T$	0.993	0.987	0.980	147.1173	0.0067
	S	$P = e^{(1.2368 - \frac{2.3422}{T})}$	0.957	0.915	0.873	21.6065	0.0433
	Inverse	$P = 3.3535 - 5.4924\frac{1}{T}$	0.927	0.859	0.788	12.1806	0.0732
	Power	$P = 1.1583T^{0.3339}$	0.994	0.989	0.984	187.3661	0.0053

The parameters of different curve regression equations are calculated, and the method of variance analysis is selected for statistical analysis. Then, the correlation coefficients (R), coefficient of determinations (R²), and adjusted coefficient of determinations (ADJ R²) of different regression equations are obtained, as well as the F values and p values of the significance test. The specific calculation results are shown in Table 3.

Table 3 shows that the linear regression equation between UCS and curing age of the CUTB at the C/T ratio of 1:4 and 1:6 is relatively low, and the adjusted coefficients of determinations are only 0.739 and 0.874, indicating that the UCS of CUTB is nonlinear with the curing age. According to the scatter plot, select the regression equations as follows: logarithmic equation, S-shaped equation, inverse equation, and power equation. The C/T ratio is 1:4, the logarithmic equation and the S-shaped equation have a high degree of regression, and the adjusted coefficients of determinations are 0.971 and 0.960. The F value of the logarithmic regression is 100.8506; the p values are 0.0098 < 0.01, showing that the significance of the logarithmic is extremely great. The C/T ratio is 1:6, the logarithmic regression equation and the power equation have a high degree of regression, and the adjusted coefficients of determinations are 0.980 and 0.984. The F values are 147.1173 and 187.3661, and the p values are 0.0067 and 0.0053. In summary, the UCS of CUTB has a logarithmic relationship with curing age, and the regression equation is as follows:

$$\begin{aligned} \text{C/T 1:4 } P &= 1.1339 + 1.1607 \ln T \\ \text{C/T 1:6 } P &= 0.7105 + 0.8172 \ln T \end{aligned} \quad (1)$$

According to the regression equation, the regression values corresponding to different observation values are calculated, and residual error analysis is performed. The specific calculation results are shown in Figure 7 and Table 4:

Analyzing the residual error of the regression equation, it can be seen that the observation value and the regression value are very small, but the residual value has a unit and cannot be directly used for comparative analysis. Generally, the residual values are standardized, and it follows the standard normal distribution N (0,1). The standardized residuals of the regression equations of UCS and curing age are all within the interval of -2~+2 and contain randomness, indicating the equation is normal.

XRD Analysis of CPB

Figure 8 shows the XRD spectrum of the ultra-fine tailings and the classified tailings under the same conditions (C/T ratio 1:4, mass concentration 70%, and curing age of 3 days). The SiO₂ diffraction peak can be clearly seen from the figures because the main component of CPB is SiO₂, which accounts for about 40% of the total mass. On the other hand, most SiO₂ particles are inert materials, which act as aggregate and do not participate in the hydration reaction. The main hydration products in CUTB are C-S-H and AFt. Among them, AFt belongs to the crystals and has obvious diffraction peaks and C-S-H is a mostly amorphous hydrate with poor crystallinity. Moreover, there is a broad, convex hull background under the diffraction peaks of 2θ between 20° and 45°. In contrast, the XRD spectrum of CCTB can observe not only AFt crystals and C-S-H but also obvious diffraction peaks of Ca (OH)₂ crystals.

The analysis shows that the content of Ca (OH)₂ crystals in the CUTB is very little or non-existent, and the area of the convex hull background of the spectrum is significantly larger than that of the CCTB. It shows that the hydration products and content of CUTB and CCTB are different, and the hydration reaction in the two kinds of CPB is different.

SEM Analysis of CPB

The CPB is mainly composed of three major types of materials, including unhydrated cement clinker, inert including in tailings and hydration product (Xu et al., 2013), and hydration products of Portland cement such as calcium silicate hydrate (C-S-H), ettringite (AFt), calcium aluminate sulfate hydrate (AFm), portlandite (Ca (OH)₂) and hydrogarnet (C₃AH₆). The composition of C-S-H gel is complex, and it is usually assumed that the molecular formula is C₃S₂H₃. C-S-H gel has extremely poor crystallinity and its morphology is not fixed; most of them are fibrous, granular, and networked. The structural formula of AFt is [Ca₃Al(OH)₆ · 12H₂O](SO₄)₁₆ · H₂O, with a high degree of crystallinity. The crystal is generally hexagonal prismatic, which grows into needle-like or columnar shape according to the growth space. The Ca (OH)₂ has a good crystallinity with a hexagonal plate shape. It is unevenly distributed and the crystal size is 10–100 μm (Fall et al., 2005).

Figures 9A,B are SEM images of CUTB and CCTB under the same conditions (C/T ratio 1:4, mass concentration 70%, and curing age of 3 days). It can be seen from the figure that there are

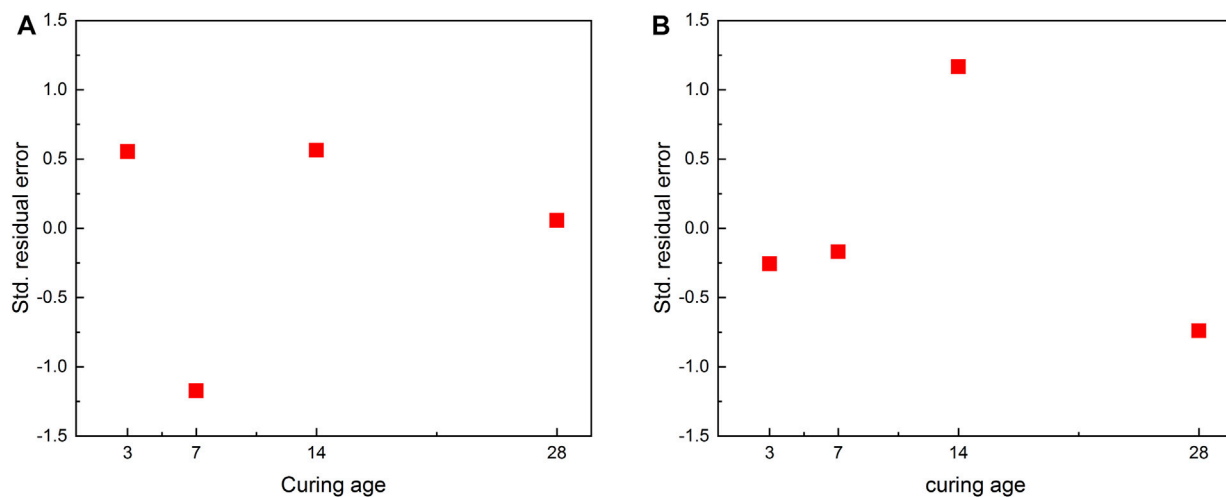


FIGURE 7 | Standardized residual error of regression equation: (A) C/T ratio 1:6; (B) C/T ratio 1:4.

TABLE 4 | Regression value and residual error analysis.

C/T ratio	Observation value	Regression value	Residual error	Standardized residual error
1:4	2.36	2.4091	-0.0491	-0.2564
	3.36	3.3925	-0.0325	-0.1697
	4.42	4.197	0.223	1.1656
	4.86	5.0015	-0.1415	-0.7395
1:6	1.67	1.6083	0.0617	0.553
	2.17	2.3008	-0.1308	-1.1723
	2.93	2.8672	0.0628	0.5628
	3.44	3.4337	0.0063	0.0566

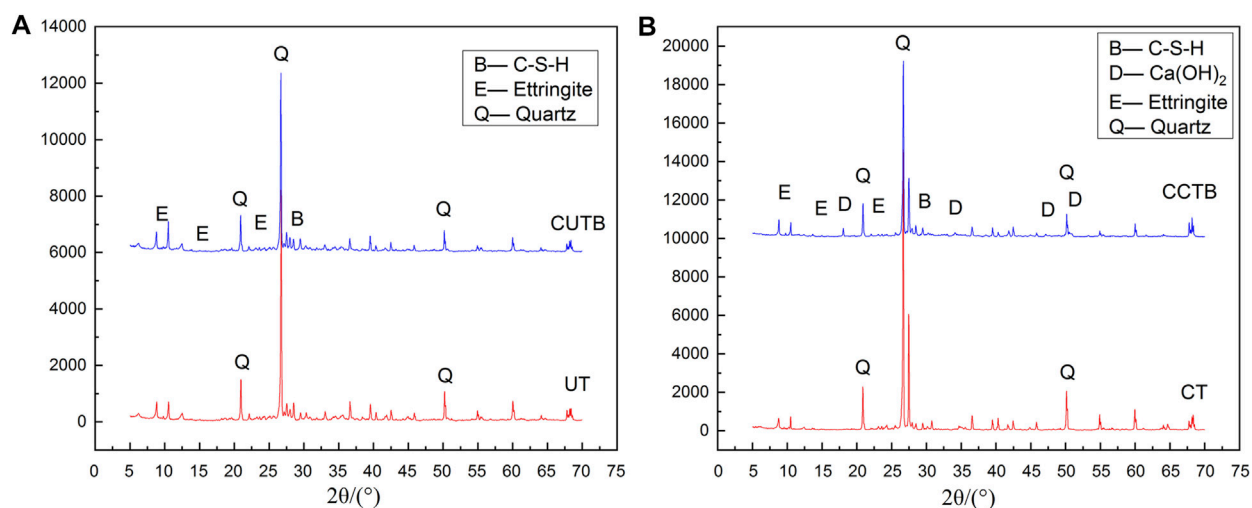


FIGURE 8 | XRD spectrum of CPB with S/W ratio 1:4 and curing age of 3 days: (A) CUTB; (B) CCTB.

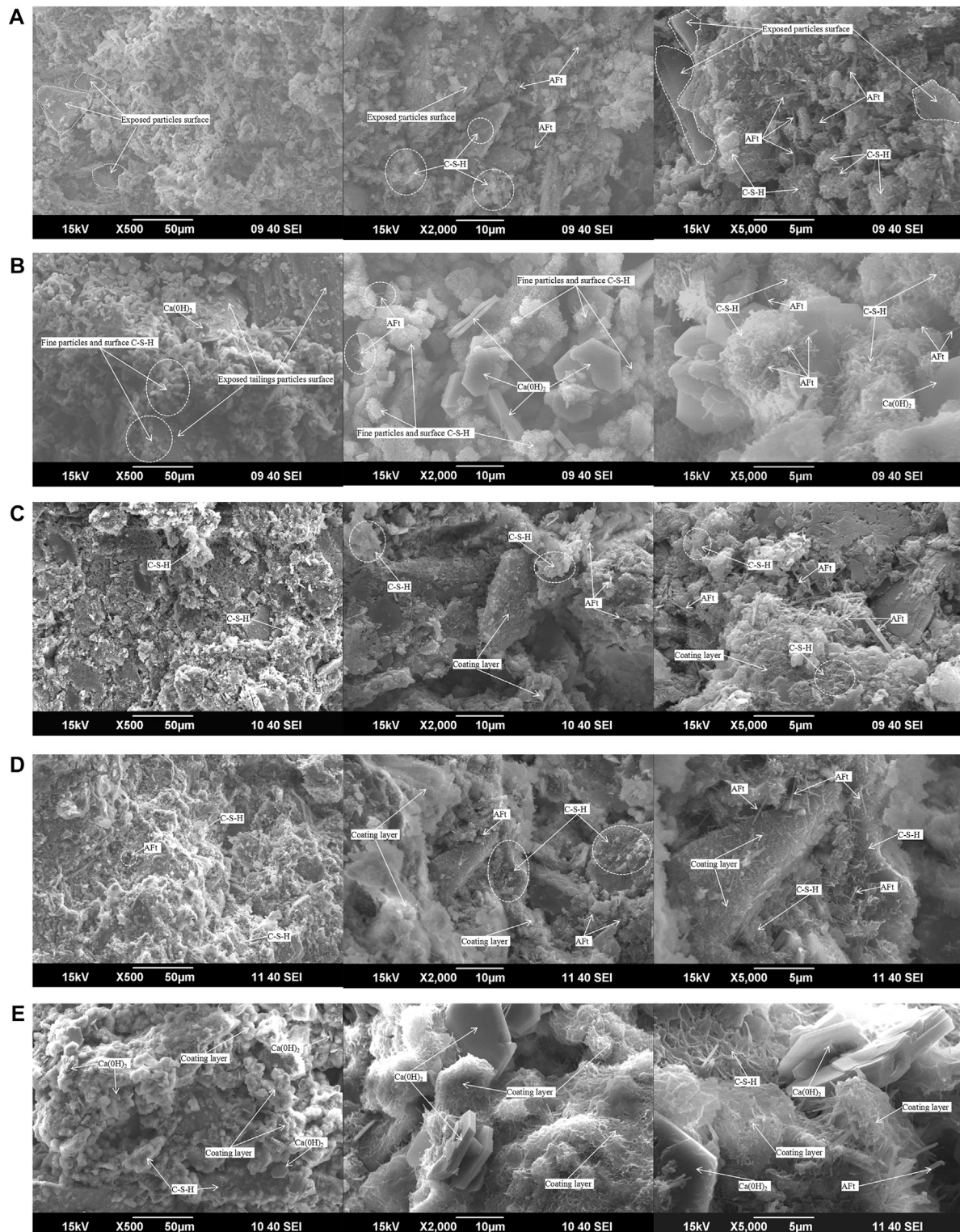


FIGURE 9 | SEM images of CPB with different C/T ratio and curing age: **(A)** CUTB, C/T ratio 1:4, curing age of 3 days; **(B)** OCTB, C/T ratio 1:4, curing age of 3 days; **(C)** CUTB, C/T ratio 1:4, curing age of 7 days; **(D)** CUTB, C/T ratio 1:4, curing age of 28 days; **(E)** CCTB, C/T ratio 1:4, curing age of 28 days.

obvious hydration products in the CPB in the early curing age, but the morphology of the hydration products is different between the CUTB and the CCTB. In the CUTB, the C-S-H gel mostly wraps fine particles and ultra-fine particles in a network shape or attaches to the surface of coarse particles in a fibrous; the AFt crystals are randomly distributed on the surface of the particles and in tiny pores, and length is about 1~3 μm . In the CCTB, the C-S-H gel basically exists on the surface of fine particles and ultra-fine particles, the AFt crystals are mostly perpendicular to the surface of fine particles and ultra-fine particles, and the length is about 1~3 μm . The $\text{Ca}(\text{OH})_2$ crystals are randomly filled in the fine pores and micro-pores, with a size of about 5–10 μm . No obvious $\text{Ca}(\text{OH})_2$ crystals are observed in the CUTB, it can be seen that the hydration products in the CUTB and CCTB are different, and the hydration reactions that occur are also different. It shows that the particle size of tailings affects the hydration process of the CPB, and the distribution and morphology of the hydration products change due to the difference in particle size.

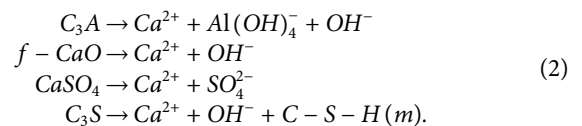
Figures 9C,D are SEM images of CUTB and CCTB under the same conditions (C/T ratio 1:4, mass concentration 70%, and curing age of 28 days). According to the hydration mechanism of the cement paste, the hydration reaction continues at 28 days of curing age, the hydration rate decreases, the hydration product grows slowly, and the internal structure of CPB is basically formed. However, the morphology of the hydration products and internal structure of CUTB and CCTB are still different. In the CUTB, the C-S-H gel forms a coating layer around fine particles and ultra-fine particles, and grows outwards. At the same time, it grows in a network on the surface of the coarse particles and connects the fine particles and ultra-fine particles with the coarse particles to form a dense three-dimensional whole. The AFt crystals are distributed on the surface of coarse particles and tiny pores, and the length is about 1~3 μm . In the CCTB, the C-S-H gel forms a coating layer around fine particles and ultra-fine particles, grows outward with particles as the center, and connects the particles into a whole. The AFt crystals mostly exist perpendicular to the surface of fine particles and ultra-fine particles, and the length is about 1~3 μm . The $\text{Ca}(\text{OH})_2$ crystals are distributed disorderly in the CCTB: some are wrapped by C-S-H gel and some are filled into pores.

There are no obvious $\text{Ca}(\text{OH})_2$ crystals in the CUTB at the curing age of 28 days. It can be seen that the difference of hydration reaction between the two CPB always exists, indicating that the particle size of tailings has always affected the hydration process in the curing process, and there is the difference in the structure of the CPB and the morphology of the hydration products. Although the C-S-H gel forms a coating layer after curing 28 days, the C-S-H gel grows with independent particles as the center in the CCTB, with the increasing thickness of the coating layer. Particles contact with each other and continue to grow at the contact point and finally form a three-dimensional whole, and obvious particle profile can be observed in the figure. In the CUTB, fine particles and ultra-fine particles are wrapped in C-S-H gel to form aggregates, and independent fine particles and ultra-fine particles are not observed. The aggregates connect with adjacent coarse particles to form a dense whole.

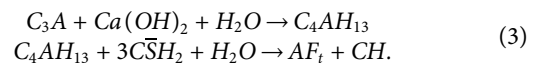
Figures 9A,D,E are SEM images of CUTB at different curing ages under the same proportion (C/T ratio 1:4, mass concentration 70%, and curing age of 28 days). It can be seen from the figures that the morphology of C-S-H gel changes with the curing age and has regularity. At the curing age of 3 days, the C-S-H gel is centered on the fine particles and ultra-fine particles and grows on the surface of the surface in a network shape, and the surface of the coarse particles is exposed and no obvious C-S-H gel is observed. At the curing age of 7 days, with the continuous growth of the C-S-H gel outside the coating layer, the particles and the C-S-H gel form agglomerates where the fine particles and ultra-fine particles are dense, and there are obvious network-shaped C-S-H gel on the surface of local coarse particles. The morphology of AFt crystals changed with the growth of the curing age, AFt crystals are mainly distributed on the particle surface and tiny pores, and the size does not change significantly, about 1~3 μm .

Hydration Reaction Mechanism of CUTB

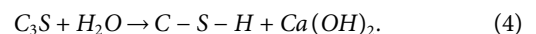
After the cement, ultra-fine tailings, and water were mixed, the chemical reaction will be produced immediately. The first is the rapid dissolution of cement clinker minerals:



At this moment, the liquid phase of cement ultra-fine tailings backfill slurry contains various ions: Ca^{2+} , OH^- , $\text{Al}(\text{OH})_4^-$, SO_4^{2-} , etc. The slurry is alkaline, and the hydration reaction of CUTB is carried out under an alkaline environment. C_3A is one of the main components of cement, and immediate hydration reaction when it is mixed with water rapidly produces C_4AH_{13} , immediately reacting with gypsum to form AFt (Myers et al., 2017):

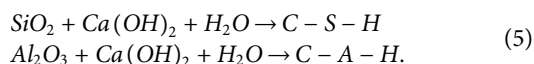


The hydration reaction rate of C_3S is slightly slower than that of C_3A because the pore solution of C_3S particles quickly reaches saturation, inhibiting the dissolution of C_3S particles. However, the formation and growth of hydration such as C-S-H take a certain time, thus hindering the hydration of C_3S particles, but this duration of this stage is very short (Scrivener et al., 2019). With the increase of curing age, the hydration reaction rate of C_3S gradually increases and reaches the maximum. The hydration product of C_3S is mainly C-S-H gel, and the concentration of $\text{Ca}(\text{OH})_2$ solution is increased continuously by the generated large amount of Ca^{2+} iron and OH^- iron:



Figures 8, 9A,B show that the hydration products of the CUTB and CCTB are different, indicating that not only does the cement itself undergo a hydration reaction, but also other components of CPB participate in the hydration reaction. According to the results of XRD energy spectrum analysis of tailings, the ultra-fine particles in the ultra-fine tailings are amorphous, with high surface energy and certain potential

activity, which can react with $\text{Ca}(\text{OH})_2$ in ultra-fine tailings filling slurry solution (Geng et al., 2017; Li et al., 2019):



Therefore, some of the mineral particles in the UT, such as SiO_2 and Al_2O_3 , do not act as a backfill aggregate but participate as active materials in the hydration reaction. It increased the amount of C-S-H and C-A-H and consumed $\text{Ca}(\text{OH})_2$.

Due to the existence of secondary hydration reaction in the CUTB, this consumes Ca^{2+} ions, OH^- ions, and gypsum in the solution and increases the production of C-S-H gel and AFt crystals. Because of the decrease in the concentration of Ca^{2+} ions and OH^- ions, the concentration of $\text{Ca}(\text{OH})_2$ can not be supersaturated, resulting in very little or not $\text{Ca}(\text{OH})_2$ crystals formation in the CUTB.

With the curing age increasing, gypsum is gradually consumed, making the C_3A in the CUTB not completely hydrated, and is exhausted. The reaction of AFt generated in the early curing age of CUTB with C_4AH_{13} formed by hydration of C_3A produces AFm:



The AFm generated by hydration reaction and the C-S-H gel coating layer on the surface of particles are mixed, where no AFm crystals could be observed on the SEM image. This reaction also consumes AFt, causing the AFt crystals to be converted into AFm without further growth, so the size of AFt crystals observed in the SEM image does not change significantly.

In summary, the hydration of CUTB is based on cement hydration, which is affected by ultra-fine tailings particles with potential activity, and can result in secondary hydration reaction, affect the hydration process, and change the hydration products and morphology.

CONCLUSION

In this study, UCS test of the CPB with different curing ages and different C/T ratios was designed, and XRD energy spectrum and SEM image were carried out. The following conclusions were drawn in this study:

- 1) The UCS of the CUTB is significantly higher than the CCTB under the same conditions, and the greater the C/T ratio and curing age, the greater the UCS difference value between the CUTB and CCTB. The variation laws of the CUTB and CCTB are different under the same mixing ratio; the UCS growth curve of the CUTB is approximately S-shaped and the UCS growth curve of the CCTB has an approximately convex shape.
- 2) There is a logarithmic relationship between the UCS of the CUTB and the curing age; the regression equation is as follows:

$$\begin{aligned}\text{C/T } 1:4 \quad P &= 1.1339 + 1.1607 \ln T \\ \text{C/T } 1:6 \quad P &= 0.7105 + 0.8172 \ln T\end{aligned}$$

The adjusted coefficient of determinations ($\text{ADJ } R^2$) is 0.971 (C/T ratio 1:4) and 0.980 (C/T ratio 1:4), respectively, and passed the significance test and residual test equations.

- 3) The XRD energy spectrum shows that the hydration products and content of CUTB and CCTB are different. In the CUTB, the content of $\text{Ca}(\text{OH})_2$ crystals is very little or non-existent, but the content of the C-S-H gel is higher than the CCTB.
- 4) The particle size of tailings affects the hydration process of the CPB and the distribution and morphology of the hydration products. In the CUTB, no obvious $\text{Ca}(\text{OH})_2$ crystals are observed during the curing. The C-S-H gel forms a coating layer around fine particles and ultra-fine particles and grows to form aggregates. In the CCTB, the C-S-H gel grows with independent particles as the center, and particles contact each other by C-S-H gel.
- 5) The ultra-fine tailings particles in the CUTB have potential activity; in the alkaline environment-generated cement hydration, the active SiO_2 and Al_2O_3 particles undergo secondary hydration reaction, C-S-H and C-A-H are generated while consuming $\text{Ca}(\text{OH})_2$, resulting in different hydration reactions of CUTB and CCTB, and the hydration products and morphology are also different.
- 6) It is well-known that the groundwater protection challenges related to cemented paste backfill have become a worldwide issue in mining areas (Chen et al., 2021). Thus, the leaching risk of CUTB to groundwater will be further studied in our future studies.

DATA AVAILABILITY STATEMENT

The original contributions presented in the study are included in the article/Supplementary Materials; further inquiries can be directed to the corresponding author.

AUTHOR CONTRIBUTIONS

GD contributed to the experiments scheme and discuss the results. CC contributed to the conception of the study. LiH contributed to the experiments and wrote the manuscript. LuH and ZY discussed the results and contributed to the final manuscript.

FUNDING

This work was supported by the National Natural Science Foundation of China (No. 51774137), the Department of Education of Hebei Province (No. ZD2015020), the Natural Science Foundation of Hebei Province (Nos. E2021209006 and E2019209326), the "333" Talent Project of Hebei Province, China (No. 202001011), and State Key Laboratory of Process Automation in Mining and Metallurgy and Beijing Key Laboratory of Process Automation in Mining and Metallurgy (No. BGRIMM-KZSKL-2018).

REFERENCES

- Benzaazoua, M., Fall, M., and Belem, T. (2004). A Contribution to Understanding the Hardening Process of Cemented Pastefill. *Minerals Eng.* 17, 141–152. doi:10.1016/j.mineng.2003.10.022
- Chen, Q., Sun, S., Liu, Y., Qi, C., Zhou, H., and Zhang, Q. (2021). Experimental and Numerical Study on Immobilization and Leaching Characteristics of Fluoride from Phosphogypsum Based Cemented Paste Backfill. *Int. J. Min. Mater. Eng.* doi:10.1007/s12613-021-2274-6
- Cihangir, F., Ercikdi, B., Kesimal, A., Turan, A., and Deveci, H. (2012). Utilisation of Alkali-Activated Blast Furnace Slag in Paste Backfill of High-Sulphide Mill Tailings: Effect of Binder Type and Dosage. *Minerals Eng.* 30, 33–43. doi:10.1016/j.mineng.2012.01.009
- Deng, D. Q., Liu, L., Yao, Z. L., Song, K. I.-I. L., and Lao, D. Z. (2017a). A Practice of Ultra-fine Tailings Disposal as Filling Material in a Gold Mine. *J. Environ. Manage.* 196, 100–109. doi:10.1016/j.jenvman.2017.02.056
- Deng, X. J., Klein, B., Hallbom, D. J., de Wit, B., and Zhang, J. X. (2018a). Influence of Particle Size on the Basic and Time-dependent Rheological Behaviors of Cemented Paste Backfill. *J. Mater. Eng. Perform.* 27, 3478–3487. doi:10.1007/s11665-018-3467-7
- Deng, X., Klein, B., Tong, L., and de Wit, B. (2018b). Experimental Study on the Rheological Behavior of Ultra-fine Cemented Backfill. *Construction Building Mater.* 158, 985–994. doi:10.1016/j.conbuildmat.2017.05.085
- Deng, X., Zhang, J., Klein, B., Zhou, N., and deWit, B. (2017b). Experimental Characterization of the Influence of Solid Components on the Rheological and Mechanical Properties of Cemented Paste Backfill. *Int. J. Mineral Process.* 168, 116–125. doi:10.1016/j.minpro.2017.09.019
- Doherty, J. P., Hasan, A., Suazo, G. H., and Fourie, A. (2015). Investigation of Some Controllable Factors that Impact the Stress State in Cemented Paste Backfill. *Can. Geotech. J.* 52, 1901–1912. doi:10.1139/cgj-2014-0321
- Ercikdi, B., Baki, H., and İzki, M. (2013). Effect of Desliming of Sulphide-Rich Mill Tailings on the Long-Term Strength of Cemented Paste Backfill. *J. Environ. Manage.* 115, 5–13. doi:10.1016/j.jenvman.2012.11.014
- Ercikdi, B., Kesimal, A., Cihangir, F., Deveci, H., and Alp, İ. (2009). Cemented Paste Backfill of Sulphide-Rich Tailings: Importance of Binder Type and Dosage. *Cement and Concrete Composites.* 31, 268–274. doi:10.1016/j.cemconcomp.2009.01.008
- Fall, M., Benzaazoua, M., and Ouellet, S. (2005). Experimental Characterization of the Influence of Tailings Fineness and Density on the Quality of Cemented Paste Backfill. *Minerals Eng.* 18, 41–44. doi:10.1016/j.mineng.2004.05.012
- Fall, M., Benzaazoua, M., and Saa, E. G. (2008). Mix Proportioning of Underground Cemented Tailings Backfill. *Tunnelling Underground Space Tech.* 23, 80–90. doi:10.1016/j.tust.2006.08.005
- Fall, M., Célestin, J. C., Pokharel, M., and Touré, M. (2010). A Contribution to Understanding the Effects of Curing Temperature on the Mechanical Properties of Mine Cemented Tailings Backfill. *Eng. Geology.* 114, 397–413. doi:10.1016/j.enggeo.2010.05.016
- Geng, G., Myers, R. J., Li, J., Maboudian, R., Carraro, C., Shapiro, D. A., et al. (2017). Aluminum-induced Dreierketten Chain Cross-Links Increase the Mechanical Properties of Nanocrystalline Calcium Aluminosilicate Hydrate. *Sci. Rep.* 7 (1). doi:10.1038/srep44032
- Helinski, M., Fahey, M., and Fourie, A. (2007). Numerical Modeling of Cemented Mine Backfill Deposition. *J. Geotech. Geoenviron. Eng.* 133, 1308–1319. doi:10.1061/(asce)1090-0241(2007)133:10(1308)
- Jiang, H., Fall, M., Li, Y., and Han, J. (2019). An Experimental Study on Compressive Behaviour of Cemented Rockfill. *Construction Building Mater.* 213, 10–19. doi:10.1016/j.conbuildmat.2019.04.061
- Kawatra, S. K. (2017). Mineral Processing and Extractive Metallurgy Review. *An Int. J. Min. Proc. Ext. Met. Rev.* 38. doi:10.1080/08827508.2017.1390966
- Ke, X., Hou, H., Zhou, M., Wang, Y., and Zhou, X. (2015). Effect of Particle Gradation on Properties of Fresh and Hardened Cemented Paste Backfill. *Construction Building Mater.* 96, 378–382. doi:10.1016/j.conbuildmat.2015.08.057
- Ke, X., Zhou, X., Wang, X., Wang, T., Hou, H., and Zhou, M. (2016). Effect of Tailings Fineness on the Pore Structure Development of Cemented Paste Backfill. *Construction Building Mater.* 126, 345–350. doi:10.1016/j.conbuildmat.2016.09.052
- Kesimal, A., Ercikdi, B., and Yilmaz, E. (2003). The Effect of Desliming by Sedimentation on Paste Backfill Performance. *Minerals Eng.* 16, 1009–1011. doi:10.1016/S0892-6875(03)00267-X
- Li, J., Geng, G., Myers, R., Yu, Y.-S., Shapiro, D., Carraro, C., et al. (2019). The Chemistry and Structure of Calcium (Alumino) Silicate Hydrate: A Study by XANES, Ptychographic Imaging, and Wide- and Small-Angle Scattering. *Cement Concrete Res.* 115, 367–378. doi:10.1016/j.cemconres.2018.09.008
- Liu, L., Fang, Z., Qi, C., Zhang, B., Guo, L., and Song, K. I.-I. L. (2019). Numerical Study on the Pipe Flow Characteristics of the Cemented Paste Backfill Slurry Considering Hydration Effects. *Powder Tech.* 343, 454–464. doi:10.1016/j.powtec.2018.11.070
- Lu, H., Qi, C., Chen, Q., Gan, D., Xue, Z., and Hu, Y. (2018). A New Procedure for Recycling Waste Tailings as Cemented Paste Backfill to Underground Stopes and Open Pits. *J. Clean. Prod.* 188, 601–612. doi:10.1016/j.jclepro.2018.04.041
- Myers, R. J., Geng, G., Li, J., Rodríguez, E. D., Ha, J., Kidkhunthod, P., et al. (2017). Role of Adsorption Phenomena in Cubic Tricalcium Aluminate Dissolution. *Langmuir* 33 (1), 45–55. doi:10.1021/acs.langmuir.6b03474
- Nircoshan, N., Sivakugan, N., and Veenstra, R. L. (2017). Laboratory Study on Strength Development in Cemented Paste Backfills. *J. Mater. Civil. Eng.* 29. doi:10.1061/(asce)mt.1943-5533.0001848
- Ouellet, S., Bussière, B., Aubertin, M., and Benzaazoua, M. (2007). Microstructural Evolution of Cemented Paste Backfill: Mercury Intrusion Porosimetry Test Results. *Cement Concrete Res.* 37, 1654–1665. doi:10.1016/j.cemconres.2007.08.016
- Qiu, J., Yang, L., Sun, X., Xing, J., and Li, S. (2017). Strength Characteristics and Failure Mechanism of Cemented Super-Fine Unclassified Tailings Backfill. *Minerals* 7, 58. doi:10.3390/min7040058
- Scrivener, K., Ouzia, A., Juilland, P., and Kunhi Mohamed, A. (2019). Advances in Understanding Cement Hydration Mechanisms. *Cement Concrete Res.* 124, 105823. doi:10.1016/j.cemconres.2019.105823
- Wang, C., Harbottle, D., Liu, Q., and Xu, Z. (2014). Current State of fine mineral Tailings Treatment: A Critical Review on Theory and Practice. *Minerals Eng.* 58, 113–131. doi:10.1016/j.mineng.2014.01.018
- Wang, X.-m., Zhao, B., and Zhang, Q.-I. (2009). Cemented Backfill Technology Based on Phosphorous gypsum. *J. Cent. South. Univ. Technol.* 16, 285–291. doi:10.1007/s11771-009-0049-8
- Wolff, A. P., da Costa, G. M., and de Castro Dutra, F. (2010). A Comparative Study of Ultra-Fine Iron Ore Tailings from Brazil. *Mineral. Process. Extractive Metall. Rev.* 32, 47–59. doi:10.1080/08827508.2010.530718
- Xu, W. B., Du, J. H., Song, W. D., and Cheng, H. Y. (2013). Experiment on the Mechanism of Consolidating Backfill Body of Extra-fine Grain Unclassified Tailings and Cementitious Materials. *Rock. Soil Mech.* 8, 2295–2302. doi:10.16285/j.rsm.2013.08.013
- Xue, G., Yilmaz, E., Song, W., and Cao, S. (2018). Compressive Strength Characteristics of Cemented Tailings Backfill with Alkali-Activated Slag. *Appl. Sci.* 8, 1537. doi:10.3390/app8091537
- Yang, L., Qiu, J., Jiang, H., Hu, S., Li, H., and Li, S. (2017). Use of Cemented Super-Fine Unclassified Tailings Backfill for Control of Subsidence. *Minerals* 7, 216. doi:10.3390/min7110216
- Yilmaz, E., Belem, T., and Benzaazoua, M. (2012). One-Dimensional Consolidation Parameters of Cemented Paste Backfills/Parametry Jednowymiarowej Konsolidacji Podsadzki W Postaci Cementowej Pasty. *Gospod. Surowcami. Min.* 28, 29–45. doi:10.2478/v10269-012-0030-2
- Yin, S., Wu, A., Hu, K., Wang, Y., and Zhang, Y. (2012). The Effect of Solid Components on the Rheological and Mechanical Properties of Cemented Paste Backfill. *Minerals Eng.* 35, 61–66. doi:10.1016/j.mineng.2012.04.008
- Yilmaz, T., Ercikdi, B., Karaman, K., and Külekçi, G. (2014). Assessment of Strength Properties of Cemented Paste Backfill by Ultrasonic Pulse Velocity Test. *Ultrasonics* 54, 1386–1394. doi:10.1016/j.ultras.2014.02.012
- Zhao, J.-w., Wang, X.-m., Peng, K., and Li, S. (2017a). Utilization of Foaming Technology in Cemented Paste Backfill of High-Mud Superfine Unclassified Tailings. *Adv. Mater. Sci. Eng.* 2017, 1–7. doi:10.1155/2017/6157869
- Zheng, J., Zhu, Y., and Zhao, Z. (2016). Utilization of limestone Powder and Water-Reducing Admixture in Cemented Paste Backfill of Coarse Copper Mine Tailings. *Construction Building Mater.* 124, 31–36. doi:10.1016/j.conbuildmat.2016.07.055

Zhou, K.-p., Gao, R., and Gao, F. (2017b). Particle Flow Characteristics and Transportation Optimization of Superfine Unclassified Backfilling. *Minerals* 7, 6. doi:10.3390/min7010006

Conflict of Interest: The authors declare that the research was conducted in the absence of any commercial or financial relationships that could be construed as a potential conflict of interest.

Publisher's Note: All claims expressed in this article are solely those of the authors and do not necessarily represent those of their affiliated organizations, or those of

the publisher, the editors and the reviewers. Any product that may be evaluated in this article, or claim that may be made by its manufacturer, is not guaranteed or endorsed by the publisher.

Copyright © 2021 Deqing, Hongbao, Chao, Hongjian and Youzhi. This is an open-access article distributed under the terms of the Creative Commons Attribution License (CC BY). The use, distribution or reproduction in other forums is permitted, provided the original author(s) and the copyright owner(s) are credited and that the original publication in this journal is cited, in accordance with accepted academic practice. No use, distribution or reproduction is permitted which does not comply with these terms.



Occurrence State of Carbon and Electrolyte in Anode Carbon Residue From Electrolytic Aluminum

Song Mao^{1,2,3} and Qin Zhang^{2,3,4*}

¹College of Resources and Environmental Engineering, Guizhou University, Guiyang, China, ²National and Local Joint Laboratory of Engineering for Effective Utilization of Regional Mineral Resources from Karst Areas, Guiyang, China, ³Guizhou Key Laboratory of Comprehensive Utilization of Non-metallic Mineral Resources, Guiyang, China, ⁴Guizhou Academy of Science, Guiyang, China

Anode carbon residue is produced in the production of electrolytic aluminum. Its properties need to be studied for secondary utilization. In this paper, mineralogy of anode carbon residue from an electrolytic aluminum plant in Guizhou was studied. The anode residue chemical composition, structure, mineral composition, occurrence state of main elements, etc., was investigated. The results show that: Anode carbon residue is mainly composed of 14 minerals such as cryolite, cryolithionite, elpasolite and graphite. Among them, the opaque minerals are mainly graphite and the transparent minerals are mainly cryolite. Carbon in the form of independent mineral occurrence in graphite; fluoride in the form of independent mineral occurrence in cryolite, cryolithionite, elpasolite and fluorite; aluminum in the form of independent mineral occurrence in cryolite, cryolithionite, elpasolite, aluminium oxide and magnesium aluminate; sodium in the form of independent mineral occurrence in cryolite, cryolithionite, elpasolite. The mineralogical characteristics and occurrence state of carbon and electrolyte were studied, which provided a basis for the separation and recovery of carbon and electrolyte in anode carbon residue.

Keywords: anode carbon residue, mineral composition, state of occurrence, graphite, cryolite

OPEN ACCESS

Edited by:

Lijie Guo,
Beijing General Research Institute of
Mining and Metallurgy, China

Reviewed by:

Huamei Duan,
Chongqing University, China
Jiaqi Li,
University of California, United States

*Correspondence:

Qin Zhang
zq6736@163.com

Specialty section:

This article was submitted to
Structural Materials,
a section of the journal
Frontiers in Materials

Received: 03 June 2021

Accepted: 28 June 2021

Published: 17 August 2021

Citation:

Mao S and Zhang Q (2021)
Occurrence State of Carbon and
Electrolyte in Anode Carbon Residue
From Electrolytic Aluminum.
Front. Mater. 8:719563.
doi: 10.3389/fmats.2021.719563

INTRODUCTION

Hall-Heroult electrolysis process is the most commonly used method for aluminum production (Grjotheim and Krohn, 2020). Anode carbon residue produced in the process of electrolytic aluminum is a kind of dangerous solid waste. For example, it contains fluorine ions, the direct storage and landfill treatment will have a serious impact on the environment (Lifeng et al., 2019). Carbon anode is one of the key components in the production of electrolytic aluminum. It is mainly composed of calcined petroleum coke, coal tar pitch and regenerated carbon materials (Bhattacharyay et al., 2017). In the process of electrolytic aluminum production, part of the carbon anode falls off and enters the electrolyte to form anode carbon residue, and the accumulation of carbon residue will affect the production of electrolytic aluminum (Jin-sheng and Qing-chun, 2017; Zhi-qian et al., 2019), and the generation of carbon residue is related to the quality of anode (Aryanpour et al., 2014; Chevarin et al., 2015). Because in the process of aluminum electrolysis, carbon anode participated in the electrolysis process and was consumed, the production of aluminum at the same time to consume a large amount of carbon, producing a large amounts of CO₂ (Huang et al., 2018) are produced resulting in voltage increases (Haupin, 1971) and current efficiency losses (Einarsrud, 2010). The carbon anode needs to be replaced in time after being consumed, to ensure the normal operation of production (Chevarin et al., 2015; Allard et al., 2019; Guo et al., 2020; Hussein et al., 2020). The production of anode carbon residue can be reduced

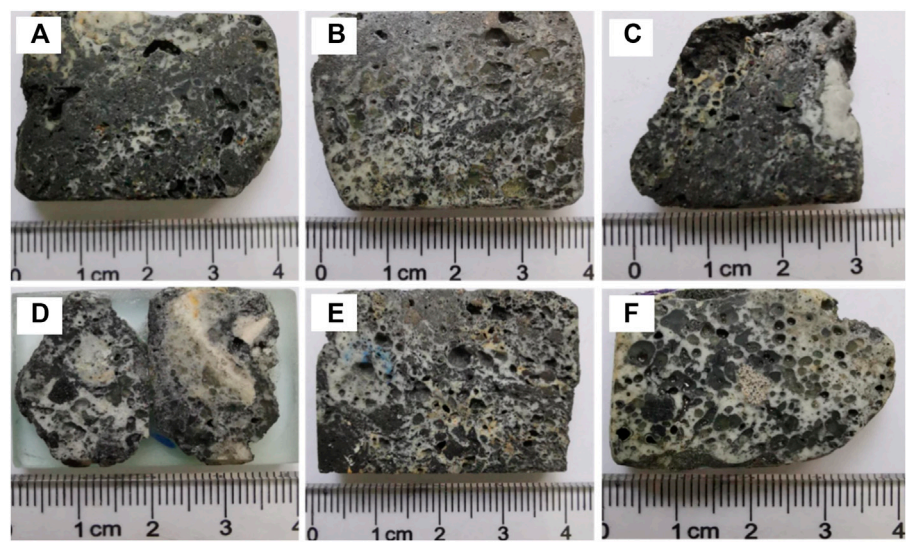


FIGURE 1 | Structure Diagram of Anode Carbon Residue. **(A–D)** Many pores, cryolite and graphite are locally enriched; **(E,F)** Multiple pores, alternating distribution of cryolite and graphite.

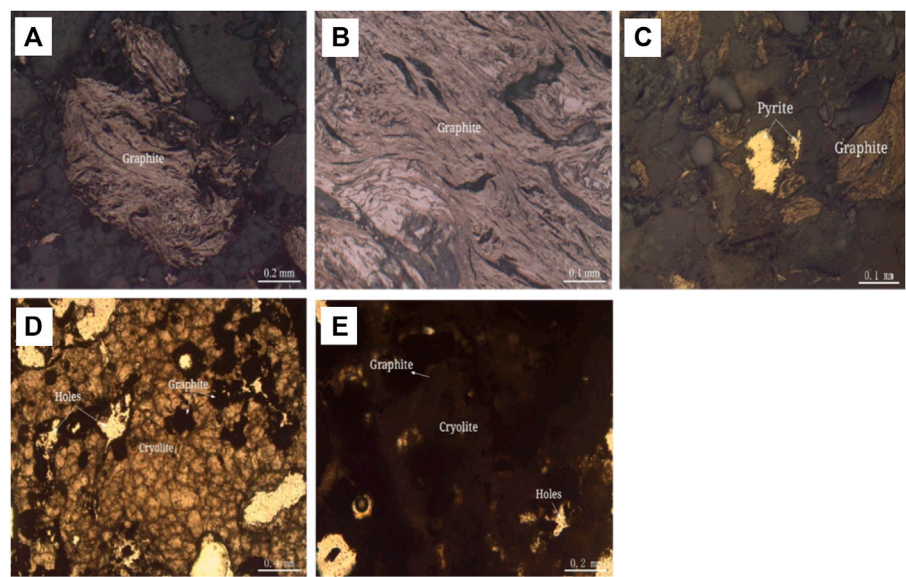


FIGURE 2 | Structure Diagram of Anode Carbon residue. **(A)** Flake and fibrous graphite aggregates are lumpy in reflected plane polarized light. **(B)** Flake and fibrous graphite is lumpy in reflected plane polarized light. **(C)** Pyrite is anamorphic granular in reflected plane polarized light. **(D)** Cryolite is microscopic granular amorphous, grain boundaries are blurred, closely inlaid, graphite aggregates embedded in them, transmission of single polarized light. **(E)** cryolite is mud-microcrystalline, particle size <0.004 mm, or 0.004–0.03 mm, transmission of single polarized light.

TABLE 1 | Chemical multi-element analysis results/%.

Chemical element	F	Al	Na	K	S	Ca	Mg
Content	43.27	11.77	22.44	2.77	0.42	1.58	0.39
Chemical element	Si	Fe	C _{total}	C _{organic}	Ni	LOI 700 °C	LOI 1,000 °C
Content	<0.50	0.58	14.16	12.28	0.23	16.53	31.00

"LOI" means loss on ignition in bold.

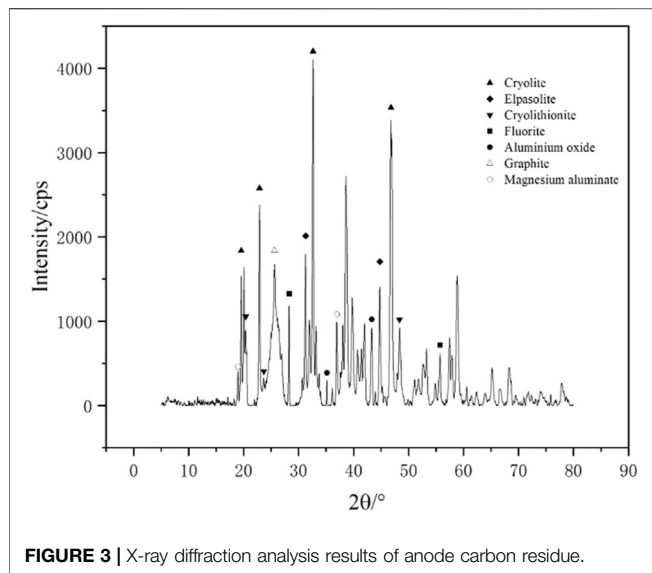


FIGURE 3 | X-ray diffraction analysis results of anode carbon residue.

by improving the quality of raw materials and strengthening the management of electrolytic aluminum production process (Hai-fei et al., 2009; Qing et al., 2015). It has been found that the shape of anode is one of the factors affecting the formation of carbon slag (Min-zhang and Xian, 2012). The anode consumption can be reduced by optimizing the structure of anode carbon block height and top shape (Xugui, 2021). The anode performance can also be improved by increasing the density of carbon anode, reducing the resistivity, air permeability, and reducing the impurity elements in the anode carbon (Batista and da Silveira, 2008; Dan-qing, 2008; Azari et al., 2013; Azari et al., 2013; Khaji and Al Qassemi, 2016). Trace elements in anode will affect anode consumption and aluminum liquid quality (Jing et al., 2010; Jing-lu et al., 2015). At the same time, the carbon and electrolyte in the anode carbon residue can be separated and recovered, which can effectively utilize the solid waste resources (Xiangyang et al., 2016; Lifeng et al., 2019). In the study of alternative materials for carbon anode, some researchers use calcined anthracite to partially replace petroleum coke to produce carbon anode (Yao-jian et al., 2009), and some researchers use bio-asphalt instead of coal asphalt to prepare carbon anode (Hussein et al., 2020). The use of inert materials instead of carbon anodes will be a promising option for the future and has been extensively investigated (Xiao et al., 2014; Kubiňáková et al., 2018). In view of the current utilization of anode carbon residue, the recycling of anode carbon residue is one of the effective ways to solve the environmental problems caused by it. The separation and recovery of carbon and electrolyte and the quantification of the key mineralogical parameters in anode carbon residue are important means for the separation of useful components (Diógenes et al., 2021).

In this paper, Polarized light microscope and X-ray diffraction (XRD), Scanning Electron Microscope and Energy Dispersive Spectroscopy (SEM-EDS) Analysis and combined with mineral liberation analyser (MLA), and other methods for anode carbon residue was studied, find out the structure of

the anode residue structure, element composition, mineral composition and embedded characteristics, find out the carbon phase, sodium, aluminum phase, fluorine equal characteristics of each phase found out C, F, Al, Na, K and other elements in the distribution law of various minerals and occurrence state, It provides a basis for the separation and recovery of useful components in anode carbon residue.

MATERIALS AND METHODS

Anode carbon residue is taken from Guizhou Hua Ren New Material Co., Ltd. The bulk anode carbon residue was selected and polished, and the structure of the anode carbon residue was analyzed by polarizing microscope (Axio Scope. A1, Zeiss, Germany), chemical multi-element analysis, X-ray diffraction analysis (Empyrean sharp shadow, Panalytical, Netherlands), MLA mineral dissociation analyzer (MLA650, FEI, American), scanning electron microscopy (Quanta600, FEI, American) and energy dispersive X-ray spectrometry (Apollo X type, EDAX, American) were used to analyze the element composition, mineral composition, embedded characteristics, symbiosis and element occurrence of anode carbon residue.

TEST RESULTS AND DISCUSSION

Structure of Anode Carbon Residue

The gross eye observation shows that the anode carbon residue is black, and the particle size less than 5 cm. In some anode carbon residue, dark mineral aggregates and light mineral aggregates are locally enriched, with multiple pores and porous structures. The structural diagram is shown in **Figures 1A–D**. Dark mineral aggregates and light mineral aggregates are alternately distributed, and the structural diagram is shown in **Figures 1E, F**.

Polarizing microscope was used to analyze the anode carbon residue. The opaque minerals in the anode carbon residue were mainly graphite, which was flaky and fibrous, forming flaky and fibrous crystalloblastic structures. Transparent minerals are mainly cryolite, cryolithionite and elpasolite, which are microscopic granular, mud-microcrystalline, forming micro-granular metamorphosis structure and mud-microcrystalline structure. The metallic minerals are mainly pyrite, magnetite, polydymite and pentlandite, which are anisotropic granular and constitute anisotropic granular structure.

Flake and fibrous crystallizing structure: graphite in anode carbon residue has good crystallizing degree, showing flaky and fibrous shape; aggregates are twisted into lumps, camboidal polygonal and other amorphous particles, which are distributed in anode carbon residue, as shown in **Figures 2A, B**. Anisotropic granular structure: there are very few metallic minerals in the anode carbon residue, which are mainly pyrite, magnetite, polydymite and pentlandite. The anisotropic granular structure is formed, as shown in **Figure 2C**. Micro-granular crystalloblastic structure: the main transparent mineral cryolite in anode carbon residue is semi-idiomorphic and other-shaped granular with particle size <0.1 mm. The particles are closely

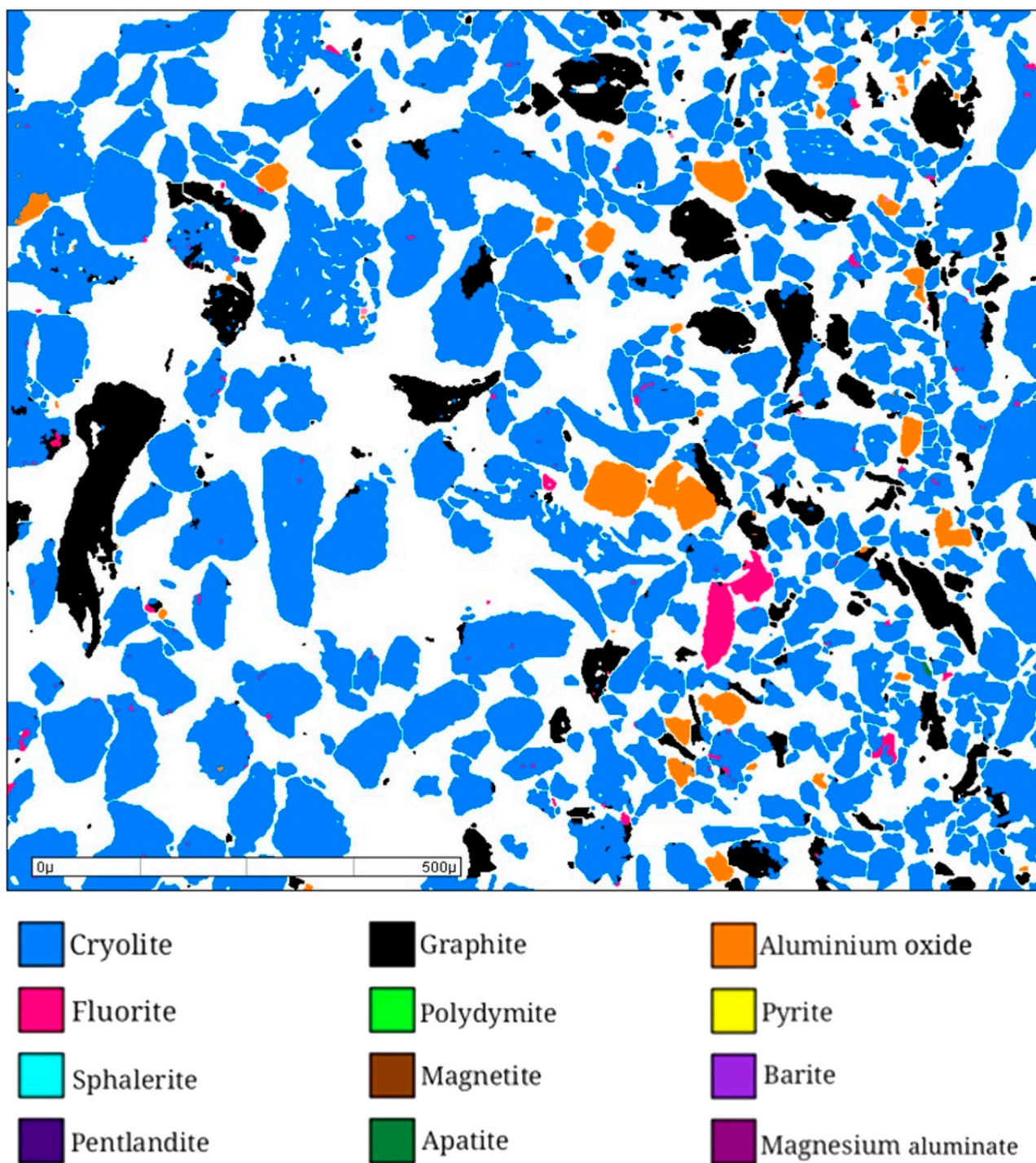


FIGURE 4 | General diagram of MLA analysis of anode carbon residue (partial area).

inlaid to form a micro-granular crystalloblastic structure, as shown in **Figure 2D**. Mud-microcrystalline structure: part of cryolite in anode carbon residue has fine crystalline particle size,

showing micrite size <0.004 mm, or micrite size between 0.004 and 0.03 mm, forming mud-microcrystalline structure, as shown in **Figure 2E**.

TABLE 2 | Mineral composition and content table/%.

Serial	Mineral name	Chemical formula	Content (%)
1	Cryolite	Na_3AlF_6	60.25
2	Cryolithionite	$\text{Na}_3 (\text{Li}_3\text{Al}_2\text{F}_{12})$	10.10
3	Elpasolite	$\text{K}_2 (\text{NaAlF}_6)$	8.41
4	Fluorite	CaF_2	2.12
5	Aluminium oxide	Al_2O_3	1.49
6	Graphite	C	14.35
7	Polydymite	Ni_3S_4	0.18
8	Pyrite	FeS_2	0.22
9	Sphalerite	ZnS	Very few
10	Magnetite	Fe_3O_4	0.43
11	Barite	BaSO_4	Very few
12	Pentlandite	$(\text{Fe,Ni}) (\text{Fe,Ni})_8\text{S}_8$	0.14
13	Magnesium aluminate	MgAl_2O_4	2.28
14	Apatite	$\text{Ca}_5 [\text{PO}_4]_3 (\text{F,OH})$	0.03
Total	—	—	100.00

Chemical Multielement Analysis of Anode Carbon Residue

Chemical Multielement Analysis

Chemical multi-element analysis was carried out on anode carbon residue, and the analysis results are shown in **Table 1**.

As can be seen from the analysis results in **Table 1**, the content of element F, Al, Na and K in anode carbon residue is 43.27%,

11.77%, 22.44% and 2.77%. The content of C_{total} was 14.16%. Other elements mainly include Ca, S, Fe, Mg and Ni. The loss on ignition is 16.53% at 700°C, 31.00% at 1,000°C, C_{organic} content is 12.28%, and a small amount of Si, etc.

Analysis of Mineral Composition of Anode Carbon Residue

X-Ray Diffraction Analysis

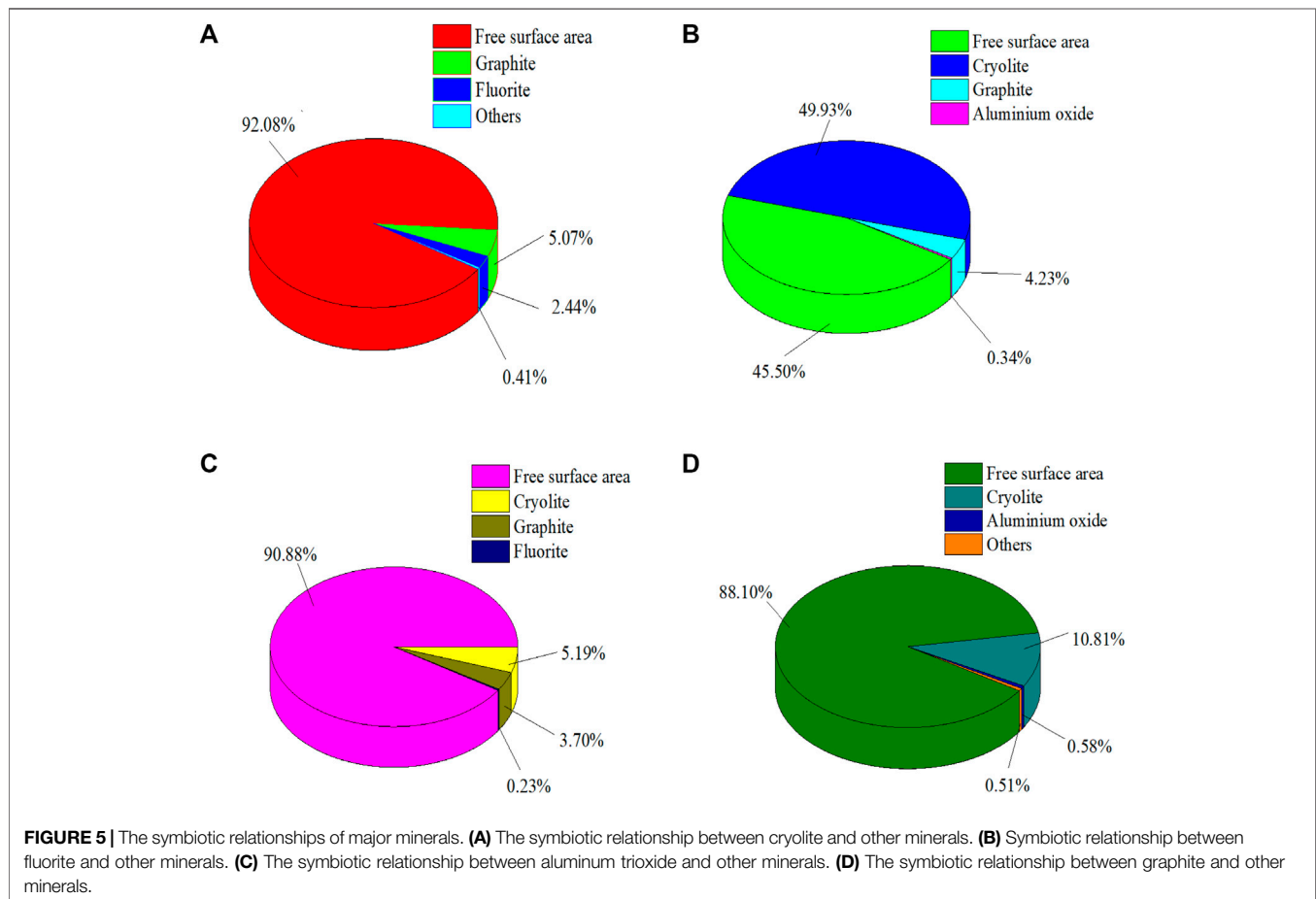
The anode carbon residue was analyzed by X-ray diffractometer. The X-ray diffraction analysis results are shown in **Figure 3**.

The results of X-ray diffraction show that the anode carbon residue is mainly composed of cryolite, cryolithionite, elpasolite, fluorite, graphite, aluminum oxide, magnesium aluminate and so on. Yang et al. (2021) analysis of anode carbon residue found similar composition.

Analysis of the Mineral Liberation Analyzer

Mineral particles in anode carbon residue were analyzed and counted by MLA, scanning electron microscope and X-ray energy spectrometer to determine their mineral composition. The general analysis diagram is shown in **Figure 4**, and the mineral composition and content results are shown in **Table 2**.

X-ray diffraction analysis shows that there are three kinds of cryolite, cryolithionite and elpasolite in anode carbon residue.



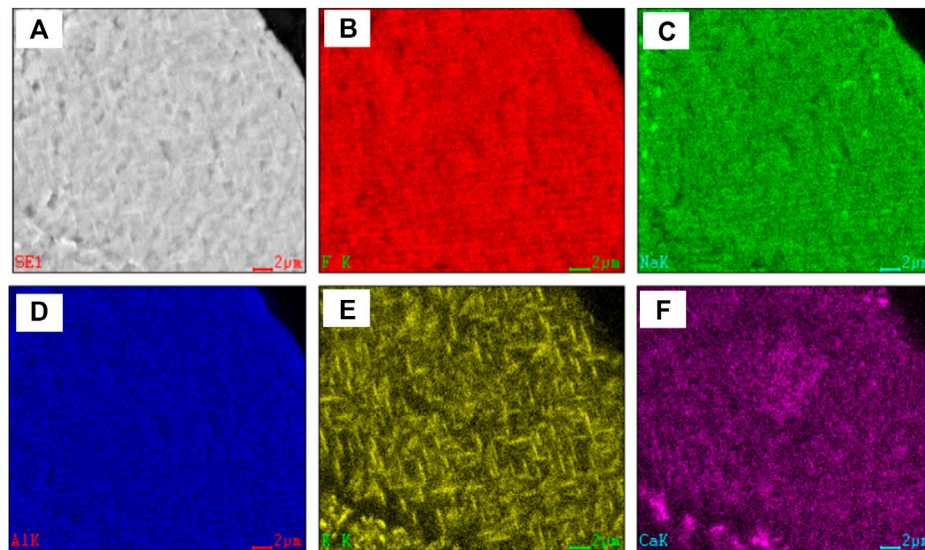


FIGURE 6 | Scanning view of cryolite surface.

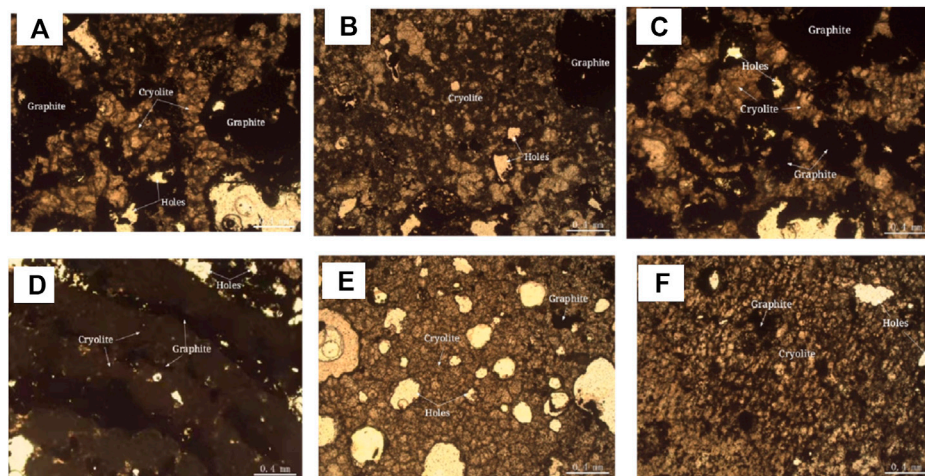


FIGURE 7 | Polarization microscope photo of cryolite (transmitted single polarization). **(A)** Microgranular cryolite, closely inlaid with blurred boundaries and embedded with graphite aggregates. **(B)** The microgranular ice crystals are alternately distributed with micritic cryolite. **(C)** Graphite aggregates are distributed in cryolite. **(D)** The cryolite is in the form of mud-microcrystalline, and the graphite aggregates are in the form of intermittent strips, which are distributed in the cryolite. **(E)** microscopic granular cryolite is shaped granular, particles are closely inlaid, the boundaries are black and thick, and there are more cavities. **(F)** Microgranular cryolite is amorphous and alternately distributed with micritic cryolite.

Because MLA has identification defects for light element lithium, and elpasolite is in fine grid shape and evenly distributed in cryolite and cryolithionite, which is beyond the lower limit of MLA identification, it is difficult to effectively distinguish them. So in MLA analysis, the cryolite, cryolithionite and elpasolite were classified as cryolite for analysis.

According to MLA analysis, combined with X-ray diffraction analysis, rock ore identification analysis and chemical multi-element analysis, the anode carbon residue is composed of

14 minerals, among which cryolite, cryolithionite, elpasolite and graphite are the most important minerals, accounting for about 93%, followed by aluminum oxide, magnesium aluminate and fluorite, accounting for about 6%.

There was only one independent mineral of carbon, graphite, with a content of 14.35%. The independent minerals of fluorine were cryolite, cryolithionite and elpasolite and fluorite, with contents of 60.25%, 10.10%, 8.41%, and 2.12%, respectively. The independent minerals of aluminum are cryolite, cryolithionite

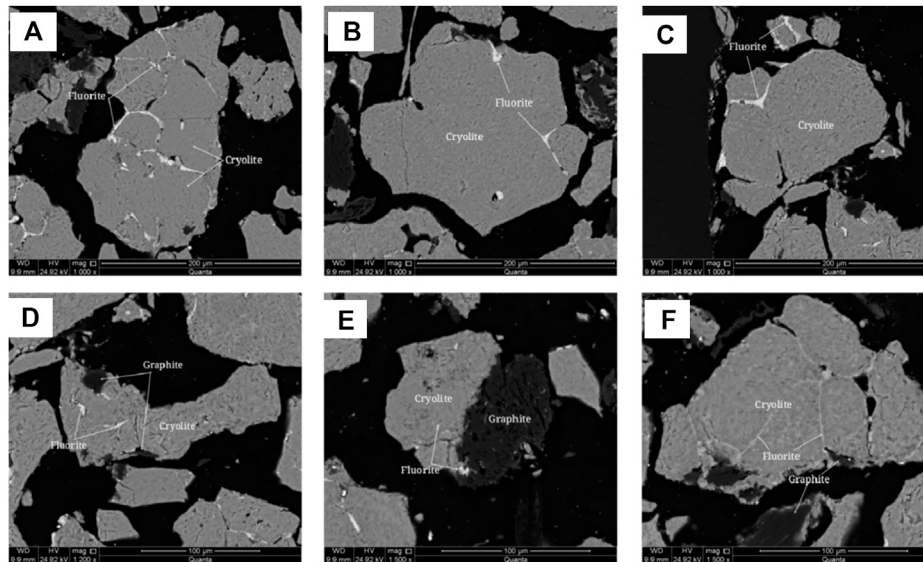


FIGURE 8 | Scanning electron microscope backscattered electron image of cryolite. (A) Fluorite filling between cryolite grains; (B) Fluorite filling between cryolite grains; (C) Fluorite filling between cryolite grains; (D) anisotropic granular cryolite particles encapsulate fine fluorite; (E) Fine-grained fluorite encapsulated in cryolite; (F) Fluorite filling between cryolite grains.

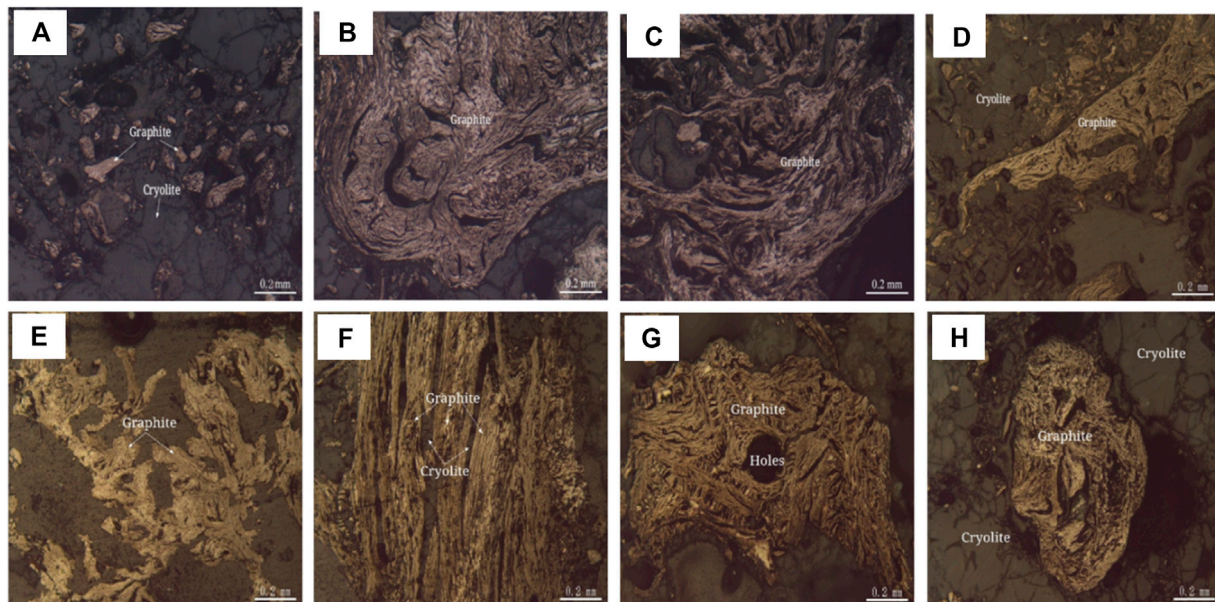


FIGURE 9 | Polarization microscope photo of graphite (Reflected Single Polarized Light). (A) Graphite aggregates are amorphous granules distributed between cryolite grains. (B) Graphite aggregates are twisted into clumps. (C) Fibrous graphite is twisted. (D) Graphite aggregates are amorphous granules. (E) Flake-like graphite, aggregates are amorphous granular. (F) The fibrous graphite aggregates are bundled with cryolite filling between the bundled aggregates. (G) Graphite is twisted to be lumpy and camboidal polygonal. (H) Graphite aggregates are spherical.

and elpasolite, aluminum oxide and magnesium aluminate, with contents of 60.25%, 10.10%, 8.41%, 1.49%, and 2.28%, respectively. The independent minerals of sodium are cryolite, cryolithionite and elpasolite. The independent mineral of potassium is only a kind of elpasolite.

Symbiotic Relationships of Major Minerals

When the grinding fineness of anode carbon residue is -0.075 mm accounting for 49.74%, MLA is used to analyze the anode carbon residue and make statistics on the symbiosis relationship between the main target minerals in anode carbon

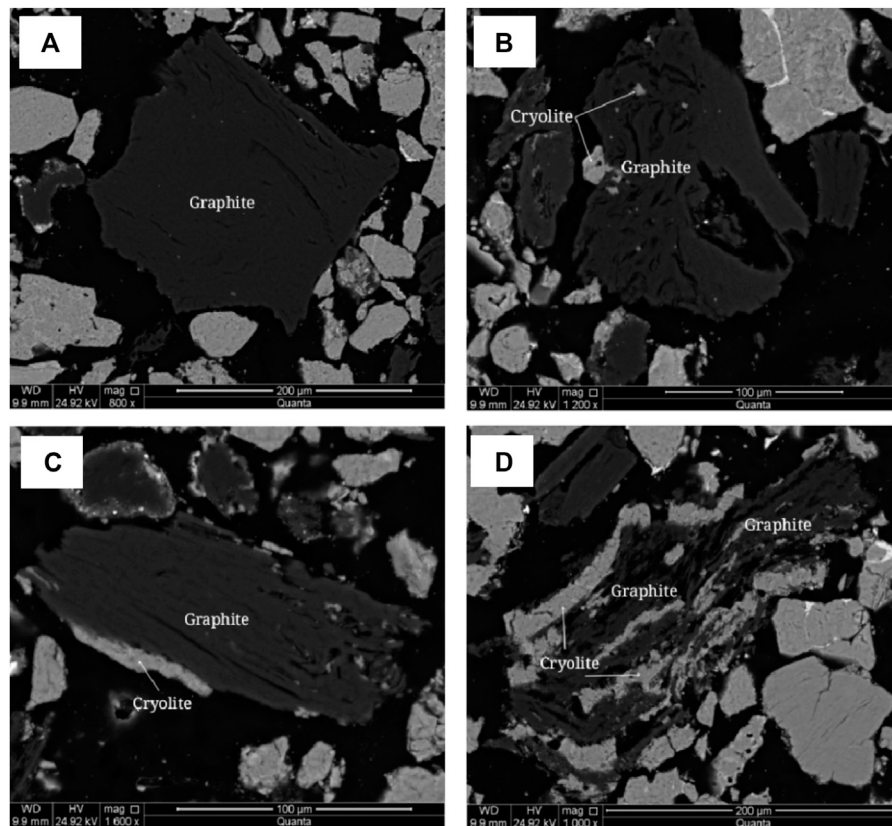


FIGURE 10 | Scanning electron microscope backscattered electron image of graphite. **(A)** Graphite dissociated from monomers. **(B)** Graphite bonded to cryolite or encapsulated with fine grained cryolite. **(C)** Graphite bonded with cryolite. **(D)** Cryolite is distributed in graphite.

residue, cryolite, fluorite, aluminum oxide, graphite and other minerals. The analysis results are shown in **Figure 5**.

The results of **Figure 5** show that the symbiosis relationship of the main minerals in anode carbon residue is relatively simple. Among them, cryolite is mainly associated with graphite fluorite, and the proportion of their common surface area is 5.07% and 2.44%, respectively. The proportion of free surface area of cryolite was 92.08%. Fluorite is mainly associated with cryolite, graphite and aluminum oxide, and the proportions of their common surface area are 49.93%, 4.23% and 0.34%, respectively. The free surface area ratio of fluorite is 45.50%. Aluminum oxide is mainly associated with cryolite, graphite and fluorite, and the proportion of its common surface area is 5.19%, 3.70% and 0.23%, respectively. The free surface area ratio of aluminum oxide was 90.88%. Graphite is mainly associated with cryolite and aluminum oxide, with a total surface area ratio of 10.81% and 0.58%, respectively. The free surface area ratio of fluorite is 88.10%.

Characteristics of Disseminated Particle Size of Carbonaceous Minerals and Fluorine Minerals

Under the condition that the grinding fineness of anode carbon residue is -0.075 mm accounting for 49.74%, the particle size of

anode carbon residue and the embedded size characteristic of the main target minerals cryolite, fluorite, aluminum oxide and graphite were analyzed and statistically by using MLA. The analysis results are shown in **Supplementary Figure 1**.

According to the analysis results in **Supplementary Figure 1**, under the current grinding fineness, the cumulative distribution rate of anode carbon residue with $+150$ μ m size is 16.50%, the cumulative distribution rate of $+75$ μ m size is 50.26%, the cumulative distribution rate of $+38$ μ m size is 77.38%, and the cumulative distribution rate of $+19$ μ m size is 92.17%. The cumulative distribution rates of cryolite $+150$, $+75$, $+38$ and $+19$ μ m were 18.24%, 51.55%, 78.91% and 93.70%, respectively. The cumulative distribution rate of fluorite $+19$ μ m was 17.10%, and the cumulative distribution rate of $+9.6$ μ m was 48.97%. The cumulative distribution rates of graphite with 150 μ m size were 5.59%, $+75$ μ m size was 29.58%, $+38$ μ m size was 55.02%, and $+19$ μ m size was 75.54%. The cumulative distribution rates of aluminum oxide $+75$, $+38$ and $+19$ μ m fractions were 31.30%, 65.53% and 86.92%, respectively.

Mineralogical Characteristics of Major Minerals

The mineralogical characteristics of the main minerals in anode carbon residue were analyzed by polarizing microscope, X-ray

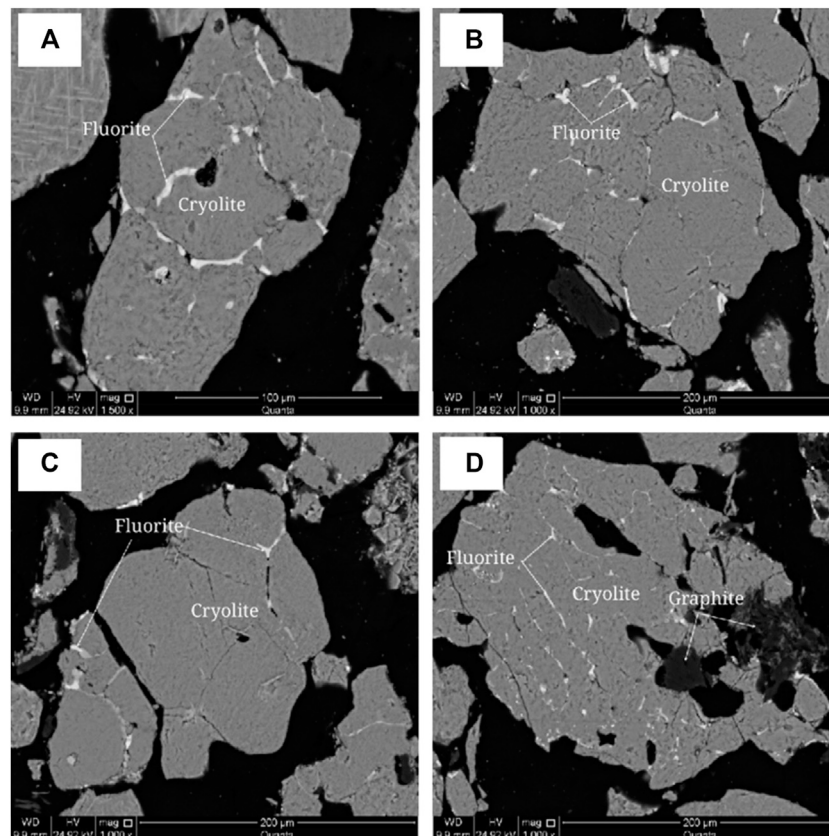


FIGURE 11 | Scanning electron microscope backscattered electron image of fluorite. (A) Fluorite aggregates are veined between cryolite grains; (B) Fluorite aggregates are veined between cryolite grains; (C) Fluorite aggregates are distributed between cryolite grains; (D) Fluorite aggregates are veined in cryolite.

energy spectrometer, scanning electron microscope and MLA mineral dissociation analyzer.

Cryolite

The cryolite was analyzed by X-ray energy spectrometer and MLA mineral dispersal analyzer. The X-ray energy spectrum analysis spectrum of cryolite is shown in **Supplementary Figure 2**, and the scanning analysis of mineral surface is shown in **Figure 6**.

As can be seen from **Figure 6**, fluoride, sodium, aluminum and calcium are uniformly distributed without obvious enrichment, while potassium is uniformly distributed, and some of them are grid-like enriched and uniformly distributed.

Polarizing microscope and scanning electron microscope were used to analyze the embedded characteristics of cryolite, as shown in **Figure 7** and **Figure 8**. It is difficult to distinguish cryolite, cryolithionite and elpasolite, so they are classified as cryolite to describe the embedded characteristics under the microscope. Crystalline particle size of cryolite is relatively uniform, most of them are microcrystalline, and the crystal particle size is about 0.1 mm, and it is semi-idiomorphic and anisotomorphic granular. A few cryolite has fine crystal particle size, which is micrite or microcrystalline, and the crystal particle size is < 0.004 mm, or between 0.004 and 0.03 mm. The cryolite particles are closely inlaid, and the boundaries are blurred. The particles are filled with

fine fluorite, and some of them are filled with micrite cryolite. The cryolite aggregates have many holes, flake and fibrous flake graphite aggregates are twisted into lumps, camboidal polygonal and other amorphous granules embedded in cryolite.

Graphite

Graphite was analyzed by X-ray energy spectrometer. The X-ray energy spectrum analysis of graphite is shown in **Supplementary Figure 3**. Graphite contained C 98.65% and S 1.35%.

The embedded characteristics of graphite were analyzed by polarizing microscope and scanning electron microscope, as shown in **Figure 9** and **Figure 10**. Graphite crystallization degree is higher, the grain size is larger, flake, fibrous flake, aggregate distortion is lumpy, camboidal polygonal, sharp edges and angles, bundles and other shaped granular. Graphite aggregates are disseminated between 0.05–0.5 and 1.00–2.0 mm, and a few aggregates are disseminated between 2.00 and 3.0 mm and the maximum is 4.0 mm. Graphite aggregates are disseminated between cryolite particles.

Fluorite

The fluorite was analyzed by X-ray energy spectrometer, and the X-ray energy spectrum of fluorite is shown in **Supplementary Figure 4**.

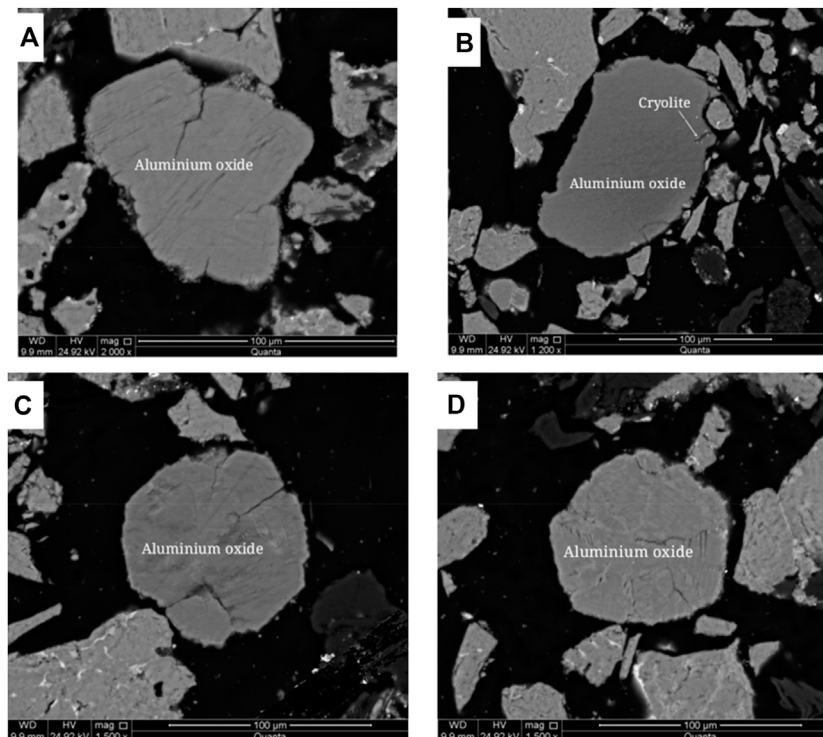


FIGURE 12 | Scanning electron microscope backscattered electron image of aluminum oxide. **(A)** Monomer dissociated aluminum oxide; **(B)** Aluminum oxide is associated with cryolite; **(C)** Monomer dissociated aluminum oxide; **(D)** Monomer dissociated aluminum oxide.

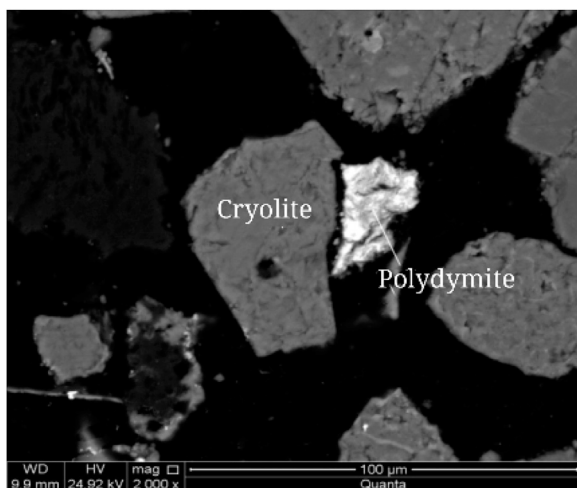


FIGURE 13 | Scanning electron microscope backscattered electron image of Polydymite (Polydymite as crushed granular).

The embedded characteristics of fluorite were analyzed by scanning electron microscopy (SEM), as shown in **Figure 11**. Fluorite is other-shaped granular with fine particle size. The aggregates are mainly other-shaped granular and vein-like distributed among cryolite grains, and a few are granular-coated in cryolite grains and graphite aggregates with disseminated particle size <0.04 mm.

Aluminum Oxide

The X-ray energy spectrometer was used to analyze aluminum oxide. The X-ray energy spectrum analysis of aluminum oxide is shown in **Supplementary Figure 5**.

The embedded characteristics of aluminum oxide were analyzed by scanning electron microscopy (SEM), as shown in **Figure 12**. Aluminum oxide is spherical, mainly associated with cryolite, graphite, and a small amount of fluorite, and the disseminated particle size is < 0.1 mm.

Polydymite

The results of X-ray energy spectrum analysis show that Ni57.86% and S42.14% are in Polydymite. The X-ray energy spectrum analysis spectrum of Polydymite is shown in **Supplementary Figure 6**.

Scanning electron microscopy (SEM) was used to analyze the embedded characteristics of Polydymite, as shown in **Figure 13**. The Polydymite is amorphous and stellate embedded in cryolite, with disseminated particle size < 0.04 mm.

Pyrite

By X-ray energy spectrum analysis, pyrite contains Fe 46.55% and S53.45%. The X-ray energy spectrum analysis spectrum of pyrite is shown in **Supplementary Figure 7**.

The embedded characteristics of pyrite were analyzed by polarizing microscope and scanning electron microscope, as shown in **Figure 14**. Pyrite is amorphous and stellate

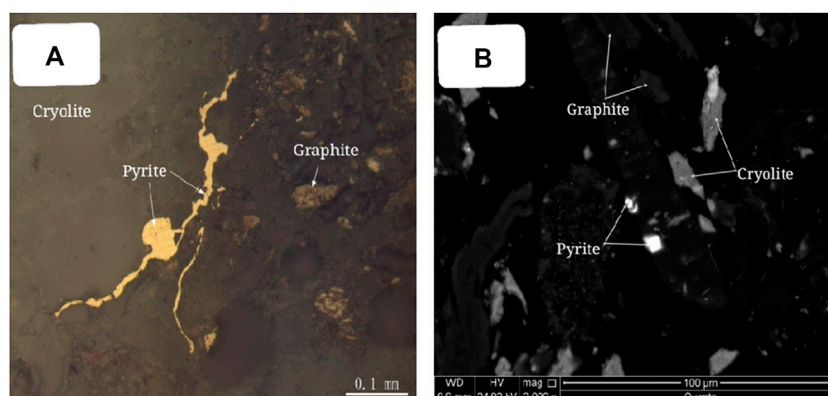


FIGURE 14 | Embedded characteristics of pyrite. **(A)** Pyrite is anamorphic granular (plane polarized light); **(B)** anamorphic granular pyrite (Scanning electron microscope image of backscattered electron).

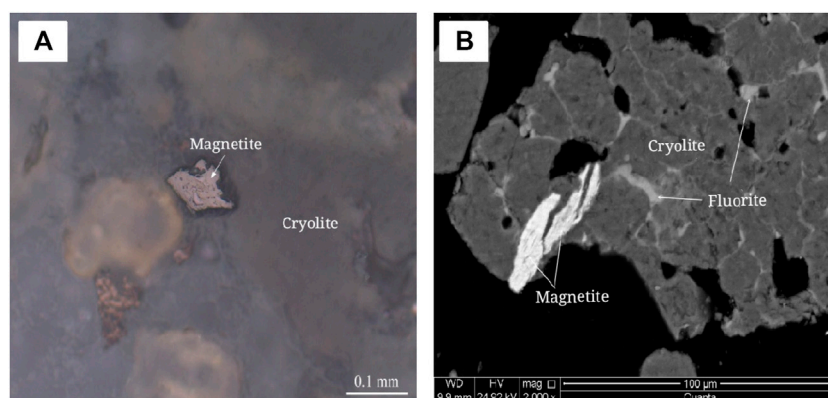


FIGURE 15 | Embedded characteristics of magnetite. **(A)** Anisotropic granular magnetite, plane polarized light. **(B)** Magnetite is encased in cryolite. Scanning electron microscope image of backscattered electron.

TABLE 3 | Calculation of carbon distribution rate in carbonaceous minerals/%.

The name of the mineral	Mineral content	The allocation of C in the mineral	The distribution rate of C in minerals
Graphite	14.35	14.16	100.00
Others	85.65	—	—
Total	100.00	14.16	100.00

embedded in transparent minerals such as cryolite, with disseminated particle size <0.05 mm.

Magnetite

By X-ray energy spectrum analysis, magnetite contains Fe 72.36% and O 27.64%. The X-ray energy spectrum analysis diagram of magnetite is shown in **Supplementary Figure 8**.

The embedded characteristics of magnetite were analyzed by polarizing microscope and scanning electron microscope, as shown in **Figure 15**. Microscopic observation shows that magnetite is

amorphous and stellate embedded in transparent minerals such as cryolite, and the disseminated particle size < 0.04 mm.

Occurrence State of the Destination Element

Occurrence State of Carbon

The carbon grade in anode carbon residue is 14.16%, and the carbon occurs in graphite in the form of independent minerals with a distribution rate of 100%. The calculation table of carbon distribution rate in carbon-bearing minerals is shown in **Table 3**.

Occurrence State of Fluorine

The fluorine grade in anode carbon residue is 43.27%, and fluorine occurs in cryolite, cryolithionite, elpasolite and fluorite as independent minerals, with the distribution rates of 74.16, 14.31, 9.15 and 2.38%, respectively. The calculation table of fluorine distribution rate in fluorine-bearing minerals is shown in **Table 4**.

TABLE 4 | Calculation table of the distribution rate of fluorine in fluorine-containing minerals/%.

The name of the mineral	Mineral content	The allocation of F in a mineral	The distribution rate of F in a mineral
Cryolite	60.25	32.09	74.16
Cryolithionite	10.10	6.19	14.31
Elpasolite	8.41	3.96	9.15
Fluorite	2.12	1.03	2.38
Others	19.12	—	—
Total	100.00	43.27	100.00

TABLE 5 | Calculation table of distribution rate of aluminum in aluminum-containing minerals/%.

The name of the mineral	Mineral content	The allocation of Al in a mineral	The distribution rate of Al in minerals
Cryolite	60.25	7.71	65.51
Cryolithionite	10.10	1.46	12.40
Elpasolite	8.41	0.94	7.99
Aluminium oxide	1.49	0.79	6.71
Magnesium aluminate	2.28	0.87	7.39
Others	17.47	—	—
Total	100.00	11.77	100.00

TABLE 6 | Calculation table of sodium distribution rate in sodium-containing minerals/%.

The name of the mineral	Mineral content	The allocation of Na in a mineral	The distribution rate of Na in minerals
Cryolite	60.25	19.76	88.06
Cryolithionite	10.10	1.88	8.38
Elpasolite	8.41	0.80	3.56
Others	21.24	—	—
Total	100.00	22.44	100.00

Occurrence State of Aluminum

The grade of aluminum in anode carbon residue is 11.77%, and aluminum occurs in cryolite, cryolithionite, elpasolite, aluminum oxide and magnesium aluminate in the form of independent minerals, with the distribution rates of 65.51%, 12.40%, 7.99%, 6.71% and 7.39%. The calculation table of aluminum distribution rate in aluminum-bearing minerals is shown in **Table 5**.

Occurrence State of Sodium

The grade of sodium in anode carbon residue is 22.44%, and sodium occurs in cryolite, cryolithionite and elpasolite as independent minerals, with the distribution rates of 88.06%, 8.38% and 3.56%, respectively. The calculation table of sodium distribution rate in sodium-bearing minerals is shown in **Table 6**.

Occurrence State of Potassium

The potassium content in anode carbon residue is 2.77%, and it occurs in the form of independent mineral in potassium cryolite with a distribution rate of 100.00%. The calculation table of potassium distribution rate in potassium-bearing minerals is shown in **Supplementary Table 1**.

CONCLUSION

By studying the occurrence state of the main elements in the anode carbon residue, the content of the main elements in the anode carbon residue was ascertained, and the mineral composition of the anode carbon residue was determined, among which cryolite, cryolithionite, elpasolite and graphite were the most important minerals. The co-associated relationship of the main minerals and the embedded characteristics of carbon minerals and fluorine minerals were investigated.

In the anode carbon residue, the content of carbon is 14.16%, which occurs in graphite as independent minerals. Fluorine content is 43.27%. It occurs in cryolite, cryolithionite, elpasolite and fluorite as independent minerals, and the distribution rate of the three kinds of cryolite reaches 97.62%. The content of aluminum is 11.77%, and it occurs in the form of independent minerals in cryolite, cryolithionite, elpasolite, aluminum oxide and magnesium aluminate. The sodium content is 22.44%, and it occurs in the form of independent mineral in cryolite, cryolithionite, elpasolite. The potassium content is 2.77%, and it occurs in the form of independent

mineral in elpasolite. In terms of occurrence state, fluorine, aluminum, sodium and potassium minerals are mainly distributed in cryolite, cryolithionite, elpasolite, presenting a relatively concentrated distribution. Therefore, the main elements of anode carbon residue, such as fluorine, aluminum, sodium and potassium, mainly occur in cryolite, while carbon mainly occurs in graphite. Effective separation of graphite and cryolite is an effective way to recover and utilize carbon residue. Flotation method can be used to separate carbon and electrolyte mainly containing cryolite.

DATA AVAILABILITY STATEMENT

The original contributions presented in the study are included in the article/**Supplementary Material**, further inquiries can be directed to the corresponding author.

REFERENCES

- Allard, F., Désilets, M., and Blais, A. (2019). Thermal, Chemical and Microstructural Characterization of Anode Crust Formed in Aluminum Electrolysis Cells. *Thermochim. Acta* 671, 89–102. doi:10.1016/j.tca.2018.11.008
- Aryanpour, G., Alamdari, H., Azari, K., Ziegler, D., Picard, D., and Fafard, M. (2014). Analysis on the Die Compaction Of Anode Paste Material Used in Aluminum Production Plants. *Powder Tech.* 254, 228–234. doi:10.1016/j.powtec.2014.01.033
- Azari, K., Alamdari, H., Aryanpour, G., Picard, D., Fafard, M., and Adams, A. (2013). Mixing Variables for Prebaked Anodes Used in Aluminum Production. *Powder Tech.* 235, 341–348. doi:10.1016/j.powtec.2012.10.043
- Azari, K., Alamdari, H., Aryanpour, G., Ziegler, D., Picard, D., and Fafard, M. (2013). Compaction Properties of Carbon Materials Used for Prebaked Anodes in Aluminum Production Plants. *Powder Tech.* 246, 650–657. doi:10.1016/j.powtec.2013.06.025
- Batista, J. d. S., and Silveira, B. I. d. (2008). Influence of the Sodium Content on the Reactivity of Carbon Anodes. *Mat. Res.* 11, 387–390. doi:10.1590/S1516-14392008000300025
- Bhattacharyay, D., Kocaefe, D., Kocaefe, Y., and Morais, B. (2017). An Artificial Neural Network Model for Predicting the CO₂ Reactivity of Carbon Anodes Used in the Primary Aluminum Production. *Neural Comput. Applic.* 28, 553–563. doi:10.1007/s00521-015-2093-7
- Chevarin, F., Lemieux, L., Picard, D., Ziegler, D., Fafard, M., and Alamdari, H. (2015). Characterization of Carbon Anode Constituents under CO₂ Gasification: A Try to Understand the Dusting Phenomenon. *Fuel* 156, 198–210. doi:10.1016/j.fuel.2015.04.035
- Dan-qing, Z. (2008). The Measures to Reduce the Consumption of Anode Carbon in Aluminum Electrolysis. *Light Met.* 08, 25–28.
- Diógenes, L., Maia, R., Bessa, I., Castelo Branco, V., Nogueira Neto, J., and Silva, F. (2021). The Influence of Crushing Processes and Mineralogy of Aggregates on Their Shape Properties and Susceptibility to Degradation. *Construction Building Mater.* 284, 122745. doi:10.1016/j.conbuildmat.2021.122745
- Einarsrud, K. E. (2010). The Effect of Detaching Bubbles on Aluminum-Cryolite Interfaces: An Experimental and Numerical Investigation. *Metall. Mater. Trans. B* 41, 560–573. doi:10.1007/s11663-010-9345-9
- Grjotheim, K., and Krohn, M. (2020). *Aluminium Electrolysis: Fundamentals of the Hall-Heroult Process*. Dusseldorf, Germany: Aluminium Verlag Marketing & Kommunikation GmbH.
- Guo, Y., Yu, Y., Ren, H., and Xu, L. (2020). Scenario-based DEA Assessment of Energy-Saving Technological Combinations in Aluminum Industry. *J. Clean. Prod.* 260, 121010. doi:10.1016/j.jclepro.2020.121010
- Hai-fei, X., Li-jun, F., Yang, Z., He-kui, L., and Yi, S. (2009). Analysis of Sources of Carbon Residue and its Control Methods. *Carbon Tech.* 28, 41–44. doi:10.3969/j.issn.1001-3741.2009.06.009

AUTHOR CONTRIBUTIONS

SM: Data curation and Writing- Original draft preparation. ZQ: Conceptualization and Methodology.

FUNDING

This work was financially supported by Project of 100 leading talents in Guizhou Province (Grant No. (2015) 4012).

SUPPLEMENTARY MATERIAL

The Supplementary Material for this article can be found online at: <https://www.frontiersin.org/articles/10.3389/fmats.2021.719563/full#supplementary-material>

- Haupin, W. E. (1971). A Scanning Reference Electrode for Voltage Contours in Aluminum Smelting Cells. *Jom* 23, 46–49. doi:10.1007/BF03355737
- Huang, Y., Wang, Z., Yang, Y., Gao, B., Shi, Z., and Hu, X. (2018). Anodic Bubble Behavior in a Laboratory Scale Transparent Electrolytic Cell for Aluminum Electrolysis. *Metals* 8, 806. doi:10.3390/met8100806
- Hussein, A., Lu, Y., Mollaabbasi, R., Tessier, J., and Alamdari, H. (2020). Bio-pitch as a Binder in Carbon Anodes for Aluminum Production: Bio-Pitch Properties and its Interaction with Coke Particles. *Fuel* 275, 117875. doi:10.1016/j.fuel.2020.117875
- Jin-sheng, L., and Qing-chun, W. (2017). XRD Measurement of Carbon Concentration of Anode Slag in Aluminum Electrolyte. *Phys. Examination Test.* 35, 27–30.
- Jing, Y., Xian-lei, L., Du, Bin-bin., Ping-fu, W., and Lu-ning, J. (2010). The Impact of Element in Pre-baked Carbon Anodes on Aluminum Electrolysis and Relevant Control Measures. *Carbon* 144, 37–41. doi:10.3969/j.issn1001-8948.2010.04-008
- Jing-lu, W., Zhong-yu, Q., Jun, L., Li, L., and Xian-yong, M. (2015). The Analysis and Control of Fe Content Influencing Factor in Electrolytic Liquid Aluminum. *Yunnan Metall.* 44, 82–85. doi:10.3969/j.issn.1006-0308.2015.05.019
- Khaji, K., and Al Qassemi, M. (2016). The Role of Anode Manufacturing Processes in Net Carbon Consumption. *Metals* 6, 128. doi:10.3390/met6060128
- Kubiňáková, E., Danielik, V., and Hiveš, J. (2018). Electrochemical Characterization of Multicomponent Sodium Cryolite Electrolytes with High Content of Aluminium Fluoride. *Electrochimica Acta* 265, 474–479. doi:10.1016/j.electacta.2018.01.174
- Lifeng, M., Shiliang, L., and Hailiang, Z. (2019). Flotation Process of Recycling Carbon Slag from Electrolytic Aluminium. *Mod. Mining* 35, 33–34. doi:10.3969/j.issn.1674-6082.2019.11.011
- Min-zhang, L., and Xian, L. (2012). The Effect of Exterior Geometric Shape of Prebaked Anode on the Formation of Carbon Residue during Electrolysis. *Carbon Tech.* 31, 64–66.
- Qing, L., Xudong, C., and Wenyi, G. (2015). Countermeasures and Origins of Carbon Residue in Aluminum Reduction Production. *Light Met.* 11, 36–38. doi:10.13662/j.cnki.qjs.2015.11.008
- Xiangyang, M., Jun, L., and Zhanliang, Y. (2016). The Research on Recycling Carbon Residue by Flotation Process. *Light Met.* 04, 28–30. doi:10.13662/j.cnki.qjs.2016.04.007
- Xiao, S.-j., Mokkelbost, T., Paulsen, O., Ratvik, A. P., and Haarberg, G. M. (2014). SnO₂-based Gas (Hydrogen) Anodes for Aluminum Electrolysis. *Trans. Nonferrous Met. Soc. China* 24, 3917–3921. doi:10.1016/S1003-6326(14)63551-2
- Xugui, Z. (2021). Production Practice of Anode Carbon Block Structure Optimization to Reduce Gross Consumption. *Light Met.* 03, 40–44. doi:10.13662/j.cnki.qjs.2021.03.009
- Yang, F., Yu, Q., Zuo, Z., and Hou, L. (2021). Thermodynamic Analysis of Waste Heat Recovery of Aluminum Dross in Electrolytic Aluminum Industry. *Energy*

- Sourc. A: Recovery, Utilization, Environ. Effects* 43, 1047–1059. doi:10.1080/15567036.2019.1634163
- Yao-jian, R., Zhi, S., Jie, T., and Wei, L. (2009). Study on Electrolytic Aluminium Carbon Anode Preparation with Calcined Anthracite. *Proced. Earth Planet. Sci.* 1, 694–700. doi:10.1016/j.proeps.2009.09.109
- Zhi-qian, W., Tie-jun, W., and Hong-tao, Z. (2019). Analysis and Research on Resource Utilization Technology of Anode Carbon Slag Disposal in Aluminum Electrolysis Production. *World Nonferrous Met.* 22, 8–9. doi:10.3969/j.issn.1002-5065.2019.22.004

Conflict of Interest: The authors declare that the research was conducted in the absence of any commercial or financial relationships that could be construed as a potential conflict of interest.

Publisher's Note: All claims expressed in this article are solely those of the authors and do not necessarily represent those of their affiliated organizations, or those of the publisher, the editors and the reviewers. Any product that may be evaluated in this article, or claim that may be made by its manufacturer, is not guaranteed or endorsed by the publisher.

Copyright © 2021 Mao and Zhang. This is an open-access article distributed under the terms of the Creative Commons Attribution License (CC BY). The use, distribution or reproduction in other forums is permitted, provided the original author(s) and the copyright owner(s) are credited and that the original publication in this journal is cited, in accordance with accepted academic practice. No use, distribution or reproduction is permitted which does not comply with these terms.



Effects of the Silicate Modulus of Water Glass on the Hydration and Mechanical Properties of Alkali-Activated Blast Furnace Ferronickel Slag

Kuisheng Liu¹, Zhenguo Liu¹ and Jianwei Sun^{2*}

¹Beijing Urban Construction Group Co., Ltd., Beijing, China, ²Department of Civil Engineering, Tsinghua University, Beijing, China

OPEN ACCESS

Edited by:

Tingting Zhang,
Dalian University of Technology, China

Reviewed by:

Xiaomei Wan,
Qingdao University of Technology,
China

Changming Li,
North China University of Water
Conservancy and Electric Power,
China

*Correspondence:

Jianwei Sun
jianwei_68@126.com

Specialty section:

This article was submitted to
Structural Materials,
a section of the journal
Frontiers in Materials

Received: 28 July 2021

Accepted: 24 August 2021

Published: 07 September 2021

Citation:

Liu K, Liu Z and Sun J (2021) Effects of
the Silicate Modulus of Water Glass on
the Hydration and Mechanical
Properties of Alkali-Activated Blast
Furnace Ferronickel Slag.
Front. Mater. 8:748833.
doi: 10.3389/fmats.2021.748833

Blast furnace ferronickel slag (BFNS), currently an underutilized metallurgical residue, was investigated for use as a precursor for alkaline activation. Water glass solutions with various moduli (0.5, 1.0, 1.5 and 2.0) were used at the same water glass concentration of 10% to investigate the influence of the modulus on hydration and mechanical properties. The results show that the modulus has a certain impact on the hydration and mechanical strength development of alkali-activated BFNS. Increasing the modulus of water glass does not change the type of hydration product and the activity of the Mg-containing phases, but it decreases the amount of C₂AS, the Ca/Si and Al/Si ratios of the (N,C)-A(M)-S-H gel. In addition, a high silicate modulus deteriorates the pore structure, which has an adverse effect on the development of compressive strength and splitting tensile strength.

Keywords: ferronickel slag, alkali activation, hydration, water glass, modulus

INTRODUCTION

Cement is the most widely used building material (Wang et al., 2011). However, during the production of cement, much energy and resources are consumed, and toxic gases such as nitrogen oxides are emitted, which obviously does not conform to the development concept of green environmental protection (Sabir et al., 2001; Siddique and Klaus, 2009; Wang et al., 2020b). To meet the environmental protection requirements for green building materials, alkali-activated cementitious materials are produced (Sun and Chen, 2019; Wang et al., 2020a). Alkali-activated cementitious material refers to a kind of cementitious material produced by alkaline activators used to destroy the vitreous structure of silicate aluminate material. Silicate aluminates are generally common industrial wastes, such as slag, fly ash, metakaolin, phosphorus slag and steel slag (Goñi et al., 2013; Abdalqader et al., 2015; Kovtun et al., 2015; Abdalqader et al., 2016; Zhuang and Wang, 2021). Because these silicate aluminates are industrial byproducts, there is no need for high-temperature calcination during the production of alkali-activated materials, and they do not produce a large amount of CO₂ and other toxic gases, so they meet the development requirements for green building materials.

Generally, alkali-activated materials can be divided into three categories according to the chemical compositions of the precursor (Rashad et al., 2013; Rashad et al., 2016; Gebregziabihier et al., 2016; Mobasher et al., 2016). The first type is a high Ca system ((Na,K)₂O-CaO-Al₂O₃-SiO₂-H₂O) (Wang and Scrivener, 1995; Aydin and Baradan, 2014; Bernal et al., 2014; Ke et al., 2016). The most typical alkali-activated material is ground blast furnace slag (GBFS), which contains more Si and Ca and less

Al, especially a more amorphous phase and higher activity (Krizan and Zivanovic, 2002; Pan et al., 2002; Puertas et al., 2011; Myers et al., 2015). The second type of alkali-activated material is low Ca (free Ca) system ($(\text{Na,K})_2\text{O}-\text{Al}_2\text{O}_3-\text{SiO}_2-\text{H}_2\text{O}$) (De Vargas et al., 2014; Chi, 2015; Leong et al., 2016). The most typical examples are fly ash and metakaolin with more Si and Al and very less Ca content (Atiş et al., 2015; Williamson and Juenger, 2016). Generally, high-temperature curing or high alkalinity is needed for activation (Junaid et al., 2015; Ma and Ye, 2015). In addition to the two typical alkali-activated cementitious material systems mentioned above, the third system is the hybrid cementitious material system, which is also a hot research topic at present. Generally, there are two combinations of hybrid cementitious materials: The first combination contains a small amount of cement, which is the most common composite method (Acevedo-Martinez et al., 2012; Escalante-Garcia et al., 2014; Li and Li, 2014); the second type does not contain cement and is made of industrial wastes, and the most common example is the GBFS-fly ash composite material system (Lee et al., 2014; Harbulakova et al., 2017).

Ferronickel slag is a byproduct from the smelting and purification of nickel-iron alloys (Coman et al., 2013; Bartzas and Komnitsas, 2015; Sagadin et al., 2016). At present, the main way of treating ferronickel slag in China is to directly store or bury it, which not only occupies land resources but also may pollute land and underground water because of infiltration or leaching for a long time (Xi et al., 2018). It may have adverse influence on marine resources. Therefore, the accumulation of ferronickel slag will seriously damage the ecological environment if it is allowed to continue. Ferronickel slag can be divided into electric furnace ferronickel slag and blast furnace ferronickel slag (BFNS) depending on the production process (Wang et al., 2018b; Sun et al., 2018). The main chemical components of BFNS in China are SiO_2 , MgO , FeO , CaO and Al_2O_3 (Choi and Choi, 2015; Tangahu et al., 2015). Because BFNS is generated by water quenching and quick cooling, it has potential for activation. The forming process and chemical composition of BFNS are similar to those of GBFS (Bartzas and Komnitsas, 2015). Alkali-activated GBFS has been widely studied, and many advantages of alkali-activated GBFS have been recognized to some extent. Therefore, in theory, alkali-activated BFNS should also have certain application promise.

Research on alkali-activated ferronickel slag cementitious material starts recently. Maragkos et al. (2009) used water glass to prepare alkali-activated electric furnace ferronickel slag and found that the compressive strength could reach 120 MPa with optimal experimental parameters, including a solid-liquid ratio of 5.4 g/ml, NaOH concentration of 7 M and SiO_2 concentration of 4 M. Meanwhile, water absorption of 0.7% and apparent density of $2,480 \text{ kg/m}^3$ could be obtained (Maragkos et al., 2009). It was also proven that the interface between unreacted particles and gel products is the weak area when the material is damaged by compression (Maragkos et al., 2009). Komnitsas et al. (2007) also studied a water glass-activated electric furnace and found that the main crystalline products were sodalite, magnetic hematite, thermonatrite, trona and calcite. They also found that the curing age was the main factor that influenced the compressive strength (Komnitsas et al., 2007).

Zhang et al. (2017b) used high-magnesium ferronickel slag to improve water glass-activated fly ash materials and found that adding 20 and 40% ferronickel slag could significantly improve the compressive strength of alkali-activated fly ash. Moreover, compared with cement-based materials, the production of this geopolymer could significantly reduce CO_2 emissions (Zhang et al., 2017b). Yang et al. (2014) also found that the main reaction product was N-M-A-S gel in alkali-activated fly ash and high-magnesium ferronickel slag paste. The optimal concentration of ferronickel slag is 20% in alkali-activated composite material, which had the highest compressive strength, the densest pore structure and the least drying shrinkage (Yang et al., 2014). Zhang et al. (2017a) also found the same gel products. Yang et al. (2017) studied the thermal stability of alkali-activated fly ash and ferronickel slag composite materials and found that the thermal stability of alkali-activated composite systems was better than that of ordinary Portland cement systems in a certain temperature range, and the volume shrinkage was also less than that of ordinary Portland cement systems resulting from the generation of dense N-A(M)-S-H gels.

The existing literature mainly focuses on the properties of electric furnace ferronickel slag, and there are few studies on alkali-activated BFNS cementitious material systems. Compared with the chemical composition of GBFS and fly ash, BFNS can be defined as a “medium Ca” system, which is a new raw material system. The alkaline environment plays an important role in the hydration and subsequent properties of alkali-activated cementitious materials. In this paper, water glass was used as an alkaline activator, and the influence of different alkaline environments on the hydration and mechanical properties of alkali-activated BFNS was studied by changing the modulus of water glass.

MATERIALS AND METHODS

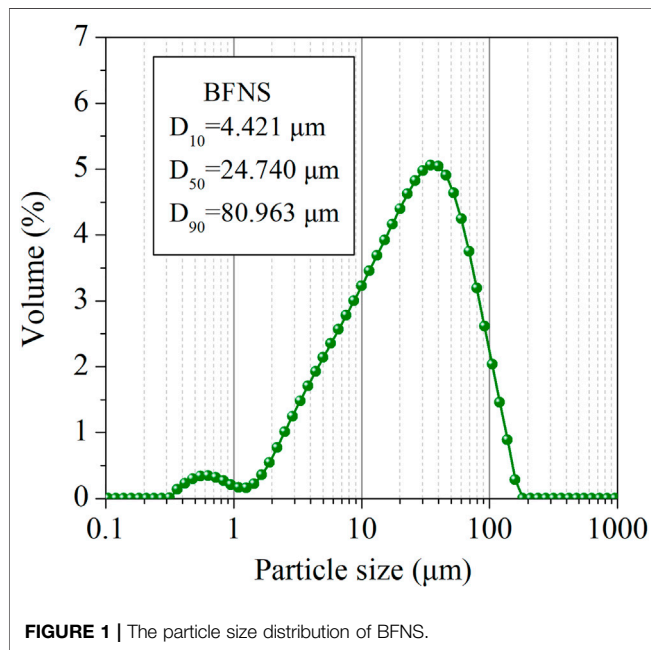
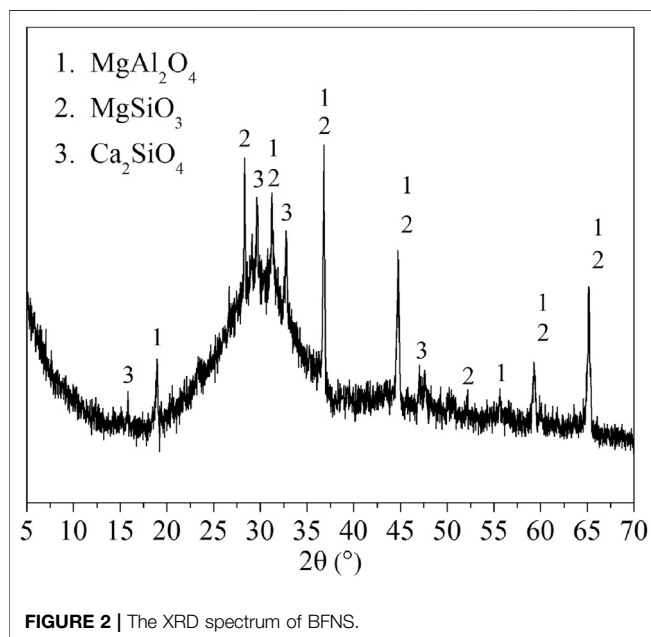
Raw Materials

The BFNS used in this paper came from Luoyuan County, Fujian Province. The chemical composition of the BFNS was determined by X-ray fluorescence spectroscopy, as shown in **Table 1**. Compared to common GBFS, the CaO content is lower in BFNS. A laser particle size analyzer (MasterSizer 2000) was used to measure the particle size distribution of the BFNS, as shown in **Figure 1**. The average particle size was $D_{50} = 24.740 \mu\text{m}$ for BFNS particles. The mineral composition of the BFNS obtained is shown in **Figure 2**. A hump appears in the range of $25^\circ\text{--}35^\circ$ (2θ) in the XRD spectrum, which indicates that there is an activated vitreous phase in the BFNS. It is worth noting that the Mg in the BFNS mainly exists as a spinel (MgAl_2O_4) and magnesium olivine (MgSiO_3).

Sodium hydroxide (NaOH) of 99% purity was obtained from Beijing Tongguang Fine Chemicals Company, China. Commercial liquid sodium silicate ($\text{Na}_2\text{O}\cdot n\text{SiO}_2$) with a silicate modulus ($\text{SiO}_2/\text{Na}_2\text{O}$ molar ratio) of 3.36 was also used. Water glass was prepared with NaOH and $\text{Na}_2\text{O}\cdot n\text{SiO}_2$ as an alkaline activator. Natural river sand with a particle size less than 5 mm and limestone with a particle size between 5 and 25 mm were selected as coarse and fine aggregates, respectively.

TABLE 1 | Main chemical composition of BFNS (%).

	SiO ₂	Al ₂ O ₃	CaO	MgO	Cr ₂ O ₃	MnO	Fe ₂ O ₃	TiO ₂	SO ₃	NiO
BFNS	29.95	26.31	25.19	8.93	2.30	2.25	1.55	1.18	0.90	0.01

**FIGURE 1** | The particle size distribution of BFNS.**FIGURE 2** | The XRD spectrum of BFNS.

Mix Proportions and Curing Method

The mix proportions of concrete are shown in Table 2. The total amount of cementitious material was 400 kg/m³, and the water-binder ratio was 0.5 which involves the water in water glass

solution. The BFNS was activated by water glass at a constant activator to slag ratio of 10% (water glass: BFNS in mass). And the modulus (molar ratio between SiO₂ and Na₂O) of the water glass was adjusted to 0.5, 1.0, 1.5 and 2.0 by adding NaOH. The alkaline activator was first mixed with water before 2 h and cooled to room temperature to avoid temperature interference, and subsequently mixed with solid materials. Concrete samples (100 × 100 × 100 mm) were prepared according to GB/T 50082-2009. The hardened paste and fresh mortar of sample BFNS-M1.0 are shown in Figure 3. According to the pre-preparation test, the initial setting time of sample BFNS-M1.0 was very short, and the moisture on the surface disappeared rapidly after stirring for 5 min. Meanwhile, cracks began to appear after 3 h, which indicated that sample BFNS-M1.0 underwent quick and large shrinkage. In terms of fresh mortar, sample BFNS-M1.0 could not be molded due to rapid setting. Therefore, only samples BFNS-M0.5, BFNS-M1.5 and BFNS-M2.0 were studied in this paper. The water-binder ratio of paste was the same as that of the concrete, and the fresh paste was put into the plastic tube. All samples were cured under the same conditions (20 ± 2°C, >90% RH) until testing.

Test Method

After 28 days and 90 days, the middle part of the hardened paste was taken, crushed and immersed in anhydrous ethanol to stop hydration and then dried at 60°C. The dried pastes were treated in two ways. First, the block pastes were directly tested as follows: an FEI Quanta-200 scanning electron microscope (SEM) was used to observe the morphology of alkali-activated BFNS under different conditions. The composition of the hydration products was also analyzed using an EDAX Genesis 2000 X-ray energy spectrometer (EDX). The pore structure of the hardened paste was tested by an Autopore IV 9500 mercury injection apparatus (MIP). Then, the other pastes were ground. A Bruker Vertex 70 Fourier transform infrared (FTIR) spectrometer was used to analyze the structure of the gel product. The types of hydration products were measured by XRD analysis with a scanning range from 5° to 70° and a measuring speed of 8°/min. At 1, 3, 7, 28 and 90 days, the compressive strength and splitting tensile strength of concrete were obtained by using three specimens for each test according to the Chinese National Standard GB/T 50081-2002.

RESULTS AND DISCUSSION

XRD Analysis

Under different hydration conditions, the XRD spectra of the alkali-activated BFNS pastes at 28 days are shown in Figure 4. Compared to the XRD spectrum of BFNS in Figure 2, diffraction peaks of MgAl₂O₄ and MgSiO₃ of alkali-activated BFNS pastes in

TABLE 2 | Mix proportions of concrete (kg/m³).

Sample	BFNS	Coarse aggregate	Fine aggregate	Concentration (%)	Modulus	Water/binder
BFNS-M0.5	400	1,000	800	10	0.5	0.5
BFNS-M1.0	400	1,000	800	10	1.0	0.5
BFNS-M1.5	400	1,000	800	10	1.5	0.5
BFNS-M2.0	400	1,000	800	10	2.0	0.5

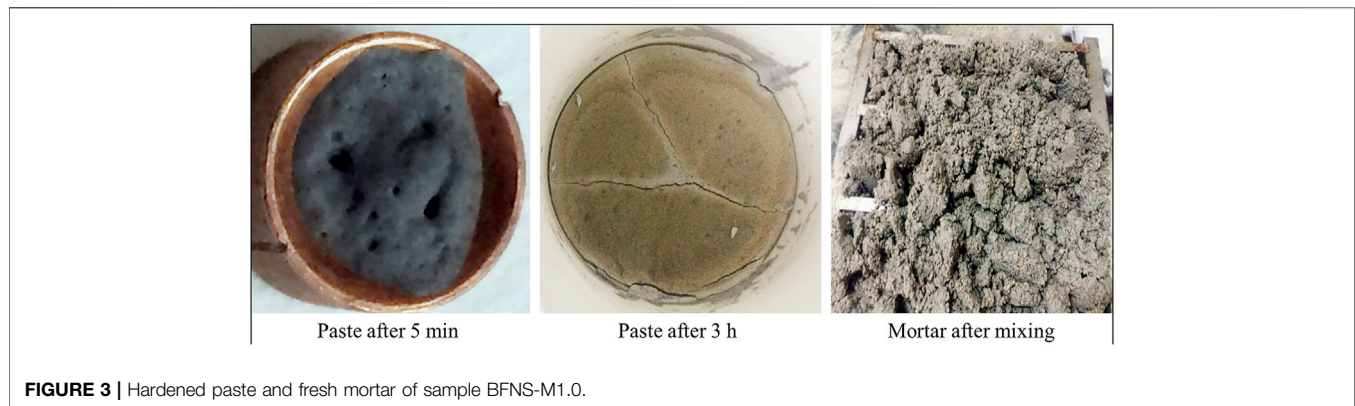
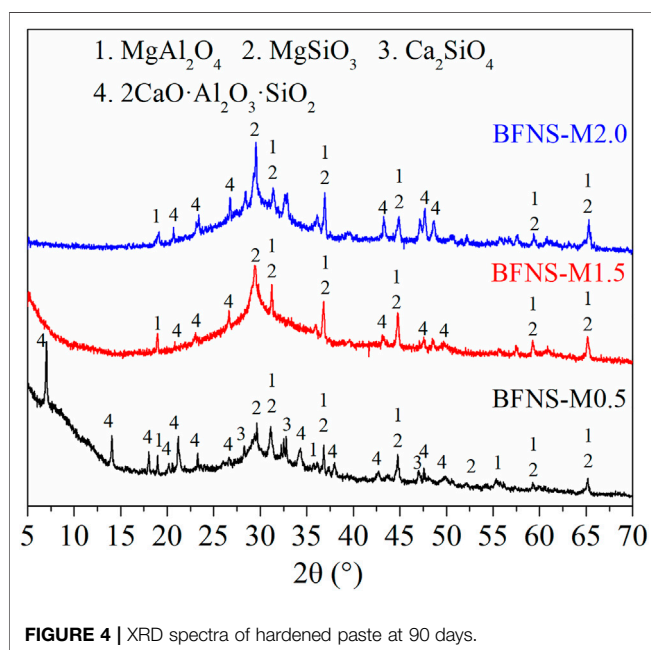
**FIGURE 3** | Hardened paste and fresh mortar of sample BFNS-M1.0.**FIGURE 4** | XRD spectra of hardened paste at 90 days.

Figure 4 are very clearly detected. There is almost no change in the peaks, which means that MgAl_2O_4 and MgSiO_3 do not participate in the reaction. This result is similar to the use of ferronickel slag as a mineral admixture in cement.

In addition, the only newly generated crystalline phase detected is $2\text{CaO} \cdot \text{Al}_2\text{O}_3 \cdot \text{SiO}_2$ (C_2AS , peak 4). This crystalline phase can also be found in alkali-activated GBFS paste. However, there are differences in the specific composition and content, which should be attributed to the similar chemical composition of GBFS and BFNS. It is worth noting that the diffraction peak of

C_2AS is obvious and high, indicating that the crystallinity is high. When the modulus of water glass increases from 0.5 to 1.5, the XRD spectra of alkali-activated BFNS pastes change significantly. The number and intensity of C_2AS diffraction peaks are significantly reduced with increasing modulus. This indicates that increasing the modulus significantly reduces the amount of C_2AS . Moreover, with the increase in the modulus of water glass, the “hump” in the XRD spectra becomes more obvious, which indicates that increasing the modulus is beneficial to the formation of amorphous products. However, it is worth noting that there is no significant difference between the XRD patterns of samples BFNS-M1.5 and BFNS-M2.0. This indicates that when the modulus of water glass is more than 1.5, increasing the content of silicate will not have a significant impact on the hydration products of alkali-activated BFNS pastes.

SEM and EDX Analyses

The microstructure of sample BFNS-M0.5 at 90 days is shown in **Figure 5**. The microstructure of the water glass-activated BFNS hardened paste is very dense, but even at 90 days, unreacted BFNS particles can still be obviously detected (point B in **Figure 5**). In the EDX spectrum at point A, a small amount of Mg was detected in the gel products. According to the XRD results, the Mg-containing phase in the BFNS almost did not participate in the reaction, which suggests that the vitreous components of the BFNS may contain Mg. According to the EDX analysis, the gel products of water glass-activated BFNS can be written as $(\text{N,C})\text{-A(M)-S-H}$. Na ions may replace some of the Ca ions to form a gel, which is similar to the reaction products of alkali-activated GBFS-based cementitious materials. Mg in the vitreous of BFNS may enter the gel structure or adsorb on the surface of the gel, which is similar to the result from previous research on alkali-activated low Ca and high Mg ferronickel slag (Yang et al., 2014; Yang et al., 2017).

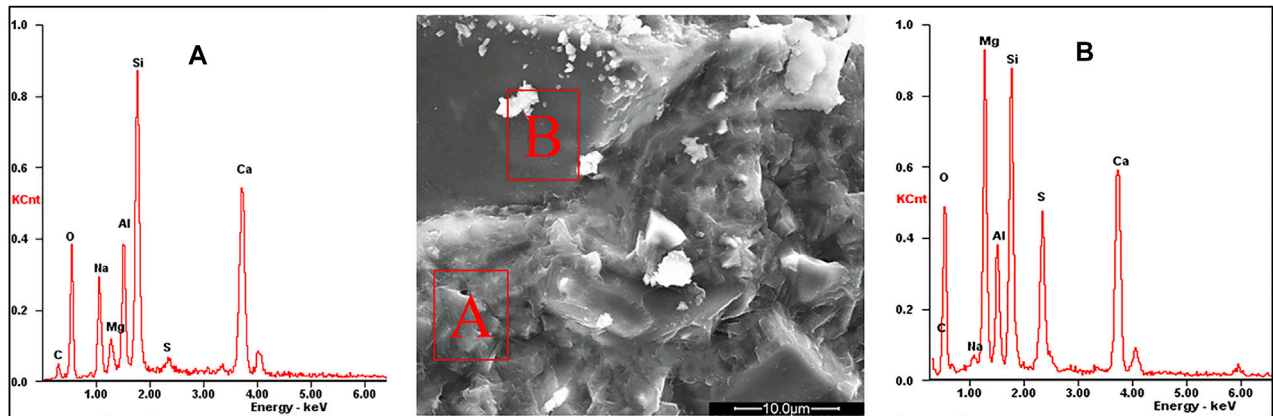


FIGURE 5 | The SEM image and EDX spectra of sample BFNS-M0.5 at 90 days.

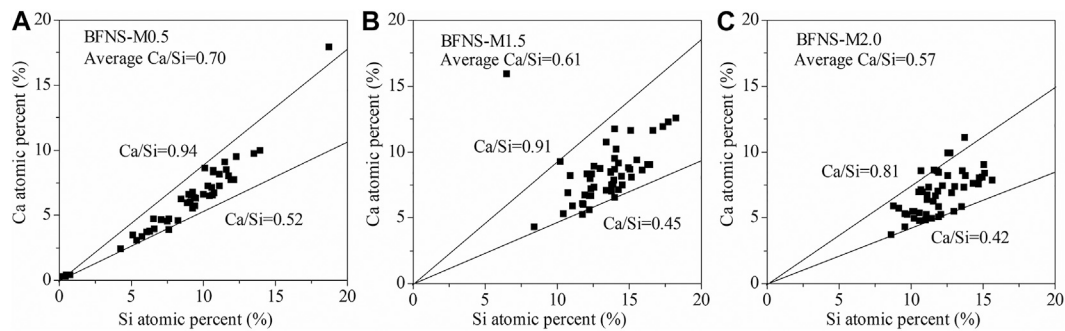


FIGURE 6 | The Ca/Si ratio in (N,C)-A(M)-S-H gel at 90 days.

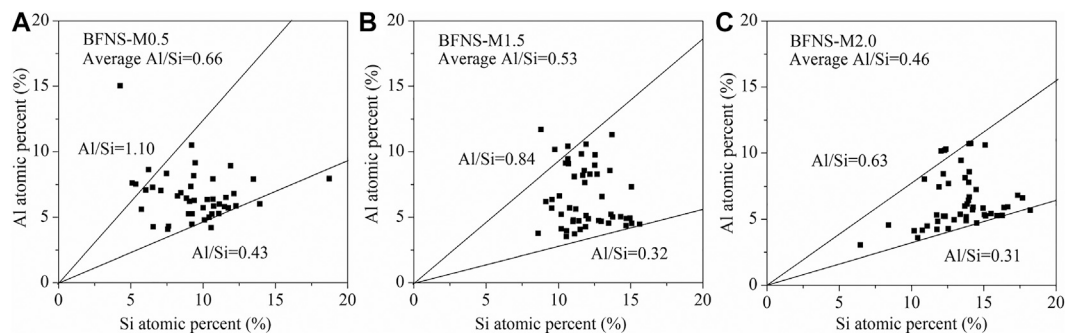


FIGURE 7 | The Al/Si ratio in (N,C)-A(M)-S-H gel at 90 days.

To further determine the effect of the modulus on the composition of the gel, a total of 50 micro-scale areas of the (N,C)-A(M)-S-H gel were analyzed by EDX. The Ca/Si and Al/Si ratios of each sample were calculated according to the EDX test results, as shown in **Figure 6** and **Figure 7**, respectively.

When the modulus of water glass is 0.5, the Ca/Si ratio of the gel varies from 0.52 to 0.94, with an average value of 0.70. When the modulus of water glass is 1.5, the Ca/Si ratio of the gel varies from

0.45 to 0.91, with an average value of 0.61. When the modulus of water glass is 2.0, the Ca/Si ratio of the gel varies from 0.42 to 0.81, with an average value of 0.57. The Ca/Si ratio of the gel decreases with increasing modulus, but the amplitude reduction is not significant. Since the increase in modulus means a significant increase in silicate content, the change in Ca/Si ratios in the gels is very small, which indicates that more silicate due to the increase in modulus does not participate in the later reaction.

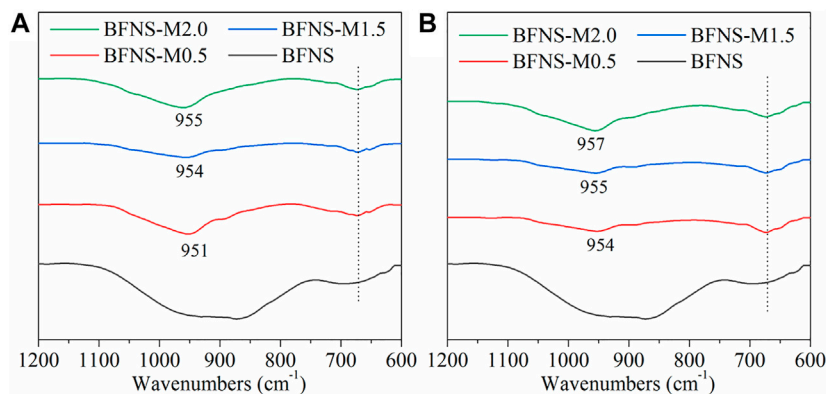


FIGURE 8 | FTIR spectra of hydration products ranging from 1,200 to 600 cm^{-1} : (A) 28 days; (B) 90 days.

Previous studies show that the Ca/Si ratio of gel in pure cement systems generally varies in the range of 1.2–2.3 (Richardson, 1999). Another study shows that the Ca/Si ratio in alkali-activated GBFS is 1.29 ± 0.33 (Kovtun et al., 2015). Therefore, the Ca/Si ratio in the gels generated by alkali-activated BFNS is significantly lower than that generated by cement and alkali-activated GBFS.

When the modulus of water glass is 0.5, the Al/Si ratio of the gels varies from 0.43 to 1.10, with an average value of 0.66. When the modulus of water glass is 1.5, the Al/Si ratio varies from 0.32 to 0.84, with an average value of 0.53. When the modulus of water glass is 2.0, the Al/Si ratio varies from 0.31 to 0.63, with an average value of 0.46. With the increase in the modulus of water glass, the Al/Si ratio gradually decreases. On the one hand, an increase in the modulus leads to an increase in silicate. On the other hand, the increase in silicate makes it easier for Al to form a gel, resulting in a reduction in the Al/Si ratio (Pardal et al., 2009; García-Lodeiro et al., 2013).

FTIR Analysis

FTIR patterns of hydration products of water glass-activated BFNS at 28 and 90 days are shown in **Figure 8A** and **Figure 8B**, respectively. In general, the peak at approximately 950 cm^{-1} is the Q^2 units of the stretching vibration peak of the Si-O bond, and some peaks at approximately $600\text{--}700 \text{ cm}^{-1}$ are the deformation vibration peaks of Si-O-Si(Al) (Wang et al., 2018a). The narrow and sharp peak indicates better crystallization of the corresponding phase, and the wide and rounded peak indicates worse crystallization (Wang et al., 2018a). It can be seen from **Figure 8** that the crystallization of Si-O and Al-O connection structures in BFNS is poor, and there is no obvious stretching vibration peak for Si-O bonds and no deformation vibration peak of Si-O-Si(Al). However, after activation, a series of deformation vibration peaks of Si-O bonds of Q^2 units and Si-O-Si(Al) appear in alkali-activated BFNS. With the increase in the modulus of water glass, the stretching vibration peak of the Si-O bond of Q^2 units tends to shift toward a higher frequency. This indicates a higher polymerization degree in the alkali-activated BFNS pastes. The FTIR results clearly reveal the polymerization process of alkali-activated BFNS. The variation after 90 days was basically the same as that after 28 days, which further verified the possibility of the above speculation.

MIP Analysis

Pore structure has a very important effect on strength and permeability resistance of concrete. According to previous studies, the pores in cementitious materials are classified as follows: harmless pores ($<20 \text{ nm}$), little harmful pores ($20\text{--}50 \text{ nm}$), harmful pores ($50\text{--}200 \text{ nm}$) and much harmful pores ($>200 \text{ nm}$) (Zhou et al., 2020). In this study, the pore structure distributions of different kinds of hardened pastes at 28 and 90 days are shown in **Figure 9**.

Obviously, with increasing modulus, the total pore volume increases. Compared to samples BFNS-M1.5 and BFNS-M2.0, sample BFNS-M0.5 has an extremely low pore volume. This indicates that increasing the modulus of water glass has an adverse impact on the pore structure. Moreover, the pores in alkali-activated BFNS hardened pastes are mainly composed of small pores, and the proportion of large pores is very small. With the prolongation of curing time, there is no obvious change in the total pore volume. The main reason is that the pore structures of alkali-activated BFNS hardened pastes at 28 days are very dense and prolonging the curing time has little influence on improving the pore structure. However, in terms of sample BFNS-M2.0, with prolonged curing age, the pore distribution obviously changes. The harmless pore volume increases, little harmful pores and harmful pores volume decreases, and much harmful pore volume change slightly.

Mechanical Properties

The changes in the compressive strength and splitting tensile strength of all concrete with age under different conditions are shown in **Figure 10A** and **Figure 10B**, respectively. As illustrated in **Figure 10**, the compressive strengths show a similar tendency to the splitting tensile strength at all ages. Apparently, increasing the modulus of water glass has an adverse impact on the development of compressive strength and splitting tensile strength, resulting from deteriorated pore structure. At 1 day, samples BFNS-M1.5 and BFNS-M2.0 have no strengths. Meanwhile, the late strength increases slowly. Thus, these two materials cannot be used in practical engineering applications due to their low strengths. In terms of sample BFNS-M0.5, the compressive strength and splitting tensile strength rapidly increase before 7 days. However, after 7 days, the growth rates

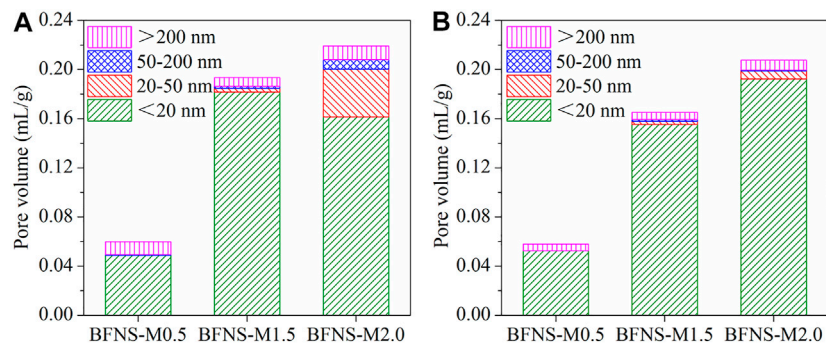


FIGURE 9 | Pore structures of hardened pastes.

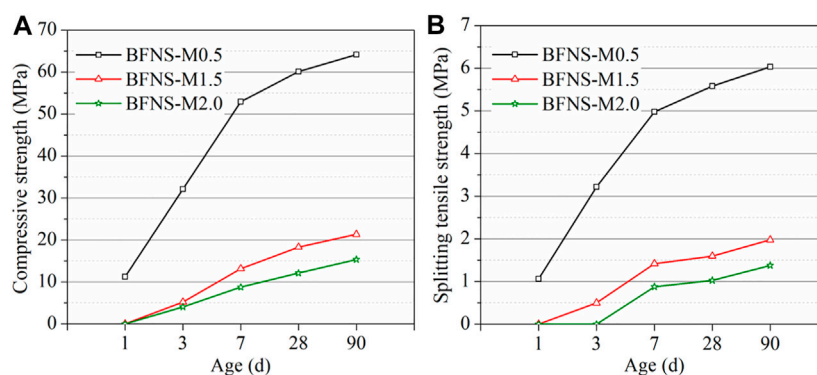


FIGURE 10 | Mechanical properties of the alkali-activated BFNS mortars at different ages: **(A)** Compressive strength; **(B)** Splitting tensile strength.

of the strength decrease. Sample BFNS-M0.5 can achieve 60 MPa compressive strength and 5.5 MPa splitting tensile strength. In this study, when the concentration of water glass is 10% in alkali-activated BFNS cementitious material, the optimum modulus for compressive strength and splitting tensile strength is 0.5.

CONCLUSION

Alkali-activated BFNS material is a low-cost product that may possibly use industrial waste and provide a solution to a current ecological problem. This study investigated the influence of the modulus of water glass on the hydration product, pore structure and strength of alkali-activated BFNS materials at the same water glass content of 10%. The main conclusions obtained from this research are as follows:

1. The crystalline product of water glass-activated BFNS is C_2AS . Increasing the modulus of water glass has no effect on the type of crystalline product but decreases the amount of C_2AS . Changing the hydration condition has little influence on the $MgAl_2O_4$ and $MgSiO_3$ phases, which almost do not participate in the reaction.
2. The amorphous product of water glass-activated BFNS is (N,C)-A(M)-S-H gel. Increasing the modulus of water glass

reduces the Ca/Si and Al/Si ratios of the gel. With the increase in the modulus of water glass, the polymerization degree increases in the alkali-activated BFNS.

3. Increasing the activator modulus can significantly increase pore size which has an adverse effect on the development of compressive strength and splitting tensile strength. With a water glass concentration of 10% and a water/binder ratio of 0.5, a silicate modulus of 0.5 is the optimum modulus based on these results.

DATA AVAILABILITY STATEMENT

The original contributions presented in the study are included in the article/supplementary material, further inquiries can be directed to the corresponding author.

AUTHOR CONTRIBUTIONS

KL contributed to conception and design of the study. ZL organized the database. KL and JS performed the statistical analysis. KL and ZL wrote sections of the manuscript. JS wrote the first draft of the manuscript. All authors contributed to manuscript revision, read, and approved the submitted version.

REFERENCES

- Abdalqader, A. F., Jin, F., and Al-Tabbaa, A. (2015). Characterisation of Reactive Magnesia and Sodium Carbonate-Activated Fly Ash/slag Paste Blends. *Construction Building Mater.* 93, 506–513. doi:10.1016/j.conbuildmat.2015.06.015
- Abdalqader, A. F., Jin, F., and Al-Tabbaa, A. (2016). Development of Greener Alkali-Activated Cement: Utilisation of Sodium Carbonate for Activating Slag and Fly Ash Mixtures. *J. Clean. Prod.* 113, 66–75. doi:10.1016/j.jclepro.2015.12.010
- Acevedo-Martinez, E., Gomez-Zamorano, L. Y., and Escalante-Garcia, J. I. (2012). Portland Cement-Blast Furnace Slag Mortars Activated Using Waterglass: - Part 1: Effect of Slag Replacement and Alkali Concentration. *Construction Building Mater.* 37, 462–469. doi:10.1016/j.conbuildmat.2012.07.041
- Atiş, C. D., Görür, E. B., Karahan, O., Bilim, C., İlkentapar, S., and Luga, E. (2015). Very High Strength (120MPa) Class F Fly Ash Geopolymer Mortar Activated at Different NaOH Amount, Heat Curing Temperature and Heat Curing Duration. *Construction Building Mater.* 96, 673–678. doi:10.1016/j.conbuildmat.2015.08.089
- Aydın, S., and Baradan, B. (2014). Effect of Activator Type and Content on Properties of Alkali-Activated Slag Mortars. *Composites B: Eng.* 57, 166–172. doi:10.1016/j.compositesb.2013.10.001
- Bartzas, G., and Komnitsas, K. (2015). Life Cycle Assessment of Ferronickel Production in Greece. *Resour. Conservation Recycling* 105, 113–122. doi:10.1016/j.resconrec.2015.10.016
- Bernal, S. A., Provis, J. L., Myers, R. J., San Nicolas, R., and van Deventer, J. S. J. (2014). Role of Carbonates in the Chemical Evolution of Sodium Carbonate-Activated Slag Binders. *Mater. Struct.* 48, 517–529. doi:10.1617/s11527-014-0412-6
- Chi, M. (2015). Effects of Modulus Ratio and Dosage of Alkali-Activated Solution on the Properties and Micro-structural Characteristics of Alkali-Activated Fly Ash Mortars. *Construction Building Mater.* 99, 128–136. doi:10.1016/j.conbuildmat.2015.09.029
- Choi, Y. C., and Choi, S. (2015). Alkali-silica Reactivity of Cementitious Materials Using Ferro-Nickel Slag fine Aggregates Produced in Different Cooling Conditions. *Construction Building Mater.* 99, 279–287. doi:10.1016/j.conbuildmat.2015.09.039
- Coman, V., Robotin, B., and Ilea, P. (2013). Nickel Recovery/removal from Industrial Wastes: A Review. *Resour. Conservation Recycling* 73, 229–238. doi:10.1016/j.resconrec.2013.01.019
- De Vargas, A. S., Dal Molin, D. C. C., Masuero, A. B., Vilela, A. C. F., Castro-Gomes, J., and de Gutierrez, R. M. (2014). Strength Development of Alkali-Activated Fly Ash Produced with Combined NaOH and Ca(OH)₂ Activators. *Cement and Concrete Composites* 53, 341–349. doi:10.1016/j.cemconcomp.2014.06.012
- Escalante-Garcia, J. I., Castro-Borges, P., Gorokhovskiy, A., and Rodriguez-Varela, F. J. (2014). Portland Cement-Blast Furnace Slag Mortars Activated Using Waterglass: Effect of Temperature and Alkali Concentration. *Construction Building Mater.* 66, 323–328. doi:10.1016/j.conbuildmat.2014.04.120
- García-Lodeiro, I., Fernández-Jiménez, A., and Palomo, A. (2013). Variation in Hybrid Cements over Time. Alkaline Activation of Fly Ash-portland Cement Blends. *Cement Concrete Res.* 52, 112–122. doi:10.1016/j.cemconres.2013.03.022
- Gebregziabihier, B. S., Thomas, R. J., and Peethamparan, S. (2016). Temperature and Activator Effect on Early-Age Reaction Kinetics of Alkali-Activated Slag Binders. *Construction Building Mater.* 113, 783–793. doi:10.1016/j.conbuildmat.2016.03.098
- Gofñi, S., Frías, M., Vigil de la Villa, R., and Vegas, I. (2013). Decalcification of Activated Paper Sludge - Fly Ash-Portland Cement Blended Pastes in Pure Water. *Cement and Concrete Composites* 40, 1–6. doi:10.1016/j.cemconcomp.2013.04.002
- Ke, X., Bernal, S. A., and Provis, J. L. (2016). Controlling the Reaction Kinetics of Sodium Carbonate-Activated Slag Cements Using Calcined Layered Double Hydroxides. *Cement Concrete Res.* 81, 24–37. doi:10.1016/j.cemconres.2015.11.012
- Komnitsas, K., Zaharaki, D., and Perdikatsis, V. (2007). Geopolymerisation of Low Calcium Ferronickel Slags. *J. Mater. Sci.* 42, 3073–3082. doi:10.1007/s10853-006-0529-2
- Kovtun, M., Kearsley, E. P., and Shekhovtsova, J. (2015). Chemical Acceleration of a Neutral Granulated Blast-Furnace Slag Activated by Sodium Carbonate. *Cement Concrete Res.* 72, 1–9. doi:10.1016/j.cemconres.2015.02.014
- Krizan, D., and Zivanovic, B. (2002). Effects of Dosage and Modulus of Water Glass on Early Hydration of Alkali-Slag Cements. *Cement Concrete Res.* 32, 1181–1188. doi:10.1016/S0008-8846(01)00717-7
- Lee, N. K., Jang, J. G., and Lee, H. K. (2014). Shrinkage Characteristics of Alkali-Activated Fly Ash/slag Paste and Mortar at Early Ages. *Cement and Concrete Composites* 53, 239–248. doi:10.1016/j.cemconcomp.2014.07.007
- Leong, H. Y., Ong, D. E. L., Sanjayan, J. G., and Nazari, A. (2016). The Effect of Different Na₂O and K₂O Ratios of Alkali Activator on Compressive Strength of Fly Ash Based-Geopolymer. *Construction Building Mater.* 106, 500–511. doi:10.1016/j.conbuildmat.2015.12.141
- Li, Y., and Li, J. (2014). Capillary Tension Theory for Prediction of Early Autogenous Shrinkage of Self-Consolidating concrete. *Construction Building Mater.* 53, 511–516. doi:10.1016/j.conbuildmat.2013.12.010
- Ma, Y., and Ye, G. (2015). The Shrinkage of Alkali Activated Fly Ash. *Cement Concrete Res.* 68, 75–82. doi:10.1016/j.cemconres.2014.10.024
- Maragkos, I., Giannopoulou, I. P., and Pnias, D. (2009). Synthesis of Ferronickel Slag-Based Geopolymers. *Minerals Eng.* 22, 196–203. doi:10.1016/j.mineng.2008.07.003
- Mobasher, N., Bernal, S. A., and Provis, J. L. (2016). Structural Evolution of an Alkali Sulfate Activated Slag Cement. *J. Nucl. Mater.* 468, 97–104. doi:10.1016/j.jnucmat.2015.11.016
- Myers, R. J., Lothenbach, B., Bernal, S. A., and Provis, J. L. (2015). Thermodynamic Modelling of Alkali-Activated Slag Cements. *Appl. Geochem.* 61, 233–247. doi:10.1016/j.apgeochem.2015.06.006
- Ondrejka Harbulakova, V., Estokova, A., and Kovalcikova, M. (2017). Correlation Analysis between Different Types of Corrosion of concrete Containing Sulfate Resisting Cement. *Environments* 4, 44–14. doi:10.3390/environments4030044
- Pan, Z., Cheng, L., Lu, Y., and Yang, N. (2002). Hydration Products of Alkali-Activated Slag-Red Mud Cementitious Material. *Cement Concrete Res.* 32, 357–362. doi:10.1016/S0008-8846(01)00683-4
- Pardal, X., Pochard, I., and Nonat, A. (2009). Experimental Study of Si-Al Substitution in Calcium-Silicate-Hydrate (C-S-H) Prepared under Equilibrium Conditions. *Cement Concrete Res.* 39, 637–643. doi:10.1016/j.cemconres.2009.05.001
- Puertas, F., Palacios, M., Manzano, H., Dolado, J. S., Rico, A., and Rodríguez, J. (2011). A Model for the C-A-S-H Gel Formed in Alkali-Activated Slag Cements. *J. Eur. Ceram. Soc.* 31, 2043–2056. doi:10.1016/j.jeurceramsoc.2011.04.036
- Rashad, A. M., Bai, Y., Basheer, P. A. M., Milestone, N. B., and Collier, N. C. (2013). Hydration and Properties of Sodium Sulfate Activated Slag. *Cement and Concrete Composites* 37, 20–29. doi:10.1016/j.cemconcomp.2012.12.010
- Rashad, A. M., Zeedan, S. R., and Hassan, A. A. (2016). Influence of the Activator Concentration of Sodium Silicate on the thermal Properties of Alkali-Activated Slag Pastes. *Construction Building Mater.* 102, 811–820. doi:10.1016/j.conbuildmat.2015.11.023
- Richardson, I. G. (1999). The Nature of C-S-H in Hardened Cements. *Cement Concrete Res.* 29, 1131–1147. doi:10.1016/S0008-8846(99)00168-4
- Sabir, B. B., Wild, S., and Bai, J. (2001). Metakaolin and Calcined Clays as Pozzolans for concrete: A Review. *Cement and Concrete Composites* 23, 441–454. doi:10.1016/S0958-9465(00)00092-5
- Sagadin, C., Luidold, S., Wagner, C., and Wenzl, C. (2016). Melting Behaviour of Ferronickel Slags. *Jom* 68, 3022–3028. doi:10.1007/s11837-016-2140-6
- Siddique, R., and Klaus, J. (2009). Influence of Metakaolin on the Properties of Mortar and concrete: A Review. *Appl. Clay Sci.* 43, 392–400. doi:10.1016/j.clay.2008.11.007
- Sun, J., and Chen, Z. (2019). Effect of Silicate Modulus of Water Glass on the Hydration of Alkali-Activated Converter Steel Slag. *J. Therm. Anal. Calorim.* 138, 47–56. doi:10.1007/s10973-019-08146-3
- Sun, J., Wang, Z., and Chen, Z. (2018). Hydration Mechanism of Composite Binders Containing Blast Furnace Ferronickel Slag at Different Curing Temperatures. *J. Therm. Anal. Calorim.* 131, 2291–2301. doi:10.1007/s10973-017-6739-9

- Talha Junaid, M., Kayali, O., Khennane, A., and Black, J. (2015). A Mix Design Procedure for Low Calcium Alkali Activated Fly Ash-Based Concretes. *Construction Building Mater.* 79, 301–310. doi:10.1016/j.conbuildmat.2015.01.048
- Tangahu, B. V., Warmadewanthi, I., Saptarini, D., Pudjiastuti, L., Tardan, M. A. M., and Luqman, A. (2015). Ferronickel Slag Performance from Reclamation Area in Pomalaa, Southeast Sulawesi, Indonesia. *Aces* 05, 408–412. doi:10.4236/aces.2015.53041
- Wang, D., Wang, Q., and Huang, Z. (2020a). New Insights into the Early Reaction of NaOH-Activated Slag in the Presence of CaSO₄. *Composites Part B: Eng.* 198, 108207. doi:10.1016/j.compositesb.2020.108207
- Wang, D., Wang, Q., and Xue, J. (2020b). Reuse of Hazardous Electrolytic Manganese Residue: Detailed Leaching Characterization and Novel Application as a Cementitious Material. *Resour. Conservation Recycling* 154, 104645. doi:10.1016/j.resconrec.2019.104645
- Wang, D., Wang, Q., Zhuang, S., and Yang, J. (2018a). Evaluation of Alkali-Activated Blast Furnace Ferronickel Slag as a Cementitious Material: Reaction Mechanism, Engineering Properties and Leaching Behaviors. *Construction Building Mater.* 188, 860–873. doi:10.1016/j.conbuildmat.2018.08.182
- Wang, Q., Feng, J. J., and Yan, P. Y. (2011). An Explanation for the Negative Effect of Elevated Temperature at Early Ages on the Late-Age Strength of concrete. *J. Mater. Sci.* 46, 7279–7288. doi:10.1007/s10853-011-5689-z
- Wang, Q., Huang, Z., and Wang, D. (2018b). Influence of High-Volume Electric Furnace Nickel Slag and Phosphorous Slag on the Properties of Massive concrete. *J. Therm. Anal. Calorim.* 131, 873–885. doi:10.1007/s10973-017-6576-x
- Wang, S.-D., and Scrivener, K. L. (1995). Hydration Products of Alkali Activated Slag Cement. *Cement Concrete Res.* 25, 561–571. doi:10.1016/0008-8846(95)00045-E
- Williamson, T., and Juenger, M. C. G. (2016). The Role of Activating Solution Concentration on Alkali-Silica Reaction in Alkali-Activated Fly Ash concrete. *Cement Concrete Res.* 83, 124–130. doi:10.1016/j.cemconres.2016.02.008
- Xi, B., Li, R., Zhao, X., Dang, Q., Zhang, D., and Tan, W. (2018). Constraints and Opportunities for the Recycling of Growing Ferronickel Slag in China. *Resour. Conservation Recycling* 139, 15–16. doi:10.1016/j.resconrec.2018.08.002
- Yang, T., Wu, Q., Zhu, H., and Zhang, Z. (2017). Geopolymer with Improved thermal Stability by Incorporating High-Magnesium Nickel Slag. *Construction Building Mater.* 155, 475–484. doi:10.1016/j.conbuildmat.2017.08.081
- Yang, T., Yao, X., and Zhang, Z. (2014). Geopolymer Prepared with High-Magnesium Nickel Slag: Characterization of Properties and Microstructure. *Construction Building Mater.* 59, 188–194. doi:10.1016/j.conbuildmat.2014.01.038
- Zhang, Z., Yang, T., and Wang, H. (2017a). Alkali-Activated Cement (AAC) from Fly Ash and High-Magnesium Nickel Slag. *Elsevier Inc.* 357–374. doi:10.1016/B978-0-12-804524-4.00013-0
- Zhang, Z., Zhu, Y., Yang, T., Li, L., Zhu, H., and Wang, H. (2017b). Conversion of Local Industrial Wastes into Greener Cement through Geopolymer Technology: A Case Study of High-Magnesium Nickel Slag. *J. Clean. Prod.* 141, 463–471. doi:10.1016/j.jclepro.2016.09.147
- Zhou, Y., Sun, J., and Liao, Y. (2020). Influence of Ground Granulated Blast Furnace Slag on the Early Hydration and Microstructure of Alkali-Activated Converter Steel Slag Binder. *J. Therm. Anal. Calorim.* doi:10.1007/s10973-020-10220-0
- Zhuang, S., and Wang, Q. (2021). Inhibition Mechanisms of Steel Slag on the Early-Age Hydration of Cement. *Cement Concrete Res.* 140, 106283. doi:10.1016/j.cemconres.2020.106283

Conflict of Interest: Authors KL and ZL are employed by Beijing Urban Construction Group Co., Ltd. Thank the company for providing the test site and test equipment support. Authors KL and ZL are employed by Beijing Urban Construction Group Co., Ltd.

The remaining author declares that the research was conducted in the absence of any commercial or financial relationships that could be construed as a potential conflict of interest.

Publisher's Note: All claims expressed in this article are solely those of the authors and do not necessarily represent those of their affiliated organizations, or those of the publisher, the editors and the reviewers. Any product that may be evaluated in this article, or claim that may be made by its manufacturer, is not guaranteed or endorsed by the publisher.

Copyright © 2021 Liu, Liu and Sun. This is an open-access article distributed under the terms of the Creative Commons Attribution License (CC BY). The use, distribution or reproduction in other forums is permitted, provided the original author(s) and the copyright owner(s) are credited and that the original publication in this journal is cited, in accordance with accepted academic practice. No use, distribution or reproduction is permitted which does not comply with these terms.



Effect of the Alkalized Rice Straw Content on Strength Properties and Microstructure of Cemented Tailings Backfill

Shi Wang^{1,2,3}, Xuepeng Song^{1,2,3*}, Meiliang Wei^{1,2,3}, Wu Liu^{1,2,3}, Xiaojun Wang^{1,2,3*}, Yuxian Ke^{1,2,3} and Tiejun Tao⁴

¹School of Resources and Environmental Engineering, Jiangxi University of Science and Technology, Ganzhou, China, ²Jiangxi Province Key Laboratory of Mining Engineering, Jiangxi University of Science and Technology, Ganzhou, China, ³Engineering Research Center for High-efficiency Development and Application Technology of Tungsten Resources (Jiangxi University of Science and Technology), Ministry of Education, Ganzhou, China, ⁴College of Civil Engineering, Guizhou University, Guiyang, China

OPEN ACCESS

Edited by:

Lijie Guo,
Beijing General Research Institute of
Mining and Metallurgy, China

Reviewed by:

Erol Yilmaz,
Recep Tayyip Erdoğan University,
Turkey
Shiqi Dong,
University of California, Los Angeles,
United States

*Correspondence:

Xuepeng Song
sxp9612@126.com
Xiaojun Wang
xiaojun7903@126.com

Specialty section:

This article was submitted to
Structural Materials,
a section of the journal
Frontiers in Materials

Received: 20 June 2021

Accepted: 02 August 2021

Published: 13 September 2021

Citation:

Wang S, Song X, Wei M, Liu W,
Wang X, Ke Y and Tao T (2021) Effect
of the Alkalized Rice Straw Content on
Strength Properties and
Microstructure of Cemented
Tailings Backfill.
Front. Mater. 8:727925.
doi: 10.3389/fmats.2021.727925

The tailings and rice straw are waste by-products, and the storage of tailings on the ground and the burning of rice straws will seriously damage the ecological environment. In this study, the effect of different contents of alkalized rice straw (ARS; rice straw was alkalized with 4% NaOH solution) on the mechanical properties and microstructure of cemented tailings backfill (CTB; ARSCTB) was studied through uniaxial compressive strength (UCS), scanning electron microscopy (SEM), and X-ray diffraction (XRD) tests. The results indicated that 1) the UCS of ARSCTB could be improved by ARS. However, with the increase in the ARS content from 0.1 to 0.4 wt%, the UCS showed a monotonous decreasing trend. The UCS improvement effect was best when the ARS content was 0.1 wt%, and at 7, 14, and 28 days curing ages, the UCS increase rate was 6.0, 8.3, 14.7% respectively. 2) The tensile strength of ARSCTB was generally higher than that of CTB and positively correlated with the ARS content. The tensile strength increase rate was 24.1–34.2% at 28 days curing age. 3) The SEM test indicated that the ARS was wrapped by cement hydration products, which improves its connection with the ARSCTB matrix. ARS performed a bridging role, inhibited cracks propagation, and provided drag or pulling force for the block that is about to fall off. Therefore, the mechanical properties of ARSCTB were enhanced. However, under high ARS content, the inhibition of ARS on hydration reaction and the overlap between ARS were not conducive to the improvement of the UCS of ARSCTB. 4) The post-peak residual strength and integrity effect of ARSCTB were greater. It is recommended to add 0.1–0.2 wt% ARS to the backfill with high compressive strength requirements such as the empty field subsequent filling mining method and the artificial pillar. 0.3–0.4 wt% ARS is incorporated into backfill with high tensile strength requirements such as high-stage filling with lateral exposure and artificial roof. This study further makes up for the blank of the application of plant fiber in the field of mine filling and helps to improve the mechanical properties of backfill through low-cost materials.

Keywords: mechanical properties, alkalized rice straw, cemented tailings backfill, damage mode, microstructure evolution

INTRODUCTION

The mined-out areas formed during the mining of metal mines lead to the movement and fragmentation of rock layers, which in turn causes surface settlement in the mining area, unbalanced ecological environment, and even a series of problems such as safety accidents (Yang et al., 2017; Xu et al., 2019a; Huang et al., 2019; Zeng et al., 2020; Zheng et al., 2021). Meanwhile, a large number of tailings will inevitably be produced in the process of mineral processing. The tailings stored in the tailings pond not only occupy a lot of land resources but also causes pollution to groundwater and the surrounding ecological environment (Huynh et al., 2006; Yilmaz et al., 2015; Qi and Fourie, 2019; Hao et al., 2021). In addition, with the gradual depletion of shallow mineral resources, mines around the world have become deeper, high ground stress, and rockburst are the key factors leading to goaf instability (Hao et al., 2020). To solve the above problems, cemented tailings backfill (CTB) is widely used in underground mines around the world because of its ability to effectively control ground pressure, reduce surface settlement, and manage tailings (Liu et al., 2016; Wang et al., 2016; Zhao et al., 2017; Cao et al., 2019a; Yang et al., 2020). CTB is a complex composite material produced by mixing tailings (70–80 wt%), cementing materials (3–7 wt%), and a corresponding proportion of water, which is then transported to underground stopes by gravity or pumping (Yang et al., 2018; Xue et al., 2019a). The hardened filling body gradually has the ability to support the goaf, absorb, and transfer stress. However, in the process of filling mining, in addition to the quasi-static load of overlying strata, the backfill was also disturbed by the excavation blasting near the ore body, which was very easy to lead to the failure of the backfill. Therefore, the mechanical properties of the backfill are the key to its function. To improve the mechanical properties of the backfill, at present, domestic and foreign scholars used chemical reagents and/or synthetic fibers to enhance the mechanical properties of the backfill (Yi et al., 2015; Ma et al., 2016; Haruna and Fall, 2017; Chen et al., 2018; Manganea et al., 2018; Ouattara et al., 2018; Cao et al., 2019b; Xue et al., 2019b; Jiang et al., 2020; Kou et al., 2020; Cao et al., 2021; Cavusoglu et al., 2021; Koohestani et al., 2021), and certain research results have been achieved. However, the application of chemical reagents and synthetic fibers will increase the filling cost. Therefore, it is necessary to seek low-cost and wide-ranging admixtures to improve the mechanical behavior of the backfill.

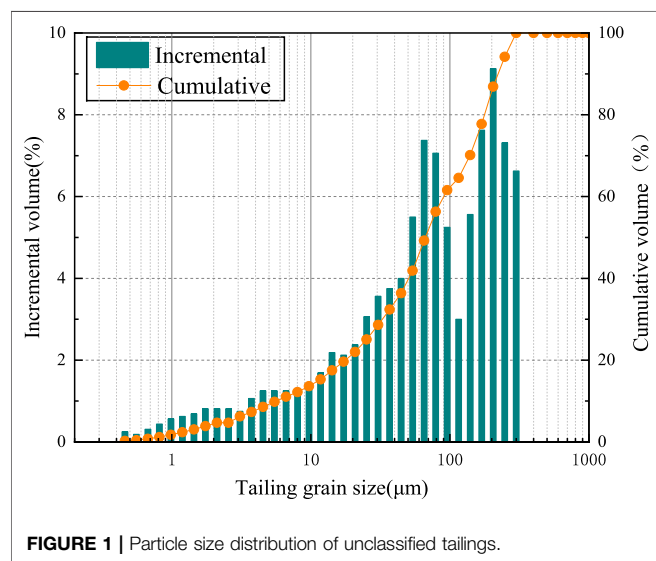
In comparison with synthetic fibers, plant fibers have the advantages of low density, low cost, wide source (Xie et al., 2015; Xie et al., 2016; Wang et al., 2020). In terms of concrete, the application of plant fibers to improve the mechanical properties of concrete has always been a hot research topic (Chakraborty et al., 2013). Rahim et al. (2016) found that lime concrete added with rape straw and hemp exhibited good moisture absorption and buffer performance. Ammari et al. (2020) studied the physical and mechanical properties of concrete with barley straw and steel fiber, and the compressive strength of concrete was improved. Farooqi and Ali (2019) found that the compressive strength and flexural strength of concrete with wheat straw (wheat straw was soaked, boiled, and chemically

treated) were all improved. Bederina et al. (2016) found that the flexural strength and shrinkage of concrete with barley straw treated with hot water, gasoline, varnish, and waste oil were enhanced. Zhang et al. (2020) concluded that the addition of rice straw significantly improved the tensile compression ratio and impact resistance of concrete. Xie et al. (2015) added different contents of rice straw to cement-based composites, which significantly improved the flexural strength and fracture toughness of cement-based composites. Chen et al. (2015) concluded that rice straw could control the development of cracks in the mortar, and the splitting toughness of the mortar was improved. Based on the above research, plant fiber can be used to improve the mechanical properties of cement-based materials, and as the oldest plant fiber used in cement-based materials, rice straw has been used for hundreds of years (Sun and Jiang, 2007; Xie et al., 2016; Zhang et al., 2020). Moreover, according to the statistics and calculation of FAOSTAT (the database of the United Nations Food and Agriculture Organization), in 2018, the amount of straw was nearly 800 million tons in China (Song et al., 2018; Li, 2020). Among them, the annual yield of rice straw reached 200 million tons. The phenomenon of random stacking and burning of rice straw is serious, and the utilization rate of resources is low [only a small percentage of rice straw is used as fodder and curtains or is biodegraded (Petrella et al., 2018; Wang et al., 2020)]. Most of the rice straw is burned in the field in spring and autumn, causing serious pollution to the surrounding environment and atmosphere (Chen et al., 2015; Ming et al., 2019). CTB is similar to cement-based materials, but there are some differences in aggregate source, size distribution of aggregate, and cement dosage between the two materials. Thus, it is of great significance to study the application of rice straw in the field of filling, to reduce the environmental pollution caused by rice straw burning, and to improve the utilization rate of resources and the mechanical properties of the backfill. Regarding the application of rice straw and other plant fibers in the field of filling, there are few related studies. Among them, Wang et al. (2020) studied the effect of alkalized rice straw of different lengths on the mechanical properties of CTB and found that the strength of CTB was significantly improved and was more sensitive to the rice straw length. As the length of the rice straw increased, the compressive strength of CTB increased first and then decreased. When the length of rice straw was 12 mm, the improvement effect of CTB strength was the best. However, the effect of different rice straw contents on the mechanical properties of CTB has not been studied. This would be resulted in an insufficient exploration of the application of plant fibers in the filling field. Therefore, it is necessary to carry out experimental research on the response of the mechanical properties of CTB with alkalize rice straw of different contents. It provides a more detailed theoretical and technical basis for the application of plant fiber in filling field.

Therefore, the aim of this experimental study is to provide a better understanding of the effect of different alkalized rice straw (ARS) contents on mechanical properties of CTB. To achieve this aim, a series of UCS and tensile strength tests were carried out. The strength changes, stress strain curve characteristics, and

TABLE 1 | Physical properties of the main tailings.

Property indexes	Porosity (vol%)	Specific gravity	Specific surface area (m ² /kg)	Content <20 μm (wt%)	Content <74 μm (wt%)	D ₁₀ (μm)	D ₅₀ (μm)	D ₉₀ (μm)	pH
Value	53.87	2.97	184.4	31.5	48.4	6.03	68.41	226.651	11



failure modes of CTB containing alkalized rice straw of different contents (ARSCTB) were determined. The influence mechanism of alkalized rice straw on CTB and ARSCTB strength was discussed by SEM and XRD tests.

MATERIALS AND METHODS

Experimental Materials and Characteristics Tailings

The unclassified tailings were obtained from a copper mine in the Jiangxi Province, China. The particle size distribution of these tailings was analyzed using the Winner 2000 LPSA. The pycnometer method was used to measure the specific gravity, a small relative density meter was used to measure the unit density, and the pH value of the unclassified tailings slurry with an original mass concentration of 35% was measured on-site using the METTLER TOLEDO pH meter. The results are presented and depicted in **Table 1** and **Figure 1**, respectively. Particles in the tailings smaller than 74 μm account for about 48.4% of the total, which corresponds to a size classification of medium to fine. X-ray fluorescence analysis test (XRF-1800) was

used to determine the main element content of the tailings, as shown in **Table 2**. The content of Si and Ca was relatively high, which was conducive to improve the strength of the backfill. The alkalinity of the tailings was $M0 = 0.49$, indicating that the tailings were acidic (<1).

Rice Straw

Rice straw was selected from the surrounding countryside of Ganzhou, Jiangxi Province. Rice straw is composed of cellulose, hemicellulose, lignin, and ash. Cellulose and hemicellulose are composed of polysaccharide units. Hydrolysis of polysaccharides under alkaline conditions will inhibit the hydration reaction of cement (Fan and Sheng, 2011; Xie et al., 2016; Wang et al., 2017). Some scholars used NaOH solution (4 wt%) to alkalized rice straw (ARS), which significantly reduced the inhibitory effect of rice straw on cement hydration reaction (Fan and Sheng, 2011; Chen et al., 2017; Wang et al., 2017; Liao et al., 2018). Thus, in this experiment, rice straw was soaked in NaOH solution (4 wt%) for 24 h, washed with water until the pH value was 7 ± 0.1 , and then dried at 50°C. According to previous research (Wang et al., 2020), the length of fixing ARS is 12 mm, and the ARS content is 0, 0.1, 0.2, 0.3, 0.4 wt% of the cement quantity, respectively. The elastic modulus, bending deformation, and diameter of rice straw are 3.66 MPa, 3.17 mm, and 1.5–2.5 mm, respectively.

Binders and Water

The cementing material used in this test is ordinary Portland cement (P.O32.5) commonly used in mines. The specific surface area of the cement used is 2,105.2 cm²/g, and the specific gravity is 2.97. Domestic water is used as the test water. The chemical composition of cement is shown in **Table 3**.

EXPERIMENTAL METHOD

The test procedure is shown in **Figure 2**. The brief introduction to the test steps is as follows:

Sample Preparation

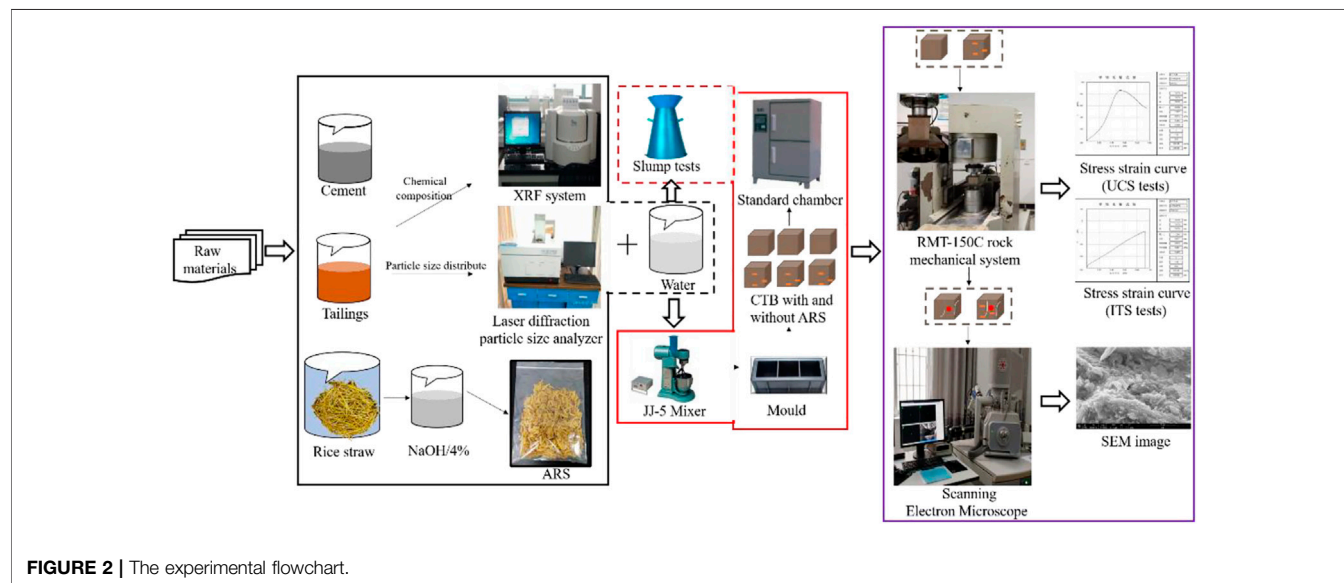
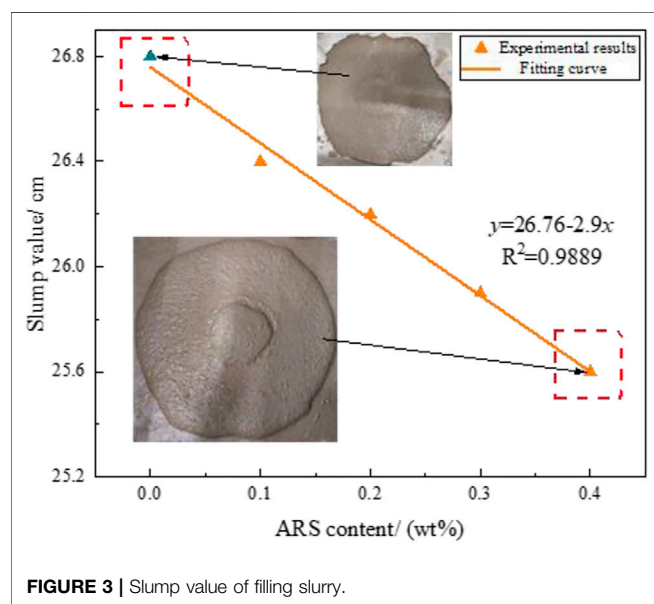
The mix proportion for the CTB and ARSCTB mixtures used a cement-to-tailings (c / t) ratio (dry weight) of 1:4 and a solid content of 74 wt%. ARS was added to filling materials at 0, 0.1, 0.2,

TABLE 2 | Composition of the main elements of the unclassified tailings (%).

Composition/%	SiO ₂	CaO	MgO	Al ₂ O ₃	Fe ₂ O ₃	SO ₂	PbO ₂	MnO ₂	K ₂ O	P ₂ O ₅	CuO
Content	33.02	15.68	1.82	2.56	10.37	4.55	0.0095	0.085	0.37	0.049	0.065

TABLE 3 | The chemical composition of cement.

Compositions	CaO	SiO ₂	Al ₂ O ₃	Fe ₂ O ₃	MgO	SO ₂	Na ₂ O	Other
wt%	63.66	21.26	4.5	2.8	1.66	2.58	0.18	3.36

**FIGURE 2** | The experimental flowchart.**FIGURE 3** | Slump value of filling slurry.

0.3, and 0.4 wt% of the cement mass. When preparing the sample, cement and tailings were first mixed evenly, and then ARS was added and mixed again. Finally, a proper amount of water was added and stirred by a JJ-5 mixer for 5 min to ensure even mixing. Part of CTB and ARSCTB slurries were tested for slump (rice straw had strong water absorption capacity, and with increased ARS content, the fluidity of filling slurry would inevitably be

TABLE 4 | The experiment scheme design of uniaxial compressive strength tests and tension tests.

NO.	c/ta	W/ (wt%)b	L (%) / (mm)c	C/ (wt%)d	Slump/ (cm)
C-0			0	0	26.8
C-1			12	0.1	26.4
C-2	1:4	74	12	0.2	26.2
C-3			12	0.3	25.9
C-4			12	0.4	25.6

^adry mass ratio of cement to tailings.

^bmass concentration.

^cARS length.

^dARS content.

affected. Hence, according to Standard Test Method for Slump of Portland Cement Concrete (ASTM C143/C143M-2015), slump test of filled slurry with ARS was carried out using cone slump cone (upper diameter: 10 cm, lower diameter: 20 cm, height: 30 cm) (Wang and Chen, 2016; Zheng et al., 2016; Deng, 2017; Chen et al., 2020). The results were shown in **Figure 3** and **Table 4**. With the ARS content increase from 0 to 0.4 wt%, the slump value decreased from 26.8 to 25.6 cm, showed a linearly decreasing trend. They have a high linear function relationship ($R^2 = 0.9889$, where x and y represent the ARS content and slump value, respectively). The results show that ARS can affect the fluidity of the filling slurry, which is due to its high water absorption capacity, which reduces the free water content in the fresh filling slurry, resulting in the decrease of the fluidity of

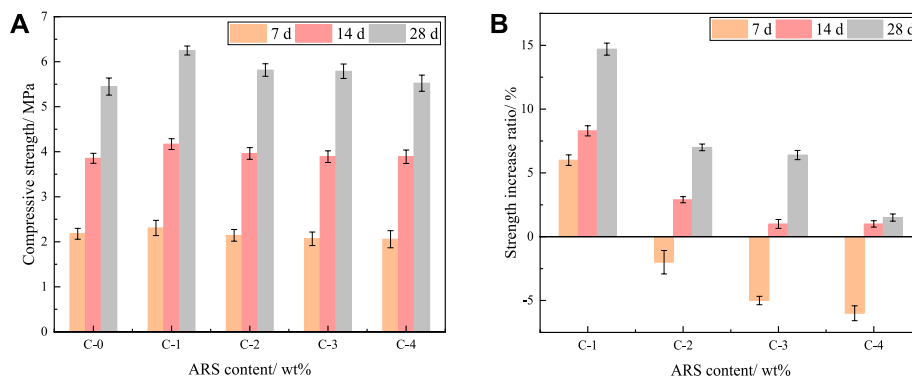


FIGURE 4 | The UCS of CTB and ARSCTB.

the fresh filling slurry (Sathiparan and De Zoysa, 2018; Chen et al., 2020). Meanwhile, since the maximum ARS content in this test was only 0.4 wt% of the cement quantity, it had little effect on the slump of the filling slurry (the maximum reduction rate was only 4.8%). The addition of ARS could ensure that the filling slurry had good fluidity. The remaining part of the filling slurry was poured into a cube mold (70.7 mm), and after demolding, the samples were placed in an HBY-40B standard curing box ($20^{\circ}\text{C} \pm 1^{\circ}\text{C}$, $90 \pm 5\%$). The experimental design is presented in **Table 4**.

Uniaxial Compressive Strength and Tensile Strength Tests

After the desired curing time (7, 14, and 28 days), the UCS test was conducted on CTB and ARSCTB (CTB and ARSCTB were cube samples with a size of 70.7 mm. The upper and lower end faces of the samples were polished before testing) according to the standard ASTM C39/C39M-18. The RMT-150C rock mechanics test system was used. The backfill was loaded continuously at a constant speed of 0.6 mm/min, the maximum load was 1,000 kN, and the piston stroke was 50 mm, recorded once every 0.5 s. On this basis, the tensile strength was tested at the same loading rate. The mechanical parameters and stress strain curves of the backfill were obtained. Three samples were tested for each backfill formulation, and the average values of the UCS and tensile strength were calculated.

Scanning Electron Microscopy and X-Ray Diffraction Tests

Microstructural tests of CTB and ARSCTB were performed by SEM equipment (XL30W/TMP, United States) at 28 days curing time. The samples were crushed and cored, and the cement hydration reaction was terminated with anhydrous ethanol after 28 days (Wang et al., 2020). The samples were sprayed with gold to improve conductivity. The samples were placed into the SEM sample chamber, a vacuum was created, and the interaction between ARS and the ARSCTB matrix was observed. In addition, XRD (Smart apex II, United States) was used to determine the type and intensity of hydration products of CTB and ARSCTB. In this experiment, the scanning speed was 10 deg/min, and the range of 2θ was $10\text{--}90^{\circ}$.

RESULTS AND DISCUSSION

The Effect of Rice Straw was Alkalized With 4% NaOH Solution Content on the Uniaxial Compressive Strength of CTB and ARSCTB

Figure 4 shows the UCS test results of CTB and ARSCTB at 7, 14, and 28 days curing ages. As the figure shows: 1) at 14 days curing age, the UCS of CTB was 3.85 MPa, and the UCS of ARSCTB decreased gradually from 4.17 MPa with 0.1 wt% ARS to 3.79 MPa with 0.4 wt%, that is, the increased rate of the UCS of ARSCTB decreased from 8.3 to 1.0%. 2) When the ARS content was 0.1 wt%, at 7, 14, and 28 days curing age, compared with CTB, the UCS of ARSCTB increased by 6.0, 8.3, 14.7%, respectively. When the ARS content was 0.2, 0.3, 0.4 wt%, it had the same properties, that is, with the increased curing age, the better the improvement effect of ARS on the UCS of ARSCTB; 3) At 7 days curing age, when the ARS content was 0.2, 0.3, 0.4 wt%, the UCS of ARSCTB was reduced by 2.0, 5.0, 6.0% compared with CTB, and the UCS of other ARSCTBs was higher than the corresponding CTB.

The above three conclusions are mainly attributed to the following three reasons. 1) ARS plays a bridging role in the ARSCTB matrix. **Figure 5** is a schematic diagram of the distribution of ARS in the ARSCTB matrix. As shown in **Figure 5**, ARS has a high adhesive strength with the ARSCTB matrix, which can inhibit the crack propagation and exert a drag force on the block that is about to fall off; thus, the effective stress area of ARSCTB is increased, and the strength is improved (Wang et al., 2020; Ramli et al., 2013; Bederina et al., 2016) (conclusion 1) and 2) ARS inhibits cement hydration reaction. Although the rice straw is alkalized, there is a slight inhibition of cement hydration (Wang et al., 2017). With the increase of ARS content, the inhibition effect of ARS on cement hydration reaction gradually appears, which leads to the decrease of adhesive strength between ARS and the ARSCTB matrix, which weakens the bridging effect and crack inhibition effect, and the UCS of ARSCTB decreases. This phenomenon is also supported by XRD results, as shown in **Figure 6**. From **Figure 6A**, the main hydration products of CTB and ARSCTB

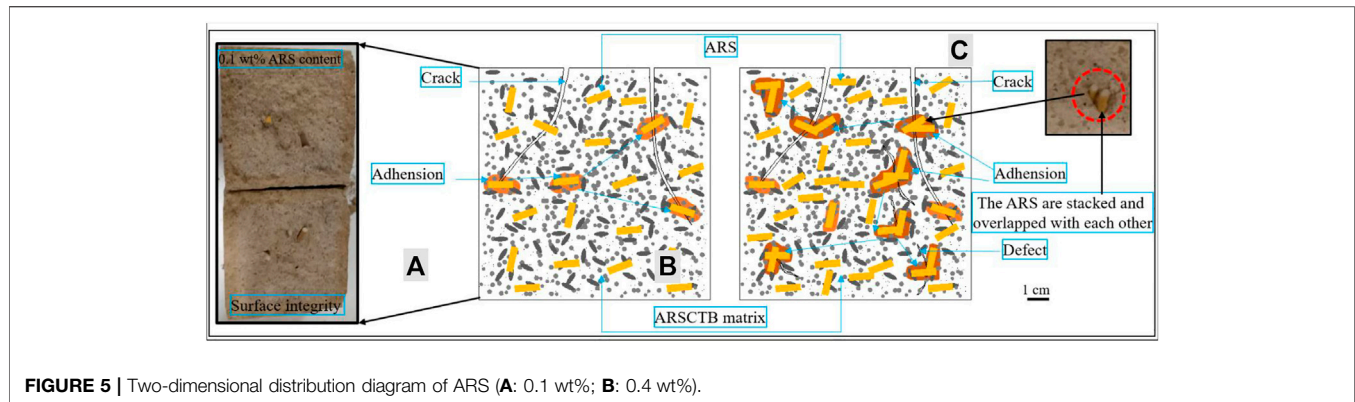


FIGURE 5 | Two-dimensional distribution diagram of ARS (A: 0.1 wt%; B: 0.4 wt%).

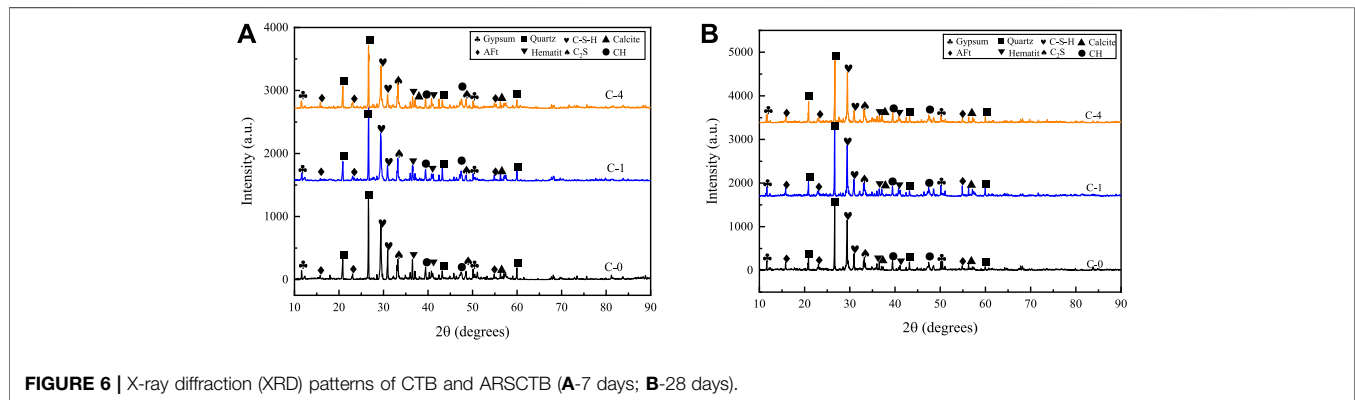


FIGURE 6 | X-ray diffraction (XRD) patterns of CTB and ARSCTB (A-7 days; B-28 days).

are calcium silicate hydrate (C-S-H), calcium hydroxide (CH), and ettringite (AFt) at 7 days curing age. When the content of ARS is 0.1 wt%, compared with CTB, the change of diffraction peak of hydration products is small. It indicated that the ARS content is less, and the inhibition effect of ARS on cement hydration is not obvious. Therefore, the adhesive force between ARS and the ARSCTB matrix is high, and the bridging effect is dominant, which effectively improved the internal structure of ARSCTB. When the ARS content is 0.4 wt%, the diffraction peak of hydration products decreases obviously. It indicated that the inhibition effect of ARS on cement hydration reaction is enhanced, which leads to the decrease of adhesive strength between ARS and the ARSCTB matrix, so the UCS of ARSCTB decreases. As the curing age increases, cement hydration products increase (Xu et al., 2019b), which can also be found in **Figure 6B** (the diffraction peak intensity of hydration products increases), and it can be seen from **Figure 6B** that the diffraction peak intensities of hydration products of CTB and ARSCTB have no obvious difference. It indicated that with the increase in curing age, the inhibition effect of ARS on cement hydration reaction is weakened. Thus, the degree of the connection between ARS and the ARSCTB matrix is enhanced, and the adhesive force and friction between ARS and the ARSCTB matrix increase significantly. Therefore, the UCS of ARSCTB is higher than that of CTB, and the bridging effect of ARS is dominant at 14 and 28 days curing ages regardless

of the ARS content (conclusion 2 and 3). 3) ARS was randomly dispersed in the ARSCTB matrix (**Figure 5A**). With increased ARS content, ARS overlapped each other in the ARSCTB matrix (Xu et al., 2019a), which caused the decrease of adhesive strength between ARS and the ARSCTB matrix, and defects were generated (as shown in **Figures 5B,C**), which was another reason why the UCS of ARS decreased gradually with increased ARS content (conclusion 1)). In summary, the addition of an appropriate amount of ARS can improve the compressive strength of the backfill, which is consistent with the previous results (Chen et al., 2020). However, compared with the previous research results (Chen et al., 2020), the improvement effect of ARS on the compressive strength of backfill in this study is relatively low, which may be related to the preparation of rice straw (rice straw is alkalized in this study, and the shape of rice straw is circular tube, while the rice straw used by Chen et al. (2017) is flocculent).

The Effect of Rice Straw was Alkalized With 4% NaOH Solution Content on the Tensile Strength of CTB and ARSCTB

Figure 7 shows the tensile strength test results of CTB and ARSCTB at 7, 14, and 28 days curing ages. As shown in **Figure 7**, the tensile strength of CTB was 0.27 MPa at 7 days curing age. As the ARS content gradually increased from 0.1 to

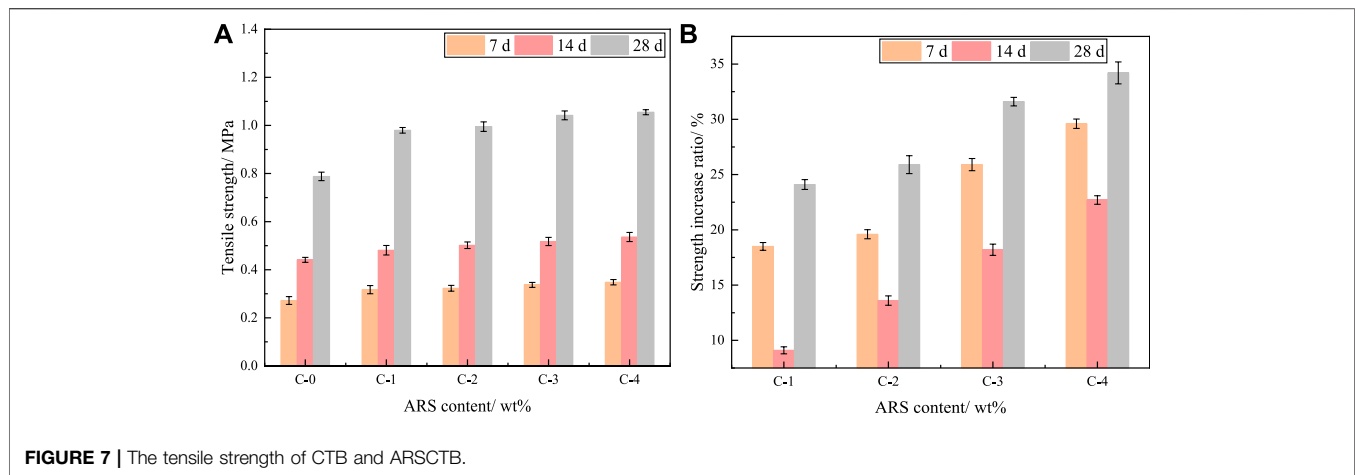


FIGURE 7 | The tensile strength of CTB and ARSCTB.

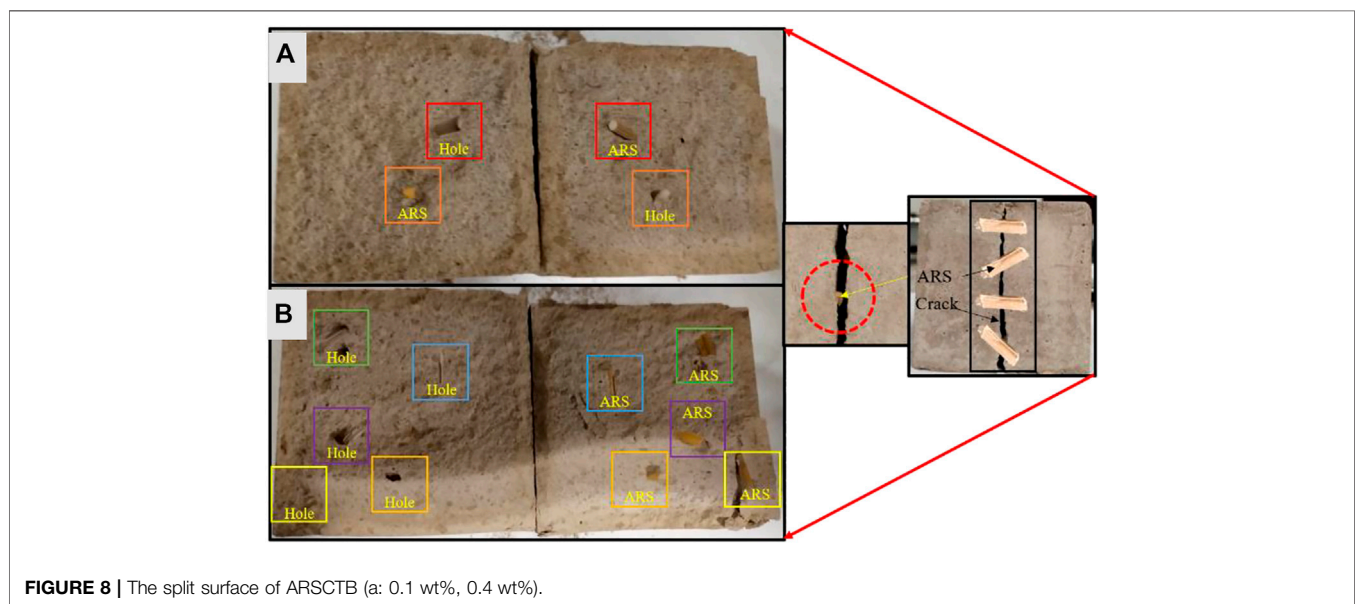


FIGURE 8 | The split surface of ARSCTB (a: 0.1 wt%, 0.4 wt%).

0.4 wt%, the tensile strength of ARSCTB increased from 0.32 to 0.36 MPa, and the increased rate of tensile strength was 18.5–29.6%. Meanwhile, the changing trend of tensile strength was the same at 14, 28 days curing ages. The increased rate of tensile strength was 9.1–22.7% and 24.1–34.2%; that is, the tensile strength of ARSCTB was generally higher than CTB. The tensile strength was positively correlated with the ARS content. This conclusion is mainly attributed to the following two reasons. 1) ARS plays as a bridging role in the ARSCTB matrix. As mentioned earlier, ARS is randomly distributed inside the ARSCTB matrix. when the ARCTB tensile failure occurs, ARS may have penetrated the positions where ARSCTB is damaged by tension, similar to “grouting anchor” (bridging effect), as shown in **Figure 8**. The adhesive force between ARS and the ARSCTB matrix can inhibit the crack propagation (Xue et al., 2019a; Wang et al., 2020) and provide pulling force for the blocks on both sides of the crack. Therefore, the tensile stress was transferred from the

ARSCTB matrix to ARS, and the pulling out of the ARS from the matrix consumed energy, thereby the tensile strength of ARSCTB is enhanced. 2) With the increase of ARS content, the number of ARS on both sides of tensile crack is increased. **Figures 8A,B** show the split surface of tensile strength test of ARSCTB with ARS content of 0.1 and 0.4 wt%, respectively. It can be seen from the figure that with the increase of ARS content, the number of ARS at the split surface increases obviously (for instance, the number of ARS increased from two at 0.1% to five at 0.4%, and there was a positive correlation between them). The bridging effect of ARS is strengthened, and the inhibition effect of ARS on cracks is enhanced. Thus, the pulling force provided by ARS for both sides of the crack is increased, and more ARSs consume more capacity when pulling out of the ARSCTB matrix, contributing to the improvement of the tensile strength of ARSCTB. In addition, the strengthening bridging effect of ARS can also make up for the inhibition of ARS on cement hydration

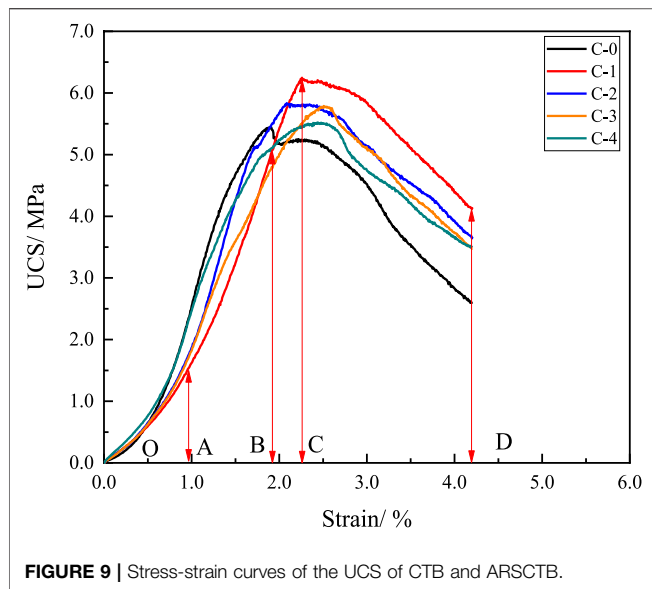


FIGURE 9 | Stress-strain curves of the UCS of CTB and ARSCTB.

at 7 days curing age, which can also be clearly found in the changing trend of the ARSCTB tensile strength.

Analysis of the Stress Strain Curves of CTB and ARSCTB

The Stress Strain Curves of Uniaxial Compressive Strength

Figure 9 shows the stress strain curves of the UCS test of CTB and ARSCTB at 28 days curing age. The failure process of CTB and ARSCTB is divided into four stages: 1) pore compaction stage (OA); 2) linear elasticity stage (AB); 3) plastic yield stage (BC); 4) failure stage (CD) (Cao et al., 2019a; Xue et al., 2019b; Wang et al., 2020). The detailed description of each stage of the curve is as follows:

In the OA stage, the curves were concave upward. Under the initial loading condition, the internal pores were compressed and closed or broken under the action of external force (28 days curing age, the backfill had high brittleness). In this stage, the strain of ARSCTB was greater than CTB. This may be due to the existence of ARS which is not completely filled by the cement tailings, resulting in increased pores. Thus, strain was increased. This phenomenon was consistent with the results of previous studies (Wang et al., 2020). In AB stage, the backfill entered the elastic deformation stage, and the curves of all samples are approximately straight line. The slope of the ARSCTB curve was smaller than CTB, and the time to break the threshold was longer. In BC stage, the cracks in the backfill gradually expanded, and the curves were convex, and gradually reached the peak strength (Cheng et al., 2018). At this stage, the peak strength of ARSCTB was generally higher than that of CTB. At this stage, ARS was the main action stage (Wang et al., 2020; Xue et al., 2020), which played a bridging role in the ARSCTB matrix. The further propagation and convergence of cracks were restrained, the stress concentration at the crack tip was relieved, and the drag force was generated on the block of ARSCTB, so that the

compressive stress was evenly distributed on the top and bottom of ARSCTB, and the strength of ARSCTB was improved. In the CD stage, after the peak strength, the crack evolution was intensified, and the load continues to be applied, and the compressive strength rapidly decreases and gradually flattens. It can be found that all the samples had a certain residual strength, the residual strength of ARSCTB was significantly higher than that of CTB, and the residual strength decreased with the increase of ARS content. This is because ARS played a bridging role in the ARSCTB matrix and produced a drag force on the block. As a result, the abscission of block of ARSCTB was reduced, and the stress area of ARSCTB was increased. The residual strength of ARSCTB was improved, and the bearing capacity was more after failure. However, the increase in ARS content increased the probability of ARS overlapping and cross, and then reduced the post-peak bearing capacity. The UCS and post-peak residual strength of the backfill are improved by the addition of ARS. It follows that in actual filling operations, ARSCTB can better ensure the stability of the goaf and improve the safety of downhole operations.

The Stress Strain Curves of Tensile Strength

Figure 10 shows the stress strain curve of tensile strength tests for CTB and ARSCTB at 28 days curing age. As shown in Figure 10, from the overall view, a higher brittleness was exhibited by CTB and ARSCTB, when the tensile stress reached the extreme tensile strength value, the stress was reduced to zero instantly. However, the peak tensile strength of ARSCTB was higher at 28 days curing age (corresponding to the results of tensile strength test), and the peak strain of ARSCTB was greater. The bridging effect of ARS in the ARSCTB matrix exerted a pilling force on the blocks of both sides of the crack, which improved the tensile strength of ARSCTB, inhibited the crack propagation, and slowed down the failure of ARSCTB. Moreover, the increase of peak strain can delay damage under tensile stress, which is beneficial to the

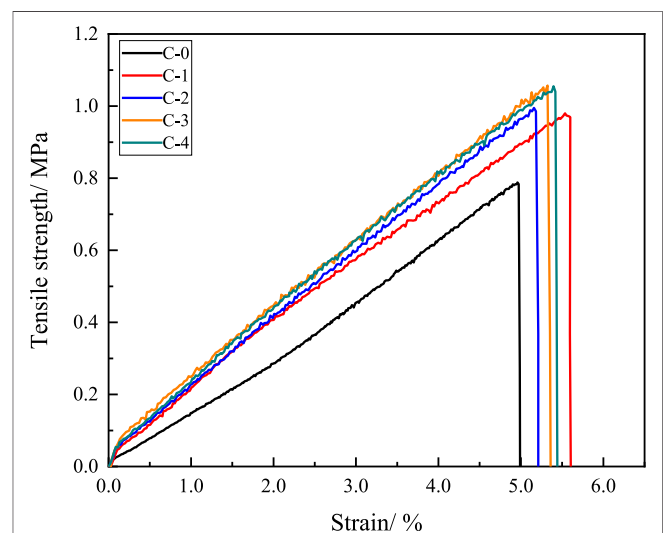


FIGURE 10 | Stress-strain curves of the tensile strength of the CTB and ARSCTB.

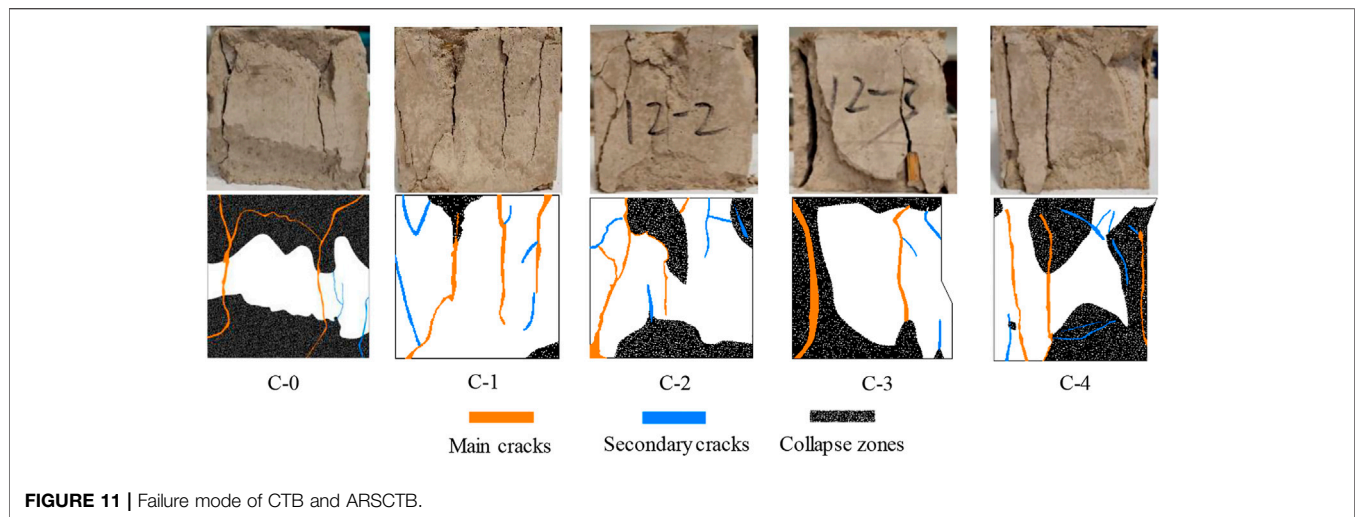


FIGURE 11 | Failure mode of CTB and ARSCTB.

safety of downhole operation. Meanwhile, ore dilution and high brittleness of the backfill can be reduced.

Analysis of Damage Mode of CTB and ARSCTB

Figure 11 shows the failure modes of CTB and ARSCTB at 28 days curing age. It can be seen from **Figure 11** that there are differences in failure mode and damage degree between CTB and ARSCTB, indicating that the internal structure of ARSCTB is changed by ARS. As shown in **Figure 11C-0**, the failure mode of CTB was mainly tensile failure; accompanied by shear failure, two nearly parallel main cracks penetrated the upper and lower sides of CTB, and they were connected by a third main crack, resulting in the block was about to separate from the CTB matrix. Two collapse areas were generated during the compression process (the area of the collapsed area was larger). CTB was seriously damaged under uniaxial compression, and the bearing capacity was poor after damage, which corresponded to the lower post-peak residual strength in **Figure 9**. However, the failure mode of ARSCTB was more complex. The failure mode of ARSCTB was tension shear mixed failure, which may be related to the significant increase of tensile strength of ARSCTB in **Figure 5**. It can be found from **Figures 11C1-4** that the main crack of ARSCTB was narrow and did not penetrate the upper and lower parts of ARSCTB, and there was no obvious large body falling off. Meanwhile, ARSCTB had more secondary cracks, and the secondary cracks were not connected with each other under this strain condition, which had little effect on the strength. In addition, with increased ARS content, the area of the ARSCTB collapse zone increased gradually. This was because the increased rate of ARS content caused the overlap of ARS in the ARSCTB matrix, which reduced the adhesive force between ARS and the ARSCTB matrix, resulting in the increased collapse area. This phenomenon was consistent with the conclusion in **Figure 4**. From overall view, after the UCS test, the integrity of ARSCTB was higher, and the block did not fall off. This phenomenon corresponded to the higher residual strength of the ARSCTB

stress strain curve. In addition, when the ARS content was 0.1 wt%, ARSCTB was most integrated after UCS test, which was consistent with the changing trend of UCS in **Figure 4**. The integrity of ARSCTB is improved by ARS, and then the stability of backfill is enhanced, which is beneficial for backfill to effectively support goaf, maintain its own self-supporting ability, better play its different functions, and improve safety of downhole operation. Meanwhile, the ARS content can be adjusted by the actual filling mining method, and then the different mechanical behaviors of the backfill can be obtained, as described in the following the engineering suggestions.

Analysis of Microstructure Evolution of CTB and ARSCTB

The mechanical properties of ARSCTB were significantly improved by the addition of ARS. To understand the micro-scale interaction relationship between ARS and the ARSCTB matrix, and based on the influence of ARS content on the UCS and tensile strength of ARSCTB, the SEM test was carried out on the representative backfill samples (C-0, C-1, C-4) at 28 days curing age, as shown in **Figure 12**. It can be seen from **Figures 12C-0,1,4** that the microstructure of CTB and ARSCTB had no obvious difference at 28 days curing age, with dense structure and less pores, and the inhibition effect of ARS on cement hydration was negligible (it is consistent with the XRD results in **Figure 6B**). Therefore, the change of the internal structure of the ARSCTB matrix by ARS is the main reason for its strength improvement. **Figures 12C-1i,4i** show the microscopic interaction relationship between ARS and the ARSCTB matrix when the ARS content was 0.1 and 0.4 wt%, respectively. It can be seen from the figure that the end and surface of ARS were wrapped by cement hydration products, and the adhesive strength between ARS and the ARSCTB matrix was improved, which help ARS play a bridging role in the ARSCTB matrix, and the crack propagation was restrained, providing a drag force or pulling force for the block that is about to fall off (Chen et al., 2020; Wang et al., 2020). Thus, the mechanical properties of ARSCTB were improved, the post-peak residual strength was increased, and the

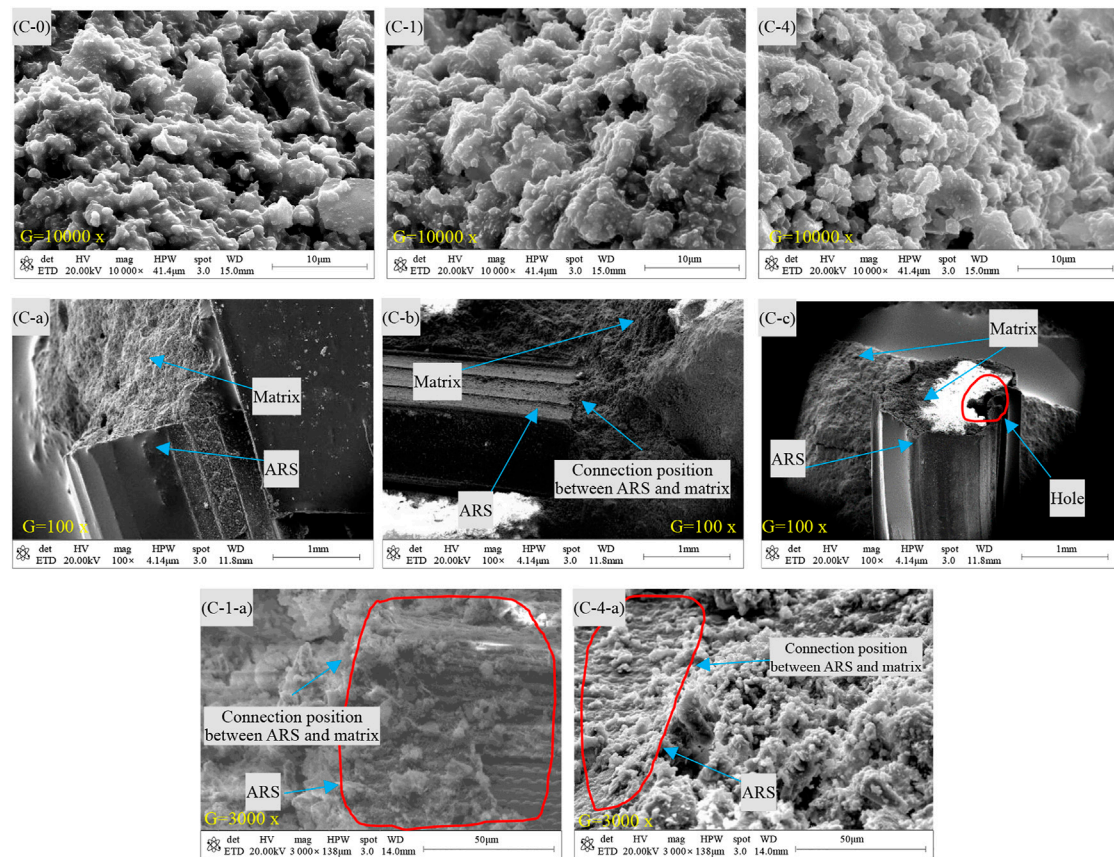


FIGURE 12 | SEM images of CTB and ARSCTB (G is the magnification).

integrity of ARSCTB was enhanced (consistent with the results in **Figure 4** and **Figure 11**). In addition, the rough texture of the ARS surface increased its friction with the ARSCTB matrix and further improved the adhesive strength between ARS and the ARSCTB matrix (strengthening the bridging effect of ARS). **Figures 12C-i,ii,iii** show the microscopic interaction between ARS (ARS content is 0.4 wt%) and the ARSCTB matrix. It can be seen from the figure that ARS was filled with cement tailings and connected to the ARSCTB matrix as a whole without obvious cracks (**Figures 12C-i,ii**), which hold ARS play a better bridging role, the morphology of ARS in the backfill matrix was consistent with that of *Chen et al., 2020*. In addition, in **Figure 12-Ciii**, there were holes in ARS that were not filled with cement tailings, but ARS was not damaged under external force, which corresponded to the large strain at the initial stage of the stress strain curve of ARSCTB in **Figure 9**.

ENGINEERING SUGGESTIONS

The mechanical properties of the backfill in filling mining method are the key to control ground pressure, reduce surface subsidence, and provide safe working environment for workers. Therefore, the backfill must have enough stability. Based on this study, the UCS and tensile strength of ARSCTB were higher than those of

CTB at 28 days curing age regardless of the ARS content (especially at 0.1 wt% ARS, the UCS of ARSCTB was best improved, and when this content of ARS was added to the backfill, the strength of ARSCTB was significantly improved compared with the strength of the backfill required by the mine, which ensured the safety of underground operation). However, the UCS and tensile strength of ARSCTB have negative correlation and positive correlation with the ARS content. Therefore, for the application of ARS in actual filling, the following suggestions are presented: 1) In the open stope and subsequent filling method with pillars, the compressive strength of the backfill is the key to its stability. Therefore, it is recommended to add 0.1 wt% ARS to the backfill. 2) In the high-stage subsequent filling mining method with two-step stoping, the backfill is exposed laterally during the second step mining, and the backfill is prone to tensile failure under the action of ground pressure and blasting stress wave. It is recommended to add 0.3–0.4 wt% ARS. 3) In the downward slicing or drift filling mining method, as artificial false roof, the backfill is prone to tensile failure, which increases the mining risk. Therefore, it is recommended to add 0.4 wt% ARS. 4) When the backfill is used as artificial pillar for residual pillar mining, the compressive strength of the backfill is required to be high. Therefore, it is recommended to add 0.1 wt% ARS.

CONCLUSIONS

1) The UCS of ARSCTB can be improved by ARS, and it is positively correlated with curing age. However, with the ARS content increases from 0.1 to 0.4 wt%, the UCS of ARSCTB gradually decreases. When the ARS content is 0.1 wt%, the UCS improvement effect is best, and the UCS increased rate is 6.0, 8.3, 14.7% at 7, 14, and 28 days curing age.

2) With the ARS content increases from 0.1 to 0.4 wt%, the increased rates of tensile strength of ARSCTB at 7, 14, and 28 days are 18.5–29.6%, 9.1–22.7%, and 24.1–34.2%, respectively. The tensile strength of ARSCTB is generally higher than that of CTB and is positively correlated with the ARS content.

3) The failure mode of ARSCTB is complex, mainly tensile shear mixed failure. However, ARSCTB has higher integrity after failure. ARSCTB is most integrated after the UCS test, when the ARS content was 0.1 wt%. Meanwhile, ARSCTB has higher residual strength and greater bearing capacity after failure.

4) The microstructure shows that ARS is wrapped by the cement hydration products and has a high adhesive force with the ARSCTB matrix. ARS plays a bridging role in the matrix. The crack propagation is restrained. However, after a content of about 0.2–0.3 wt%, the inhibition of ARS on hydration reaction and the overlap between ARS are not conducive to the improvement of the UCS of ARSCTB.

5) In the actual filling operation, it is recommended to add 0.1 wt% of ARS to the backfill of open stope and subsequent filling method, and 0.3–0.4 wt% of ARS to the backfill that needs to be laterally exposed in the high stage, 0.4 wt% ARS is added to the backfill of the false roof, and 0.2–0.3 wt% ARS is added to the backfill used as the artificial pillar mining residual pillar.

The change of ARS content significantly affects the strength of changing trend of backfill, which indicates that it is valuable to study the effect of ARS content on the mechanical properties of backfill. Meanwhile, according to the influence of ARS content on

UCS and tensile strength, ARS contents can be determined according to the actual filling situation. Moreover, it is a green and sustainable development method to improve the mechanical properties of backfill by using rice straw waste with low cost and wide sources.

DATA AVAILABILITY STATEMENT

The original contributions presented in the study are included in the article/Supplementary Material; further inquiries can be directed to the corresponding authors.

ETHICS STATEMENT

Written informed consent was obtained from the individual(s), and minor(s)' legal guardian/next of kin, for the publication of any potentially identifiable images or data included in this article.

AUTHOR CONTRIBUTIONS

All authors listed have made a substantial, direct and intellectual contribution to the work, and approved it for publication.

FUNDING

This study was supported by the National Natural Science Foundation of China (No. 51804134, No. 51804135), the Natural Science Foundation of Jiangxi Province (No. 20181BAB216013), and the Program of Qingjiang Excellent Young Talents, Jiangxi University of Science and Technology (JXUSTQJYX2019007).

REFERENCES

- Ammari, M. S., Belhadji, B., Bederina, M., Ferhat, A., and Quéneudec, M. (2020). Contribution of Hybrid Fibers on the Improvement of Sand concrete Properties: Barley Straws Treated with Hot Water and Steel Fibers. *Constr. Build. Mater.* 233, 117374. doi:10.1016/j.conbuildmat.2019.117374
- Bederina, M., Belhadji, B., Ammari, M. S., Gouilleux, A., Makhoulfi, Z., Montrelay, N., et al. (2016). Improvement of the Properties of a Sand concrete Containing Barley Straws - Treatment of the Barley Straws. *Constr. Build. Mater.* 115, 464–477. doi:10.1016/j.conbuildmat.2016.04.065
- Cao, S., Yilmaz, E., and Song, W. (2019a). Fiber Type Effect on Strength, Toughness and Microstructure of Early Age Cemented Tailings Backfill. *Constr. Build. Mater.* 223, 44–54. doi:10.1016/j.conbuildmat.2019.06.221
- Cao, S., Yilmaz, E., Song, W., Yilmaz, E., and Xue, G. (2019b). Loading Rate Effect on Uniaxial Compressive Strength Behavior and Acoustic Emission Properties of Cemented Tailings Backfill. *Constr. Build. Mater.* 213, 313–324. doi:10.1016/j.conbuildmat.2019.04.082
- Cao, S., Xue, G., Yilmaz, E., and Yin, Z. (2021). Assessment of Rheological and Sedimentation Characteristics of Fresh Cemented Tailings Backfill Slurry. *Int. J. Mining. Reclam. Environ.* 35 (5), 319–335. doi:10.1080/17480930.2020.1826092
- Cavusoglu, I., Yilmaz, E., and Yilmaz, A. O. (2021). Sodium Silicate Effect on Setting Properties, Strength Behavior and Microstructure of Cemented Coal Fly Ash Backfill. *Powder Technol.* 384, 17–28. doi:10.1016/j.powtec.2021.02.013
- Chakraborty, S., Kundu, S. P., Roy, A., Adhikari, B., and Majumder, S. B. (2013). Polymer Modified Jute Fibre as Reinforcing Agent Controlling the Physical and Mechanical Characteristics of Cement Mortar. *Constr. Build. Mater.* 49, 214–222. doi:10.1016/j.conbuildmat.2013.08.025
- Chen, H. T., Ming, X. L., Liu, S., Zhang, Y., and Zhang, H. C. (2015). Optimization of Technical Parameters for Making Mulch from Waste Cotton and Rice Straw Fiber. *Trans. Chin. Soc. Agric. Eng.* 20, 300–308. doi:10.11975/j.issn.1002-6819.2015.13.041
- Chen, B., Lu, Y. B., Su, S., and Luo, D. (2017). Influence of Straw Fiber on Tensile Properties of Concrete. *China Concr. Cem. Prod.* (10), 85–88. doi:10.19761/j.1000-4637.2017.10.020
- Chen, X., Shi, X., Zhou, J., Chen, Q., Li, E., and Du, X. (2018). Compressive Behavior and Microstructural Properties of Tailings Polypropylene Fibre-Reinforced Cemented Paste Backfill. *Constr. Build. Mater.* 190, 211–221. doi:10.1016/j.conbuildmat.2018.09.092
- Chen, X., Shi, X., Zhou, J., Yu, Z., and Huang, P. (2020). Determination of Mechanical, Flowability, and Microstructural Properties of Cemented Tailings Backfill Containing rice Straw. *Constr. Build. Mater.* 246, 118520. doi:10.1016/j.conbuildmat.2020.118520
- Cheng, A., Zhang, Y., Dai, S., Dong, F., Zeng, W., and Li, D. (2018). Spatiotemporal Evolution Law and Fracture Prediction of Acoustic Emission Parameters of Uniaxial Compressed Cemented Backfill. *Rock Soil Mech.* 40, 2–9. doi:10.16285/j.rsm.2018.1940
- Deng, X. J. (2017). Ground Control Mechanism of Mining Extra-thick Coal Seam Using Upward Slicing Longwall-Roadway Cemented Backfilling

- Technology. Xuzhou, China: China University of mining and technology. Doctoral Dissertation.
- Fan, H., and Sheng, L. (2011). Experimental Studies on Performance of Cement-Based Straw Fiber Material. *J. Anhui Agric. Univ.* 38, 159–162. doi:10.13610/j.cnki.1672-352x.2011.04.015
- Farooqi, M. U., and Ali, M. (2019). Effect of Pre-treatment and Content of Wheat Straw on Energy Absorption Capability of concrete. *Construct. Build. Mater.* 224, 572–583. doi:10.1016/j.conbuildmat.2019.07.086
- Hao, X., Du, W., Zhao, Y., Sun, Z., Zhang, Q., Wang, S., et al. (2020). Dynamic Tensile Behaviour and Crack Propagation of Coal under Coupled Static-Dynamic Loading. *Int. J. Mining Sci. Technol.* 30 (5), 659–668. doi:10.1016/j.ijmst.2020.06.007
- Hao, X., Zhang, Q., Sun, Z., Wang, S., Yang, K., Ren, B., et al. (2021). Effects of the Major Principal Stress Direction Respect to the Long axis of a Tunnel on the Tunnel Stability: Physical Model Tests and Numerical Simulation. *Tunnelling Underground Space Technol.* 114 (7), 103993. doi:10.1016/j.tust.2021.103993
- Haruna, S., and Fall, M. (2017). “Enhanced Flow Ability and Mechanical Characteristics of Cemented Paste Backfill with a Chemical Admixture,” in Proceedings of the 12th International Symposium on Mining with Backfill (Ottawa, Canada: Minefill).
- Huang, Y., Li, J., Ma, D., Gao, H., Guo, Y., and Ouyang, S. (2019). Triaxial Compression Behaviour of Gangue Solid Wastes under Effects of Particle Size and Confining Pressure. *Sci. Total Environ.* 693, 133607. doi:10.1016/j.scitotenv.2019.133607
- Huynh, L., Beattie, D. A., Fornasiero, D., and Ralston, J. (2006). Effect of Polyphosphate and Naphthalene Sulfonate Formaldehyde Condensate on the Rheological Properties of Dewatered Tailings and Cemented Paste Backfill. *Minerals Eng.* 19, 28–36. doi:10.1016/j.mineng.2005.05.001
- Jiang, H., Fall, M., Yilmaz, E., Li, Y., and Yang, L. (2020). Effect of mineral Admixtures on Flow Properties of Fresh Cemented Paste Backfill: Assessment of Time Dependency and Thixotropy. *Powder Technol.* 372, 258–266. doi:10.1016/j.powtec.2020.06.009
- Koohestani, B., Mokhtari, P., Yilmaz, E., Mahdipour, F., and Darban, A. K. (2021). Geopolymerization Mechanism of Binder-free Mine Tailings by Sodium Silicate. *Constr. Build. Mater.* 268, 121217. doi:10.1016/j.conbuildmat.2020.121217
- Kou, Y., Jiang, H., Ren, L., Yilmaz, E., and Li, Y. (2020). Rheological Properties of Cemented Paste Backfill with Alkali-Activated Slag. *Minerals* 10 (3), 288. doi:10.3390/min10030288
- Li, D. X. (2020). *Agricultural Waste Changes from “waste” to “treasure” to Promote green and Sustainable Development of Agriculture Vegetables* 7, 1–9.
- Liao, Q., Li, B., and Wu, J. Y. (2018). Experimental Study on Preparation Technology of Straw Fiber Concrete. *Sichuan Build. Sci.* 44, 99–104. doi:10.19794/j.cnki.1008-1933.2018.02.019
- Liu, G., Li, L., Yang, X., and Guo, L. (2016). Stability Analyses of Vertically Exposed Cemented Backfill: A Revisit to Mitchell’s Physical Model Tests. *Int. J. Mining Sci. Technol.* 26, 1135–1144. doi:10.1016/j.ijmst.2016.09.024
- Ma, G. W., Li, Z. J., Yi, X. W., and Guo, L. J. (2016). Macro-meso experiment of Fiber-Reinforced Cement Paste Filling Material. *J. Beijing Univ. Technol.* 42, 407–412. doi:10.11936/bjtxb2015040024
- Mangane, M. B. C., Argane, R., Trauchessec, R., Lecomte, A., and Benzaazoua, M. (2018). Influence of Superplasticizers on Mechanical Properties and Workability of Cemented Paste Backfill. *Minerals Eng.* 116, 3–14. doi:10.1016/j.mineng.2017.11.006
- Ming, X. L., Chen, H. T., and Wei, Z. P. (2019). Optimization of Technical Parameters for Making Light-Basis-Weight and Environment-Friendly rice Straw Fiber Film. *Trans. Chin. Soc. Agric. Eng.*, 259–266. doi:10.11975/j.issn.1002-6819.2019.19.032
- Ouatara, D., Belem, T., Mbonimpa, M., and Yahia, A. (2018). Effect of Superplasticizers on the Consistency and Unconfined Compressive Strength of Cemented Paste Backfills. *Constr. Build. Mater.* 181, 59–72. doi:10.1016/j.conbuildmat.2018.05.288
- Petrella, A., Spasiano, D., Liuzzi, S., Ayr, U., Cosma, P., Rizzi, V., et al. (2018). Use of Cellulose Fibers from Wheat Straw for Sustainable Cement Mortars. *J. Sustainable Cem.-Based Mater.* 3, 1–8. doi:10.1080/21650373.2018.1534148
- Qi, C., and Fourie, A. (2019). Cemented Paste Backfill for mineral Tailings Management: Review and Future Perspectives. *Minerals Eng.* 144, 106025. doi:10.1016/j.mineng.2019.106025
- Rahim, M., Douzane, O., Tran Le, A. D., Promis, G., and Langlet, T. (2016). Characterization and Comparison of Hygric Properties of Rape Straw concrete and Hemp concrete. *Constr. Build. Mater.* 102, 679–687. doi:10.1016/j.conbuildmat.2015.11.021
- Ramli, M., Kwan, W. H., and Abas, N. F. (2013). Strength and Durability of Coconut-Fiber-Reinforced concrete in Aggressive Environments. *Constr. Build. Mater.* 38, 554–566. doi:10.1016/j.conbuildmat.2012.09.002
- Sathiparan, N., and De Zoysa, H. T. S. M. (2018). The Effects of Using Agricultural Waste as Partial Substitute for Sand in Cement Blocks. *J. Build. Eng.* 19, 216–227. doi:10.1016/j.jobte.2018.04.023
- Song, D. L., Hou, S. P., and Wang, X. B. (2018). The Amount of Straw Nutrient Resources in China and the Potential of Replacing Chemical Fertilizers. *J. Plant Nutr. Fert.* 24, 1–21. doi:10.11674/zwyf.17348
- Sun, Z. F., and Jiang, E. C. (2007). Study on Mechanical Properties of rice Straw. *J. Northeast Agric. Univ.* 38 (5), 660–664. doi:10.19720/j.cnki.issn.1005-9369.2007.05.020
- Wang, H.-Y., and Chen, K.-W. (2016). A Study of the Engineering Properties of CLSM with a New Type of Slag. *Constr. Build. Mater.* 102, 422–427. doi:10.1016/j.conbuildmat.2015.10.198
- Wang, Y., Fall, M., and Wu, A. X. (2016). Initial Temperature-Dependence of Strength Development and Self-Desiccation in Cemented Paste Backfill that Contains Sodium Silicate. *Cem. Concr. Compos.* 67, 101–110. doi:10.1016/j.cemconcomp.2016.01.005
- Wang, X. Y., Hu, C. G., and Feng, X. X. (2017). Strength of Modified Wheat Straw/Cement Composites. *J. Mater. Sci. Eng.* 35, 140–143. doi:10.14136/j.cnki.issn1673-2812.2017.01.028
- Wang, S., Song, X., Chen, Q., Wang, X., Wei, M., Ke, Y., et al. (2020). Mechanical Properties of Cemented Tailings Backfill Containing Alkalized rice Straw of Various Lengths. *J. Environ. Manage.* 276, 111124. doi:10.1016/j.jenvman.2020.111124
- Xie, X., Zhou, Z., Jiang, M., Xu, X., Wang, Z., and Hui, D. (2015). Cellulosic Fibers from rice Straw and Bamboo Used as Reinforcement of Cement-Based Composites for Remarkably Improving Mechanical Properties. *Compos. B: Eng.* 78, 153–161. doi:10.1016/j.compositesb.2015.03.086
- Xie, X., Gou, G., Wei, X., Zhou, Z., Jiang, M., Xu, X., et al. (2016). Influence of Pretreatment of rice Straw on Hydration of Straw Fiber Filled Cement Based Composites. *Constr. Build. Mater.* 113, 449–455. doi:10.1016/j.conbuildmat.2016.03.088
- Xu, W., Cao, Y., and Liu, B. (2019a). Strength Efficiency Evaluation of Cemented Tailings Backfill with Different Stratified Structures. *Eng. Struct.* 180, 18–28. doi:10.1016/j.engstruct.2018.11.030
- Xu, W., Li, Q., and Zhang, Y. (2019b). Influence of Temperature on Compressive Strength, Microstructure Properties and Failure Pattern of Fiber-Reinforced Cemented Tailings Backfill. *Constr. Build. Mater.* 222, 776–785. doi:10.1016/j.conbuildmat.2019.06.203
- Xue, G., Yilmaz, E., Song, W., and Yilmaz, E. (2019a). Influence of Fiber Reinforcement on Mechanical Behavior and Microstructural Properties of Cemented Tailings Backfill. *Constr. Build. Mater.* 213, 275–285. doi:10.1016/j.conbuildmat.2019.04.080
- Xue, G., Yilmaz, E., Song, W., and Cao, S. (2019b). Mechanical, Flexural and Microstructural Properties of Cement-Tailings Matrix Composites: Effects of Fiber Type and Dosage. *Compos. Part B: Eng.* 172, 131–142. doi:10.1016/j.compositesb.2019.05.039
- Xue, G., Yilmaz, E., Song, W., and Cao, S. (2020). Fiber Length Effect on Strength Properties of Polypropylene Fiber Reinforced Cemented Tailings Backfill Specimens with Different Sizes. *Constr. Build. Mater.* 241, 118113. doi:10.1016/j.conbuildmat.2020.118113
- Yang, L., Qiu, J., Jiang, H., Hu, S., Li, H., and Li, S. (2017). Use of Cemented Super-fine Unclassified Tailings Backfill for Control of Subsidence. *Minerals* 7, 216. doi:10.3390/min7110216
- Yang, L., Yilmaz, E., Li, J., Liu, H., and Jiang, H. (2018). Effect of Superplasticizer Type and Dosage on Fluidity and Strength Behavior of Cemented Tailings Backfill with Different Solid Contents. *Constr. Build. Mater.* 187, 290–298. doi:10.1016/j.conbuildmat.2018.07.155
- Yang, L., Xu, W., Yilmaz, E., Wang, Q., and Qiu, J. (2020). A Combined Experimental and Numerical Study on the Triaxial and Dynamic Compression Behavior of Cemented Tailings Backfill. *Eng. Struct.* 219, 110957. doi:10.1016/j.engstruct.2020.110957

- Yi, X. W., Ma, G. W., and Fourie, A. (2015). Compressive Behaviour of Fibre-Reinforced Cemented Paste Backfill. *Geotextiles Geomembr.* 43, 207–215. doi:10.1016/j.geotextmem.2015.03.003
- Yilmaz, E., Belem, T., and Benzaazoua, M. (2015). Specimen Size Effect on Strength Behavior of Cemented Paste Backfills Subjected to Different Placement Conditions. *Eng. Geol.* 185, 52–62. doi:10.1016/j.enggeo.2014.11.015
- Zeng, W., Huang, Z., Wu, Y., Li, S., Zhang, R., and Zhao, K. (2020). Experimental Investigation on Mining-Induced Strain and Failure Characteristics of Rock Masses of Mine Floor. *Geomatics, Nat. Hazards Risk* 11 (01), 491–509. doi:10.1080/19475705.2020.1734102
- Zhang, X. Y., Lv, C., Zhang, D. M., Wang, L., and Li, Y. (2020). Performance of Increasing Toughness of Straw Fiber in Lightweight Aggregate concrete and its Prediction Model of Splitting Tensile Strength. *Mater. Rep.* 34 (02), 34–38.
- Zhao, G. Y., Wu, H., Chen, Y., Xu, Z., Li, Z., and Wang, E. J. (2017). Experimental Study on Loadbearing Mechanism and Compaction Characteristics of Mine Filling Materials. *J. China Univ. Min. Technol.* 46, 1251–1258. doi:10.13247/j.cnki.jcumt.000759
- Zheng, J., Zhu, Y., and Zhao, Z. (2016). Utilization of limestone Powder and Water-Reducing Admixture in Cemented Paste Backfill of Coarse Copper Mine Tailings. *Constr. Build. Mater.* 124, 31–36. doi:10.1016/j.conbuildmat.2016.07.055
- Zheng, Y., Chen, C. X., Liu, T. T., and Ren, Z. H. (2021). A New Method of Assessing the Stability of Anti-dip Bedding Rock Slopes Subjected to Earthquake. *Bull. Eng. Geol. Environ.* 80 (4), 1–18. doi:10.1007/s10064-021-02188-4

Conflict of Interest: The authors declare that the research was conducted in the absence of any commercial or financial relationships that could be construed as a potential conflict of interest.

Publisher's Note: All claims expressed in this article are solely those of the authors and do not necessarily represent those of their affiliated organizations, or those of the publisher, the editors and the reviewers. Any product that may be evaluated in this article, or claim that may be made by its manufacturer, is not guaranteed or endorsed by the publisher.

Copyright © 2021 Wang, Song, Wei, Liu, Wang, Ke and Tao. This is an open-access article distributed under the terms of the Creative Commons Attribution License (CC BY). The use, distribution or reproduction in other forums is permitted, provided the original author(s) and the copyright owner(s) are credited and that the original publication in this journal is cited, in accordance with accepted academic practice. No use, distribution or reproduction is permitted which does not comply with these terms.



Effect of Cr^{6+} on the Properties of Alkali-Activated Slag Cement

Fu Bo^{1,2*} and Cheng Zhenyun¹

¹College of Civil Engineering, North Minzu University, Yinchuan, China, ²Coal Chemical Industry Technology Research Institute, National Energy Group, Ningxia Coal Industry Co., Ltd, Yinchuan, China

In order to investigate the effect of Cr^{6+} on the properties of alkali-activated slag cement (AAS), the effects of added dosage of $\text{Na}_2\text{Cr}_2\text{O}_4$ on the setting time and compressive strength of AAS were measured. The leaching concentration of Cr^{6+} from AAS cement stone was measured using dual-beam UV-visible spectrophotometry. The effect of $\text{Na}_2\text{Cr}_2\text{O}_4$ on the hydration kinetics of AAS cement was monitored by microcalorimetry and the corresponding kinetic parameters were analyzed. The pore solution from AAS was collected and analyzed using the high pressure press method. The effects of $\text{Na}_2\text{Cr}_2\text{O}_4$ on the hydration products of AAS cement were observed and compared using X-ray diffraction (XRD) and scanning electron microscopy (SEM). The experimental results showed that the AAS hydration process was markedly affected by $\text{Na}_2\text{Cr}_2\text{O}_4$ dosage. The setting time of AAS pastes was increased and the compressive strength of cement stones was reduced with increasing dosage of $\text{Na}_2\text{Cr}_2\text{O}_4$. With the development of AAS hydration, the leaching concentration of $\text{Na}_2\text{Cr}_2\text{O}_4$ gradually decreased. $\text{Na}_2\text{Cr}_2\text{O}_4$ did not affect the dissolution of slag particles, but impeded the formation of C-S-H gel. The Cr^{6+} was immobilized chemically in the form of needle-like CaCrO_4 particles formed by the chemical reaction between $\text{Na}_2\text{Cr}_2\text{O}_4$ and Ca^{2+} leaching from the slag.

Keywords: sodium chromate, alkaline activated slag cement, hydration behavior, hydration kinetic, hydration products

INTRODUCTION

Domestic and industrial waste in urban areas are both increasing with the rapid development of China's economy. Most industrial waste contains toxic heavy metals, such as lead, chromium, copper, zinc, cadmium, nickel, etc., which exist mainly in the form of oxides, hydroxides, silicates, insoluble salts, and organic complexes. Such toxic wastes pollute the soil, water courses, and the atmosphere if not properly disposed of, which thereby results in serious environmental pollution that threatens human life and health (Liu et al., 2020).

Chromium (Cr), a typical heavy metal element, comes mainly from pigments, electroplating, metallurgy, leather tanning, Cr-containing wastewater in electronics, and from other industries. The sludge retains Cr following treatment of these Cr-containing wastewaters and of untreated and newly produced Cr residues from enterprises. Cr is toxic and can cause human respiratory and gastrointestinal diseases, as well as skin damage. In addition, Cr^{6+} is carcinogenic when inhaled into the respiratory tract, which leads to death if the amount of inhalation is large through the skin and digestive tract (I.C.D. Association, 2007).

At present, solidification technology is one of the important methods for the treatment of heavy metal lead (Pb) wastes worldwide, and cement-based materials have also been the most widely studied and applied cementing materials in developed countries in recent decades (Gougar et al., 1996; Halim et al., 2004). Research on cement-cured heavy metal Cr is quite mature, and it has been

OPEN ACCESS

Edited by:

Tingting Zhang,
Dalian University of Technology, China

Reviewed by:

Linwen Yu,
Chongqing University, China
Zhuqing Yu,
Nanjing Tech University, China

*Correspondence:

Fu Bo
20100901036@cqu.edu.cn

Specialty section:

This article was submitted to
Structural Materials,
a section of the journal
Frontiers in Materials

Received: 06 August 2021

Accepted: 23 September 2021

Published: 18 October 2021

Citation:

Bo F and Zhenyun C (2021) Effect of
 Cr^{6+} on the Properties of Alkali-
Activated Slag Cement.
Front. Mater. 8:754463.
doi: 10.3389/fmats.2021.754463

found that cement-cured bodies have high leaching toxicity, poor durability, and poor corrosion resistance.

Alkali-activated slag cement (AAS) is a new kind of cementitious material, which is activated by alkali metal compounds from finely granulated blast furnace slag. The alkali-slag concrete derived from this process has excellent physical and mechanical properties and chemical resistance (Gougar et al., 1996; Halim et al., 2004).

AAS has an excellent pore structure, which is beneficial for reducing the leaching of Cr⁶⁺ into alkali-slag cement stones. AAS has a high initial strength, a stable long-term strength, and exhibits excellent mechanical sealing effects, which can comprehensively block Cr⁶⁺ in cement stone, thereby reducing Cr⁶⁺ leaching. The main product generated by the hydration of AAS is a low Ca/Si ratio C-S-H gel (Shi and Roy, 2006), which has a larger specific surface area, higher surface energy, and can strongly adsorb additional Cr⁶⁺. In addition, the C-S-H gel formed by AAS hydration has a cage-like microstructure, which is more conducive to the adsorption and solidification of Cr⁶⁺.

Deja (2002) studied the solidification of Cr⁶⁺ with slag cement and found that the nanoscale micropores in the alkali-slag gel had a great physical package effect on heavy metals. Palomo and Palacios (2003) pointed out that CrO₃ could not only solidify heavy metal ions but its addition could also improve the mechanical properties of AAS. Xu et al. (2006) studied the effect of alkali solution concentration and curing time on the solidification effect, and the results showed that the alkali concentration had little effect on the solidification effect of Cr. A large number of studies have pointed out that the effective solidification of Cr⁶⁺ by AAS is due to the presence of sulfides, which can convert Cr⁶⁺ into Cr³⁺ in a reducing environment, thereby reducing precipitation (Wang and Scrivener, 1995; Xu et al., 2006; Chen et al., 2020). Hence, AAS plays an active role in the solidification process. Zhang et al. (2016), Ponzoni et al. (2015), and Guo et al. (2017) all found that the silicate and aluminosilicate anions of the AAS system can partially chemically react with Cr⁶⁺ to form compounds with extremely low solubility, thus reducing the amount of Cr⁶⁺ leached in aqueous media.

A large number of studies have reported the solidification effect of AAS on Cr⁶⁺. However, the effect of Cr⁶⁺ on the hydration performance of alkali-slag cement is still unclear. In this paper, the effect of Na₂Cr₂O₄ on the hydration process of AAS was studied under conditions where the water-binder ratio, alkali equivalent, and the modulus of the water glass were kept unchanged. First, the effect of Na₂Cr₂O₄ on the hydration performance of AAS was studied. Then, the effect of Na₂Cr₂O₄ on the hydration dynamics of AAS was investigated. Finally, the effect of Na₂Cr₂O₄ on the hydration products of AAS was examined.

MATERIALS AND METHODS

Raw Materials

Granulated blast furnace slag (GBFS) (Chongqing Iron and Steel Group Co., Ltd., Chongqing Municipality, China) was vibrated

and ground for 40 min. This material had a specific surface area of 452 m²/kg, a density of 2.91 g/cm³, an alkalinity coefficient (M₀) of 1.00, an activity coefficient (M_a) of 0.45, and a mass coefficient (M_k) of 1.76. **Table 1** lists the chemical composition (main oxides) of GBFS.

NaOH (AR, Chongqing Chuanjiang Chemical Reagent Factory) was added to the purchased water glass (Chongqing Jingkou Chemical Plant; the main physical and chemical indicators are listed in **Table 2**) and its modulus adjusted to the needs of the experiment.

Tap water was used for the preparation of the solidified body, and deionized water was used for chemical analysis, including heavy metal leaching.

The chromium in Na₂CrO₄·4H₂O (AR, Chongqing Chuandong Chemical Co., Ltd.) is hexavalent, which is carcinogenic. Na₂Cr₂O₄ has strong oxidizing properties and is soluble in water, giving a solution that is slightly alkaline.

Table 3 lists their mix ratios (in terms of mass), the modulus of sodium silicate was fixed at 1.5, the alkali equivalent was 5%, and the water-binder ratio was 0.3. The mechanism of solidification of AAS was studied by varying the content of Na₂Cr₂O₄.

Methods

Slurry Curing Time Test

The determination of the curing time of AAS was carried out in accordance with the method specified in the Chinese cement standard GB/T 1346-2001 "Water consumption for standard consistency of cement, setting time, and stability test method".

Forming and Curing of the Test Block

The slag, alkali component, water, and Na₂Cr₂O₄·4H₂O were weighed out in a fixed ratio and mixed evenly in a cement slurry mixer. A 40 × 40 × 40 mm mold was used to form a solid specimen, and the molding surface was covered with a plastic film to prevent moisture evaporating. The mold was removed after 24 h at room temperature. In order to prevent the precipitation of Cr⁶⁺ in the specimen and the diffusion of alkali components to the condensed water on the surface of the specimen, which could lead to insufficient hardening of the surface of the cured body, the cured body specimen was placed in a sealed bag and kept in a standard indoor environment (temperature 20 ± 2°C, RH ≥ 90%) for the specified length of time.

Compressive Strength Test

The 40 × 40 × 40 mm specimens cured to 3, 7, and 28 d were removed from the standard curing room, and a universal material testing machine was employed to test the compressive strength of 3, 7, and 28 d for different cured bodies according to "Test Method for Strength of Glue Sand" (ISO Method).

Heat of Hydration Test

The heat detector of a TAM air microcalorimeter (TA Instruments, New Castle, DE, United States) was used for the heat of hydration test. The basic principle of the instrument is as follows: the heats of hydration of the sample and reference

TABLE 1 | Chemical composition of ground granulated blast furnace slag.

Chemical component	CaO	SiO ₂	Al ₂ O ₃	MgO	Fe ₂ O ₃	Na ₂ O	K ₂ O	SO ₃	MnO	Loss
wt%	36.18	32.61	14.44	9.39	1.03	0.40	0.42	0.27	0.72	0.47

TABLE 2 | Chemical composition and physical properties of water glass.

Index	SiO ₂ /%	Na ₂ O/%	Baume degree	Modulus	Density/g·cm ⁻³	Moisture content/%
Value	28.52	12.18	46	2.42	1.46	52.18

TABLE 3 | Mix proportions of alkali-activated slag cement (AAS) with Na₂Cr₂O₄.

No.	Water/cement	Na ₂ O (%)	Modulus of water glass	Na ₂ Cr ₂ O ₄ content (%)
1	0.30	5.0	1.5	0.0
2				0.5
3				1.0
4				1.5
5				2.0

sample are measured using a thermocouple (water or the completely hydrated cement stone is usually selected as the reference sample) in a constant temperature environment, and the exothermic rate and cumulative heat release of the sample are calculated. The test temperature was set at 20°C. Measurements were carried out on 4 g samples of the pastes. The solution of Na₂Cr₂O₄ was added in the proportions given in **Table 3**. Heat development was measured for 72 h, with a step of 50 s between consecutive measurements. Before the experiment, slag was placed in an ampoule, the solution was placed in a syringe, and the ampoule was placed in the calorimeter. After the syringe had been installed, the solution was injected into the ampoule when the temperature had stabilized at 20°C, when measurement began.

Heavy Metal Concentration Measurement

According to the national standards GB 5086.1-1997 “Solid Waste Leaching Toxicity Leaching Method Reversal Method” and GB/T 15555.4-1995 “Solid Waste Determination of Hexavalent Chromium Diphenylcarbazide Spectrophotometer Method,” the molded test piece was broken and a sample passing through a 5 mm sieve was placed in an oven and dried at 60°C, and then soaked in deionized water at a liquid-to-solid ratio (L/g) of 1:10. Subsequently, the mixture was vibrated at 23 ± 2°C for 18 h with a flip-type shaking device at a speed of 30 ± 2 rev/min, and kept for 30 min, and then the leaching solution was collected with a vacuum filter. A dual-beam UV-Vis spectrophotometer TU-190 made by Beijing General Instrument Co. Ltd. was used to measure the concentration of Cr⁶⁺ in the leaching solution.

Testing of Block Hole Solution

The alkali-slag-Cr⁶⁺ solidified body pore solution extrusion test piece was prepared using a special molding test mold (Jiangsu Subote Materials Co., Ltd., Nanjing, Jiangsu, China). The test piece was sealed in a plastic bag and then placed in standard storage environment (temperature: 20 ± 2°C; RH ≥ 90%) for the specified time. The hole solution pressing device of cement-based material was then used to squeeze the hole solution, and the dual-beam spectrophotometer was used to test the Cr⁶⁺ concentration in the hole solution.

X-Ray Diffraction Test

The sample was broken following curing for the specified time and hydration was immediately terminated using absolute ethanol. The sample was then baked to a constant weight at 60°C and passed through a 0.08 mm sieve. The powder was then sealed in an ampoule for later testing.

A Rigaku D/Max-5A 12 kW rotating target X-ray diffractometer (Rigaku Corporation, Tokyo, Japan) was used for testing, with Cu Kα radiation at a voltage of 40 kV and a scanning speed of 4°/min. The sample was dried to constant weight in a vacuum drying oven at 60°C before the test.

Scanning Electron Microscope Test

The sample was broken following curing for the specified time and hydration was immediately terminated with absolute ethanol. The sample was then baked to a constant weight at 60°C and sprayed with gold on a cross-section for later testing.

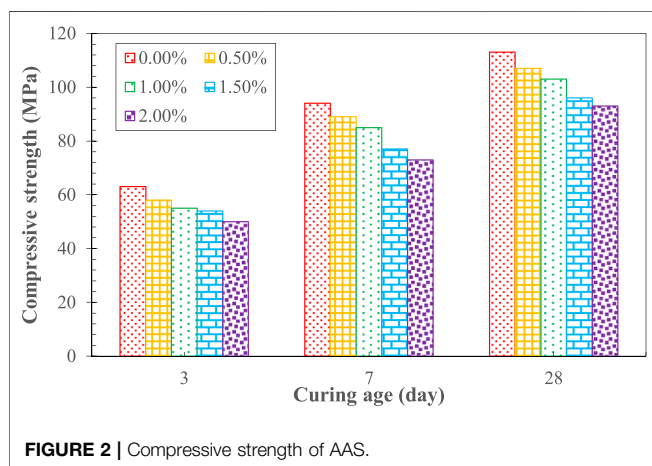
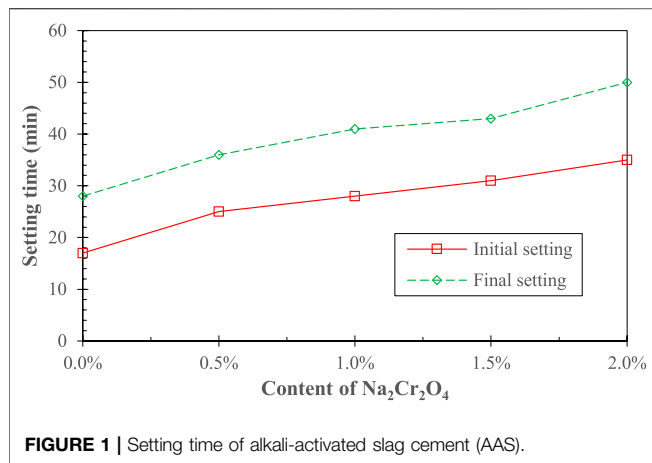
A variable vacuum scanning electron microscope (TESCAN VEGA2, Tescan Brno, s.r.o, Brno, Czech Republic) was adopted for morphological characterization, and an INCA Energy 350X energy dispersive X-ray spectrometer (Oxford Instruments, Oxford, United Kingdom) was employed for elemental analysis.

RESULTS AND DISCUSSION

Macroscopic Performance of Na₂Cr₂O₄-AAS

Variation in Curing Time

Figure 1 shows the effect of Na₂Cr₂O₄ on the curing time of AAS. It can be seen that the latter gradually increased as the Na₂Cr₂O₄ content increased. The initial setting time of AAS

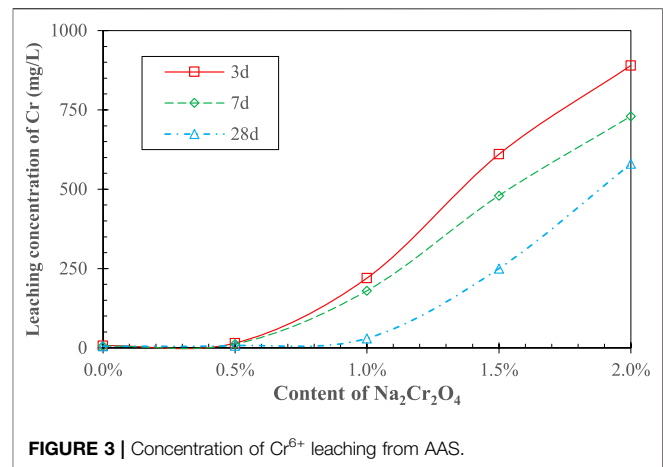


with 2% Na₂Cr₂O₄ increased from 17 to 35 min, compared with that of the control AAS, and the final curing time increased from 28 to 50 min, both of which were doubled. This is consistent with the results of previous studies (Palomo and Palacios, 2003).

Variation in Compressive Strength

Figure 2 shows the effect of Na₂Cr₂O₄ on the compressive strength of AAS. It can be seen that the latter decreased with increasing concentration of Na₂Cr₂O₄ for the same curing age. The compressive strength of cement with different Na₂Cr₂O₄ content increased with age.

The curing time and strength development of AAS are two important macro indicators that reflect the hydration process (Shi and Roy, 2006; Pacheco-Torgal et al., 2015). As shown in **Figures 1, 2**, the addition of Na₂Cr₂O₄ played a significant role in the hydration process of AAS, and the effect increased with increasing concentration of Na₂Cr₂O₄. Fang et al. (2020) pointed out that when the chemical substances introduced into the AAS hydration system combine with the Ca²⁺ ions or [SiO₄]⁴⁻ ions generated by the disintegration of the slag and OH⁻ ions in the system under the action of the alkali component,



forming small-sized particles of insoluble substances, they may form precipitates on the surface of the slag particles, hindering further hydration reactions with OH⁻ ions and activating components.

Leaching Concentration of Cr⁶⁺

Figure 3 shows the concentration of Cr⁶⁺ leaching from the AAS stone. It can be seen that at both 3 and 7 d, Cr⁶⁺ was effectively solidified in the AAS when the Na₂Cr₂O₄ content was less than 0.5%. The concentration of Cr⁶⁺ leaching out increased significantly when the Na₂Cr₂O₄ content was greater than 0.5%, and it rose sharply with increasing amounts of Na₂Cr₂O₄. Therefore, it can be conjectured that the initial leaching concentration of Cr⁶⁺ has a critical value when the concentration of Na₂Cr₂O₄ is 0.5% for this cement mix. In addition, the Cr⁶⁺ leaching concentration for AAS stone at 28 d also appeared to follow a similar pattern, whereas the Na₂Cr₂O₄ content for a critical leaching concentration increased from 0.5 to ~1.0%.

From the previous analysis, it can be seen that the introduction of Na₂Cr₂O₄ led to a low degree of initial hydration of AAS, so that the porosity of the initial cement stone and the leaching rate of Cr⁶⁺ are both increased, leading to a low leaching concentration threshold. The density of the AAS stone gradually increased, and the porosity gradually decreased with increasing age, so that the leaching rate of Cr⁶⁺ was small, and the Na₂Cr₂O₄ content for a critical leaching concentration increased with extension of the hydration time.

Hydration Exothermic Behavior of Na₂Cr₂O₄-AAS

From the previous analysis, it can be seen that the solidification of Cr⁶⁺ is closely related to the hydration process of AAS. In order to further study the solidification mechanism of AAS on Cr⁶⁺, the effect of Na₂Cr₂O₄ on the hydration exothermic process of AAS was studied (**Figure 4**).

Figure 4A shows the exothermic hydration rate of AAS for the Na₂Cr₂O₄ group and the control group, among which the control group was AAS without Cr⁶⁺. In the Na₂Cr₂O₄ group, the Na₂Cr₂O₄ content was 1.0%, and the content of the rest of the material was the same as that of the control group. The figure

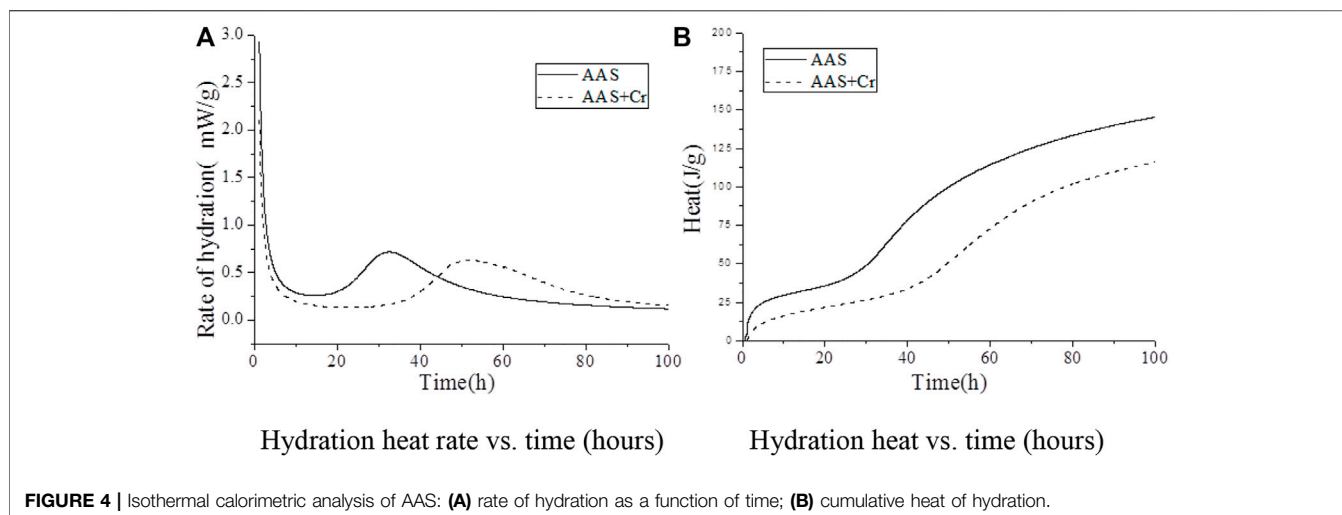


FIGURE 4 | Isothermal calorimetric analysis of AAS: **(A)** rate of hydration as a function of time; **(B)** cumulative heat of hydration.

shows that, compared with the control group, the AAS exothermic hydration rate of the $\text{Na}_2\text{Cr}_2\text{O}_4$ group was significantly prolonged.

Figure 4B shows the total hydration heat released by AAS in the $\text{Na}_2\text{Cr}_2\text{O}_4$ group and the control group. It can be seen that the AAS hydration of the $\text{Na}_2\text{Cr}_2\text{O}_4$ group was always significantly lower than that of the control group and that the variation in the total hydration heat released by the two groups were completely different. It can be seen from **Figure 4A** that there is an obvious exothermic peak in the early stages for the two groups, which was caused by the destruction of the slag surface by OH^- ions and the formation of C-S-H gel on the surface of the slag particles (Shi and Roy, 2006). However, it can be seen from the total quantity of heat released during the corresponding time in **Figure 4B** that the total quantity of heat released in the $\text{Na}_2\text{Cr}_2\text{O}_4$ group during this time was significantly lower than that of the control group. It is inferred that $\text{Na}_2\text{Cr}_2\text{O}_4$ prevents OH^- ions from destroying the slag structure or forming C-S-H gel on the slag surface. The $\text{Na}_2\text{Cr}_2\text{O}_4$ group showed a longer induction period (**Figure 4A**), and the total quantity of corresponding hydration heat released was much lower than that of the control group (**Figure 4B**). It can be inferred that $\text{Na}_2\text{Cr}_2\text{O}_4$ chemically reacts with the ions in the liquid phase to form insoluble substances on the surface of the slag particles, which prevents Ca^{2+} ions from reacting with SiO_4^{4-} in the liquid phase to form C-S-H gel. After entering the acceleration period, the variation in heat released for the two groups was identical, although the heat released by the $\text{Na}_2\text{Cr}_2\text{O}_4$ group was always lower than that of the control group. The effect of $\text{Na}_2\text{Cr}_2\text{O}_4$ on the hydration process of AAS was therefore weakened. In summary, the introduction of $\text{Na}_2\text{Cr}_2\text{O}_4$ significantly changed the hydration process of AAS according to Hess's law (Gersten and Gersten, 2001). In order to further understand the effect of $\text{Na}_2\text{Cr}_2\text{O}_4$ on the hydration process of AAS, the corresponding hydration kinetic parameters were calculated from the hydration heat release curve of the alkali-slag cement, the Knudson hydration heat model, and the Jander equation (**Table 4**).

TABLE 4 | Hydration kinetic parameters of AAS.

Hydration process	—	AAS	AAS +1% Cr6+
Acceleration stage	Time	15.80–32.5	38.44–54.35
	<i>N</i>	1.95	1.36
	<i>K</i>	1.71×10^{-3}	3.21×10^{-3}
Deceleration stage	Time	32.53–59.4	54.35–89.18
	<i>N</i>	2.01	1.37
	<i>K</i>	2.51×10^{-3}	3.37×10^{-3}
Attenuation stage	Time	59.43–100	89.18–100
	<i>N</i>	2.22	2.01
	<i>K</i>	1.17×10^{-4}	1.12×10^{-4}

Table 4 lists the AAS hydration kinetic parameters of the $\text{Na}_2\text{Cr}_2\text{O}_4$ group and the control group. It can be seen from the data listed in the table that the start time of the acceleration period in the $\text{Na}_2\text{Cr}_2\text{O}_4$ group was about 2.4 times that of the control group, and the start time of the deceleration period was about 1.7 times that of the control group. $\text{Na}_2\text{Cr}_2\text{O}_4$ significantly prolonged the curing time of AAS. In **Table 4**, *N* represents the order of the chemical reaction, which mainly characterizes the degree of difficulty of the reaction. The latter is controlled by chemical reactions on the particle surfaces and by the dissolution of reactants or the deposition of reaction products when $N \leq 1$. The reaction is controlled by the diffusion of reactants through the porous reaction product layer when $1 \leq N \leq 2$. The reaction is controlled by the diffusion of reactants through the dense product layer when $2 \leq N$ (Shi and Roy, 2006). *K* represents the rate constant of the chemical reaction, which characterizes the speed of the chemical reaction (Gersten and Gersten, 2001).

It can be seen from **Table 4** that the reaction rate of AAS in the $\text{Na}_2\text{Cr}_2\text{O}_4$ group during both the acceleration and deceleration periods was significantly higher than that of the control group, yet the reaction order was significantly lower than that of the control group. According to the AAS hydration process (Zhang et al., 2016), the chemical reaction order *N* of the whole hydration process was around 2 for the control group,

TABLE 5 | Pore solution obtained from solidification of AAS-Cr⁶⁺ (mg/L).

Age/kind	1 d			3 d			7 d		
	Total Cr	Cr ⁶⁺	Ca ²⁺	Total Cr	Cr ⁶⁺	Ca ²⁺	Total Cr	Cr ⁶⁺	Ca ²⁺
AAS	2.267	2.035	1.64	2.253	2.241	0.85	2.357	2.301	0.475
AAS + Cr	9635.58	7,125.65	2.3	7,056.616	6,023.65	1.4	6,245.069	4,952.26	0.775

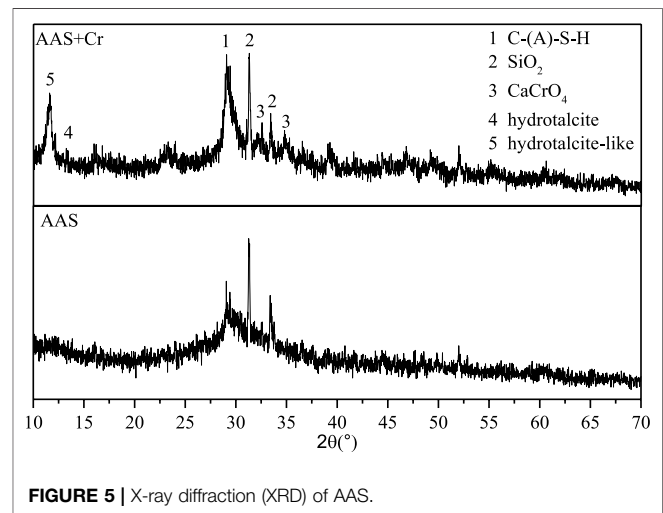
indicating that the hydration process of the control group was more prone to being controlled by the diffusion of reactants through the dense product layer from the acceleration period. The main hydration products of sodium silicate activated in AAS were mainly low calcium-to-silicon ratio C-S-H gel, which has low porosity and a compact structure (Shi and Roy, 2006). Although the reaction rate of Ca²⁺ and SiO₄⁴⁻ was rapid in the liquid phase, it is not easy for Ca²⁺ to penetrate the hydration product layer and enter the liquid phase in order to react. For the Na₂Cr₂O₄ group, the reaction order *N* was closer to 1, although the reaction rate was faster during both the acceleration and deceleration periods, indicating that the hydration process was more prone to being controlled by the diffusion of reactants through the porous reaction product layer from the acceleration period. Based on this, it can be further speculated that Na₂Cr₂O₄ first forms a poorly soluble porous product on the surface of the slag particles with the substance in the liquid phase. After entering the decay period, the reaction rate constants and reaction orders of the two groups were equivalent, and both were controlled by the diffusion of the reactants through the dense product layer, at which time C-S-H gel should have been generated.

Pore Solution and Hydration Products of Na₂Cr₂O₄-AAS

Analysis of Pore Solution of AAS

In this study, a cement-based material pore solution pressing device (Jiangsu Subote Materials Co., Ltd.) was used to collect different cement paste and pore solutions of the paste solidification body. The solidification effect of AAS on heavy metal Cr⁶⁺ ions during the hydration process was investigated by analyzing the ion concentration of the pore solution and using the analysis of hydration kinetics described above.

Table 5 shows that the total Cr, Cr⁶⁺, and Ca²⁺ concentrations in the liquid phase gradually decreased with the progress of hydration. The Ca²⁺ concentration of the pore solution in the AAS stone depended mainly on the degree of disintegration of the slag glass body and the amount of C-S-H gel hydration product. With the extension of hydration time, OH⁻ ions were continuously consumed, and the formation of hydration products gradually increased. The hydration product layer gradually changed from a porous structure to a dense structure, which reduced the amount available for disintegration of the slag glass structure as well as the concentration of Ca²⁺. The concentrations of total Cr and Cr⁶⁺ in the alkali-slag solidified body were reduced as a function of time due to the reduction of Cr⁶⁺ by S²⁻ or HS⁻ in the slag and the enhanced adsorption of Cr⁶⁺ by the hydration products.

**FIGURE 5** | X-ray diffraction (XRD) of AAS.

At 1 d, the Ca²⁺ content in the AAS pore solution of the Na₂Cr₂O₄ group was significantly higher than that of the control group. This shows that Na₂Cr₂O₄ can promote the dissolution of slag particles. At 3 and 7 d, the Ca²⁺ content in the AAS pore solution of the Na₂Cr₂O₄ group was higher than that of the control group. The heat of hydration experiment showed that the rates of hydration of the Na₂Cr₂O₄ group in the initial age were lower than those of the control group, indicating that Na₂Cr₂O₄ delayed the Ca²⁺, which dissolved from the slag, from reacting with SiO₄⁴⁻ in the liquid phase to form C-S-H gel, which led to a delay in the second hydration reaction peak in the heat of hydration experiment.

Hydration Products of AAS

Figure 5 shows the XRD pattern of AAS stone at 28 d. It can be seen that a typical “Bailey broad peak” appeared around 30°, which originated from the C-S-H gel. There are two obvious peaks at 32.3° and 35.2°, both originating from CaCrO₄ (Wang and Vipulanandan, 2000; Chen et al., 2009). Combined with the analysis of the hydration kinetic process, it can be known that Na₂Cr₂O₄ hydrolyzes to form CrO₄²⁻, which reacts with the dissolved Ca²⁺ in the slag to form CaCrO₄, hence preventing Ca²⁺ from interacting with SiO₄⁴⁻ in the liquid phase to generate C-S-H gel. This reduces the strength of AAS.

Figure 6 shows the SEM images of AAS stones in both the Na₂Cr₂O₄ group and control groups at 28 d. It can be seen from the control group that the slag was basically hydrated, forming a continuous dense structure with fewer pores. In addition, it can be seen from the Na₂Cr₂O₄ group that the structure of the

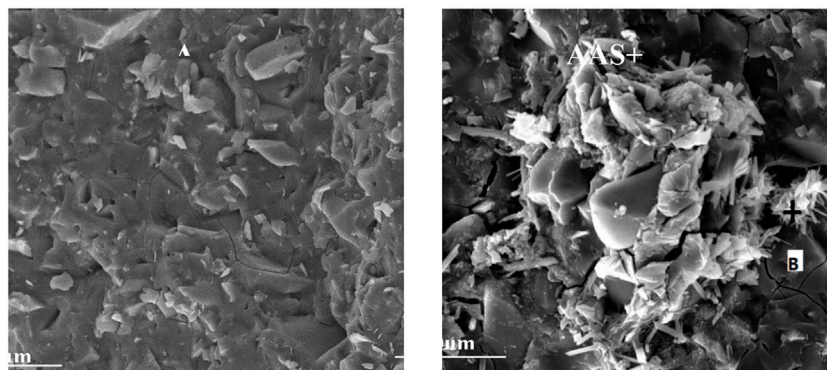


FIGURE 6 | Scanning electron micrograph (SEM) of AAS-Cr⁶⁺ solidification.

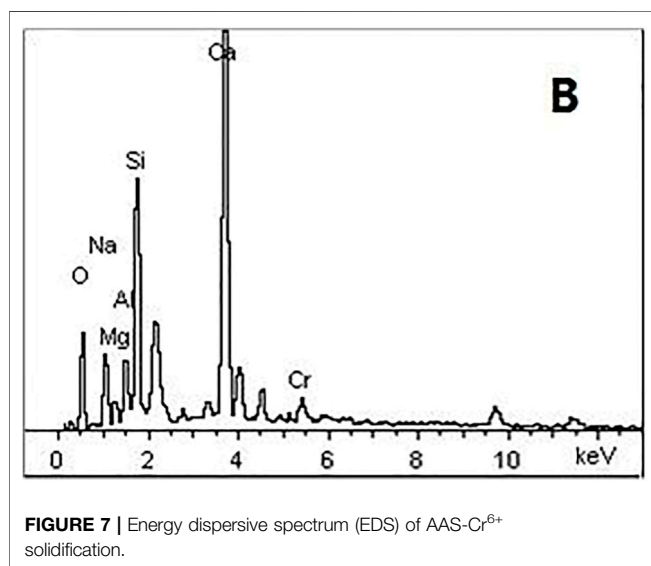


FIGURE 7 | Energy dispersive spectrum (EDS) of AAS-Cr⁶⁺ solidification.

hydration products was relatively loose, and needles and rods were formed. The needles and rods (point B) were analyzed using energy dispersive spectroscopy (EDS) (Figure 7). The results showed that the weight percentage of elemental Cr at this point was 3.23%, which was much higher than the original amount in the mix (1%). In addition, a large amount of Ca was enriched here. According to the results of Laforest and Duchesne (2005), the rod-shaped crystals here were CaCrO₄.

CONCLUSION

The curing time of AAS in our experiments was prolonged and the strength of the cement stone gradually decreased with

increasing Na₂Cr₂O₄ content. The leaching of Na₂Cr₂O₄ gradually decreased with increasing hydration age. At this AAS mix ratio, the leaching limit value of Na₂Cr₂O₄ at 3 and 7 d was 0.5% and at 28 d was 1.0%. Na₂Cr₂O₄ did not affect the way OH⁻ ions destroyed the slag structure, but mainly affected the reaction of Ca²⁺ ions dissolved in the slag with SiO₄⁴⁻ ions in the liquid phase to form C-S-H gel. Na₂Cr₂O₄ and Ca²⁺ precipitated in the slag to form rod-shaped CaCrO₄ particles, which chemically solidified Cr⁶⁺.

DATA AVAILABILITY STATEMENT

The original contributions presented in the study are included in the article/Supplementary Material, further inquiries can be directed to the corresponding author.

AUTHOR CONTRIBUTIONS

FB investigated the data and wrote the manuscript. CZ designed the experiments and was involved in data analysis.

FUNDING

This study was financially supported by 2019 Key Research Project of North Minzu University (2019KJ31). The support of the National Natural Science Foundation of China (Grant No. 51668001), the Key Research and Development Program of Ningxia Hui Autonomous Region (2020BDE03009) and the Natural Science Foundation of Ningxia Hui Autonomous Region (2020AAC03195; 2021AAC03187) is also gratefully acknowledged.

REFERENCES

I.C.D. Association. (2007). *Health Safety and Environment Guidelines for Chromium, Revision*.

Chen, H., Yuan, H., Mao, L., Hashmi, M. Z., Xu, F., and Tang, X. (2020). Stabilization/solidification of Chromium-Bearing Electroplating Sludge with Alkali-Activated Slag Binders. *Chemosphere* 240, 124885. doi:10.1016/j.chemosphere.2019.124885

Chen, Q. Y., Tyrer, M., Hills, C. D., Yang, X. M., and Carey, P. (2009). Cheminform Abstract: Immobilization of Heavy Metal in Cement-Based Solidification/

- stabilisation: A Review. *ChemInform* 40 (23), 390–403. doi:10.1002/chin.200923207
- Deja, J. (2002). Immobilization of Cr⁶⁺, Cd²⁺, Zn²⁺ and Pb²⁺ in Alkali-Activated Slag Binders. *Cement Concrete Res.* 32, 1971–1979. doi:10.1016/S0008-8846(02)00904-3
- Fang, S., Lam, E. S. S., Li, B., and Wu, B. (2020). Effect of Alkali Contents, Moduli and Curing Time on Engineering Properties of Alkali Activated Slag. *Construction Building Mater.* 249 (6), 118799. doi:10.1016/j.conbuildmat.2020.118799
- Gougar, M. L. D., Scheetz, B. E., and Roy, D. M. (1996). Ettringite and C-S-H Portland Cement Phases for Waste Ion Immobilization: A Review. *Waste Management* 16 (4), 295–303. doi:10.1016/S0956-053X(96)00072-4
- Guo, X., Zhang, L., Huang, J., and Shi, H. (2017). Detoxification and Solidification of Heavy Metal of Chromium Using Fly Ash-Based Geopolymer with Chemical Agents. *Construction Building Mater.* 151, 394–404. doi:10.1016/j.conbuildmat.2017.05.199
- Halim, C. E., Amal, R., Beydoun, D., Scott, J. A., and Low, G. (2004). Implications of the Structure of Cementitious Wastes Containing Pb(II), Cd(II), As(V), and Cr(VI) on the Leaching of Metals. *Cement Concrete Res.* 34, 1093–1102. doi:10.1016/j.cemconres.2003.11.025
- Laforest, G., and Duchesne, J. (2005). Immobilization of Chromium (VI) Evaluated by Binding Isotherms for Ground Granulated Blast Furnace Slag and Ordinary Portland Cement. *Cement Concrete Res.* 35 (12), 2322–2332. doi:10.1016/j.cemconres.2004.12.011
- Liu, M., Li, X., He, Y., and Li, H. (2020). Aquatic Toxicity of Heavy Metal-Containing Wastewater Effluent Treated Using Vertical Flow Constructed Wetlands. *Sci. Total Environ.* 727, 138616. doi:10.1016/j.scitotenv.2020.138616
- Pacheco-Torgal, F., Labrincha, J. A., Leonelli, C., Palomo, A., and Chindapasirt, P. (2015). *Handbook of Alkali-Activated Cements, Mortars and Concretes*. Cambridge: Woodhead Publishing. doi:10.1016/C2013-0-16511-7
- Palomo, A., and Palacios, M. (2003). Alkali-activated Cementitious Materials: Alternative Matrices for the Immobilisation of Hazardous Wastes. *Cement Concrete Res.* 33 (2), 289–295. doi:10.1016/S0008-8846(02)00964-X
- Ponzoni, C., Lancellotti, I., Barbieri, L., Spinella, A., Saladino, M. L., and Martino, D. C. (2015). Chromium Liquid Waste Inertization in an Inorganic Alkali Activated Matrix: Leaching and NMR Multinuclear Approach. *J. Hazard. Mater.* 286, 474–483. doi:10.1016/j.jhazmat.2014.12.054
- Gersten, J. I., and Gersten, J. I. (2002). *The Physics and Chemistry of Materials*, 55. New York: John Wiley & Sons, 59–60. doi:10.1063/1.1506755
- Shi, C., and Roy, D. (2006). *Alkali-Activated Cements and Concretes*. Boca Raton: CRC Press.
- Wang, S. D., and Scrivener, K. L. (1995). Hydration Products of Alkali Activated Slag Cement. *Cement Concrete Res.* 25 (3), 561–571. doi:10.1016/0008-8846(95)00045-E
- Wang, S., and Vipulanandan, C. (2000). Solidification/stabilization of Cr(VI) with Cement: Leachability and XRD Analyses. *Cement Concrete Res.* 30, 385–389. doi:10.1016/S0008-8846(99)00265-3
- Xu, J. Z., Zhou, Y. L., Chang, Q., and Qu, H. Q. (2006). Study on the Factors of Affecting the Immobilization of Heavy Metals in Fly Ash-Based Geopolymers. *Mater. Lett.* 60 (6), 820–822. doi:10.1016/j.matlet.2005.10.019
- Zhang, W., Yang, C., Yang, K., and Pan, Q. (2016). Effect of Sal Perlatum-Water Glass on the Hydration Behavior of Alkali-Activated Slag Cements. *J. Building Mater.* 19, 803–809. doi:10.3969/j.issn.1007-9629.2016.05.003

Conflict of Interest: FB was employed by the company Coal Chemical Industry Technology Research Institute, National Energy Group, Ningxia Coal Industry Co., Ltd.

The remaining author declare that the research was conducted in the absence of any commercial or financial relationships that could be construed as a potential conflict of interest.

Publisher's Note: All claims expressed in this article are solely those of the authors and do not necessarily represent those of their affiliated organizations, or those of the publisher, the editors and the reviewers. Any product that may be evaluated in this article, or claim that may be made by its manufacturer, is not guaranteed or endorsed by the publisher.

Copyright © 2021 Bo and Zhenyun. This is an open-access article distributed under the terms of the Creative Commons Attribution License (CC BY). The use, distribution or reproduction in other forums is permitted, provided the original author(s) and the copyright owner(s) are credited and that the original publication in this journal is cited, in accordance with accepted academic practice. No use, distribution or reproduction is permitted which does not comply with these terms.



Filling Treatment of Surface Subsidence Resulted From Underground Mining in a High-Altitude Mine

Daiqiang Deng^{1,2}, Guodong Cao^{1*} and Yihua Liang^{3*}

¹College of Civil Engineering and Mechanics, Xiangtan University, Xiangtan, China, ²College of Mining Engineering, Guizhou Institute of Technology, Guiyang, China, ³Guizhou Industrial Development Research Center, Guizhou Institute of Technology, Guiyang, China

OPEN ACCESS

Edited by:

Lijie Guo,
Beijing General Research Institute of
Mining and Metallurgy, China

Reviewed by:

Ping Duan,
China University of Geosciences
Wuhan, China
Yanli Huang,
China University of Mining and
Technology, China

*Correspondence:

Guodong Cao
gdcao@xtu.edu.cn
Yihua Liang
20150631@git.edu.cn

Specialty section:

This article was submitted to
Structural Materials,
a section of the journal
Frontiers in Materials

Received: 05 June 2021

Accepted: 11 October 2021

Published: 25 October 2021

Citation:

Deng D, Cao G and Liang Y (2021)
Filling Treatment of Surface
Subsidence Resulted From
Underground Mining in a High-
Altitude Mine.
Front. Mater. 8:720915.
doi: 10.3389/fmats.2021.720915

In the process of filling the goaf of Huashugou copper mine, the filling aggregate was the mine's self-produced copper flotation tailings. The physical and chemical property tests showed that the tailings were relatively fine, and the cumulative contents of the 7.5, 15, 80, and 90 μm particles were 56.99, 79.46, 99.88, and 100%, respectively. PSA42.5 Portland slag cement was selected as the cementing material for the tests. The amount of finely ground blast furnace slag added to the cement was 20–50%. The filling test blocks of all proportions were demolded within 24–36 h, and the integrity of the formed filling bodies was satisfactory. Among them, the uniaxial compressive strength of the test block formed by the filling slurry with a tailings-to-cement ratio of 3/1 and a concentration of 74% after 3, 7, 28, and 60 days reached 0.833, 2.026, 4.520, and 6.560 MPa, respectively. The strengths of the other filling blocks also met the engineering design requirements. Based on the statistical regression analysis method, the influences of the slag cement content χ_1 and the tailings water content χ_2 on the filling body's strength σ were analyzed. The regression calculation also considered the interaction between χ_1 and χ_2 , and the obtained multiple nonlinear regression model successfully predicted σ . In production and application, the large density of tailings would accelerate their settling, which could easily cause blockage during the transportation of filling slurry through the pipeline. Regarding a series of existing filling materials and technical conditions, the filling process investigated in this study overcomes several unfavorable conditions. Using advanced and reliable technology and an industrial filling pump with a delivery pressure of 10 MPa, the prepared filling slurry concentration was 68–72% and the flow rate was 56–79 m^3/h . The tailings and PSA42.5 Portland slag cement combined quite well. The filling body in the goaf demonstrated excellent homogeneity, and the various industrial indicators met the technical requirements for mining deposits. The preparation of high-quality filling materials with a smooth filling process has played a positive role in the prevention and treatment of surface mountain cracks and collapse during underground mining in high-altitude areas.

Keywords: high-altitude mine, portland slag cement, surface collapse and damage, blast furnace slag, environmental protection

INTRODUCTION

When using a mine's own tailings for goaf filling, the supply of tailings should be convenient and sufficient. In addition, the physical and mechanical properties of the cemented filling materials should satisfy the technical requirements and should ultimately have a certain technological and economic competitiveness (Behera et al., 2019; Zheng and Li, 2020). In the search for technically feasible, safe, and reliable filling materials, many recent studies have conducted relevant filling material development and performance analysis, and they have achieved some progress in developing economically viable filling materials (Chen et al., 2020; Li et al., 2020). For example, in terms of block stone cemented filling materials, several studies have optimized the gradation of the waste rock produced during the mining process, compared and verified the combination of different tailings and stone contents, and obtained a filling material with a better density (Wu et al., 2021). In the high-grade iron ore mining process in the Ukrainian PJSC zaporizhzhia and Pivdenno-Bilozerske mines, cemented rock fill materials were used for goaf filling, which provided stable surrounding rock conditions for safe production, reduced industrial waste emissions, and inhibited surface subsidence hazards (Oleg et al., 2021). To obtain filling materials with stable mechanical properties, several researchers have comprehensively studied the interaction between cemented filling bodies and rock interfaces, analyzed the factors influencing the fracture toughness, and established a theoretical basis for the resource utilization of mining solid waste (Fang and Mamadou, 2020). In the treatment of ultra-fine particle tailing backfill materials, some researchers have adopted the method of flocculation and sedimentation of fine-particle tailings to accelerate the concentration of the tailings. This enabled the fine particle tailing mortar to reach the concentration required for the process in a shorter period. Combining the filling mortar and cementitious materials in a certain ratio can form a filling body with a strength suitable for the mining approach, thereby creating feasible conditions for the preparation of the filling slurry (Cui, 2018; Zhao et al., 2020).

When using tailings and cementitious materials to prepare a filling slurry, due to the particularity of the physical and chemical properties of the tailings, the mechanical properties of the filling formed by the combination of fine particle tailings and cementitious materials are less ideal, and the low strength of the filling body will affect the subsequent mining process (Na et al., 2021; chao et al., 2020). For example, the low strength of the filling body can cause many safety problems in the roof of the large section of roadway and in the chamber roof in the high stress area. The filling body can collapse after being exposed through mining of the adjacent pillar. This can affect the ore extraction operation of the scraper and the subsequent ore grade, which can in turn reduce the beneficiation efficiency and increase the beneficiation costs. The filling slurry cannot become consolidated and harden normally for a long time after entering the goaf, which can cause the filling retaining wall to exhibit excessive hydrostatic pressure and potentially crack. To address these problems, several researchers have optimized and

developed filling materials for the specific conditions of mine filling projects (Ouattara et al., 2018; Zhang et al., 2020). In studies focused on improving the strength of the filling body, researchers have optimized the combination of different filling aggregates. Based on theoretical analysis and experimental verification, the densities and mechanical strengths of the filling materials were improved, and the effect of the filling bodies on maintaining the stability of the rock formation was also improved (Wenbin et al., 2021; Zhang et al., 2021). In the evaluation of the *in-situ* performance of cement paste, researchers have developed a curing under applied pressure system (CUAPS) to understand the consolidation behavior of *in-situ* cement paste materials in field tests (Bruno et al., 2010). In split Hopkinson pressure bar (SHPB) tests of the dynamic mechanical behavior of cemented backfill materials, it has been shown that the failure mode of cemented backfill materials is similar to that of low-strength concrete. This finding can be used to guide the strength design of deep mining backfill (Tan et al., 2019). For a similar case, another study tested the geotechnical characteristics of peat-based cover materials. The test items included the properties of compaction, consolidation, and hydraulic and thermal conductivities. These methods provide a reference for studies of the performances of filling bodies (Khoshand and Fall, 2016).

The stability of the backfill is an important part of the backfill's stop design. A good backfill can effectively protect the pillar and roof from being damaged. In view of the stability of the backfill, some researchers have determined the aspect ratio H/B of the stope workspace and have verified the calculations through field implementation (Li and Aubertin, 2012). Based on a dynamic model of blasting vibration monitoring of mine backfill and field instruments, it is possible to use blasting vibration data to understand the state of the backfill, which can be used to effectively deal with the adverse consequences of backfill damage (Emad et al., 2018). Regarding the influence of blasting vibrations on filling damage, several researchers have used dynamic numerical simulations to characterize the blasting vibrations and have confirmed that they are the main reason for the wedge-shaped damage to the filling body (Zaka and MitriHani, 2014). In terms of blasting vibration damage of cemented rock fill (CRF), related studies have utilized monitoring blasting vibrations to evaluate the stability of CRF and have provided a theoretical basis for related drilling and blasting mining design (Emad et al., 2015). In terms of improving the stability of the filling body, a previous study adopted several feasible techniques to strengthen the filling body, which greatly reduced the probability of the collapse of the filling body (Emad et al., 2012). For example, in terms of shortening the consolidation and hardening time of the cemented filling slurry, the addition of fillers/additives and microscopic analysis provided a basis for accelerating the consolidation and hardening of the filling slurry (Belem et al., 2001; Benzaazoua et al., 2004; XU et al., 2017). Regarding cemented backfill with a high sulfur content, some researchers have analyzed multiple aspects (involving physics, chemistry, and mineralogy) and proposed feasible ideas for improving the performance of the backfill (Benzaazoua et al., 1999). Regarding the influence of sulfate-rich mine water on the mechanical behavior of cemented paste

backfill (CPB), researchers have immersed CPB samples in sulfate solutions of different concentrations (0, 0.1, 1, and 10 g/L). By testing the strength of each curing time, the microstructure changes of the CPB were observed. This study revealed the significant influence of the sulfate concentration on the formation and crystallization of hydration products and provided several reasonable suggestions for the engineering design of goaf filling (Belem et al., 2000).

To make full use of the limited mineral resources, properly disposing of the solid waste generated in the production processes in metal and non-metal mines can avoid subsequent environmental pollution and achieve safe production of mineral deposits. As an important means of preventing and managing the potential risks of environmental pollution in mines, the current filling mining technique has become one of the main techniques used in various mines (Deng et al., 2014). In the mining of deep mineral resources, in the face of more complex rock mechanics conditions, underground mining can encounter many unknown difficulties. Thus, it is essential to improve goaf filling and its maintenance in order to create a safe working environment for daily production (Cai and Brown, 2017). Among various mining methods, the filling method combines the output of coal gangue or tailings with the formation of the goaf, creating a circular relationship between the supply and demand. The feedback is to provide enterprises with a positive state of environmental safety and efficient ore recovery (Lu and Fall, 2018). In view of the many advantages of backfill mining, the related research has gradually received extensive attention (for both metal and non-metal mines), and scientific research on the properties of various materials and engineering conditions is making positive progress (Sun and Ren, 2012). The Huashugou copper mine in the Jingtieshan mining area of the Jiuquan Iron and Steel Group in Gansu Province is a high mountain area located in the western part of the North Qilian Mountains, with an altitude of 2,700–3,200 m, a relative elevation difference of about 500 m, and an average slope of 48°. To better recover the copper resources, filling mining was implemented in the Huashugou copper mine to mine the ore body in order to achieve the purpose of timely backfilling of the goaf and reducing the tailings discharge (Liang et al., 2013; Wang, 2013; Ran et al., 2014). From the perspective of environmental protection and comprehensive utilization of minerals, the application of this approach has played a positive role in the sustainable development of mines.

MATERIALS AND METHODS

Tailings

The experiments used tailings as the aggregate of the filling materials. The tailings were obtained from the copper concentrator plant (with an annual copper ore processing capacity of 300,000 t) of the Jingtieshan iron mine. In order to easily obtain the typical tailing samples on site, the tailing mortar was discharged into several 75 L plastic buckets with DN50 plastic pipes at different time intervals during the normal operation of the mine's concentrator for 3–5 days. After filling the plastic



FIGURE 1 | The tailing was dried in the laboratory.

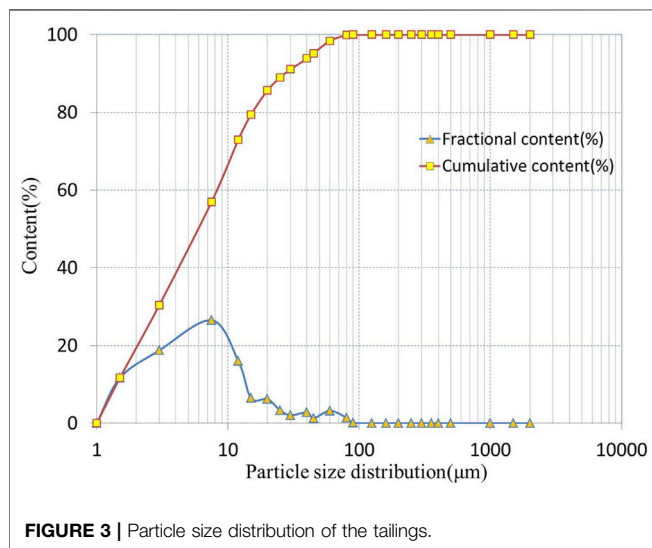
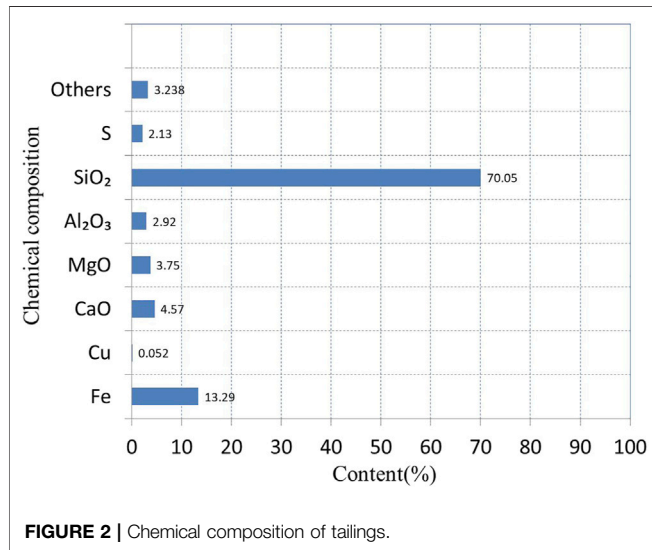
buckets with low concentrations of tailing mortar, the plastic buckets were gradually tilted after a period of natural sedimentation (until the tailing particles no longer moved and settled) to allow the water in the upper part of the buckets to flow out slowly. To make the sampled tailings more representative, the operation of this process needs to be stable and orderly to avoid the loss of fine particle tailings. The tailings in each plastic bucket were collected and bagged in three layers of woven bags with inner bile. After completing the sample collection, all of the samples were transported by car to the laboratory in Changsha. In preparation for the experiments, all of the samples were oven-dried, sun-dried, and evenly mixed. Before test, the tailing was naturally dried in the laboratory, as shown in **Figure 1**.

To ensure that the test results were representative, the sun-dried tailings used for the physical and chemical properties test were sampled using the quartile method. The physical properties of the tailings have a great impact on the performance of the filling materials. After several multi-point sampling measurements, representative data were obtained. The measurement results for the commonly used physical properties are presented in **Table 1**. The chemical composition of tailings is shown in **Figure 2**. After even mixing, the particle size distribution of the tailings was measured using a Malvern 2000 laser particle size analyzer. The particle size distribution is presented in **Figure 3**.

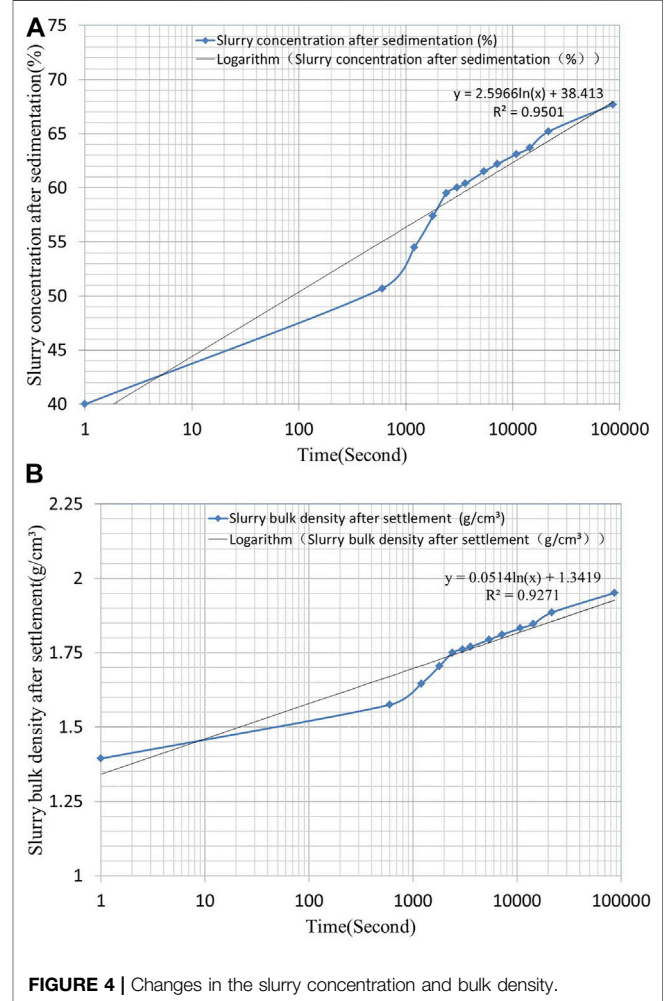
Combined with the on-site filling process, because the concentration of tailing delivered from the copper concentrator plant to the filling station is about 40%, so in this paper the tailings were mixed with an appropriate amount of water to prepare a tailing mortar with a concentration of 40%. The natural sedimentation parameters of the tailing mortar were measured. For more close to the actual production situation, the changes in the final concentration and bulk density of the tailings mortar after 24 h of natural sedimentation are displayed in **Figure 4**. As shown in **Figure 4A**, the sedimentation concentration of tailings with initial concentration of 40% increase with time. The concentration is linear with

TABLE 1 | Test results of the physical properties of the tailings.

Density	Loose bulk density (t/m ³)	Compacted bulk density (t/m ³)	Maximum porosity (%)	Minimum porosity (%)	Angle of repose (°)
2.963	1.298	1.695	56.19	42.79	38.9



sedimentation time from 1 to 600 s. The settling velocity of the tailing mortar is obviously accelerated, the trend of settling curve becomes steeper, inflection point of rise appears, and the settling concentration increases greatly from 600 to 1150 s. After 1,150 s, the settlement velocity slows down and reaches the final settlement state. The settlement concentration is close to 67.7% after 24 h. As can be seen from the curve in **Figure 4B**, the settlement bulk density basically follows the same variation



trend as the settlement concentration. Similarly, after 24 h of natural settlement, the settlement bulk density is 1.951 g/cm³.

Cement

In the proportioning test, we used cement as the filling and cementing material. The cement named as Gobi P.S.A 42.5 Portland slag cement was produced by the Hongda Building Materials Co., Ltd., JISCO Group. After sampling the standard packaged cement, a series of laboratory tests was conducted to determine the properties of the cement, (e.g., density, loose bulk density, compacted bulk density, and angle of repose of natural accumulation). Then, the maximum and minimum porosities were calculated. The chemical composition of cement is shown in

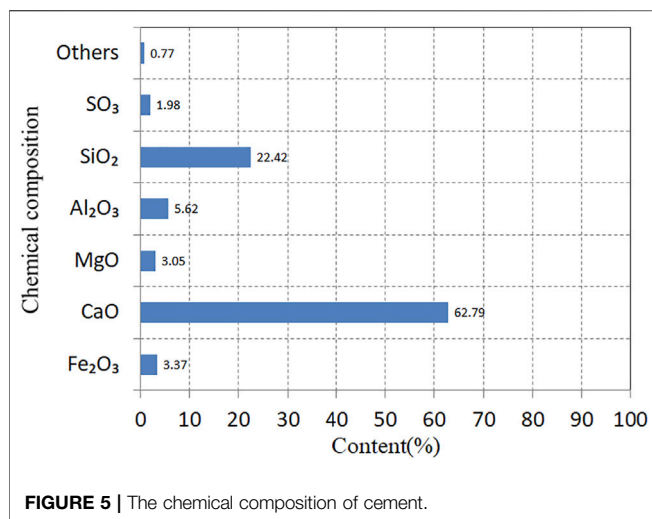


Figure 5. Through testing and data analysis, the basic physical properties of the cement were obtained (Table 2).

Tailings Water

The water used to make the cemented filling test blocks was the tailing water discharged from the Jingtieshan Copper Mine Concentrator. After the basic performance index tests, the density of the tailings water after beneficiation is basically 1 g/cm³, the pH value is about 6.9. The water was neutral, and the water temperature during the test was 18–22°C. The collection of tailing water is shown in Figure 6.

LABORATORY FILLING SLURRY PREPARATION AND FILLING BODY PERFORMANCE TESTS

Filling Slurry

In the proportioning test of the filling materials conducted in the laboratory, the tailings from the copper concentrator were used as the filling aggregate. Gobi Brand P.S.A42.5 Portland slag cement was used as the filling and cementing material; and the water used to make the test blocks was the tailings water from the concentrator. Combined with the mining conditions of the deposit, according to the main factors affecting the mechanical properties of the filling materials and the slurry flow performance during the transportation process, the tests included three groups of filling slurry with concentrations of 70–74% at equal intervals, and four tailings-to-cement ratios of 3:1, 4:1, 6:1, and 8:1. Since the test materials were all fine-grained materials, the size of the test blocks were cubes with a side length of 70.7 mm. After



FIGURE 6 | The cistern of tailing water.

loading all of the materials into the same container and mixing evenly, the test blocks were poured in stages and placed statically. Stage controlled backfilling method is adopted and then the strength of filling body is not strict. Therefore, in the process of laboratory test, the fabricated test block was demolded within 24–36 h, which did not affect the mining technology requirements. The test blocks were demolded according to the consolidation and hardening conditions (more than 24 h), and the temperature of the laboratory curing box was adjusted to 18–22°C. After regular moisturizing and curing at the corresponding times, we used an NYL-300 concrete compression testing machine to test the uniaxial compressive strength of each test block.

By combining the basic physical properties of the test materials, the bulk density parameters of the filling slurry were calculated. The material preparation and consumption of the test materials are presented in Table 3. The materials were uniformly mixed in the laboratory, and the filling slurry after fully mixing is shown in Figure 7A. A filling test block made using the triple concrete test mold is shown in Figure 7B.

Filling Performance Tests

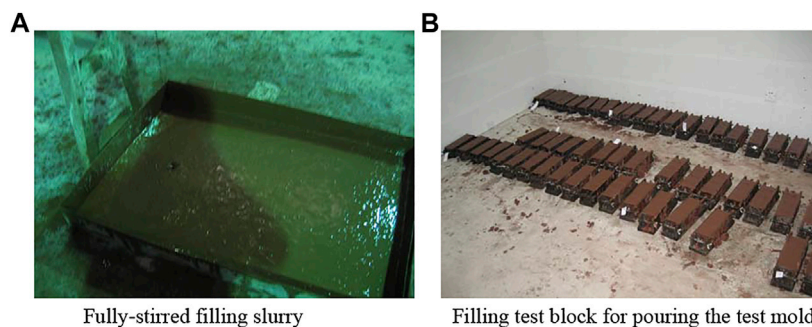
After curing the cemented filling body test blocks in the curing box for 3, 7, 28, and 60 days, the test blocks were taken out of the curing box. The unconfined uniaxial compressive strengths of the filling body test blocks corresponding to each curing time were tested. The strength parameters of the different filling body test blocks were obtained through experiments. After summarizing and sorting, mathematical methods were used to perform statistical analysis, and the variation in the strength of the filling body under different conditions was analyzed. By keeping the tailings-to-cement ratio of the filling material constant, the variation in the strength of the test blocks of each concentration and curing time is shown in Figure 8.

TABLE 2 | Measurement of the physical properties of the cement.

Density	Loose bulk density (t/m ³)	Compacted bulk density (t/m ³)	Maximum porosity (%)	Minimum porosity (%)	Angle of repose (°)
3.132	1.298	1.785	58.55	43.01	39.7

TABLE 3 | Preparation and consumption of the filling materials.

No.	Water/cement	Cement/tailings	Water/(cement + tailings)	Bulk density (t/m ³)	Material consumption (kg/m ³)		
					Water	Tailings	Cement
1	1.714	0.333	0.428	1.876	563	985	328
2	1.555	0.333	0.389	1.924	539	1,039	346
3	1.405	0.333	0.351	1.975	513	1,096	365
4	2.142	0.250	0.428	1.874	562	1,049	262
5	1.944	0.250	0.389	1.922	538	1,107	277
6	1.756	0.250	0.351	1.972	513	1,168	292
7	3.000	0.167	0.428	1.871	561	1,123	187
8	2.722	0.167	0.389	1.919	537	1,184	197
9	2.459	0.167	0.351	1.969	512	1,249	208
10	3.857	0.125	0.428	1.870	561	1,163	145
11	3.500	0.125	0.389	1.917	537	1,227	153
12	3.162	0.125	0.351	1.968	512	1,294	162

**FIGURE 7 |** Filling slurry stirring and test block production.

When the concentration of the filling slurry is kept constant, the change in the strength of the test block for each curing time with a given tailings-to-cement ratio is presented in **Figure 9**. For the filling test blocks with the same curing time, the variation in the strength of the test blocks of each concentration with the tailings-to-cement ratio is illustrated in **Figure 10**.

To understand the influences of the different factors on the strength of the filling body, the cement-tailings ratio χ_1 and the concentration of the filling slurry χ_2 were taken as independent variables, and the interaction between the cement-tailings ratio χ_1 and the concentration of the filling slurry χ_2 was also considered. In addition, the day 3, day 7, day 28, and day 60 uniaxial compressive strengths of the test blocks σ_{03} , σ_{07} , σ_{28} , and σ_{60} were used as dependent variables. At the initial stage of the original data induction and arrangement, the relevant data should be listed in the spreadsheet. The strength of the backfill corresponding to the specific cement-sand ratio and the concentration of the backfill slurry should be listed. The strength samples at the same curing age should be grouped into a column to clarify the strict correspondence between the data. Using data processing methods similar to those described in previous studies, the statistical regression analysis of the test parameters was performed using mathematical software, e.g., Excel or Matlab (Quan et al., 2007; Qiao et al., 2019; de Souza et al., 2021; Freise et al., 2021). Regression statistical analysis is

shown in **Table 4**. The analytical relationships between the uniaxial compressive strength and the influencing factors of each group of filling test blocks were established. The obtained multiple regression equation for the strength of the filling body is presented in **Table 5**.

FIELD FILLING INDUSTRIAL TEST AND RESULT ANALYSIS

Field Filling Industrial Test

In the industrial testing stage of the filling, when the tailings entering process was completed, after a period of natural sedimentation, the concentration of the tailing mortar was increased after deposition. A certain amount of water was secreted from the upper part, and the sidewalls of the tailings silo were opened row by row from top to bottom. The stepped drain valve gradually drained part of the clarified water from the upper part of the tailings mortar, leaving some for the slurry adjustment and concentration adjustment. Then, the air compressor was turned on to compress the tailings mortar in the horizontal sand silo. After about 40–50 min, the tailings mortar throughout the entire horizontal sand silo exhibited a uniform boiling state and became a porridge-like fluid, which rolled up and down due to the agitation of the bubbles. At this

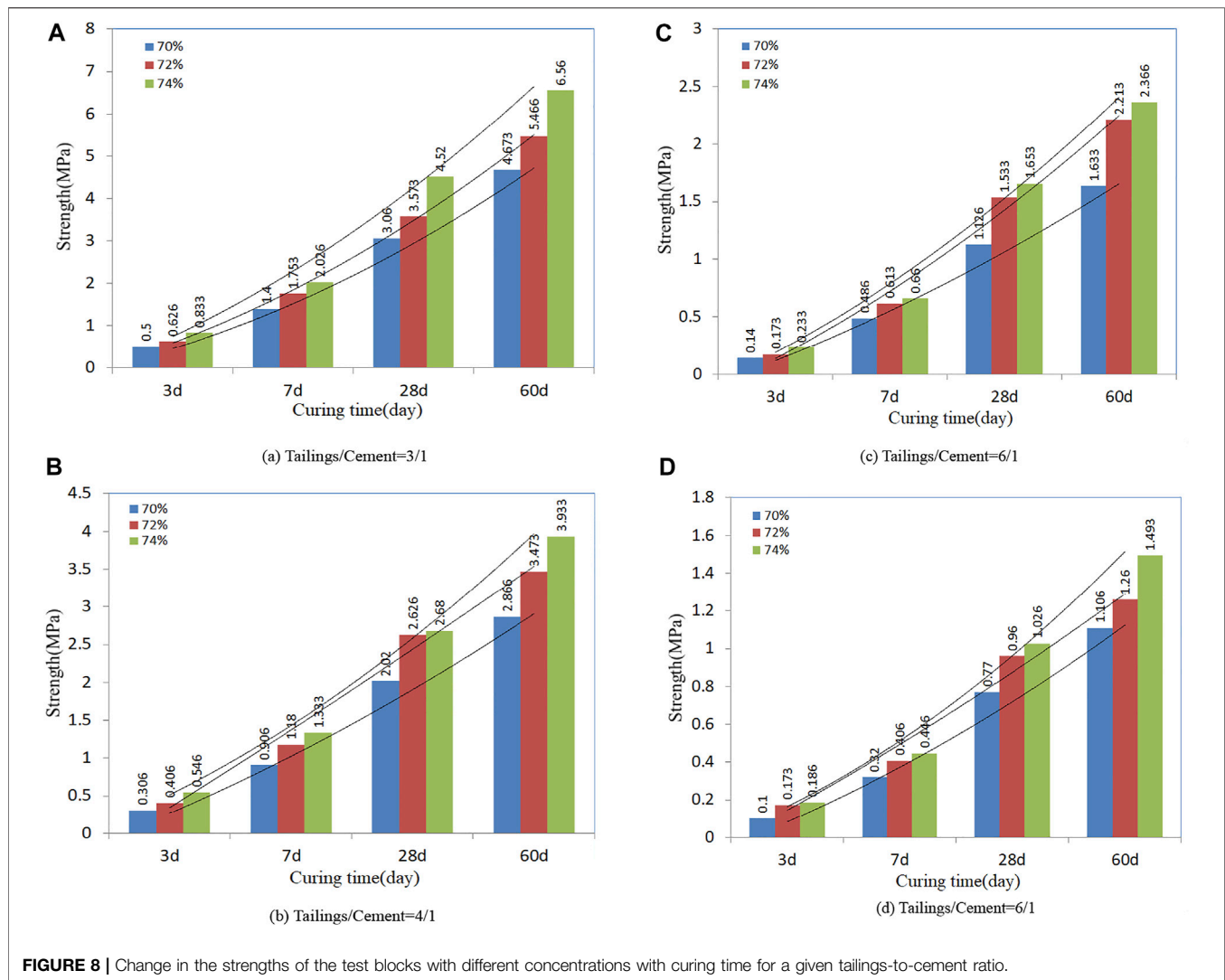


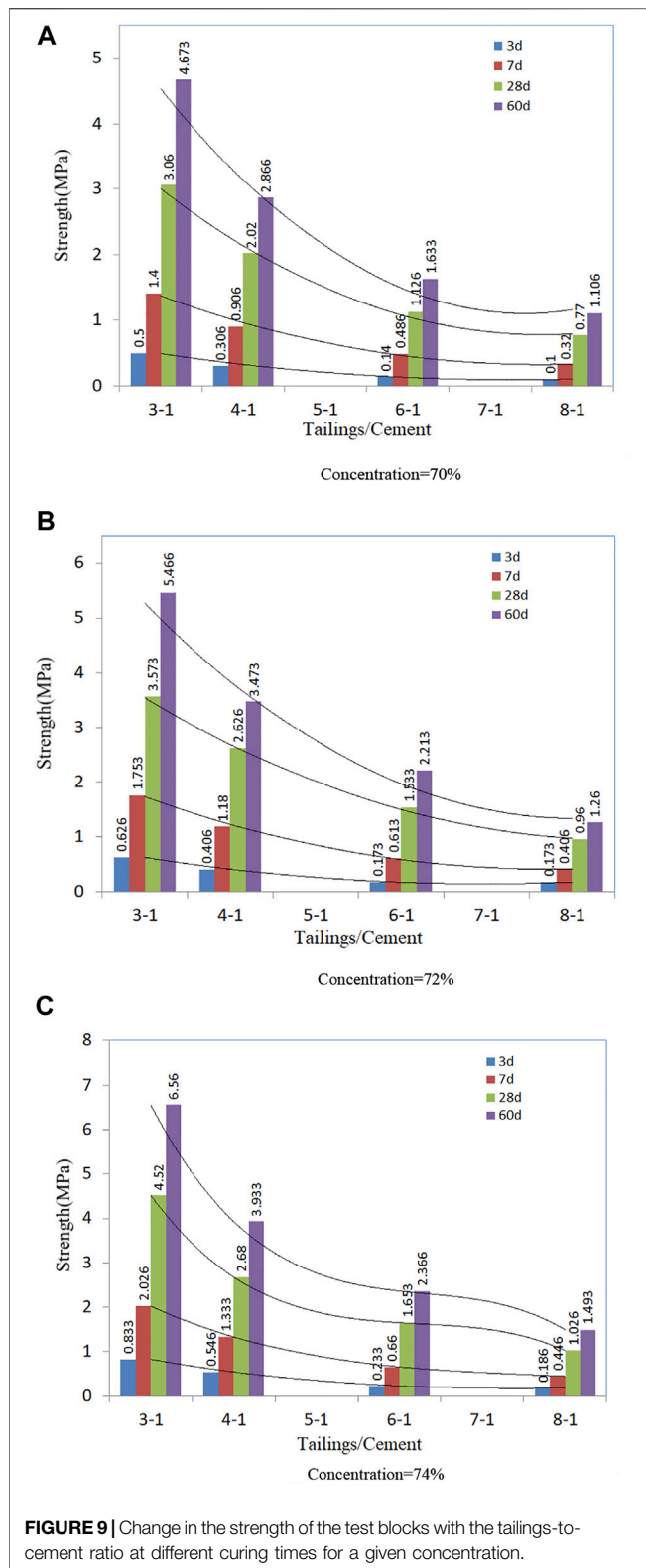
FIGURE 8 | Change in the strengths of the test blocks with different concentrations with curing time for a given tailings-to-cement ratio.

time, the liquefaction of the tailings mortar was completely uniform. Then, the sand discharge valve at the bottom of the horizontal sand silo was opened to discharge the sand. The flow chart of filling process is shown in **Figure 11**.

The uniform activation and stirring of the two-stage mixer after the addition of the cement enabled the filling slurry to flow into the suction tank of the filling industrial pump. After being pressurized by the filling industrial pump, it was transported to the distant goaf for cementation and filling. The first phase filling slurry preparation station was located in a huge mountain with an altitude of +2,880 m. The equipment in the filling slurry preparation station was located in a large rock chamber. The equipment in the chamber is shown in **Figure 12**. The underground cement silo fed the horizontal mixer through a screw conveyor and an electronic scale. The cement silo and screw conveyor are shown in **Figure 13**. The connecting roadway at the end of the goaf was filled with a brick filling retaining wall. Three DN150 pipelines were installed on the retaining wall as observation tubes.

Filling Operation and Result Analysis

Throughout the period of filling operations and adjustments, the downhole filling system underwent a smooth process and the technical conditions were sufficient for long-term operation. When the material supply was sufficient, the filling system fully satisfied the filling capacity requirements of the goaf generated by the mining and a separation capacity of 300,000 t/a of copper ore. The horizontal sand silo had a sand concentration of 40–47%. After 8–12 h of flocculation and sedimentation, the sand concentration basically stabilized at about 65–69% for a long time. The flow rate was controlled at around 65–75 m³/h through the control valve, and the concentration of the filling slurry was approximately 71%. After adding PSA42.5 Portland slag cement, the hydration reaction of the cement was sufficient, and the flow rate of the filling slurry after the addition of the cement also increased. When the filling slurry passed through the filling retaining wall, a higher tailings-to-cement ratio of 3:1–4:1 was used (i.e., the cement content of the dry material was 25–20%), and the increase in the height of the filling slurry level was controlled



at 1.85–2.25 m. In each stage of the filling operation, there was no slurry leakage around the filling retaining wall, indicating that the surface of the filling retaining wall and the surrounding rock wall

were maintained by the M7.5 sprayed cement mortar. The cracks were filled, and it was difficult for the water in the filling slurry to flow out of the periphery. Thus, the filling retaining wall was relatively stable.

After several episodes of operation and adjustment, the filling system was able to operate stably for a long time. For the case of two 8 h shifts per day, the working conditions of the equipment were good and the filling efficiency was fully reflected. By measuring the exposed filling body within a height of 1.5–8 m from the bottom, the strength of the filling body test block was determined to be 2.75–4.65 MPa. The integrity of the filling body was intact, and its color was grayish brown and grayish white. The filling body did not collapse when the self-standing height exceeded 20 m. From the perspective of the fracture feel of the unexposed part, the filling body was relatively hard and dense, with a bulk density of about 1.87–2.15 g/cm³. An accidental shutdown was caused by a cement supply problem, and the production had to be suspended. This means that when the supply of various filling materials is sufficient, the filling system can operate for a long time.

DISCUSSION

1) On the basis of uniform sampling and testing, the relevant physical properties of the copper flotation tailings were obtained. According to the results of the laser particle size tests, the content of the 7.5 μ m particles in the tailings from the Huashugou copper mine was relatively high, with fractional and cumulative contents of 26.53 and 56.99%, respectively. The fractional and cumulative contents of the 15 μ m particles were 6.46 and 79.46%, respectively. The fractional and cumulative contents of the 80 μ m particles were 1.43 and 99.88%, respectively. When the particle size was 90 μ m, the cumulative content of the particles reached 100%. Therefore, the tailings were extremely fine-grained tailings (i.e., less than 90 μ m). In the pipeline transportation process, very fine particle tailings typically have a strong viscosity, so the tailings can easily adhere to the pipe wall and reduce the cross-sectional area of the transportation pipeline. At this time, the transportation pipeline's pressure will increase sharply. In the process of selecting a filling slurry conveying pump, after considering this problem, an industrial filling pump with an outlet pressure of greater than 10 MPa was selected. Based on the daily production situation, the prepared filling slurry delivery conditions were normal. The conveying flow and pressure were normal and stable. In the preliminary filling process, the height difference of the filling pipeline is not large, and the conveying distance is about 450–1,000 m. With the increase of the mining depth, the conveying resistance of the filling slurry will be further reduced. Therefore, the filling industrial pump with the outlet pressure of 10 MPa can meet the technical requirements of the filling process.

2) During the natural sedimentation of the tailings with an initial concentration of 40%, as the settling time increased, due to the combined actions of gravity and buoyancy of the tailings

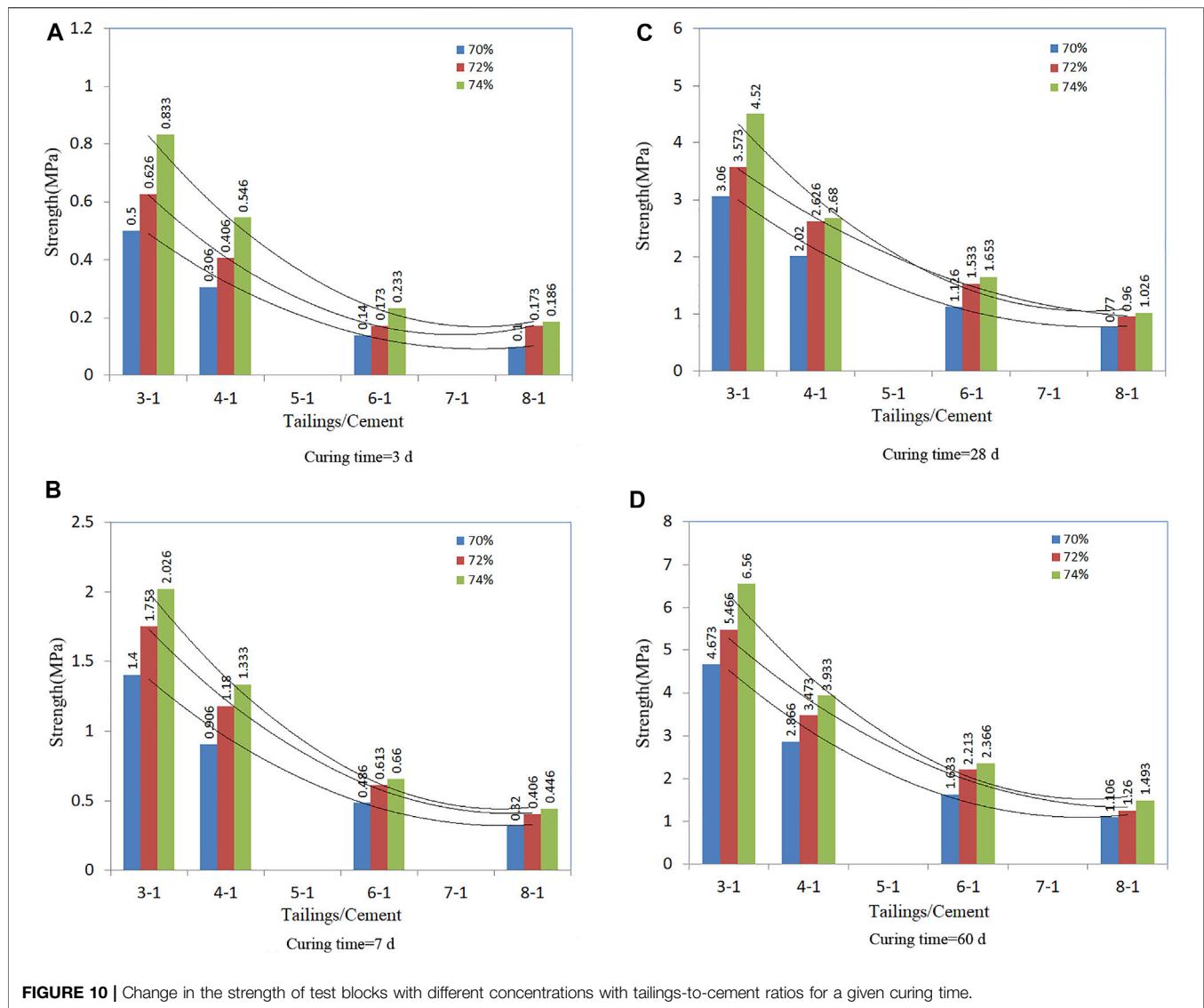


FIGURE 10 | Change in the strength of test blocks with different concentrations with tailings-to-cement ratios for a given curing time.

TABLE 4 | Regression statistics.

Regression analysis	σ_{03}	σ_{07}	σ_{28}	σ_{60}
Multiple R	0.996592	0.995982	0.986532	0.989930
R^2	0.993196	0.991981	0.973245	0.979961
Adjusted R^2	0.986393	0.983962	0.946489	0.959922
Standard error	0.027637	0.073348	0.276656	0.355912
Observed value	11	11	11	11

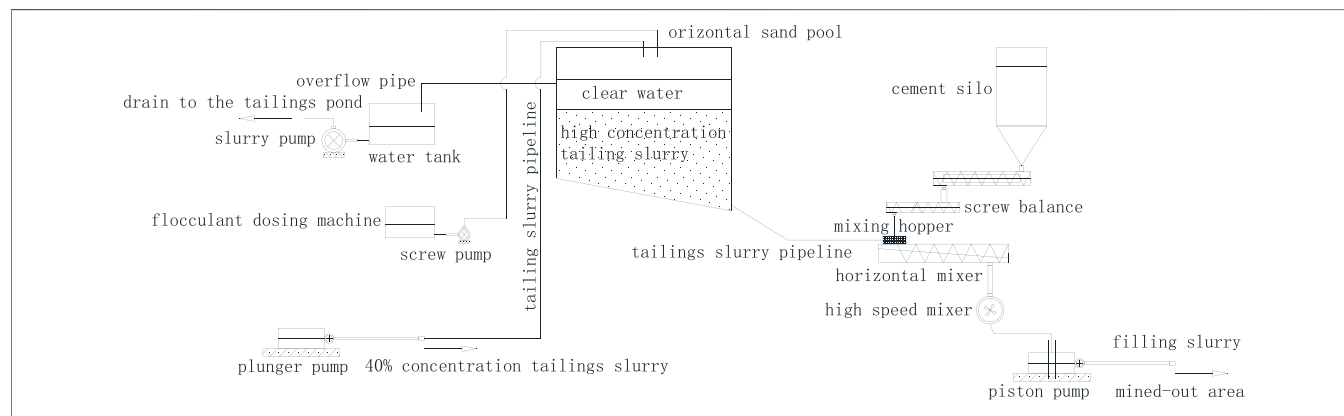
particles, the initial slurry buoyancy was small due to the low concentration, so the tailings particles settled faster. As the slurry concentration continued to increase, the buoyancy of the slurry caused by the tailings particles during the sedimentation process also increased and the settling speed gradually decreased. Therefore, the net increment of water initially increased and then decreased. The total amount of water increased to the maximum and then stabilized. The

amount of slurry decreased with the continuous settlement of the tailings. When the pores of the tailings were completely filled with water, the total amount of tailings mortar was constant. Throughout the entire sedimentation process, the trends of both the tailings slurry concentration and the bulk density of the slurry gradually reached their maximums. In the natural settlement process of tailings, under the combined action of self-gravity and buoyancy of slurry paste, the large particles precipitate in advance, and the small particles settle gradually. With the increasing pressure between settling particles, the pore volume between the tailings gradually decreases, thus increasing the bulk density of the tailings. In the production process, flocculant is always added to speed up the settling speed of small particles tailings to meet the daily production demand.

- After evenly mixing the tailings and slag cement with the tailings water, the filling slurries with different mixing ratios were prepared and poured into 70.7 mm³ cube test blocks to

TABLE 5 | Multiple regression equation for the strength of the filling body at different curing times.

No.	Regression models
1	$\sigma_{03} = 13.5672 - 27.984\chi_1 - 35.916\chi_2 + 13.6323\chi_1\chi_2 + 23.9709\chi_2\chi_2 + 36.9638\chi_1\chi_2$
2	$\sigma_{07} = 0.55438 - 36.832\chi_1 - 1.6721\chi_2 + 29.2287\chi_1\chi_1 + 1.64595\chi_2\chi_2 + 49.5529\chi_1\chi_2$
3	$\sigma_{28} = 4.19585 - 84.865\chi_1 - 10.510\chi_2 + 62.3888\chi_1\chi_1 + 7.83846\chi_2\chi_2 + 112.936\chi_1\chi_2$
4	$\sigma_{60} = 36.3514 - 117.77\chi_1 - 98.950\chi_2 + 124.100\chi_1\chi_1 + 70.7577\chi_2\chi_2 + 141.086\chi_1\chi_2$

**FIGURE 11** | Flow chat of filling process.**FIGURE 12** | Part of the filling equipment chamber.**FIGURE 13** | Quantitative feeding of the underground cement silo.

test their mechanical properties. For each group of test blocks with different curing times, the test results suggest that as the slag cement content increases and the water content decreases, the uniaxial compressive strength of the filling body increases. The slag cement content plays the dominant role in the strength of the filling body, while the addition of tailings water has little effect on the strength of the filling body. In the statistical analysis of the strength test results of the cemented filling body, the slag cement content (cement-to-tailings ratio)

χ_1 and the tailings water content (filler slurry concentration) χ_2 were taken as two independent variables, and the interaction between the independent variables was taken into account. Multivariate non-linear statistical regression analysis was conducted to obtain the uniaxial compressive strengths of the cemented filling bodies σ_{03} , σ_{07} , σ_{28} , and σ_{60} at 3, 7, 28, and 60 days, respectively.

- 4) Taken the variation characteristics and influencing factors of backfill strength into account, the value of significance level α

was set as 0.05. $n-m-1 = 11-2-1 = 8$, where n and m were the number of samples tested and the dimension of unknown quantity respectively. As can be seen from the “Correlation coefficient Critical value Table”, $R_{0.05}(8)$ is equal to 0.6319. For the 3, 7, 28 and 60 days strength of the backfill, $R_{03} = 0.996592$, $R_{07} = 0.995982$, $R_{28} = 0.986532$, $R_{60} = 0.989930$, which are greater than $R_{0.05}(8)$. It indicates that the regression Equations 1 and 2, 3 and 4 are significant at the level of $\alpha = 0.05$. That is to say, the cement-sand ratio and the filling slurry concentration have a significant effect on the strength of the backfill. Through the above correlation coefficient analysis, it can be well explained that the multiple regression model of uniaxial compressive strength at each curing age is of good feasibility, which can provide relevant theoretical basis for the future detection of filling quality.

- 5) In the daily operation of the filling system, the long-distance pipeline transportation process of the tail mortar was relatively stable, and there was basically no large-scale pipe blockage accident. In the process of pumping and conveying the filling slurry, due to the finer tailings and cement particles, the prepared filling slurry adhered to the inner wall of the pipeline, which reduced the friction of the filling particles with the inner wall of the pipeline and protected the pipeline. During the disassembly inspection of the seamless steel pipes on site, it was found that the filling pipes were less worn. Taking into account the field industrial conditions, the annual ore processing capacity of the Huashugou copper mine is 300,000 t of copper ore, and the annual discharge of the tailings is 277,200 t. By adopting the filling method, about 103950 t of copper ore flotation tailings can be continuously filled underground, which can greatly reduce the damage caused to the ecological environment by the tailings discharge, and a large amount of solid waste can be properly treated. After goaf filling, the surrounding broken rock strata can be supported and maintained by high-quality fillings. The fillings can absorb a large amount of the high stress transferred from the strata. Therefore, the movement of the underground strata will decrease and gradually disappear. The collapse and cracking of the surface mountains in the mining area can also be effectively resolved.
- 6) The goaf filling is adopted to treat the surface collapse in the underground mining in high altitude areas. Although this kind of technology has a broad application prospect, it faces many technical challenges. The climate in high altitude areas is usually harsh, and the low temperature environment in winter is extremely unfavorable to the long-distance pipeline transportation of the filling slurry. Meanwhile, the mineral composition, physical and mechanical property of the filling materials have a great influence on the transportation and mechanical properties of filling materials, which makes the application of filling materials limited. However, all kinds of adverse factors may occur on site, so it is necessary to consider the physical and chemical properties of the filling material, the engineering conditions when select the filling material. The filling

material can finally obtain a more reliable promotion value in terms of technology, economy and safety.

CONCLUSIONS

Limited to the field industrial and engineering conditions, the Huashugou copper mine implemented an underground filling system for goaf filling. Compared with the ground filling station, its design and construction are extremely difficult. This project is typical of similar engineering conditions. It is an underground full tailings-cement cementing filling system, which is rare in China and abroad. The project successfully filled the copper tailings in an underground alpine cold region, and the harmless utilization rate of the tailings filling was about 60%. The remaining 40% of the tailings were filtered or dry piled, and all of the tailings were treated to achieve harmlessness, thus playing an active role in environmental protection and pollution prevention.

Another difference between the underground filling system and the surface filling station is that because it is deeply buried in a huge mountain, the daily production, construction, and operation spaces are narrow and compact, and the light and ventilation conditions are far poorer than those on the surface. The sensory perspective of the operator is limited. Because these various unfavorable factors will have a series of negative effects on people, the system includes high-efficiency ventilation facilities for pedestrians, lighting, and dust collectors, which improve the quality of the underground working environment and the safety of the operators. Therefore, the construction and completion of the project is innovative.

For the downhole pumping cemented filling system, the safety and reliability of the pump is the key to the smooth operation of the entire system. The particle gradation of the total tailings-cement mixture slurry of the Huashugou copper mine is relatively reasonable, and the formed slurry does not have obvious segregation, which is convenient for pipeline pumping and conveying. After the filling slurry enters the goaf, it can basically be consolidated and hardened within 24–36 h, and the resulting filling body has uniform and reliable mechanical properties, which meet the double-layer technical requirements of large-scale copper deposit mining and bulk mine industrial solid waste disposal.

DATA AVAILABILITY STATEMENT

The original contributions presented in the study are included in the article/Supplementary Material, further inquiries can be directed to the corresponding authors.

AUTHOR CONTRIBUTIONS

DD wrote the main text of the manuscript. GC and YL collected and analyzed the data. All authors reviewed and commented on the manuscript.

FUNDING

The authors gratefully acknowledge support for this research from the National Natural Science Foundation of China (51764009), and the Guizhou Province Science

and Technology Support Plan Project [Grant No. (2018) 2836], and the Scientific Research Fund of Hunan Province Education Department (20A475), and the High-level Talent Gathering Project in Hunan Province (2019RS1059).

REFERENCES

- Behera, S. K., Mishra, D. P., Ghosh, C. N., Mandal, P. K., Singh, K. M. P., Buragohain, J., et al. Characterization of lead-zinc Mill Tailings, Fly Ash and Their Mixtures for Paste Backfilling in Underground Metalliferous Mines. 2019, 78(14):1–13. doi:10.1007/s12665-019-8395-9
- Belem, T., Benzaazoua, M., and Bussi re, B., 2000. Mechanical Behaviour of Cemented Paste Backfill. In: Proc. of 53rd Canadian Geotechnical Conference, Montreal, Canada, October 2000, pp. 373–380.
- Belem, T., Bussi re, B., and Benzaazoua, M. (2001). "The Effect of Microstructural Evolution on the Physical Properties of Paste Backfill," in Proc. Of Tailings and Mine Waste'01 Janvier, 2001, Fort Collins, Colorado, USA, 16–19 January 2001, 365–374.
- Benzaazoua, M., Fall, M., and Belem, T. (2004). A Contribution to Understanding the Hardening Process of Cemented Pastefill. *Minerals Eng.* 17 (2), 141–152. doi:10.1016/j.mineng.2003.10.022
- Benzaazoua, M., Ouellet, J., Servant, S., Newman, P., and Verburg, R. (1999). Cementitious Backfill with High Sulfur Content Physical, Chemical, and Mineralogical Characterization. *Cement Concrete Res.* 29, 719–725. doi:10.1016/s0008-8846(99)00023-x
- Bruno, B., Bruno, B., Yilmaz, E., Benzaazoua, M., and Belem, T., (2010). Assessment of the Modified CUAPS Apparatus to Estimate *In Situ* Properties of Cemented Paste Backfill. *Geotechnical Test. J.* 33(5). doi:10.1520/GTJ102689
- Cai, M., and Brown, E. T. (2017). Challenges in the Mining and Utilization of Deep Mineral Resources. *Engineering* 3 (4), 432–433. doi:10.1016/j.eng.2017.04.027
- Chao, X. Y., Xu, T., Wasantha, P. L. P., Yang, T. H., and Fu, T. F. (2020). Dynamic Disaster Control of Backfill Mining under Thick Magmatic Rock in One Side Goaf. *A case study* 27 (10), 3103–3117. doi:10.1007/s11771-020-4532-6
- Chen, S., Du, Z., Zhang, Z., Yin, D., Feng, F., and Ma, J. (2020). Effects of Red Mud Additions on Gangue-Cemented Paste Backfill Properties. *Powder Tech.* 367, 833–840. doi:10.1016/j.powtec.2020.03.055
- Cui, L. (2018). Mamadou Fall. Multiphysics Modeling and Simulation of Strength Development and Distribution in Cemented Tailings. *Backfill Structures* 12 (1), 1–22. doi:10.1186/s40069-018-0250-y
- de Souza, A., Manoel dos Santos, C., Ihaddadene, R., Cavazzana, G., Abreu, M. C., Pobocikova, I., et al. (2021). Analysis of Extreme Monthly and Annual Air Temperatures Variability Using Regression Model in Mato Grosso Do Sul, Brazil. *Model. Earth Syst. Environ.* 2021, 1–17. doi:10.1007/s40808-021-01096-6
- Deng, X., Zhang, J., Zhou, N., An, T., and Guo, S., (2014). The Research and Application of Longwall-Roadway Cemented Backfilling Mining Technology in Extra-thick Coal Seam. *J. Mining Saf. Eng.* 31(06):857–862. doi:10.1007/s12665-017-7120-9
- Emad, M. Z., Mitri, H., and Kelly, C. (2018). Dynamic Model Validation Using Blast Vibration Monitoring in Mine Backfill. *Int. J. Rock Mech. Mining Sci.* 107, 48–54. doi:10.1016/j.ijrmms.2018.04.047
- Emad, M. Z., Mitri, H., and Kelly, C. (2015). In-situ Blast Vibration Monitoring in Cemented Rockfill Stope - a Case Study. *Int. J. Mining, Reclamation Environ.* 31 (2), 119–136. doi:10.1080/17480930.2015.1123600
- Emad, M. Z., Mitri, H. S., and Henning, J. G. (2012). Effect of Blast Vibrations on the Stability of Cemented Rockfill. *Int. J. Mining, Reclamation Environ.* 26 (3), 233–243. doi:10.1080/17480930.2012.707527
- Fang, K., and Mamadou, F. (2020). Insight into the Mode I and Mode II Fracture Toughness of the Cemented Backfill-Rock Interface: Effect of Time, Temperature and Sulphate. *Construction Building Mater.* 262, 120860. doi:10.1016/j.conbuildmat.2020.120860
- Freise, F., Gaffke, N., and Schwabe, R., (2021). Convergence of Least Squares Estimators in the Adaptive Wynn Algorithm for Some Classes of Nonlinear Regression Models. *Metrika.* 84(6)1–24. doi:10.1007/s00184-020-00803-0
- Khoshand, A., and Fall, M. (2016). Geotechnical Characterization of Peat-Based Landfill Cover Materials. *J. Rock Mech. Geotechnical Eng.* 8(05):596–604. doi:10.1016/j.jrmge.2016.05.007
- Li, B., Zhou, N., Qi, W., Li, A., and Cui, Z. (2020). Surface Subsidence Control during Deep Backfill Coal Mining: A Case Study. *Adv. Civil Eng.* 2020, 1–12. doi:10.1155/2020/6876453
- Li, L., and Aubertin, M. (2012). A Modified Solution to Assess the Required Strength of Exposed Backfill in Mine Stopes. *Can. Geotech. J.* 49 (8), 994–1002. doi:10.1139/t2012-056
- Liang, P., Ran, W., Ying, X., and Yao, Z., (2013) Experimental Study on Flocculant Selection for Tailings Settlement. *Mining Tech.* 13(6), 47–49. doi:10.3969/j.issn.1671-2900.2013.06.019
- Lu, G., and Fall, M. (2018). Modeling Postblasting Stress and Pore Pressure Distribution in Hydrating Fill Mass at an Early Age. *Int. J. Geomechanics,* 18(8). doi:10.1061/(asce)gm.1943-5622.0001141
- Na, H., Lv, G., Wang, L., Liao, L., Zhang, D., Guo, L., et al. (2021). A New Expansion Material Used for Roof-Contacted Filling Based on Smelting Slag. *Sci. Rep.* 11 (1), 2607. doi:10.1038/s41598-021-81891-4
- Oleg, B., Mykhailo, P., Vasy, L., Serhii, Z., Sai, K., Saik, P., et al. (2021). Sustainable Underground Iron Ore Mining in Ukraine with Backfilling Worked-Out Area, *Sustainability,* 13(2):834. doi:10.3390/su13020834
- Quattara, D., Mbonimpa, M., Yahia, A., and Belem, T. (2018). Assessment of Rheological Parameters of High Density Cemented Paste Backfill Mixtures Incorporating Superplasticizers. *Construction Building Mater.* 190, 294–307. doi:10.1016/j.conbuildmat.2018.09.066
- Qiao, D., Cheng, W., Xie, J., Wang, J., Huang, F., Mo, Y., et al. (2019). Analysis of the Influence of Gradation on the Strength of a Cemented Filling Body and the Cementation Strength Model. *Integrated Ferroelectrics* 199 (1), 12–21. doi:10.1080/10584587.2019.1592593
- Quan, f. Y., He, J., and Wang, Z. (2007). Application of Multiple Linear Regression in Ore Body Mining. *J. Xi'an Univ. Sci. Technol.* (04), 555–558. doi:10.3969/j.issn.1672-9315.2007.04.004
- Ran, W., Kang, R., and Liang, P. (2014). Experimental Study on Adding Amount of Flocculant. *Mining Tech.* 14 (4), 52–53. 81. doi:10.3969/j.issn.1671-2900.2014.04.021
- Sun, Y. X., and Ren, D. W., (2012). Preparation System Design of Filling Material with Coal Gangue as Coarse Aggregate, 1480:135–138. doi:10.4028/www.scientific.net/AMR.361-363.135
- Tan, Y.-y., Yu, X., Elmo, D., Xu, L.-h., and Song, W.-d Experimental Study on Dynamic Mechanical Property of Cemented Tailings Backfill under SHPB Impact Loading. *Int. J. Minerals Metall. Mater.*, 2019, 26(04): 404–416. doi:10.1007/s12613-019-1749-1
- Wang, J., (2013). Study on the Properties of Cemented Filling Material of Whole Tailings in Huashugou Copper Mine, Jingtieshan Mine. *Sci. Tech. Info.* 46 (12), 90–91. doi:10.3969/j.issn.1672-3791.2013.12.054
- Wen bin, X., Liu, B., and Wu, W. L., (2021). Strength and Deformation Behaviors of Cemented Tailings Backfill under Triaxial Compression. *J. Cent. South Univ.*, 27(12), 3531–3543. doi:10.1007/s11771-020-4568-7
- Wu, J., Yin, Q., and Gao, Y., (2021). Particle Size Distribution of Aggregates Effects on Mesoscopic Structural Evolution of Cemented Waste Rock Backfill. *Environ. Sci. Pollut. Res.* 28, (2):1–13. doi:10.1007/s11356-020-11779-9
- Xu, W., Tian, X., Qiu, Y., Dang, P., and Yin, T., (2017). Experiment of the Resistivity Characteristic of Cemented Backfill Mass during the Whole Consolidation Process. *J. China Univ. Mining Tech.* 46(02):265–272+344. doi:10.13247/j.cnki.jcumat.000648

- Zaka, E. M., and MitriHani, K. C., (2014). Effect of Blast-Induced Vibrations on Fill Failure in Vertical Block Mining with Delayed Backfill. *Can. Geotechnical J.* 51(9):975–983. doi:10.1139/cgj-2013-0305
- Zhang, S., Yang, L., and Qiu, J. (2021). Fluidity and Strength Behaviors of Cemented Foam Backfill: Effect of Particle Size Distribution and Foaming Agent Dosage. *Bull. Eng. Geology. Environ.* 80(4):3177–3191. doi:10.1007/s10064-021-02117-5
- Zhang, X., Xu, M., Liu, L., Huan, C., Zhao, Y., Qi, C., et al. (2020). Experimental Study on thermal and Mechanical Properties of Cemented Paste Backfill with Phase Change Material. *J. Mater. Res. Tech.* 9 (2), 2164–2175. doi:10.1016/j.jmrt.2019.12.047
- Zhao, K., Xiang, Y., and Zhu, S. (2020). Acoustic Emission Investigation of Cemented Paste Backfill Prepared with Tantalum–Niobium Tailings. *Construction Building Mater.* 237, 117523. doi:10.1016/j.conbuildmat.2019.117523
- Zheng, J., and Li, L. (2020). Experimental Study of the "Short-Term" Pressures of Uncemented Paste Backfill with Different Solid Contents for Barricade Design. *J. Clean. Prod.* 275 (1), 123068. doi:10.1016/j.jclepro.2020.123068
- Conflict of Interest:** The authors declare that the research was conducted in the absence of any commercial or financial relationships that could be construed as a potential conflict of interest.
- Publisher's Note:** All claims expressed in this article are solely those of the authors and do not necessarily represent those of their affiliated organizations, or those of the publisher, the editors and the reviewers. Any product that may be evaluated in this article, or claim that may be made by its manufacturer, is not guaranteed or endorsed by the publisher.
- Copyright © 2021 Deng, Cao and Liang. This is an open-access article distributed under the terms of the Creative Commons Attribution License (CC BY). The use, distribution or reproduction in other forums is permitted, provided the original author(s) and the copyright owner(s) are credited and that the original publication in this journal is cited, in accordance with accepted academic practice. No use, distribution or reproduction is permitted which does not comply with these terms.



Strength Prediction of Coal-Based Solid Waste Filler Based on BP Neural Network

Feisheng Feng¹, Lirong Li², Jiqiang Zhang^{1*}, Zhen Yang³ and Xiaolou Chi¹

¹State Key Laboratory of Mining Response and Disaster Prevention and Control in Deep Coal Mine, Anhui University of Science and Technology, Huainan, China, ²Shanxi Coking Coal Group Co., Ltd., Taiyuan, China, ³College of Information Science and Engineering, Henan University of Technology, Zhengzhou, China

The compressive strength of filling body is an important index to characterize the filling and mining effect of coal mine. In order to accurately predict the strength of coal-based solid waste filler (CBSWF) to guide the safe, efficient, and green mining of coal mine, coal gangue is used as coarse material; fly ash, desulfurization gypsum, gasification slag, and furnace bottom slag are used as fine materials; and cement is used as gelling agent. The compressive strength and bleeding rate of CBSWF are tested through orthogonal test, and the strength of CBSWF at different curing ages is predicted by using a 4-11-3 three-layer BP neural network structure. The results show that the correlation coefficient r of strength prediction of CBSWF is 0.99987, which can accurately predict the strength of CBSWF. Orthogonal test combined with the BP neural network can reduce the number of tests without losing generality, make full use of the advantages of adaptive nonlinear optimization of the BP neural network, and improve the operation efficiency of the model, fast prediction speed, and high accuracy.

Keywords: BP neural network, coal based solid waste, filling mining, strength prediction, orthogonal test

OPEN ACCESS

Edited by:

Tingting Zhang,
Dalian University of Technology, China

Reviewed by:

Yun Gao,
Southeast University, China
Xianjie Hao,
China University of Mining and
Technology, China

*Correspondence:

Jiqiang Zhang
2390912295@qq.com

Specialty section:

This article was submitted to
Structural Materials,
a section of the journal
Frontiers in Materials

Received: 30 August 2021

Accepted: 18 October 2021

Published: 03 November 2021

Citation:

Feng F, Li L, Zhang J, Yang Z and Chi X
(2021) Strength Prediction of Coal-
Based Solid Waste Filler Based on BP
Neural Network.
Front. Mater. 8:767031.
doi: 10.3389/fmats.2021.767031

INTRODUCTION

In recent years, China's coal output has remained high, reaching 3.9 billion tons of raw coal in 2020. With the large-scale coal production capacity, there are also ecological problems such as surface subsidence, coal-based solid waste discharge, water system, and environmental pollution. In view of these problems, more and more mines adopt filling coal mining technology to effectively solve the coal-based solid waste generated in the process of coal deep processing. It has achieved good social and economic benefits (Wu et al., 2016; Wu et al., 2018; Zhang et al., 2020a).

Coal-based solid waste refers to the solid waste generated in the process of coal development and utilization, such as coal gangue, fly ash, desulfurization gypsum, and coal chemical waste residue. The multi-source coal-based solid waste forms a filling body by setting the ratio to avoid the deformation and damage of the rock mass around the stope. Therefore, exploring the strength characteristics, composition, and mechanical properties of coal-based solid waste filling is a necessary research content to ensure the filling effect. Exploring the performance of coal-based solid waste filling is mainly characterized by its compressive strength (Hao et al., 2021a). Uniaxial compressive strength (UCS) is an important parameter for rock mass classification and rock engineering design (Hao et al., 2020; Hao et al., 2021b). At present, empirical analogy method, empirical formula method, physical simulation method, elastic mechanics analysis method, and other methods are mainly used to predict the strength of filling body, but there are some problems such as lack of scientificity and low accuracy

of prediction results (Chang et al., 2009). With the rapid development of big data and artificial intelligence, intelligent algorithm has been introduced into the field of coal mine filling mining to predict the strength of filling body. Deng et al. (2021) predict the strength of aeolian sand filling body from the aspects of data fitting degree, network error analysis, and prediction results, and constructs a prediction model based on the BP neural network model and PCA-BP neural network model. Zhang et al. (2020b) used artificial intelligence algorithm to study the proportion development of mining cementitious materials from the perspective of “black box”, and obtains the optimal proportion of cementitious materials through orthogonal test and an artificial neural network model. Zhang and Deng (2020) extracted the strength prediction model of deep connected deep belief network (DBN) with input parameters, and used quantum particle swarm optimization algorithm to determine the number of hidden layer nodes and learning rate of DBN. The prediction performance of the BP neural network, RVM (relevance vector machine), and SVM (support vector machine) was compared and analyzed. Bai et al. (2020) improved the initial weight and threshold of the BP neural network through genetic algorithm, established the compressive strength prediction model of recycled thermal insulation concrete, and compared and analyzed the performance of the GA-BP neural network and BP neural network prediction model. Moon and Munira (2021) used 3-days concrete strength as the prior information in neural network training, developed a neural network model based on prior information (pi-nnm) to obtain the 28-days concrete strength prediction model, and verified the prediction ability of the prediction model through practical production application. Huang et al. (2021) used the orthogonal test method to analyze the sensitivity of compressive strength and splitting strength of hybrid fiber reinforced recycled aggregate concrete (HYFRAC), proposed a hyfrac compressive strength prediction model based on the convolution neural network (CNN), and compared and analyzed the prediction effects of the back propagation (BP) neural network model and multiple linear regression model. Zhang et al. (2021) support vector machine and a modified cuckoo algorithm are utilized to predict the compressive strength of geopolymer concrete. An orthogonal factor is introduced to modify the traditional cuckoo algorithm to update new species and accelerate computation convergence. Then, the modified cuckoo algorithm is employed to optimize the parameters in the support vector machine model. Then, the compressive strength predictive model of coal gangue-based geopolymer concrete is established with oxide content of raw materials as the input and compressive strength as the output of the model.

In the development history of the artificial neural network, the MLP (multi-layer perceptron) network has played a great role in the development of the artificial neural network. It is also considered as a real artificial neural network model. Its emergence has set off an upsurge of people's research on artificial neural network. As the initial neural network, the single-layer perceptual network (M-P model) has the following advantages: clear model, simple structure, and small amount of

calculation. However, with the deepening of research work, it is found that it still has some shortcomings. For example, it cannot deal with nonlinear problems. Even if the action function of the calculation unit does not use the valve function and uses other more complex nonlinear functions, it can only solve the linear separable problem and cannot realize some basic functions, which limits its application. The only way to enhance the classification and identification ability of the network and solve the nonlinear problem is to use a multi-layer feedforward network, that is, add an implicit layer between the input layer and the output layer. A multilayer feedforward perceptron network is formed. In the mid-1980s, David Rumelhart, Geoffrey Hinton, Ronald Williams, and David Parker independently discovered the error BP training algorithm, which systematically solved the learning problem of hidden layer connection weight of the multilayer neural network and gave a complete derivation mathematically. The multilayer feedforward network using this algorithm for error correction is called BP network.

The basic BP algorithm includes two processes: signal forward propagation and error BP. That is, the error output is calculated in the direction from input to output, while the weight and threshold are adjusted in the direction from output to input. During forward propagation, the input signal acts on the output node through the hidden layer and generates the output signal through nonlinear transformation. If the actual output is inconsistent with the expected output, it will turn into the BP process of error. Error BP is to back transmit the output error layer by layer to the input layer through the hidden layer, allocate the error to all units of each layer, and take the error signal obtained from each layer as the basis for adjusting the weight of each unit. By adjusting the connection strength between the input node and the hidden layer node, and the connection strength and threshold between the hidden layer node and the output node, the error decreases along the gradient direction. After repeated learning and training, the network parameters (weight and threshold) corresponding to the minimum error are determined, and the training stops (Wang et al., 2021). At this time, the trained neural network can process the input information of similar samples and output the non-linear converted information with the minimum error.

Compared with traditional methods, the BP neural network has become the most widely used neural algorithm with its good nonlinear mapping ability, self-learning, and self-adaptive ability, and has actively explored and studied strength prediction (Hu et al., 2021; Ji et al., 2021; Qing et al., 2021). Wei et al. (2020) studied the influence of fly ash content on the strength of cemented backfill based on orthogonal test, and analyzed and predicted the influence law by using the BP neural network model. In Jiang et al. (2021), aiming at the influence of heterogeneity on rock strength under different strain rates, 42 quasi-static and 42 dynamic Brazilian disk experimental tests were trained, verified, and tested by the artificial neural network, and the relationship between rock strength and heterogeneity parameters under different strain rates was obtained. Through sensitivity analysis, it is found that strain rate is the most important physical quantity affecting the strength of heterogeneous rock.

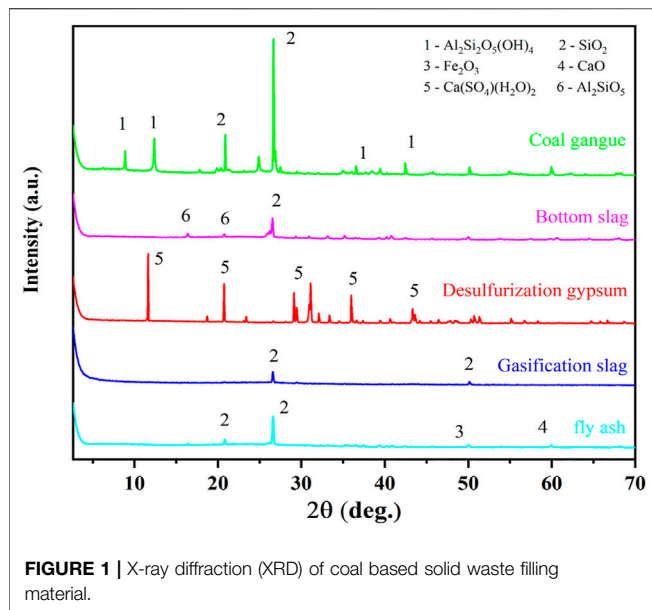


FIGURE 1 | X-ray diffraction (XRD) of coal based solid waste filling material.

Based on the BP neural network, taking coal gangue as coarse material; fly ash, desulfurization gypsum, gasification slag, and furnace bottom slag as fine material; and cement as gelling agent, the compressive strength and bleeding rate of coal-based solid waste filler (CBSWF) are tested through orthogonal test. The three-layer BP neural network of 4-11-3 is used to predict the strength of CBSWF, and the strength prediction model of CBSWF is established. The prediction results are evaluated.

TEST MATERIALS AND METHODS

Material Composition

The chemical composition of the dried CBSWF material is determined by x-ray diffraction (XRD) and x-ray fluorescence spectrum analysis (XRF). As shown in **Figure 1**, the main component of coal gangue is SiO_2 , accompanied by some silica compounds. A large amount of SiO_2 ensures the high hardness and deformation resistance of gangue. Fly ash is the dry discharged ash of the Yuanyanghu power plant. The main components are SiO_2 , Fe_2O_3 , and CaO . The content of CaO and SiO_2 reaches 92.27%, which reduces the polymerization degree of glass in fly ash and increases its activity. The gasification slag is mainly composed of SiO_2 , the bottom slag is mainly composed of SiO_2 , $\text{Al}_2\text{O}_3 \cdot \text{SiO}_2$, and Fe_2O_3 , and the desulfurization gypsum is mainly composed of CaSO_4 and $\text{CaSO}_4 \cdot 2\text{H}_2\text{O}$.

Test Scheme

Using $L_{16}(4^4)$ orthogonal test, without special explanation, the ratio involved in the text is the quality ratio. Selecting the quality of coal gangue and cement as invariants, the cement content shall not exceed 5% of the total mass of coal-based solid waste. Set four research factors, namely, A (concentration), B (ash–gangue ratio), C (gasification slag: furnace bottom slag), and D (gasification slag:desulfurization gypsum), and set four horizontal gradients, as shown in **Table 1**.

Source and Preparation of Test Materials

Ningdong energy and chemical base are located in the Middle East of Ningxia. In 2018, the coal output was about 91.55 million tons, the coal chemical production capacity was 22.25 million tons, and the thermal power capacity was 14.95 million kW. In recent years, it has produced more than 90 million tons of coal-based solid wastes such as coal gangue, fly ash, desulfurization gypsum, gasification slag, and furnace bottom slag (Yang et al., 2021). Coal gangue was used as coarse material; fly ash, gasification slag, furnace bottom slag, and desulfurization gypsum were used as fine material; and 42.5 ordinary Portland cement was used as cementitious material. Among them, coal gangue comes from Renjiazhuang and Meihuajing coal mines, and fly ash, desulfurization gypsum, gasification slag, and bottom slag come from the Yuanyanghu power plant. The geographical location of the mining area is shown in **Figure 2**.

The large gangue is crushed by a small jaw crusher and screened into coal gangue with a particle size of 0–5 mm through a standard screen. The cemented block in the material is crushed and ground and screened with a 0- to 5-mm standard screen for standby. According to GB 50080-2016 national standard (Ministry of Housing and Urban and Rural Construction, 2016), all kinds of coal-based solid waste materials are weighed successively according to the quality fraction requirements of the design scheme. The required water is poured into the evenly mixed filling materials, and a small amount of cement is mixed. After 30 s of mixing, the mixed cementation material is cast into the standard cube mold of $70.7 \times 70.7 \times 70.7$ mm, and the surface of the mold is smooth with a scraper. Then, add some mixed cementitious materials into the plexiglass container with a height of about 120 mm to ensure that the height of the measured filling surface is consistent, and then seal it tightly with fresh-keeping film. After standing indoors for 24 h, measure the separated water surface and cement slurry expansion surface. After the flat mold is placed indoors and cured for 12 h, the sample is taken out of the mold after the test block is initially self-supporting and placed in a curing box with constant temperature and humidity of 20°C and humidity of $90\% \pm 5\%$ until taken out for testing. According to the national standard (General Institute of Coal Science Research, 2010) of GB 23561.12-2010, complete the strength test on the electro-hydraulic servo universal press (loading rate is 0.05 kn/s), as shown in **Figure 3**.

Test Results

The bleeding rate and uniaxial compressive strength (3, 7, and 28 days) of CBSWF are tested by $L_{16}(4^4)$ orthogonal experiment, as shown in **Table 2**.

The results of bleeding rate and uniaxial compressive strength (3, 7, and 28 days) of CBSWF are shown in **Figure 4**. The $A_i B_j C_k D_l$ is used to characterize the optimal test scheme combination of strength, in which A, B, C, and D represent four factors, and i (taking 1,2,3,4) represents different horizontal gradients of the corresponding factors. It can be seen that among the 16 groups of specimens, when the curing age is 3 days, the compressive strength of S15 is the largest and the compressive strength of S5 is the smallest. At this time, given A (concentration

TABLE 1 | L16 (4^4) orthogonal experimental factors and levels.

Level	Factor			
	A (Concentration/%)	B (Ash-to-gangue ratio)	C (Gasification slag:Bottom slag)	D (Gasification slag:Desulfurization gypsum)
L1	74	0.3	0.2	0.1
L2	76	0.4	0.25	0.15
L3	78	0.5	0.3	0.2
L4	80	0.6	0.35	0.25

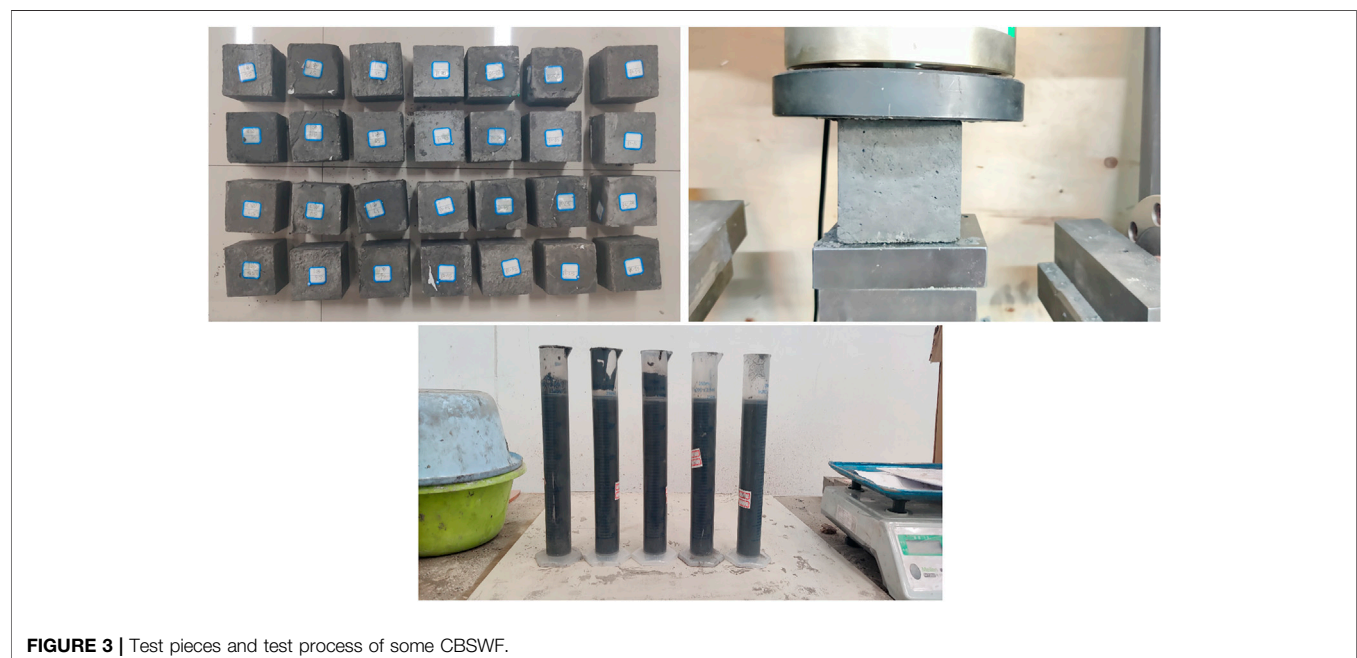
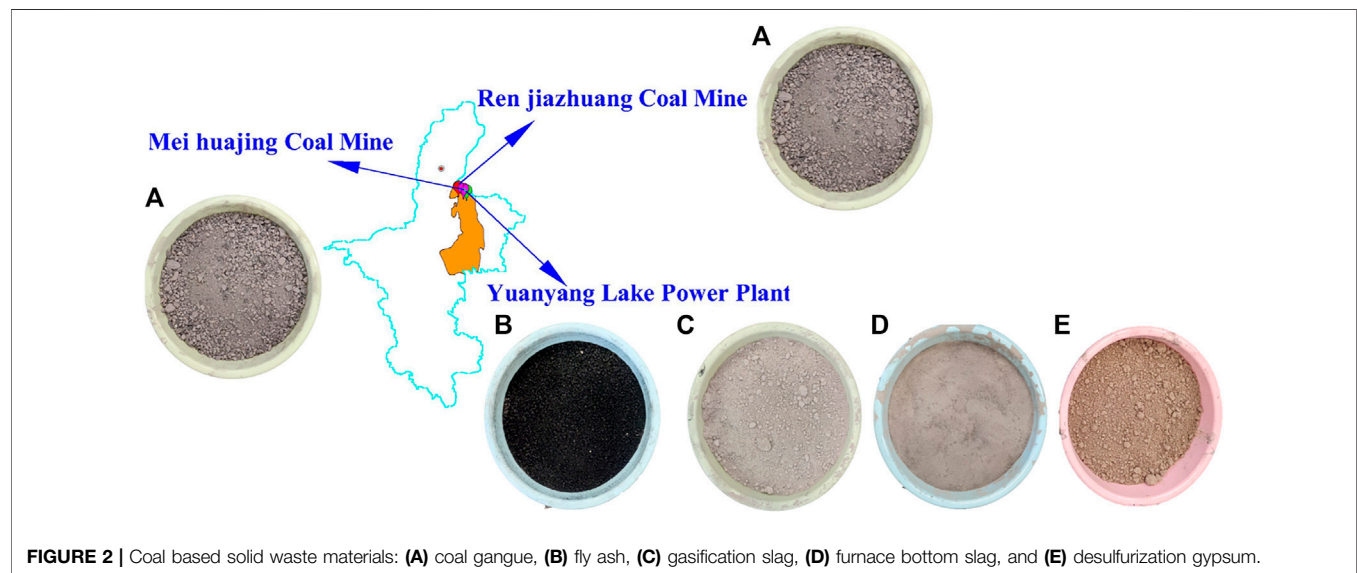
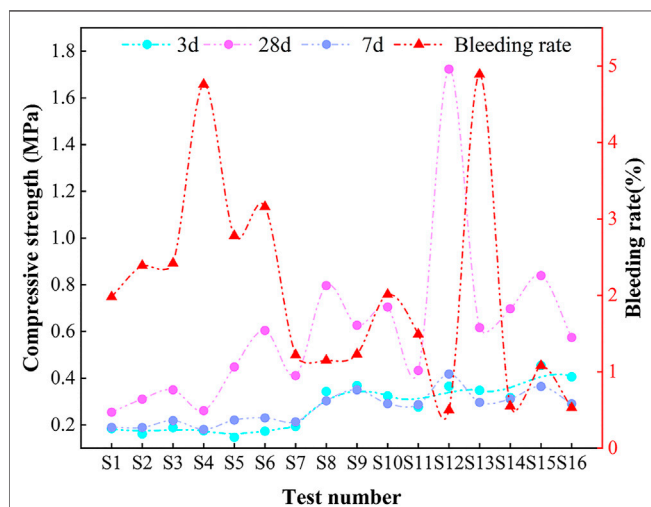


TABLE 2 | Orthogonal experimental results of L16 (4^4) CBSWF.

Group number	Factor				UCS/MPa			Bleeding rate/%
	A	B	C	D	3 days	7 days	28 days	
S1	1	1	1	1	0.184	0.272	0.254	1.98
S2	1	2	2	2	0.161	0.27	0.31	2.39
S3o	1	3	3	3	0.188	0.361	0.35	2.42
S4	1	4	4	4	0.175	0.245	0.261	4.76
S5	2	1	2	3	0.147	0.369	0.448	2.78
S6	2	2	1	4	0.173	0.396	0.604	3.16
S7	2	3	4	1	0.193	0.345	0.411	1.22
S8	2	4	3	2	0.343	0.621	0.796	1.15
S9	3	1	3	4	0.368	0.764	0.626	1.23
S10	3	2	1	3	0.324	0.583	0.704	2.01
S11	3	3	4	2	0.276	0.571	0.433	1.49
S12	3	4	2	1	0.365	0.971	1.723	0.5
S13	4	1	4	2	0.348	0.601	0.616	4.89
S14	4	2	3	1	0.317	0.643	0.697	0.55
S15	4	3	2	4	0.454	0.809	0.839	1.08
S16	4	4	1	3	0.406	0.582	0.574	0.53

**FIGURE 4 |** Bleeding rate and UCS of CBSWF in different test groups.

is 80%), B (ash–gangue ratio is 0.5), C (gasification slag:bottom slag is 1.67), and D (gasification slag:desulfurization gypsum is 0.7), the combination with the largest strength in the previous period is $A_4B_3C_2D_4$. When the curing age is 7 and 28 days, the compressive strength and bleeding rate of S12 are the largest. At this time, given A (concentration is 78%), B (ash–gangue ratio is 0.6), C (gasification slag:bottom slag is 1.67), and D (gasification slag:desulfurization gypsum is 1), the combination with the largest strength in the later stage is $A_3B_4C_2D_1$.

Establishment of Filling Strength Prediction Model

The BP neural network is a multilayer feedforward neural network trained according to the error BP algorithm. It is the most widely used neural network at present. Its basic idea is the

gradient descent method, which uses gradient search technology to minimize the error mean square deviation between the actual output value and the expected output value of the network. The artificial neural network does not need to determine the mathematical equation of the mapping relationship between input and output in advance. It only learns some rules through its own training and obtains the result closest to the expected output value when the input value is given.

From the orthogonal test results, it can be seen that A (concentration), B (ash–gangue ratio), C (gasification slag: furnace bottom slag), and D (gasification slag:desulfurization gypsum) all have an impact on the strength of CBSWF, and each factor has a nonlinear relationship with the compressive strength. It is impossible to consider all factors in the test. The neural network model can be constructed based on the existing test data to predict the unknown data. By establishing the filling strength prediction model based on the BP neural network, the disadvantages of experimental test and field monitoring being costly and time-consuming can be overcome, and a new method for filling strength prediction is provided.

Taking the bleeding rate and uniaxial compressive strength (3, 7, and 28 days) of coal-based solid waste material filling in L16 (4^4) orthogonal experiment as samples, the strength prediction model of CBSWF is constructed. The main structure of the model is composed of an input layer, a hidden layer, and an output layer, with A (concentration), B (ash–gangue ratio), C (gasification slag: furnace bottom slag), and D (gasification slag:desulfurization gypsum) as the network input factor in the input layer, and the 3-, 7-, and 28-days compressive strength and bleeding rate of CBSWF are taken as the network output factors. Groups S4, S8, S12, and S16 in the table are taken as the test set samples, and the other 12 groups of data are taken as the training set samples. The number of neurons in the hidden layer can determine the convergence of the training function, the length of training, and the size of training error, which is very important for the effect of model fitting. Many scholars have conducted a lot of research on the selection of the number of neurons in the hidden

TABLE 3 | Average relative error of number and intensity prediction of neurons in different hidden layers.

Number of hidden layer neurons	Average relative error/%		
	3-days UCS	7-days UCS	28-days UCS
2	7.207781	16.93408	37.81255
3	5.026197	14.04447	29.14075
4	4.596087	11.57161	29.00382
5	6.75147	12.54053	26.81211
6	4.668387	13.38517	27.68315
7	3.87042	11.80098	24.66333
8	7.376976	9.197673	23.89781
9	8.618736	9.572023	15.31264
10	5.594761	7.986225	23.74555
11	3.955781	8.210314	19.59745
12	2.952257	8.844902	23.51462

layer (Adil et al., 2020; Chin and Zhang, 2021; Karmakar and Goswami, 2021). Dong et al. (2018) believe that the number of neurons in the hidden layer is optimal when m is $(2a + 1)$, which can also be selected according to Eq. 1:

$$\begin{cases} m = \sqrt{(a+b)} + k \\ m = \log_2 a \\ m = \sqrt{ab} \end{cases} \quad (1)$$

In the equation, a and b are the number of input factors and output factors, respectively, and k is a constant between 0 and 10. The number of neurons in the hidden layer determined according to the above formula is 2–12. The average relative error of compressive strength is used as the basis for screening the number of neurons in the hidden layer. The number of neurons in the hidden layer is determined through comparative analysis, and the network performance when the number of neurons in the hidden layer is 2–12 is checked respectively. The prediction results and relative errors of compressive strength at different curing ages (3, 7, and 28 days) are obtained. The relative errors obtained from each neuron are averaged, as shown in Table 3. It is found that the relative error increases with the increase of curing age, and the worse the prediction effect. When the number of neurons in the hidden layer is 12, the average relative error of 3-days compressive strength is the smallest, which is 2.952257%. When the number is 10, the average relative error of 7-days compressive strength is the smallest, which is 7.99%. When the number is 9, the average relative error of 28-days compressive strength is the smallest, which is 15.31%. The average relative error of different curing ages is taken as the average value. It is found that when the number of neurons in the hidden layer is 11, the relative average error is the smallest, which is 10.59%. At this time, the training error will be closer to the target error. Therefore, the number of neurons in the hidden layer is 11 to predict the strength of the filling body.

At the same time, set the transfer function of input layer and output layer as purelin function, the transfer function of hidden layer as logarithmic S-type transfer function logsig, and the traingdx function is selected as the training function. The

three-layer BP neural network, i.e., 4-11-3, is used to construct the strength prediction model of CBSWF, as shown in Figure 5.

In order to avoid the situation that the training time is too long to converge, before formal modeling, the data shall be preprocessed by data normalization method, the input or output data shall be transformed into dimensionless values of interval $[0,1]$ or $[-1,1]$, and the accuracy of prediction results shall be judged by means of average relative error analysis. Eq. 2 is used for normalization:

$$x'_k = (x_k - x_{min}) / (x_{max} - x_{min}) \quad (2)$$

Where x'_k is normalized data, x_k is the original data, and x_{max} and x_{min} are the maximum and minimum of each group of factors, respectively. When outputting the prediction results, the data also need to be inverse normalized.

DISCUSSION

Literature (Dong et al., 2018) based on 18 groups of orthogonal test samples with mixing level, taking the content of cement clinker, desulfurization ash, Glauber's salt, and steel slag as four input factors and the 7- and 28-days compressive strength of the filling body as the output factor, $4 \times 9 \times 2$, the maximum relative errors of predicted strength at 7 and 28 days are 4.33 and 0.84%. Liang et al. (2017) collected 47 groups samples. With the help of MATLAB R2015a platform and based on the BP neural network, the three-layer neural network model with single hidden layer is taken as the input with the amount of water, cement, sand, gravel, and recycled coarse aggregate per unit volume and the 28-days prism compressive strength of recycled concrete as the output. Its structure is 5-21-1. The simulation results show that the maximum relative error of prediction is 18.69%. The prediction error is less than 5%, accounting for 78.72% of the total sample. These studies show that using the BP neural network model to predict material strength is feasible and accurate.

Based on the above research basis, in MATLAB software, the 4-11-3 three-layer BP neural network is used to predict the strength of CBSWF. The number of training iterations is set to 1,000 steps, and the error target is set to 0.0001. The strength

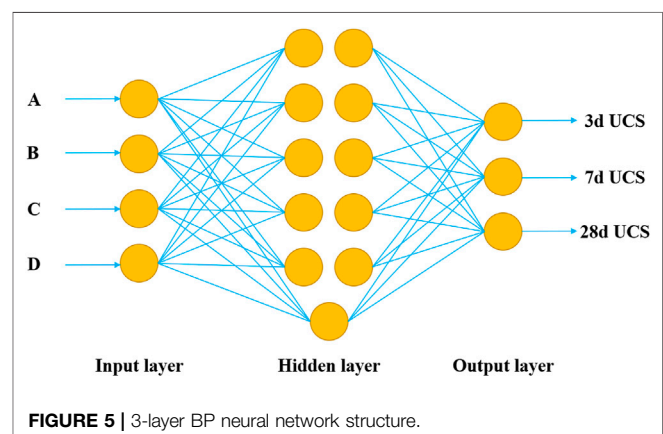
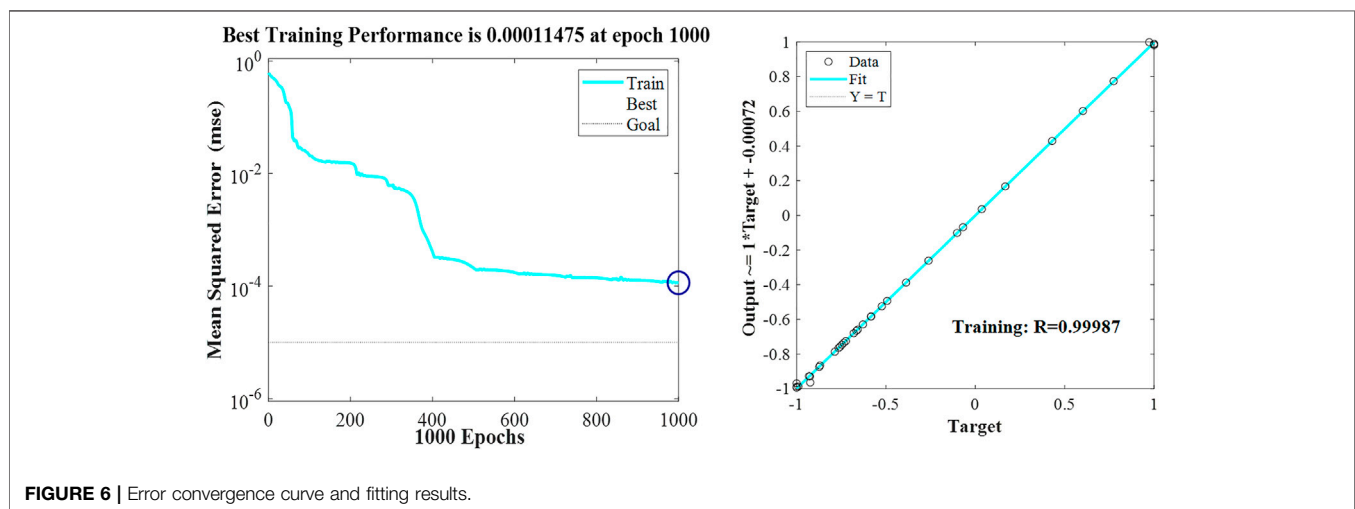


TABLE 4 | Predicted values and relative error results of strength at different curing ages.

Training sample/MPa			Predicted value/MPa			Relative error/%		
3 days	7 days	28 days	3 days	7 days	28 days	3 days	7 days	28 days
0.184	0.272	0.254	0.184071657	0.271676	0.266955	0.038944	0.1192	5.10047
0.161	0.27	0.31	0.160392243	0.271525	0.304933	0.377489	0.564856	1.634526
0.188	0.361	0.35	0.188221329	0.360484	0.350406	0.117728	0.143045	0.115964
0.175	0.245	0.261	0.174891347	0.251718	0.261637	0.062087	2.742047	0.243983
0.147	0.369	0.448	0.149428932	0.368958	0.448361	1.652335	0.011319	0.080494
0.173	0.396	0.604	0.173030869	0.396149	0.604181	0.017843	0.037714	0.030044
0.193	0.345	0.411	0.193019851	0.345267	0.411082	0.010285	0.07745	0.019952
0.343	0.621	0.796	0.343120889	0.621032	0.796219	0.035245	0.005078	0.027552
0.368	0.764	0.626	0.365257374	0.764429	0.626038	0.745279	0.056097	0.006131
0.324	0.583	0.704	0.324107366	0.583084	0.704275	0.033138	0.014345	0.039103
0.276	0.571	0.433	0.276281022	0.571502	0.433244	0.10182	0.087912	0.056465
0.365	0.971	1.723	0.36465307	0.968911	1.715123	0.095049	0.215088	0.457157
0.348	0.601	0.616	0.363147038	0.385663	0.286349	4.352597	35.82976	53.51477
0.317	0.643	0.697	0.362841108	0.674051	0.39525	14.46092	4.829079	43.29265
0.454	0.809	0.839	0.337911612	0.592709	0.564493	25.57013	26.73558	32.71838
0.406	0.582	0.574	0.34257626	0.930597	1.585512	15.62161	59.89647	176.2215

**FIGURE 6** | Error convergence curve and fitting results.

prediction value and relative error results are shown in **Table 4**. Obviously, it can be found that the strength prediction value of S1–S12 training data in the input layer by the BP neural network is close to the test value. The maximum relative error is 5.1% of the 28-days strength and the minimum is 0.0051% of the 7-days strength. However, the strength prediction value of S13–S16 test data in the output layer is quite different from the test value. The relative error of the 28-days strength in S16 reaches 176.22%, and the minimum value is 4.35% of the 3-days strength in S13. The average error of the 3-days strength is 3.95%, that of the 7-days strength is 8.21%, and that of the 28-days strength is 19.59%.

The BP neural network training error convergence curve and fitting characterization of the filling strength are shown in **Figure 6**. The best training error is 0.0115% after 1,000 times of training in the whole training process. The effect of the whole filling strength prediction can be evaluated by fitting characterization. The solid line represents the simulation

fitting curve, and the dotted line represents that the predicted value is equal to the experimental value. The R value is the correlation coefficient between the predicted output and the target output. The closer the R value is to 1, it shows that the greater the correlation between the predicted output and the target output, the higher the fitting degree of the prediction model, and the better the prediction effect. It can be concluded that the correlation coefficient r of the strength prediction of coal-based solid waste filling body is 0.99987, indicating that the BP neural network is used to predict the compressive strength of filling body with high accuracy.

CONCLUSION

The following conclusions could be drawn from the current study:

- 1) The compressive strength and bleeding rate of CBSWF are tested through orthogonal test. It is found that the combination with the largest early strength is $A_4B_3C_2D_4$. When the curing age is 7 and 28 days, the compressive strength and bleeding rate of S12 are the largest; that is, the combination with the largest later strength is $A_3B_4C_2D_1$.
- 2) The 4-11-3 three-layer BP neural network is used to predict the compressive strength of coal-based solid waste filling at different curing ages (3, 7, and 28 days). It is concluded that the correlation coefficient r of strength prediction of coal-based solid waste filling is 0.99987, and the prediction accuracy is high.
- 3) Orthogonal test combined with the BP neural network can reduce the number of tests without losing generality, make full use of the advantages of adaptive nonlinear optimization of the BP neural network, and improve the operation efficiency of the model, fast prediction speed, and high accuracy.

DATA AVAILABILITY STATEMENT

The original contributions presented in the study are included in the article/**Supplementary Material**, further inquiries can be directed to the corresponding author.

REFERENCES

- Adil, M., Ullah, R., Noor, S., and Gohar, N. (2020). Effect of Number of Neurons and Layers in an Artificial Neural Network for Generalized concrete Mix Design. *Neural Comput. Applic.*, 1–9. doi:10.1007/s00521-020-05305-8
- Bai, H., Liu, Y., Guo, Y., and Zhao, M. (2020). Prediction of the Strength of Recycled Insulation concrete Based on GA-BP Neural Network. *Concrete* 11, 16–19+25.
- Chang, Q., Zhou, H., Qing, J., Fan, J., and Wang, Y. (2009). Using Artificial Neural Network Model to Determine the Prescription of Paste Filling Materials. *J. Mining Saf. Eng.* 26 (01), 74–77.
- Chin, C. S., and Zhang, R. (2021). Noise Modeling of Offshore Platform Using Progressive Normalized Distance from Worst-Case Error for Optimal Neuron Numbers in Deep Belief Network. *Soft Comput.* 25 (1), 495–515. doi:10.1007/S00500-020-05163-5
- Deng, N., Ding, Y., Xing, C., Cao, X., and Shang, H. (2021). Wind-accumulated Sand Filler Strength Prediction Based on PCA-BP Neural Network. *Mining Res. Develop.* 41 (02), 109–113. doi:10.13827/j.cnki.kyyk.2021.02.019
- Dong, Y., Yang, Z., and Gao, Q. (2018). Orthogonal Test in Collaboration with BP Neural Network Model to Predict Filler Strength. *Mater. Guide* 32 (06), 1032–1036.
- General Institute of Coal Science Research (2010). *The Method of Determining the Physical and Mechanic Properties of Coal and Rock Part 12: The Method of Determining the Robustness Coefficient of Coal*, 8. Beijing: China's National Standardization Management Committee.
- Hao, X., Du, W., Zhao, Y., Sun, Z., Zhang, Q., Wang, S., et al. (2020). Dynamic Tensile Behaviour and Crack Propagation of Coal under Coupled Static-Dynamic Loading. *Int. J. Mining Sci. Techn.* 30 (5), 659–668. doi:10.1016/j.ijmst.2020.06.007
- Hao, X., Zhang, Q., Sun, Z., Wang, S., Yang, K., Ren, B., et al. (2021a). Effects of the Major Principal Stress Direction Respect to the Long axis of a Tunnel on the Tunnel Stability: Physical Model Tests and Numerical Simulation. *Tunnell. Undergr. Space Techn.* 114 (114), 103993. doi:10.1016/J.TUST.2021.103993

AUTHOR CONTRIBUTIONS

FF contributed to the conception of the study. LL helped perform the analysis with constructive discussions. JZ performed the data analyses and wrote the article. ZY and XC helped perform the analysis with constructive discussions. All authors agree to be accountable for the content of the work.

FUNDING

We acknowledge the financial support for this work provided by the Youth Science Foundation Project (52104115), Open Foundation of State Key Laboratory of Mining Response and Disaster Prevention and Control in Deep Coal Mine (SKLMRDPC19KF10), National Key Research and Development Program (2019YFC1904304), Major special projects of science and technology in Shanxi Province (No: 20191101016).

SUPPLEMENTARY MATERIAL

The Supplementary Material for this article can be found online at: <https://www.frontiersin.org/articles/10.3389/fmats.2021.767031/full#supplementary-material>

- Hao, X., Wei, Y., Yang, K., Su, J., Sun, Y., Zhu, G., et al. (2021b). Anisotropy of Crack Initiation Strength and Damage Strength of Coal Reservoirs. *Pet. Explor. Develop.* 48 (1), 243–255. doi:10.1016/s1876-3804(21)60020-4
- Hu, S., Wang, T., Guan, Y., and Yang, Z. (2021). Regional Crustal Horizontal Motion Model of Euler-GABP Neural Network Construction. *Mapp. Sci.* 46 (02), 25–33. doi:10.16251/j.cnki.1009-2307.2021.02.005
- Huang, W., Quan, W., and Ge, P. (2021). Orthogonal Tests Investigation into Hybrid Fiber-Reinforce Recycled Aggregate Concrete and Convolutional Neural Network Prediction. *J. Asian Architect. Build. Eng.*, 1–16. doi:10.1080/13467581.2021.1918553
- Ji, K., Han, B., Hu, Y., Wu, F., and Qiu, J. (2021). Based on the Underground Filler Strength Prediction of Strength Reduction and Intelligent Algorithm. *China Nonferrous Met. J.* 31 (03), 796–805.
- Jiang, S., Sharafisafa, M., and Shen, L. (2021). Using Artificial Neural Networks to Predict Influences of Heterogeneity on Rock Strength at Different Strain Rates. *Materials* 14 (11), 3042. doi:10.3390/MA14113042
- Karmakar, S., and Goswami, S. (2021). A New Procedure for Optimization of Hidden Layer Neurons during Learning through Gradient Descent Process of Neural Network and Improvement of Performance in the Chaos Forecasting. *Iran J. Comput. Sci.*, 1–11. doi:10.1007/S42044-021-00089-Z
- Liang, J., Yan, L., Hu, P., and Yang, Y. (2017). Application of BP Neural Network in Forecast to Recycled concrete Strength. *Concrete* (06), 9–12+16.
- Ministry of Housing and Urban and Rural Construction (2016). *Standard for the Performance Test Method of Ordinary concrete Mixes*. Beijing: China Construction Industry Press.
- Moon, S., and Munira Chowdhury, A. (2021). Utilization of Prior Information in Neural Network Training for Improving 28-Day Concrete Strength Prediction. *J. Constr. Eng. Manage.* 147 (5), 04021028. doi:10.1061/(ASCE)CO.1943-7862.0002047
- Qing, N., Ge, Q., Liang, Z., Sun, J., and Wang, Y. (2021). Study on the Prediction of the Strength of the Single axis of the High Temperature on sandstone Macroscopic Damage and BP Neural Network. *Exp. Mech.* 36 (01), 105–113.
- Wang, Y., Zhang, Y., and Chen, Y. (2021). Prediction of Concrete Slump Model Based on BP Neural Network. *Int. Core J. Eng.* 10 (7), 252–259. doi:10.6919/ICJE.202110_7(10).0038

- Wei, H., Ba, L., and Gao, Q. (2020). Study on the Effect of Fly Ash Doping on the Strength of the Glycolic Filling Body. *Mining Res. Develop.* 40 (12), 28–32. doi:10.13827/j.cnki.kyyk.2020.12.006
- Wu, A., Wang, Y., Zhou, B., and Shen, J. (2016). Effect of Initial Backfill Temperature on the Deformation Behavior of Early Age Cemented Paste Backfill that Contains Sodium Silicate. *Adv. Mater. Sci. Eng.* 2016, 1–10. doi:10.1155/2016/8481090
- Wu, A., Yang, Y., Cheng, H., Cheng, S., and Han, Y. (2018). Status and Prospects of Paste Technology in China. *Chin. J. Eng.* 40 (05), 517–525. doi:10.13374/j.issn2095-9389.2018.05.001
- Yang, K., Wei, Z., Zhao, X., He, X., Zhang, J., and Ji, J. (2021). Theory and Technology of green Filling Mining of Solid Waste Underground in Coal Power Base of Yellow River Basin. *J. China Coal Soc.*, 1–14. doi:10.13225/j.cnki.jccs.T21.0284
- Zhang, A., and Deng, F. (2020). Phosphate gypsum Filling Material Strength Prediction Based on Deep Belief Network. *Sci. Techn. Eng.* 20 (18), 7220–7225.
- Zhang, J., Ju, F., Li, M., Zhou, N., and Zhang, Q. (2020a). Method of Coal Gangue Separation and Coordinated In-Situ Backfill Mining. *J. China Coal Soc.* 45 (01), 131–140. doi:10.13225/j.cnki.jccs.YG19.1826
- Zhang, G., Cheng, Y., Hu, Y., and Gao, Q. (2020b). Based on the Comparison of New Filling Gel Materials of Artificial Intelligence Neural Network. *Mining Res. Develop.* 40 (09), 143–148. doi:10.13827/j.cnki.kyyk.2020.09.027
- Zhang, D., Sun, F., and Liu, T. (2021). Prediction of Compressive Strength of Geopolymer Concrete Based on Support Vector Machine and Modified Cuckoo Algorithm. *Adv. Mater. Sci. Eng.* 2021, 1–14. doi:10.1155/2021/4286810

Conflict of Interest: Author LL was employed by the company Shanxi Coking Coal Group Co., Ltd.

The remaining authors declare that the research was conducted in the absence of any commercial or financial relationships that could be construed as a potential conflict of interest.

Publisher's Note: All claims expressed in this article are solely those of the authors and do not necessarily represent those of their affiliated organizations, or those of the publisher, the editors and the reviewers. Any product that may be evaluated in this article, or claim that may be made by its manufacturer, is not guaranteed or endorsed by the publisher.

Copyright © 2021 Feng, Li, Zhang, Yang and Chi. This is an open-access article distributed under the terms of the Creative Commons Attribution License (CC BY). The use, distribution or reproduction in other forums is permitted, provided the original author(s) and the copyright owner(s) are credited and that the original publication in this journal is cited, in accordance with accepted academic practice. No use, distribution or reproduction is permitted which does not comply with these terms.



Experimental Investigation on Strength and Failure Characteristics of Cemented Paste Backfill

Zhihong Zhang* and Jiacheng Li

Key Laboratory of Urban Security and Disaster Engineering, Ministry of Education, Beijing University of Technology, Beijing, China

OPEN ACCESS

Edited by:

Lijie Guo,
Beijing General Research Institute of
Mining and Metallurgy, China

Reviewed by:

Jiaqi Li,
University of California, Berkeley,
United States
Xinglan Cui,
General Research Institute For
Nonferrous Metals, China

*Correspondence:

Zhihong Zhang
zhangzh2002@126.com

Specialty section:

This article was submitted to
Structural Materials,
a section of the journal
Frontiers in Materials

Received: 10 October 2021

Accepted: 19 October 2021

Published: 15 November 2021

Citation:

Zhang Z and Li J (2021) Experimental
Investigation on Strength and Failure
Characteristics of Cemented
Paste Backfill.
Front. Mater. 8:792561.
doi: 10.3389/fmats.2021.792561

The strength characteristics of cemented paste backfill (CPB) in mining areas are key control factors for the safety assessment of overlying strata. A series of experiments about uniaxial compression and triaxial compression were carried out to study the influence of cement content of filling slurry, curing age, and curing temperature on strength behavior of CPB specimens. The failure mechanism and damage feature of CPB have been investigated. The results show the following: (1) The uniaxial compressive strength of CPB specimens exhibits an upward trend with the increase of cement content and curing age. When the cement content is high, the uniaxial compressive strength increases sharply with increasing curing age. (2) The cohesion of CPB specimens increases with the increase of cement content of filling slurry, curing age, and curing temperature. The cohesion of CPB specimens with curing age 7 days and 14 days increases linearly with increasing cement content. At the later stage of curing age, the strength growth of high cement content backfill is significantly greater than that of low cement content. The internal friction angle of the filling increases slightly with increasing filling cement content, curing age, and curing temperature. (3) The shear strength of CPB specimens at curing age 7 days exhibits an upward trend with the increase of confining pressure, while the shear strength at 14 days and 28 days curing age decreases slightly as the confining pressure increases. (4) With the increase of cement content in backfill, the brittleness increases significantly when the backfill is damaged. The failure mode of CPB specimens changes from monoclinic section shear failure to X-type failure with increasing curing age, and the failure process is divided into four stages: pore compaction, linear elastic deformation, plastic deformation, and post-peak failure.

Keywords: cemented paste backfill, uniaxial compression, triaxial compression, shear strength, failure mode

INTRODUCTION

With the increase of mining depth, geological disasters, such as underground rock burst and roof caving, occur frequently. At same time, there are potential risks, for instance, dam failure and environmental pollution in the tailing reservoir, formed by tailings accumulation (Cai, 2009; Yang et al., 2018). Tailings cemented filling mining method can effectively use mine tailings and prepare cemented filling slurry to backfill the goaf, so as to control the ground pressure, support the stope, reduce the surface subsidence, and improve ore recovery (Zhao and Hu, 2008; Lu et al., 2008). Therefore, the tailings cemented filling mining method is widely adopted by many mines (Ghirian and Fall, 2014; Jiang et al., 2019).

The mechanical properties of cemented paste backfill (CPB) are the key to the safe application of backfill mining method, and it is also the main controlling factor for safety assessment of overlying strata in the mine goaf. In order to better utilize the mechanical properties of the CPB to serve the mining operation, many scholars have conducted a lot of research work on compressive tests. Fall et al. (2005), Guo and Li, 2017, and Hou et al. (2021) explored the relationship between uniaxial compressive strength and material ratio of CPB. Li et al. (2005), Wang et al. (2015), and Zhang et al. (2020) optimized the filling material ratio to meet the actual demand of project through orthogonal test. Cao et al. (2016, 2019) studied the influence of CPB stratification on strength by simulating the interval between actual filling groups. Nie et al. (2016) tested the strength of CPB with different water contents and determined the influence of water content on the strength of CPB. Meanwhile, the microscopic damage evolution law of CPB during compression has also been widely concerned. Xie et al. (2015), Li, 2019, and Zhao et al. (2020) tested the acoustic emission parameters of specimens under compression, and analyzed the influence of curing temperature and cement content on the development of microcracks in CPB specimens. Yi et al., 2020 investigated the internal response of CPB during compression by rock CT scanner. Wei et al. (2020) explored the crack propagation process using crack camera observation system. The relationship between fracture area and tensile strength of cement paste with supplementary cementitious materials and the influence of new SCM on the long-term durability of concrete have been analyzed (Li and Li, 2015; Juenger et al., 2019). Richardson (2008) reviewed the model of calcium silicate hydrates. Li et al. (2020a) measured the intrinsic nanomechanical properties of C-S-H under different Ca/Si conditions by high-pressure X-ray diffraction method and made fibrillar C-S-H seeds from hydrated tricalcium silicate lower cement demand. The effects of curing time, cement content, and saturation state on mode-I fracture toughness of CPB have been studied (Libos and Cui, 2020). In addition, Zhou et al., 2019 and Wang, 2014 carried out the numerical simulation of uniaxial compression process of CPB. In triaxial compression test, Wu et al. (2019, 2021) studied the influence of cement content and inclined interface angle on the strength characteristics and failure mode of CPB. Yang et al. (2018) and Xu et al. (2019) analyzed the failure mode and energy dissipation characteristics of CPB. Fall et al. (2007), Rankine and Sivakugan, 2007, and Xu et al., 2014 revealed the deformation characteristics of CPB in compression. Those studies are valuable in stope engineering, yet it is worth noting that most research focus on uniaxial compression, which does not agree with reality, the actual three-dimensional stress state (Liu et al., 2019). Furthermore, the occurrence environment of backfill is complex, which indicates that the mechanical property of CPB could be affected by various factors.

The objective of this study is to determine the influence of cement content, curing age, and curing temperature on uniaxial compressive and triaxial shear strength of CPB. A series of uniaxial compression tests and triaxial compression tests are carried out to analyze the strength and failure characteristics of the CPB. The quantitative relationship between uniaxial compressive strength and triaxial shear strength has been obtained. This study can provide a valuable reference for the efficient application of CPB.

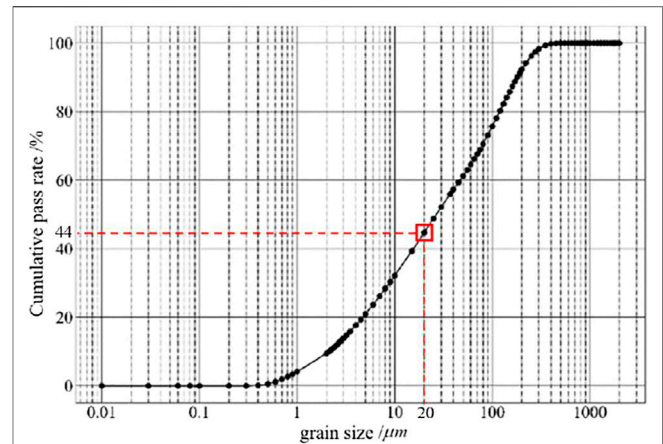


FIGURE 1 | Particle size distribution curve of tailings.

MATERIALS AND METHODOLOGY

Test Materials

The tailings utilized in this test were obtained from a copper mine, located in Anhui Province of China. The basic physical properties of the tailings were determined according to Rock Test Regulations for Water Conservancy and Hydropower Engineering (SL/T 264-2020). The natural density of the tailings is 1.424 g/cm^3 , the dry density is 1.420 g/cm^3 , and the moisture content is 0.977%. The particle size distribution (PSD) is shown in Figure 1.

It can be seen from Figure 1 that the cumulative pass rate of the tailings with particle size less than 20 microns reaches 44% (more than 35%), which belongs to the finer-grained tailings. This particle gradation can effectively reduce the layering and segregation in the slurry mixing process and make the internal aggregate distribution of the specimens more uniform, which makes the mechanical properties more stable.

Specimen Preparation

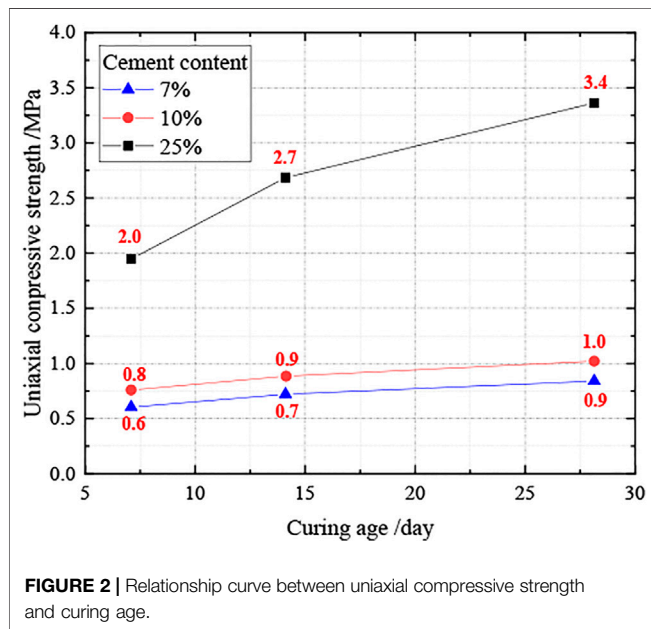
With full tailings as aggregate and P. O 42.5 Portland cement as cementing material, multiple cylindrical tailings CPB specimens ($\varnothing 50 \text{ mm} \times 100 \text{ mm}$) were prepared. The mass concentration of filling specimen was 72%, and the cement contents were 7, 10, and 25% (mass ratio). Afterwards, the CPB specimens were cured at room temperature $20 \pm 0.5^\circ\text{C}$ and humidity $95 \pm 5\%$ for 7, 14, and 28 days, respectively. These specimens were used to conduct experiments investigating the influence of cement content and curing age of CPB strength.

Test Method

A series of uniaxial and triaxial compression tests of CPB specimens were performed by TruePath automatic stress path triaxial apparatus. The loading rate is 1 mm/min , and the confining pressures of triaxial compression test are set to 100, 200, 300, and 400 kPa, respectively. The influence of three factors, namely, cement content, curing age, and curing temperature, on strength was discussed in this section. The specific test scheme is shown in Table 1.

TABLE 1 | Test conditions for the strength characteristics of the CPB.

Test types	Cement content (%)	Curing age (day)	Curing temperature (°C)	Specimen number
Uniaxial compression	7%	7	20	45
	10%	14	25	
			30	
Triaxial compression	25%	28	35	60
			40	
			45	



RESULTS AND ANALYSIS OF UNIAXIAL COMPRESSION TEST

The uniaxial compression test of CPB specimens focuses on the influence of slurry cement content and curing age on the uniaxial compressive strength. The experimental results are shown in **Figure 2**. The uniaxial compressive strength exhibits an upward trend with the increase of cement content and curing age. It is evident that the compressive strength increases slowly and maintains constant amplitude when the cement content is less than 10%, yet the compressive strength of specimens increases sharply as the cement content is greater than 10% (25% this test). It is worth noting that the strength value reaches 3.4 MPa at 28 days curing age (25% cement content), which is 1.7 times higher than that of 7 days (2.0 MPa/7% cement content) under the same working condition. The trends of relationship curve are obviously different with various cement content and curing age, even for the same specimens. The results of specimens with curing age (days) and cement content (25%) are the most prominent. So, it can be concluded that the curing age has a more significant effect on the strength increase of high cement content specimens.

It can be seen from the results of **Figure 2** that when the cement content is higher (25%) and the curing age is longer

(28 days), the compressive strengths of CPB specimens are significantly higher than those under other conditions. Increasing cement content can efficiently enhance the cementing effect of CPB, reduce the internal pores and gaps of the specimen, and cause increase of the uniaxial compressive strength. Meanwhile, prolonging the curing age is beneficial to promote the internal hydration reaction, so that the hydration reaction of a large number of gelling materials inside CPB specimens is more fully developed, and more calcium silicate hydrate is generated, so as to significantly increase the uniaxial compressive strength (Hou et al., 2021). When the cement content is higher (25%) and the curing period is longer (28 days), the compressive strength value of CPB is significantly higher than the strength of the samples under other working conditions, which indicates when the curing time is longer and the cement content is higher, the hydration reaction of a large amount of cementitious material inside the CPB will react more fully, which can significantly improve the uniaxial compressive strength of CPB specimens. However, for the specimens with low cement content and short curing age, due to the insufficient progress of the cement hydration reaction and insufficient hydration products, there are many pores and micro-cracks inside the specimens and the original defects are serious. The corresponding compressive strength is lower and damage is more likely to occur.

RESULTS AND ANALYSIS OF TRIAXIAL COMPRESSION TEST

A total of 60 sets of triaxial compression tests with different cement contents and curing ages were carried out in this study. By drawing the molar stress circles of filling bodies with different cement contents under different curing ages and confining pressures, the Mohr-Coulomb criterion was adopted. The shear failure line of each CPB specimen is fitted, and the cohesion and internal friction angle of the corresponding specimen are obtained. The fitting results are shown in **Figure 3**.

Influence of Cement Content and Curing Age on Shear Strength Indexes

The relationship curves between the cohesion, internal friction angle, and curing age of the CPB specimens with different cement contents are shown in the following figures:

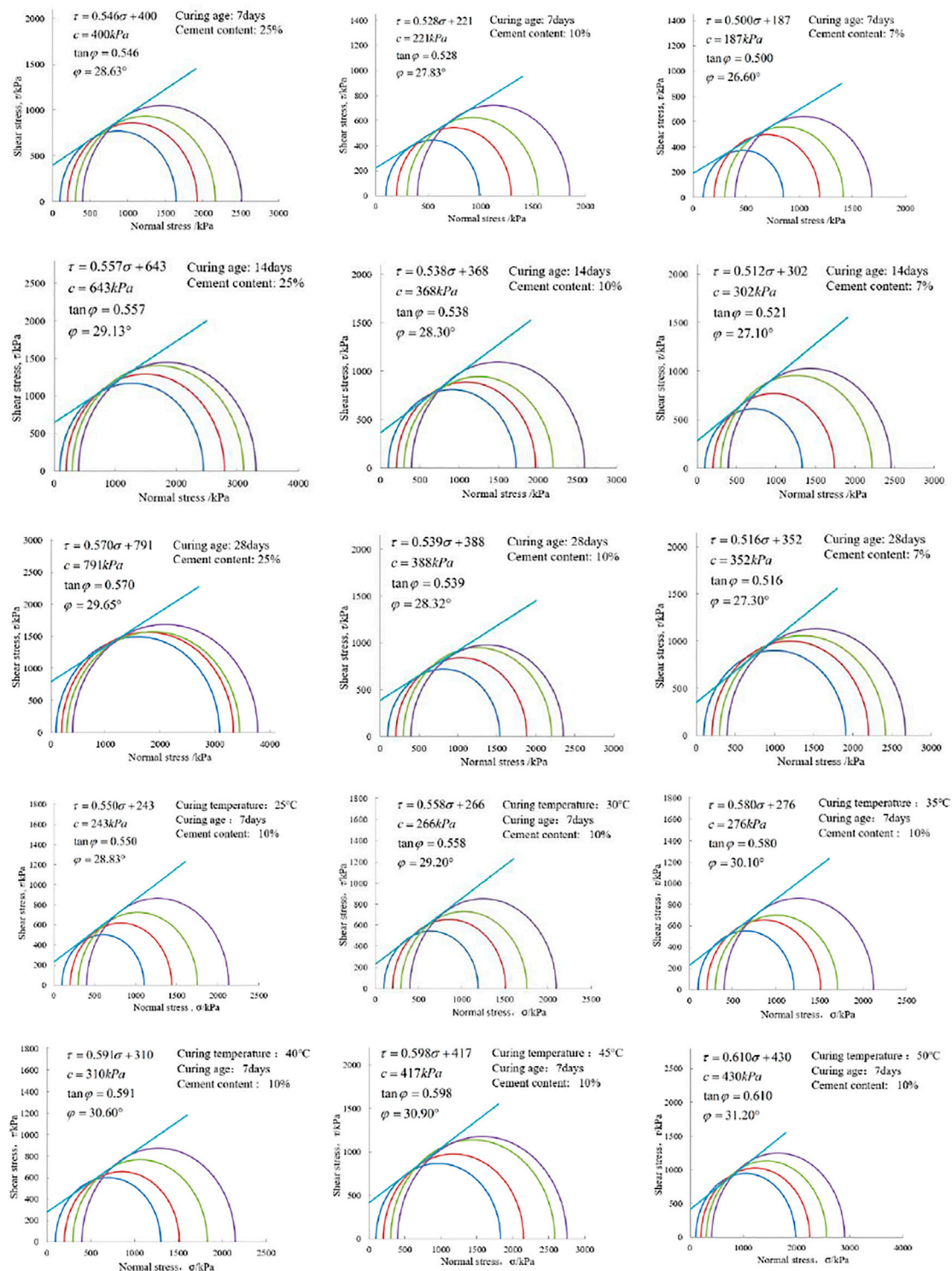
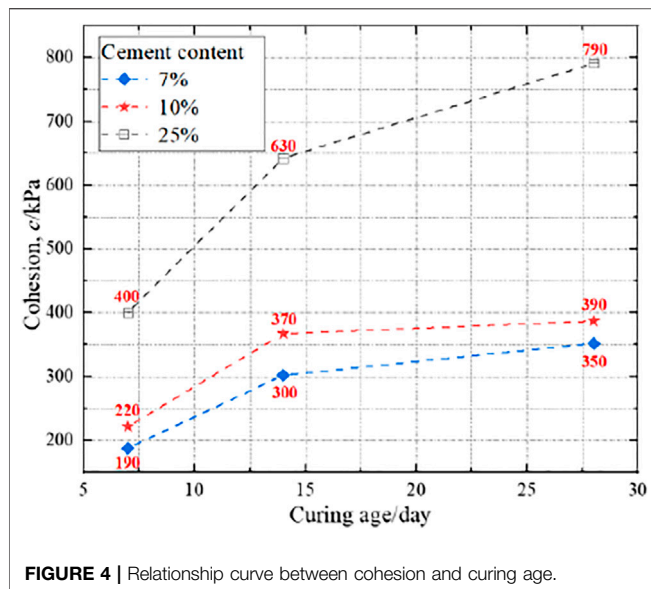


FIGURE 3 | Triaxial compression test results of CPB specimens.

As shown in Figure 4; Figure 5, the cohesion of CPB specimens increases with the increase of cement content and curing age, and the greater the cement content, the more obvious the increase. The values of specimens range from

190 to 790 kPa. When the cement content is 25%, the cohesion with curing age (28 days) reaches 790 kPa, which is 390 kPa higher than that (400 kPa) at 7 days. The main reason is that the CPB specimens with higher cement content will

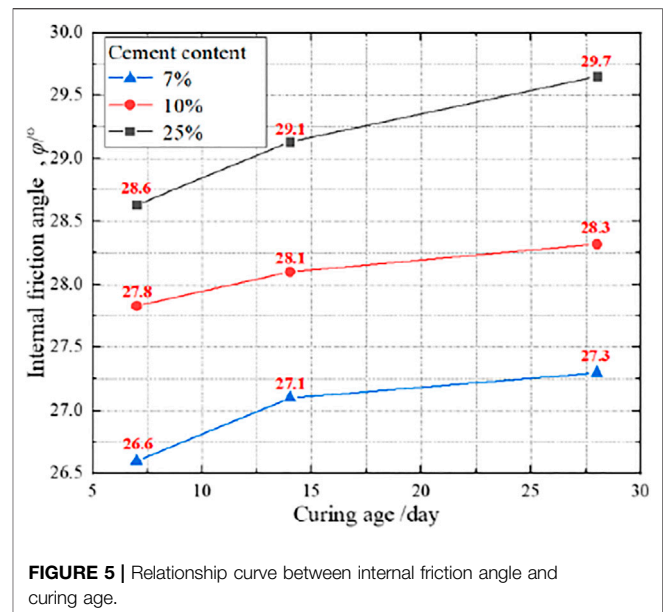


generate more binding phases (calcium silicate hydrate), which makes the bonding between tailings particles and cement tighter, and the bonding effect is better. It can be seen that, to achieve a cohesive strength of about 400 kPa, from the perspective of saving filling costs, a design scheme with low cement content and high curing age can be preferred. The friction angle increases slowly with increasing curing age and cement content. However, comparing the internal friction angle values of the specimens, there is a little difference between the friction angles of the CPB specimens with different curing ages and cement contents. The values of internal friction angle range from 26.6° to 29.7°; the change is only about 3.1°. This result shows that the influence of cement hydration on the friction angle of the CPB is relatively small.

Influence of Curing Temperature on Shear Strength Indexes

In order to study the influence of curing temperature on shear strength, a series of triaxial tests were carried out for the specimens with cement 10% and curing age 7 days at seven curing temperatures (20°C, 25°C, 30°C, 35°C, 40°C, 45°C, and 50°C). The relationship curves between shear strength indexes and curing temperature are shown as **Figure 6**.

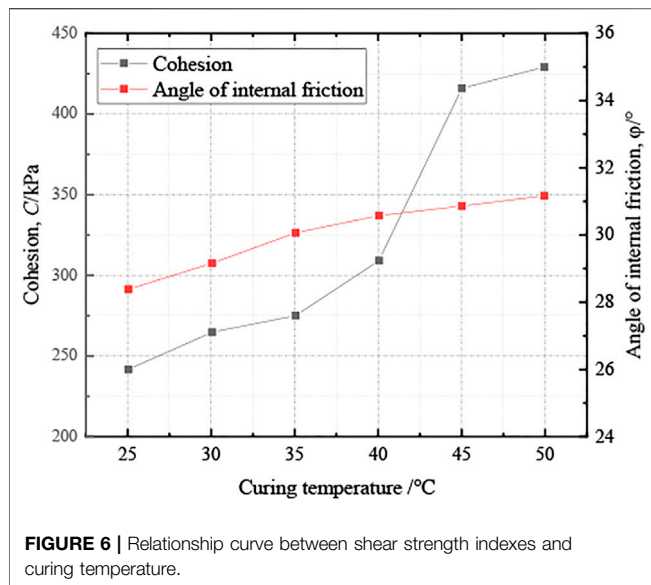
With the increase of curing temperature, the cohesive forces of CPB specimens increase rapidly and significantly, from 243 kPa corresponding to 25°C to 430 kPa corresponding to 50°C, which nearly doubled. This is because the higher curing temperature accelerates the hydration of the binder, and the hydration products increase with the increasing curing temperature, and the cement hydration product (C-S-H) is the main binding phase. The friction angle increases slightly with the increase of curing temperature, and the change value is only about 2.4°. Therefore, the increase of curing temperature can significantly increase the cohesive strength, but the effect of increasing the friction strength is not obvious.



FAILURE CHARACTERISTICS OF CPB SPECIMENS

Under a confining pressure of 300 kPa, the failure conditions of CPB specimens in the triaxial compression test are shown in **Figure 7**. When the specimen with a curing age 7 days and cement content 25% is broken, a penetrating and inclined tensile-shear failure surface appears, and there is a slight surface peeling. However, the shape of two other cement content tests is still relatively complete without obvious cracks, but the height reduction and lateral expansion appear, and there are some wrinkles and small cracks on the surface. This indicates that as the cement content decreases, the ductility of CPB specimens gradually increases when it is broken. This is due to the fact that when the cement content is relatively low, enough hydration products are not generated inside the CPB to cement and fill the pores, and there is still compressible space inside, so it has a strong deformability. The surface wrinkles decrease with the increase of the cement content during the curing age of 14 days and 28 days, and there is no obvious sign of damage. The reason is that with the increase of curing age, the amount of C-S-H generated inside the specimens increases and tends to be stable gradually, so that the brittleness of CPB specimens improves when it is damaged. As the curing age increases to 28 days, the failure form of the CPB changes from a single oblique cross-section shear failure to an X-shaped failure, and there is a local fall-off phenomenon in the specimen with a cement content of 25%, and the damage becomes more serious and there exist lumps. In the actual engineering, the design of cement content and curing age of CPB should not only consider the strength, but also take the deformation characteristics into account, so that it can better provide support for the safety of surrounding rock.

Taking the stress-strain curve of backfill under confining pressure of 300 kPa, 25% cement content after 28 days of curing as an example (curing temperature 20 ± 0.5°C), the compression failure process of specimen has been analyzed. The result is shown in **Figure 8**.



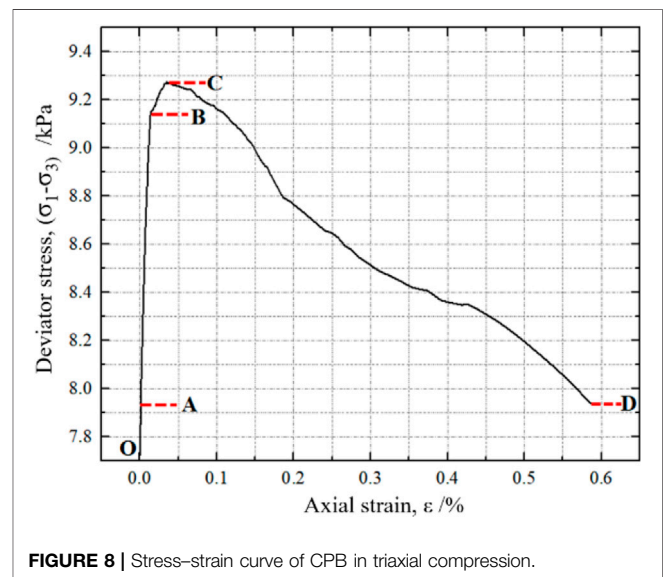
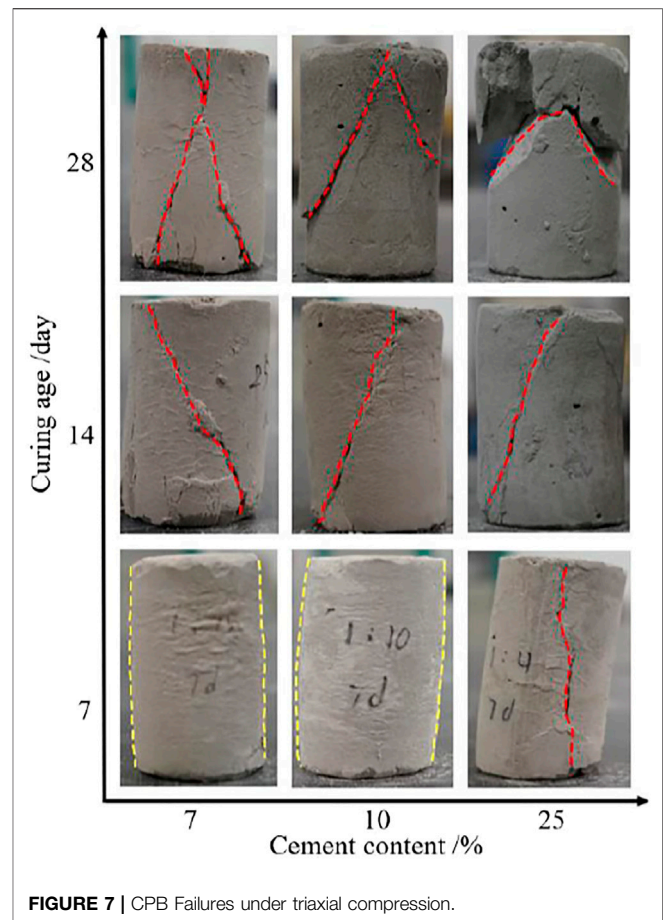
It can be concluded that the compression deformation and failure of the CPB can be roughly divided into the following four stages:

- 1) Pore compaction stage (section OA). In the initial stage of compression, the internal pores and cracks are gradually compacted and closed, so that the strength of the specimen is improved.
- 2) Linear elastic deformation stage (section AB), the internal cracks gradually develop and penetrate in the end. At this stage, the stress–strain curve of the CPB is close to a straight line, and the stress growth rate gradually slows down.
- 3) Plastic deformation stage (section BC). As the load further increases, new cracks continue to be generated and intertwined with the original cracks, gradually extending and converging in the direction of stress action, and then the specimen enters the stage of yield failure.
- 4) Post-peak failure stage (section CD). Plastic deformation further develops, the load-bearing capacity of the CPB decreases rapidly, and visible macroscopic cracks are formed on the surface. The bearing capacity of specimen continues to decrease rapidly until it is completely destroyed.

DISCUSSIONS

Taking the CPB specimens with curing age 7, 14, and 28 days as an example (curing temperature $20 \pm 0.5^\circ\text{C}$), the relationships between the maximum principal stress and the confining pressure under uniaxial compression and triaxial compression test conditions are compared and analyzed, as shown in **Figure 9**.

It can be found from **Figure 9** that the maximum principal stress of the CPB under the axial force state is significantly lower than that of three-direction force state. Furthermore, the maximum principal stress increases nearly linearly with the increase of the confining pressure. Taking the confining pressure 400 kPa and curing age 28 days as an example, the differences between confining pressure



400 kPa and confining pressure-free (cement content 7, 10, and 25%) are 1.5, 1.7, and 0.4 MPa, respectively. The reason is that under the three-way stress state, the confining pressure limits the material deformation caused by the axial force, thereby improving the compressive resistance of the specimens.

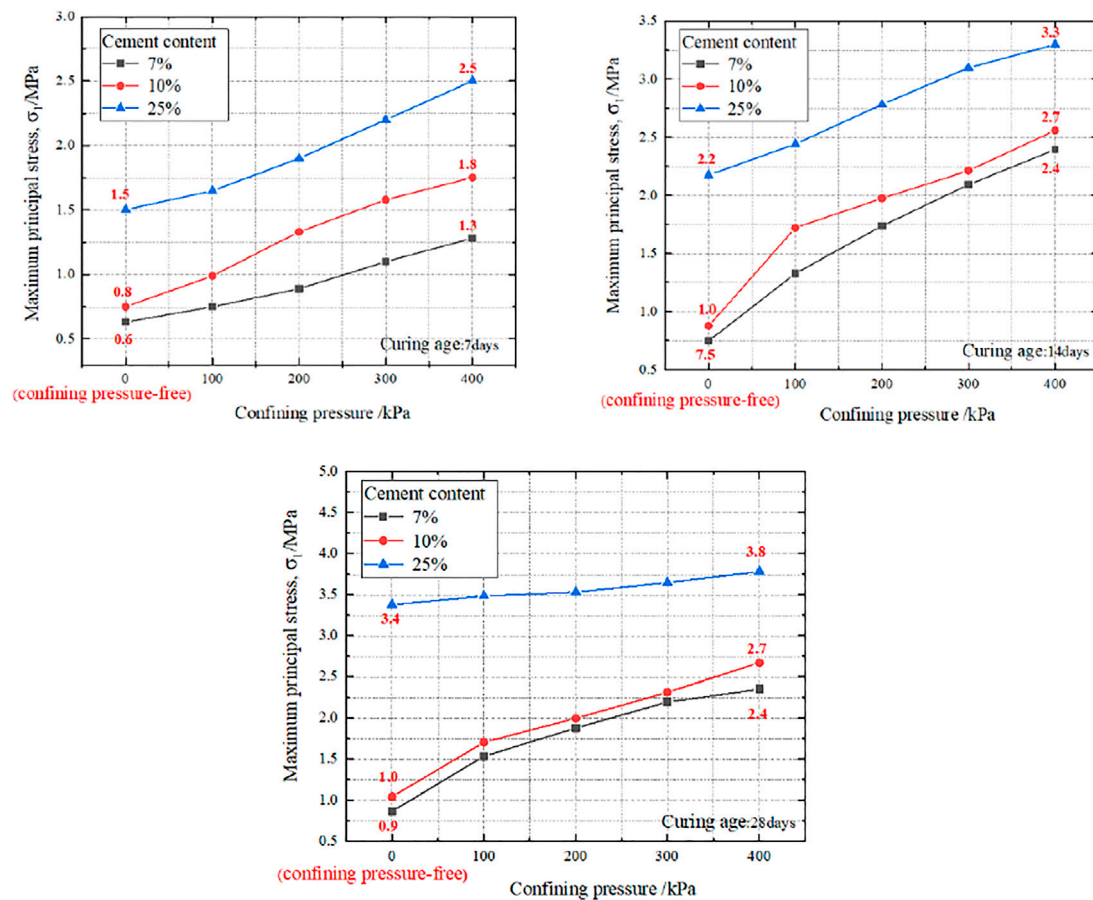


FIGURE 9 | Relation curve between maximum principal stress and confining pressure.

CONCLUSION

In this study, the results of an experimental investigation on the influence of cement content, curing age, and curing temperature on the compression behavior of CPB specimens are presented. The following conclusions were drawn:

- 1) The uniaxial compressive strength of CPB increases with the increase of cement content and curing age. When the cement content is high, the influence of curing age on the strength of CPB is more obvious.
- 2) The cement content, curing age, and curing temperature have an important influence on strength and cohesion. In the curing temperature range 25°C–50°C, increasing the curing temperature can significantly increase the cohesion. As the cement content is relatively low, after 14 days of curing age, the compressive strength and cohesion slow down.
- 3) The internal friction angle increases gradually with the increase of the cement content, curing age, and curing temperature, but the degree of influence is small.
- 4) With the increase of the curing age, the failure form of the CPB changes from the single oblique section shear failure to

the X-shaped failure. The failure process is divided into four stages: pore compaction, linear elastic deformation, plastic deformation, and post-peak failure.

DATA AVAILABILITY STATEMENT

The raw data supporting the conclusions of this article will be made available by the authors, without undue reservation.

AUTHOR CONTRIBUTIONS

ZZ contributed to design of the study and wrote the draft of the manuscript. JL carried out the experiment and performed the data analysis. All authors contributed to manuscript revision, read, and approved the submitted version.

FUNDING

This research was supported by the Key Program of the National Natural Science Foundation of China (No. 52130905).

REFERENCES

- Cai, S.-j. (2009). *Mechanical Basis of Mine Filling*. Berlin: Metallurgical Industry Press.
- Cao, S., Song, W.-d., Xue, G.-l., Ma, R.-w., and Zhu, P.-r. (2016). Variation Law of Mechanical Properties and Failure Mode of Layered Tailings Cemented CPB. *J. China Univ. Min. Technol.* 45, 717–722.
- Cao, S., Yilmaz, E., Song, W. D., and Xue, G. L. (2019). Assessment of Acoustic Emission and Triaxial Mechanical Properties of Rock-Cemented Tailings Matrix Composites. *Adv. Mater. Sci. Eng.* 2019, 6742392. doi:10.1155/2019/6742392
- Fall, M., Belem, T., Samb, S., and Benzaazoua, M. (2007). Experimental Characterization of the Stress-Strain Behaviour of Cemented Paste Backfill in Compression. *J. Mater. Sci.* 42, 3914–3922. doi:10.1007/s10853-006-0403-2
- Fall, M., Benzaazoua, M., and Ouellet, S. (2005). Experimental Characterization of the Influence of Tailings Fineness and Density on the Quality of Cemented Paste Backfill. *Minerals Eng.* 18, 41–44. doi:10.1016/j.mineng.2004.05.012
- Ghirian, A., and Fall, M. (2014). Coupled Thermo-Hydro-Mechanical-Chemical Behaviour of Cemented Paste Backfill in Column Experiments. *Eng. Geology.* 170, 11–23. doi:10.1016/j.enggeo.2013.12.004
- Guo, T.-r., and Li, Z.-j. (2017). Experimental Study on Reasonable Proportion of Cemented CPB for Iron Ore Tailings. *China Met. Bull.* 9, 112–113.
- Hou, Y.-q., Yin, S.-h., Cao, Y., Yang, S.-x., Zhang, M.-z., Kou, P.-f., et al. (2021). Uniaxial Compressive Stress-Strain Relationship and Damage Constitutive Model of Tailings Cemented Backfill. *Mater. Rep.* 16, 1–15.
- Jiang, H., Fall, M., Li, Y., and Han, J. (2019). An Experimental Study on Compressive Behaviour of Cemented Rockfill. *Construction Building Mater.* 213, 10–19. doi:10.1016/j.conbuildmat.2019.04.061
- Juenger, M. C. G., Snellings, R., and Bernal, S. A. (2019). Supplementary Cementitious Materials: New Sources, Characterization, and Performance Insights. *Cement Concrete Res.* 122, 257–73. doi:10.1016/j.cemconres.2019.05.008
- Li, J., Zhang, W., and Monteiro, P. J. M. (2020a). Structure and Intrinsic Mechanical Properties of Nanocrystalline Calcium Silicate Hydrate. *ACS Sustainable Chem. Eng.* 8, 12453–61. doi:10.1021/acssuschemeng.0c03230
- Li, J., Zhang, W., Xu, K., and Monteiro, P. J. M. (2020b). Fibrillar Calcium Silicate Hydrate Seeds from Hydrated Tricalcium Silicate Lower Cement Demand. *Cement Concrete Res.* 137, 106195. doi:10.1016/j.cemconres.2020.106195
- Li, K.-b. (2019). *The Mechanical and Acoustic Emission Characteristics of CPB under Uniaxial Compression under Temperature Influence*. China: Wuhan University of Technology.
- Li, Y.-f., Zhang, J.-m., Deng, F., and Bai, S.-w. (2005). Experimental Study on Strength Characteristics of CPB in Deep Goaf. *Rock. Soil Mech.* 26, 865–8. doi:10.3969/j.issn.1000-7598.2005.06.00
- Li, Y., and Li, J. (2015). Relationship between Fracture Area and Tensile Strength of Cement Paste with Supplementary Cementitious Materials. *Construction Building Mater.* 79, 223–8. doi:10.1016/j.conbuildmat.2015.01.052
- Libos, I. L. S., and Cui, L. (2020). Effects of Curing Time, Cement Content, and Saturation State on Mode-I Fracture Toughness of Cemented Paste Backfill. *Eng. Fracture Mech.* 235, 107174. doi:10.1016/j.engfracmech.2020.107174
- Liu, G.-s., Yang, X.-c., and Guo, L.-j. (2019). Three-Dimensional Arch Stress and Strength Demand Model of Subsequent CPB in Stage Open Field. *J. China Coal Soc.* 44, 1391–1403. doi:10.13225/j.cnki.jccs.2019.6025
- Lu, S.-b., Li, X., and Liao, Q.-l. (2008). Application Prospect and Environmental Protection of Filling Mining Method. *Nonferrous Met. (Mining Section)*. doi:10.3969/j.issn.1001-1277.2008.01.006
- Nie, Y.-l., Wang, X.-j., Huang, G.-l., Chao, L.-s., Feng, X., and Cao, S.-r. (2016). Strength and Damage Model Analysis of CPB with Different Moisture Content. *Bull. Chin. Ceram. Soc.* 37, 2008–2013. doi:10.16552/j.cnki.issn1001-1625.2018.06.035
- Rankine, R. M., and Sivakugan, N. (2007). Geotechnical Properties of Cemented Paste Backfill from Cannington Mine, Australia. *Geotech. Geol. Eng.* 25, 383–393. doi:10.1007/s10706-006-9104-5
- Richardson, I. G. (2008). The Calcium Silicate Hydrates. *Cement Concrete Res.* 38, 137–58. doi:10.1016/j.cemconres.2007.11.005
- Wang, X.-m., Hu, Y.-b., Wang, S., Liu, J.-x., Chen, Y., and Bian, J.-w. (2015). Orthogonal Experimental Study on Optimization of Filling Ratio of Superfine Tailings. *Gold. Sci. Technol.* 3, 45–49. doi:10.11872/j.issn.1005-2518.2015.03.045
- Wang, Y.-p. (2014). *Study on Cemented Waste Rock Filling Process and Numerical Simulation of Meso-Level Mechanical Properties of CPB*. China: Central South University.
- Wei, X.-m., Guo, L.-j., Zhou, X.-l., Li, C.-h., and Zhang, L.-x. (2020). Research on Full Time Sequence Stress Evolution Law and Prediction Model of High Stage Cemented. *CPB. Rock. Soil Mech.* 41, 3613–3620. doi:10.16285/j.rsm.2020.0585
- Wu, W.-l., Liu, G.-s., Guo, L.-j., Fan, C., Zhang, Z.-h., and Zhang, X.-m. (2019). Study on Mechanical Properties of Interface between Cemented CPB and Rock Based on Direct Shear Test. *China Min. Mag.* 28, 116–122. doi:10.12075/j.issn.1004-4051.2019.12.008
- Wu, W.-l., Xu, W.-b., and Zuo, J.-p. (2021). Effect of Inclined Interface Angle on Shear Strength and Deformation Response of CPB-Rock under Triaxial Compression. *Constr. Build. Mater.* 279, 122478. doi:10.1016/j.conbuildmat.2021.122478
- Xie, Y., He, W., Zhu, Z.-c., Liu, H., and Xie, T. (2015). Acoustic Emission Characteristics and Damage Evolution of CPB under Uniaxial Compression. *Chin. J. Appl. Mech.* 32, 670–676. doi:10.11776/cjam.32.04.D034
- Xu, W.-b., Song, W.-d., Dong, X., and Ma, Y. (2019). Analysis of Triaxial Compression Deformation Failure and Energy Dissipation Characteristics of Cemented. *CPB. Rock. Soil Mech.* 35, 3421–3429. doi:10.16285/j.rsm.2014.12.025
- Xu, W.-b., Song, W.-d., Wang, D.-x., and Ma, Y. (2014). Characteristic Analysis of Deformation Failure and Energy Dissipation of Cemented CPB Body under Triaxial Compression. *Rock. Soil Mech.* 35, 3421–3429. doi:10.16285/j.rsm.2014.12.025
- Yang, S.-x., Fu, Y.-h., Peng, J.-h., and Yang, M.-s. (2018). Analysis of Failure Mode and Energy Dissipation Characteristics of Full Tailings CPB under Triaxial Compression. *Ind. Miner. Process.* 47, 30–33. doi:10.16283/cnki.hgkwyjg.0.2018-06-008
- Yang, X., and Guo, L.-j. (2018). *Comprehensive Utilization Technology of Tailings and Waste Rock*. Beijing: Chemical Industry Press.
- Yi, X.-F., Liu, C.-K., and Wang, Y. (2020). *In Situ* CT Scanning Experimental Study on Fracture Evolution Process of Metal Tailings Cemented CPB. *Rock. Soil Mech.* 41, 3365–3373. doi:10.16285/j.rsm.2019.1962
- Zhang, L., Guo, L.-j., and Li, W.-c. (2020). Experimental Study on Preparation of Filling Cementitious Materials Based on Copper-Nickel Smelting Slag. *Gold. Sci. Technol.* 28, 669–677. doi:10.11872/j.issn.1005-2518.2020.05.106
- Zhao, C.-q., and Hu, N.-l. (2008). Development and Application of Filling Cementitious Materials. *Gold* 29, 25–29. doi:10.3969/j.issn.1001-1277.2008.01.006
- Zhao, K., Yu, X., Zhu, S., Yan, Y., and Huang, M. (2020). Acoustic Emission Fractal Characteristics and Mechanical Damage Mechanism of CPB Prepared with Tantalum Niobium Mine Tailings. *Constr. Build. Mater.* 258, 1–11. doi:10.1016/j.conbuildmat.2020.119720
- Zhou, X., Hu, S., Zhang, G., Li, J., Xuan, D., and Gao, W. (2019). Experimental Investigation and Mathematical Strength Model Study on the Mechanical Properties of Cemented Paste Backfill. *Construction Building Mater.* 226, 524–533. doi:10.1016/j.conbuildmat.2019.07.148

Conflict of Interest: The authors declare that the research was conducted in the absence of any commercial or financial relationships that could be construed as a potential conflict of interest.

Publisher's Note: All claims expressed in this article are solely those of the authors and do not necessarily represent those of their affiliated organizations, or those of the publisher, the editors and the reviewers. Any product that may be evaluated in this article, or claim that may be made by its manufacturer, is not guaranteed or endorsed by the publisher.

Copyright © 2021 Zhang and Li. This is an open-access article distributed under the terms of the Creative Commons Attribution License (CC BY). The use, distribution or reproduction in other forums is permitted, provided the original author(s) and the copyright owner(s) are credited and that the original publication in this journal is cited, in accordance with accepted academic practice. No use, distribution or reproduction is permitted which does not comply with these terms.



Basic Properties of fly Ash/Slag-Concrete Slurry Waste Geopolymer Activated by Sodium Carbonate and Different Silicon Sources

Yingli Gao^{1*}, Kairui Duan¹, Shuncheng Xiang¹ and Wei Zeng²

¹School of Traffic and Transportation Engineering, Changsha University of Science and Technology, Changsha, China, ²China West Construction Hunan Group Co., Ltd., Changsha, China

OPEN ACCESS

Edited by:

Tingting Zhang,
Dalian University of Technology, China

Reviewed by:

Ping Duan,
China University of Geosciences
Wuhan, China
Peng Zhang,
National Natural Science Foundation
of China, China

*Correspondence:

Yingli Gao
yingligao509@126.com

Specialty section:

This article was submitted to
Structural Materials,
a section of the journal
Frontiers in Materials

Received: 01 August 2021

Accepted: 12 October 2021

Published: 19 November 2021

Citation:

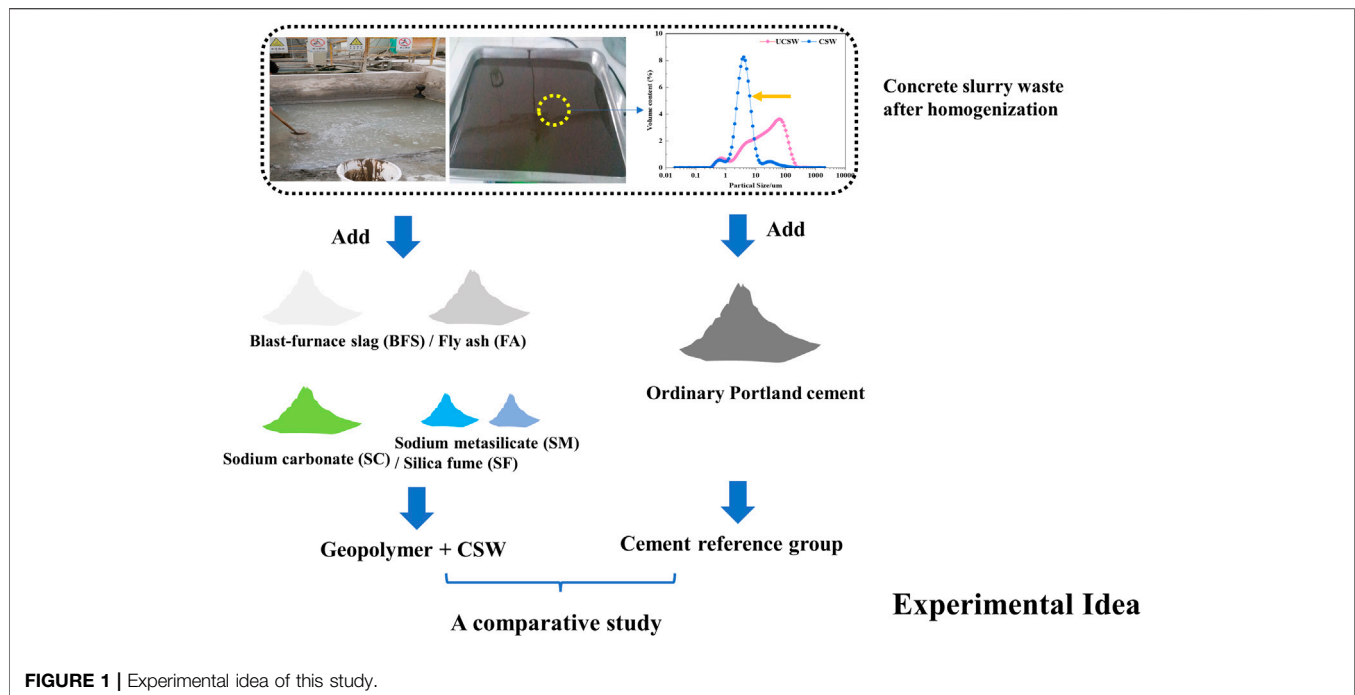
Gao Y, Duan K, Xiang S and Zeng W
(2021) Basic Properties of fly Ash/Slag
-Concrete Slurry Waste Geopolymer
Activated by Sodium Carbonate and
Different Silicon Sources.
Front. Mater. 8:751585.
doi: 10.3389/fmats.2021.751585

As a kind of granular waste with complex composition and alkali corrosiveness, concrete slurry waste (CSW) has severe recycling limitations in the ordinary Portland cement (OPC). Considering this, a new type of geopolymer, prepared by granulated blast furnace slag/fly ash, concrete slurry waste, and powdered activators (sodium carbonate and different silicon sources including sodium metasilicate pentahydrate and silica fume), was adopted to conduct a comparative study with the OPC counterpart. In this study, the homogenized CSW was mixed in the OPC and geopolymer with a constant ratio of 50 wt%, respectively. Then the properties were studied in terms of the flowability, setting times, mechanical strengths, and microstructures. The results showed that better flowability (200 mm) could be achieved in the obtained geopolymer than in the OPC reference group (95 mm) by increasing the powdered activators. The setting time of the OPC was significantly shortened due to the addition of CSW. The strengths of geopolymer were supported by the produced C-A-S-H and carbonates, with less chemically bonded water than the hydration products in the reference group. The dominant size of pores in the hardened geopolymer was much smaller than that in the OPC group which was 80 nm. Silica fume could be the alternate of the sodium metasilicate pentahydrate and had an insignificant negative impact on the fresh and hardened properties and microstructures of the geopolymer when the incorporation rate was within 5%.

Keywords: concrete slurry waste, fly ash, slag, geopolymer, properties

INTRODUCTION

As an energy-intensity industry, the production of ordinary Portland cement is accompanied by a massive amount of CO₂ emission and has left a large amount of hardened or unhardened waste (Ali et al., 2011; Singh et al., 2015; Miller et al., 2016; Shen et al., 2017). Among these, the reuse of the unhardened waste generated from the concrete batching plant (CBP) in China is greatly restricted, especially for concrete slurry waste (CSW). Concrete slurry waste is an unhardened residue of returned fresh concrete that has been treated by washing and aggregate recycling systems due to excess supply or unsatisfactory performance. According to the previous studies, concrete waste is produced every day in CBP (about 165–350 million tonnes), and most of it is deposited in landfills, which not only results in a detrimental effect on the ecosystem but also occupy many free lands for its storage (Vieira and Figueiredo, 2016; Xuan et al., 2016; Iizuka et al., 2017). It has been revealed that



the incorporation of CSW into mortar or concrete is an efficient stabilization method in terms of the heavy metals' leaching behavior (Audo et al., 2018). However, the activity of CSW is very low owing to the long storage period in the sediment pit with high alkalinity (pH normally ranging from 11.0 to 13.0) (Vieira and Figueiredo, 2016). Thus, it is reasonable to consider CSW as aggregate or filler substitutes in concrete productions after dewatering, drying, crushing, and sieving. The relevant studies highlighted that the substitute rate should not exceed 30% because of its poor qualities (high porosity, weak adhesion of the old mortar, and low strength), which can cause the degradations of the workability, strengths, fire resistance, and durability (Correia et al., 2009; Kou S.-c. et al., 2012; Kou et al., 2012 S.-C.; Audo et al., 2016; Rughooputh et al., 2017). A similar situation is also observed when the CSW is used for cement or fly ash substitute after drying, dry milling, or calcination. The dried CSW powder can replace about 0–6% cement with little degradation of the strengths and workability (Zervaki et al., 2013; Ferriz-Papia, 2014). Generally, the CSW may not be suitable to use in new concrete productions. Thus, a new cementitious system is desired to solve the disposal problem of the CSW.

CSW is rich in calcium and silicate components and can act as an alkaline substance. Based on this, it is understandable to consider CSW as a raw material in geopolymer (Elyamany et al., 2018; Thakur et al., 2019). At present, there are two kinds of geopolymers that have been described by researchers in their studies: one is called conventional geopolymer, the other is named as “one-part” geopolymer (Luukkonen et al., 2018a; Ng et al., 2018; Askarian et al., 2019). However, considering the safety problems and the impracticalities related to handling large amounts of viscous, corrosive, and hazardous alkaline

solutions, conventional geopolymer might not be suitable to combine with the original alkaline CSW. Accordingly, the “one-part” geopolymer is proposed to solve the mentioned worries.

So far, there is little study conducting experiments about the recycling of CSW in the “one-part” geopolymer, but the advantages of it are outstanding: Firstly, it only needs dry mixtures that consist of solid aluminosilicate and activator powders rather than using alkaline solutions; Secondly, the water is regarded as the initial reaction trigger in the “one-part” AAMs, which is similar to that of OPC (Duxson and Provis, 2008; Adesanya et al., 2018). The experimental idea is shown in **Figure 1**. Specifically, granulated blast-furnace slag/fly ash were regarded as the supplements of precursors in the geopolymer, and powdered sodium carbonate was chosen as the primary activator because its buffer capacity can moderate the corrosive of the CSW-composite and improve the handling safety for the researchers (Peng et al., 2017; Ishwarya et al., 2019). Besides, sodium metasilicate pentahydrate, as an auxiliary activator, was adopted to enhance the properties of geopolymer, and the silica fume was expected to substitute it to expand the environmental benefits (Sturm et al., 2016; Ye et al., 2016).

This paper aimed to provide a new preparation method of cementitious materials containing CSW and the basic properties (flowability, setting times, and mechanical strengths) and microstructures (including X-ray diffraction/XRD, Fourier transform Infrared spectroscopy/FTIR, Thermal gravity analysis/TG-DTG, and Mercury intrusion porosimetry/MIP) of the geopolymer and the cement reference group were investigated. Then, the advantages and disadvantages of these two cementitious composites were discussed. The obtained

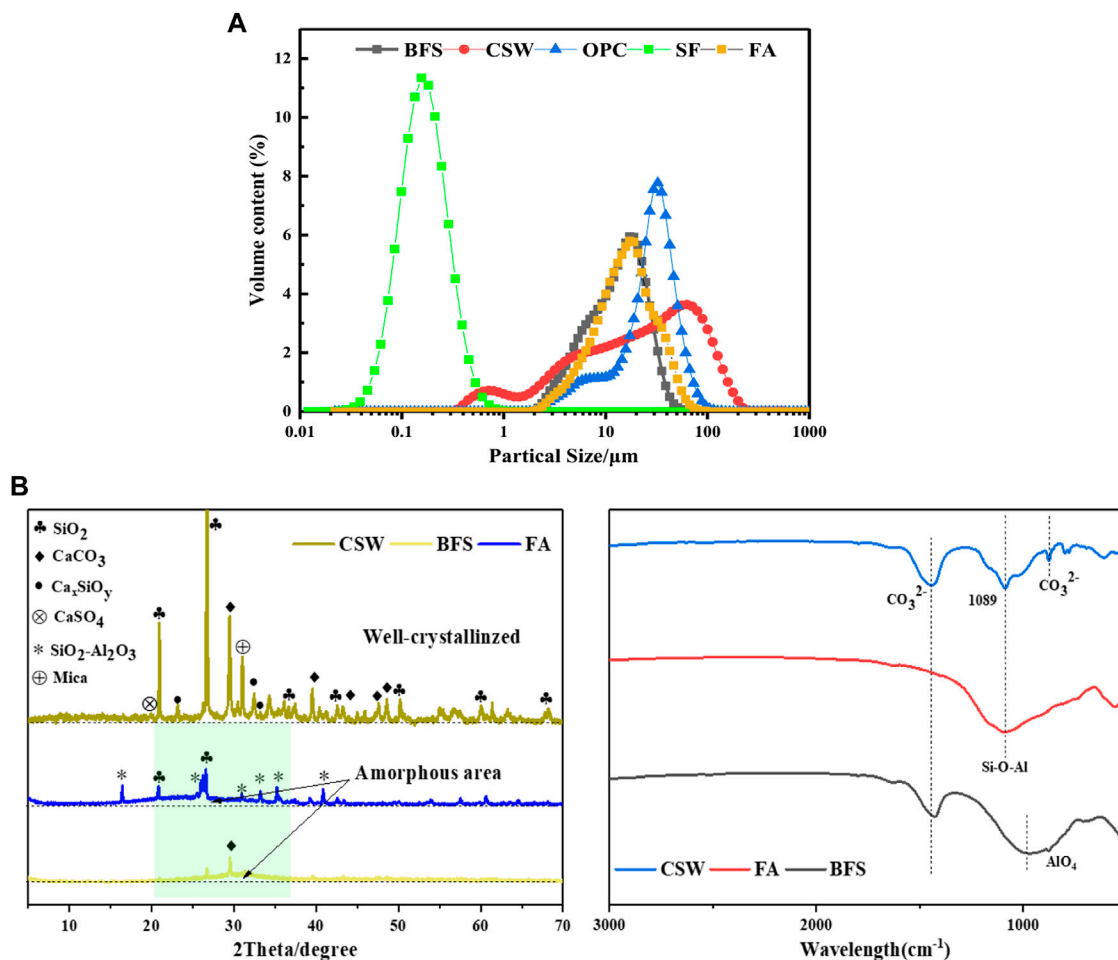


FIGURE 2 | Basic characteristics of raw materials.

geopolymer mixed with concrete slurry waste in this study provides new ideas and references for preparing a new type of cementitious material and is beneficial to recycling various wastes.

MATERIALS AND METHODS

Materials

Blast-furnace slag (BFS), fly ash (FA), silica fume (SF), and P.O 42.5 ordinary Portland cement (OPC) were provided by China West Construction Hunan Group Co., Ltd., and the concrete slurry waste (CSW) with solid to water ratio of 1:1 was collected from the concrete mixing plant of the same company (CSW sedimented within 1 week). The particle size distributions of the raw materials are shown in **Figure 2A**, and the chemical compositions of these raw materials were determined by the X-ray fluorescence spectrometer (XRF), as shown in **Table 1**. As can be seen, there is high content of SiO_2 and LOI value in the CSW, which implies that CSW contains much sand and some carbon particles/organic components (He et al., 2020). This is in line with the results of X-ray diffraction (XRD) and Fourier

TABLE 1 | Chemical compositions of raw materials by XRF.

Main chemical oxides	BFS (%)	FA (%)	SF (%)	Cement (%)	CSW (%)
SiO_2	32.80	57.53	95.5	23.35	39.35
Al_2O_3	14.30	31.30	1.15	5.42	10.09
CaO	39.50	2.73	0.4	61.18	23.11
MgO	9.20	0.81	0.75	2.64	1.74
Fe_2O_3	0.88	5.04	0.72	2.78	6.29
Na_2O	0.20	0.08	1.2	0.07	0.33
K_2O	0.63	1.33	0.6	0.69	1.54
MnO	0.07	0.03	—	—	0.10
SO_3	1.32	0.45	0.55	2.42	1.12
LOI	1.1	0.7	—	1.45	16.38

transform infrared spectroscopy (FTIR), as shown by **Figure 2B**. CSW is a well-crystallized substance with complex components, and there are complex bands ranging from 469 to 875 cm^{-1} . It is worth noticing that the bands at approximately 1,089, 1,092, and 967 cm^{-1} in the CSW, FA, and BFS, respectively, represent the asymmetric stretching vibration of Si-O-T (T = Al or Si) and are

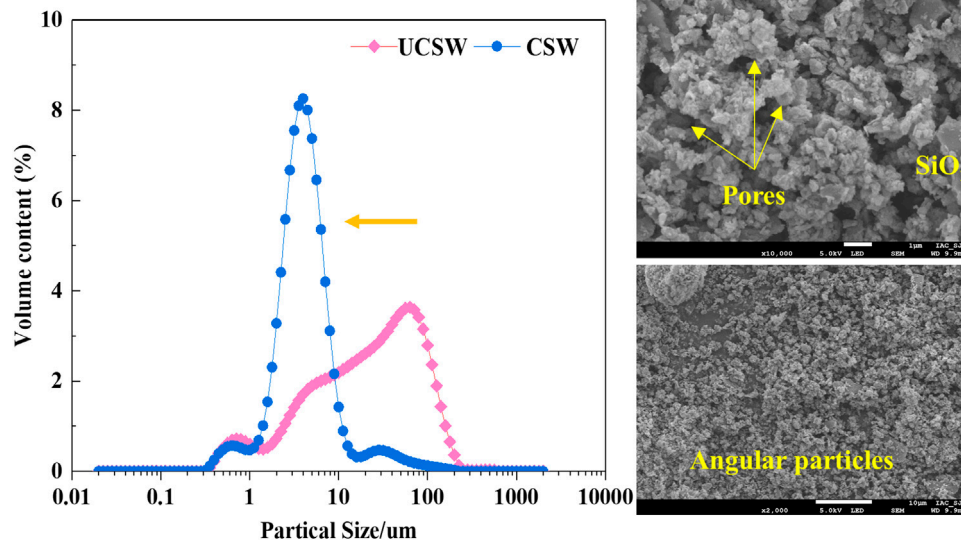


FIGURE 3 | Particle size distribution and SEM morphology of the homogenized CSW.

closely related to the alkaline activation process (Hajimohammadi and van Deventer, 2017; Kaja et al., 2018). The commercial powdered activators used in this study were sodium carbonate anhydrous ($\text{Na}_2\text{CO}_3/\text{SC}$, AR, Purity \geq 99.8%) and sodium metasilicate pentahydrate ($\text{Na}_2\text{SiO}_3 \cdot 5\text{H}_2\text{O}/\text{SM}$, AR, modulus of 0.93). Silica fume (SF) with ultra-fine particle size, as depicted in **Figure 2A**, was expected to substitute the commercial silicon source (SM).

Preparation of Homogenized Concrete Slurry Waste

To develop the filling effect of CSW, as reported by He et al. (He et al., 2020), and obtain a CSW-composite with dense microstructures, CSW was treated by wet-grinding before being added into the geopolymer and OPC (Tan et al., 2018). The grinding balls were made of zirconium silicate, and the mass ratio of the balls with different diameters (3 mm:2.5 mm:0.7 mm) equaled to 2:5:3. Moreover, the mass ratio of the balls and CSW (weight of the solids content) was 2.5:1. Then the grinding balls and CSW were poured into the machine for grinding (45 min). The parameters of the control cabinet were as follows: electric current for 7–10 A, voltage for 380 V, and frequency for 35–45 Hz. The wet-grinding CSW (pH = 11.0) with uniform particle size distribution was obtained when the separation of the balls and slurry was completed. The target size of homogenized CSW was consistent with the previous studies, $D_{50} \approx 3\text{--}5\text{ }\mu\text{m}$ (Tan et al., 2018; He et al., 2020).

Figure 3 shows the particle size distribution and SEM morphology of the homogenized CSW. It can be seen that the uniform particle size was obtained in the CSW, with a D_{50} of $3.757\text{ }\mu\text{m}$. The SEM morphology shows that many fine particles with an angular shape and clusters scatter randomly, and there are many pores on the surface of those clusters. Besides, many smooth flake particles, identified as SiO_2 , embedded in those observed clusters.

Mix Proportions and Mixing Procedures

Mix proportions of one reference group (cement + CSW, CCSW) and 11 geopolymer groups (geopolymer + CSW, GCSW) are shown in **Table 2**. The water to binder ratio (W/B) was kept at 0.5 in all specimens. The mass ratio of binders and CSW was 1:1, and the ratio of sodium carbonate and silicon sources (sodium metasilicate pentahydrate + silica fume) was kept at 1.5:1 (Ishwarya et al., 2019). Specifically, in the GCSW groups of No.1 to No.4, 9% sodium carbonate and 6% sodium metasilicate (total 15%, mass ratio of the binders) were utilized as the activators, and the effect of different binder proportions (fly ash and slag) was evaluated. The effect of activator dosages (10–25%) was investigated in GCSW groups of No.5 to No.8, and the influence of silica fume substitution for sodium metasilicate was explored in GCSW groups of No.8 to No.11.

A cement mixer was used to prepare all the specimens. Firstly, the homogenized CSW was poured into the container and then mixed for 1 min at a rotation speed of $140 \pm 5\text{ r/min}$ and revolution speed of $62 \pm 5\text{ r/min}$. Afterward, fly ash and slag were added into the CSW and mixed for another 2 min at a rotation speed of $280 \pm 10\text{ r/min}$ and revolution speed of $125 \pm 10\text{ r/min}$. Secondly, the activators were wet mixed with the matrix obtained from above for 2 min. Finally, the homogenized matrix was completed and cast into $40 \times 40 \times 160\text{ mm}$ detachable steel prism molds immediately. Each specimen was prepared in triplicate. A vibrating table (1×60 shocks, one shock/s) was used to improve compactness and eliminate the air bubbles in the matrix. All the specimens were de-molded after 24 h and cured at $20 \pm 1^\circ\text{C}$ and 90% relative humidity for 3, 7, and 28-days tests.

Test Methods

Flowability of mixtures was tested by a conical mold (36 mm, 60 mm, and 36 mm) and a smooth glass plate. Before the homogenized matrix that got from the mixer was cast, it

TABLE 2 | Mix proportions of the 12 groups.

Target	No	Labelled	Binders (g)			CSW (g)	Activator (%)		
			FA	BFS	OPC		SC	SM	SF
Reference	0	CCSW	0	0	900	900 (water to solid ratio = 1:1)	—	—	—
GCSW: influence of binder proportions	1	1:0 15% (0%)	900	0	—		9%	6%	0%
	2	4:1 15% (0%)	720	180					
	3	2:1 15% (0%)	600	300					
	4	1:1 15% (0%)	450	450					
GCSW: Influence of activators and different silicon sources	5	1:1 10% (0%)	450	450	—		6%	4%	
	6	1:1 15% (0%)					9%	6%	
	7	1:1 20% (0%)					12%	8%	
	8	1:1 25% (0%)					15%	10%	0%
	9	1:1 25% (2.5%)					15%	7.5%	2.5%
	10	1:1 25% (5%)					15%	5%	5%
	11	1:1 15% (10%)					15%	0%	10%

¹ CCSW-concrete slurry waste; FA-fly ash; BFS-slag; OPC-cement; SC-sodium carbonate; SM-sodium metasilicate pentahydrate; SF-silica fume; CCSW-"Cement + CSW" for reference; GCSW-"Geopolymer + CSW".

² Labelled explanations of GCSW: for example, "1:1 15% (0%)" means: FA: BFS = 1:1, content of total activators = 15%, SF incorporation rate = 0%.

³ W/B = 0.5, SC:(SM + SF) = 1.5:1, CSW: binder = 1:1.

would be poured into the conical mold. When the conical mold was full of the matrix, the top surface of it would be scraped flat, and then the conical mold was lifted so that the matrix could flow freely on the surface of the plate. The flow diameter was defined as the mean values of two perpendicular directions. Setting times of the CCSW and GCSW were measured by a Vicat apparatus according to the standard ASTM C191. Compressive and flexural strengths were tested according to the standard ASTM C349. The flexural strength was measured on three specimens for each group, and the compressive strength was further measured on the rest of the six broken half-specimens. After completing the tests of 28-days, the pieces within dimensions of 15 mm × 15 mm × 15 mm were collected and immersed into the anhydrous ethanol for 3 days to stop the reactions. Then the pieces were dried at 40°C in a vacuum environment for 24 h. Thereafter, some of the pieces were ground and passed the 0.75 mm sieve for XRD, FTIR, and TG-DTG analysis.

FTIR was taken using Nicolet Nexus 410 FTIR Spectrometer Spectrum, and the data was collected in transmittance mode from 4,000 cm⁻¹ to 500 cm⁻¹ with an accuracy of 0.01 cm⁻¹. The mineral phase analysis was launched with X-ray diffraction with Cu(Kα) source (XRD, German BRUKERD8 ADVANCE Diffractometer) at a scanning rate of 2°/min with the 2θ ranging from 5° to 80°. Thermal gravity analysis experiments (TGA, TGA5500) were conducted with 20 ± 2 mg powder under the nitrogen atmosphere and heated at 10°C/min from ambient temperature to 1,000°C. Besides, pore size characteristics of the CCSW and GCSW were tested by Mercury intrusion porosimetry (MIP, AutoPore IV 9500, America). The surface tension of Mercury was 485 mN/m, and the contact angle was 140°.

RESULTS AND DISCUSSIONS

Flowability

Figure 4 shows the flow diameters of CSW-composites. As can be seen, the flow diameter of CCSW is only 95 mm, which is significantly lower than that of the GCSW groups. This may be

related to the morphology of CSW and the reaction characteristics between the two kinds of cementitious materials. In other words, CSW is mainly composed of many extremely porous, absorbent, and coarse clusters, as shown in *Preparation of homogenized CSW*. These clusters in the CSW can increase the friction between particles and reduce the local water-binder ratio by absorbing part of free water, thus weakening the flow performance of CCSW (He et al., 2020). Besides, due to the cement hydration, the free water was consumed, and the flow diameter of CCSW decreased furtherly. The flow diameters of GCSW groups fluctuate between 93 and 200 mm. When the level of activators is fixed at 15%, and the SF incorporation rate kept at 0%, the flow diameters of GCSW gradually decrease from 192 to 165 mm with the increase of BFS, which can be attributed to the existence of CaO and rough morphology of BFS (Ismail and El-Hassan, 2018). On the contrary, the flow diameters of GCSW are proportional to the dosages of activators. With the activators increase from 10 to 25%, the flow diameters of GCSW increase from 130 to 200 mm. As reported, with the increase of activators, more BFS and FA particles could be dissolved, and the particle concentration in the GCSW decreased accordingly. Thus the flow diameters of GCSW were improved (Ishwarya et al., 2019). Besides, when the SF incorporation rate keeps within 2.5%, the flowability of GCSW has an insignificant decrease. However, when the incorporation rate of SF reaches over 5%, a significant decrease in the flow diameter of GCSW could be observed. In particular, when SF completely replaces the SM (10% SF incorporation rate), the flow diameter of GCSW is almost equal to that of the CCSW. Ultra-fine SF particles have a large specific surface area, and the increase of SF content would increase the water requirement for the GCSW to reach the same flow diameter. Therefore, when the SF substitution rate exceeds a certain range, the flow performance of GCSW would suffer a significant loss. This result is consistent with the experimental conclusions obtained by Liu et al., 2020.

Setting Times

The results of the setting time are presented in **Figure 5**. After adding CSW into the OPC, the initial and final setting times of

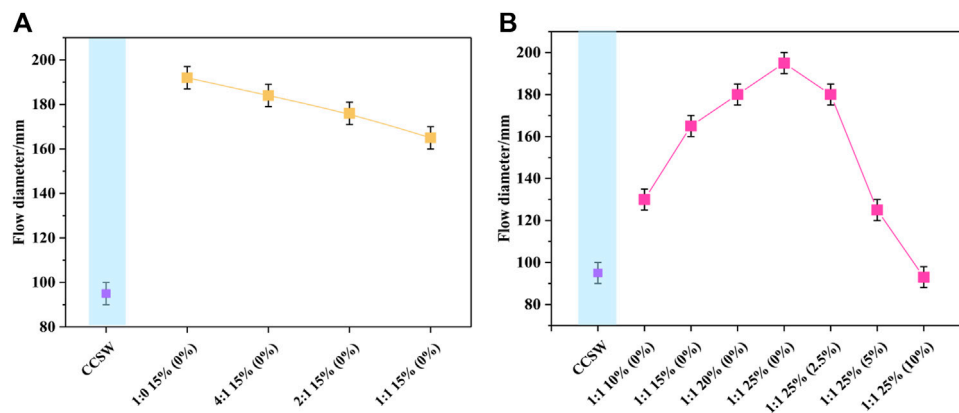


FIGURE 4 | Flowability of the CCSW and GCSW (A: influence of slag; B: influence of activator and silica fume).

CCSW are reduced to about 80 and 145 min, respectively. As reported by Liu et al. (2019), He et al. (2020), the setting time of the cementitious system was greatly influenced by the filling effect and nucleation effect of CSW. On the one hand, CSW would replace the unhydrated substances in the CCSW to fill the pores inside the structure at an early stage, densifying the internal structure and facilitating the skeleton formation. On the other hand, CSW could also act as a nucleation site to provide contact sites for the connection of hydration products, while some of the hydration products contained in the CSW could induce and accelerate the reaction process of the OPC, thus accelerating the initial and final setting times (Soliman and Nehdi, 2011). Compared to CCSW, the initial and final setting times of GCSW fluctuate between 70–255 min and 115–300 min, respectively. For example, when the activator's dosage is fixed at 15%, and the SF incorporation rate keeps at 0%, the setting times of GCSW are gradually shortened with the increase of BFS. This is due to the higher activity of BFS than FA, and the addition of BFS provides more CaO to GCSW, which can accelerate the reaction rate (Figure 5A). A similar situation can also be observed when the dosage of activators is increased. It can be seen from Figure 5B), when the dosage of activators is increased from 10 to 25%, the initial and final setting times of GCSW are shortened by about 63.16 and 53.06%, respectively. Increasing the dosage of the activators is equivalent to providing more Na₂O to GCSW, which results in a higher pH value of pore solution in the GCSW groups, thereby increasing the dissolution and reaction rate of the raw materials (Yousefi Oderji et al., 2019). However, it is worth noticing that the setting times of GCSW can be gradually prolonged as the SF incorporation rate increases (0–10%), especially when the rate of SF exceeds 5%. The initial and final setting times of GCSW are almost equal to that of the pure OPC, reaching 180 and 215 min, respectively. On the one hand, it is speculated that, compared to SM, SF cannot provide additional Na₂O, resulting in lower alkalinity of pore solutions. On the other hand, SF may have weaker solubility than SM under alkaline conditions, leading to more undissolved SF particles and hindering the connection of the generated alkali-activated products (Luukkonen et al., 2018a). Moreover, this

phenomenon also explains the decrease of flow diameters of GCSW with high SF incorporation rates.

Mechanical Strengths

Figure 6 shows the compressive and flexural strengths of the hardened CSW-composites at 3, 7, and 28 days, respectively. For CCSW, the 3-days strength reaches 32.5 MPa with the addition of CSW to the cement, and increases to 40.2 and 43.6 MPa at 7 and 28 days, respectively. Moreover, the compressive strength of CCSW only increases by 8.46% during the curing period from 7 to 28 days. In the case of GCSW, the compressive strength increases with the increase of BFS. The 3, 7 and 28 days compressive strengths of GCSW without adding BFS are only 0.9, 3.4, and 4.9 MPa, respectively, whereas, when the mass ratio of FA to BFS reaches 1:1, the corresponding compressive strengths of GCSW increases to 19.4, 28.9, and 38.7 MPa, respectively, and its 28 days strength is almost the same as that of the CCSW. This indicates that the sodium carbonate type activator cannot effectively activate the precursors consisting of only FA and CSW particles under ambient temperatures, while the incorporation of BFS greatly enhances the reactivity of GCSW. According to the previous studies, the mechanical properties of geopolymer usually reach a more satisfactory level when FA: BFS is equal to 1:1 (Chen et al., 2015; Abdalqader et al., 2016). Besides, when the FA: BFS keeps at 1:1, and the SF incorporation rate is 0%, the variation of the activators also significantly affects the compressive strengths of GCSW groups. For instance, when the activators are reduced from 15 to 10%, the 3, 7, and 28 days strengths of GCSW decrease by 26.29, 29.41, and 24.40%, respectively. They reach 29, 41.1, and 60 MPa when the activators are increased from 15 to 25%, and the corresponding improvement rate reaches nearly 55.04%. The change in the strengths of GCSW is mainly attributed to the alkaline equivalent provided by the activators. With the increase of pH values, the dissolution of reactive species in FA and BFS increases, thus generating more products to improve specimens' early and late strengths (Jeong et al., 2019). In addition, the type of additional silica source (activator) is also one of the most important parameters affecting the strength development of

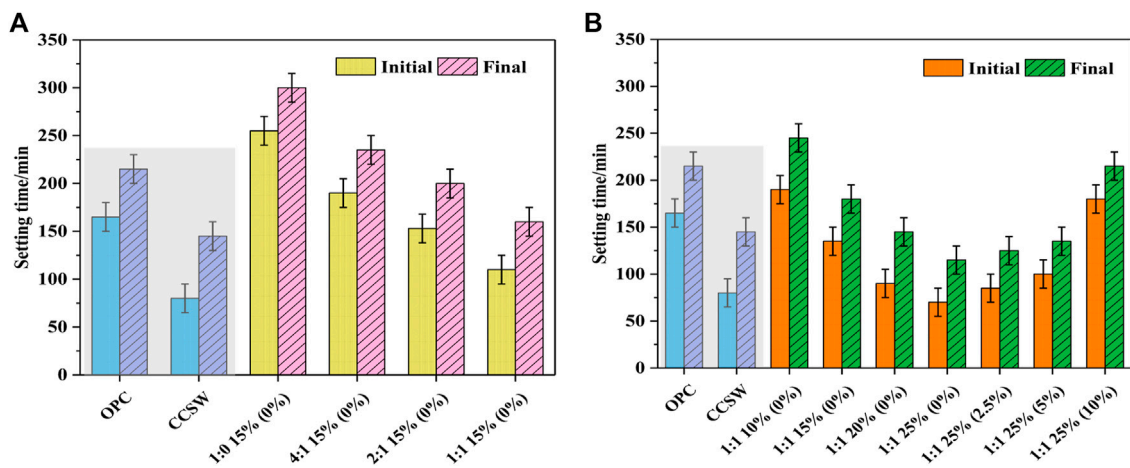


FIGURE 5 | Setting times of the CCSW and GCSW (A: influence of slag; B: influence of activator and silica fume).

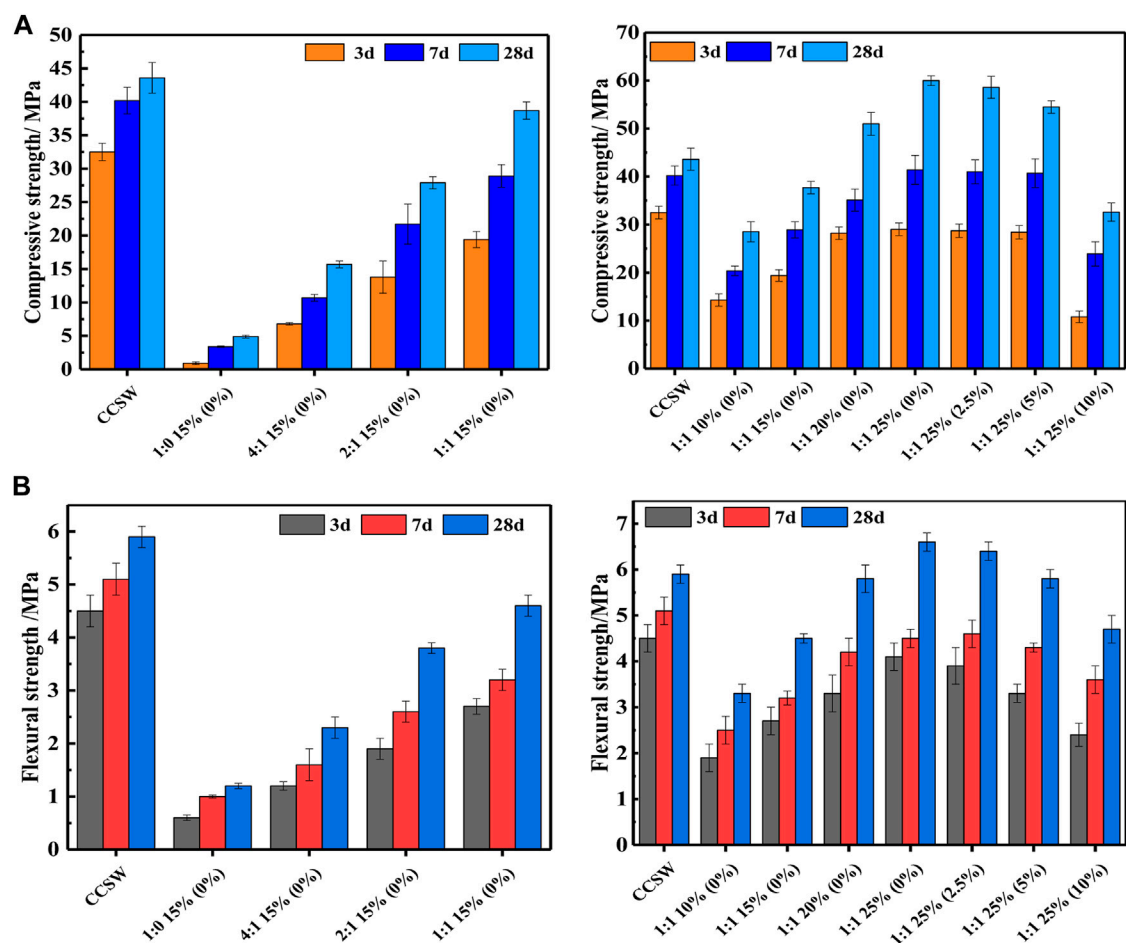


FIGURE 6 | Mechanical performances of CCSW and GCSW composites.

GCSW (Luukkonen et al., 2018b). It is worth noting that there is almost no adverse effect on the early strength of the GCSW group (3 and 7 days) with FA: BFS of 1:1 and activator dosage of 25%, when the SF incorporation rate reaches 2.5%. However, when the SF incorporation rate exceeds 5%, a significant reduction in the compressive strengths of GCSW is observed at all ages. This phenomenon is not difficult to be understood by combining the results of flow diameters and setting times of the corresponding specimens. Compared to commercial SM, the ability of SF to provide a soluble silicon source in an alkaline environment is limited, and its substitution rate should be kept within 5% (Luukkonen et al., 2018a).

The development of flexural strength is similar to that of compressive strength. The flexural strength could be effectively improved by increasing the content of BFS and activators. The 28 days flexural strength of GCSW increases to approximately 7 MPa when the FA: BFS is 1:1, and the dosage of activators is 25%. In this study, the set ratio of FA and BFS is scientific and reasonable because it was reported that the high-level content of BFS may cause severe shrinkage, which could leave many microcracks inside the specimen and have a negative effect on the flexural strength (Yousefi Oderji et al., 2019). Besides, the 28 days flexural strength of GCSW reaches the same level as CCSW when the FA: BFS is 1:1, and the activator's dosage reaches 20%.

X-Ray Diffraction Analysis

Figure 7 presents the XRD patterns of CCSW and typical GCSW, in which the main crystalline products of the CSW-composites can be observed when the 2θ ranged from 5 to 70° (Pan et al., 2018). Although the peak intensities of the minerals can reflect the relative content of particular phases, the XRD results were mainly used for qualitative analysis rather than quantitative analysis. Firstly, it needs to be noted that the peaks of quartz, calcium carbonate, and calcium-silica with different Ca/Si ratios in the CSW are still detectable in the CCSW and GCSW, which is consistent with the high crystallinity of CSW. For the CCSW, no new crystalline phases are observed, except for the cement hydration products (e.g., ettringite, gypsum, calcium silicate hydrate, and calcium hydroxide). In the GCSW, the XRD patterns show slight differences under the influence of BFS and activators. As for the GCSW with 15% activator, 0% BFS and 0% SF incorporation rate, a broad diffuse hump, and crystalline peaks of mullite and quartz are observed in the range of $20\text{--}40^\circ 2\theta$, which are mainly attributed to the nature of BFS and FA in the raw materials. Referring to the lowest mechanical strengths of the GCSW specimen, "1:0 15% (0%)", it can be inferred that the reaction degree of this specimen is still low at 28 days. Also, a high-intensity peak is detected at $28.8^\circ 2\theta$, which is identified as gaylussite ($\text{Na}_2\text{Ca}(\text{CO}_3)_2 \cdot 5\text{H}_2\text{O}$) (Bernal et al., 2014). The formation of this phase indicates that a precipitate is preferentially formed due to the reaction between the carbonate and sodium ions released from the activators and the calcium ions dissolved from the precursors (FA, BFS, and CSW). However, such phases do not effectively enhance the strength of the GCSW, as shown by the mechanical strength of "1:1 15%, 0%" (Abdalqader et al., 2016). It is worth noticing that the peak intensities of both the mullite and gaylussite in the range of $25.0\text{--}30.0^\circ 2\theta$ decrease as the content of BFS and activators

increases, while the peak at $29.5^\circ 2\theta$ increases significantly, suggesting a change in the composition of the main products in the GCSW groups. In particular, the peak at $29.5^\circ 2\theta$ is identified as the calcium silicate hydrate (C-S-H) and calcium carbonate phases. The gaylussite's intensity decrease may suggest the involvement of sodium and calcium ions in the formation of C-S-H (Samantasinghar and Singh, 2018). According to the previous studies, the formation of the C-(A)-S-H phase plays a key role in the early and final strength development of the geopolymer with FA-BFS as the main precursors (Ben Haha et al., 2011a). For instance, when the dosage of activators reaches 25%, and the SF incorporation rate is within 5%, the intensity of the peak located at $29.5^\circ 2\theta$ is even more than that of the quartz peak located at $26.7^\circ 2\theta$, which is also in good agreement with the excellent mechanical strengths exhibited by the corresponding GCSW groups. When the SM is completely substituted by SF, the intensity of the C-S-H peak decreases and it is generally consistent with the reduction in the 28 days compressive and flexural strengths for the "1:1 25% (10%)" GCSW specimen. Furthermore, the hydrotalcite phase is usually detected in sodium carbonate-activated slag or slag/fly ash mixtures with a 2θ of 11.7° , however, it is difficult to be observed here, considering that the peak intensity of the hydrotalcite phase is too weak to determine its presence (Ben Haha et al., 2011b).

FT-IR Characterization

Figure 8 illustrates the FT IR spectra of CCSW and typical GCSW groups. All specimens exhibit similar band characteristics, indicating a similar product composition. Major bands are detected at approximately 3,450, 1,650, 1,450, 1,080, 995, and 875 cm^{-1} . The structure of interlayer water in GCSW and CCSW is characterized by the O-H stretching band located at around $3,450\text{ cm}^{-1}$, whereas the bending of the chemically bonded H-O-H is located at approximately $1,650\text{ cm}^{-1}$ owing to the water capture effect and surface absorption of the gel cavities (Ishwarya et al., 2019). Compared to CCSW, the absorption band due to chemically bonded water is barely visible in the GCSW specimen of "1:0 15% (0%)", suggesting that less alkali-activated products are produced, and the corresponding mechanical strengths of the specimen are the lowest. With the increase of BFS and activators, the absorption band of GCSW at $1,650\text{ cm}^{-1}$ is enhanced but still generally lower than that of the CCSW. The absorption bands at $1,450\text{ cm}^{-1}$ and 875 cm^{-1} are mainly caused by carbonates: In CCSW, it is mainly due to the existed calcium carbonate in the CSW and a small proportion of carbonized hydration products. As for the GCSW, these bands could be attributed to the presence of calcium carbonate and gaylussite detected in the XRD, and the excessive carbonate ions from the activators. It is worth noticing that the GCSW specimen of "1:0 15% (0%)" has a stronger absorption band at 875 cm^{-1} than that of the other GCSW specimens, and the intensity of this band gradually decreases with the increase of BFS and activators. Combined with the XRD results, it seems that the absorption band at such wavenumbers may be related to the formation and transformation of gaylussite. It is well known that the bands located at 950 cm^{-1} - 995 cm^{-1} are assigned to the Si-O vibration in C-S-H and also imply the formation of C-A-S-H (Puertas and Fernández-Jiménez, 2003).

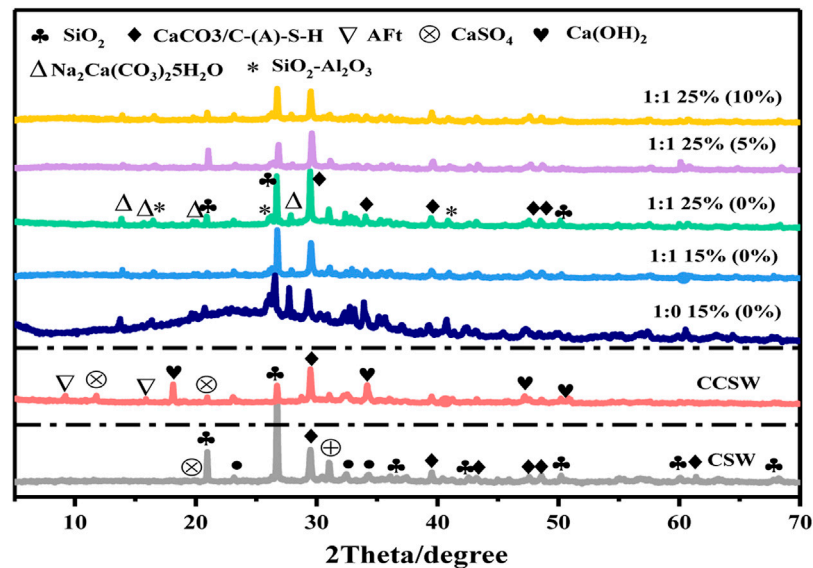


FIGURE 7 | XRD for CCSW and GCSW composite.

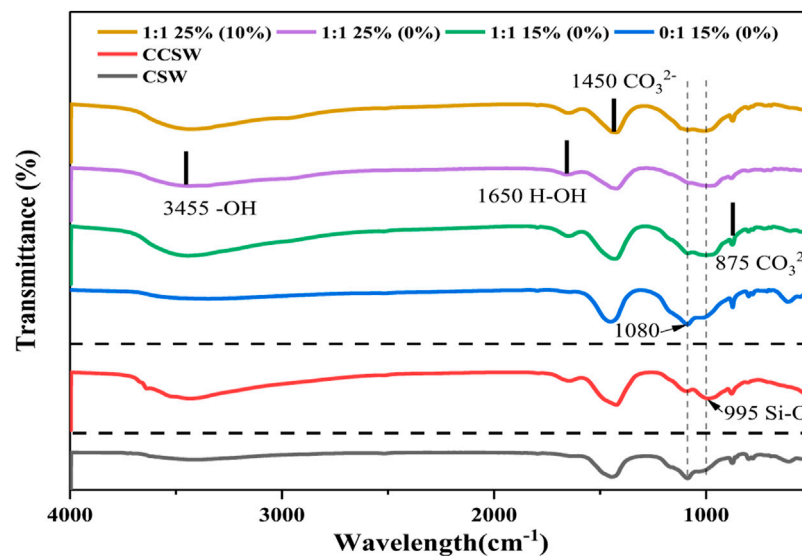


FIGURE 8 | FTIR analysis for CCSW and GCSW composites.

As can be seen from GCSW: On the one hand, the absorption band of C-A-S-H gradually shifts towards lower wavenumbers with the increase of BFS and activators, which is possibly affected by calcium ions and tetrahedral aluminum in the BFS or the more formation of C-A-S-H with short chains that could decrease the network connectivity of alkali-activated products (Yang et al., 2012). On the other hand, the gradual enhancement of the C-A-S-H absorption band directly leads to a significant improvement in the mechanical properties of the GCSW specimens. Furthermore, it is interesting to notice that the characteristic absorption band of CSW at $1,080\text{ cm}^{-1}$, which could still be observed in CCSW,

gradually disappears in GCSW with the continuous generation of C-A-S-H, as shown in the corresponding band of “1:1 25% (0%)”. It is speculated that some minerals in the CSW are also involved in the formation of alkali-activated products, such as mica-like minerals (Bassani et al., 2019). However, further investigation is still needed to be conducted.

TG-DTG Analysis

Figure 9 shows four typical TG and DTG curves of CCSW and GCSW. There are mainly two mass losses in the DTG curves of GCSW composites, while three losses in CCSW, suggesting the

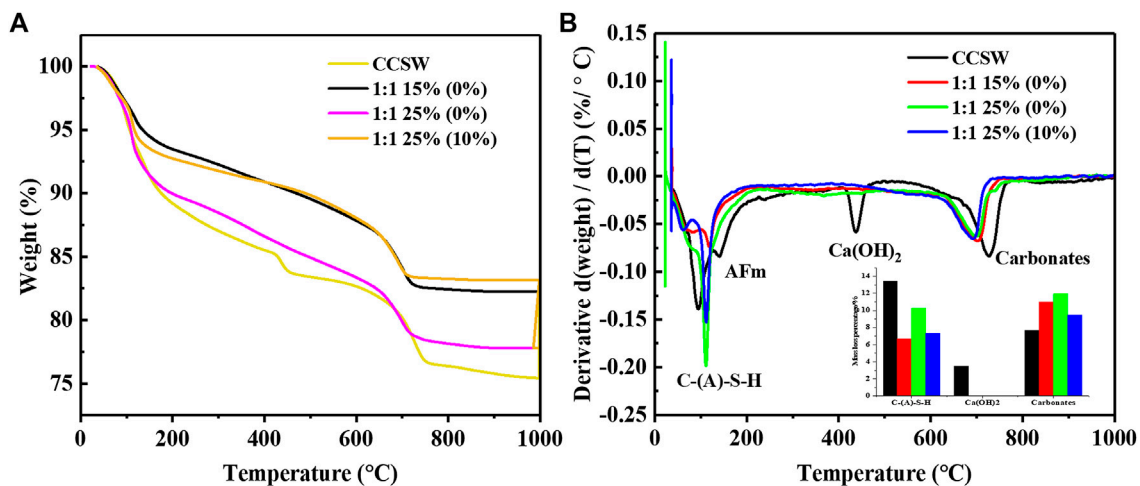


FIGURE 9 | TG-DTG results of CCSW and GCSW composites (**A**: TG curves, **B**: DTG curves).

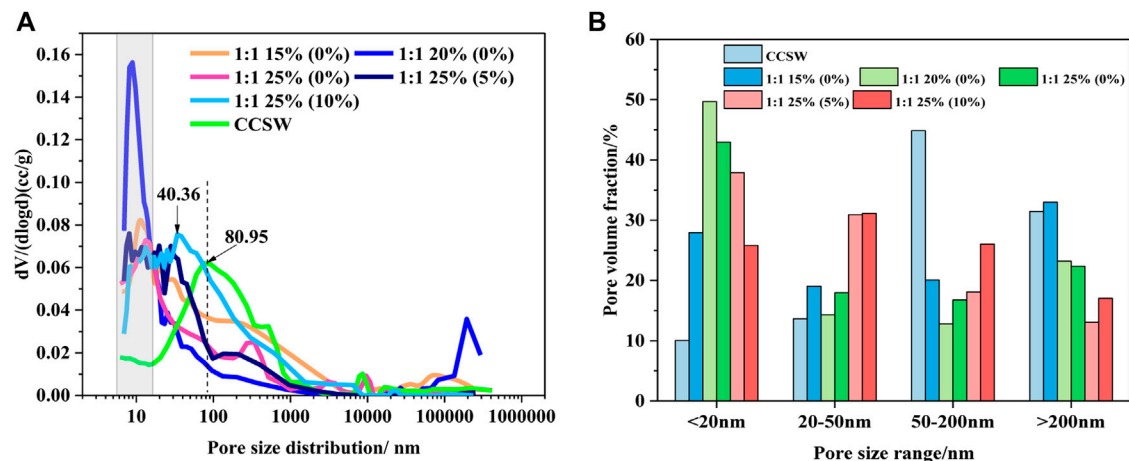


FIGURE 10 | Pore characteristics of CCSW and GCSW composites (**A**: pore distribution, **B**: pore volume fraction).

difference in the production components of these two cementitious systems. As shown by the specimens of GCSW, two kinds of productions match well with two weight losses. The first mass loss is mainly at 110°C and ascribed to the evaporation of water existing in the pores of C-(A)-S-H gel (Ismail et al., 2013). The mass loss between 690°C and 727°C is owing to the decomposition of the bonded water in the stable carbonates, which come from the CSW and alkali-activated products, such as calcium carbonate and gaylussite detected by XRD and FTIR (Jin et al., 2014). Meanwhile, it should be noticed that the mass losses appearing in the CCSW are quite different from the GCSW. Firstly, the decomposition temperature of C-(A)-S-H gel in the CCSW (approximately 100°C) was lower than that of the GCSW (111°C–118°C). The evaporation of the bonded water in the AFm often occurs at around 160°C–200°C in the CCSW, whereas there is no mass loss in the same temperature range of GCSW. Secondly, the mass loss at 350–500°C is the typical sign belong

to OPC, resulting from the decomposition of $\text{Ca}(\text{OH})_2$ (Suraneni et al., 2019). The mass loss at around 700°C in CCSW is primarily due to the decomposition of the carbonates from CSW, and a small part is attributed to the carbonized hydration products. It should be mentioned that, according to the TG curves, the mass loss of GCSW is basically less than that of CCSW, suggesting that the amount of chemically bonded water in GCSW is less than that of the CCSW, and it is in line with the corresponding analysis of FTIR section.

It is worth noticing that the mass-loss rate associated with C-(A)-S-H gel becomes sharper in “1:1 25% (0%)” than that of the “1:1 15% (0%)”. The mass loss percentage of the main production gel increases from 6.72% in “1:1 15% (0%)” to 10.27% in “1:1 25% (0%)” as shown by the small graph in **Figure 9B**, indicating a great number of C-(A)-S-H gel is produced, which is well in line with the best mechanical properties of the “1:1 25% (0%)” GCSW group. Besides, the outstanding mechanical performance is not

only due to the increase of C-(A)-S-H gel, but also the increase of carbonates with high crystallinity and stability, as shown in the increase mass loss from the decomposition of the carbonates, which is from 10.99% in “1:1 15% (0%)” to 11.93% in “1:1 25% (0%)”. Moreover, a significant reduction of the mechanical properties in “1:1 25% (10%)” can also be explained by its DTG curve. The complete substitution of SF leads to a decrease of C-(A)-S-H gel dehydration, which is from 10.27% in “1:1 25% (0%)” to 7.35% in “1:1 25% (10%)”, as well as the decomposition of the carbonates, which is from 11.93 to 9.49%. The nearly overlapping TG curves and the similar C-A-S-H mass loss percentage of “1:1 15% (0%)” and “1:1 25% (10%)” also suggest that these two groups have similar mechanical properties. The weight loss may be closely related to the mechanical properties of GCSW.

Pore Size Characteristics

The pore structure has been reported to be closely related to some basic properties of cementitious materials, such as mechanical properties and durability (Ahmad and Chen, 2018). Therefore, the pore structure distribution characteristics of CCSW and GCSW were tested, and the results are shown in **Figure 10**. It can be seen that the most probable aperture of CCSW and GCSW is significantly different from each other. GCSW specimens present the most probable apertures around 10 nm, while CCSW is mainly around 80 nm. This suggests that a denser pore structure is more likely to be obtained by combining CSW with the geopolymer prepared in this study. Although this result cannot imply that the GCSW always achieves higher mechanical strengths than that of the CCSW, it is still an essential reference for the later durability investigation of CSW-composites (Tan et al., 2019; He et al., 2020). The pore sizes of CSW-composites can be classified into the following four types: harmless pores less than 20 nm, less harmful pores of 20–50 nm, harmful pores of 50–200 nm, and much harmful pores of more than 200 nm (Tan et al., 2018). As can be seen from the percentages of the pore size distribution, 44.84% of the pores in CCSW belong to the harmful pores, and the percentage of the much harmful pores is also high, reaching 31.46%, which may explain the limitations of CSW recycling in the OPC system. On the contrary, most of the pore sizes in GCSW belong to the less harmful pores with the fluctuating percentage between 25.81 and 49.68%, which depends on the geopolymer's design parameters. When the dosage of the activators is increased, the proportion of pores less than 20 nm in GCSW rises accordingly, and these pores mainly belong to the gel pores in C-A-S-H and play a major role in supporting the strengths of GCSW. The increase of the SF incorporation rate makes the pore structure of GCSW more complex. When the SF incorporation rate reaches 5%, the most probable aperture of GCSW becomes finer. However, as the rate reaches 10%, the most probable aperture develops towards coarse pores (40.36 nm). Overall, with the increase of SF, the proportion of gel pores appears to decrease, while the proportion of harmful pores tends to increase. And its corresponding decrease in the mechanical strengths of GCSW specimens can also be explained by the pore changes.

Reaction Mechanism

Combined with the results of macroscopic and microscopic tests, this study clarified the reaction characteristics of CSW-based geopolymer. The properties of the prepared geopolymer were mainly related to the ratio of fly ash/slag, the amount of activator, and the type of silicon sources. The combined activator composed of sodium carbonate and sodium metasilicate is much moderate than the sodium hydroxide type. It is because when sodium carbonate touches the water-containing slurry, the carbonate ion is first released. At this time, the alkalinity of the reaction system is low, and the alkaline environment required for the early reaction is supported only by sodium metasilicate. Therefore, fly ash, as the dominant active raw material, is difficult to be stimulated. And the role of CSW particles is only to provide nucleation sites and fill the pores, which cannot facilitate strength development substantially. However, when the slag content and activator content increase, the activity of the raw material and the alkali equivalent of the system is improved, thus the reaction degree is intensified. The hydration of slag is accelerated, and the reaction rate of fly ash is improved. On the other hand, when silica fume is used in place of sodium metasilicate pentahydrate, the ultra-fine silica fume provides a soluble silicon source with the system in an alkaline environment forming C-A-S-H with calcium ions. But unlike the sodium silicate, silica fume does not provide additional sodium oxide, and its dissolution rate in the alkaline environment is much slower than that of commercial sodium silicate. Accordingly, the excessive replacement of silica fume will result in a lower alkali equivalent and higher particle concentration of the system, which leads to a decrease in the strength and flow diameter, and a prolonged setting time.

CONCLUSION

This paper showed an innovative way to recycle CSW, and a comparative study was made between the GCSW and CCSW in terms of the flowability, setting times, mechanical strengths, and microstructures (XRD, FTIR, TG-DTG, and MIP). The main conclusions are as follows:

1. With the addition of homogenized CSW into OPC and geopolymer, the flow diameter of CCSW is only 95 mm, while the GCSW could achieve higher flow diameters by adjusting the dosage of BFS and powdered activators (~200 mm), and the flow diameter increases with the increase of the powdered activators. The negative effect on the flowability of the cementitious materials caused by CSW could be mitigated in the GCSW.
2. The setting time of the OPC is greatly shortened by the incorporation of CSW, with the initial setting time reduced from 165 to 80 min and the final setting time reduced from 215 min to 145 min. This is mainly due to the filling and nucleation effects of CSW. The setting time of GCSW is mainly affected by the content of BFS and activators. The initial and final setting times fluctuate between 70–255 min and 115–300 min, respectively, and the increase in both BFS and activators shortens the setting times of GCSW.
3. When BFS: FA keeps at 1:1, and the activator content reaches 15–20%, GCSW could achieve comparable mechanical

strengths as the CCSW did at 28 days. The gained strengths of CCSW mainly come from the cement hydration products, while the GCSW is mainly supported by C-A-S-H and carbonates (calcium carbonate and gaylussite). The amount of chemically bonded water in the products of GCSW is lower than that of the CCSW.

4. Compared to CCSW, it is easier to obtain a dense microstructure by mixing the homogenized CSW with geopolymers prepared in this study. Increasing the dosage of BFS and activators could effectively increase the proportion of gel pores (< 20 nm) in the GCSW (25.81–49.68%). SF has a certain ability to replace SM, but the recommended incorporation rate for SF should be less than 5% without significantly affecting the fresh and hardened properties of GCSW.

5. In this study, the slag content is limited. Further increasing the slag content will greatly improve the mechanics and shorten the setting time. For satisfactory properties, the dosage of the activator should be 10–20% of the total amount of slag and fly ash, because excessive activator may cause the problems such as efflorescence and worried durability. If the silica fume substitution (0–10%) is considered, the activator content should not exceed 25%. It is an innovative attempt to recycle CSW into alkali-activated materials, which shows advantages compared with traditional cement materials.

REFERENCES

- Abdalgader, A. F., Jin, F., and Al-Tabbaa, A. (2016). Development of Greener Alkali-Activated Cement: Utilisation of Sodium Carbonate for Activating Slag and Fly Ash Mixtures. *J. Clean. Prod.* 113, 66–75. doi:10.1016/j.jclepro.2015.12.010
- Adesanya, E., Ohenoja, K., Luukkainen, T., Kinnunen, P., and Illikainen, M. (2018). One-Part Geopolymer Cement from Slag and Pretreated Paper Sludge. *J. Clean. Prod.* 185, 168–175. doi:10.1016/j.jclepro.2018.03.007
- Ahmad, M. R., and Chen, B. (2018). Effect of Silica Fume and basalt Fiber on the Mechanical Properties and Microstructure of Magnesium Phosphate Cement (MPC) Mortar. *Constr. Build. Mater.* 190, 466–478. doi:10.1016/j.conbuildmat.2018.09.143
- Ali, M. B., Saidur, R., and Hossain, M. S. (2011). A Review on Emission Analysis in Cement Industries. *Renew. Sustain. Energ. Rev.* 15, 2252–2261. doi:10.1016/j.rser.2011.02.014
- Askarian, M., Tao, Z., Samali, B., Adam, G., and Shuaibu, R. (2019). Mix Composition and Characterisation of One-Part Geopolymers with Different Activators. *Constr. Build. Mater.* 225, 526–537. doi:10.1016/j.conbuildmat.2019.07.083
- Audo, M., Mahieux, P.-Y., and Turcry, P. (2016). Utilization of Sludge from Ready-Mixed concrete Plants as a Substitute for limestone Fillers. *Constr. Build. Mater.* 112, 790–799. doi:10.1016/j.conbuildmat.2016.02.044
- Audo, M., Mahieux, P.-Y., Turcry, P., Chateau, L., and Churlaud, C. (2018). Characterization of Ready-Mixed concrete Plants Sludge and Incorporation into Mortars: Origin of Pollutants, Environmental Characterization and Impacts on Mortars Characteristics. *J. Clean. Prod.* 183, 153–161. doi:10.1016/j.jclepro.2018.02.155
- Bassani, M., Tefa, L., Coppola, B., and Palmero, P. (2019). Alkali-activation of Aggregate Fines from Construction and Demolition Waste: Valorisation in View of Road Pavement Subbase Applications. *J. Clean. Prod.* 234, 71–84. doi:10.1016/j.jclepro.2019.06.207
- Ben Haha, M., Le Saout, G., Winnefeld, F., and Lothenbach, B. (2011a). Influence of Activator Type on Hydration Kinetics, Hydrate Assemblage and Microstructural Development of Alkali Activated Blast-Furnace Slags. *Cem. Concr. Res.* 41, 301–310. doi:10.1016/j.cemconres.2010.11.016
- Ben Haha, M., Lothenbach, B., Le Saout, G., and Winnefeld, F. (2011b). Influence of Slag Chemistry on the Hydration of Alkali-Activated Blast-Furnace Slag - Part I:

DATA AVAILABILITY STATEMENT

The original contributions presented in the study are included in the article/Supplementary Material, further inquiries can be directed to the corresponding author.

AUTHOR CONTRIBUTIONS

YG: Conceptualization, Methodology, Funding acquisition, review and editing. KD: Methodology, Data curation, Writing-original draft, Funding acquisition, review and editing. SX: Funding acquisition, Conceptualization, Data curation. WZ: Resources, Methodology, review and editing.

FUNDING

The Authors gratefully acknowledge the financial support from the National Natural Science Foundation of China (51978080), Joint Fund of the National Natural Science Foundation of China and the China Civil Aviation Administration (U1833127), Hunan Province Innovation Foundation for Postgraduate (CX20190668), Natural Science Foundation of Hunan Province (2021JJ40602) and Scientific Research Project of Hunan Provincial Department of Education (20B014).

- Effect of MgO. *Cem. Concr. Res.* 41, 955–963. doi:10.1016/j.cemconres.2011.05.002
- Bernal, S. A., Provis, J. L., Myers, R. J., San Nicolas, R., and van Deventer, J. S. J. (2014). Role of Carbonates in the Chemical Evolution of Sodium Carbonate-Activated Slag Binders. *Mater. Struct.* 48, 517–529. doi:10.1617/s11527-014-0412-6
- Chen, C.-T., Nguyen, H.-A., Chang, T.-P., Yang, T.-R., and Nguyen, T.-D. (2015). Performance and Microstructural Examination on Composition of Hardened Paste with No-Cement SFC Binder. *Constr. Build. Mater.* 76, 264–272. doi:10.1016/j.conbuildmat.2014.11.032
- Correia, S. L., Souza, F. L., Dienstmann, G., and Segadaes, A. M. (2009). Assessment of the Recycling Potential of Fresh concrete Waste Using a Factorial Design of Experiments. *Waste Manage.* 29, 2886–2891. doi:10.1016/j.wasman.2009.06.014
- Duxson, P., and Provis, J. L. (2008). Designing Precursors for Geopolymer Cements. *J. Am. Ceram. Soc.* 91, 3864–3869. doi:10.1111/j.1551-2916.2008.02787.x
- Elyamany, H. E., Abd Elmoaty, A. E. M., and Elshaboury, A. M. (2018). Setting Time and 7-day Strength of Geopolymer Mortar with Various Binders. *Constr. Build. Mater.* 187, 974–983. doi:10.1016/j.conbuildmat.2018.08.025
- Férriz Papi, J. A. (2014). Recycling of Fresh concrete Exceeding and Wash Water in concrete Mixing Plants. *Mater. Construcc.* 64, e004. doi:10.3989/mc.2013.00113
- Hajimohammadi, A., and van Deventer, J. S. J. (2017). Characterisation of One-Part Geopolymer Binders Made from Fly Ash. *Waste Biomass Valor.* 8, 225–233. doi:10.1007/s12649-016-9582-5
- He, X., Zheng, Z., Ma, M., Su, Y., Yang, J., Tan, H., et al. (2020). New Treatment Technology: The Use of Wet-Milling concrete Slurry Waste to Substitute Cement. *J. Clean. Prod.* 242, 118347. doi:10.1016/j.jclepro.2019.118347
- Iizuka, A., Sasaki, T., Honma, M., Yoshida, H., Hayakawa, Y., Yanagisawa, Y., et al. (2017). Pilot-Scale Operation of a Concrete Sludge Recycling Plant and Simultaneous Production of Calcium Carbonate. *Chem. Eng. Commun.* 204, 79–85. doi:10.1080/00986445.2016.1235564
- Ishwarya, G., Singh, B., Deshwal, S., and Bhattacharyya, S. K. (2019). Effect of Sodium Carbonate/Sodium Silicate Activator on the Rheology, Geopolymerization and Strength of Fly Ash/slag Geopolymer Pastes. *Cem. Concr. Compos.* 97, 226–238. doi:10.1016/j.cemconcomp.2018.12.007
- Ismail, N., and El-Hassan, H. (2018). Development and Characterization of Fly Ash-Slag Blended Geopolymer Mortar and Lightweight Concrete. *J. Mater. Civ. Eng.* 30, 04018029. doi:10.1061/(asce)mt.1943-5533.0002209

- Ismail, I., Bernal, S. A., Provis, J. L., Hamdan, S., and Van Deventer, J. S. J. (2013). Microstructural Changes in Alkali Activated Fly Ash/slag Geopolymers with Sulfate Exposure. *Mater. Struct.* 46, 361–373. doi:10.1617/s11527-012-9906-2
- Jeong, Y., Kang, S.-H., Du, Y., and Moon, J. (2019). Local Ca-Structure Variation and Microstructural Characteristics on One-Part Activated Slag System with Various Activators. *Cem. Concr. Compos.* 102, 1–13. doi:10.1016/j.cemconcomp.2019.04.009
- Jin, F., Gu, K., and Al-Tabbaa, A. (2014). Strength and Drying Shrinkage of Reactive MgO Modified Alkali-Activated Slag Paste. *Constr. Build. Mater.* 51, 395–404. doi:10.1016/j.conbuildmat.2013.10.081
- Kaja, A. M., Lazaro, A., and Yu, Q. L. (2018). Effects of Portland Cement on Activation Mechanism of Class F Fly Ash Geopolymer Cured under Ambient Conditions. *Constr. Build. Mater.* 189, 1113–1123. doi:10.1016/j.conbuildmat.2018.09.065
- Kou, S.-c., Zhan, B.-j., and Poon, C.-s. (2012a). Feasibility Study of Using Recycled Fresh concrete Waste as Coarse Aggregates in concrete. *Constr. Build. Mater.* 28, 549–556. doi:10.1016/j.conbuildmat.2011.08.027
- Kou, S.-C., Zhan, B.-J., and Poon, C.-S. (2012b). Properties of Partition wall Blocks Prepared with Fresh concrete Wastes. *Constr. Build. Mater.* 36, 566–571. doi:10.1016/j.conbuildmat.2011.08.063
- Liu, M., Tan, H., and He, X. (2019). Effects of Nano-SiO₂ on Early Strength and Microstructure of Steam-Cured High Volume Fly Ash Cement System. *Constr. Build. Mater.* 194, 350–359. doi:10.1016/j.conbuildmat.2018.10.214
- Liu, Y., Zhang, Z., Shi, C., Li, N., and Lei, L. (2020). Influence of Silica Fume on Performance of High-Strength Geopolymer. *J. Chin. Ceram. Soc.* 48 (11), 1689–1699. doi:10.14062/j.issn.0454-5648.20200234
- Luukkonen, T., Abdollahnejad, Z., Yliniemi, J., Kinnunen, P., and Illikainen, M. (2018a). Comparison of Alkali and Silica Sources in One-Part Alkali-Activated Blast Furnace Slag Mortar. *J. Clean. Prod.* 187, 171–179. doi:10.1016/j.jclepro.2018.03.202
- Luukkonen, T., Abdollahnejad, Z., Yliniemi, J., Kinnunen, P., and Illikainen, M. (2018b). One-part Alkali-Activated Materials: A Review. *Cem. Concr. Res.* 103, 21–34. doi:10.1016/j.cemconres.2017.10.001
- Miller, S. A., Horvath, A., and Monteiro, P. J. M. (2016). Readily Implementable Techniques Can Cut Annual CO₂ Emissions from the Production of concrete by over 20. *Environ. Res. Lett.* 11, 1–7. doi:10.1088/1748-9326/11/7/074029
- Ng, C., Alengaram, U. J., Wong, L. S., Mo, K. H., Jumaat, M. Z., and Ramesh, S. (2018). A Review on Microstructural Study and Compressive Strength of Geopolymer Mortar, Paste and concrete. *Constr. Build. Mater.* 186, 550–576. doi:10.1016/j.conbuildmat.2018.07.075
- Pan, Z., Tao, Z., Cao, Y. F., Wuhrer, R., and Murphy, T. (2018). Compressive Strength and Microstructure of Alkali-Activated Fly Ash/slag Binders at High Temperature. *Cem. Concr. Compos.* 86, 9–18. doi:10.1016/j.cemconcomp.2017.09.011
- Peng, M. X., Wang, Z. H., Shen, S. H., Xiao, Q. G., Li, L. J., Tang, Y. C., et al. (2017). Alkali Fusion of Bentonite to Synthesize One-Part Geopolymeric Cements Cured at Elevated Temperature by Comparison with Two-Part Ones. *Constr. Build. Mater.* 130, 103–112. doi:10.1016/j.conbuildmat.2016.11.010
- Puertas, F., and Fernández-Jiménez, A. (2003). Mineralogical and Microstructural Characterisation of Alkali-Activated Fly Ash/slag Pastes. *Cem. Concr. Compos.* 25, 287–292. doi:10.1016/S0958-9465(02)00059-8
- Rughooputh, R., Rana, J. O., and Joarawon, K. (2017). Possibility of Using Fresh concrete Waste in concrete for Non Structural Civil Engineering Works as a Waste Management Strategy. *KSCE J. Civ. Eng.* 21, 94–99. doi:10.1007/s12205-016-0052-1
- Samantasinghar, S., and Singh, S. P. (2018). Effect of Synthesis Parameters on Compressive Strength of Fly Ash-Slag Blended Geopolymer. *Constr. Build. Mater.* 170, 225–234. doi:10.1016/j.conbuildmat.2018.03.026
- Shen, W., Liu, Y., Yan, B., Wang, J., He, P., Zhou, C., et al. (2017). Cement Industry of China: Driving Force, Environment Impact and Sustainable Development. *Renew. Sustain. Energ. Rev.* 75, 618–628. doi:10.1016/j.rser.2016.11.033
- Singh, B., Ishwarya, G., Gupta, M., and Bhattacharyya, S. K. (2015). Geopolymer concrete: A Review of Some Recent Developments. *Constr. Build. Mater.* 85, 78–90. doi:10.1016/j.conbuildmat.2015.03.036
- Soliman, A. M., and Nehdi, M. L. (2011). Self-accelerated Reactive Powder concrete Using Partially Hydrated Cementitious Materials. *Mater. j.* 108, 1–7. doi:10.14359/51683462
- Sturm, P., Gluth, G. J. G., Simon, S., Brouwers, H. J. H., and Kühne, H.-C. (2016). The Effect of Heat Treatment on the Mechanical and Structural Properties of One-Part Geopolymer-Zeolite Composites. *Thermochim. Acta* 635, 41–58. doi:10.1016/j.tca.2016.04.015
- Suraneni, P., Hajibabae, A., Ramanathan, S., Wang, Y., and Weiss, J. (2019). New Insights from Reactivity Testing of Supplementary Cementitious Materials. *Cem. Concr. Compos.* 103, 331–338. doi:10.1016/j.cemconcomp.2019.05.017
- Tan, H., Zhang, X., He, X., Guo, Y., Deng, X., Su, Y., et al. (2018). Utilization of Lithium Slag by Wet-Grinding Process to Improve the Early Strength of Sulphoaluminate Cement Paste. *J. Clean. Prod.* 205, 536–551. doi:10.1016/j.jclepro.2018.09.027
- Tan, H., Nie, K., He, X., Guo, Y., Zhang, X., Deng, X., et al. (2019). Effect of Organic Alkali on Compressive Strength and Hydration of Wet-Grinded Granulated Blast-Furnace Slag Containing Portland Cement. *Constr. Build. Mater.* 206, 10–18. doi:10.1016/j.conbuildmat.2019.02.028
- Thakur, A. K., Pappu, A., and Thakur, V. K. (2019). Synthesis and Characterization of New Class of Geopolymer Hybrid Composite Materials from Industrial Wastes. *J. Clean. Prod.* 230, 11–20. doi:10.1016/j.jclepro.2019.05.081
- Vieira, L. d. B. P., and Figueiredo, A. D. d. (2016). Evaluation of concrete Recycling System Efficiency for Ready-Mix concrete Plants. *Waste Manage.* 56, 337–351. doi:10.1016/j.wasman.2016.07.015
- Xuan, D., Zhan, B., Poon, C. S., and Zheng, W. (2016). Innovative Reuse of concrete Slurry Waste from Ready-Mixed concrete Plants in Construction Products. *J. Hazard. Mater.* 312, 65–72. doi:10.1016/j.jhazmat.2016.03.036
- Yang, T., Yao, X., Zhang, Z., and Wang, H. (2012). Mechanical Property and Structure of Alkali-Activated Fly Ash and Slag Blends. *J. Sustain. Cem. Based Mater.* 1, 167–178. doi:10.1080/21650373.2012.752621
- Ye, N., Yang, J., Liang, S., Hu, Y., Hu, J., Xiao, B., et al. (2016). Synthesis and Strength Optimization of One-Part Geopolymer Based on Red Mud. *Constr. Build. Mater.* 111, 317–325. doi:10.1016/j.conbuildmat.2016.02.099
- Yousefi Oderji, S., Chen, B., Ahmad, M. R., and Shah, S. F. A. (2019). Fresh and Hardened Properties of One-Part Fly Ash-Based Geopolymer Binders Cured at Room Temperature: Effect of Slag and Alkali Activators. *J. Clean. Prod.* 225, 1–10. doi:10.1016/j.jclepro.2019.03.290
- Zervaki, M., Leptokaridis, C., and Tsimas, S. (2013). Reuse of By-Products from Ready-Mixed concrete Plants for the Production of Cement Mortars. *J. Sustain. Dev. Energy Water Environ. Syst.* 1, 152–162. doi:10.13044/j.sdwes.2013.01.0011

Conflict of Interest: WZ was employed by the China West Construction Hunan Group Co., Ltd.

The remaining authors declare that the research was conducted in the absence of any commercial or financial relationships that could be construed as a potential conflict of interest.

Publisher's Note: All claims expressed in this article are solely those of the authors and do not necessarily represent those of their affiliated organizations, or those of the publisher, the editors, and the reviewers. Any product that may be evaluated in this article, or claim that may be made by its manufacturer, is not guaranteed or endorsed by the publisher.

Copyright © 2021 Gao, Duan, Xiang and Zeng. This is an open-access article distributed under the terms of the Creative Commons Attribution License (CC BY). The use, distribution or reproduction in other forums is permitted, provided the original author(s) and the copyright owner(s) are credited and that the original publication in this journal is cited, in accordance with accepted academic practice. No use, distribution or reproduction is permitted which does not comply with these terms.



Synergistic Excitation Mechanism of CaO-SiO₂-Al₂O₃-SO₃ Quaternary Active Cementitious System

Fusheng Niu¹, Yukun An^{1,2*}, Jinxia Zhang^{1*}, Wen Chen¹ and Shengtao He¹

¹College of Mining Engineering, North China University of Science and Technology, Tangshan, China, ²Hebei Provincial Laboratory of Inorganic Nonmetallic Materials, College of Material Science and Engineering, North China University of Science and Technology, Tangshan, China

OPEN ACCESS

Edited by:

Lijie Guo,
Beijing General Research Institute of
Mining and Metallurgy, China

Reviewed by:

Ruidong Wu,
University of Science and Technology
Beijing, China
Xinglan Cui,
General Research Institute For
Nonferrous Metals, China

*Correspondence:

Yukun An
anyukun@ncst.edu.cn
Jinxia Zhang
Zhangjinxia163@163.com

Specialty section:

This article was submitted to
Structural Materials,
a section of the journal
Frontiers in Materials

Received: 11 October 2021

Accepted: 08 November 2021

Published: 29 November 2021

Citation:

Niu F, An Y, Zhang J, Chen W and He S
(2021) Synergistic Excitation
Mechanism of CaO-SiO₂-Al₂O₃-SO₃
Quaternary Active
Cementitious System.
Front. Mater. 8:792682.
doi: 10.3389/fmats.2021.792682

In this study, the influence of steel slag (SS) content on the strength of the cementitious materials was investigated. The quaternary active cementitious material (CaO-SiO₂-Al₂O₃-SO₃) was prepared using various proportions of steel slag (SS), granulated blast furnace slag (BFS), and desulfurized gypsum (DG). The mechanism of synergistic excitation hydration of the cementitious materials was examined using various techniques such as X-ray diffraction (XRD), scanning electron microscopy (SEM) and Fourier transform infrared spectrometry (FTIR). The strength of the mortar test block was initially increased and decreased later with the increase of the SS content. Mortar test block with 20% steel slag, 65% granulated blast furnace slag, and 15% desulfurized gypsum with 0.35 water-binder ratio showed the highest compressive strength of 57.3 MPa on 28 days. The free calcium oxide (f-CaO) in the SS reacted with water and produced calcium hydroxide (Ca(OH)₂) which created an alkaline environment. Under the alkaline environment, the alkali-activated reaction occurred with BFS. In the early stage of hydration reaction, calcium silicate hydrate (C-S-H) gel and fibrous hydration product ettringite (Aft) crystals were formed, which provided early strength to the cementitious materials. As the hydration reaction progressed, the interlocked growth of C-S-H gel and Aft crystals continued and promoted the increase of the strength of the cementitious system.

Keywords: steel slag, granulated blast furnace slag, full solid waste cementitious materials, AFT, C-S-H gel

INTRODUCTION

Solid waste refers to the garbage and discarded material resulting from commercial, industrial, and community activities (Chen et al., 2010). Among all types of solid waste, seven (coal gangue, fly ash, tailings, industrial by-product gypsum, smelting slag, construction waste, and crop straw) can be considered as bulk solid waste owing to their high annual production which exceeds 100 million tons (National Development and Reform Commission of the People's Republic of China, 2021). Bulk solid waste is a key area in the field of comprehensive utilization of resources due to its large quantity, wide range, adverse environmental impact, and broad utilization prospects (S Yüksel, 2018).

The generation of smelting slag has been substantially increased over the last few decades in China due to the rapid development in iron and steel industries (Li, 2020). The smelting slag accumulated on soil occupies a large area of land and easily form fine dust when exposed to air, thereby seriously impact on the local environment. Consequently, increasing attention has been paid to proper disposal and resource utilization of smelting slag generated from the iron and steel industries. A

large-scale application of smelting slag in the construction industry is one such example of resource utilization. For a long time, solid waste such as fly ash, granulated blast furnace, silica fume, etc., is used to make cementitious material which is an important substance added alongside cement in concrete production (Jagadisha et al., 2020). The application of cementitious materials reduces the amount of cement required to be added in concrete production. Cement production consumes a large amount of energy and emits a high amount of CO₂. Therefore, these environmental impacts can be reduced when the amount of cement used in concrete production is reduced (Ansai et al., 2009).

Cementitious material is a substance that can change a slurry to a solid stone-like body through a series of physical and chemical reactions and can cement other solid materials into a whole with mechanical strength. They are used to increase the performance of concrete. Active Si-Al components can be used effectively to prepare high-quality cementitious materials from smelting slag. As a consequence, the utilization of steel slag has been enhanced and the production of CO₂ has been greatly reduced when making cement (Wang et al., 2019).

For example, using the similarity of mineral composition between blast furnace slag, converter slag, and cement clinker, homogeneously mixed them under a hot melting state can produce the same components of cement clinker (Gudim et al., 2009; Zhu, 2002). However, in this process, it is difficult to control the production parameters and the heat consumption is too large. Zhao et al. (2007), prepared mortar test blocks having 28 days strength of 49 MPa using blast furnace slag and fly ash with the desulfurized gypsum as the activator. The performance of these mortar test blocks was improved using the “partial ultra-fine grinding process.” However, the ultra-fine grinding is an expensive process consequently, the actual production cost was very high. According to Jiang et al. (2019), high-strength composite cementitious materials can be prepared using optimum mixture ratio of steel slag: fly ash 1:2 with 1.4 water glass modules at an early curing temperature (80°C).

The above studies highlighted the importance of low energy consumption when preparing cementitious materials using smelting slag. Therefore, subsequent research was more focused on the reaction mechanism of making cementitious materials from smelting slag to reduce energy consumption. Yan and Wang. (2009) found that the steel slag-based cementitious materials can significantly shorten the induction period thereby can accelerate the hydration reaction rate under high-temperature curing. The steel-based cementitious materials had low dissolved Si-Al matter in the early stage of hydration reaction compared to the later stage suggesting a rapid reaction rate at the later stage (Cui et al., 2017). Calcium silicate hydrate (C-S-H) gel and Aft were the main hydration products obtained from steel-based cementitious materials.

Therefore, further research is needed to improve the early strength of steel slag-based cementitious materials. The chemical activation and hydration mechanism of cementitious materials have been studied with different dosages of activators such CaO or Na₂SO₄. However, these activators are unable to influence the

hydration product types (Cui et al., 2018). During the hydration, the generation of Ca(OH)₂ through the reaction of tricalcium silicate in the steel slag could promote the breaking of Si-O-Al and O-Si-O bonds (Xu et al., 2019). Although the crystallinity of Ca(OH)₂ and the strength of the cementitious material were weak, the second exothermic peak of steel slag After the alkali activation was strong (Sun, 2019). Water glass was used to activate the steel slag in place of traditional cement clinker (Sun, 2019).

Compared with an ordinary mortar, the strength of the mortar prepared with steel slag powder was increased by 72%, and the chloride ion permeability was decreased by 52% at high temperatures indicating better mechanical properties and durability (Jihad Miah et al., 2021). In recent years, research has used advanced methods to study the reaction mechanism of smelting slag cementitious materials. However, only a few of them have been applied in engineering practice. Therefore, it is important to solve the possible utilization of large quantities of smelting slag to prepare cementitious materials at a low cost. In this study, steel slag, granulated blast furnace slag, and desulfurized gypsum were used to prepare solid waste based cementitious materials. The strength and the hydration mechanism were studied to lay a theoretical foundation for the utilization of solid waste in the iron and steel industry.

MATERIALS AND METHODS

Materials

Chemical Composition and Phase Composition

The steel slag, granulated blast furnace slag, and desulfurized gypsum used in the experiment were obtained from Tangshan, Hebei Province, China. The chemical composition of the three raw materials is shown in **Table 1**, and XRD scans of the raw materials are shown in **Figure 1**.

The major mineral phases in steel slag are dicalcium silicate (C₂S), tricalcium silicate (C₃S), FeO/MgO(RO phase), and free calcium oxide (f-CaO). According to Mason's theory (Mason, 1994), the basicity coefficient of the steel slag was calculated using **Eq. 1**. Here, the basicity coefficient value indicates high alkalinity in steel slag with excess f-CaO that can provide an alkaline environment for the cementitious system.

$$M = W(\text{CaO})/[W(\text{SiO}_2) + W(\text{P}_2\text{O}_5)] = 3 \cdot 31 \quad (1)$$

The diffuse peak at 25°–35° in the XRD pattern (**Figure 1**) of the granulated blast furnace slag confirms the occurrence of glassy substances and a small amount of gehlenite (peak 6, **Figure 1**). The quality coefficient of granulated blast furnace slag was determined using **Eq. 2** (Saafan et al., 2020).

$$K = [m(\text{CaO}) + m(\text{MgO}) + m(\text{Al}_2\text{O}_3)]/[m(\text{SiO}_2) + m(\text{MnO}) + m(\text{TiO}_2)] = 2 \cdot 31 \quad (2)$$

The main component of desulfurized gypsum is dihydrate gypsum (peak 7, **Figure 1**). The alkalinity coefficient of

TABLE 1 | Chemical compositions of raw materials.

Raw material (%)	SiO ₂	Al ₂ O ₃	Fe ₂ O ₃	CaO	MgO	K ₂ O	Na ₂ O	TiO ₂	SO ₃	P ₂ O ₅	MnO
SS	11.944	2.92	29.365	46.122	3.582	0.05	0.104	1.235	0.542	1.996	1.525
BFS	24.895	10.858	8.038	44.778	5.447	0.445	0.363	1.123	2.253	0.735	0.431
DG	1.614	0.5	2.355	46.738	0.573	0.098	0.052	0.104	47.171	0.237	0.107

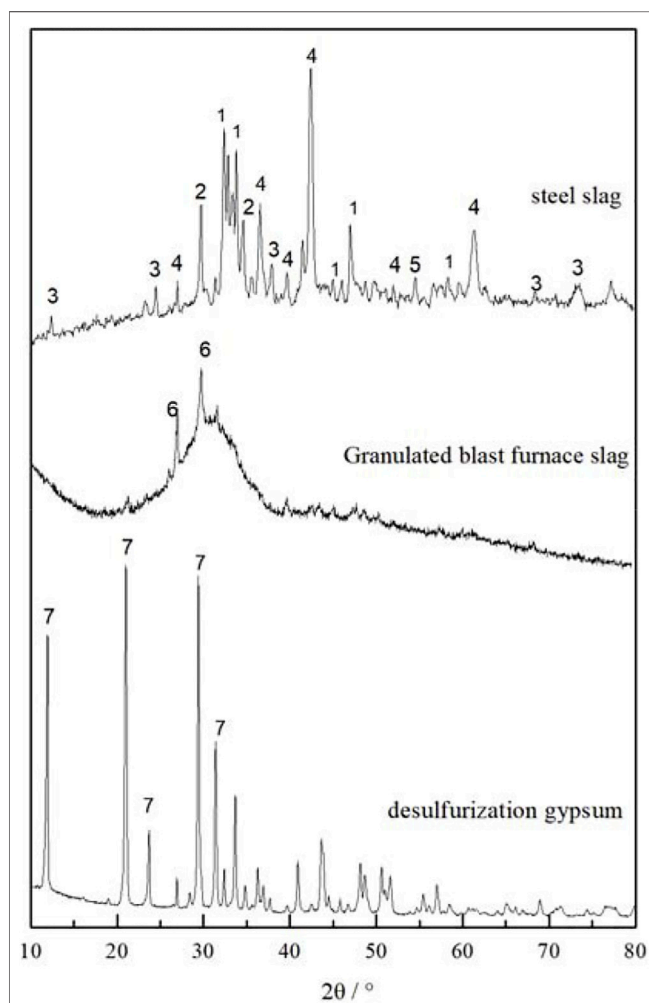


FIGURE 1 | XRD scans of raw materials. Peaks of the different mineral phases are numbered 1- Dicalcium silicate (C₂S) 2- Tricalcium silicate (C₃S) 3- Dicalcium ferrite (C₂F) 4- FeO/MgO(RO phase) 5-f-CaO 6- Gehlenite (C₂AS) 7- CaSO₄·2H₂O.

desulfurized gypsum was determined from Eq. 3 (Hou et al., 2006).

$$M = [m(\text{CaO}) + m(\text{MgO})] / [m(\text{SiO}_2) + m(\text{Al}_2\text{O}_3)] = 1.40 \quad (3)$$

The alkalinity coefficient of desulfurized gypsum indicates that it is easier to simulate the activity and to improve the strength of the cementitious system.

TABLE 2 | Cement mortar test scheme.

Number	SS/%	BFS/%	DG/%
A	5	80	15
B	10	75	15
C	15	70	15
D	20	65	15
E	25	60	15
F	35	55	15
G	40	50	15

Physical Properties

Steel slag contains high iron content which makes it difficult to grind. These excess iron in the slag must be removed to maximize the activity of raw materials under low energy consumption. Therefore, the circular iron removal method called “magnetic separation grinding” was used to remove the iron minerals in steel slag. After grinding, the density of steel slag and granulated blast furnace were 3.27 g/cm³ and 2.86 g/cm³ and the specific surface areas were 440 m²/kg and 480 m²/kg, respectively.

Experiment Procedure

The approximate proportions of three raw materials for the pilot study were determined based on the previous research. According to the pilot study, the proportion of steel slag should be less than 40% and that of desulfurization gypsum should be between 13 and 17%. Beyond these limits the workability of the mortar test block is poor and the strength would grow slowly. The water-binder ratio was determined as 0.35 by following the water consumption experiment of standard consistency. A test scheme with different proportions of SS, BFS, and DG was designed to further study the effect of steel slag content on the strength of the mortar test block (Table 2).

A homogenised mixture of raw materials was obtained by mixing them according to the above ratios in a mixer, and the mortar test blocks were shaped following the standard method called “Method of testing cements-Determination of strength (ISO Method)” (ISO, 1999). The mortar test blocks were then cured in a standard curing room and the strength and the workability were determined at a specified age.

Based on the strength of the mortar the ideal proportion of the raw materials was selected to prepare the paste test block. The selected best raw materials proportion mixture was ground to powder and dried at the specified age to carry out microscopic tests. The micromorphology of the cementitious system was analyzed by the SEM. The mineralogical phases of the

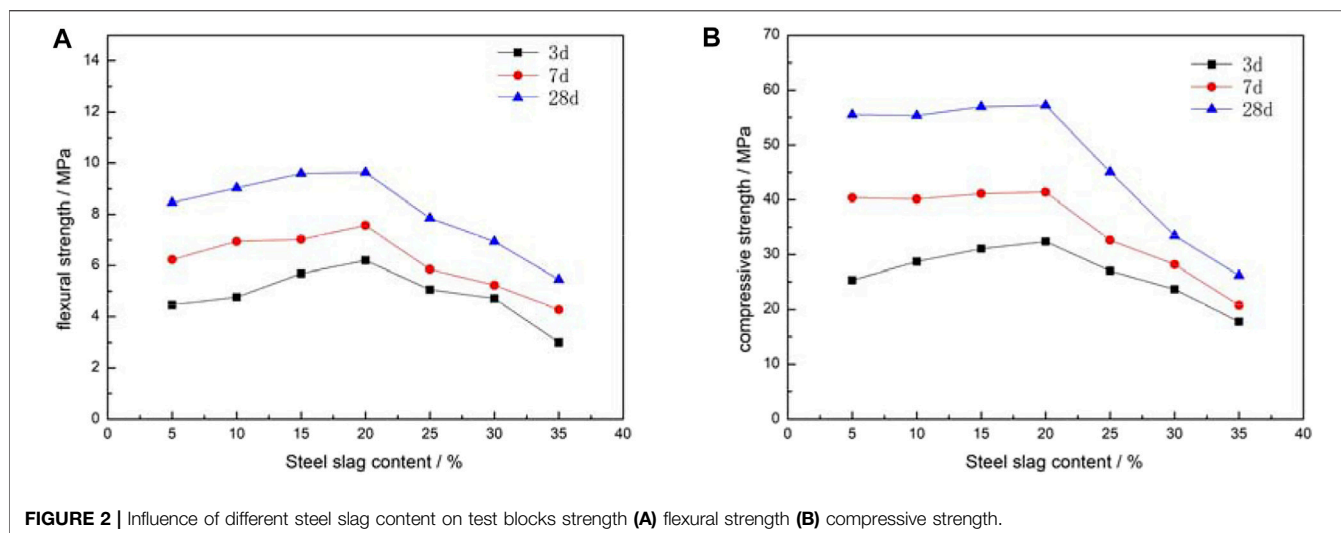


FIGURE 2 | Influence of different steel slag content on test blocks strength (A) flexural strength (B) compressive strength.

cementitious system were determined using the XRD. The molecular structure of the gelling system was analyzed by FTIR at the spectral scanning range of 400–4,000 cm^{-1} (Li et al., 2011).

RESULTS AND DISCUSSION

Influence of Steel Slag Content on the Strength of the Mortar Test Block

The strength of the cementitious material After hardening is an important indicator of its performance (Han et al., 2020).

Figure 2 shows the variation of the mortar test block strength with steel slag content. The ideal ratio to prepare cementitious material was in Group D with a steel slag content of 20% (Figure 2; Table 2). At steel slag content of 20%, the highest flexural (9.64 MPa) and compressive (57.26 MPa) strengths were observed in the test block aged for 28 days (Figure 2). A slight increase in both flexural and compressive strengths occurred at steel slag content from 5 to 20%. However, a significant decrease in both types of strengths occurred when steel slag content was greater than 20% (Figure 2).

The strength can be changed when the Ca-Si-Al-S system in the raw materials stimulates each other and when a hydration reaction occurs. The strength of the cementing system can be promoted as Aft and C-S-H gel are continuously formed during the hydration. The increase in the steel slag content results in a decrease in the granulated blast furnace slag content together with the content of the active ingredients in the system. However, the increase in f-CaO content led to an increase in the basicity of the system. The hydration product Aft is prone to swell, which can ultimately lead to a decrease in the strength of the mortar test block (Ni et al., 2019).

Hydration Reaction Mechanism

During the curing period, hydration reaction occurs in the cementitious system. This process leads to a change in the

mineralogy and the micromorphology of the mortar which in turn affects the strength of the mortar (Chen et al., 2019; Ni et al., 2019).

Micromorphological Analysis of Mortar Test Blocks

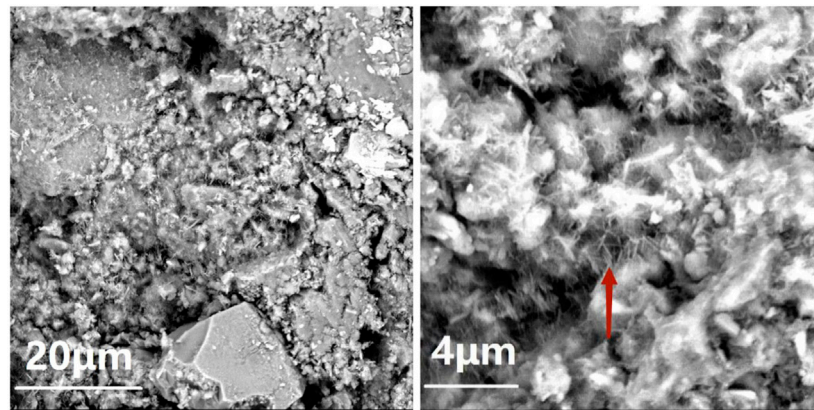
The SEM images of pastes at different ages are shown in Figure 3.

The SEM images of the cementitious system paste test cubes After 3, 7, and 28 days of hydration are shown in Figures 3A–C, respectively. A large number of needle-like Aft crystals were in the cementitious system After 3 days of hydration (Li et al., 2013). These Aft crystals, interspersed in irregularly shaped C-S-H gel, formed a spatial framework that provided an early strength to the cementitious system (Figure 3A). However, this framework was not dense hence, had low intensity at the early stage. By 7 days, the Aft crystals had grown stronger and the growth continued to a stable crystal form. The C-S-H gel was wrapped more tightly and the structure porosity had been reduced. As a result, the strength of the test cubes continued to increase during the hydration (Figure 3B) (Cui and Ni, 2016). By 28 days of hydration, the structure became more compact as the unreacted fine particles in the raw material were interweaved and wrapped by the Aft crystals and the C-S-H gel in the cementitious system (Figure 3C) (Cui and Ren, 2016). This lead to increase the strength of the test cubes further and was consistent with the strength test results.

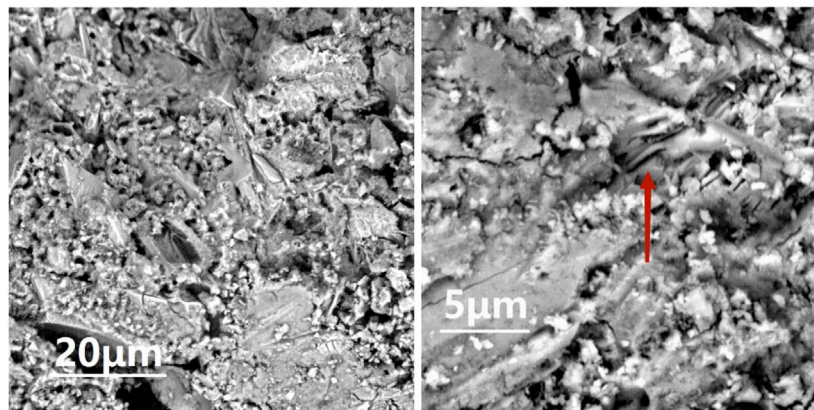
Mineralogical Analysis of Mortar Test Blocks

The XRD scans of the pastes at different ages are shown in Figure 4.

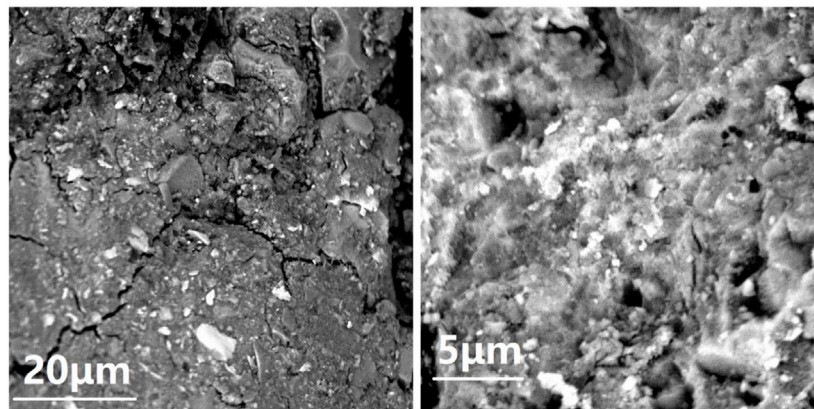
The main mineral phases of the cementitious system under standard curing conditions were Aft, $\text{Ca}(\text{OH})_2$, gypsum, RO phase, and C_2S (Figure 4). The RO phase derived from the steel slag showed no evident activation and did not participate in the reaction. At the early hydration period, Aft and $\text{Ca}(\text{OH})_2$ were formed (Figure 4). The diffuse peak near the diffraction angle of 30° , indicates the formation of C-S-H gel with lower crystallinity (Figure 4). The gradual decrease in diffraction peaks of gypsum



A Low power diagram and high power diagram at 3 days of hydration



B Low power diagram and high power diagram at 7 days of hydration

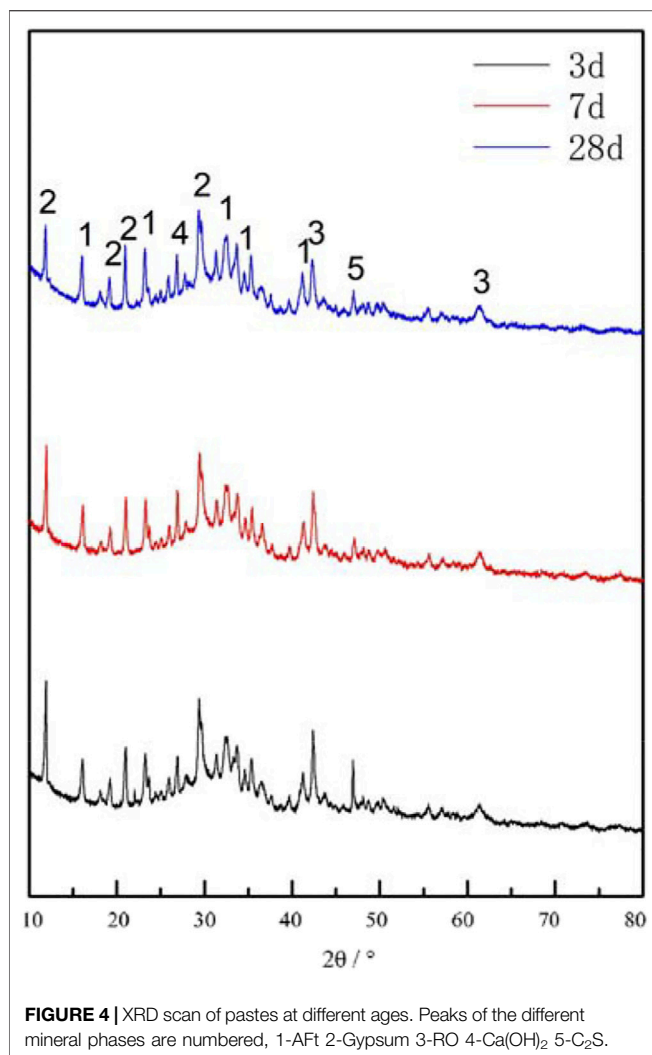


C Low power diagram and high power diagram at 28 days of hydration

FIGURE 3 | SEM images of pastes at different ages **(A)** Day 3 **(B)** Day 7 **(C)** Day 28. **(A)** Low power diagram and high power diagram at 3 days of hydration. **(B)** Low power diagram and high power diagram at 7 days of hydration. **(C)** Low power diagram and high power diagram at 28 days of hydration.

and C_2S with prolonged hydration indicates the disappearance of the two minerals. This could be due to their participation in the hydration reaction and subsequent formation of Aft and

$Ca(OH)_2$ (**Figure 4**). ThereAfter, the $Ca(OH)_2$ was reacted with the active salic minerals in the system, causing a pozzolanic reaction and eventually forming C-S-H gel (Chang et al., 2021).



XRD results confirmed that the acicular substance in the corresponding SEM was Aft, and the amorphous substance is C-S-H gel.

FTIR and Analysis Mortar Test Blocks

FTIR analysis was carried out on the paste test cube at different ages to identify and understand the molecular structure of the mineral phases. The corresponding FTIR spectra are shown in Figure 5.

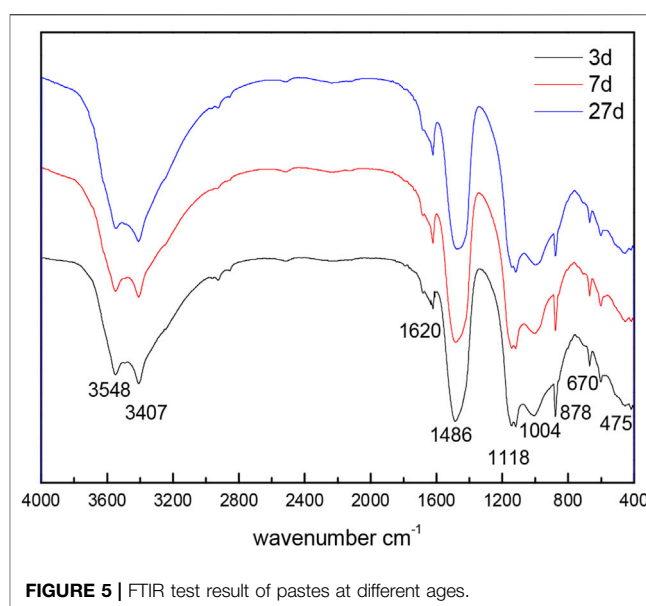
The absorption bands at $3548\sim 3407\text{ cm}^{-1}$ and 1620 cm^{-1} indicate the asymmetric stretching band of H₂O and the flexural vibration peak of OH⁻, respectively, in the hydration product. With aging, the absorption peaks were increased and broadened indicating a continuous increase of OH in the system. As the hydration reaction continued, more hydration products were gradually added. The asymmetric stretching band of CO₃²⁻ at 1486 cm^{-1} suggests the occurrence of carbonation reaction in the air. The asymmetric stretching bands of Si-O at 1118 , 1004 , and 475 cm^{-1} , and the characteristic peak of C-S-H gel near 1004 cm^{-1} indicates the reaction of the f-CaO in the steel slag

with water at the initial stage of hydration. During this hydration reaction, Ca(OH)₂ was produced which provided an alkaline environment to the system.

In the alkaline environment, the Si-O-Al bond breaks and oxygen-silicon tetrahedron depolymerizes with the aluminum-oxygen tetrahedron. This follows another reaction with SO₄²⁻ in the desulfurized gypsum and the Ca²⁺ in the system to produce Aft. The Aft formation through the hydration reaction was facilitated by a small amount of C₂S in steel slag and the pozzolanic effect by the C-S-H gel. The C-S-H gel and the Aft were interconnected and the gaps were filled by the steel slag powder which acted as a microaggregate thereby resulting in an early strength (Zhang, 2016; Xiao et al., 2018). As the reaction continued, with the progress of the hydration reaction, the characteristic peak of the C-S-H gel shifted slightly to a high wavenumber. This shift indicates an increase in the degree of polymerization of the C-S-H gel thereby promoting the strength of the cementitious system.

CONCLUSION

In this study, the effect of steel slag content on the strength of the CaO-SiO₂-Al₂O₃-SO₃ quaternary active cementitious system was investigated using metallurgical slag as the primary raw material. The strength was initially increased and decreased thereafter with the increase of the steel slag content. The steel slag content of 20% was the ideal percentage which showed the highest compressive strength of 57 MPa on the 28th day. The synergistic excitation of steel slag, granulated blast furnace slag, and desulfurized gypsum promoted the staggering growth of hydration products, Aft, and C-S-H gel. These hydration products formed a network structure, making the system more compact and



ensuring further development of strength. Steel slag has low hydration activity and poor stability. Therefore, in depth research is required to further excite the activity of steel slag in the cementitious material, to increase the steel slag consumption, and to improve the efficiency of solid waste resource utilization.

DATA AVAILABILITY STATEMENT

The raw data supporting the conclusion of this article will be made available by the authors, without undue reservation.

REFERENCES

- Ansai, T., Nishikawa, M., Ikeo, Y., and Sakai, E. (2009). Hydration Reaction Analysis of Cement Having High Blast-Furnace Slag. *Cement and Concrete Tech.* 63 (1), 22–27. doi:10.14250/cement.63.22
- Chang, J., Zhang, X., Gu, Y. Y., and Zhang, Y. Y. (2021). Effects of Pozzolanic Reaction on Carbonation Degree and Strength of Steel Slag Compacts Containing Zeolite. *Construction Building Mater.* 277 (277), 122334. doi:10.1016/j.conbuildmat.2021.122334
- Chen, X., Geng, Y., and Fujita, T. (2010). An Overview of Municipal Solid Waste Management in China. *Waste Manage.* 30 (4), 716–724. doi:10.1016/j.wasman.2009.10.011
- Chen, X., Wan, D.-W., Jin, L.-Z., Qian, K., and Fu, F. (2019). Experimental Studies and Microstructure Analysis for Ultra High-Performance Reactive Powder concrete. *Construction Building Mater.* 229 (Dec.30), 116924–116924. doi:10.1016/j.conbuildmat.2019.116924
- Cui, X., and Ni, W. (2016). Hydration Behavior of Cementitious Materials with All Solid Waste Based of Steel Slag and Blast Furnace Slag. *Revista de la Facultad de Ingeniería* 31 (7), 172–181. doi:10.21311/002.31.7.17
- Cui, X., Ni, W., and Ren, C. (2016). Early Hydration Kinetics of Cementitious Materials Containing Different Steel Slag Powder Contents. *Ijht* 34 (4), 590–596. doi:10.18280/ijht.34.4.06
- Cui, X., Ni, W., and Di, Y. (2018). Chemical Activation of Cementitious Materials with All Solid Waste Based of Steel Slag and Blast Furnace Slag. *Bull. Chin. Ceram. Soc.* 37 (4), 1411–1417. doi:10.16552/j.cnki.issn1001-1625.2018.04.047
- Cui, X., Ni, W., and Ren, C. (2017). Hydration Reaction Mechanism of Steel Slag Slag Based Solid Waste Cementitious Material. *Chin. J. Mater. Res.* 31 (09), 687–694. doi:10.11901/1005.3093.2016.741
- Gudim, Y. A., Golubev, A. A., Ovchinnikov, S. G., and Zinurov, I. Y. (2009). Waste-free Processing of Steel-Smelting Slag. *Steel Transl.* 39 (7), 612–614. doi:10.3103/s0967091209070237
- Han, X., Feng, J., Shao, Y., and Hong, R. (2020). Influence of a Steel Slag Powder-Ground Fly Ash Composite Supplementary Cementitious Material on the Chloride and Sulphate Resistance of Mass concrete. *Powder Tech.* 370, 176–183. doi:10.1016/j.powtec.2020.05.015
- Hou, X., Xu, D., Cao, H., Han, T., and Shang, B. (2006). Effects of Ground Blast-Furnace-Slag with Highly Hydraulic Activity on the Cement Properties. *J. Xi'an Univ. Architecture Tech. (NATURAL SCIENCE EDITION)* 01, 9–17. doi:10.3969/j.issn.1006-7930.2006.01.003
- ISO (1999). *Method of testing cements—Determination of strength*. China National Standardization Administration Committee. GB/T 17671-2020. Available at: <https://kns.cnki.net/kcms/detail/detail.aspx?FileName=SCSF00023001&DbName=SCSF>.
- Jagadisha, K., Rao, B., Nayak, G., and Shenoy, B. A. (2020). A Review on Properties of Sustainable Concrete Using Iron and Steel Slag Aggregate as Replacement for Natural Aggregate. doi:10.1007/978-981-15-8293-6_7
- Jiang, Y., Jia, L. J., Wen, M. Y., and Niu, Y. H. (2019). Preparation of Alkali-Activated Fly Ash/steel Slag Cementitious Materials. *Bull. Chin. Ceram. Soc.* (07), 2152–2156+2161. doi:10.16552/j.cnki.issn1001-1625.2019.07.027

AUTHOR CONTRIBUTIONS

All authors listed have made a substantial, direct, and intellectual contribution to the work and approved it for publication.

FUNDING

This work was supported by the Key R and D Plan of Hebei Province (20373801D). Key R and D Plan of Hebei Province (18273807D); Hebei graduate innovation funding project 2021(CXZZBS2021099) and Tangshan Basic Innovation team for clean utilization of industrial solid waste (19130207C).

- Jihad Miah, M., Kawsar Ali, M., Lo Monte, F., Chandra Paul, S., John Babafemi, A., and Šavija, B. (2021). The Effect of Furnace Steel Slag Powder on the Performance of Cementitious Mortar at Ambient Temperature and After Exposure to Elevated Temperatures. *Structures* 33 (2), 2811–2823. doi:10.1016/j.istruc.2021.06.047
- Li, C., Zhang, Z. F., Liu, S. Y., and Cheng, L. (2013). Ettringite Formation in Lime and Cement-Stabilized clay. *Chin. J. Geotechnical Eng.* 35 (zk2), 662–665.
- Li, X. (2020). *Development Road of China's Modern Iron and Steel Industry*. China: Metallurgical Industry Press. doi:10.1007/978-981-15-2074-7_1
- Li, L., Xie, Y., Feng, Z., and Zhu, C. H. (2011). Hydration Mechanism of Cement and its Research Methods. *Concrete* (06), 76–80.
- Mason, B. (1994). The Constitution of Some Open-Heart Slag. *J. Iron Steel Inst.* 11, 69–80.
- National Development and Reform Commission of the people's Republic of China. (2021). Available at: <https://www.163.com/dy/article/G60SC6FI05148IM8.html>.
- Ni, W., Li, Y., Xu, C., Xu, D., Jiang, Y., and Gao, G. (2019). Hydration Mechanism of Slag Electric Furnace Reduction Slag All Solid Waste Cementitious Material. *J. Cent. South Univ. (NATURAL SCIENCE EDITION)* 50 (10), 2342–2351. doi:10.11817/j.issn.1672-7207.2019.10.002
- Saafan, M. A., ZeinabEtman, A., and Lakany, D. (2020). Microstructure and Durability of Ground Granulated Blast Furnace Slag Cement Mortars. *Iranian J. Sci. Technology-Transactions Civil Eng.* 45 (6), doi:10.1007/s40996-020-00533-3
- Sun, J. (2019). *Properties of Alkali Activated Steel Slag Cementitious Material and concrete*. Beijing: China University of mining and Technology. doi:10.27624/d.cnki.gzkb.2019.000009
- Wang, A., Zheng, Y., Zhang, Z., Liu, K., Rui, M. A., and Sun, D. (2019). Research Progress of Geopolymer Cementitious Material Modification for Improving Durability of concrete. *Mater. Rep.* 33 (15), 2552–2560. doi:10.11896/cldb.19040211
- Xiao, J., Li, H., Zhu, H., and Dang, Y. (2018). Analysis of Hydration Products of Slag Silicate Composite Cementitious Materials by Infrared and Nuclear Magnetic Spectroscopy. *J. Mater. Sci. Eng.* 36 (04), 132–137. doi:10.14136/j.cnki.issn1673-2812.2018.04.025
- Xu, C., Ni, W., Li, K., Zhang, S., Li, Y., and Xu, D. (2019). Hydration Mechanism and Orthogonal Optimisation of Mix Proportion for Steel Slag-Slag-Based Clinker-free Prefabricated concrete. *Construction Building Mater.* 228, 117036. doi:10.1016/j.conbuildmat.2019.117036
- Yan, P., and Wang, Q. (2009). Effect of High Temperature Curing on Early Hydration Properties of Steel Slag Composite Cementitious Materials. *J. Tsinghua Univ. Nat. Sci. Edition* 4, 790–793. doi:10.3321/j.issn:1000-0054.2009.06.003
- Yüksel, S. (2018). A Review of Steel Slag Usage in Construction Industry for Sustainable Development. *Environ. Dev. Sustainability* 19 (2), 1–16. doi:10.1007/s10668-016-9759-x
- Zhang, G. (2016). Formation and Evolution Mechanism of C-S-H Microstructure of Slag Cement Composite Slurry under the Action of Aggressive Ions. *Doctoral dissertation*. Wuhan University of Technology. Available at: <https://kns.cnki.net/KCMS/detail/detail.aspx?dbname=CDFLAST2019&filename=1019809008.nh>.
- Zhao, F.-Q., Ni, W., Wang, H.-J., and Liu, H.-J. (2007). Activated Fly Ash/slag Blended Cement. *Resour. Conservation Recycling* 52 (2), 303–313. doi:10.1016/j.resconrec.2007.04.002
- Zhu, G. (2002). “Current Situation and Trend of Comprehensive Utilization of Solid Wastes of Iron and Steel Industry in PRC,” in CISA International Steel

Congress 2002 and High-Ranking Conference on Innovation and Sustainable Development, Beijing, June 26, 2002 Research Institute for Processing and Utilization of Metallurgical Solid Waste, Central Research Institute of Building & Construction, MCC Group.

Conflict of Interest: The authors declare that the research was conducted in the absence of any commercial or financial relationships that could be construed as a potential conflict of interest.

Publisher's Note: All claims expressed in this article are solely those of the authors and do not necessarily represent those of their affiliated organizations, or those of

the publisher, the editors and the reviewers. Any product that may be evaluated in this article, or claim that may be made by its manufacturer, is not guaranteed or endorsed by the publisher.

Copyright © 2021 Niu, An, Zhang, Chen and He. This is an open-access article distributed under the terms of the Creative Commons Attribution License (CC BY). The use, distribution or reproduction in other forums is permitted, provided the original author(s) and the copyright owner(s) are credited and that the original publication in this journal is cited, in accordance with accepted academic practice. No use, distribution or reproduction is permitted which does not comply with these terms.



Synergetic–Complementary Use of Industrial Solid Wastes to Prepare High-Performance Rapid Repair Mortar

Jingwei Li^{*†}, Dong Xu[†], Xujiang Wang, Kun Wang and Wenlong Wang

National Engineering Laboratory for Reducing Emissions From Coal Combustion, Engineering Research Center of Environmental Thermal Technology of Ministry of Education, Shandong Key Laboratory of Energy Carbon Reduction and Resource Utilization, School of Energy and Power Engineering, Shandong University, Jinan, China

OPEN ACCESS

Edited by:

Lijie Guo,
Beijing General Research Institute of
Mining and Metallurgy, China

Reviewed by:

Jiaqi Li,
University of California, Berkeley,
United States
Shiqi Dong,
University of California, Los Angeles,
United States

*Correspondence:

Jingwei Li
ljw@sdu.edu.cn

[†]These authors have contributed
equally to this work

Specialty section:

This article was submitted to
Structural Materials,
a section of the journal
Frontiers in Materials

Received: 10 October 2021

Accepted: 02 November 2021

Published: 03 December 2021

Citation:

Li J, Xu D, Wang X, Wang K and
Wang W (2021)
Synergetic–Complementary Use of
Industrial Solid Wastes to Prepare
High-Performance Rapid
Repair Mortar.
Front. Mater. 8:792299.
doi: 10.3389/fmats.2021.792299

With the vigorous development of infrastructure engineering, there are growing demands for high-performance rapid repair mortar, especially those using environmental-friendly and low-carbon cementitious materials. Hereupon, this work explored an innovative approach for rapid repair mortar preparation using solid waste-based calcium sulfoaluminate cement. The calcium sulfoaluminate cement was first prepared via synergetic–complementary use of industrial solid wastes and then adopted to prepare rapid repair mortar by proportionally mixing with standard sand and four additives (i.e., polycarboxylate superplasticizer, lithium carbonate, boric acid, and latex powder). The mechanistic analysis indicated that the four additives comprehensively optimized the mechanical strengths, fluidity, and setting time of rapid repair mortar by adjusting the hydration process of calcium sulfoaluminate cement. The test results showed that the 2-h compressive and flexural strength, and 1-day bonding strength of the prepared rapid repair mortar were 32.5, 9.2, and 2.01 MPa, respectively, indicating excellent early-age mechanical performance. In addition, the 28-day compressive and flexural strengths of the rapid repair mortar reached 71.8 and 17.7 MPa. Finally, a life cycle assessment and economic analysis indicated that this approach achieved environmental-friendly utilization of industrial solid wastes, and cost-effective and energy-saving natures, which supports current trends towards a circular economy and green sustainable development.

Keywords: rapid repair mortar, sulfate-based cements, industrial wastes, recycling, environmental friendliness

INTRODUCTION

Recently, large-scale infrastructure engineering such as railways, highways, bridges, water conservancy, and buildings are developing vigorously in China, and the number of these engineering infrastructures is more than that in foreign countries combined. Statistically, the annual output of concrete has reached more than 2.5 billion m³ in China (Chinaconcretes., 2020). However, the concrete structures can be damaged due to natural disasters, climate change, or continuous load, which affect the safety and normal of the facilities (Han et al., 2015; Song et al., 2018; Feng et al., 2019). Therefore, the maintenance and repair industries of concrete structures and facilities are likely to develop rapidly, and there will be massive demands for rapid repair mortars (RRMs) with properties of fast hardening, high fluidity, and early compressive

strength (i.e., ≥ 20 MPa in 2–4 h) (Moffatt and Thomas, 2017). For decades, ordinary Portland cement (OPC) has been commonly used as a cementing material for RRM preparation (Feng et al., 2019; Phoo-ngernkham et al., 2019). However, traditional OPC production consumes massive resources and energy, and contributes up to $\sim 9\%$ global anthropogenic CO_2 emissions and $\sim 7\%$ primary energy consumption (Huynh et al., 2018; Li et al., 2020). Hence, there are growing demands for replacing OPC with eco-friendly and low-carbon alternatives for the sake of energy and environment sustainability (Gartner and Sui, 2018; Juenger et al., 2019).

Calcium sulfoaluminate (CSA) cement features high early strength, low permeability, rapid setting, and slight expansion properties, which are primarily attributed to the rapid crystallization of ettringite ($3\text{CaO} \cdot \text{Al}_2\text{O}_3 \cdot 3\text{CaSO}_4 \cdot 32\text{H}_2\text{O}$), produced by the hydration of the key mineral, ye'elimite ($3\text{CaO} \cdot 3\text{Al}_2\text{O}_3 \cdot \text{CaSO}_4$) (Telesca et al., 2014; Du et al., 2021). Researchers have found that CSA cement is very suitable as the cementing material for RRM preparation (Zhang J. et al., 2018; Long et al., 2019; Yeung et al., 2019). Moffatt and Thomas (2017) prepared RRM by blending 30% CSA cement with 70% OPC as the cementing material, and achieved a compressive strength of 22 MPa at 3 h. Shi et al. (2021) also prepared RRM using CSA cement, and the flexural and compressive strengths at 1 day reached ~ 7 and ~ 36 MPa. Furthermore, CSA cement is regarded as a green cement category because of its low calcination temperature ($\sim 1,250^\circ\text{C}$) and low carbon dioxide emissions (Benhelal et al., 2013; Ren et al., 2017a).

However, the annual production of CSA cement is only several million tons worldwide (Ren et al., 2017a). Traditional raw materials to prepare CSA-based cements include high-grade bauxite, natural gypsum, and limestone, which lead to high production costs and significantly restrict its large-scale application (Ren et al., 2017b), in particular, in concrete rapid repair. Researchers tried to use industrial solid wastes as substitute raw materials for CSA cement preparation. Wang et al. (2013) successfully prepared high-performance CSA cement by synergistically using low-priced industrial solid wastes, such as red mud, desulfurization gypsum, aluminum dust, and carbide slag. A comparative life cycle assessment of CSA clinker production derived from industrial solid wastes and natural raw materials by Ren et al. (2017) showed that the total environmental burden could be reduced by 38.62% with the comprehensive waste utilization compared with the traditional process. In addition, the solid waste-based CSA cement (WCSA) exhibited a good immobilization ability on heavy metals introduced from industrial solid wastes (Yao et al., 2020). Collectively, the synergistic utilization of solid waste not only can prepare high-performance CSA cement, but also has great environmental benefits and reduces the production costs. Furthermore, some researchers verified the feasibility of preparing green building materials, i.e., ready-to-use low-density foamed concrete (Yao et al., 2019), construction 3D printing material (Shahzad et al., 2020), lightweight porous concrete (Yang et al., 2021), and foamed concrete for road embankment (Ge et al., 2020). However, there are few studies

that have explored the combination of WCSA and RRM preparation.

This paper proposes an innovative, technical approach for RRM preparation with WCSA as the primary cementing material. The WCSA was first prepared by the synergetic-complementary use of four types of bulk industrial solid wastes, and was then mixed with standard sand and four additives to prepare RRM. The compressive and flexural strengths, bonding strength, and fluidity of the prepared RRM were tested. The effects of the four additives on the hydration and mechanical properties of the prepared RRM were studied. Finally, the environmental impact and economics of this approach were assessed by both a life cycle assessment and economic analysis. This paper may provide a promising pathway to realize the preparation of high-performance solid waste-derived RRM and synergetic treatment of industrial solid wastes, which is in line with current trends towards green industrial chain.

MATERIALS AND METHODS

Materials

To prepare WCSA clinker, four kinds of industrial solid wastes were used with complementary matching of their ingredients. Carbide slag was sampled from the Tai'an Jiepu Technology Science and Technology Ltd. (Tai'an, China); aluminum dust was sampled from Xinfu Group (Liaocheng, China); red mud was sampled from Xinfu Group (Liaocheng, China); flue gas desulfurization (FGD) gypsum was sampled from Liaocheng Coal-fired Power Plants (Liaocheng, China). The chemical compositions and x-ray diffraction (XRD) patterns for the raw materials are provided in **Supplementary Table S1** and **Supplementary Figure S1**, respectively. Standard sand was used as the aggregate for RRM. Four kinds of additives, including polycarboxylic acid water reducer, lithium carbonate, boric acid, and dispersible latex powder, were used to adjust the hydration characteristics of RRM, i.e., fluidity, setting time, and mechanical strengths.

Experimental Procedure

The schematic overview of this study is shown in **Figure 1**. The above-mentioned industrial solid waste materials were proportionally mixed based on the following three modulus values in **Eqs 1–3**. The three modulus values were set as $\text{Cm} = 0.98$, $P = 1.85$, and $N = 3.09$, and the corresponding proportion of solid wastes is provided in **Supplementary Table S2**. The mixture of solid waste materials was caked and calcined at $1,250^\circ\text{C}$ (holding 30 min) to prepare the WCSA clinker. Then, the clinker was mixed with 5 wt% anhydrous gypsum, ground together, to prepare WCSA.

$$\text{Cm} = \frac{\text{CaO} - 0.7\text{TiO}_2}{1.87\text{SiO}_2 + 0.73(\text{Al}_2\text{O}_3 - 0.64\text{Fe}_2\text{O}_3) + 1.40\text{Fe}_2\text{O}_3} \quad (1)$$

$$P = \frac{\text{Al}_2\text{O}_3}{\text{SO}_3} \quad (2)$$

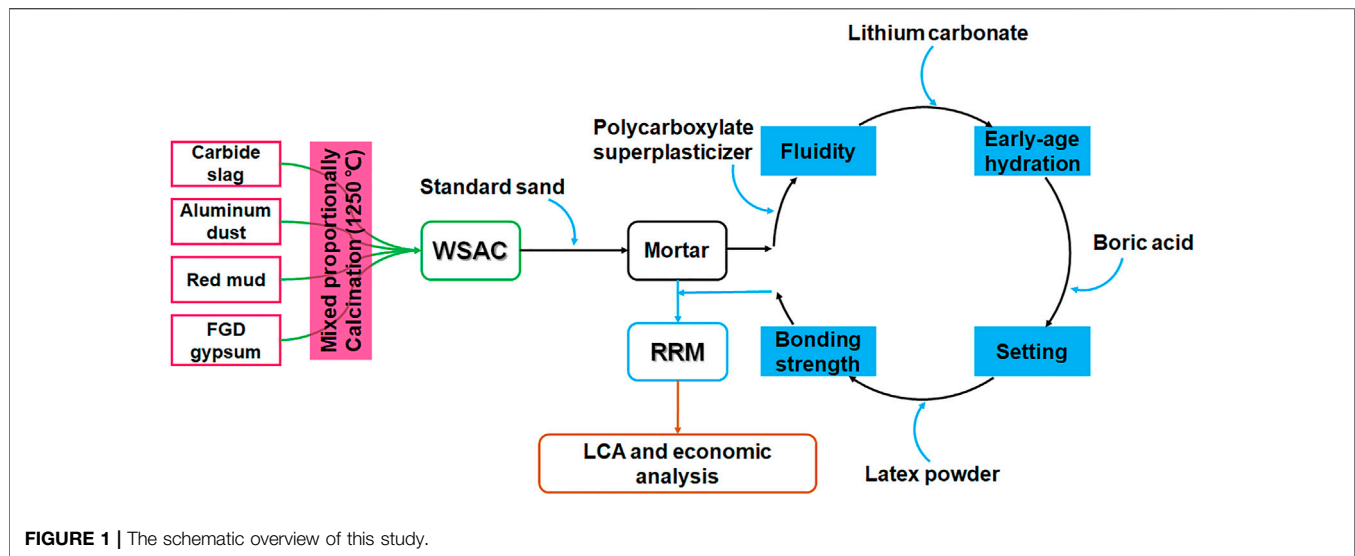


FIGURE 1 | The schematic overview of this study.

$$N = \frac{\text{Al}_2\text{O}_3}{\text{SiO}_2} \quad (3)$$

The prepared WCSA was mixed with standard sand at a weight ratio of 1:1 and then the mixture was blended with water at a water-to-binder ratio (W/B) of 0.28. Different amounts of the four additives were added into the mortar to adjust its hydration characteristics one by one: (i) polycarboxylate superplasticizer was added to adjust the fluidity at a low W/B ratio (Li et al., 2021; Tian et al., 2019), (ii) lithium carbonate was added to improve the early-age compressive and flexural strengths (Zhang Y. et al., 2018), (iii) boric acid was added to adjust the setting time (Cau Dit Coumes et al., 2017a), and (iv) dispersible latex powder was added to improve the bonding strength (Shi et al., 2021). With the optimized amounts of additives, the WCSA-based RRM was successfully prepared.

Analytical Methods

The compressive and flexural strengths of the prepared RRM were tested according to International Standard ISO 679-2009 "Cement - Test methods - Determination of strength"^[24]. The prepared RRM was mixed with water at a water-to-binder ratio of 0.28, and then stirred using a mixer. After stirring, the mortar was cast into 40 mm × 40 mm × 160 mm molds and de-molded after 24 h. The de-molded samples were cured at 95% humidity and 20 ± 2°C. The compressive and flexural strengths of the cured samples were tested using an electronic universal testing machine (YAW-300C; Zhongluchang Co., Ltd., China) after 2-h, 1-day, 3-day, and 28-day curing ages. The compressive and flexural strengths (1 day, 3 days, and 28 days) of the prepared WCSA were also tested according to International Standard ISO 679-2009, and the mass ratio of WCSA:standard sand:water was 1: 3: 0.5.

The bonding strength of the prepared RRM was tested according to Chinese Industry standard JC/T 2381-2016 "Repairing mortar, 2016"^[25]. A base mortar with dimensions of 70 mm × 70 mm × 20 mm was prepared using OPC and cured

at 95% humidity and 20 ± 2°C for 28 days. A forming frame was placed on the base mortar and then the RRM slurry was poured into the forming frame and cured at 95% humidity and 20 ± 2°C. The bonding strength was determined after 1-day curing age.

The fluidity test for the prepared RRM was conducted on the basis of Chinese national standard GB/T 2419-2005 "Test method for fluidity of cement mortar"^[26]. The RRM slurry was added to truncated cone dies, where the round die was slowly filled, allowing the slurry to flow undisturbed and freely before it eventually stopped. Then, measurements of the largest diameter of the slurry diffusion and the vertical height were conducted, and the average value was calculated. The slurry was stirred for 6 min and measured again to complete the test.

The initial and final setting times of the prepared RRM were determined according to International Standard ISO 9597-2008 "Cement-Test methods-Determination of setting time and soundness, NEQ"^[27]. The mortar was mixed and blended to a workable consistency. A Vicat apparatus was then used to perform needle penetrations at fresh locations for each measurement. The initial and final setting times were taken as the elapsed time required to achieve a penetration of 4 ± 1 and 0.5 mm, respectively.

The chemical compositions of raw materials and WCSA were characterized by x-ray fluorescence spectrometry (XRF; Spectro XEPOS 05C, SPECTRO, Germany). The mineral phases of the raw materials, WCSA clinkers, and RRM hydration products were characterized by x-ray diffraction (XRD; Rigaku Dmax-2500 PC, Rigaku, Japan) using Cu-Kα radiation with 50 kV voltage, 100 mA current, and a scanning speed of 2.4°/min over a range of 5°–65°. The morphologies and structures of RRM samples were characterized with scanning electron microscopy coupled with an energy-dispersive spectrometer (SEM/EDS; Zeiss Supra 55, Carl Zeiss MERLIN Compact, Germany). The hydrated WCSA samples were characterized using a thermogravimetric analysis combined with the differential scanning calorimetry (TGA/DSC; TGA/DSC 1, Mettler Toledo, Switzerland) under nitrogen atmosphere with a heating rate of 10°C/min from 30°C to 400°C.

TABLE 1 | Mechanical properties of the WCSA mortar.

Compressive strength (MPa)			Flexural strength (MPa)			Setting time (min)	
1 day	3 days	28 days	1 day	3 days	28 days	Initial	Final
41.9	59.9	73.4	7.2	8.0	9.1	20	28

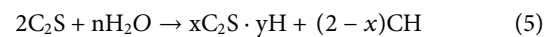
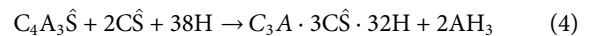
Life cycle assessment (LCA) was conducted using the SimPro ReCiPe2016 H 1.01 model according to ISO 14040 (ISO, 2006). The goal of this LCA study was to appraise the environmental impact of WCSA, CSA, and OPC clinker production chains, and the boundary considered in this study was from the cradle to the gate of the materials' production facility. The processes included mainly raw material transportation, raw material preparation, and production of the three cementitious materials. The function unit for the three techniques was established as 1 ton production of clinker. LCA inventory data were collected for each step in each material's production process. The inventory included mainly inputs of energy and source inputs, and outputs of waste and pollutants. Diesel was used for raw material transportation, and the vehicle used was assumed to be a diesel truck with 28 tons, and the transportation distance of each raw material was assumed to be 50 km from the mining facility or the solid waste facility to the gates of the production facility. Electricity was used mainly for raw material preparation and equipment, and coal was mainly used for material production. Data for raw material consumption, energy consumption, waste, and pollution emission were obtained mainly from industry statistics and literature (Huntzinger and Eatmon, 2009; Li et al., 2014; Li et al., 2019a; Chen et al., 2015; Jeswiet and Szekeres, 2016; Ren et al., 2017b; Ren et al., 2020). Detailed system boundary, function unit, and life cycle inventory are provided in **Supplementary Table S3**.

RESULTS AND DISCUSSION

Physicochemical and Mechanical Properties of WCSA

The main mineral components of WCSA were ye'elimite ($\text{Ca}_4\text{Al}_6\text{O}_{12}\text{SO}_4$, $\text{C}_4\text{A}_3\hat{\text{S}}$), dicalcium silicate (C_2S , mainly α' - C_2S and β - C_2S), and anhydrite (CaSO_4 , $\text{C}\hat{\text{S}}$) (**Supplementary Figure S2**), which were similar to those of ordinary CSA cement (Ren et al., 2020). During the hydration process of WCSA, $\text{C}_4\text{A}_3\hat{\text{S}}$ can quickly react with H_2O and $\text{C}\hat{\text{S}}$ to form ettringite (**Eq. 4**) (Telesca et al., 2014), which can contribute to much of the early-age mechanical strength. C_2S can also react with H_2O to form C-S-H gel (**Eq. 5**) (Li et al., 2019b; Yao et al., 2019), which can contribute to the later strength development. The mechanical properties of the WCSA mortar are shown in **Table 1**. The prepared WCSA had compressive strengths of 41.9, 59.9, and 73.4 MPa and flexural strengths of 7.2, 8.0, and 9.1 MPa after a curing age of 1 day, 3 days, and 28 days, respectively. The ratio of 3-day compressive strength to 28-day compressive strength was above 0.8, owing to the rapid hydration of the main mineral $\text{C}_4\text{A}_3\hat{\text{S}}$ and the relatively lower hydration reactivity of C_2S (Wang et al., 2016; Li et al., 2019b; Yao et al., 2020). The initial and final

setting times of the WCSA were only 20 and 28 min, respectively. These results indicated high early strength, high later strength, and fast hardening properties of the WCSA, which were suitable for RRM preparation.



Effect of Polycarboxylate Superplasticizer

Polycarboxylate superplasticizer was added into the prepared RRM to adjust its fluidity at a low W/B ratio. The influence of different amounts of polycarboxylate superplasticizer on the fluidity and 2-h strength development of the WCSA-based RRM was studied. As shown in **Figure 2A**, the fluidity of the RRM increased with the increase of the amount of polycarboxylate superplasticizer added. The SEM images of RRM (**Supplementary Figure S3**) indicated that the minerals were more dispersed at 0.2% polycarboxylate superplasticizer than those at 0% polycarboxylate superplasticizer, and more needle-like ettringite was observed. Polycarboxylate superplasticizer preferentially could absorb on aluminate phases that have a positively charge surface and modify the fluidity of the fresh mixture by producing electrostatic repulsion between the anhydrous and hydrated cement particles (Tian et al., 2019; Li et al., 2021), which contributed to the increase of fluidity of RRM with polycarboxylate superplasticizer added. A recent study reported that the use of polycarboxylate superplasticizer did not significantly influence the hydration process of ye'elimite after the main hydration period and could reduce expansion after 4 days of curing (Li et al., 2021). With these effects, this work used polycarboxylate superplasticizer to promote the constructability and durability of the RRM.

The existing literature has shown that the adsorption of polycarboxylate superplasticizer on ettringite could inhibit the growth of ettringite crystals and delay the setting time of CSA cement in the early-age hydration period (Sun et al., 2011; Ma et al., 2014; Su et al., 2019; Li et al., 2021), which may affect the early-age strengths of RRM. In this work, the 2-h compressive and flexural strengths of RRM fluctuated with the addition of polycarboxylate superplasticizer, and the maximum values occurred when the addition amount was 0.2% (**Figure 2B**). However, the overall compressive and flexural strengths of RRM at 2-h hydration age were relatively low and were decreased significantly when the amount of polycarboxylate superplasticizer content was higher than 0.2%. The XRD patterns of hydrated WCSA samples with different amounts of polycarboxylate superplasticizer at 2-h hydration age (**Figure 3**) showed that the main mineral phases of all samples were ettringite, anhydrite, and ye'elimite. When the polycarboxylate superplasticizer was 0.2%, the ettringite peak was the highest and the anhydrite peak was the lowest, indicating the

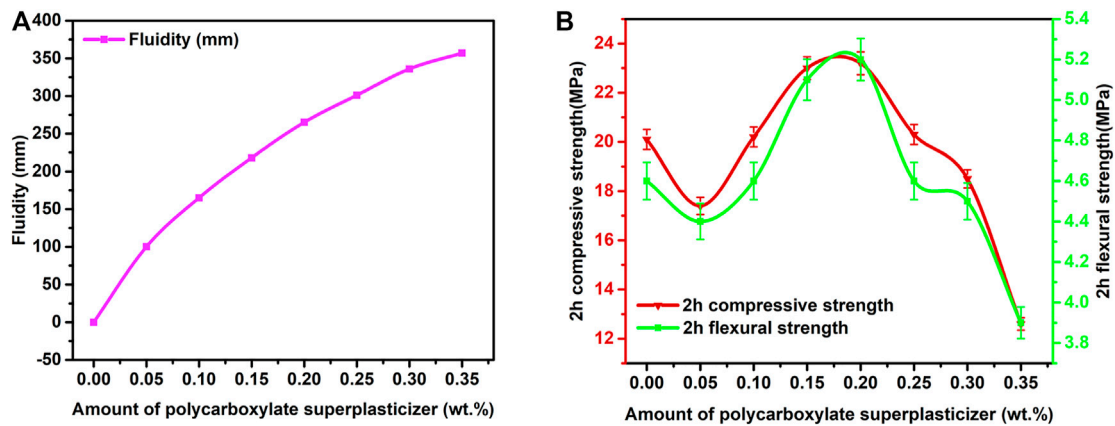


FIGURE 2 | Effect of polycarboxylate superplasticizer on the (A) fluidity and (B) 2-h strength development of RRM.

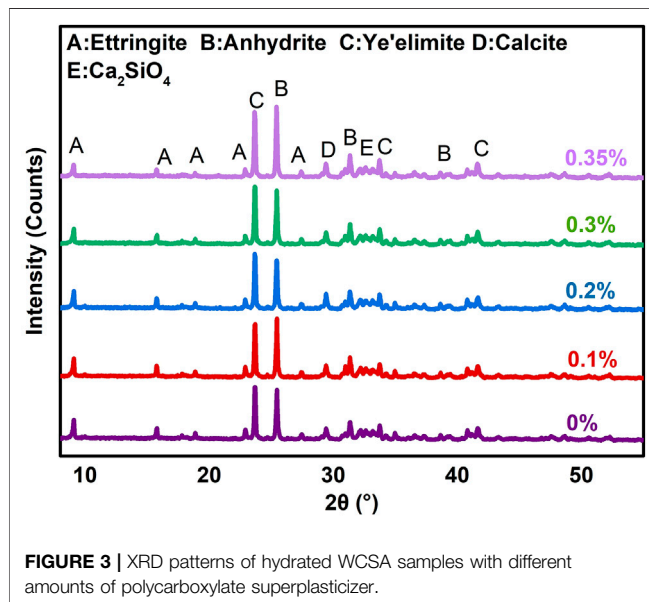


FIGURE 3 | XRD patterns of hydrated WCSA samples with different amounts of polycarboxylate superplasticizer.

highest degree of hydration among the samples. The TG/DTG curves (Supplementary Figure S4A) indicated that, with the increasing amounts of added polycarboxylate superplasticizer, the amounts of ettringite first increased and then decreased, which was consistent with the change trend of the 2-h compressive and flexural strengths of RRM.

The above results indicated that a small content of polycarboxylate superplasticizer could increase the fluidity of WCSA effectively. However, excessive polycarboxylate superplasticizer would inhibit the hydration of WCSA and the formation of ettringite, thereby reducing the early-age strength of RRM.

Effect of Lithium Carbonate and Boric Acid

When the amount of added polycarboxylate superplasticizer was set at 0.2%, to deal with the decline of the early-age strength of

RRM caused by polycarboxylate superplasticizer, lithium carbonate was added. The influence of different amounts of lithium carbonate on the initial setting time and 2-h strength development of the WCSA-based RRM is shown in Figure 4. The 2-h compressive and flexural strengths obviously increased with the addition of lithium carbonate and then dropped when the addition amount was over 0.2% (Figure 4A). Correspondingly, the initial setting time of RRM initially decreased and then increased (Figure 4B). The highest 2-h compressive and flexural strengths reached 36.5 and 8.5 MPa, respectively, which were much higher than those without lithium carbonate addition, indicating that lithium carbonate strongly accelerated the early-age hydration of WCSA in RRM.

During the hydration process of RRM, Li⁺ introduced by lithium carbonate would induce a fast precipitation of amorphous Li-containing Al(OH)₃ and the consumption of aluminate ions from the solution (Cau Dit Coumes et al., 2017b). Consequently, it would induce a fast dissolution of ye'elimite. Meanwhile, Li-containing Al(OH)₃ would provide seeds for the heterogeneous nucleation of amorphous Al(OH)₃, leading to massive precipitation of hydrates (mainly ettringite) (Cau Dit Coumes et al., 2017b). Therefore, the early-age WCSA hydration was significantly accelerated and the mechanical strengths were quickly increased. However, the acceleration effect of lithium carbonate was not linear with the addition amount. The XRD patterns and TG/DTG curves of hydrated WCSA samples with different amounts of lithium carbonate at 2-h hydration age (Supplementary Figures S4B, S5A) showed that, the ettringite peak intensity was the highest at 0.2% addition amount, rather than increased with the addition amount of lithium carbonate. As shown in Figure 4A, the compressive and flexural strengths decreased when the addition amount exceeded 0.2%. Cau Dit Coumes et al. (2017a) found that, the duration of period of low thermal activity produced by WCSA hydration tended to decrease at higher lithium additions, indicating the lack of sustainability of the acceleration effect induced by excessive lithium carbonate. Parr et al. (2004) also mentioned that the higher the lithium concentration, the faster the hydration of calcium aluminate

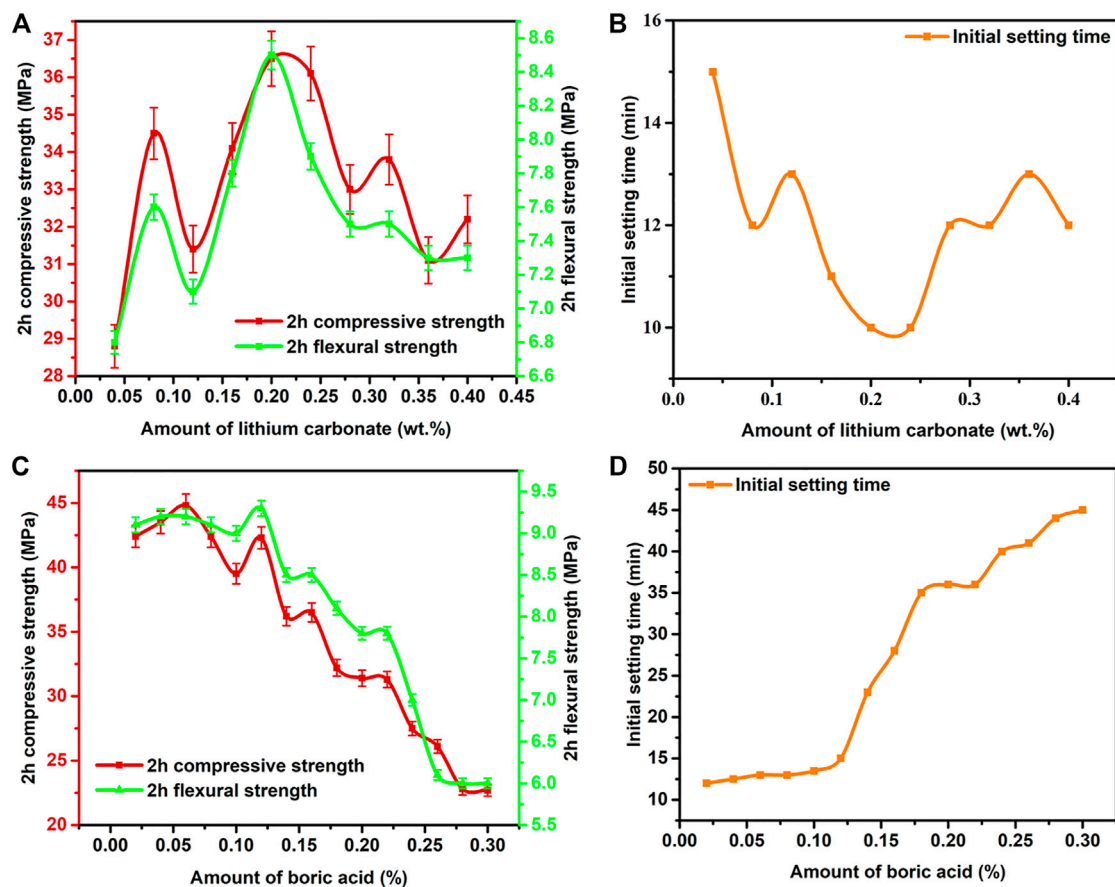


FIGURE 4 | (A, B) Effect of lithium carbonate on the initial setting time and 2-h strength development of RRM. **(C, D):** Effect of boric acid on the initial setting time and 2-h strength development of RRM.

cement until a limit above which a plateau effect occurred. These might explain the limited increase in compressive and flexural strengths induced by excessive lithium carbonate.

The above results indicated that small addition of lithium carbonate could effectively increase the early-age mechanical strengths of RRM and reduce the setting time. However, as shown in **Figure 4B**, the initial setting time was decreased to less than 15 min, which was unfavorable to the actual engineering application of RRM. Borate compound is well known for acting as set retarder during the hardening of cement (Hu et al., 2017; Chen et al., 2019). In this work, boric acid was added to extend the initial setting time of RRM (added 0.2% polycarboxylate superplasticizer and 0.2% lithium carbonate). As shown in **Figures 4C,D**, the initial setting time of RRM was prolonged with the addition of boric acid, but the compressive and flexural strengths decreased quickly as the addition amount increased.

In **Figure 4C**, small addition of boric acid ($\leq 0.06\%$) slightly increased the mechanical strengths of RRM. It might be explained that a small amount of boric acid neutralized OH^- and promoted the release of Li^+ , which accelerated the hydration of RRM. However, a higher amount of boric acid significantly reduced the mechanical strengths of RRM. It has been reported that a poorly crystallized borate compound [ulexite, $\text{NaCaB}_5\text{O}_6(\text{OH})_6\text{A}$

$5\text{H}_2\text{O}$] was formed during the CSA cement hydration, which covered the surface of CSA clinker particles and prevented the further dissolution of ye'elimite, producing a strong retarding effect (Champenois et al., 2015; Chen et al., 2019). The SEM images of RRM (**Figure 5**) showed that, some substances were attached to the surface of the hydration products when 0.16% boric acid was added, indicating the formation of poorly crystallized borate compound. Meanwhile, excessive H^+ in boric acid neutralized OH^- in $\text{Al}(\text{OH})_3$ and inhibited the formation of ettringite. These effects led to the obvious decrease in mechanical strengths of RRM.

When the addition amount of boric acid was 0.16%, the initial setting time was 28 min, which was close to the requirement of ≤ 30 min in JC/T 2381-2016 "Repairing mortar, 2016"^[25]. Meanwhile, the compressive and flexural strengths still reached 36.1 and 8.5 MPa at 0.16% addition amount, respectively. Therefore, 0.16% addition amount of boric acid might be more suitable for the RRM and was chosen in this study.

Effect of Latex Powder

When the addition amount of polycarboxylate superplasticizer, lithium carbonate, and boric acid added were set at 0.2%, 0.2%, and 0.16%, respectively, latex powder was added to increase the

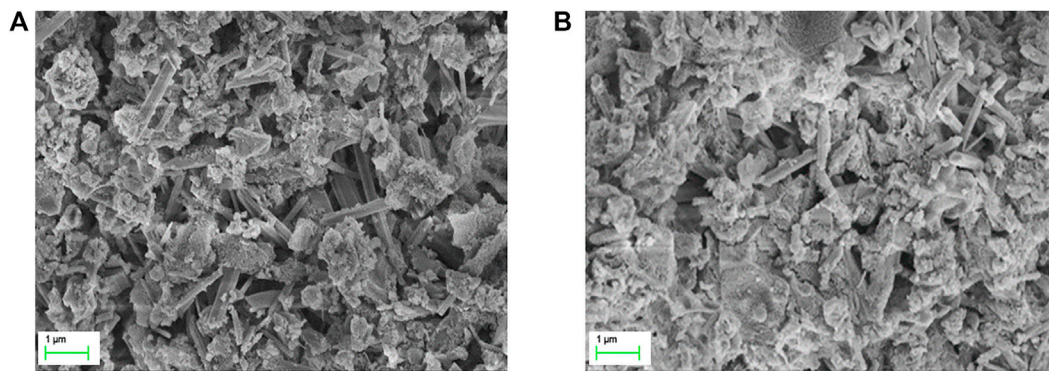


FIGURE 5 | SEM images of RRM: (A) 0% boric acid; (B) 0.16% boric acid.

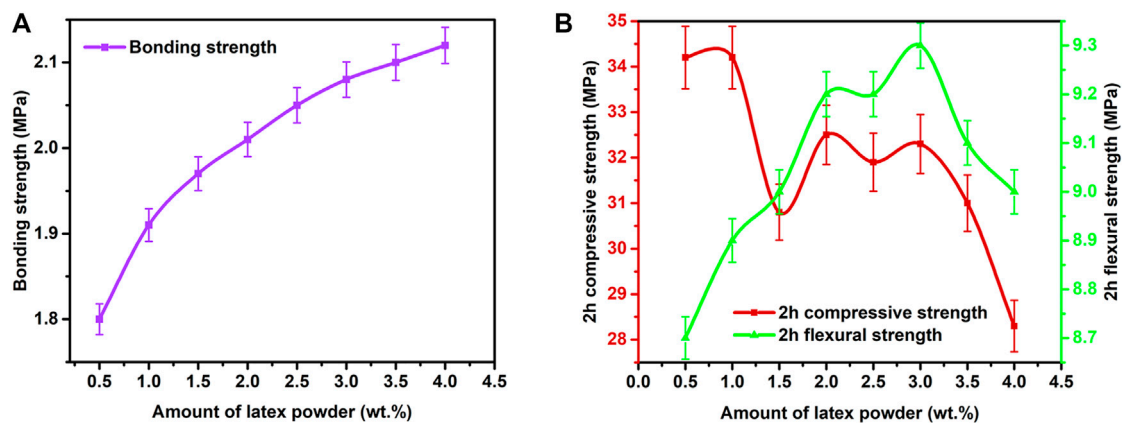


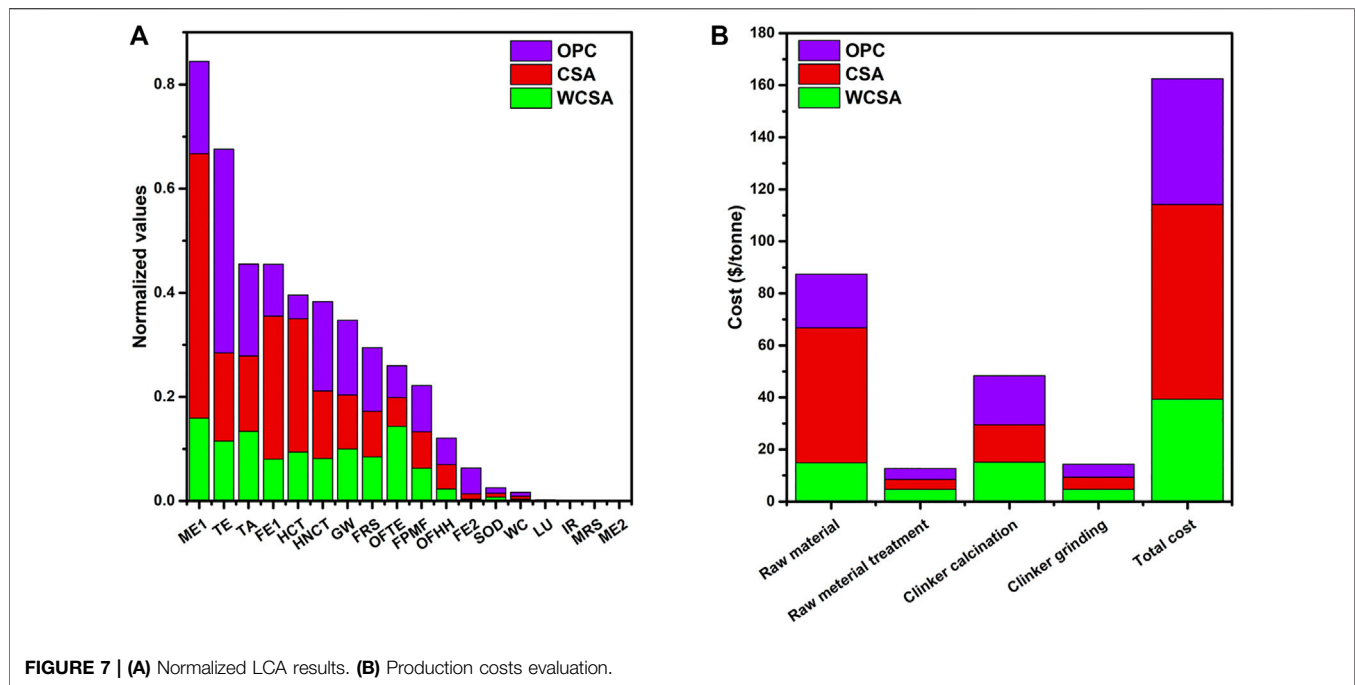
FIGURE 6 | Effects of latex powder on the 1-day bonding strength and 2-h mechanical strengths of RRM.

bonding strength of RRM. Redispersible latex powder could increase the flexural strength and bonding strength of the mortar, but it would reduce the compressive strength (Wang Peiming, 2018; Liu et al., 2019; Fan Chengwen, 2020; Lin et al., 2020). In this work, the influencing effects of latex powder on the 1-day bonding strength and 2-h mechanical strengths of RRM were studied (Figure 6). In the presence of an increased amount of latex powder, the bonding strength and flexural strength of the RRM generally increased; however, the 2-h compressive strength showed an overall downward trend. When the addition amount of latex powder exceeded 3%, the compressive strengths significantly decreased and the flexural strengths also decreased slightly.

The latex powder was able to increase the mortar bonding strength and flexural strength because it could form an emulsion with water and became evenly dispersed in the RRM slurry. The polymer particles distributed in the emulsion then gradually deposited onto the cement particle surfaces during the hydration process. The polymer particles were connected by mutual fusion to form membranes, and they eventually formed a continuous network structure into which the RRM hydrates became intertwined (Wang Peiming, 2018). This process

increased the contact area between the internal RRM particles and played a bridging role to decrease the tensile stress, and it was able to effectively absorb and transmit energy (Fan Chengwen, 2020; Wang Peiming, 2018). As a result, the bonding strength and flexural strength of the RRM was increased. However, the XRD patterns of hydrated WCSA samples with different amounts of latex powder added (Supplementary Figure S5B) showed that the anhydrite peak intensity generally increased when the addition amount increased from 1% to 4%, indicating the inhibitory effect of latex powder on the hydration of WCSA. In addition, Zhao et al. (2019) found that there were enlargement effects of redispersible polymer powders on porosity, average pore diameter, and mean pore diameter of pores in cement mortars. These effects probably led to the reduction of the compressive strength.

When the addition amount of latex powder was 2%, the 1-day bonding strength and 2-h compressive and flexural strength were 2.01, 32.5, and 9.2 MPa, respectively, which were much higher than the requirements for rigid repair mortar in JC/T 2381-2016. After curing age of 1 day, 3 days, and 28 days, the compressive strengths of RRM reached 57.2, 58.6, and 71.8 MPa, and the flexural strengths reached 12.6, 15.3, and 17.7 MPa, respectively. These results indicated



that a high-performance RRM was successfully prepared *via* using solid waste-based CSA cement as binding material, standard sand as aggregate, and four additives as performance modifiers. Collectively, the optimal addition amounts of polycarboxylate superplasticizer, lithium carbonate, boric acid, and latex powder were set at 0.2 wt%, 0.2 wt%, 0.16 wt%, and 2 wt%.

Life Cycle Assessment and Economic Analysis

Both CSA cement and OPC are usually used as the cementing materials for RRM. In order to evaluate the potential environmental benefits of using WCSA to prepare RRM, the LCA analysis of the production of WCSA, CSA cement, and OPC was conducted. The LCA results of 18 environmental impact categories are shown in **Figure 7A**. The LCA results indicated that, the WCSA production had a much lower overall environmental impact than traditional CSA cement and OPC production. It had obvious environmental benefits in the following major categories, i.e., marine ecotoxicity, terrestrial ecotoxicity, freshwater ecotoxicity, human carcinogenic and non-carcinogenic toxicity, and global warming. Previous studies also concluded that the process for preparing WCSA was more environment-friendly than that for producing traditional CSA cement (Ren et al., 2017b; Yao et al., 2019).

(ME1—Marine ecotoxicity; TE—Terrestrial ecotoxicity; TA—Terrestrial acidification; FE1—Freshwater ecotoxicity; HCT—Human carcinogenic toxicity; HNCT—Human non-carcinogenic toxicity; GW—Global warming; FRS—Fossil resource scarcity; OFTE—Ozone formation, Terrestrial ecosystems; FPMF—Fine particulate matter formation; OFHH—Ozone formation, Human health; FE2—Freshwater eutrophication; SOD—Stratospheric ozone depletion; WC—Water consumption;

LU—Land use; IR—Ionizing radiation; MRS—Mineral resource scarcity; ME2—Marine eutrophication.)

The production of WCSA could consume large amounts of industrial solid wastes, reduce the use of high-grade raw materials, and increase the added value of industrial solid wastes. Production costs of WCSA, CSA, and OPC clinkers were also evaluated (**Figure 7B**), and the total production costs for WCSA, CSA, and OPC clinkers were estimated at 39.33\$, 74.78\$, and 48.42\$, respectively (detailed data are provided in **Supplementary Table S4**). The use of industrial solid wastes significantly contributed to the cost reduction for WCSA production. In addition, a comparison of the mechanical properties among WCSA, CSA, and OPC (**Supplementary Table S5**) showed that WCSA had much higher compressive strengths than commercial CSA and OPC with lower cost, especially the early-age strengths of WCSA were two to three times that of OPC. The high early-age strength property of WCSA (i.e., 3-day hydration to achieve 80% of 28-day compressive strength) could effectively reduce the curing time of RRM, thereby improving repair efficiency. Therefore, WCSA obtained better performance at a lower cost and had greater advantages in preparing RRM. These results indicated that the production of WCSA would achieve large-scale utilization of industrial solid wastes and high performance, reducing environmental burden and production cost, which might have the potential to promote the industrial chain development of solid waste-derived high-performance RRM.

CONCLUSION

The prepared RRM exhibited excellent early-age compressive, flexural, and bonding strengths, which were mainly attributed to the high early strength and fast hardening properties of WCSA. In addition, the fluidity, early-age hydration, and mechanical strengths of

RRM were well adjusted and optimized using four additives, including polycarboxylate superplasticizer, lithium carbonate, boric acid, and latex powder.

The polycarboxylate superplasticizer could effectively improve the fluidity of RRM, but it also had an adverse effect on the early-age strength development. As a solution to the above problem, a very small amount of lithium carbonate could significantly improve the early-age hydration and strength development of RRM by promoting the dissolution of ye'elimite and the precipitation of hydrates (mainly ettringite). In addition, adding a small amount of boric acid prolonged the too short setting time of RRM caused by lithium carbonate, with ensuring its high early-age compressive and flexural strengths. Finally, the addition of a certain amount of latex powder could effectively increase the mortar bonding and flexural strengths, and only caused a limited and acceptable decrease in compressive strength.

Collectively, the WCSA production can significantly reduce the consumption of natural resources and production costs, which is more environmental-friendly than that for traditional CSA cement and OPC. This work provides an innovative and promising method for the production of high-performance RRM using WCSA, standard sand, and four suitable additives, which is in line with the current trend towards a circular economy and green sustainable development.

DATA AVAILABILITY STATEMENT

The original contributions presented in the study are included in the article/**Supplementary Material**. Further inquiries can be directed to the corresponding author.

REFERENCES

- Benhelal, E., Zahedi, G., Shamsaei, E., and Bahadori, A. (2013). Global Strategies and Potentials to Curb CO₂ Emissions in Cement Industry. *J. Clean. Prod.* 51, 142–161. doi:10.1016/j.jclepro.2012.10.049
- Cau Dit Coumes, C., Dhoury, M., Champenois, J.-B., Mercier, C., and Damidot, D. (2017a). Combined Effects of Lithium and Borate Ions on the Hydration of Calcium Sulfoaluminate Cement. *Cement Concrete Res.* 97, 50–60. doi:10.1016/j.cemconres.2017.03.006
- Cau Dit Coumes, C., Dhoury, M., Champenois, J.-B., Mercier, C., and Damidot, D. (2017b). Physico-chemical Mechanisms Involved in the Acceleration of the Hydration of Calcium Sulfoaluminate Cement by Lithium Ions. *Cement Concrete Res.* 96, 42–51. doi:10.1016/j.cemconres.2017.03.004
- Cement-Test methods-Determination of strength Cement - Test Methods - Determination of Strength, ISO 679-2009. <https://www.iso.org/standard/4848.html>.
- Cement-Test methods-Determination of setting time and soundness Cement-Test Methods-Determination of Setting Time and Soundness, NEQ, ISO 9597-2008.
- Champenois, J.-B., Dhoury, M., Cau Dit Coumes, C., Mercier, C., Revel, B., Le Bescop, P., et al. (2015). Influence of Sodium Borate on the Early Age Hydration of Calcium Sulfoaluminate Cement. *Cement Concrete Res.* 70, 83–93. doi:10.1016/j.cemconres.2014.12.010
- Chen, W., Hong, J., and Xu, C. (2015). Pollutants Generated by Cement Production in China, Their Impacts, and the Potential for Environmental Improvement. *J. Clean. Prod.* 103, 61–69. doi:10.1016/j.jclepro.2014.04.048
- Chen, W., Ling, X., Li, Q., Yuan, B., Li, B., and Ma, H. (2019). Experimental Evidence on Formation of Ulexite in Sulfoaluminate Cement Paste Mixed with High Concentration Borate Solution and its Retarding Effects. *Construction Building Mater.* 215, 777–785. doi:10.1016/j.conbuildmat.2019.04.242

AUTHOR CONTRIBUTIONS

JL: Investigation, Writing—Original draft, Formal analysis, Data curation, and Visualization. DX: Experimental analysis, Writing—Original draft, Review, and Editing. XW: Supervision, Methodology, and Review. KW: Investigation and Editing. WW: Formal analysis and Funding acquisition.

FUNDING

This work was funded by the National Key R&D Program of China (No. 2020YFC1910000) and the Natural Science Foundation of Shandong Province (CN) Youth Project (No. ZR2020QE201).

ACKNOWLEDGMENTS

We thank the support of the National Engineering Laboratory of Coal-fired Pollutants Emission Reduction (Shandong University).

SUPPLEMENTARY MATERIAL

The Supplementary Material for this article can be found online at: <https://www.frontiersin.org/articles/10.3389/fmats.2021.792299/full#supplementary-material>

- Chinaconcretes, (2020). Production and Market Analysis of Commercial concrete in China's Provinces and Cities in 2019. <http://www.cnrmc.com/news/show.php?itemid=120134>.
- Du, P., Li, X., Zhou, Z., Lu, X., Zhang, X., Xu, D., et al. (2021). Preparation and Properties of Alite-Modified Calcium Sulfoaluminate Cement. *Adv. Cement Res.* 33, 135–143. doi:10.1680/jadcr.19.00092
- Fan Chengwen, B. Y. L. P. (2020). Study on Early Performance of Rapid Hardening Sulphoaluminate Cement-Based Sealing Material. *Hydro-Science Eng.* 000, 30–35.
- Feng, L., Chen, X.-q., Wen, X.-d., Zhang, Z.-y., and Shou, L.-y. (2019). Investigating and Optimizing the Mix Proportion of Sustainable Phosphate-Based Rapid Repairing Material. *Construction Building Mater.* 204, 550–561. doi:10.1016/j.conbuildmat.2019.01.195
- Gartner, E., and Sui, T. (2018). Alternative Cement Clinkers. *Cement Concrete Res.* 114, 27–39. doi:10.1016/j.cemconres.2017.02.002
- Ge, Z., Yuan, H., Sun, R., Zhang, H., Wang, W., and Qi, H. (2020). Use of green Calcium Sulphoaluminate Cement to Prepare Foamed concrete for Road Embankment: A Feasibility Study. *CONSTR BUILD MATER.* 237, 117791. doi:10.1016/j.conbuildmat.2019.117791
- Han, J.-W., Jeon, J.-H., and Park, C.-G. (2015). Mechanical and Permeability Characteristics of Latex-Modified Pre-packed Pavement Repair Concrete as a Function of the Rapid-Set Binder Content. *MATERIALS* 8, 6728–6737. doi:10.3390/ma8105339
- Hu, Y., Li, W., Ma, S., and Shen, X. (2017). Influence of Borax and Citric Acid on the Hydration of Calcium Sulfoaluminate Cement. *Chem. Pap.* 71, 1909–1919. doi:10.1007/s11696-017-0185-9
- Huntzinger, D. N., and Eatmon, T. D. (2009). A Life-Cycle Assessment of Portland Cement Manufacturing: Comparing the Traditional Process with Alternative Technologies. *J. Clean. Prod.* 17, 668–675. doi:10.1016/j.jclepro.2008.04.007
- Huynh, T.-P., Vo, D.-H., and Hwang, C.-L. (2018). Engineering and Durability Properties of Eco-Friendly Mortar Using Cement-free SRF Binder. *Construction Building Mater.* 160, 145–155. doi:10.1016/j.conbuildmat.2017.11.040

- ISO (2006). *ISO/DIS 14040. Environmental Management - Life Cycle Assessment - Principles and Framework*. Brussels, Belgium: International Standard Iso.
- Jeswiet, J., and Szekeres, A. (2016). Energy Consumption in Mining Communion. *Proced. CIRP* 48, 140–145. doi:10.1016/j.procir.2016.03.250
- Juenger, M. C. G., Snellings, R., and Bernal, S. A. (2019). Supplementary Cementitious Materials: New Sources, Characterization, and Performance Insights. *Cement Concrete Res.* 122, 257–273. doi:10.1016/j.cemconres.2019.05.008
- Li, C., Li, J., Telesca, A., Marchon, D., Xu, K., Marroccoli, M., et al. (2021). Effect of Polycarboxylate Ether on the Expansion of Ye'elimite Hydration in the Presence of Anhydrite. *CEMENT CONCRETE RES.* 140. doi:10.1016/j.cemconres.2020.106321
- Li, C., Nie, Z., Cui, S., Gong, X., Wang, Z., and Meng, X. (2014). The Life Cycle Inventory Study of Cement Manufacture in China. *J. Clean. Prod.* 72, 204–211. doi:10.1016/j.jclepro.2014.02.048
- Li, J., Geng, G., Zhang, W., Yu, Y.-S., Shapiro, D. A., and Monteiro, P. J. M. (2019a). The Hydration of β - and α' -H-Dicalcium Silicates: An X-ray Spectromicroscopic Study. *ACS Sustain. Chem. Eng.* 7, 2316–2326. doi:10.1021/acssuschemeng.8b05060
- Li, J., Zhang, W., Li, C., and Monteiro, P. J. M. (2019b). Green concrete Containing Diatomaceous Earth and limestone: Workability, Mechanical Properties, and Life-Cycle Assessment. *J. Clean. Prod.* 223, 662–679. doi:10.1016/j.jclepro.2019.03.077
- Li, J., Zhang, W., Xu, K., and Monteiro, P. J. M. (2020). Fibrillar Calcium Silicate Hydrate Seeds from Hydrated Tricalcium Silicate Lower Cement Demand. *CEMENT CONCRETE RES.* 137, 106195. doi:10.1016/j.cemconres.2020.106195
- Lin, R., Yang, L., Li, S., Li, R., Sheng, X., and Song, G. (2020). Influences of Polymers on the Properties of Cement-Sodium Silicate Grouts with a High Water-Binder Ratio. *J. CERAM. PROCESS RES.* 21, 393–399.
- Liu, G. J., Bai, E. L., Xu, J. Y., and Yang, N. (2019). Mechanical Properties of Carbon Fiber-Reinforced Polymer Concrete with Different Polymer-Cement Ratios. *Materials (Basel)* 12. doi:10.3390/ma12213530
- Long, W. R., Doyle, J. D., Freyne, S. F., and Ramsey, M. A. (2019). Effects of Impure Water Sources on the Early-Age Properties of Calcium Sulfoaluminate (CSA) Cement. *Adv. Civil Eng. Mater.* 8, 20–30. doi:10.1520/acem20180115
- Ma, B., Ma, M., Shen, X., Li, X., and Wu, X. (2014). Compatibility between a Polycarboxylate Superplasticizer and the Belite-Rich Sulfoaluminate Cement: Setting Time and the Hydration Properties. *Construction Building Mater.* 51, 47–54. doi:10.1016/j.conbuildmat.2013.10.028
- Moffatt, E. G., and Thomas, M. D. A. (2017). Performance of Rapid-Repair concrete in an Aggressive marine Environment. *Construction Building Mater.* 132, 478–486. doi:10.1016/j.conbuildmat.2016.12.004
- Parr, C., Simonin, F., Touzo, B., Wöhrmeyer, C., Valdelièvre, B., and Namba, A. (2004). The Impact of Calcium Aluminate Cement Hydration upon the Properties of Refractory Castables. *Proc. TARJ Meet.*, 1–17.
- Phoo-ngernkham, T., Hanjitsuwan, S., Li, L.-y., Damrongwiriyanupap, N., and Chindaprasit, P. (2019). Adhesion Characterisation of Portland Cement concrete and Alkali-Activated Binders. *Adv. Cement Res.* 31, 69–79. doi:10.1680/jadcr.17.00122
- Repairing mortar (2016). *Repairing Mortar, JC/T, 2381-2016*. Beijing, China
- Ren, C., Wang, W., and Li, G. (2017a). Preparation of High-Performance Cementitious Materials from Industrial Solid Waste. *Construction Building Mater.* 152, 39–47. doi:10.1016/j.conbuildmat.2017.06.124
- Ren, C., Wang, W., Mao, Y., Yuan, X., Song, Z., Sun, J., et al. (2017b). Comparative Life Cycle Assessment of Sulfoaluminate Clinker Production Derived from Industrial Solid Wastes and Conventional Raw Materials. *J. Clean. Prod.* 167, 1314–1324. doi:10.1016/j.jclepro.2017.05.184
- Ren, C., Wang, W., Yao, Y., Wu, S., Qamar, S., and Yao, X. (2020). Complementary Use of Industrial Solid Wastes to Produce green Materials and Their Role in CO₂ Reduction. *J. Clean. Prod.* 252, 119840. doi:10.1016/j.jclepro.2019.119840
- Shahzad, Q., Wang, X., Wang, W., Wan, Y., Li, G., Ren, C., et al. (2020). Coordinated Adjustment and Optimization of Setting Time, Flowability, and Mechanical Strength for Construction 3D Printing Material Derived from Solid Waste. *Construction Building Mater.* 259, 119854. doi:10.1016/j.conbuildmat.2020.119854
- Shi, C., Wang, P., Ma, C., Zou, X., and Yang, L. (2021). Effects of SAE and SBR on Properties of Rapid Hardening Repair Mortar. *J. Building Eng.* 35, 102000. doi:10.1016/j.job.2020.102000
- Song, Z., Zhang, A., Li, G., Liu, S., and Zhang, J. (2018). Study of Seawater Corrosion Resistance of Ordinary Portland Cement-Calcium Aluminate Cement-gypsum Mortar Containing Slag. *ADV. CEM RES.* 32, 1–24.
- Su, T., Kong, X., Tian, H., and Wang, D. (2019). Effects of Comb-like PCE and Linear Copolymers on Workability and Early Hydration of a Calcium Sulfoaluminate Belite Cement. *Cement Concrete Res.* 123, 105801. doi:10.1016/j.cemconres.2019.105801
- Sun, N., Chang, W., Wang, L., Zhang, J., and Pei, M. (2011). Effects of the Chemical Structure of Polycarboxy-Ether Superplasticizer on its Performance in Sulphoaluminate Cement. *J. Dispersion Sci. Tech.* 32, 795–798. doi:10.1080/01932691.2010.488132
- Telesca, A., Marroccoli, M., Pace, M. L., Tomasulo, M., Valenti, G. L., and Monteiro, P. J. M. (2014). A Hydration Study of Various Calcium Sulfoaluminate Cements. *Cement and Concrete Composites* 53, 224–232. doi:10.1016/j.cemconcomp.2014.07.002
- Test method for fluidity of cement mortar Test Method for Fluidity of Cement Mortar, GB/T, 2419-2005. Beijing, China. Available at: <http://html.rhhz.net/GLJTKJYWB/20130303.htm>.
- Tian, H., Kong, X., Cui, Y., Wang, Q., and Wang, D. (2019). Effects of Polycarboxylate Superplasticizers on Fluidity and Early Hydration in Sulfoaluminate Cement System. *Construction Building Mater.* 228, 116711. doi:10.1016/j.conbuildmat.2019.116711
- Wang Peiming, Z. G. Z. G. (2018). Mechanism of Redispersible Polymer Powder in Cement Mortar. *J. Chin. Ceram. Soc.* 46, 256–262.
- Wang, W., Wang, X., Zhu, J., Wang, P., and Ma, C. (2013). Experimental Investigation and Modeling of Sulfoaluminate Cement Preparation Using Desulfurization Gypsum and Red Mud. *Ind. Eng. Chem. Res.* 52, 1261–1266. doi:10.1021/ie301364c
- Wang, Z., Wang, M., Wen, Z., and Zhang, W. (2016). Progress on Study of Dicalcium Silicate and Low Calcium Cement with Dicalcium Silicate as a Main Mineral Composition. *Mater. Rev.* doi:10.11896/j.issn.1005-023X.2016.01.012
- Yang, S., Yao, X., Li, J., Wang, X., Zhang, C., Wu, S., et al. (2021). Preparation and Properties of Ready-To-Use Low-Density Foamed concrete Derived from Industrial Solid Wastes. *Construction Building Mater.* 287, 122946. doi:10.1016/j.conbuildmat.2021.122946
- Yao, X., Wang, W., Liu, M., Yao, Y., and Wu, S. (2019). Synergistic Use of Industrial Solid Waste Mixtures to Prepare Ready-To-Use Lightweight Porous concrete. *J. Clean. Prod.* 211, 1034–1043. doi:10.1016/j.jclepro.2018.11.252
- Yao, Y., Wang, W., Ge, Z., Ren, C., Yao, X., and Wu, S. (2020). Hydration Study and Characteristic Analysis of a Sulfoaluminate High-Performance Cementitious Material Made with Industrial Solid Wastes. *Cement and Concrete Composites* 112, 103687. doi:10.1016/j.cemconcomp.2020.103687
- Yeung, J. S. K., Yam, M. C. H., and Wong, Y. L. (2019). 1-Year Development Trend of concrete Compressive Strength Using Calcium Sulfoaluminate Cement Blended with OPC, PFA and GGBS. *Construction Building Mater.* 198, 527–536. doi:10.1016/j.conbuildmat.2018.11.182
- Zhang, J., Li, G., Yang, X., Ren, S., and Song, Z. (2018). Study on a High Strength Ternary Blend Containing Calcium Sulfoaluminate Cement/calcium Aluminate Cement/ordinary Portland Cement. *Construction Building Mater.* 191, 544–553. doi:10.1016/j.conbuildmat.2018.10.040
- Zhang, Y., Wang, Y., Li, T., Xiong, Z., and Sun, Y. (2018). Effects of Lithium Carbonate on Performances of Sulphoaluminate Cement-Based Dual Liquid High Water Material and its Mechanisms. *Construction Building Mater.* 161, 374–380. doi:10.1016/j.conbuildmat.2017.11.130
- Zhao, G., Wang, P., and Zhang, G. (2019). Principles of Polymer Film in Tile Adhesive Mortars at Early Ages. *MATER. RES. EXPRESS* 6. doi:10.1088/2053-1591/ab25c2

Conflict of Interest: The authors declare that the research was conducted in the absence of any commercial or financial relationships that could be construed as a potential conflict of interest.

Publisher's Note: All claims expressed in this article are solely those of the authors and do not necessarily represent those of their affiliated organizations, or those of the publisher, the editors, and the reviewers. Any product that may be evaluated in this article, or claim that may be made by its manufacturer, is not guaranteed or endorsed by the publisher.

Copyright © 2021 Li, Xu, Wang, Wang and Wang. This is an open-access article distributed under the terms of the Creative Commons Attribution License (CC BY). The use, distribution or reproduction in other forums is permitted, provided the original author(s) and the copyright owner(s) are credited and that the original publication in this journal is cited, in accordance with accepted academic practice. No use, distribution or reproduction is permitted which does not comply with these terms.



Improvement of Calcium Aluminate Cement Containing Blast Furnace Slag at 50°C and 315°C

Wu Zhiqiang^{1*}, Liu Hengjie², Qu Xiong³, Wu Guangai¹, Xing Xuesong¹, Cheng Xiaowei^{4*} and Ni Xiucheng⁴

¹CNOOC Research Institute Co., Ltd., Beijing, China, ²PetroChina Southwest Oil and Gas Field Company, Chengdu, China, ³CNPC Chuangqing Drilling Engineering Company Limited, Chengdu, China, ⁴School of New Energy and Materials, Southwest Petroleum University, Chengdu, China

OPEN ACCESS

Edited by:

Weina Meng,
Stevens Institute of Technology,
United States

Reviewed by:

E. Chen,
Chalmers University of Technology,
Sweden
Xinmei Hou,
University of Science and Technology
Beijing, China
Mohamed Amin,
Ain Sham University, Egypt

*Correspondence:

Wu Zhiqiang
wuzhq2@cnooc.com.cn
Cheng Xiaowei
chengxw@swpu.edu.cn

Specialty section:

This article was submitted to
Structural Materials,
a section of the journal
Frontiers in Materials

Received: 02 November 2021

Accepted: 13 December 2021

Published: 05 January 2022

Citation:

Zhiqiang W, Hengjie L, Xiong Q,
Guangai W, Xuesong X, Xiaowei C and
Xiucheng N (2022) Improvement of
Calcium Aluminate Cement Containing
Blast Furnace Slag at 50°C and 315°C.
Front. Mater. 8:807596.
doi: 10.3389/fmats.2021.807596

During the thermal recovery of heavy oil thermal recovery wells, improving the mechanical properties and integrity of the cement ring is of great significance for the safe and efficient exploitation of heavy oil resources. This paper studies the relative properties of calcium aluminate cement and three kinds of slags under the conditions of 50°C × 1.01 MPa and 315°C × 20.7 MPa. CAC-slag composite material performance was evaluated using the cement paste compressive strength and permeability tests to study the physical properties of CAC with blast furnace slag. X-ray diffraction analysis, scanning electron microscopy (SEM), and thermal analysis (DSC/TG) were carried out to investigate the mineralogical composition of CAC with blast furnace slag. Results show that adding blast furnace slag did not affect the performance of cement slurry. Moreover, C₂ASH₈ curing occurred at low temperature, the microstructure of CAC paste was compact, and the permeability resistance was improved, thus improving the low-temperature properties of neat CAC. When cured at a high temperature, the CAC paste was mainly hydrated with C₃ASH₄ and AIO(OH), which had a well-developed crystal structure. Adding blast furnace slag can improve the CAC resistance to high temperature.

Keywords: thermal recovery, blast furnace slag, CAC, high temperature, mechanical properties, phase and microstructure

INTRODUCTION

Steam flooding is a thermal-recovery technique of heavy oil exploitation. During the process of thermal recovery, a cement sheath is used as a supporting casing and isolates the cementing intervals that can withstand steam environments of up to 300–350°C. This is a challenge for cementing materials for heavy oil thermal-recovery wells (Nabih and Chalaturnyk, 2014; Pang et al., 2018; Chai et al., 2022; Ding et al., 2021). However, silicate cement added to sand is often used at high temperatures in hot and humid environments for long periods of heavy oil thermal recovery; the compressive strength declines sharply, causing zonal isolation invalidation and shortening the working life of the oil well (Walker, 1962; Salehpour et al., 2014). Calcium aluminate cement (CAC) is used as refractory material and has characteristics of high strength, rapid hardening, and resistance to high temperatures over a long period of time (Kar et al., 2012; Idrees et al., 2021; Roig-Flores et al., 2021; Abolhasani et al., 2021). Thus, CAC

Abbreviations: A, Al₂O₃; C, CaO; H, H₂O; S, SiO₂

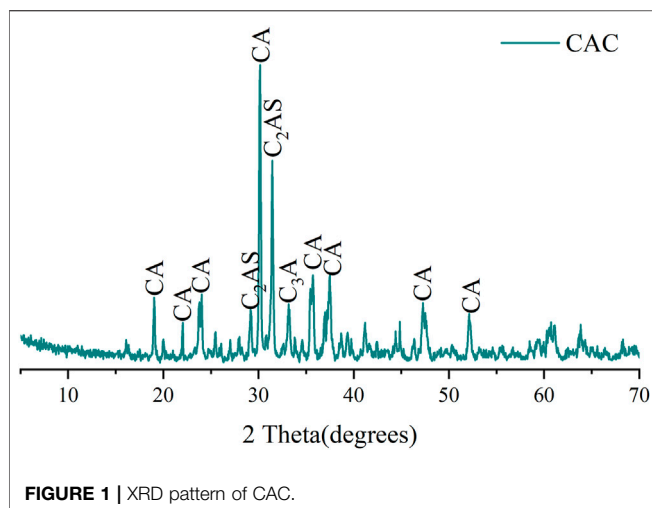
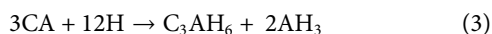
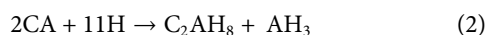
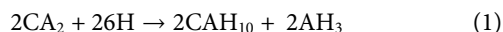


FIGURE 1 | XRD pattern of CAC.

has potential use in heavy oil thermal recovery well cementing. CAC has previously been used as a building or refractory material in simpler environments compared with thermal recovery. The curing temperature of the CAC hydration products and its structure are vital roles. Recent research on CAC have reported (Goberis and Antonovich, 2004; Ukrainczyk and Matusinović, 2010; Kirca et al., 2013; Pacewska et al., 2013) that temperatures used are mostly in the range of 20–70°C and few experiments have been performed on CAC paste curing at 300–350°C. In recent years, research on CAC has mostly focused on hydration characteristics and fracture toughness, using slag as an auxiliary cementing material to improve the mechanical performance of CAC (Amin et al., 2012; Cheng et al., 2019), and often perform collaborative analysis with concrete (Wang et al., 2021a; Wang et al., 2021b; Huang et al., 2021). Therefore, research on the resistance performance of CAC in hot and humid environments at high temperatures has great significance.

Alternately, CAC is sensitive when cured at low temperatures. CAH_{10} is mainly generated when cured below 20°C, C_2AH_8 , AH_3 are generated when cured at 30°C, and C_3AH_6 and AH_3 are mainly generated when cured at more than 45°C. The hydration reaction is as follows (Sakai et al., 2010; Mostafa et al., 2012):



The hydration products CAH_{10} and C_2AH_8 are in the metastable phase, which occurs during the conversion reaction to a product that is more stable. The reaction for cubic C_3AH_6 compounds at high temperature curing is as follows:



Based on these reaction results, the strength of CAC at low temperature is unstable, especially when cured at 50–60°C. This

unstable strength greatly limits the use of CAC in cementing engineering applications. According to previous reports (Heikal et al., 2005), adding blast furnace slag to CAC can improve the mechanical properties of CAC when cured at low temperature.

This paper aims to explore the influence of the three blast furnace slags on the high temperature resistance of CAC for heavy oil thermal recovery, the physical and microscopic properties of CAC change during the simulated processes of cementing at 50°C × 1.01 MPa and steam drive oil at 315°C × 20.7 MPa.

EXPERIMENTAL

Materials

CAC was produced by the Zhengzhou Xinxing special cement plant, China. The XRD pattern of CAC is shown in Figure 1. Three types of blast furnace slag: FSa, FSb, and FSc are all from Chengdu Hongsheng Technology Co., Ltd., China (Table 1). A filtrate reducer G33S (AMPS/AM/AA terpolymer), a retarder SR (lignin sulfonate and boric acid salt mixture), and tap water (waterworks Chengdu) were also used.

Preparation of Samples

The preparation procedure of the cement slurry is in accordance with the API standard. The neat cement slurry consisted of CAC, 1.5% (relative to the cement weight) filtrate reducer G33S, 0.45% retarder SR, and tap water, mark as Ms. The cement slurry with furnace blast furnace slag consisted of CAC with 30% FSa, FSb, or FSc, 2% filtrate reducer G33S, 0.6% retarder SR, and tap water, marked as Ma, Mb, and Mc respectively. The density of both cement slurries was 1.85 g/cm³. Four CAC formulas were designated with the codes Ms, Ma, Mb, and Mc. The experimental formula is shown in Table 2.

The cement slurry was poured into 50.8 × 50.8 × 50.8 mm³ cubic molds and cured in a bath (HH-8; Jintan City Jerry Electric Appliance Co., Ltd., China) at 50°C for 7 days to simulate the thermal recovery process. The cured samples were then moved to a water-cycling, high-temperature, and high-pressure curing reactor (OWC-9390Y; Shenyang Institute of Aviation Industry Application Technology Research Institute, China) and cured at

TABLE 1 | Chemical composition and percentage content of slag and CAC.

Materials	CAC	FSa	FSb	FSc
Specific gravity	3.10	2.70	2.95	2.70
Average specific area (m ² /g)	0.36	1.36	1.503	1.01
CaO(%)	37.85	32.7	50.8	38.2
SiO ₂ (%)	4.94	33.5	27.3	31.8
Al ₂ O ₃ (%)	55.29	16.6	6.93	14.0
MgO(%)	—	6.25	3.81	9.60
Fe ₂ O ₃ (%)	1.68	2.87	3.58	1.24
SO ₃ (%)	—	2.77	2.70	1.90
TiO ₂ (%)	—	2.60	2.31	1.26
K ₂ O(%)	—	1.09	0.755	0.581
MnO ₂ (%)	—	0.526	0.320	0.68
Na ₂ O(%)	—	0.409	0.359	0.322
Others(%)	0.24	0.685	1.136	0.417

TABLE 2 | Cement slurry formula.

Id	CAC/%	Slag		G33S/%	SR/%	Water/%	Density/g/cm ³
		Type	Amount/%				
Ms	100	—	—	1.5	0.45	44	1.85
Ma	100	FSa	30	2	0.6	44	1.85
Mb	100	FSb	30	2	0.6	44	1.85
Mc	100	FSb	30	2	0.6	44	1.85

TABLE 3 | Properties of the CAC slurry.

Formula	Density (g/cm ³)	Fluidity (cm)	Free fluid (%)	API fluid loss (ml)	100Bc thickening time (min)	Stability($\Delta\rho$ sc/%)		
						Top	Middle	Bottom
Ms	1.85	26.5	0.5	50	143	99.9	100.0	100.1
Ma	1.85	25	0.3	39	151	99.9	99.9	100.1
Mb	1.85	24	0.2	44	156	99.8	100.0	100.2
Mc	1.85	25	0.2	35	152	100.0	100.0	100.0

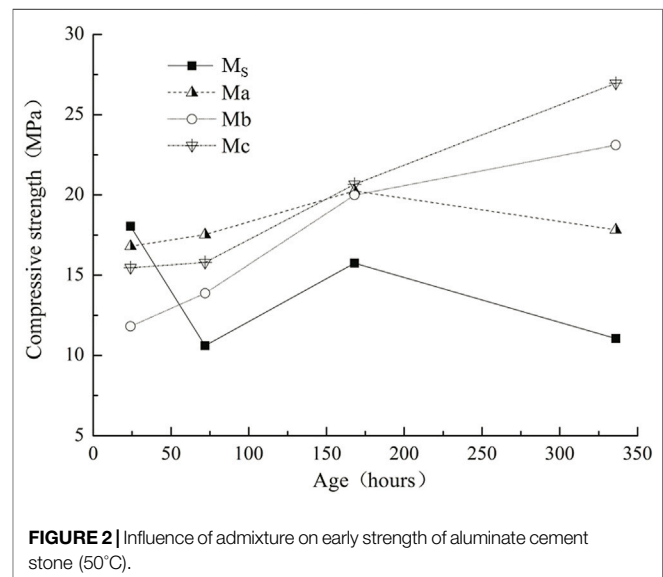
Note: The thickening time is tested under the conditions of a pressure of 45 MPa, a temperature of 50°C, and a heating time of 30 min.

315°C and 20.7 MPa for 7 days. The cubic molds were maintained in a constant temperature water bath for low-temperature curing and completely immersed in high temperature thickened oil for high-temperature and high-pressure curing.

Testing Methods

The method for the slurry performance test is in accordance with the API standard. Density, fluidity, free fluid, API fluid loss, and thickening time at 100 Bc were evaluated.

The compressive strength of cubic samples was determined using a testing machine (TA300; Beijing Ha Wisdom Technology Co., Ltd., China). Six samples were used to determine the compressive strengths at each specified age. The loading rate is 2000N/s. Permeability was determined on cylindrical samples with a size of Φ 200 mm \times 500 mm by using a core permeability measuring instrument (DSK III; Changzhou Yiyong Technology Co., Ltd., China). The rock sample was dried at 60°C for 3 days, and the absolute permeability of the rock sample was measured by the gas method. The results were the arithmetic average of three specimens at the minimum. The hydration products of cement paste were determined by X-ray diffraction (XRD; DX-1000; Dandong Fangyuan Instrument Co., Ltd., China). Samples were prepared by grinding compressive specimens with the test step length at 0.08°, scan rate at 2° per minute, and 2-theta angle range of 5°–70°. The voltage and current of the test equipment are 30 kV and 20 mA respectively. The microstructure morphology of the cement paste was determined using an environmental scanning electron microscope (FEI Quanta450; USA) with a vacuum ion sputtering apparatus (LDM150D type; USA) that coats a layer of Au to all of the samples. The morphology of the cement was then observed through SEM. Resolution: high vacuum mode, 3.0 nm (30 kV); Magnification: 5X–300000X; Accelerating voltage: 0.3–30 kV; Sample stage stroke X = 100 mm and above,

**FIGURE 2** | Influence of admixture on early strength of aluminate cement stone (50°C).

Y = 100 mm and above, Z = 100 mm and above; T = 10°–90°; R = 360°. The cement was tested for heat absorption at 25–900°C, with a heating rate of 10°C/min, sensitivity of 0.04 μ W, and calorimeter precision of 0.1% in a thermal analyzer (TGA/SDTA85; Mettler-Toledo, Switzerland). The reaction gas is air with a flow rate of 10 ml/min; the shielding gas is nitrogen with a flow rate of 20 ml/min.

RESULTS AND DISCUSSION

Properties of the CAC Slurry

Table 3 shows the fundamental properties of the CAC slurry. The CAC slurry had a density of 1.85 g/cm³, good liquidity, and

TABLE 4 | Influence of slag on the high temperature resistance of aluminate cement stone.

Formula	Permeability (mD)		Compressive strength (MPa)	
	50°C	315°C	50°C	315°C
Ms	0.0498	0.0446	11.05	15.10
Ma	0.0280	0.0344	17.82	16.56
Mb	0.0200	0.0341	23.10	19.70
Mc	0.0112	0.0338	26.96	25.49

less free fluid. API fluid loss was within 50 ml and was reduced when mixed with 30% furnace blast furnace slag. The thickening time of the 100 Bc control was within 2–3 h, which satisfies the Liaohe oilfield blocks Q cementing operation requirements in China.

Mechanical Behavior

Early Compressive Strength

This experiment demonstrated the early compressive strength of a CAC paste under low-temperature (50°C) curing in a water bath, as shown in **Figure 2**. Under this curing condition, the pure aluminate cement compressive strength changed. Moreover, the intensity fluctuation was larger after only 1 day (24 h), and the strength was higher than that of the CAC paste mixed with blast furnace slag. Fentiman et al. (Fentiman et al., 2020) also found that, in the early days, the compressive strength of CAC paste with blast furnace slag is lower than that of pure CAC paste. Compared with pure CAC paste, the compressive strength of CAC paste mixed with blast furnace slag exhibited a larger increase and was relatively stable after 3 days (72 h), and the compressive strength gradually increased with curing time. The compressive strength increased because the hydration

reaction produced C_2ASH_8 (also called stratlingite) instead of C_3AH_6 (Antonović et al., 2013).

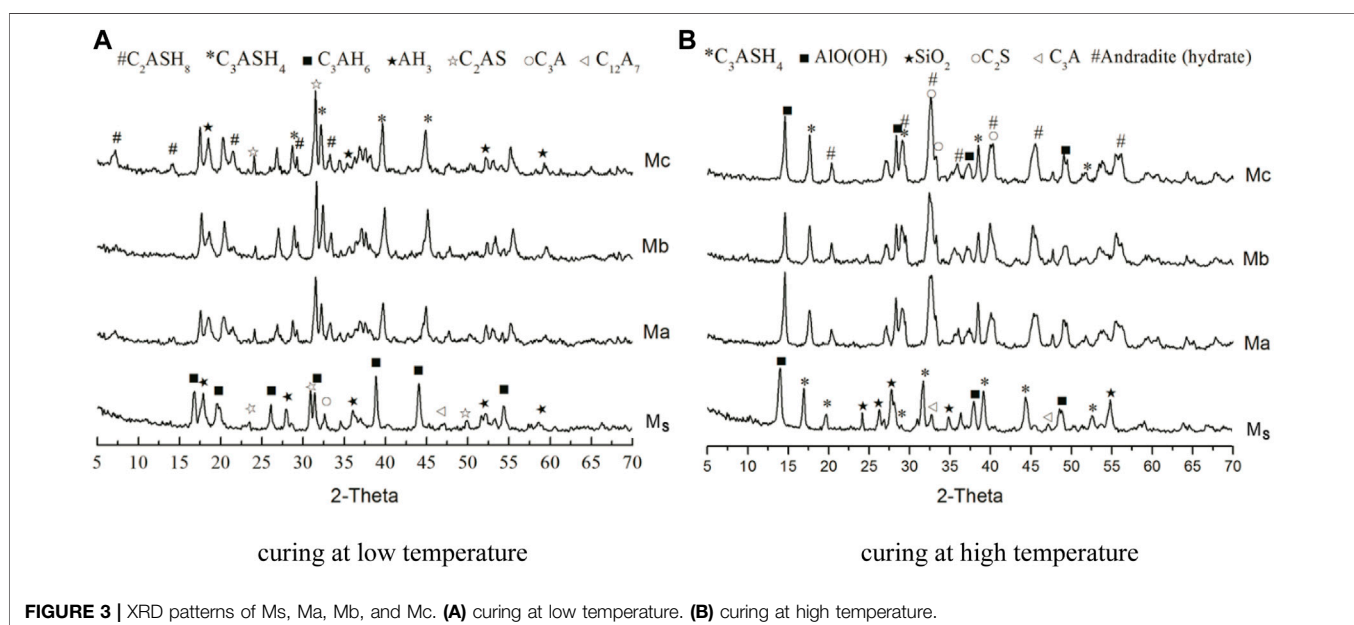
High-Temperature Performance of CAC Paste With Blast Furnace Slag

The permeability and compressive strength of CAC paste cured at 50°C × 1.01 MPa and 315°C × 20.7 MPa are shown in **Table 4**. The permeability of Ms is larger. However, the relative permeability of Ma, Mb, and Mc was improved substantially compared with Ms. This result indicates that the structure of CAC paste with blast furnace slag was denser and had increased compressive strength. In particular, the resistance of the permeability of Mc was higher than that of Ms by 77.5%, and its compressive strength increased by 74.2% at 50°C curing. This is because the CAC with blast furnace slag hydration reaction produces stratlingite crystal and the pure CAC hydration reaction produces C_3AH_6 . The volume of the C_3AH_6 crystal phase is smaller. Thus, the apparent porosity increases, thereby weakening permeability resistance and compressive strength (Tseng and Nian, 2004). The anti-permeability property of the CAC paste was reduced by curing at high temperature. However, the anti-permeability of Ma, Mb, and Mc was still higher than that of Ms by at least 22.8%, and the compressive strength of Ma, Mb, and Mc was higher than that of Ms by at least 9.7%. This result indicates that the three types of blast furnace slag can improve the anti-permeability and compressive strength properties of CAC paste at 50 and 315°C.

Hydration Products and Microstructure Testing

XRD Analysis

The hydrated phases formed by Ms, Ma, Mb, and Mc were investigated using XRD. **Figure 3A** shows the XRD pattern of



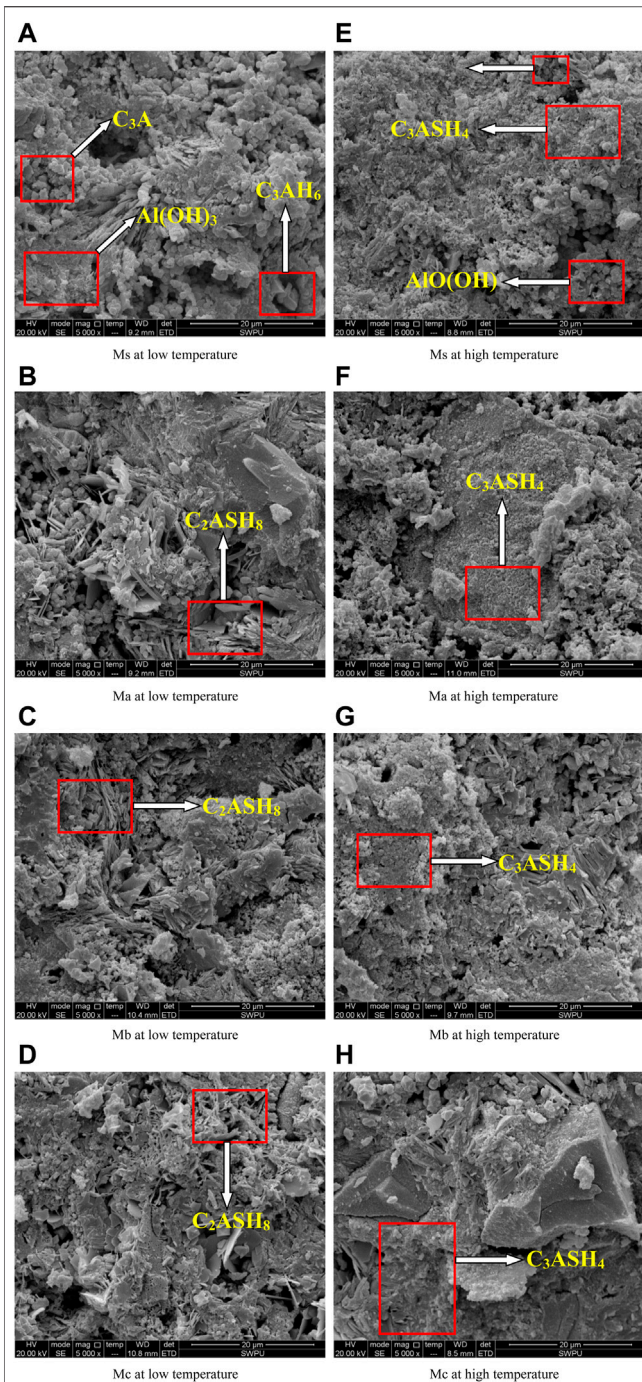


FIGURE 4 | SEM pictures of CAC stone(5,000x). (A) Ms at low temperature. (B) Ma at low temperature. (C) Mb at low temperature. (D) Mc at low temperature. (E) Ms at high temperature. (F) Ma at high temperature. (G) Mb at high temperature. (H) Mc at high temperature.

CAC paste cured at $50^{\circ}\text{C} \times 1.01 \text{ MPa}$ for 14 days. **Figure 3B** shows the XRD pattern of CAC paste cured at $50^{\circ}\text{C} \times 1.01 \text{ MPa}$ for 7 days, followed by curing at $315^{\circ}\text{C} \times 20.7 \text{ MPa}$ for 7 days. Combining previous research results (Guo et al., 2020), under low curing temperature, the main hydrated phases of Ms were

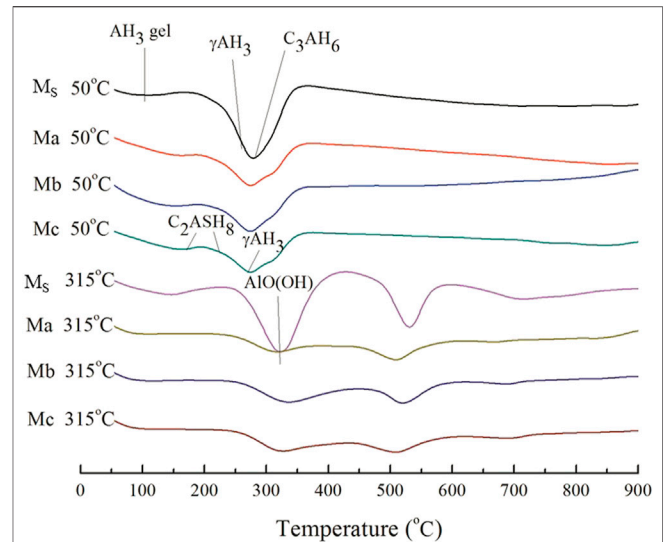


FIGURE 5 | DSC thermograms of CAC pastes.

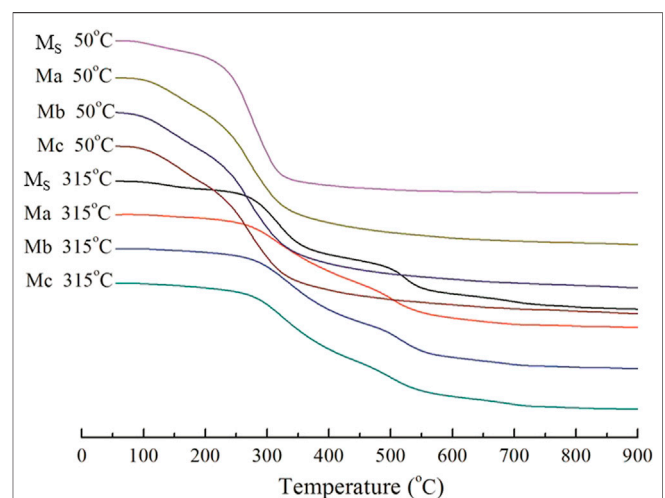


FIGURE 6 | TG of CAC pastes.

C_3AH_6 , C_2AS , $\text{Al}(\text{OH})_3$, C_3A , and C_{12}A_7 , and the main hydrated phases of Ma, Mb, and Mc were C_2ASH_8 , C_3ASH_4 , $\text{Al}(\text{OH})_3$, and C_2AS . Under high curing temperature, the main hydrated phases of Ms were C_3ASH_4 , $\text{AlO}(\text{OH})$ and C_3A . Meanwhile, the main hydrated phases of Ma, Mb, and Mc were C_3ASH_4 , $\text{AlO}(\text{OH})$, hydrated andradite $[\text{Ca}_3(\text{Fe}_{0.87}\text{Al}_{0.13})_2(\text{SiO}_4)_{1.65}(\text{OH})_{5.4}]$, and a small amount of C_2S . As shown in **Figure 3A**, the CAC paste mixed with FSa, FSb, or FSc converted C_3AH_6 into C_2ASH_8 . This conversion is the reason for the compressive strength of the CAC paste that was stably cured at low temperature. Mostafa et al. showed that the main function of Na_2SO_4 in CAC with blast furnace slag as an activator is to promote C_2ASH_8 generation. Comparing **Figures 3A,B**, the new products of Ms were C_3ASH_4 and $\text{AlO}(\text{OH})$ after curing at high temperature, and the new

phases of Ma, Mb, and Mc were C_3ASH_4 , $AlO(OH)$, and andradite (hydrated). C_3AH_6 or C_2ASH_8 converted into C_3ASH_4 , and $Al(OH)_3$ converted into $AlO(OH)$ at $315^\circ C \times 20.7$ MPa. The strength of Ma, Mb, and Mc was reduced after high-temperature curing, but the reduction rate of the compressive strength was within 15%, meeting the cementing requirements (Adolfsson et al., 2011; Li et al., 2014).

Scanning Electron Microscopy

The fracture surfaces of CAC paste were studied using SEM. The microstructures of hydrated Ms, Ma, Mb, and Mc cured at $50^\circ C \times 1.01$ MPa for 14 days, $50^\circ C \times 1.01$ MPa for 7 days, and $315^\circ C \times 20.7$ MPa for another 7 days are shown in **Figures 4A–H**. **Figure 4A** shows that Ms generated cubic C_3AH_6 , fine particles of C_3A , and an amorphous $Al(OH)_3$ gel when cured at low temperature (Ewais et al., 2009). This finding explains the increased quantity of holes and low compression strength of Ms. The micrographs of Ma, Mb, and Mc cured at $50^\circ C$ (**Figures 4B–D**) indicate the presence of the thin flaky plate-like morphology of stratlingite (C_2ASH_8) and small amounts of amorphous $Al(OH)_3$ gel. This observation reveals that the microstructures of CAC mixed with blast furnace slag were more closed and compact. The micrographs of Ms, Ma, Mb, and Mc curing at $315^\circ C$ are shown in **Figures 4E–H**. Neat CAC paste and CAC with blast furnace slag mainly generated C_3ASH_4 and dehydrated $Al(OH)_3$ $AlO(OH)$. With fewer fine particles, C_3A filled in the crystal gaps in the high-temperature environment where crystal structures are dense and well developed as well as have high crystallinity and good mechanical properties. Those are the root cause of the high-temperature resistance of CAC paste.

Thermal Analysis

The types of hydration products in CAC paste composites were investigated using differential scanning calorimetry (DSC) and thermogravimetric (TG). DSC and TG thermographs of hydrated CAC paste (Ms, Ma, Mb, and Mc) cured at low and high temperatures are shown in **Figures 5, 6**, respectively. The analysis of **Figures 5, 6** revealed that Ms cured at low temperatures; 70 – $100^\circ C$ and $278^\circ C$, displayed an endothermic peak because of $Al(OH)_3$. Given that $Al(OH)_3$ is a polycrystalline (Mac et al., 2014), a mass loss of approximately 5.4% occurred. At 270 – $350^\circ C$, the endothermic peak was due to C_3AH_6 , and the mass loss was approximately 19.8%. For Ma, Mb, and Mc at 163 and $210^\circ C$, the peak was mainly due to C_2ASH_8 (Sitnikov et al., 2009), leading to a mass loss of approximately 16.4, 16.4, and 16.1%, respectively. Heikal et al. found that CAC mixed with 25% air-cooled or water-cooled blast furnace slag can reduce C_3AH_6 formation by 54.6% when cured at $40^\circ C$ to ensure the strength of the generated CAC paste. When cured at high temperature and high pressure, the positions of the endothermic peak of Ms, Ma,

Mb, and Mc were 300 and $500^\circ C$, respectively. This result shows the location of the endothermic peak at higher temperatures. The endothermic peak of Ms was prominent and absorbed more heat, whereas the endothermic peaks of Ma, Mb, and Mc were relatively small. Compared with the TG curve for curing at low and high temperatures, the mass loss rates decreased with an increase in curing temperature. Thus, blast furnace slag added to CAC can lead to more stable hydration products at high temperature and can increase high-temperature resistance performance. XRD results showed that the endothermic peak at $325^\circ C$ may be attributed to $AlO(OH)$, which causes a loss of crystallized water (Ptáček et al., 2010).

CONCLUSION

- 1) The reaction of blast furnace slag and CAC can generate C_2ASH_8 , which can effectively improve its low temperature sensitivity;
- 2) The compressive strength and permeability resistance of Mc increased by 74.2 and 77.5%, respectively, compared with Ms.
- 3) The main reason for the high temperature resistance of CAC is C_3ASH_4 and $AlO(OH)$ produced by hydration under high temperature curing; The addition of blast furnace slag can make the high temperature performance of CAC more stable.

DATA AVAILABILITY STATEMENT

The original contributions presented in the study are included in the article/Supplementary material, further inquiries can be directed to the corresponding authors.

AUTHOR CONTRIBUTIONS

WZ is responsible for the overall idea of the article and writing the paper; LH, QX, WG, and XX are responsible for providing experimental materials and conducting specific experiments; CX and NX are responsible for data analysis and article verification.

ACKNOWLEDGMENTS

The authors appreciate the support of the CNOOC project “Feasibility Study on Low Permeability Development of Bozhong 25-1S Oilfield 5 Well Block and Sha 3 Member” (No. 2021FS-02). The authors would also like to thank the Advanced Cementing Materials Research Center of SWPU for their kind assistance with the experiments.

REFERENCES

- Abolhasani, A., Nazarpour, H., and Dehestani, M. (2021). Effects of Silicate Impurities on Fracture Behavior and Microstructure of Calcium Aluminate Cement concrete. *Eng. Fracture Mech.* 242, 107446. doi:10.1016/j.engfracmech.2020.107446
- Adolfsson, D., Robinson, R., Engström, F., and Björkman, B. (2011). Influence of Mineralogy on the Hydraulic Properties of Ladle Slag. *Cement Concrete Res.* 41, 865–871. doi:10.1016/j.cemconres.2011.04.003
- Amin, M. S., Habib, A. O., and Abo-El-Enein, S. A. (2012). Hydrothermal Characteristics of High-Slag Cement Pastes Made with and without Silica Sand. *Adv. Cement Res.* 24, 23–31. doi:10.1680/adcr.2012.24.1.23
- Antonović, V., Kerić, J., Boris, R., and Aleknevičius, M. (2013). The Effect of Temperature on the Formation of the Hydrated Calcium Aluminate Cement Structure. *Proced. Eng.* 57, 99–106. doi:10.1016/j.proeng.2013.04.015
- Chai, M., Yang, M., and Chen, Z. (2022). Analytical and Numerical Study of thermal and Solvent-Based Gravity Drainage for Heavy Oil Recovery. *J. Pet. Sci. Eng.* 208, 109214. doi:10.1016/j.petrol.2021.109214
- Cheng, X., Dong, Q., Ma, Y., Zhang, C., Gao, X., Yu, Y., et al. (2019). Mechanical and thermal Properties of Aluminate Cement Paste with Blast Furnace Slag at High Temperatures. *Construction Building Mater.* 228, 116747. doi:10.1016/j.conbuildmat.2019.116747
- Ding, B., Dong, M., Chen, Z., and Kantzas, A. (2021). Enhanced Oil Recovery by Emulsion Injection in Heterogeneous Heavy Oil Reservoirs: Experiments, Modeling and Reservoir Simulation. *J. Pet. Sci. Eng.* 2021, 109882. doi:10.1016/j.petrol.2021.109882
- Ewais, E. M. M., Khalil, N. M., Amin, M. S., Ahmed, Y. M. Z., and Barakat, M. A. (2009). Utilization of Aluminum Sludge and Aluminum Slag (Dross) for the Manufacture of Calcium Aluminate Cement. *Ceramics Int.* 35, 3381–3388. doi:10.1016/j.ceramint.2009.06.008
- Fentiman, C. H., and Science, C. (2020). “The Effect of Curing Conditions on the Hydration and Strength Development of Fondu Slag Calcium Aluminate Cements,” in Proceedings of the International Symposium Held at Queen Mary and Westfield. Editor R. J. Mangabhai (London; New York: E. & F.N. Spon).
- Goberis, S., and Antonovich, V. (2004). Influence of Sodium Silicate Amount on the Setting Time and EXO Temperature of a Complex Binder Consisting of High-Aluminate Cement, Liquid Glass and Metallurgical Slag. *Cement Concrete Res.* 34, 1939–1941. doi:10.1016/j.cemconres.2004.01.004
- Guo, C., Wang, E., Hou, X., Chen, J., Zhang, W., Ye, J., et al. (2020). Characterization and Mechanism of Early Hydration of Calcium Aluminate Cement with Anatase-TiO₂ Nanospheres Additive. *Construction Building Mater.* 261, 119922. doi:10.1016/j.conbuildmat.2020.119922
- Heikal, M., Morsy, M. S., and Radwan, M. M. (2005). Electrical Conductivity and Phase Composition of Calcium Aluminate Cement Containing Air-Cooled and Water-Cooled Slag at 20, 40 and 60 °C. *Cement Concrete Res.* 35, 1438–1446. doi:10.1016/j.cemconres.2004.09.027
- Huang, J., Li, W., Huang, D., Wang, L., Chen, E., Wu, C., et al. (2021). Fractal Analysis on Pore Structure and Hydration of Magnesium Oxysulfate Cements by First Principle, Thermodynamic and Microstructure-Based Methods. *Fractal Fract* 5, 164. doi:10.3390/fractalfract5040164
- Idrees, M., Ekinoglu, O., and Sonyal, M. S. (2021). Hydration Behavior of Calcium Aluminate Cement Mortars with mineral Admixtures at Different Curing Temperatures. *Construction Building Mater.* 285, 122839. doi:10.1016/j.conbuildmat.2021.122839
- Kar, A., Ray, I., Unnikrishnan, A., and Davalos, J. F. (2012). Estimation of C-S-H and Calcium Hydroxide for Cement Pastes Containing Slag and Silica Fume. *Construction Building Mater.* 30, 505–515. doi:10.1016/j.conbuildmat.2011.12.029
- Kırca, Ö., Özgür Yaman, İ., and Tokyay, M. (2013). Compressive Strength Development of Calcium Aluminate Cement-GGBFS Blends. *Cement and Concrete Composites* 35, 163–170. doi:10.1016/j.cemconcomp.2012.08.016
- Li, Z., Wang, Y., Cheng, X., and Guo, X. (2014). The Slag Influence on High Temperature Resistance of Aluminophosphate Cement for Heavy Oil Thermal Recovery. *High Temp. Mater. Process.* 33, 325–328. doi:10.1515/htmp-2013-0064
- Mac, F., Diego, O., Hollman, N., Energy, P. R., Javier, U., and Alberto, G. (2014). “Long-Term Calcium Phosphate Cement for In-Situ Combustion Project Synchronized Thermal Additional Recovery (STAR) Project,” in SPE Heavy Oil Conference (Alberta, Canada: SPE), 1–10.
- Mostafa, N. Y., Zaki, Z. I., and Abd Elkader, O. H. (2012). Chemical Activation of Calcium Aluminate Cement Composites Cured at Elevated Temperature. *Cement and Concrete Composites* 34, 1187–1193. doi:10.1016/j.cemconcomp.2012.08.002
- Nabih, A., and Chalaturnyk, R. (2014). Stochastic Life Cycle Approach to Assess Wellbore Integrity for CO₂ Geological Storage. *Soc. Pet. Eng. - SPE Heavy Oil Conf. Can.* 3, 2071–2090. doi:10.2118/170183-ms
- Pacewska, B., Nowacka, M., Aleknevičius, M., and Antonović, V. (2013). Early Hydration of Calcium Aluminate Cement Blended with Spent FCC Catalyst at Two Temperatures. *Proced. Eng.* 57, 844–850. doi:10.1016/j.proeng.2013.04.107
- Pang, Z., Lyu, X., Zhang, F., Wu, T., Gao, Z., Geng, Z., et al. (2018). The Macroscopic and Microscopic Analysis on the Performance of Steam Foams during thermal Recovery in Heavy Oil Reservoirs. *Fuel* 233, 166–176. doi:10.1016/j.fuel.2018.06.048
- Ptáček, P., Kubátová, D., Havlica, J., Brandšter, J., Šoukal, F., and Opravil, T. (2010). Isothermal Kinetic Analysis of the thermal Decomposition of Kaolinite: The Thermogravimetric Study. *Thermochim. Acta* 501, 24–29. doi:10.1016/j.tca.2009.12.018
- Roig-Flores, M., Lucio-Martin, T., Alonso, M. C., and Guerreiro, L. (2021). Evolution of Thermo-Mechanical Properties of concrete with Calcium Aluminate Cement and Special Aggregates for Energy Storage. *Cement Concrete Res.* 141, 106323. doi:10.1016/j.cemconres.2020.106323
- Sakai, E., Sugiyama, T., Saito, T., and Daimon, M. (2010). Mechanical Properties and Micro-structures of Calcium Aluminate Based Ultra High Strength Cement. *Cement Concrete Res.* 40, 966–970. doi:10.1016/j.cemconres.2010.01.001
- Salehpour, A. G., Pershikova, E., Chougnet-Sirapian, A., Taoutaou, S., and Adiningtyas, D. A. (2014). Novel Steam-Resilient Cement System for Long-Term Steam Injection Well Integrity: Case Study of a Steamflooded Field in Indonesia. *Soc. Pet. Eng. - SPE Heavy Oil Conf. Can.* 1, 525–533. doi:10.2118/170048-ms
- Sitnikov, P. A., Belykh, A. G., Fedoseev, M. S., Vaseneva, I. I., and Kuchin, A. V. (2009). Study of Chemical Processes in the Modification of Epoxide Polymers by Aluminum Oxide. *Russ. J. Gen. Chem.* 79, 2594–2598. doi:10.1134/S1070363209120068
- Tseng, W. J., and Nian, J. (2004). Effect of Ammonium Polyacrylate on Rheology of Anatase TiO₂ Nanoparticles Dispersed in Silicon Alkoxide Sols. *Ceramics Int.* 30, 2305–2311. doi:10.1016/j.ceramint.2004.01.011
- Ukrainczyk, N., and Matusinović, T. (2010). Thermal Properties of Hydrating Calcium Aluminate Cement Pastes. *Cement Concrete Res.* 40, 128–136. doi:10.1016/j.cemconres.2009.09.005
- Walker, W. A. (1962). Cementing Compositions for Thermal Recovery Wells. *J. Pet. Technol.* 14, 139–142. doi:10.2118/131-pa
- Wang, L., Li, G., Li, X., Guo, F., Tang, S., Lu, X., et al. (2021). Influence of Reactivity and Dosage of MgO Expansive Agent on Shrinkage and Crack Resistance of Face Slab concrete. *Cement and Concrete Composites* 2021, 104333. doi:10.1016/j.cemconcomp.2021.104333
- Wang, L., Luo, R., Zhang, W., Jin, M., and Tang, S. (2021). Effects of Fineness and Content of Phosphorus Slag on Cement Hydration, Permeability, Pore Structure and Fractal Dimension of concrete. *Fractals* 29, 2140004. doi:10.1142/S0218348X21400041

Conflict of Interest: WZ, WG, and XX were employed by the company CNOOC Research Institute Co., Ltd. LH was employed by the company PetroChina Southwest Oil and Gas Field Company. QX was employed by the company CNPC Chuanqing Drilling Engineering Company Limited.

The remaining author declares that the research was conducted in the absence of any commercial or financial relationships that could be construed as a potential conflict of interest.

Publisher's Note: All claims expressed in this article are solely those of the authors and do not necessarily represent those of their affiliated organizations, or those of the publisher, the editors and the reviewers. Any product that may be evaluated in this article, or claim that may be made by its manufacturer, is not guaranteed or endorsed by the publisher.

Copyright © 2022 Zhiqiang, Hengjie, Xiong, Guangai, Xuesong, Xiaowei and Xiucheng. This is an open-access article distributed under the terms of the Creative Commons Attribution License (CC BY). The use, distribution or reproduction in other forums is permitted, provided the original author(s) and the copyright owner(s) are credited and that the original publication in this journal is cited, in accordance with accepted academic practice. No use, distribution or reproduction is permitted which does not comply with these terms.



Mechanical Characteristics and Stress Evolution of Cemented Paste Backfill: Effect of Curing Time, Solid Content, and Binder Content

Chen Hou^{1*}, Liu Jun Yang¹, Lei Li¹ and Baoxu Yan²

¹Center for Rock Instability and Seismicity Research, School of Resource and Civil Engineering, Northeastern University, Shenyang, China, ²Energy School, Xi'an University of Science and Technology, Xi'an, China

OPEN ACCESS

Edited by:

Lijie Guo,
Beijing General Research Institute of
Mining and Metallurgy, China

Reviewed by:

Zhihong Zhang,
Beijing University of Technology,
China
Ferdi Cihangir,
Karadeniz Technical University, Turkey

*Correspondence:

Chen Hou
houchengood@yeah.net

Specialty section:

This article was submitted to
Structural Materials,
a section of the journal
Frontiers in Materials

Received: 10 November 2021

Accepted: 06 December 2021

Published: 07 January 2022

Citation:

Hou C, Yang L, Li L and Yan B (2022)
Mechanical Characteristics and Stress
Evolution of Cemented Paste Backfill:
Effect of Curing Time, Solid Content,
and Binder Content.
Front. Mater. 8:812402.
doi: 10.3389/fmats.2021.812402

The clarification of the variation on the strength of the cemented paste backfill (CPB) under the coupling of multi-factor is the foundation of the CPB design of the mine. In this article, the physical and mechanical properties of the CPB under the coupling effect of curing time, solid content, and binder content were experimentally and theoretically investigated. The results show that 1) the increase in binder content can effectively increase the later strength of CPB. 2) A sensitivity parameter considering the span of multi-factor was constructed, indicating that the curing time has the greatest impact on the uniaxial compressive strength (UCS), and the variation in solid content has the least impact on it, which can be verified by the stress-strain curves. 3) Curing time and binder content can effectively change the stress evolution, which is reflected in reducing the strain corresponding to the peak stress, enhancing the characteristics of the peak stress and increasing stress drop. The results of this study aim to explain the essence of the influence of each factor on the mechanical behavior of CPB in the view of stress-strain evolution, which will help to better understand the mechanical characteristics of CPB and quantify the sensitivity of the mechanical properties to various factors.

Keywords: cemented paste backfill, multi-factor, uniaxial compressive strength, sensitivity analysis, stress-strain behavior

INTRODUCTION

With the demands of social development and the rapid economic development, mining activities are becoming more and more active all over the world. As a byproduct in the mining process, tailings are accumulated as solid waste from mining when recovering valuable mineral resources. It is estimated that the global annual discharged tailings is between 5 and 7 billion tons (Edraki et al., 2014). However, China's annual discharged tailings exceed 1 billion tons, with the total emission amounting to 10 billion tons (Rong et al., 2017). These massively discharged tailings will inevitably pose a serious threat to the environmental protection and safe production of mines.

Therefore, the safe and effective disposal of tailings under severe background is a mining engineering problem that needs to be solved urgently. The mine backfill method, a safe, environmentally friendly, and efficient method, has been widely used in underground mines (Yilmaz, 2011; Gorakhki and Bareither, 2017). Generally, the cemented paste backfill (CPB) is an engineered mixture of tailings, water, and hydraulic binders (2–9% by weight). It contains typically between 65 and 85% solids (Ercikdi et al., 2014; Cao et al., 2021). In mine production, goaf

management, mine environmental protection, and mine economic benefits, it has multiple advantages such as supporting goafs, increasing ore recovery rate, controlling surface subsidence, reducing tailings accumulation, and reducing tailings recovery costs (Wu et al., 2015; Sun et al., 2018). Therefore, it is widely used in mining and management of mines all over the world (Ding et al., 2018; Jiang et al., 2018; Mu et al., 2019). However, the prerequisite for the successful application of filling mining method in mines is the reasonable setting of CPB strength (Deng et al., 2017; Cao et al., 2018).

The uniaxial compressive strength is considered to be one of the important parameters in the design of underground mine operations, so scholars have carried out research on it. Deng et al. (2021) carried out the uniaxial compressive strength test and porosity determination test, which showed that the total porosity decreased and the CPB strength increased with the curing time. Li et al. (2020) designed the uniaxial compression test that considers the solid content of 65, 67, and 69% and cement–tailing ratio of 1:4, 1:10, and 1:20, and the result showed that the UCS increases with the increase in solid content and cement–tailing ratio. Ghirian and Fall (2016) showed that the curing stress can significantly affect the strength of CPB, for which the UCS of CPB was increased with the curing stress within a certain range. Hou et al. (2020) investigated the influence of curing time on the damage characteristics and energy dissipation of CPB. The results show that the prolongation of curing time can effectively hinder the initiation and expansion of cracks in the specimen to improve the UCS of the CPB. The strain energy and energy storage limit required for the deformation and failure of the CPB increase with the longer curing time. Hou et al. (2018) used fiber Bragg gratings to monitor the temperature and internal strain evolution of the after 7-day cured cemented tailings backfill (CTB) specimens. The results show that the binder content has a significant effect on the temperature and internal strain. CTB with a high binder content takes less time to reach the skeleton formation stage. Ghirian and Fall (2014) studied the evolution of coupled thermal, hydraulic, mechanical, and chemical properties of underground CPB by the insulated-undrained high column test. The results have demonstrated that the UCS values significantly increase with time due to the cement hydration process and suction development. Chen et al. (2021) showed that the increase in curing stress and curing temperature will increase cement hydration products to enhance UCS. Kesimal et al. (2005) showed that the binder mixtures can effectively increase the strength of CPB produced from sulphide rich tailings. Wu et al. (2020) indicated that increasing the curing humidity helps the hydration cycle, thereby generating more products to enhance the strength of CPB. Li et al. (2020) showed that a 2% increase in solid content (65, 67 and 69 wt%) results in a 55–88% increase in yield stress. Xu et al. (2018) constructed the relationship between UCS and electrical resistivity of CPB. UCS and electrical resistivity increased with increasing cement-to-tailing ratio, solid content, and curing time.

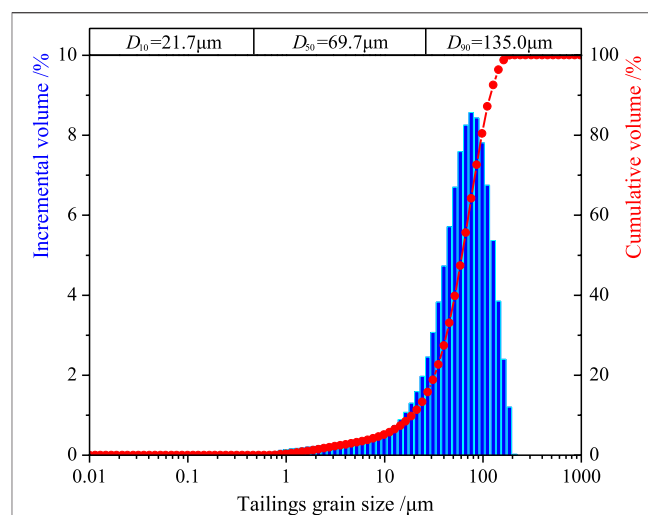


FIGURE 1 | Particle size distribution of tailings.

TABLE 1 | The main chemical composition of tailings.

Material	Composition						
Tailings	SiO ₂	Al ₂ O ₃	K ₂ O	TiO ₂	Fe ₂ O ₃	CaO	P ₂ O ₅
	93.214	4.984	1.271	0.245	0.227	0.022	0.016

TABLE 2 | Main chemical composition of PCI-I.

Material	Chemical composition						
PCI-I (%)	CaO	SiO ₂	Al ₂ O ₃	Fe ₂ O ₃	MgO	SO ₃	K ₂ O
	43.648	33.930	12.381	3.265	2.655	1.674	1.516

To sum up, the scholars used indoor tests to analyze the effects of single or two factors on the strength of the CPB. However, the mine condition in different regions has obvious differences and particularities. Therefore, it is extremely important to consider the coupling of multiple internal factors in the process of designing backfill that meet the needs of different mines according to the mine situation. However, the current research status is relatively lacking. For this reason, combining the shortcomings of the above research fields, the investigation of the strength variation of the CPB were carried out under multi-factor coupling in the time domain, which can provide a reference for the design of the strength of CPB under different conditions.

This article is to consider multi-factors and adopt multiple methods to explore the evolution mechanism of the CPB in the strength. XRD technology was used to analyze the formation mechanism of the CPB strength by consideration of curing time, solid content, and binder content, and the uniaxial compression test was carried out to measure the UCS of CPB. The influence of multi-factor on strength was quantitatively analyzed by introducing sensitivity parameter *S*. Meanwhile, the

TABLE 3 | The growth rate of UCS with curing time.

Soild content (%)	x_1-x_2	3 (%)	5 (%)	7 (%)	9 (%)
Binder content (%)					
68	1d-3d	10.34	27.76	34.64	39.32
	3d-7d	0.59	6.40	10.61	3.68
	7d-14d	1.38	1.23	1.86	2.98
	14d-28d	0.83	0.98	0.96	0.86
72	1d-3d	11.05	22.13	33.60	32.32
	3d-7d	3.13	3.64	2.97	7.10
	7d-14d	0.05	2.15	2.08	1.86
	14d-28d	1.24	0.58	1.56	1.60
76	1d-3d	12.13	13.80	35.03	18.79
	3d-7d	2.77	3.22	2.31	5.73
	7d-14d	0.88	0.49	1.21	2.76
	14d-28d	0.42	0.60	1.34	0.80

Note: $r = \frac{(UCS_i - UCS_0)}{UCS_0(x_1 - x_2)}$ r is growth rate of UCS, UCS_i is the strength after the change, UCS_0 is the strength of the reference condition, and x_1-x_2 is shown in **Table 3**.

stress-strain curves were used to analyze the difference of the stress evolution under the influence of multi-factor, and the essence of the influence of multi-factor on the mechanical properties of the CPB was clarified.

EXPERIMENTAL PROGRAM

Materials

Tailings

This article selects synthetic silica tailings (ST) as the test aggregate to achieve the test purposes: 1) The simplicity of the mineral composition and chemical elements of ST can avoid the differential process of cement hydration so that the test results are reasonably explained. 2) Because of the long duration of the test, it can avoid the difference in chemical stability and mechanical properties of the CPB caused by the different pouring time. The particle size distribution with finer particle sizes of the tailing was selected according to the engineering application (Xincheng Gold in Shandong province, China) as shown in **Figure 1**. The main chemical compositions of tailings determined by x-ray fluorescence spectroscopy were listed in **Table 1**.

Hydraulic Binder

Portland cement Type I was used as the binder. The main chemical composition is shown in **Table 2**.

Mixing Water

Deionized water was used as the mixing water to prepare the slurry to ensure that the components in the mixing water would not affect the test results.

Testing Procedures

Specimen Preparation

Considering the solid content (68, 72, and 76%), binder content (3, 5, 7, and 9%), and curing time (1, 3, 7, 14, and 28 days) as influencing factors, the specimen preparation was carried out as

TABLE 4 | Sensitivity parameter values of factors.

Factor	Variable value (m_i)	$\Delta R/R_0$	Sensitivity parameter (S)
Curing time	3d	37.58%	0.188
	7d	84.92%	0.142
	14d	151.35%	0.116
	28d	205.49%	0.076
Solid content	72%	12.24%	0.009
	76%	31.28%	0.012
Binder content	5%	53.41%	0.059
	7%	176.10%	0.098
	9%	320.14%	0.119

follows: the required tailings, cement, and deionized water were calculated and weighed. After mixing the tailings and cement evenly, pour into deionized water and stir for 7 min. The slurry was poured into a cylindrical standard mold with a diameter of 50 mm and a height of 100 mm for uniaxial compression tests. Specimens were removed from molds after 24 h and were placed in a standard curing chamber at 20°C. In addition, the specimens were sealed before being placed in the chamber to prevent the influence of moisture in the curing chamber on the hydration reaction, and then the specimens were taken out to carry out the test when it reaches the specified curing time.

Testing and Analysis Method

To obtain the physical and mechanical properties of specimens under different test conditions in the time domain, XRD component analysis test and uniaxial compression test were carried out.

XRD test was carried out by used Bruker D8 Advance x-ray powder diffractometer, which uses a copper target with a wavelength of 0.15418 nm. The composition analysis of the cement paste that had reached the designated curing time was carried out. The samples were crushed first, and the hydration reaction of the cement paste was terminated with ethanol, then dried, and sieved to prepare the samples for XRD component analysis. The continuous scanning time was 2°/min, and the scanning angle range was 5°–50°.

When the specified curing time was reached, the cylindrical specimen was taken out to be tested from the chamber. The uniaxial compression tests were carried out according to ASTM C39. Additionally, three specimens were tested at each condition. A mechanical loading system was used to conduct uniaxial tests to evaluate the mechanical properties of the CPB specimen, and the loading rate was 0.3 mm/min. The displacement and pressure were monitored by the laser displacement sensor and the pressure sensor during loading. The axial strain and stress of the specimen during the uniaxial compression process were calculated, and the stress-strains curves of different conditions were shown.

In order to explore the sensitivity of UCS to curing time, solid content, and binder content, the parameter N_i was introduced to normalize the range of factors. Then, the parameter S was introduced to calculate the sensitivity coefficient when factors change and to quantify the sensitivity of the UCS to each factor.

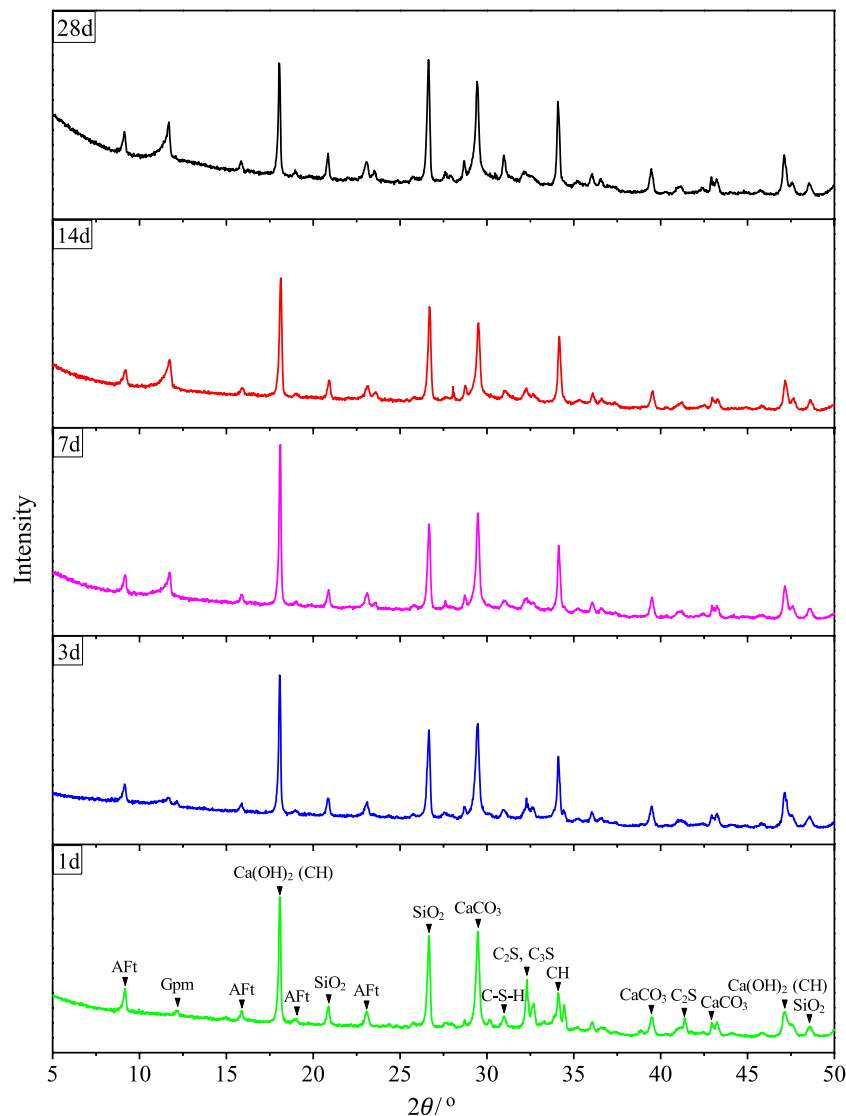


FIGURE 2 | XRD patterns of hydration products on CPB.

RESULTS AND DISCUSSION

Characteristics of Hydration Products on CPB

It can be seen from **Figure 2** that the hydration products change with the curing time. In the early curing time, gypsum and cement clinker are disintegrated, dispersed, and suspended in the liquid under the action of higher moisture content and dissolved to produce SO_4^{2-} , Ca^{2+} , OH^- , and $\text{Al}(\text{OH})^-$, which provide an ionic foundation for the production of AFt (Ettringite). In the early hydration, the hydration reaction of C_3A ($3\text{CaOAl}_2\text{O}_3$) is relatively active. Therefore, it is conducive to the production of AFt. With the continuous dissolution of the components in the cement, the increase in ion concentration, and the continuous progress of the hydration reaction, $\text{Ca}(\text{OH})_2$ reaches a larger value when the curing time is 3 days after the

unsaturated, saturated, and supersaturated stages. Then, its content declined as the curing time increased (Ma et al., 2019). The hydration reaction of C_3S generates C-S-H gel and CH after the first hydration reaction of C_3A . Therefore, the C_3S content decreases as the hydration reaction deepens, and the C-S-H gel content increases as the curing time increases (Cui and Fall 2016).

Variation of UCS Under the Multi-Factor Coupling

Variation of Curing Time on UCS

According to the curve between the curing time and UCS from **Figure 3**, it can be seen that UCS shows the same increasing trend with curing time, that is, it shows a parabolic shape, and the growth rate of UCS increases with curing time, as shown in **Table 3**. The

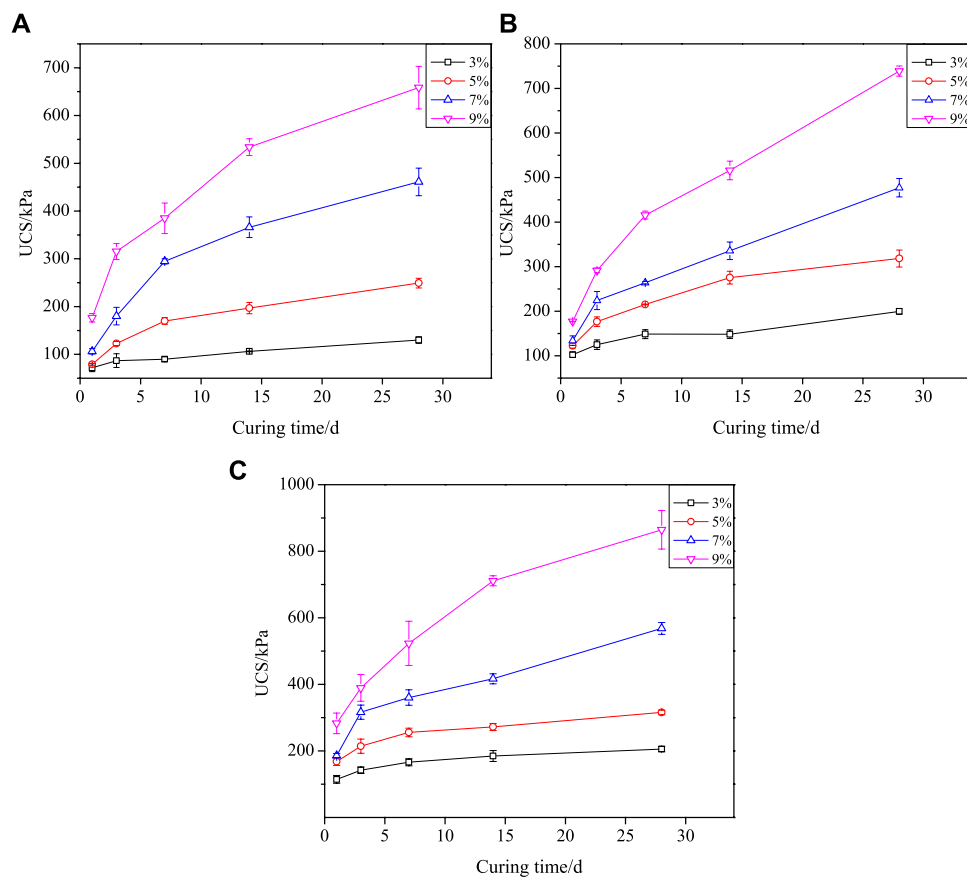


FIGURE 3 | The value of UCS corresponding to curing times under different solid content. **(A)** 68% solid content **(B)** 72% solid content **(C)** 76% solid content.

growth of UCS increases at the highest rate from 1 to 3 days, and the value can reach up to 39.32%, which corresponds to a 68% solid content and 9% binder content. After that, the growth rate of UCS decreases gradually when the curing time increases.

The essence of curing time reflects the degree and process of the hydration reaction. In the early hydration process of CPB, the space filling effect of AFt crystals is the main reason for the early strength of CPB (Xu et al., 2013). However, flocculent C-S-H gel, needle-shaped AFt crystals, and cement particles have not fully participated in the hydration reaction, and discrete tailings particles form a loose structure, which makes the early strength of CPB lower. With the increase in hydration degree, the AFt crystals are formed in large quantities and distributed in clusters, and contact points are formed with the increasing quantities of C-S-H gels (Zhang et al., 2018). The water-filled space is constantly being filled and the gap is reduced by hydration products, and the strength of CPB is continuously increasing; when the curing time at 28 days, the hydration process is gradually complete, a large amount of C-S-H gel is formed in CPB, and meanwhile, AFt crystals and $\text{Ca}(\text{OH})_2$ crystals are completely formed. The hydration products are evenly distributed, interconnected, and intertwined (Hu et al., 2018). Hydration products, hydration particles, and tailings are complexly combined in the space to form a dense and stable multilayer network structure, which makes the CPB have long-

term strength and sufficient resistance to external loads (Hu et al., 2018). The binder content increases as the solid content and binder content increase, and the cement particles that can participate in the hydration reaction increase. The hydration products generated by the hydration reaction develop into a denser and stable bearing structure, which strengthens the densification of the structure and has a stronger compressive strength.

Variation of Binder Content on UCS

The value of UCS increases with the increase in the binder content and the increase rate is significantly affected by the curing time from **Figure 4**. In the early period of the hydration reaction, the content of hydration products is low and a stable supporting framework structure has not yet formed. At the same time, sufficient water in the pores increases the lubrication between tailings particle, hydration products, and hydration raw materials. Therefore, when the curing time is 1 day, the increase in UCS caused by the increase in binder content is relatively small. With the increase in the curing time, higher initial binder content increases the amount of the hydration product, and the generated hydration products fill the water-filled space between the pores. The well-connected pore network gradually transforms into a dense supporting framework formed by the interlacing of hydration products, which made the CPB to

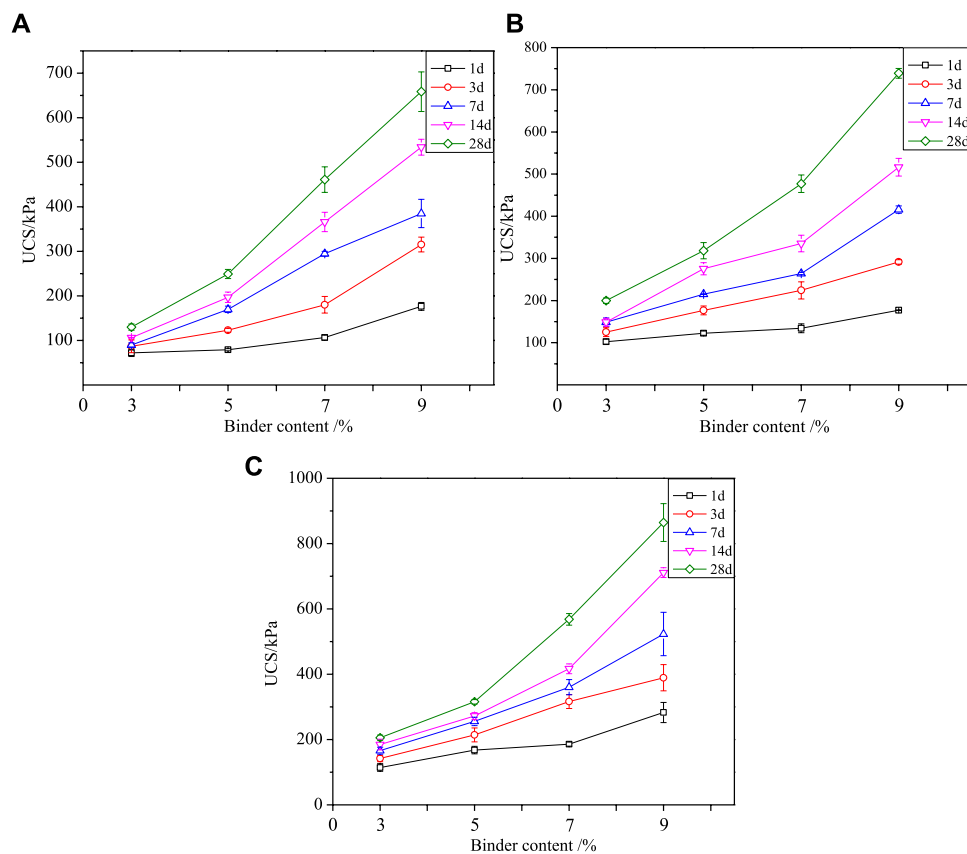


FIGURE 4 | The value of UCS corresponding to binder content under different solid content. **(A)** 68% solid content **(B)** 72% solid content **(C)** 76% solid content.

have higher strength with the increase in binder content. When the curing time is 28 days, it can be observed that UCS exhibits a relatively obvious increasing trend under the influence of binder content. That is, with the hydration reaction gradually becoming integrity, the influence of the binder content on UCS gradually appears, indicating that the increase in the binder content can effectively increase the advanced age of strength.

Variation of Solid Content on UCS

The UCS shows an increasing trend as the solid content from **Figure 5**. At the early curing time, the volume of air and free water in the pores of the CPB sample is relatively small as the solid content, which effectively reduces the connection and penetration of the pores, and forms an effective contact framework between tailings particles, hydration products, and unhydrated cement particles (Liu et al., 2020). The CPB with higher solid content has more particles (Liu et al., 2021). The load-bearing framework formed between the tailings particles and the unhydrated cement particles to form an effective lap between the solid particles. With the gradual advancement of the hydration process, the amount of hydration products produced in CPB with higher solids content increases and the degree of development is improved. The self-desiccation of CPB in the hydration process not only reduces the water-filled space in the pores but also provides development space for the generation and development of hydration products. The spatial distribution of

hydration products greatly improves the framework structure of CPB, which fills the pore space and creates bonds between the particles (Ercikdi et al., 2014). The complex, dense, and stable load-bearing system is formed that combines a gel network composed of hydration products and a solid particle structure dominated by tailings. In other words, the enhancement of cohesion of structure effectively improves the later mechanical strength.

Sensitivity Analysis of Multi-Factor on UCS

It can be seen from the above results that the curing time, binder content, and solid content can all affect the value of UCS. In order to describe the effect of the three on the UCS, the three-dimensional coordinate system is constructed with the binder content (X axis), solid content (Y axis), and curing time (Z axis) as the coordinate axis and color to distinguish the value of the UCS under different conditions, as shown in **Figure 6**.

According to the value of UCS under different conditions, 68%, 72%, and 76% solid content are indicated by circles, squares, and triangles, respectively. It can be known from the color distribution of the spheres that the smaller values of UCS are mainly concentrated in the lower left area, and the color change difference is small along the Y axis, which means that the smaller UCS is determined by the shorter curing time and the lower binder content, and the increase in the solid content contributes relatively little to the increase in the UCS. The

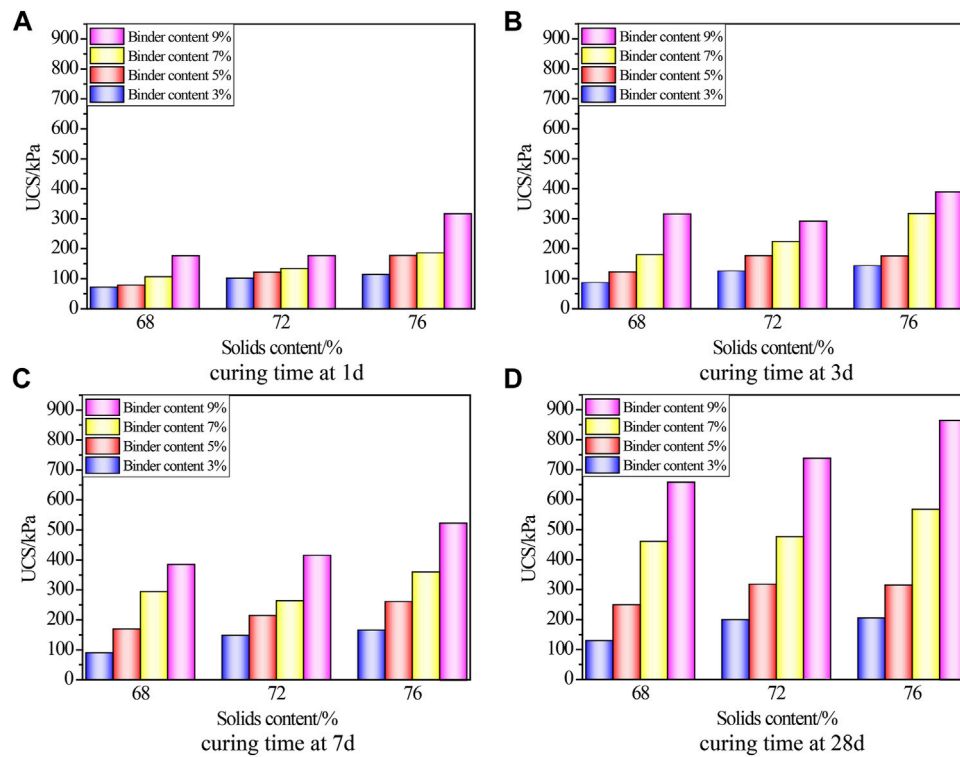


FIGURE 5 | The value of UCS corresponding to binder content under different cutting time.

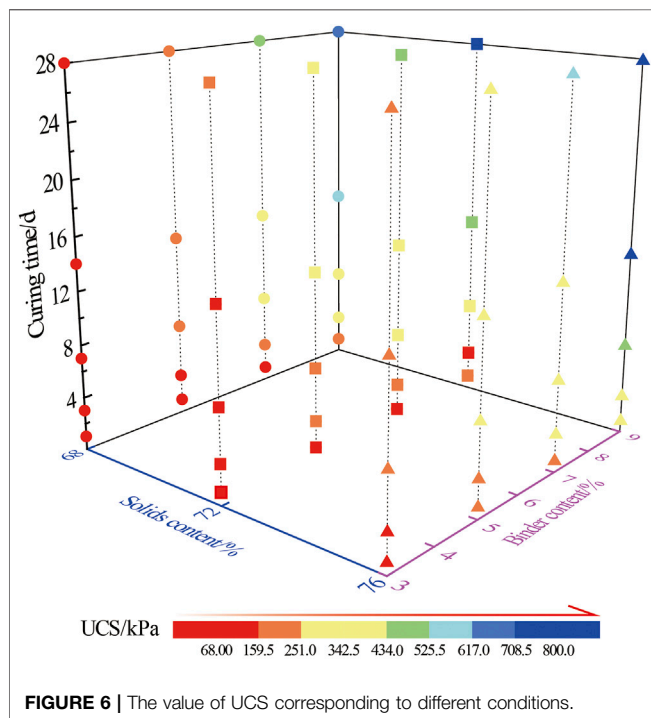


FIGURE 6 | The value of UCS corresponding to different conditions.

sphere color shows an obvious difference when the spheres are along the X-axis or Z-axis, and the color difference of the spheres are more obvious along the direction of the Y-axis and the Z-axis.

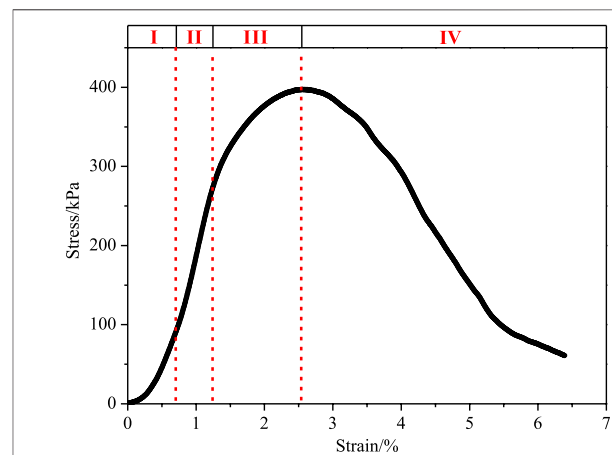


FIGURE 7 | The stress-strain curve of uniaxial compression.

The larger values of UCS are concentrated in the upper right area and reach the maximum UCS in this area.

In order to quantify and evaluate the variation in UCS which shows the sensitivity of UCS to the factors due to changes in curing time, binder content, and solid content, the sensitivity of UCS to the three is evaluated by defining the sensitivity coefficient S . Since the value ranges and spans of the curing time (1–28 days), binder content (3–9%), and solid content (68–72%) are not within the same scale, the normalized

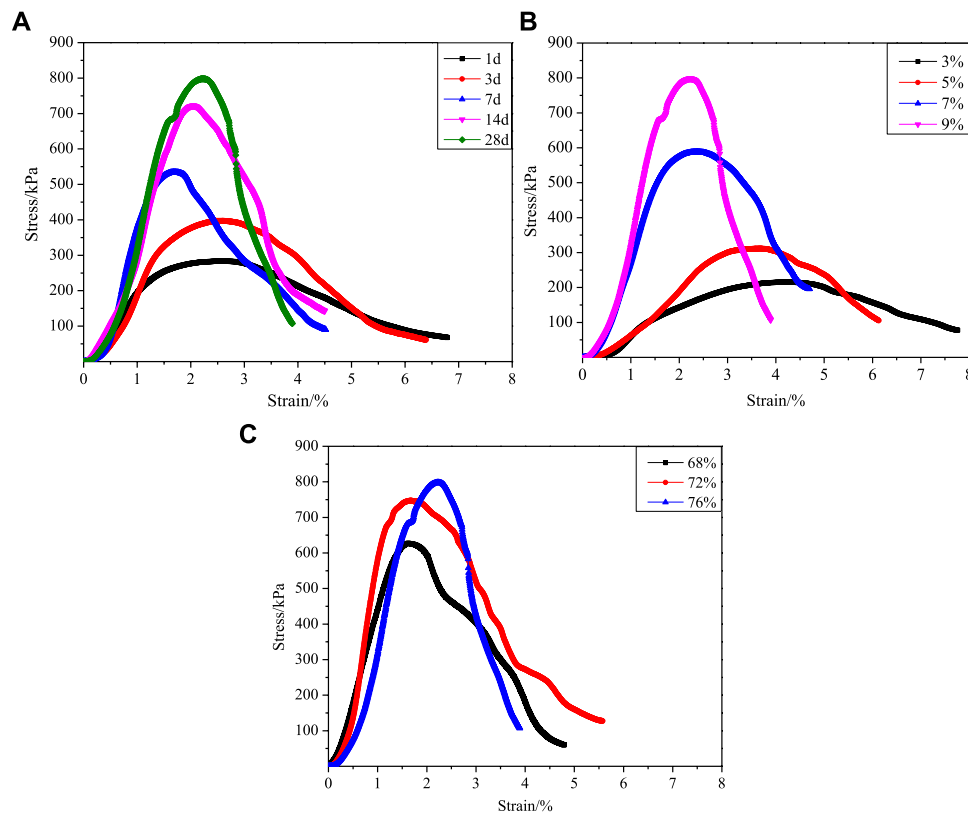


FIGURE 8 | The stress-strain curve of multi-factor. **(A)** Curves of different curing time. **(B)** Curves of different binder content. **(C)** Curves of different solid content.

parameter N_i was introduced to quantify the sensitivity of the three subsequently,

$$N_{ij} = \frac{\max \{\Delta m_{ij}\}}{\max \{\Delta m_{1j}, \Delta m_{2j}, \Delta m_{3j}\} \cdot (m_{ij} - m_{i1})}, \quad (1)$$

$$m_{ij} = \begin{bmatrix} m_{11} & m_{12} & m_{13} & m_{14} & m_{15} \\ m_{21} & m_{22} & m_{23} & m_{24} & \\ m_{31} & m_{32} & m_{33} & & \end{bmatrix}$$

$$= \begin{bmatrix} 1 & 3 & 7 & 14 & 28 \\ 3 & 5 & 7 & 9 & \\ 68 & 72 & 76 & & \end{bmatrix} \begin{matrix} i = 1, \\ i = 2, \\ i = 3, \end{matrix} \quad \begin{matrix} j = 1, 2, 3, 4, 5 \\ j = 1, 2, 3, 4 \\ j = 1, 2, 3 \end{matrix}, \quad (2)$$

where the subscript i is the influencing factors; the values 1, 2, and 3 indicate that the factors are curing time, binder content, and solid content, respectively; and j represents the conditions of each factor. The representative condition of m_{ij} is shown in Eq. 2. m_{i1} is the value of the reference condition; Δm_{ij} represents the difference between the changed value and the reference value,

$$S = \frac{R - R_0}{R_0} \cdot N_{ij}, \quad (3)$$

where S represents the sensitivity of factors, R is the value of UCS after the change, and R_0 is UCS of the reference conditions.

When the sensitivity of factors (curing time, solid content, and binder content) was analyzed, the UCS values were selected as solid content 76%, binder content 9%, curing time 1 day; the binder content

9%, curing time 28 days, solid content 68%; and solid content 76%, curing time 28 days, binder content 3% for reference conditions. Among them, the relative variation $\Delta R/R_0$ can better represent the change in UCS due to the variable value of different factors, and S is used to represent the influence of Δm to quantify the difference of UCS caused by the variation of different variable value.

As shown in Table 4, the relative variation $\Delta R/R_0$ shows different degrees of growth as the variable value increases under different factors. The sensitivity analysis based on the value of the sensitivity parameter shows that the value of S is small and it increases from 0.009 to 0.012 when the solid content increases to 72 and 76%, which indicates that the increase in the solid content causes a small variation in UCS, that is, UCS is weakly sensitive to solid content.

The maximum S appears when the curing time is 3 days, which UCS has the most significant variation in the curing time indicating the strongest sensitivity. The value of S is big, but it gradually decreases with the increase in curing time, indicating that the early strength is more sensitive to the curing time. S gradually increases with binder content, indicating that the sensitivity of UCS gradually increases as the cement binder increases.

Stress Evolution

The stress-strain curve can be divided into four stages according to the characteristics of the curve from Figure 7. Pore compaction stage (Stage I): the curve is of “superior fovea” shape; CPB is a

heterogeneous material, in which there are more uneven “sponge” structures with pores; under the action of a small load, the “spongy” structure with pores is easy to be compressed; and the pores are tightly closed under the action of the load, which makes the CPB produce greater deformation. Elastic deformation stage (Stage II): the curve is linear in this stage, and the pores in the CPB are further compacted as the stress continues to increase. Plastic deformation stage (Stage III): In this stage, the curve is of “inferior fovea” shape, the slope of the curve gradually slows down, and the stress reaches the peak. Meanwhile, new micro-cracks sprout in the CPB, and the continuous increase in stress leads to the expansion of old cracks and the development of new cracks. Damage and failure stage (Stage IV): the curve shows obvious “softening” characteristics. The internal structure of the specimen is constantly destroyed, and the existing cracks continue to expand, gradually intersect, and merge, causing the isolated cracks to gradually penetrate, forming a macroscopic failure zone, and leading to stress drop.

The stress–strain curve of the curing time is 1, 3, 7, 14, and 28 days, for which the corresponding solid content is 76% and the binder content is 9%, which are selected to analyze the effect of curing age on the stress–strain curve in **Figure 8**. The curing time is taken as a variable. From the stress–strain curves, it can be seen that the stress–strain curves have obvious differences under different curing times, which are mainly reflected in the following three aspects: 1) The strain corresponding to UCS decreases with curing time. The strain value decreased from 2.715 to 2.225% when the curing time increases from 1 to 7 days, indicating that the deformation ability of the CPB against external loads is enhanced. When the curing age is 1 and 3 days, the phenomenon of compression swelling can be observed during the test, and it is extremely significant when the curing age is 1 day. The phenomenon can also be derived from the trend of the stress–strain curve. It can be seen that the curve appears smooth when the curing time is 1 and 3 days, and the increase in stress is small with strain. 2) The peak stress characteristics of the stress–strain curve become more obvious. With the increase in the curing time, the stress value corresponding to the later curing period increases and also the growth rate increases accordingly under the same strain condition. In the curve at the early curing period, the strain in a certain range corresponding to the peak stress is basically the same as the peak stress. When the curing time increases to 7 days, this range is significantly reduced, and the peak stress can be clearly observed. It is mainly due to an increase in the degree of binder hydration and the precipitation of a larger amount of hydration products, as well as suction increase within the CTB specimen with curing time (Xu et al., 2019). 3) The post-peak characteristics show obvious differences with the change in curing time. The stress drop caused by the internal damage of the sample increases, which can be intuitively observed from the curve shape; the smooth shape in the early curing period turns into the steep peak shape in the later curing period. Therefore, the steeper change in the post-peak response of CPB with the curing time indicates the development of CPB brittleness (Libos and Cui, 2020).

It can be seen from **Figure 8B** that with the increase in the binder content, the stress–strain curve shows obvious differences. The strain corresponding to the peak stress decreases from 4.31 to 2.225% when the binder content increases from 3 to 5% and is similar to the effect of curing time on the stress evolution, that is, the change in the

binder content can enhance the peak stress characteristics and also increase the stress drop. The hydration products increase with binder content. The hydration product combines individual particles to form a skeleton structure, and the strength is derived from the cohesion and friction between the particles (Jiang et al., 2017).

From the sensitivity analysis in *Sensitivity Analysis of Multi-Factor on UCS*, it can be seen that the sensitivity of UCS to solid content is the weakest. This conclusion can be confirmed by the curves in **Figure 8C**. The curves of different solid content all show the obvious peak stress characteristics, and the difference caused by the variation of solid content is small.

CONCLUSION

In this article, a series of experiments and theoretical analysis were carried out to explore the law of the strength difference of the CPB under multi-factor coupling, quantify the sensitivity of the strength to multi-factor, and clarify the variation of stress evolution. The main conclusions are as follows:

- (1) Compared with the early strength, the increase in the binder content has a greater impact on the later strength of CPB. Under the same binder content, as the increased solid content enhances the particle density inside the CPB, the UCS also increases.
- (2) The sensitivity parameter was constructed considering the effect of multi-factor. The maximum values of the sensitivity parameters given by the curing time, solid content, and binder content are 0.202, 0.01, and 0.1, respectively, showing that the sensitivity of UCS to multi-factor is curing time > binder content > solid content.
- (3) The curing time and binder content can effectively change the stress–strain evolution referred to three aspects: reducing the strain corresponding to the peak stress, enhancing the peak stress characteristics, and increasing the stress drop.

DATA AVAILABILITY STATEMENT

The raw data supporting the conclusions of this article will be made available by the authors, without undue reservation.

AUTHOR CONTRIBUTIONS

CH completed the writing and revision of the manuscript; LY completed the experiment, data processing and graphics drawing; and LL and BY assisted in completing the experiment.

FUNDING

This work was funded by the National Natural Science Foundation of China (Grant No.51904055), the Fundamental Research Funds for the Central Universities of China (Grant No. N2001010) and the fellowship of China Postdoctoral Science Foundation (2021MD703874). These supports are gratefully acknowledged.

REFERENCES

- Cao, S., Song, W., and Yilmaz, E. (2018). Influence of Structural Factors on Uniaxial Compressive Strength of Cemented Tailings Backfill. *Construction Building Mater.* 174, 190–201. doi:10.1016/j.conbuildmat.2018.04.126
- Cao, S., Xue, G., Yilmaz, E., and Yin, Z. (2021). Assessment of Rheological and Sedimentation Characteristics of Fresh Cemented Tailings Backfill Slurry. *Int. J. Mining, Reclamation Environ.* 35 (5), 319–335. doi:10.1080/17480930.2020.1826092
- Chen, S., Wu, A., Wang, Y., and Wang, W. (2021). Coupled Effects of Curing Stress and Curing Temperature on Mechanical and Physical Properties of Cemented Paste Backfill. *Construction Building Mater.* 273, 121746. doi:10.1016/j.conbuildmat.2020.121746
- Cui, L., and Fall, M. (2016). Mechanical and thermal Properties of Cemented Tailings Materials at Early Ages: Influence of Initial Temperature, Curing Stress and Drainage Conditions. *Construction Building Mater.* 125, 553–563. doi:10.1016/j.conbuildmat.2016.08.080
- Deng, D. Q., Liu, L., Yao, Z. L., Song, K. I.-I. L., and Lao, D. Z. (2017). A Practice of Ultra-fine Tailings Disposal as Filling Material in a Gold Mine. *J. Environ. Manage.* 196, 100–109. doi:10.1016/j.jenvman.2017.02.056
- Deng, H., Liu, Y., Zhang, W., Yu, S., and Tian, G. (2021). Study on the Strength Evolution Characteristics of Cemented Tailings Backfill from the Perspective of Porosity. *Minerals* 11 (1), 82. doi:10.3390/min11010082
- Ding, K., Ma, F., Guo, J., Zhao, H., Lu, R., and Liu, F. (2018). Investigation of the Mechanism of Roof Caving in the Jinchuan Nickel Mine, China. *Rock Mech. Rock Eng.* 51 (4), 1215–1226. doi:10.1007/s00603-017-1374-0
- Edraki, M., Baumgartl, T., Manlapig, E., Bradshaw, D., Franks, D. M., and Moran, C. J. (2014). Designing Mine Tailings for Better Environmental, Social and Economic Outcomes: a Review of Alternative Approaches. *J. Clean. Prod.* 84, 411–420. doi:10.1016/j.jclepro.2014.04.079
- Ercikdi, B., Yilmaz, T., and Kulekci, G. (2014). Strength and Ultrasonic Properties of Cemented Paste Backfill. *Ultrasonics* 54 (1), 195–204. doi:10.1016/j.ultras.2013.04.013
- Ghirian, A., and Fall, M. (2014). Coupled Thermo-Hydro-Mechanical-Chemical Behaviour of Cemented Paste Backfill in Column Experiments. *Eng. Geology* 170, 11–23. doi:10.1016/j.enggeo.2013.12.004
- Ghirian, A., and Fall, M. (2016). Strength Evolution and Deformation Behaviour of Cemented Paste Backfill at Early Ages: Effect of Curing Stress, Filling Strategy and Drainage. *Int. J. Mining Sci. Tech.* 26 (5), 809–817. doi:10.1016/j.ijmst.2016.05.039
- Gorakhi, M., and Bareither, C. (2017). Sustainable Reuse of Mine Tailings and Waste Rock as Water-Balance Covers. *Minerals* 7 (7), 128. doi:10.3390/min7070128
- Hou, C., Zhu, W., Yan, B., Guan, K., and Du, J. (2018). Influence of Binder Content on Temperature and Internal Strain Evolution of Early Age Cemented Tailings Backfill. *Construction Building Mater.* 189, 585–593. doi:10.1016/j.conbuildmat.2018.09.032
- Hou, Y. Q., Yin, S. H., Cao, Y., and Dai, C. Q. (2020). Analysis of Damage Characteristics and Energy Dissipation of Cemented Tailings Backfill with Different Curing Ages under Uniaxial Compression. *J. Cent. South Univ. (Science Technology)* 51 (7), 1955–1965.
- Hu, C., Wang, X., Bai, R., Liu, G., Feng, X., and Ding, Q. (2018). Influence of Polyepoxysuccinic Acid on Solid Phase Products in Portland Cement Pastes. *J. Wuhan Univ. Technol.-Mat. Sci. Edit.* 33 (5), 1140–1149. doi:10.1007/s11595-018-1946-1
- Jiang, G., Wu, A., Wang, Y., and Lan, W. (2018). Low Cost and High Efficiency Utilization of Hemihydrate Phosphogypsum: Used as Binder to Prepare Filling Material. *Construction Building Mater.* 167, 263–270. doi:10.1016/j.conbuildmat.2018.02.022
- Jiang, H., Fall, M., and Cui, L. (2017). Freezing Behaviour of Cemented Paste Backfill Material in Column Experiments. *Construction Building Mater.* 147, 837–846. doi:10.1016/j.conbuildmat.2017.05.002
- Kesimal, A., Yilmaz, E., Ercikdi, B., Alp, I., and Devci, H. (2005). Effect of Properties of Tailings and Binder on the Short-And Long-Term Strength and Stability of Cemented Paste Backfill. *Mater. Lett.* 59 (28), 3703–3709. doi:10.1016/j.matlet.2005.06.042
- Li, J., Yilmaz, E., and Cao, S. (2020). Influence of Solid Content, Cement/Tailings Ratio, and Curing Time on Rheology and Strength of Cemented Tailings Backfill. *Minerals* 10 (10), 922. doi:10.3390/min10100922
- Libos, I. L. S., and Cui, L. (2020). Effects of Curing Time, Cement Content, and Saturation State on Mode-I Fracture Toughness of Cemented Paste Backfill. *Eng. Fracture Mech.* 235, 107174. doi:10.1016/j.engfracmech.2020.107174
- Liu, H.-L., Hou, C., Li, L., Du, J.-f., and Yan, B.-x. (2021). Experimental Investigation on Flow Properties of Cemented Paste Backfill through L-Pipe and Loop-Pipe Tests. *J. Cent. South. Univ.* 28 (9), 2830–2842. doi:10.1007/s11771-021-4810-y
- Liu, L., Xin, J., Qi, C., Jia, H., and Song, K.-I. (2020). Experimental Investigation of Mechanical, Hydration, Microstructure and Electrical Properties of Cemented Paste Backfill. *Construction Building Mater.* 263, 120137. doi:10.1016/j.conbuildmat.2020.120137
- Ma, S., Li, W., and Shen, X. (2019). Study on the Physical and Chemical Properties of Portland Cement with THEED. *Construction Building Mater.* 213, 617–626. doi:10.1016/j.conbuildmat.2019.03.109
- Mu, W., Li, L., Guo, Z., Du, Z., and Wang, S. (2019). Novel Segmented Roadside Plugging-Filling Mining Method and Overlying Rock Mechanical Mechanism Analyses. *Energies* 12 (11), 2073. doi:10.3390/en12112073
- Rong, H., Zhou, M., and Hou, H. (2017). Pore Structure Evolution and its Effect on Strength Development of Sulfate-Containing Cemented Paste Backfill. *Minerals* 7 (1), 8. doi:10.3390/min7010008
- Sun, W., Wang, H., and Hou, K. (2018). Control of Waste Rock-Tailings Paste Backfill for Active Mining Subsidence Areas. *J. Clean. Prod.* 171, 567–579. doi:10.1016/j.jclepro.2017.09.253
- Wu, A., Wang, Y., Wang, H., Yin, S., and Miao, X. (2015). Coupled Effects of Cement Type and Water Quality on the Properties of Cemented Paste Backfill. *Int. J. Mineral Process.* 143, 65–71. doi:10.1016/j.minpro.2015.09.004
- Wu, D., Zhao, R.-k., Xie, C.-w., and Liu, S. (2020). Effect of Curing Humidity on Performance of Cemented Paste Backfill. *Int. J. Miner Metall. Mater.* 27 (8), 1046–1053. doi:10.1007/s12613-020-1970-y
- Xu, L., Wang, P., and Zhang, G. (2013). Influence Mechanism of Calcium Sulfate Variety on Strength of Portland Cement-Calcium Aluminate Cement Blends. *J. Chin. Ceram. Soc.* 41 (11), 1499–1506.
- Xu, W., Cao, Y., and Liu, B. (2019). Strength Efficiency Evaluation of Cemented Tailings Backfill with Different Stratified Structures. *Eng. Structures* 180, 18–28. doi:10.1016/j.engstruct.2018.11.030
- Xu, W., Tian, X., and Cao, P. (2018). Assessment of Hydration Process and Mechanical Properties of Cemented Paste Backfill by Electrical Resistivity Measurement. *Nondestructive Test. Eval.* 33 (2), 198–212. doi:10.1080/10589759.2017.1353983
- Yilmaz, E. (2011). Advances in Reducing Large Volumes of Environmentally Harmful Mine Waste Rocks and Tailings. *Gospodarka Surowcami Mineralnymi* 27, 89–112.
- Zhang, Y., Yu, P., Pan, F., and He, Y. (2018). The Synergistic Effect of AFT Enhancement and Expansion in Portland Cement-Aluminate Cement-FGD gypsum Composite Cementitious System. *Construction Building Mater.* 190, 985–994. doi:10.1016/j.conbuildmat.2018.09.139

Conflict of Interest: The authors declare that the research was conducted in the absence of any commercial or financial relationships that could be construed as a potential conflict of interest.

Publisher's Note: All claims expressed in this article are solely those of the authors and do not necessarily represent those of their affiliated organizations, or those of the publisher, the editors and the reviewers. Any product that may be evaluated in this article, or claim that may be made by its manufacturer, is not guaranteed or endorsed by the publisher.

Copyright © 2022 Hou, Yang, Li and Yan. This is an open-access article distributed under the terms of the Creative Commons Attribution License (CC BY). The use, distribution or reproduction in other forums is permitted, provided the original author(s) and the copyright owner(s) are credited and that the original publication in this journal is cited, in accordance with accepted academic practice. No use, distribution or reproduction is permitted which does not comply with these terms.



Effect of Aluminum Incorporation on the Reaction Process and Reaction Products of Hydrated Magnesium Silicate

Yuan Jia^{1,2*}, Yuxin Zou², Xinmei Zou², Yaoting Jiang², Fangyuan Li², Wangkun Ma³, Hongli Yan⁴ and Rui Hua⁴

¹Hebei Provincial Laboratory of Inorganic Nonmetallic Materials and Hebei Provincial Industrial Solid Waste Comprehensive Utilization Technology Innovation Center, Tangshan, China, ²College of Materials Science and Engineering, North China University of Science and Technology, Tangshan, China, ³Technical Information Research Institute of Building Materials Industry, Beijing, China, ⁴China Railway 14th Bureau Group 2nd Engineering Co., Ltd., Taian, China

OPEN ACCESS

Edited by:

Lijie Guo,
Beijing General Research Institute of
Mining and Metallurgy, China

Reviewed by:

Zhihong Zhang,
Beijing University of Technology,
China
Daqiang Deng,
Xiangtan University, China

*Correspondence:

Yuan Jia
jia132012@ncst.edu.cn

Specialty section:

This article was submitted to
Structural Materials,
a section of the journal
Frontiers in Materials

Received: 07 November 2021

Accepted: 08 December 2021

Published: 12 January 2022

Citation:

Jia Y, Zou Y, Zou X, Jiang Y, Li F, Ma W,
Yan H and Hua R (2022) Effect of
Aluminum Incorporation on the
Reaction Process and Reaction
Products of Hydrated
Magnesium Silicate.
Front. Mater. 8:810535.
doi: 10.3389/fmats.2021.810535

In this study, we investigated the impact of aluminium ion (Al^{3+}) incorporation on the microstructure and the phase transformation of the magnesium silicate hydrate system. The magnesium silicate hydrate system with aluminium was prepared by mixing magnesium oxide and silica fume with different aluminium ion contents (the Al/Si molar ratios of 0.01, 0.02, 0.05, 0.1, 0.2) at room temperature. The high degree of polymerization of the magnesium silicate hydrate phases resulted in the limited incorporation of aluminium in the structure of magnesium silicate hydrate. The silicon-oxygen tetrahedra sites of magnesium silicate hydrate layers, however, were unable to substitute for silicon sites through inverted silicon-oxygen linkages. The increase in aluminium ion content raised the degree of polymerization of the magnesium silicate hydrate phases from 0.84 to 0.92. A solid solution was formed from residual aluminum-amorphous phases such as hydroxyl-aluminum and magnesium silicate hydrate phases. X-ray diffraction (XRD), field emission scanning electron microscope (F-SEM), and ^{29}Si and ^{27}Al MAS NMR data showed that the addition of Al^{3+} promotes the hydration process of MgO and has an obvious effect on the appearance of M-S-H gel. The gel with low aluminum content is fluffy, while the gel with high aluminum content has irregular flakes. The amount of Al^{3+} that enters the M-S-H gel increased with the increase of Al^{3+} content, but there was a threshold: the highest Al/Si molar ratio of M-S-H gel can be maintained at about 0.006.

Keywords: magnesium silicate hydrate system, hydroxyl-aluminum, phase transformation, microstructure, aluminium ion content

INTRODUCTION

As we all know, the hydration product of $\text{CaO-SiO}_2\text{-H}_2\text{O}$ system is calcium silicate hydrate (C-S-H) gel, like C-S-H, at normal temperatures and pressures, and the main hydration product of $\text{MgO-SiO}_2\text{-H}_2\text{O}$ system is magnesium silicate hydrate (M-S-H) gel (Li et al., 2014; Jia et al., 2017a). The molecular structures of magnesium silicate hydrate (M-S-H) and calcium silicate hydrate (C-S-H) phases are significantly different. The former is an amorphous precursor of talc or sepiolite with layered silica structure (Lothenbach et al., 2015; Bernard et al., 2019), while the latter is a silica-deficient solid solution and is a precursor of two crystalline phases, tobermorite and jennite

TABLE 1 | Chemical composition of the raw materials.

%	SiO ₂	MgO	Al ₂ O ₃	CaO	Fe ₂ O ₃	K ₂ O	Na ₂ O	P ₂ O ₅	SO ₃	Others
SF	94.9	1.1	0.3	0.8	0.2	1.6	0.3	0.4	0.4	0.08
MgO	—	98.5	—	0.02	< 0.01	< 0.01	0.05	< 0.01	0.02	1.85

(Maruyama et al., 2014; Li et al., 2020a). Various studies show that the system has many excellent properties, such as excellent adsorptive properties, especially for heavy metal ions like Cu, Ni (Jia et al., 2016). The M-S-H has a similar structure with sepiolite: it has a large specific surface area and there are unique nano-scale pores in molecular structure, and it has the ability to adsorb heavy metals (Ji et al., 2014; Jia et al., 2017b; Jia et al., 2019; Liu et al., 2021). Magnesium silicate hydrate (M-S-H) phases can be considered as a potential cementitious material for nuclear waste immobilization (Walling et al., 2015) owing to its moderate pH value (varying from ~9.5 to ~10.5) and the Radionuclide (Cs, Sr) sorption potential (Li et al., 2014; Zhang et al., 2020).

The interface region between cement-based material and clay can be observed in the generation of M-S-H, the main components of clay are SiO₂ and Al₂O₃ (Bonen and Cohen, 1992; Santhanam et al., 2020). This study aims to understand the influence of Al³⁺ content on the phase transformation and the structural change of M-S-H. However, the impact of Al³⁺ on the reaction processes during the hydration of M-S-H is poorly investigated. On the contrary, in the presence of Al³⁺, the molecular structure of C-S-H will change (Song et al., 2021). According to Richardson et al. (Richardson, 1999) the incorporation of aluminium ions (Al³⁺) could change the molecular structure of the C-S-H phase. For example, tetrahedrally coordinated Al³⁺ [Al (Bernard et al., 2019), Al for tetra-coordination] can substitute for silicon sites in the structure of tobermorite, occupying the bridging tetrahedra sites of C-S-H chains (Bernard et al., 2020; Li et al., 2020b). Magnesium silicate hydrate is formed by reacting MgO with silica fume (SF) and MgO dissolved in water, with one part disassociating with Mg²⁺ and the other part hydrated with water to form Mg(OH)₂, and at the same time the SiO₂ dissociates in water to form H₂SiO₄²⁻, and finally the Mg(OH)₂, SiO₂, and H₂SiO₄²⁻ react to form M-S-H (Li et al., 2014; Tang and Chen, 2020). The MgO dissolves slowly in water and forms a poorly soluble weak electrolyte, and the Mg(OH)₂ is incomplete, which leads to a decrease in the hydration rate of M-S-H (Bernard et al., 2017). The hydration rate of M-S-H can be increased by adding Al³⁺ and thereby can increase the early strength of M-S-H (Li et al., 2019). The M-S-H hydration product was prepared by mixing the reactive MgO, silica fume (SF) and Al(NO₃)₃, and the synthesized solids were characterized after 300 days. Advanced testing methods were used to characterize the M-S-H phases prepared under different Al³⁺ contents.

MATERIALS AND METHODS

Materials

Light burned technical grade MgO (Martin Marietta Magnesia Specialties, United States) and SF (Elkem, China) were used to

TABLE 2 | Mix proportion.

Sample ID	Mg:Si(molar ratio)	SiO ₂ (g)	Al:Si(molar ratio)	w/c
AMSH-1	1:1	6.0	0.01:1	10
AMSH-2	1:1	6.0	0.02:1	10
AMSH-3	1:1	6.0	0.05:1	10
AMSH-4	1:1	6.0	0.10:1	10
AMSH-5	1:1	6.0	0.20:1	10

synthesize M-S-H phase. Aluminium nitrate (Al(NO₃)₃, (Chempur, China) was used as the aluminium salt. The chemical composition data of the raw materials as reported by the manufacturers are presented in **Table 1**. The median particle sizes of the MgO and silica fume were 3.5 and 0.5 μm respectively.

Experiment Method and Analytical Techniques

The aluminium magnesium silicate hydrate (AMSH) specimens were prepared by mixing the aqueous solutions of MgO, SF, and Al(NO₃)₃ at Mg/Si molar ratio of 1:1 and Al/Si molar ratios of 0.01, 0.02, 0.05, 0.1, and 0.2 were presented in **Table 2**. Complete hydration was obtained by adopting a water/solids (W/S) ratio of 10, where S was the total mass of MgO and SF.

In order to speed up the reaction process and make sure the samples were homogenized, the prepared samples were placed in a horizontal oscillator to oscillate for 7 days, and then the solutions were stored at room temperature (25 ± 1°C) in 250 ml sealed polyethylene bottles for up to 300 days. After 300 days the granular residue was separated by filtration and the collected solids were soaked in absolute ethyl alcohol for 24 h to inhibit further hydration, and then dried at 40°C for 48 h. The specimens were characterized using multiple techniques, such as X-ray diffraction analysis (XRD D/Max 2400 V diffractometer with Cu Kα radiation at a scan rate of 0.5 2θ min⁻¹), thermogravimetric and derivative thermo-gravimetric analysis (TGA/DTG, alumina crucibles were used and sample were heated in a nitrogen atmosphere between 50°C and 1,000°C at 10°C/min), and field emission scanning electron microscopy (F-SEM: NOVA Nano-SEM 450) on gold coated samples that had been sputter coated for 2 min using 15 mA and 30 Pa pressure and ²⁹Si/²⁷Al nuclear magnetic resonance spectroscopy (NMR).

RESULTS AND DISCUSSION

Figure 1 shows the phases transformation in the MgO-SiO₂-H₂O system with different Al³⁺ content curing for 1 day and 300 days.

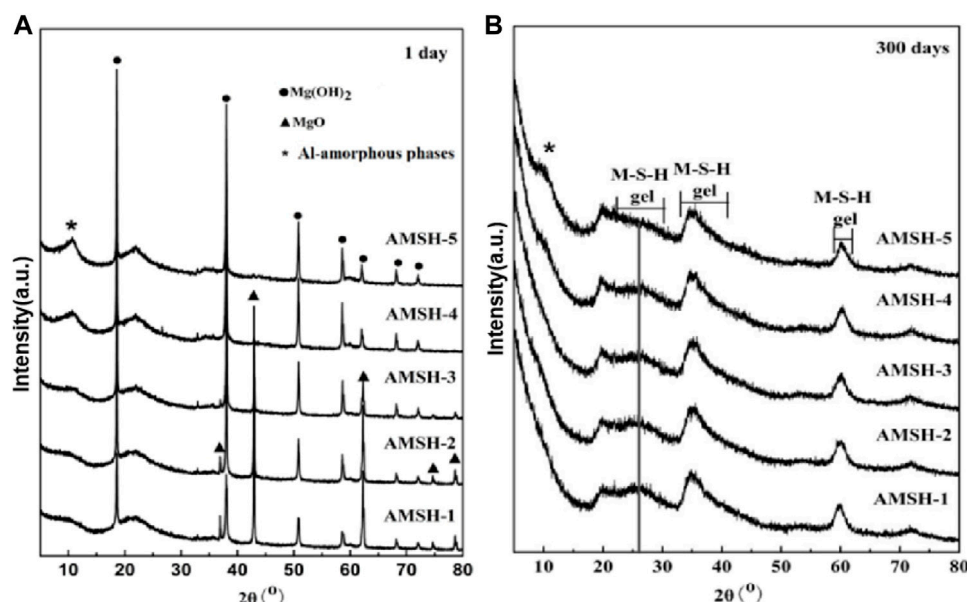


FIGURE 1 | The XRD patterns of magnesium silicate hydrate (M-S-H) samples with different Al³⁺ contents after curing for **(A)** 1 day and **(B)** 300 days.

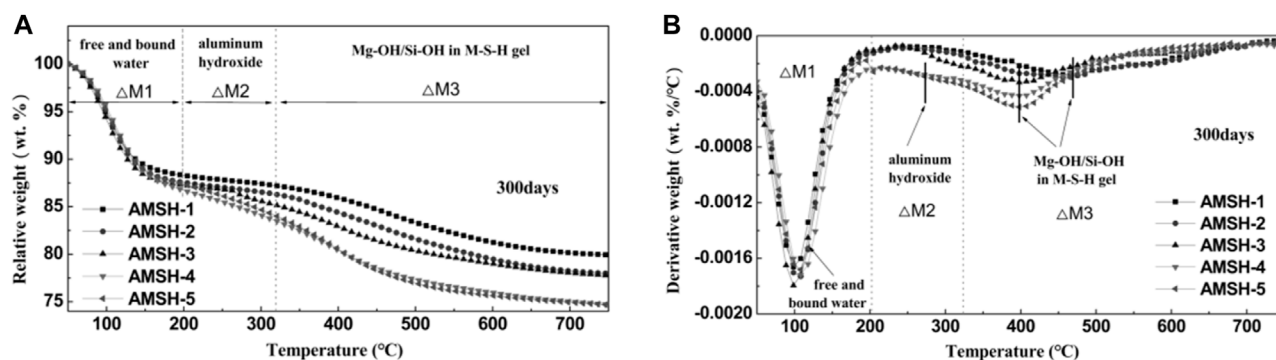


FIGURE 2 | (A) Thermo-gravimetric (TG) and **(B)** Derivative thermo-gravimetric (DTG) data for MSH samples with different Al³⁺ contents after curing for 300 days.

Curing for 1 day it is obvious that with the increase of the dosage of Al (NO₃)₃, the content of residual MgO in the system decreases greatly, while the content of Mg (OH)₂ increases gradually, which indicates that the addition of Al³⁺ promotes the hydration of MgO and the formation of Mg (OH)₂ (Figure 1A). At the same time, a dispersion peak appears around 2θ about ~10.6° and it is gradually obvious with the increase of Al³⁺ content, it indicates that there was the formation of a new phase and amorphous type of micro-crystalline hydroxy aluminium. By the later stage of hydration (300 days), the crystalline phases were completely transformed to the amorphous phases due to the reaction of MgO and Mg (OH)₂ with silica fume (SF) (Figure 1B). The cementitious system is all amorphous phase; and the characteristic peak of M-S-H gel at the broad diffraction at 22–30° becomes weaker with the increase of the dosage of Al³⁺, which may be the result of the change of molecular

structure. The broad diffraction at 20–28°, 33–40° and 58–62° ranges are attributable to the M-S-H phases (Zhang et al., 2014; Jia et al., 2016) (Figure 1B) while the diffraction peak between 8° and 12° represents the Al-amorphous phases (Figures 1A,B).

Three weight loss stages occurred during the curing of M-S-H for 300 days (Figure 2). The first weight loss occurred in the temperature range from 50 to 200°C and is attributed to the removal of free/bound water. The second and third weight losses in the 200–320°C and 320–700°C ranges are attributed to the removal of constitutional water in aluminum hydroxide (Al-amorphous phases) and M-S-H phase respectively (Jia et al., 2016; Nied et al., 2016) (Figure 2A). As the dosage of Al³⁺ increases, the weight loss of the phase in the cementitious system increases gradually in the weight loss range of 200°C–400°C, and the weight loss phase in this range may be amorphous or microcrystalline hydroxyl aluminum. According to the weight

TABLE 3 | Mass percents of various components in AMSH samples after curing for 300 days.

	(wt.%)	Free and bound water	Mg (OH) ₂ (Mg-OH)	gel (Al-OH/Si-OH/Mg-OH)
		$\Delta M1$	$\Delta M2$	$\Delta M3$
300 days	AMSH-1	12.85	—	7.49
	AMSH-2	13.08	—	7.22
	AMSH-3	13.90	—	8.32
	AMSH-4	12.37	—	10.22
	AMSH-5	11.81	—	13.95

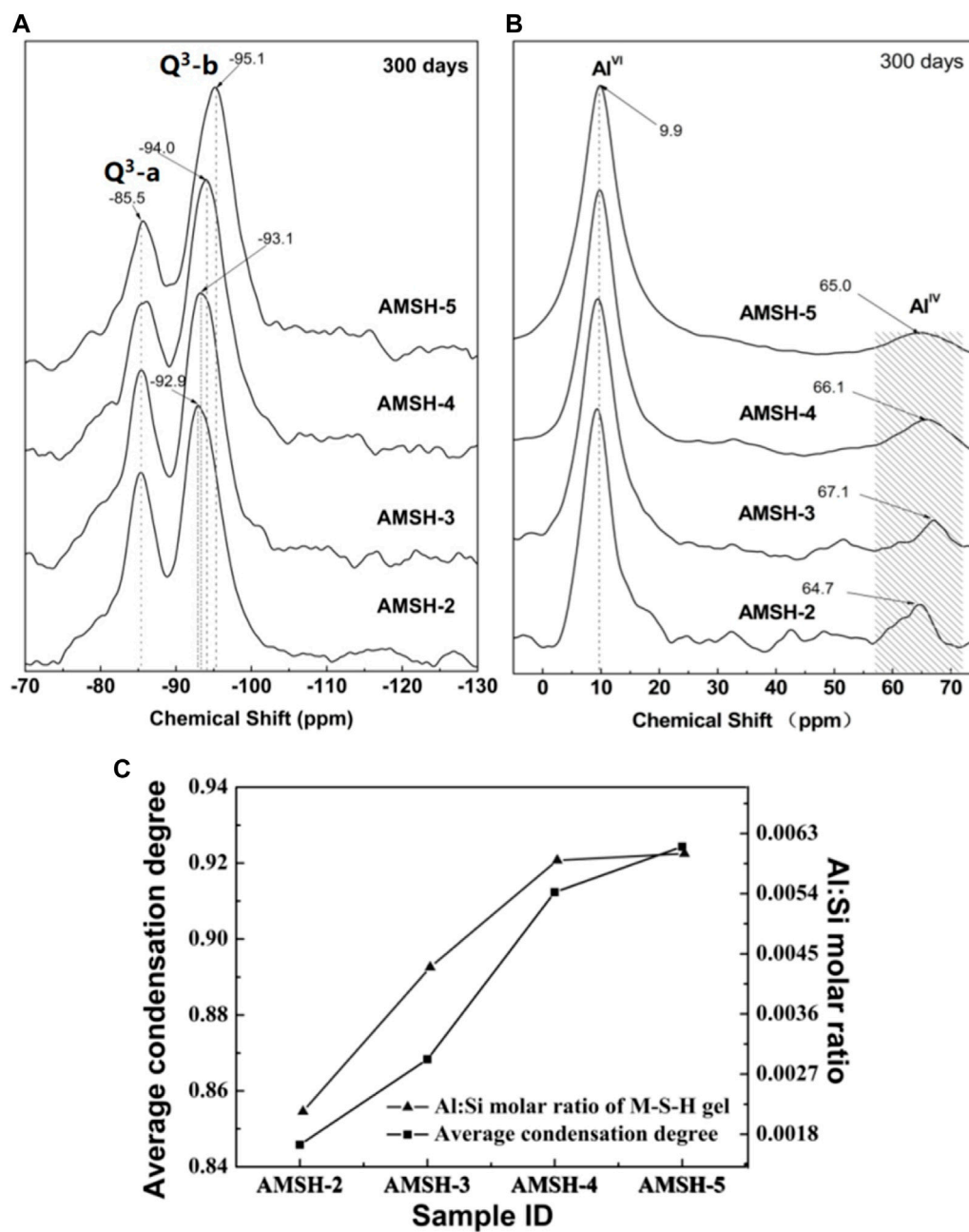
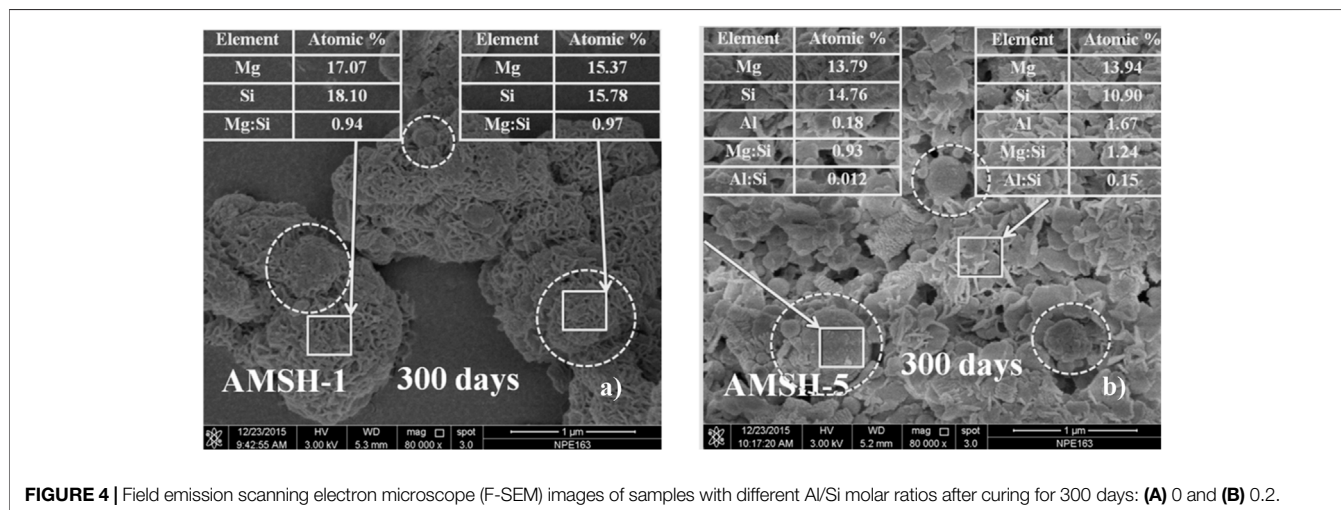
**FIGURE 3** | ²⁹Si NMR chemical shifts of MSH samples with different Al³⁺ contents after curing for 300 days (A) silica (B) aluminum (C) changes of the average condensation degree.

TABLE 4 | ²⁹Si NMR chemical shifts (ppm) and relative intensities (%) from de-convolution of the ²⁹Si/²⁷Al NMR spectra for the AMSH-2 ~ 5 samples after curing for 300 days.

Sample ID	Q ¹		Q ²		Q ³		Al ^{VI}		Al ^{IV}	
	Center (ppm)	Area (%)	Center (ppm)	Area (%)	Center (ppm)	Area (%)	Center (ppm)	Area (%)	Center (ppm)	Area (%)
AMSH-2	-79.6 (p)	10.8	-85.3 (p)	24.7	-92.9 (p/Q ³ -a)	64.6	9.3 (p)	89.3	64.4 (p)	10.7
AMSH-3	-79.2 (p)	5.8	-85.3 (p)	27.9	-93.1 (p/Q ³ -a)	66.3	9.7 (p)	91.4	67.0 (p)	8.6
AMSH-4	-80.2 (p)	4.6	-85.5 (p)	17.1	-94.0 (p/Q ³ -a)	78.3	9.9 (p)	94.1	66.0 (p)	5.9
AMSH-5	-78.3 (p)	2.3	-85.5 (p)	18.1	-95.1 (p/Q ³ -a)	79.6	9.9 (p)	97.0	65.0 (p)	3.0

Key: p—peak, sh—shoulder, Q¹—Q¹(3OH), Q²—Q²(2OH), Q³-a—Q³(OH) as continuous layer silicates, Q³-b—Q³(OH) as inverted silicates, Q³-SF—Q³(OH) in SF.

**FIGURE 4** | Field emission scanning electron microscope (F-SEM) images of samples with different Al/Si molar ratios after curing for 300 days: (A) 0 and (B) 0.2.

loss data, the contents of free water and bound water in different samples are basically consistent, indicating that the addition of Al³⁺ did not affect the generation of M-S-H gel when the curing age is long enough and the initial ratio of Al/Si is less than 0.20. As the mass of free and bonding water depends on the porous channel in the MgO-SiO₂-H₂O system but not on the aluminium incorporated, the original structure of the M-S-H phase was unaffected by the incorporated aluminium (Figure 2B). The mass percents of various components in AMSH samples after curing for 300 days were shown in Table 3.

The molecular structure of the solid solution which included aluminum-amorphous phases (hydroxyl-aluminum) and M-S-H phases was characterized using the NMR. The coordination of the spectrum of ²⁹Si NMR is usually expressed by Qⁿ, where n represents the bridge oxygen number between each silicon-oxygen tetrahedral unit and other Si atoms. The chemical migration of ²⁹Si in silicate minerals ranges from -60 to -120 ppm and according to different coordination, it can be divided into the following four intervals: -60 to -70 ppm represents a single free island silicate (Q⁰); -70 to -83 ppm represents the endpoint of *p*-silicate or chain silicate (Q¹); -83 to -90 ppm represents the silicon-oxygen tetrahedron in the chain silicate (Q²); -90 to -100 ppm represents the silicon-oxygen tetrahedron in the chain silicate (Q³); -100 to -120 ppm represents the silicon-oxygen tetrahedron in the three-dimensional reticular silicate (Q⁴) (Wei et al., 2006; Wei et al.,

2011). The transformation of the microstructure of the M-S-H phase is indicated by the peaks at -85.5 ppm (Q³-a) and -92.9 to -95.1 ppm (Q³-b) (Figure 3A). In Figure 3A, Q³-a indicates the Si unit via inverted Si-O-Si linkages, while Q³-b reflects the Si unit in the Si-O tetrahedral layer (Tonelli et al., 2016). Figure 3B shows that the coordination of a few Al³⁺ that entered the structure of the M-S-H phase and changed to the tetrahedral coordination [Al (Bernard et al., 2019)]. The chemical shift from -92.9 to -95.1 ppm suggests that Al³⁺ only occupied the Q³-b tetrahedra sites of the M-S-H layers and did not substitute for the Si⁴⁺ via inverted Si-O-Si linkages (Q³-a). Although the initial structure of the M-S-H phases was remained unchanged the average condensation degree was increased from 0.84 to 0.92 after the incorporation of Al³⁺ (Figure 3C).

Using the deconvolution technique to fit the data of the NMR Test curve, we can figure out the percentage of Si and Al with different coordinations, and the specific data are shown in Table 4. After curing for 300 days, the polymerization average degree of M-S-H and Al/Si molar ratio (M(Al: Si)) in M-S-H can be computed by formula 1 and formula 2.

$$CD = (3I(Q^3 - b) + 3I(Q^3 - a) + 2I(Q^2) + I(Q^1)) \times 3 / (I(Q^3 - b) + I(Q^3 - a) + I(Q^2) + I(Q^1)) \quad (1)$$

$$M(Al: Si) = n \times I(Al^{IV}) \quad (2)$$

Where n is the initial Al/Si molar ratio in M-S-H, I(Al^{IV}) is the percentage of moles of tetrahedral-Al.

According to **Figure 3C**, with the increase of Al³⁺ incorporation, the polymerization average degree of M-S-H increase from 0.85 to 0.93, but obviously the adding amount of Al³⁺ is still low. When the initial Al/Si molar ratio exceeds 0.1, both the adding amount of Al³⁺ and the polymerization average degree of M-S-H remain at a constant value. The adding of Al³⁺ plays a filling role, as it connects the silicon oxygen tetrahedron chains together and increases the degree of polymerization of the stratified structure. The molecular structure of M-S-H was already highly aggregated, which limits the adding amount of Al³⁺. It also shows that the number of Si sites in the silicon oxygen tetrahedral chain replaced by Al³⁺ is not large, and that the main function is to connect.

The F-SEM data show that the M-S-H phase has honeycomb morphology and grown on the surface of the SF particles extending to the gaps (**Figure 4A**). The Mg/Si molar ratio of pure M-S-H phases was 0.95. After the incorporation of Al³⁺, the Mg/Si molar ratio remained unchanged in the M-S-H phases grown on the surface of SF particles, however, increased to 1.24 in M-S-H phases grown in the gaps (**Figures 4A,B**). After curing for 300 days, samples AMSH-1 and AMSH-5 both A and B had only amorphous specimens. The amorphous substance in sample AMSH-1 was still M-S-H gel with villous shape, the villi size was about 10–20 nm and there were a lot of nano-scale pores between the villi. Aluminium incorporation changed the morphology of M-S-H phases from honeycomb to petaline shape (**Figure 4B**).

CONCLUSION

The hydration process of MgO in the magnesium silicate hydrate system was accelerated by the addition of Al³⁺, and the rate of conversion from MgO to Mg(OH)₂ increases with the increase of Al³⁺ content. However, it does not influence the formation of hydration products (M-S-H phases) and it slows down the M-S-H generation. According to TGA/DTG we know that Mg(OH)₂ crystals with amorphous hydroxy aluminum are mixed together, which led to the position of weight loss peak being offset, and the

increase of the weight loss range from 200°C to 300°C proved that there is a new phase formation in the M-S-H.

Irrespective of the amount of Al³⁺ doped, a limited amount of Al³⁺ entered the structure of the M-S-H phase, consequently, the initial molecular structure of the M-S-H remained unchanged. Aluminium ions occupied the Q³-b tetrahedra sites of the M-S-H layers and did not substitute for Si⁴⁺ via inverted Si-O-Si linkages (Q³-a). The average condensation degree and the Mg/Si molar ratio of the M-S-H phase raised with the increase of Al³⁺ content. Hydroxyl-aluminum, a residual aluminium amorphous phase, and the M-S-H phases formed a solid solution. The addition of Al³⁺ morphology of the M-S-H phase from honeycomb-like to petal-like.

DATA AVAILABILITY STATEMENT

The original contributions presented in the study are included in the article/Supplementary Material, further inquiries can be directed to the corresponding author.

AUTHOR CONTRIBUTIONS

YJ: Conception and design of study. YZ and XZ: Drafting the manuscript. YJ and FL: analysis and/or interpretation of data. WM, HY and RH: revising the manuscript critically for important intellectual content.

FUNDING

This work was supported by the National Natural Science Foundation of China (Grant No. 51808217), the Natural Science Foundation of Hebei Province (Grant No. E2019209403), the S and T Program of Hebei Province (Grant No. 19273803D), and the Research Project of Hebei Province (Grant No. B2019003028).

REFERENCES

- Bernard, E., Lothenbach, B., Cau-Dit-Coumes, C., Pochard, I., and Rentsch, D. (2020). Aluminum Incorporation into Magnesium Silicate Hydrate (M-S-H). *Cement concrete Res.* 128, 105931. doi:10.1016/j.cemconres.2019.105931
- Bernard, E., Lothenbach, B., Chlique, C., Wyrzykowski, M., Dauzères, A., Pochard, I., et al. (2019). Characterization of Magnesium Silicate Hydrate (M-S-H). *Cement concrete Res.* 116, 309–330. doi:10.1016/j.cemconres.2018.09.007
- Bernard, E., Lothenbach, B., Rentsch, D., Pochard, I., and Dauzères, A. (2017). Formation of Magnesium Silicate Hydrates (M-S-H). *Phys. Chem. Earth, Parts A/B/C* 99, 142–157. doi:10.1016/j.pce.2017.02.005
- Bonen, D., and Cohen, M. D. (1992). Magnesium Sulfate Attack on portland Cement Paste - II. Chemical and Mineralogical Analyses. *Cement Concrete Res.* 22, 707–718. doi:10.1016/0008-8846(92)90023-o
- Ji, X. Y., Guan, W., and Pei, L. (2014). Effect of Polyethylene Glycol Modification on Microstructure and Solubility of Hydrated Calcium Silicate. *J. Funct. Mater.* 45 (1), 1089–1094. doi:10.3969/j.issn.1001-9731.2014.01.020
- Jia, S. B., Zhang, X. X., and Li, Y. Y. (2019). Experimental Study on Strength and Leaching Characteristics of Alkali Activated Cement Stabilized Heavy Metal Contaminated Soil. *Ind. Construction* 49 (08), 142–146. doi:10.13204/j.gyjz201908023
- Jia, Y., Wang, B. M., Wu, Z. L., and Zhang, T. T. (2017). Effect of CaO on the Reaction Process of MgO-SiO₂-H₂O Cement Pastes. *Mater. Lett.* 192, 48–51. doi:10.1016/j.matlet.2017.01.072
- Jia, Y., Wang, B. M., and Zhang, T. T. (2017). *Study on Reaction Mechanism of MgO-SiO₂-H₂O Cementing System under the Action of NA-HMP and CaO*. Dalian: Dalian University of Technology.
- Jia, Y., Wang, B., Wu, Z., Han, J., Zhang, T., Vandeperre, L. J., et al. (2016). Role of Sodium Hexametaphosphate in MgO/SiO₂ Cement Pastes. *Cement concrete Res.* 89, 63–71. doi:10.1016/j.cemconres.2016.08.003
- Li, J., Geng, G., Myers, R., Yu, Y.-S., Shapiro, D., Carraro, C., et al. (2019). The Chemistry and Structure of Calcium (Alumino) Silicate Hydrate: A Study by XANES, Ptychographic Imaging, and Wide- and Small-Angle Scattering. *Cement Concrete Res.* 115, 367–378. doi:10.1016/j.cemconres.2018.09.008
- Li, J., Zhang, W., Garbev, K., Beuchle, G., and Monteiro, P. J. M. (2020). Influences of Cross-Linking and Al Incorporation on the Intrinsic Mechanical Properties

- of Tobermorite. *Cement Concrete Res.* 136, 106170. doi:10.1016/j.cemconres.2020.106170
- Li, J., Zhang, W., and Monteiro, P. J. M. (2020). Structure and Intrinsic Mechanical Properties of Nanocrystalline Calcium Silicate Hydrate. *ACS Sustain. Chem. Eng.* 8, 12453–12461. doi:10.1021/acssuschemeng.0c03230
- Li, Z. H., Zhang, T. S., Hu, J., Tang, Y., Niu, Y. F., Wei, J. X., et al. (2014). Characterization of Reaction Products and Reaction Process of MgO-SiO₂-H₂O System at Room Temperature. *Construction Building Mater.* 61, 252–259. doi:10.1016/j.conbuildmat.2014.03.004
- Liu, Y., Mao, Z., Y., Wang, Z., Y., He, Y., Yu, J., and Zhu, Y. (2021). Study on Preparation and Adsorption Properties of Dopamine Modified Sepiolite. *Speciality Petrochemicals* 38 (02), 50–56. doi:10.3969/j.issn.1003-9384.2021.02.010
- Lothenbach, B., Nied, D., L'Hôpital, E., Achiedo, G., and Dauzères, A. (2015). Magnesium and Calcium Silicate Hydrates. *Cement concrete Res.* 77, 60–68. doi:10.1016/j.cemconres.2015.06.007
- Maruyama, I., Nishioka, Y., Igarashi, G., and Matsui, K. (2014). Microstructural and Bulk Property Changes in Hardened Cement Paste during the First Drying Process. *Cement concrete Res.* 58, 20–34. doi:10.1016/j.cemconres.2014.01.007
- Nied, D., Enemark-Rasmussen, K., L'Hôpital, E., Skibsted, J., and Lothenbach, B. (2016). Properties of Magnesium Silicate Hydrates (M-S-H). *Cement concrete Res.* 79, 323–332. doi:10.1016/j.cemconres.2015.10.003
- Richardson, I. G. (1999). The Nature of C-S-H in Hardened Cements. *Cement concrete Res.* 29, 1131–1147. doi:10.1016/s0008-8846(99)00168-4
- Santhanam, M., Cohen, M. D., and Olek, J. (2020). Mechanism of Sulfate Attack: a Fresh Look: Part 1: Summary of Experimental Results. *Cement concrete Res.* 32, 915–921. doi:10.1016/s0008-8846(02)00724-x
- Song, Q., Nie, J., Wu, D., Hu, Y. R., and Chen, Y. X. (2021). Effect of SO₄²⁻, Cl⁻ and Mg²⁺ on the System of C-S-H and Ca(OH)₂. *Construction Building Mater.* 285, 122955. doi:10.1016/j.conbuildmat.2021.122955
- Tang, Y., and Chen, W. (2020). Effect of Magnesium on the Structure and Chemical Composition of Calcium Silicate Hydrate at Elevated Temperature. *Construction Building Mater.* 240 (C), 117925. doi:10.1016/j.conbuildmat.2019.117925
- Tonelli, M., Martini, F., Calucci, L., Fratini, E., Geppi, M., Ridi, F., et al. (2016). Structural Characterization of Magnesium Silicate Hydrate: towards the Design of Eco-Sustainable Cements. *Dalton Trans.* 45, 3294–3304. doi:10.1039/c5dt03545g
- Walling, S. A., Kinoshita, H., Bernal Collier, S. A. N. C., Collier, N. C., and Provis, J. L. (2015). Structure and Properties of Binder Gels Formed in the System Mg(OH)₂-SiO₂-H₂O for Immobilization of Magnox Sludge. *Dalton Trans.* 44, 8126–8137. doi:10.1039/c5dt00877h
- Wei, J. X., Chen, Y., and Li, Y. (2006). The Reaction Mechanism between MgO and Microsilica at Room Temperature. *J. Wuhan Univ. Technology-Materials Sci.* 21 (2), 88–91. doi:10.1007/bf02840848
- Wei, J. X., Yu, Q. J., Zhang, W. S., and Zhang, H. T. (2011). Reaction Products of MgO and Microsilica Cementitious Materials at Different Temperatures. *J. Wuhan Univ. Technology-Materials Sci.* 4 (26), 745–748. doi:10.1007/s11595-011-0304-3
- Zhang, T., Li, T., Zou, J., Li, Y., Zhi, S., Jia, Y., et al. (2020). Immobilization of Radionuclide ¹³³Cs by Magnesium Silicate Hydrate Cement. *Materials (Basel)* 13, 1–17. doi:10.3390/ma13010146
- Zhang, T., Vandeperre, L. J., and Cheeseman, C. R. (2014). Formation of Magnesium Silicate Hydrate (M-S-H) Cement Pastes Using Sodium Hexametaphosphate. *Cement concrete Res.* 65, 8–14. doi:10.1016/j.cemconres.2014.07.001

Conflict of Interest: HY and RH was employed by China Railway 14th Bureau Group 2nd Engineering Co., Ltd.

The remaining authors declare that the research was conducted in the absence of any commercial or financial relationships that could be construed as a potential conflict of interest.

Publisher's Note: All claims expressed in this article are solely those of the authors and do not necessarily represent those of their affiliated organizations, or those of the publisher, the editors and the reviewers. Any product that may be evaluated in this article, or claim that may be made by its manufacturer, is not guaranteed or endorsed by the publisher.

Copyright © 2022 Jia, Zou, Zou, Jiang, Li, Ma, Yan and Hua. This is an open-access article distributed under the terms of the Creative Commons Attribution License (CC BY). The use, distribution or reproduction in other forums is permitted, provided the original author(s) and the copyright owner(s) are credited and that the original publication in this journal is cited, in accordance with accepted academic practice. No use, distribution or reproduction is permitted which does not comply with these terms.



Durability of Concrete With Coal Gasification Slag and Coal Gangue Powder

Xiaoliang Zhu¹, Zhaoheng Guo², Wen Yang³ and Wenjing Song^{1*}

¹China Western Construction Academy of Building Materials Co., Ltd, Chengdu, China, ²School of Materials Science and Engineering, Southeast University, Nanjing, China, ³China West Construction Group Co., Ltd, Chengdu, China

OPEN ACCESS

Edited by:

Tingting Zhang,
Dalian University of Technology, China

Reviewed by:

Peng Zhang,
National Natural Science Foundation
of China, China
Neven Ukrainczyk,
Darmstadt University of Technology,
Germany

*Correspondence:

Wenjing Song
soubunnsei@foxmail.com

Specialty section:

This article was submitted to
Structural Materials,
a section of the journal
Frontiers in Materials

Received: 08 October 2021

Accepted: 22 November 2021

Published: 26 January 2022

Citation:

Zhu X, Guo Z, Yang W and Song W
(2022) Durability of Concrete With Coal
Gasification Slag and Coal
Gangue Powder.
Front. Mater. 8:791178.
doi: 10.3389/fmats.2021.791178

Lack and quality decrease of supplementary cementing materials (SCMs) such as fly ash and granulated blast-furnace slag is increasingly prominent in China. Thus, the use of coal gangue (CG) and coal gasification slag (CGS) as SCMs in concrete attracted more researcher's attention. This paper investigated the mechanical strength, porosity, and durability of CG-and CGS-added concrete. Experimental results showed that the activity of the treated CG and CGS is better than that of ordinary mineral SCMs, indicating that CG and CGS concrete can satisfy the requirements of ordinary construction under reasonable processing technology. Both CG-added and CGS-added concrete illustrated better chloride penetration resistance. The aluminum element contained in CG and CGS causes the C_3S hydration to generate ettringite which is an erosion product under sulfate erosion, and it will intensify the damage of sulfate erosion. After 125th freeze-thaw cycles, the CGS-added concrete has no obvious failure which indicates that CGS-added concrete has great capacity in the frost resistance.

Keywords: coal gangue, durability, coal gasification slag, compressive strength, supplementary cementitious material

INTRODUCTION

Concrete is the most used material in construction and building engineering. Supplementary cementing materials (SCMs) such as fly ash (FA) and granulated blast-furnace slag (GGBS) are also used in the concrete systems to reduce the use dosage of cement (Kaur et al., 2012; Cyr, 2013), and durability of concrete is increased when high-quality SCMs were used in suitable dosage (Borosnyói, 2016; Lollini et al., 2016; Rahla et al., 2019).

In recent years, lack and quality decrease of SCMs such as fly ash and granulated blast-furnace slag are increasingly prominent, which directly affected the performance of concrete (Purebase, 2021). Low-quality SCMs in cement-based materials would lead to the slow strength development, weak durability, and service life of concrete (National Precast Concrete Association, 2010). The permeability will increase due to the slow pozzolanic reactivity and insufficient curing time of SCM-added cementitious materials, which promoted the diffusion of the harmful ions and thus aggravated the durability problems. The study by Gao et al. showed the larger water-soluble SO_4^{2-} content in concrete under sulfate attack because of the high content of porosity and defects (Gao et al., 2017). Thus, research and development of other new SCMs was needed in the concrete area.

Coal gangue (CG) and coal gasification slag (CGS) contain a large amount of siliceous and aluminous minerals and have certain pozzolanic reactivity. In recent years, the use of CG and CGS as SCMs in concrete attracted more researcher's attention. Wang et al. studied the effects of CG

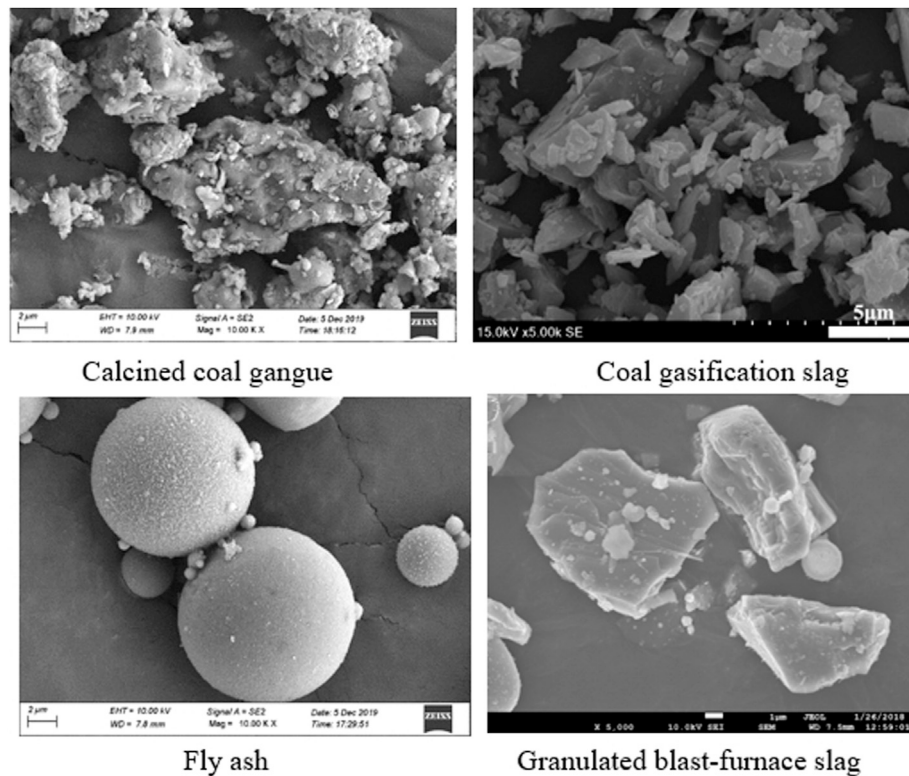


FIGURE 1 | SEM image of raw materials.

with different fineness (200, 325, 500, 1250, and 2000 mesh) on the mechanical properties, frost resistance, and chloride penetration resistance of concrete (Wang et al., 2020). Zhou using CG powder partially replaces Portland cement (PC) at 10, 20, 30, and 40% by weight for the blended cement paste mixes, and observes the degree of reaction of calcined coal gangue powder (Zhou, 2009). Pomykala proved the possibility of using slag from gasification of coal as a component of concrete and binding mixtures (Pomykala, 2014). Luo et al. investigated the influence of CGS on the fluidity of cement mortar as the admixture, which shows conducive to the fluidity (Luo et al., 2021).

At present, most of the research is mainly focused on the mechanical properties of coal gangue and coal gasification slag powder; for its application in cement-based materials, there are few studies on its impact on durability. As we all know, when concrete is used in engineering, it needs to meet not only mechanical properties, but also durability. Therefore, in order to make up for the lack of scientific research on the durability of coal gangue and coal gasification slag and promote the application of coal gangue and coal gasification slag in concrete, this paper studies the chloride ion penetration, freeze-thaw cycle, carbonation, and sulfate resistance of concrete mixed with CG/CGS, and comprehensively discusses the influence of CG/CGS on the durability of concrete. It is expected to provide the research foundation and theoretical support

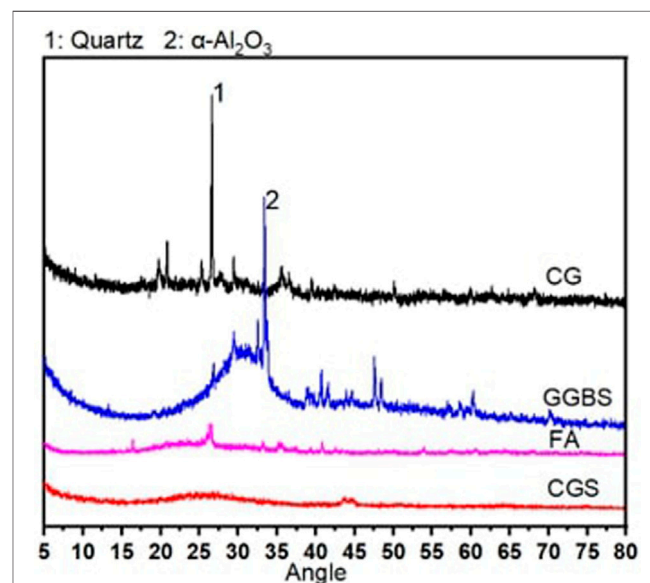


FIGURE 2 | XRD spectra of CG, CGS, GGBS and FA.

for CG/CGS as SCM. However, this study only analyzed the concrete with the replacement rate of SCMs of 30%, and the test work of other additives needs to be carried out further.

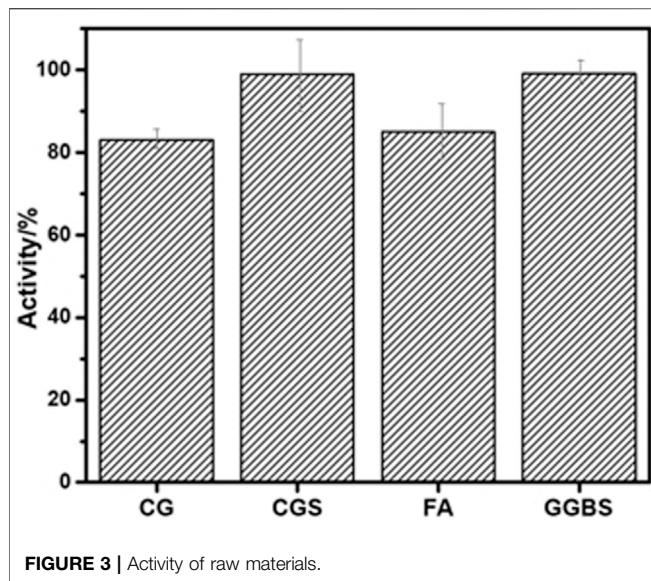


FIGURE 3 | Activity of raw materials.

MATERIALS AND METHODS

Materials

Following four types of supplementary cementitious materials and ordinary Portland cement were selected in this study: 1) Low-calcium CG: calcined at 800°C; 2) CGS: grinded for 50 min and sieved to a particle size below 200 mesh size; 3) FA: from Yibin City, Sichuan Province; 4) GGBS: obtained from Chongqing municipality; 5) C: Ordinary Portland cement, CEM I 42.5. The morphology was determined using a scanning electron microscope (SEM), as illustrated in **Figure 1**. CGS particles have several shapes such as platy and prismatic, and most of them were agglomerated with the dense smooth surface with few pores on the exterior surface. The structure of CG turns to irregular and porous at 800°C heating temperature, which may be caused by the dehydroxylation of kaolinite and phase change to metakaolin. The XRD spectra of CG, CGS, GGBS, and FA are shown in **Figure 2**. There are obvious characteristic peaks of crystalline SiO₂ in CG. GGBS and FA contain a small amount of crystalline SiO₂. There is no obvious characteristic peak of crystalline phase in CGS, indicating that most of them are amorphous phase. GGBS contains more alumina phase.

The chemical composition results and the activity of the cementitious materials were determined (**Figure 3**; **Table 1**). It can be seen from the table that CG and CGS have similar contents of SiO₂ and Al₂O₃, which are lower than FA and higher than

GGBS. CGS has a higher content of CaO than CG, which indicates that the hydraulic activity of cementitious materials is influenced by its chemical composition.

Preparation of Samples

Concrete specimens were cast at a water to cement ratio of 0.37. Aggregates smaller than 4.75 mm and up to 0.075 mm are considered fine aggregate. The total amount of cementing material was 450 kg, and the other samples except C were replaced by CG, CGS, and FA at the contents of 30% by the mass of cement, respectively. Coarse aggregate, cementite, fine aggregate, and water were added in a standard mixer after all the ingredients were prepared, and blend for 2 min until smooth. After that, the performance of concrete mixture was inspected according to the Chinese standard GB/T50080-2016. **Table 2** lists the different SCMs used in the concrete mixes that influence the workability of concrete. The effect of FA, GGBS, and CGS enhanced the slump; on the other hand, CG shows a reduction in workability compared to the C. The reason is that CG particles are porous and loose, which will absorb part of the water and affect fluidity.

METHODS

Mechanical Properties

The compressive strength testing of the samples has been started at the age of 28 days. Concrete cubes 100 mm × 100 mm × 100 mm in size were cast according to Chinese standard GB/T 50,081. The loading rate is 3 kN/s, and the average value of three samples was used for the determination of compressive strength values. The compressive strength was calculated by following formula.

$$f_{cc} = \frac{F}{A} \times \lambda$$

f_{cc} : compressive strength of concrete cube sample, MPa;

F : sample failure loads, kN/s;

A : sample bearing pressure area, mm²;

λ : dimensional conversion factor, herein is 0.95.

Pore Structure Parameters

In this paper, mercury intrusion porosimetry is used to determine the pore structure parameters of concrete. For the sample preparation, core-drilling is the core sampling method that was adopted for the consideration of protecting the original pore structure of samples. After that, the samples were dried in a 50-degree vacuum oven for 48 h to remove free water before

TABLE 1 | Chemical composition of cement CG, CGS, FA, and GGBS (wt%).

	SiO ₂	Al ₂ O ₃	CaO	Fe ₂ O ₃	K ₂ O	MgO	TiO ₂	Na ₂ O	MnO	SO ₃	C	f-CaO	LOI
Cement	21.39	5.15	61.04	3.86	0.62	2.82	0.85	0.64	-	3.10	-	-	-
CG	4.12	23.98	6.36	14.76	1.48	1.48	4.26	1.09	0.19	1.71	-	-	1.1
CGS	45.44	26.37	12.30	9.29	1.28	1.11	1.04	0.91	0.37	0.17	1.08	2.8	0.7
FA	0.39	27.49	4.47	8.47	2.03	0.95	2.92	0.1.41	-	1.16	-	-	1.5
GGBS	34.64	13.96	33.10	2.51	0.79	5.68	6.14	1.42	-	-	-	-	0.8

TABLE 2 | Proportion of concrete samples (kg/m³).

Sample	W/c	Cement/kg	FA/kg	GGBS/kg	CG/kg	CGS/kg	Sand/kg	Gravel/kg	Slump/kg	Air content/%
C	0.37	450	—	—	—	—	795	1,000	12.0	1.25
FA	0.37	315	135	—	—	—	795	1,000	22.0	1.50
GGBS	0.37	315	—	135	—	—	795	1,000	24.0	1.25
CG	0.37	315	—	—	135	—	795	1,000	11.5	1.20
CGS	0.37	315	—	—	—	135	795	1,000	21.0	0.95

the test. The instrument uses the American PM60GT-18 mercury porosimeter, in which the maximum pressure of the instrument is 325 Mpa, and the range of pore size is 3 nm to 950 μ m. The porosity tests were made on the evenly corroded cement paste samples of 2 mm thick, which ensured the reproducibility of the measurements.

Chloride Penetration Resistance

The tests for chloride ion penetration were in accordance with Chinese standard GB/T 50,082.

The method of electric flux was as follows: 1) Cylinder specimens with diameter of (100 \pm 1) mm and height of (50 \pm 2) mm were cured for 28 days; 2) Silica gel or resin sealing material was applied to brush the cylinder side of the specimen, and the specimen was vacuum-saturated; 3) 0.3 mol/L NaOH solution and 3% NaCl solution were placed in the testing cells on two sides of the sample, respectively, and connected to the power supply; 4) the DC power was switched on 60 \pm 0.1V, record the results each 30 min.

Freezing and Thawing Resistance

After curing for 24 days, the prismatic specimens of 100 mm \times 100 mm \times 400 mm were taken out and immersed in water with a temperature of (20 \pm 2) $^{\circ}$ C for 4 days, and the initial value of fundamental frequency and weight of the specimens was measured. Then, put the specimens into the freeze-thaw testing machine. Each cycle of freezing and thawing was completed within 2–4 h; the transverse fundamental frequency and the quality of the specimen should be measured every 25 freeze-thaw cycles.

Sulfate Attack Resistance

For sulfate attack resistance test, concrete specimens of 100 mm \times 100 mm \times 100 mm cube were prepared. The test as following procedure: 1) specimens were initially placed in an oven to be dried at (80 \pm 5) $^{\circ}$ C for 48 h and cool down to room temperature; 2) immersed the specimens in 5% sodium sulfate solution. The solution was replaced each month. One cycle included 15 h of soaking time and 5.5 h of drying time which was maintaining at the temperature of 80 \pm 5 $^{\circ}$ C, then cooling after drying. Each cycle lasted for about (24 \pm 2) h. Also, it is worth noting that according to GB/T 50,082 standard, the test can be stopped when the corrosion resistance coefficient of compressive strength reaches 75%.

Carbonation Resistance

Prism specimens were cast and left in the cast area and demolded 24 h after casting. After demolding, the specimens were cured in

standard curing room for 26 days. Subsequently, take out the test piece and bake it at 60 $^{\circ}$ for 48 h. The specimens were moved to a carbonization chamber with carbon dioxide concentration, relative humidity and temperature of (20 \pm 3)% (70 \pm 5)% and (20 \pm 2)%, respectively, for carbonization test. On days 3, 7, 14, and 28, split the samples and spray 1% phenolphthalein ethanol solution (the ethanol solution contains 20% distilled water) to measure the carbonization depth.

RESULTS

Mechanical Properties

The compressive strength and strength ratio of CG-, CGS-, FA-, and GGBS-added concrete is shown in **Figure 4**. It could be known that the strength of all samples was increased with a curing time increase of 3–56 days. C samples showed the highest strength as 100% cement was used.

Both CG and CGS samples suggested that the strength development trend is better than FA and GGBS. The strength is higher than that of C45 concrete after 28 days of curing, which fully meets the construction requirements. CG samples showed peak strength when compared with CGS-, FA-, and GGBS-added samples before 14 days curing time. It indicated that CG has higher activity at the early age compared with CGS, FA, and GGBS. The highest strength about 63 MPa was shown by CG sample when curing age up to 56 days. CGS-added concrete revealed higher strength than FA-added samples. Strength of concrete with CG, CGS, FA, and GGBS-added (CG, CGS, GGBS, FA for short) was inconsistent with the activity results of CG, CGS, FA, and GGBS. It may be related to the powder fineness and the accumulation state in the concrete system (Martin et al., 2006; Berodier and Scrivener, 2014; Zunino and Lopez, 2016; Hemalatha and Santhanam, 2018).

Porosity and Pore Diameter

It has been well accepted that the addition of supplementary materials modifies the microstructure of cement paste. The total porosity of cement-based materials with SCMs can be affected by chemical (pozzolanic reaction) and physical (compactness) influences (Cyr, 2013). The structure of cement mortar is complex, and the size of the internal pores has a large span. Bout et al. roughly divide the pore size into four categories and give the impact of each level of pores on the performance: the gel pore, with pore size of less than 20 nm (harmless pore); the transition pore, with diameter in the range of 10–100 nm (less harmful pores); the capillary pore, with diameter in the range of

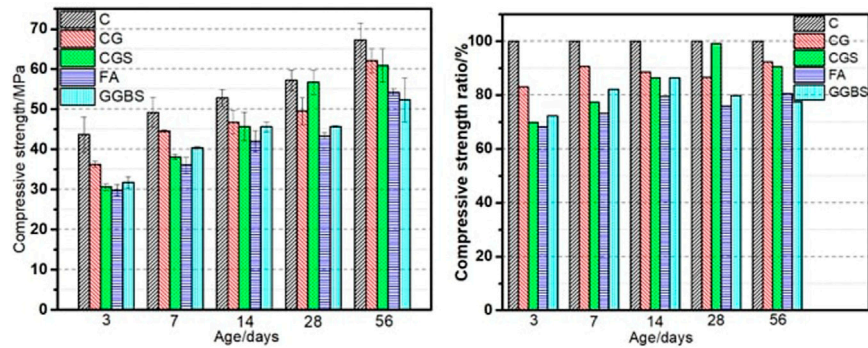


FIGURE 4 | Compressive strength and compressive strength ratio of concrete samples.

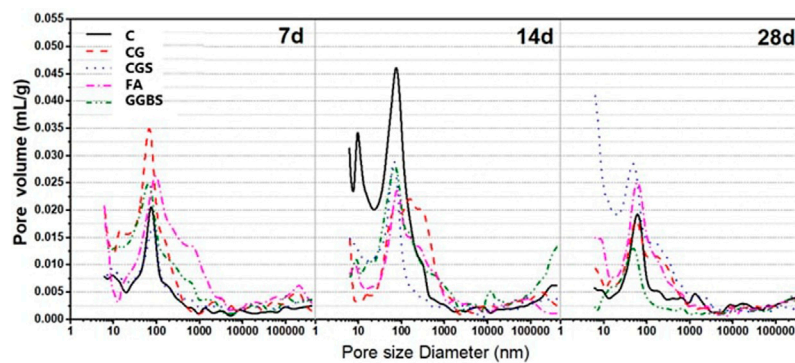


FIGURE 5 | Pore size distribution of concrete samples.

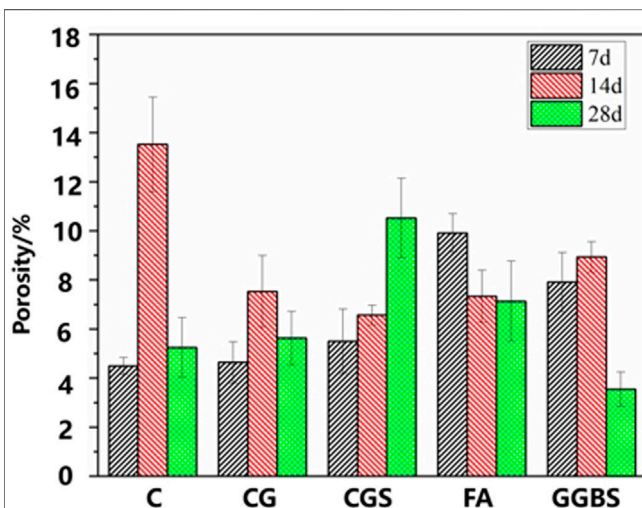


FIGURE 6 | Porosity of concrete samples.

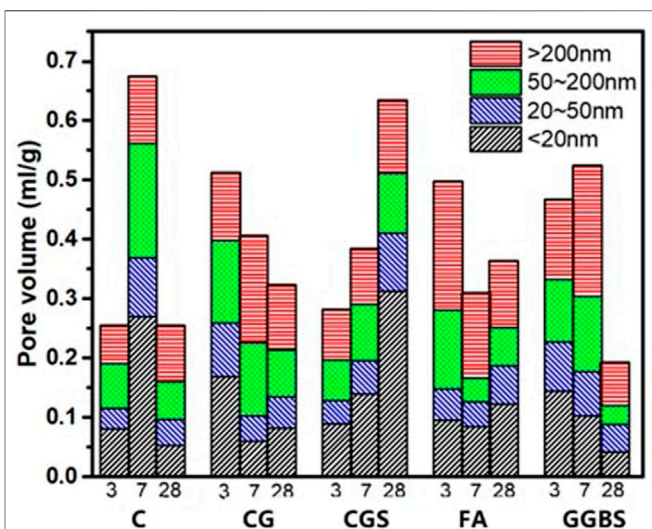


FIGURE 7 | Pore volume of concrete samples.

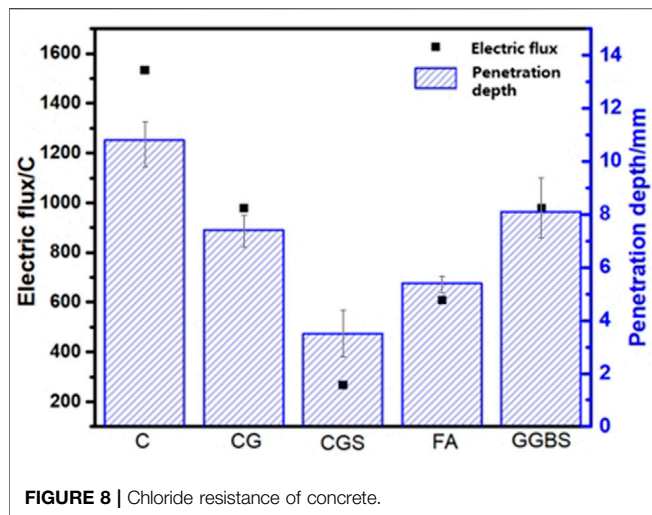


FIGURE 8 | Chloride resistance of concrete.

100–1000 nm (harmful pores); and the macro pores, with pore size of greater than 1000 nm (Long et al., 2017). Figures 5–7 exhibit the pore structure of concrete at different ages. The concrete addition of SCMs has larger porosity, and the size of pores owing to a smaller quantity of hydrates is formed in the paste at the early age. At this time, the pozzolanic reaction has hardly occurred to produce calcium silicate hydrate, and the concrete mixed with SCMs will generally last for several days (when the amount of SCMs is added, the time may be prolonged; however, when the activity of SCMs is high, the time may be shortened, depending on the situation).

It can be found that the samples cured for 7 days with CG illustrated more pores, which is because the SCMs have lower activity at the early age and the structure is relatively loose at the early of hydration; Wang et al. published the same results (Wang et al., 2012). All specimens except CGS (it should be noted that the porosity of CGS concrete increases significantly with the hydration process, considering that the test operation may cause errors in the results; however, the reasons for this phenomenon need further study) showed the same trend that the hydration products C-S-H gel filled the pores and reduced the porosity with the hydration proceeding after curing for 14 days. The 5.63% porosity of CG is similar to C (5.25%), and less than FA (7.13%) at the curing age of 28 days.

Chloride Penetration Resistance

Mineral admixtures can effectively improve the internal pore structure and interface area of concrete, and to a large extent hinder the chloride ion erosion of concrete, which is one of the effective measures to improve the chloride ion erosion resistance of concrete. The reasons that mineral admixtures is able to improve the resistance of concrete to chloride ion erosion mainly include the following two aspects: first, the addition of mineral admixtures can effectively optimize the internal microstructure of concrete, thus improving its diffusion resistance to chloride ion infiltration; second, the secondary hydration reaction of cement after the addition of

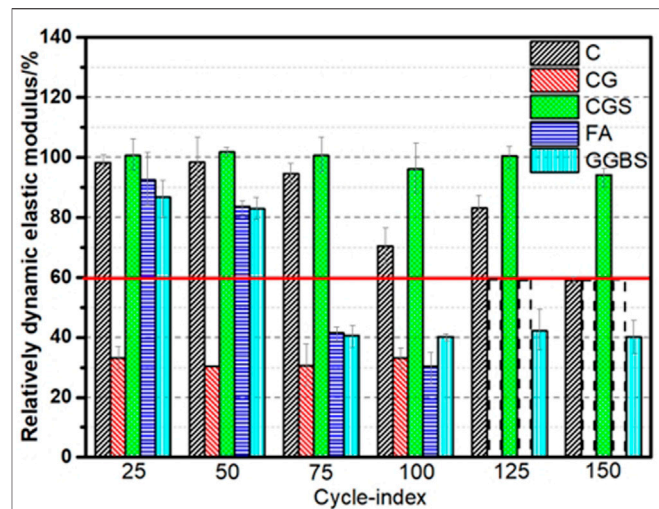


FIGURE 9 | Relatively dynamic elastic modulus of concrete under different freezing and thawing cycles.

mineral admixtures generates low-alkaline C-S-H gel, which can enhance the chemical binding ability and physical adsorption ability of concrete to chloride ions. The following contents will summarize and analyze the influence of various mineral admixtures on the chloride ion resistance of concrete.

The results of electric flux and penetration depth of concrete are summarized in Figure 8. It can be obviously seen that the electric flux of C is larger than CGS and CG, which indicates that CGS and CG significantly reduced the electric flux of concrete. CGS has the best effect, and CG is similar to FA.

The penetration depth of chloride ions is consistent with the electrical flux. The penetration depth of chloride ions in the C was the largest at 10.8 mm, and the smallest of CGS at 1.8 mm. The CG was lower than GGBS at 7.8 mm. Such a phenomenon perhaps due to high amounts of alumina contents exhibited a much better resistance to chloride ion penetration (Mucteba et al., 2012).

Freeze-Thaw Resistance

At present, the evaluation indexes of concrete freeze-thaw damage include relative dynamic elastic modulus change, mass loss rate, compressive strength loss rate, and damage layer thickness. The relative dynamic elastic modulus change is used as the evaluation index in this study.

Figure 9 shows that the relative dynamic elasticity modulus of CG is always lower than other concrete, which is less than 35% after 25th freeze-thaw cycle. According to the GB/T50082 standard, it is stipulated that the test needs to be stopped when the freeze-thaw cycle has reached the specified number of times, the relative dynamic elastic modulus has dropped to 60% ($\leq 60\%$), or the mass loss rate has reached 5%. The relative dynamic elastic modulus of the CG has been low as 30.3%, indicating that it has been destroyed, which proved the CG has little resistance to freeze-thaw damage. The reason why the CG

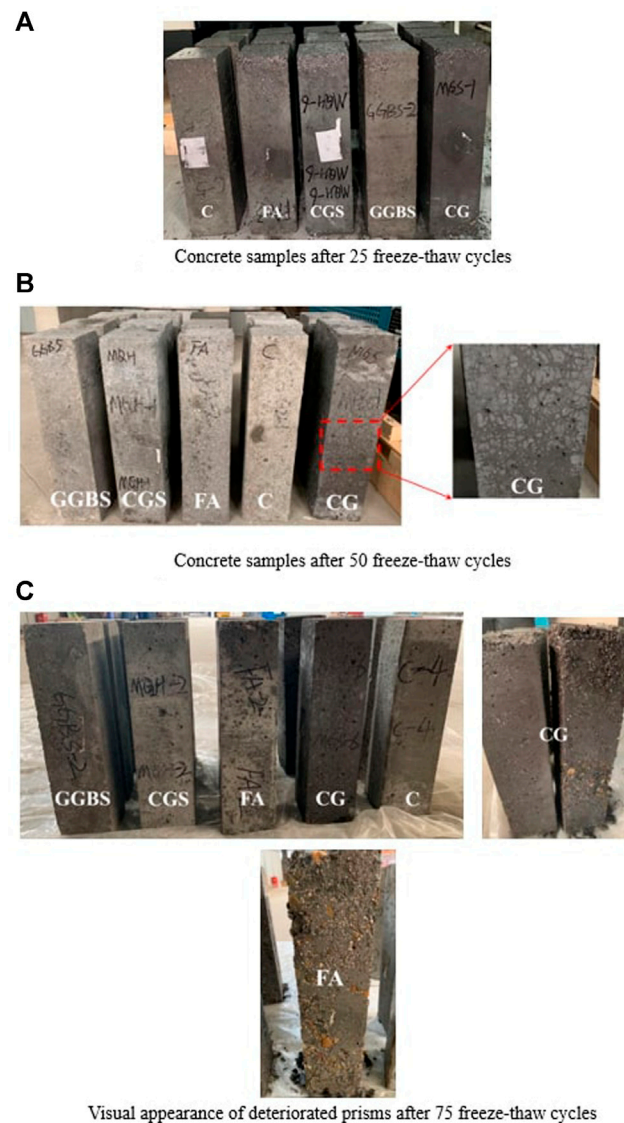


FIGURE 10 | Freezing and thawing resistance of concrete (A) Concrete samples after 25 freeze-thaw cycles (B) Concrete samples after 50 freeze-thaw cycles (C) Visual appearance of deteriorated prisms after 75 freeze-thaw cycles.

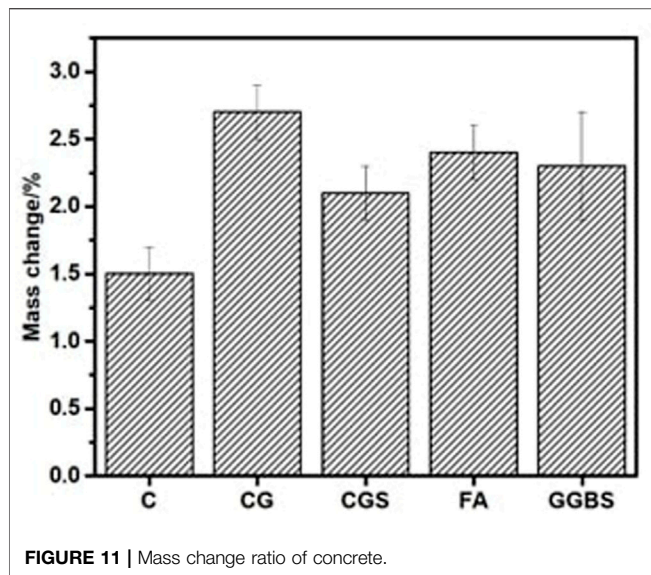
specimens were first frozen and damaged may also be due to the good water absorption of the CG after calcination (Wang et al., 2021; Zhang et al., 2021), and the previous slump results also confirmed this view. The external water is more likely to enter the interior of the concrete. After freezing at low temperature, frost heave pressure will be generated, which will promote the development of cracks. Accelerate the frost heave and fall off of the outer layer of the specimen. The freeze-thaw resistance grade of the FA and GGBS is F50. With the freeze-thaw cycle reaching 150 times, no obvious damage was found in the concrete mixed with CGS. It illustrates that the CGS has excellent resistance to freeze-thaw damage.

The apparent quality of the freeze-thaw cycle of concrete is shown in **Figure 10**. When the freeze-thaw cycle reaches 25

cycles, no distinct cracks appeared. As the freeze-thaw cycle reaches 50 cycles, micro-cracks appear on the surface of CG; meanwhile, the internal freeze-thaw water flows out through the cracks, which indicates that its internal structure has been significantly damaged. The other samples showed no obvious damage except for the upper and lower surfaces. When 75 cycles of freezing and thawing were done, a large amount of aggregate fell off and broken during the sampling process of one of the CG specimens; similarly, the FA and GGBS specimens also appeared evident damage.

Sulfate Attack Resistance

There are two main reasons for the influence of Na_2SO_4 solution on the quality of concrete under the combined action of dry and

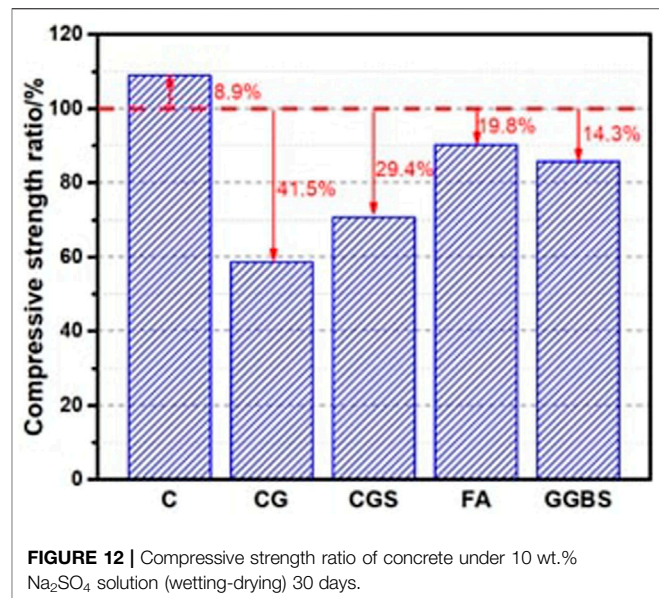


wet cycles: on the one hand, the SO_4^{2-} that enter the concrete reacted with the hydration products and generated the erosion products which fill and accumulate in the pores of the concrete, temporarily increasing the quality of concrete; on the other hand, the corrosion products are expansive. Under the combined action of dry and wet cycles, the expansion stress will cause the concrete to crack and peel, reducing the quality.

The mass change ratio and the compressive strength ratio of all specimens after 30 cycles of immersion were recorded and illustrated in **Figures 11, 12**. It can be found that each specimen presented a decline in mass. Compared with ordinary concrete, concrete mixed with SCMs shows weak resistance to sulfate erosion. The reason is that there are many hydration products that can participate in chemical reactions in ordinary concrete, and the amount of corrosion products generated is large, which improves the compactness. However, the degradation of CG mass (-2.7%) is the most obvious among all the specimens. Meanwhile, the compressive strength ratio (41.5%) of CG is also the highest loss (**Figure 12**). Not only CG, but also CGS showed a similar trend. Therefore, in certain sense, the change ratio of mass also reflects the change ratio of compressive strength. The aluminum element contained in CG and CGS causes the C_3S hydration to generate ettringite which is an erosion product under sulfate erosion, and it will intensify the damage of sulfate erosion (Wang et al., 2018). The reason for this phenomenon may be due to the fact that the aluminum phase in CG combines with other elements to form another compound. Therefore, Al_2O_3 was not founded in CG.

Carbonation Resistance

Figure 13 shows the carbonation depth of the samples using CG and CGS after 28 days of the accelerated carbonation test. A carbonation phenomenon of all the samples was not observed at the first 3 days, and the carbonation depth increases gradually with an increase in exposure time. It is not difficult to see that C showed a lower carbonation depth



than other groups at 28 days of curing, about 5 mm, and the carbonization depth of concrete mixed with CG was the largest, about 7.9 mm, followed by CGS, about 7.6 mm.

Although many researchers have done comparative experiments on concrete carbonization with and without SCMs, generalizations remain difficult. The overall trend found in the literature is that the depth of carbonation increases with the use of pozzolan in concretes (Shi et al., 2009). The author considers that there are two reasons that lead to this carbonization experiment results: the first one, the pozzolanic reaction consumes $\text{Ca}(\text{OH})_2$, which implies that a smaller amount of CO_2 is required to carbonate the remaining hydrates; when the amount of $\text{Ca}(\text{OH})_2$ present is lower, the carbonization depth is larger. This view is consistent with the conclusion drawn by (Bier, 1986). The second one, a large SCM content weakens the accumulation effect of SCM particle, and the increases of the capillary pore content of the specimen will accelerate the carbonization depth. Although concretes containing SCMs are sometimes considered as less resistant to carbonation (especially in accelerated tests) due to their low portlandite content, this property should not be considered alone regarding the risk of corrosion since the SCMs can sometimes reduce the permeability of the concrete (Bouikni et al., 2009). Moreover, it has been shown that many concrete with SCMs have very low probabilities of corrosion after several tenths of years (due to lower permeability), meaning that in the whole life cycle of concrete, the influence of carbonization effect at the early stage is insignificant (Ciaran and Emma, 2012).

DISCUSSION

From the observed relationship between SCM activity and 28 days compressive strength, it can be seen that activity is positively correlated with compressive strength. The higher the







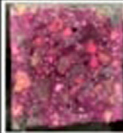



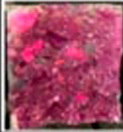



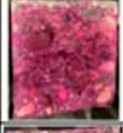





	3d	Depth /mm	7d	Depth /mm	14d	Depth /mm	28d	Depth /mm
C		0		0.8		0.8		5.0
CG		0		4.6		4.8		7.9
CGS		0		1.3		2.6		7.6
FA		0		6.6		7.0		7.3
GGBS		0		1.0		1.9		6.4

FIGURE 13 | Carbonation depth and visual appearance of concrete with different time.

activity, the greater the compressive strength. From the results of concrete electric flux, it can be seen that the permeability resistance performance of CG and CGS is better than that of C. In addition, a comparative analysis of porosity and electric flux results shows that CG has lower porosity but poorer permeability, which may be due to better connectivity of pore structure. The better the pore connectivity, the easier it is for external material to enter the concrete and reduce durability. However, CGS has high porosity but poor interconnectivity, resulting in strong impermeability and good durability. Therefore, we consider that there is no strong correlation between concrete durability and porosity. Moreover, the pore distribution results show that CGS concrete has a large porosity and is easier to form gel pores during the hydration process, but considering the reason of insufficient sample quantity in this study, there may be errors in the results, and future investigations are necessary to validate the kinds of conclusions. Besides, since this study only discussed the concrete performance of CG and CGS with 30% content, the durability of concrete with 40 and 50% content of CG and CGS will be studied (Osborne believes that when 60% gasification slag is used instead of Portland cement to produce concrete, the resistance to sulfate attack and chloride invasion is not obvious (Osborne, 1994); therefore, the future work mainly studies the durability of concrete with CG and CGS content less than 60%), and the influence of the content on its durability will be analyzed in the future work.

CONCLUSION

Overall, CG and CGS can affect the durability of concrete. The chief conclusions of this study can be drawn as follows:

- 1) The strength of the concrete with CG and CGS added after curing for 56 days can reach more than 60 Mpa, indicating that CG and CGS concrete can satisfy the requirements of ordinary construction under reasonable processing technology.
- 2) Both CG-added and CGS-added concrete illustrated great chloride penetration resistance. If it is used in a chloride salt environment, it shows a strong advantage by adding CGS.
- 3) CG and CGS concrete have weak sulfate attack resistance compared to ordinary Portland cement. The aluminum element contained in CG and CGS will intensify the damage of sulfate erosion.
- 4) CGS-added concrete has great capacity in the freeze-thaw resistance. On the contrary, CG has little resistance to freeze-thaw damage.
- 5) The results for the use of CG and CGS revealed that the two SCMs could not effectively contribute to a better performance in carbonation resistance.

DATA AVAILABILITY STATEMENT

The raw data supporting the conclusions of this article will be made available by the authors, without undue reservation.

AUTHOR CONTRIBUTIONS

XZ from China Western Construction Academy of Building Materials Co., Ltd. was responsible for the experimental design. ZG from Southeast University was in charge of the experiment. WY from China West Construction Group Co., Ltd. was in charge of the analysis experiment. WS from China Western Construction Academy of Building Materials Co., Ltd. was responsible for data collation.

REFERENCES

- Berodier, E., and Scrivener, K. (2014). Understanding the Filler Effect on the Nucleation and Growth of C-S-H. *J. Am. Ceram. Soc.* 97 (12), 3764–3773. doi:10.1111/jace.13177
- Bier, T. A. (1986). Influence of Type of Cement and Curing on Carbonation Progress and Pore Structure of Hydrated Cement Pastes. *MRS Proc.* 85, 123. doi:10.1557/PROC-85-123
- Borosnyói, A. (2016). Long Term Durability Performance and Mechanical Properties of High Performance Concretes with Combined Use of Supplementary Cementing Materials. *Construction Building Mater.* 112, 307–324. doi:10.1016/j.conbuildmat.2016.02.224
- Bouikni, A., Swamy, R. N., and Bali, A. (2009). Durability Properties of concrete Containing 50% and 65% Slag. *Construction Building Mater.* 23 (8), 2836–2845. ISSN 0950-0618. doi:10.1016/j.conbuildmat.2009.02.040
- Ciaran, M., and Emma, S. (2012). Probability-Based Assessment of the Durability Characteristics of Concretes Manufactured Using CEM II and GGBS Binders. *Construction Building Mater.* 30, 22–29. doi:10.1016/j.conbuildmat.2011.11.029
- Cyr, M. (2013). Influence of Supplementary Cementitious Materials (SCMs) on concrete Durability. *Eco-Efficient Concrete*, 153–197. doi:10.1533/9780857098993.2.153
- Hemalatha, M. S., and Santhanam, M. (2018). Characterizing Supplementary Cementing Materials in Blended Mortars. *Construction Building Mater.* 191, 440–459. doi:10.1016/j.conbuildmat.2018.09.208
- Kaur, G., Singh, S. P., and Kaushik, S. K. (2012). Reviewing Some Properties of concrete Containing mineral Admixtures. *Indian Concrete J.* 86, 7.
- Lollini, F., Redaelli, E., and Bertolini, L. (2016). A Study on the Applicability of the Efficiency Factor of Supplementary Cementitious Materials to Durability Properties. *Construction Building Mater.* 120, 284–292. doi:10.1016/j.conbuildmat.2016.05.031
- Long, W., Xiao, B., Zhou, B., and Liang, P. (2017). Research on the Internal Pores in Alkali-Activated Slag Cementing Material via X-CT Three-Dimensional Imaging Microscopy. *AIP Conf. Proc.* 1794 (1), 020001. doi:10.1063/1.4971883
- Luo, F., Jiang, Y., and Wei, C. (2021). Potential of Decarbonized Coal Gasification Residues as the mineral Admixture of Cement-Based Material. *Construction Building Mater.* 269, 121259. doi:10.1016/j.conbuildmat.2020.121259
- Martin, C., Philippe, L., and Erick, R. (2006). Efficiency of Mineral Admixtures in Mortars: Quantification of the Physical and Chemical Effects of Fine Admixtures in Relation with Compressive Strength. *Cement Concrete Res.* 36 (2), 264–277. doi:10.1016/j.cemconres.2005.07.001
- Mucteba, U., Kemalettin, Y., and Metin, I. (2012). The Effect of mineral Admixtures on Mechanical Properties, Chloride Ion Permeability and Impermeability of Self-Compacting concrete. *Construction Building Mater.* 27 (1), 263–270. doi:10.1016/j.conbuildmat.2011.07.049
- National Precast Concrete Association (2010). Using Fly Ash in Concrete. Available at: <https://precast.org/2010/05/using-fly-ash-in-concrete/> (Accessed September 26, 2021).
- Osborne, G. (1994). *The Durability of Gasifier Slag and Fly Ash Cement Concretes in Aggressive Environments*. South Africa.
- Pomykala, R. (2014). The Mechanical Properties of Coal Gasification Slag as a Component of Concrete and Binding Mixtures. *Polish J. Environ. Stud.* 23 (4), 1403–1406.
- Purebase (2021). About SCM. Available at: <https://purebase.com/supplementary-cementitious-materials/> (Accessed September 6, 2021).
- Qi, B., Gao, J., Chen, F., and Shen, D. (2017). Evaluation of the Damage Process of Recycled Aggregate Concrete under Sulfate Attack and Wetting-Drying Cycles.

FUNDING

This work was supported by National key research and development plan for key projects of solid waste recycling (2019YFC1907200), Sichuan Science and Technology Program (2021YJ0530), and Major science and technology project of Jiangxi Provincial Department of water resources (202124zdk28).

Construction Building Mater. 138, 254–262. doi:10.1016/j.conbuildmat.2017.02.022

- Rahla, K. M., Mateus, R., and Bragança, L. (2019). Comparative Sustainability Assessment of Binary Blended Concretes Using Supplementary Cementitious Materials (SCMs) and Ordinary Portland Cement (OPC). *J. Clean. Prod.* 220, 445–459. doi:10.1016/j.jclepro.2019.02.010
- Shi, H.-S., Xu, B.-W., and Zhou, X.-C. (2009). Influence of Mineral Admixtures on Compressive Strength, Gas Permeability and Carbonation of High Performance Concrete. *Construction Building Mater.* 23 (5), 1980–1985. doi:10.1016/j.conbuildmat.2008.08.021
- Wang, A., Liu, P., Mo, L., Liu, K., Ma, R., Guan, Y., et al. (2021). Mechanism of thermal Activation on Granular Coal Gangue and its Impact on the Performance of Cement Mortars. *J. Building Eng.* [Preprint] Available at: <https://www.sciencedirect.com/science/article/abs/pii/S2352710221014741> (Accessed November 13, 2021).
- Wang, Q., Yan, P., and Mi, G. (2012). Effect of Blended Steel Slag-GBFS mineral Admixture on Hydration and Strength of Cement. *Construction Building Mater.* 35, 8–14. doi:10.1016/j.conbuildmat.2012.02.085
- Wang, Y., He, X., Su, Y., Ma, B., Chu, J., and Jiang, B. (2018). Effect of Aluminium Phases on Thaumassite Formation in Cement Slurries Containing limestone Powder. *Mag. Concrete Res.* 70 (12), 610–616. doi:10.1680/jmacr.16.00521
- Wang, Y., Tan, Y., Wang, Y., and Liu, C. (2020). Mechanical Properties and Chloride Permeability of Green Concrete Mixed with Fly Ash and Coal Gangue. *Construction Building Mater.* 233, 117166. doi:10.1016/j.conbuildmat.2019.117166
- Zhang, J., Chen, T., and Gao, X. (2021). Incorporation of Self-Ignited Coal Gangue in Steam Cured Precast concrete. *J. Clean. Prod.* 292, 126004. doi:10.1016/j.jclepro.2021.126004
- Zhou, S. (2009). Study on the Reaction Degree of Calcined Coal Gangue Powder in Blended Cement by Selective Solution Method. *Proced. Earth Planet. Sci.* 1, 634–639. doi:10.1016/j.proeps.2009.09.100
- Zunino, F., and Lopez, M. (2016). Decoupling the Physical and Chemical Effects of Supplementary Cementitious Materials on Strength and Permeability: A Multi-Level Approach. *Cement and Concrete Composites* 65, 19–28. doi:10.1016/j.cemconcomp.2015.10.003

Conflict of Interest: XZ and WS were employed by China Western Construction Academy of Building Materials Co., Ltd. WY was employed by China West Construction Group Co., Ltd.

The remaining author declares that the research was conducted in the absence of any commercial or financial relationships that could be construed as a potential conflict of interest.

Publisher's Note: All claims expressed in this article are solely those of the authors and do not necessarily represent those of their affiliated organizations, or those of the publisher, the editors and the reviewers. Any product that may be evaluated in this article, or claim that may be made by its manufacturer, is not guaranteed or endorsed by the publisher.

Copyright © 2022 Zhu, Guo, Yang and Song. This is an open-access article distributed under the terms of the Creative Commons Attribution License (CC BY). The use, distribution or reproduction in other forums is permitted, provided the original author(s) and the copyright owner(s) are credited and that the original publication in this journal is cited, in accordance with accepted academic practice. No use, distribution or reproduction is permitted which does not comply with these terms.

Advantages of publishing in Frontiers



OPEN ACCESS

Articles are free to read for greatest visibility and readership



FAST PUBLICATION

Around 90 days from submission to decision



HIGH QUALITY PEER-REVIEW

Rigorous, collaborative, and constructive peer-review



TRANSPARENT PEER-REVIEW

Editors and reviewers acknowledged by name on published articles

Frontiers

Avenue du Tribunal-Fédéral 34
1005 Lausanne | Switzerland

Visit us: www.frontiersin.org

Contact us: frontiersin.org/about/contact



REPRODUCIBILITY OF RESEARCH

Support open data and methods to enhance research reproducibility



DIGITAL PUBLISHING

Articles designed for optimal readership across devices



FOLLOW US

@frontiersin



IMPACT METRICS

Advanced article metrics track visibility across digital media



EXTENSIVE PROMOTION

Marketing and promotion of impactful research



LOOP RESEARCH NETWORK

Our network increases your article's readership